

# Expanding the landscape of tidal disruption events

Thesis by  
Jean J. Somalwar

In Partial Fulfillment of the Requirements for the  
Degree of  
Doctor of Philosophy

The logo for the California Institute of Technology (Caltech), featuring the word "Caltech" in a bold, orange, sans-serif font.

CALIFORNIA INSTITUTE OF TECHNOLOGY  
Pasadena, California

2026  
Defended June 4, 2025

© 2026

Jean J. Somalwar

ORCID: 0000-0001-8426-5732

All rights reserved except where otherwise noted

## ACKNOWLEDGEMENTS

I would like to thank my advisor, Vikram Ravi, for his guidance, support, and helpful discussions. I would like to thank my committee members, Profs. Gregg Hallinan, Shri Kulkarni, Fiona Harrison, and Philip Hopkins, for their thoughtful advice. I would particularly like to thank Profs. Gregg Hallinan and Shri Kulkarni for their insights and scientific encouragement throughout my Ph.D. I would like to thank both past and current members of the Zwicky Transient Facility TDE team and the Caltech VLA Sky Survey groups for their guidance and help. In particular, Profs. Matthew Graham, Wenbin Lu, Raffaella Margutti, Ryan Chornock, as well as Casey Law, Steve Myers, and Erica Hammerstein. I would like to thank all the Caltech astronomy professors for fostering a fruitful academic environment, as well as the broader ZTF and VLASS teams, who were fundamental to both my work and so much other science. Likewise, thank you to those who made Keck, Palomar, and all telescope facilities possible, as well as the IT teams at Caltech and elsewhere, without whom my thesis would not have been feasible.

Thanks to all my roommates through grad school, Ivey, Sam, Yashvi, Kaustav, Shreya, Tony, Merry, and Pippin. Thanks to the present and past astronomy graduate students at Caltech, including Yuhan, Dillon, Kritti, Jess, Nik, Adolfo, and Zhuyun. Thanks to Ollie, Mickey, and Bruce, and finally, thank you to my family for their constant encouragement and support.

## ABSTRACT

Massive black holes (black hole masses  $M_{\text{BH}} \gtrsim 100 M_{\odot}$ ) are key to our understanding of galaxy evolution, reionization, and physics that is as fundamental as general relativity. Many open questions remain surrounding MBH formation, growth, and demographics. We require methods of discovering BHs, as well as probes of accretion, that expand beyond analyses of the most luminous, accreting MBHs. Tidal disruption events (TDEs) occur when a star enters an orbit around an MBH with pericentric distance small enough that tidal forces from the MBH overcome the stellar self-gravity. They produce accretion flares on human timescales, lighting up otherwise quiescent MBHs and enabling direct observations of a newly formed accretion disk. Efforts to identify TDEs in optical, X-ray, and infrared survey data have led to the first populations of such events, but selection effects may be limiting our view of the TDE landscape; for example, we may be missing the lowest mass black holes or populations with certain types of host galaxies.

In my thesis, I expand our understanding of the TDE landscape using novel TDE discovery methods. The first part of my thesis discusses eight examples of radio-selected TDEs with a range of multiwavelength properties. The first event was a long-lived, jetted TDE candidate, with evidence for ongoing energy injection into the jet despite a highly sub-Eddington accretion state, as has been observed in X-ray binary systems. The second event was an infrared, and radio bright TDE, which, despite showing no optical flare, can be modeled as a TDE analogous to optically-selected event but with significantly more dust and gas in the circumnuclear medium. I identified the final six events as radio-selected, optically-detected TDEs. I show that these events are largely analogous to the optically-selected events, despite being identified in a search with largely different selection effects.

In the second part of my thesis, I expand to optical searches for nuclear transients, and I present two events that were identified in optical TDE searches aimed at identifying events that are excluded by typical selection criteria. The first is a candidate repeating, partial TDE, where a star is grazing the tidal radius on successive orbits and a small fraction of its mass is accreted. This event shows a fast-cooling, fast-evolving optical flare, unlike previously identified TDEs. Finally, I present a candidate accretion event onto an IMBH, identified in a search for hostless TDEs in optical data. My work shows the significant potential of current and upcoming surveys to identify flaring and variable MBHs in new regimes.

## PUBLISHED CONTENT AND CONTRIBUTIONS

1. J. J. Somalwar, V. Ravi, W. Lu, *ApJ* **983**, 159, arXiv: 2310.03795 (astro-ph.HE) (Apr. 2025),

J.J.S. discovered the tidal disruption events, obtained and analyzed follow-up data, and wrote the manuscript.

2. J. J. Somalwar *et al.*, *arXiv e-prints*, arXiv:2505.11597, arXiv: 2505.11597 (astro-ph.HE) (May 2025),

J.J.S. discovered the transient, obtained and analyzed follow-up data, and wrote the manuscript.

3. J. J. Somalwar *et al.*, *ApJ* **982**, 163, arXiv: 2310.03791 (astro-ph.HE) (Apr. 2025),

J.J.S. discovered the tidal disruption events, obtained and analyzed follow-up data, and wrote the manuscript.

4. J. J. Somalwar *et al.*, *ApJ* **945**, 142, arXiv: 2207.02873 (astro-ph.HE) (Mar. 2023),

J.J.S. obtained and analyzed follow-up data on the tidal disruption event, interpreted the results, and wrote the manuscript.

5. J. J. Somalwar *et al.*, *arXiv e-prints*, arXiv:2310.03782, arXiv: 2310.03782 (astro-ph.HE) (Oct. 2023),

J.J.S. helped discover the tidal disruption events, obtained and analyzed follow-up data, and wrote the manuscript.

6. J. J. Somalwar, V. Ravi, D. Dong, M. Graham, G. Hallinan, C. Law, W. Lu, S. T. Myers, *ApJ* **929**, 184, arXiv: 2108.12431 (astro-ph.HE) (Apr. 2022),

J.J.S. discovered the tidal disruption event, obtained and analyzed follow-up data, and wrote the manuscript.

## TABLE OF CONTENTS

Acknowledgements . . . . .	iii
Abstract . . . . .	iv
Published Content and Contributions . . . . .	v
Table of Contents . . . . .	v
List of Illustrations . . . . .	viii
List of Tables . . . . .	xxvii
Chapter I: Introduction . . . . .	1
1.1 The astrophysics of black holes and open questions . . . . .	2
1.2 Tidal disruption events . . . . .	11
1.3 This thesis . . . . .	18
Chapter II: A candidate relativistic tidal disruption event at 340 Mpc . . . . .	20
2.1 Introduction . . . . .	21
2.2 Target Selection . . . . .	22
2.3 Observations and Data Reduction . . . . .	22
2.4 Analysis . . . . .	28
2.5 Discussion . . . . .	39
2.6 Conclusion . . . . .	49
Chapter III: The nascent milliquasar VT J154843.06+220812.6: tidal disruption event or extreme accretion-state change? . . . . .	53
3.1 Introduction . . . . .	54
3.2 Target Selection . . . . .	57
3.3 Observations and Data Reduction . . . . .	57
3.4 Host Galaxy Analysis . . . . .	60
3.5 Analysis of transient spectral features . . . . .	63
3.6 Analysis of transient broadband features . . . . .	72
3.7 Discussion . . . . .	83
3.8 Conclusions . . . . .	96
3.9 Appendix . . . . .	97
Chapter IV: VLASS tidal disruption events with optical flares I: the sample and a comparison to optically-selected TDEs . . . . .	101
4.1 Introduction . . . . .	101
4.2 Sample Selection . . . . .	104
4.3 Observations and Data Reduction . . . . .	106
4.4 Summary of detailed transient properties . . . . .	109
4.5 Host galaxies . . . . .	111
4.6 Optical transient broadband emission analysis . . . . .	119
4.7 Radio emission properties and mechanism . . . . .	122
4.8 Discussion . . . . .	126
4.9 Conclusions . . . . .	129

4.10 Appendix . . . . .	131
Chapter V: VLASS tidal disruption events with optical flares II: discovery of two TDEs with intermediate width Balmer emission lines and connections to the ambiguous extreme coronal line emitters . . . . .	139
5.1 Introduction . . . . .	140
5.2 Sample Selection . . . . .	142
5.3 Summary of transient properties . . . . .	143
5.4 The transient optical spectral features . . . . .	150
5.5 Discussion . . . . .	163
5.6 Conclusions . . . . .	172
Chapter VI: The first systematically identified repeating partial tidal disruption event . . . . .	175
6.1 Introduction . . . . .	176
6.2 Observation of the initial flare . . . . .	178
6.3 Observations of the rebrightening . . . . .	182
6.4 Constraints on previous flares from AT 2020vdq . . . . .	198
6.5 Discussion . . . . .	199
6.6 Conclusions . . . . .	208
6.7 Appendix . . . . .	209
Chapter VII: A luminous and hot infrared through X-ray transient at a 5 kpc offset from a dwarf galaxy . . . . .	212
7.1 Introduction . . . . .	213
7.2 Discovery . . . . .	216
7.3 Multiwavelength Observations and Data Reduction . . . . .	218
7.4 Data Analysis . . . . .	223
7.5 Results . . . . .	239
7.6 Discussion . . . . .	252
7.7 Conclusions . . . . .	260
7.8 Appendix . . . . .	262
7.9 The Compton equilibrium temperature . . . . .	267
7.10 MOSFIT . . . . .	269
Chapter VIII: Conclusions . . . . .	271
8.1 Summary . . . . .	271
8.2 Future prospects . . . . .	272
Bibliography . . . . .	276

## LIST OF ILLUSTRATIONS

<i>Number</i>	<i>Page</i>
1.1 Summary of SMBH formation models and resulting observable properties of IMBHs in the local universe, reproduced from (38). . . . .	3
1.2 The structure of an AGN, from <a href="https://fermi.gsfc.nasa.gov/science/eteu/agn/">https://fermi.gsfc.nasa.gov/science/eteu/agn/</a> , with the type of source perceived by the observer along different lines-of-sight noted. . . . .	9
1.3 The optical lightcurve of the first TDE discovered by the Zwicky Transient Facility, reproduced from (116). Each color denotes a different band. The flare has a constant, blue color and evolves on month timescales. . . . .	13
1.4 The preferred host galaxies of optically-selected TDEs, reproduced from (135). The <i>left</i> panel shows that the TDE hosts are over-abundant in the green valley (colored points) relative to a background sample (contours). The <i>right</i> panel shows that TDE hosts tend to be hosted by E+A galaxies, with $\sim 1$ Gyr old stellar populations. . . . .	15
1.5 Radio evolution of TDEs at GHz frequencies, reproduced from (149). TDEs show a range of evolution. The on-axis, jetted TDEs are the luminous events at the top of the figure. . . . .	17

- 2.1 ( *top*) From top to bottom, X-ray, optical, mid-infrared, and radio lightcurves for VT J0243. In the topmost panel, the black triangles represent three sigma upper limits from the MAXI and XMM slew surveys. The squares and circles show recent detections by Swift/XRT and XMM/EPIC, and the inset axis magnifies this data. The colored lines show the X-ray lightcurves for two of the three X-ray detected jetted TDEs, Sw J1644+57 (1) and Sw J2058+05 (2). We do not show the X-ray lightcurve for the final X-ray detected jetted TDE, Sw J1112-8283 (3), as it largely overlaps with the Sw J1644+57 lightcurve but is poorly sampled in comparison. Regardless of the binning of the MAXI observations, an X-ray flare of the same luminosity as those detected for previous jetted TDEs would have been detected in the first  $\sim 100$  days. An optical flare is detected in PanSTARRS around MJD 56000. The MIR emission is measured using forced photometry on NEOWISE images, and is variable. The MIR color appears to have reddened after the first three epochs. The radio lightcurves are extrapolated from the model fits described in Section 2.4, and the non-detection on the far left of the plot corresponds to the 1990 NVSS observation. (*bottom*) LRIS (*top*) and 2dFGRS (*bottom*) optical spectra, normalized. The red regions of each spectrum show wavelengths flagged by the respective reduction pipelines. No significant transient features are detected. No broad emission lines are significantly detected. The emission line ratios are consistent with weak Seyfert emission on a BPT diagram. . . . . 50
- 2.2 Five versions of the BPT diagram (4–6), following Figure 13 from (199). Line ratios measured from the LRIS (2dFGRS) observations of 2dFGRS TGS314Z138 are shown as black squares (red triangles). 2dFGRS TGS314Z138 is consistent with a Seyfert in most of the diagrams. . . . . 51
- 2.3 The evolution of VT J0243’s radio SED. The circles with errorbars correspond to our observations, and are colored with the observation epoch. We fit a synchrotron model to the three main observation epochs (see Section 2.4 for details), and show the best-fit model and  $1\sigma$  errors as lines and bands. . . . . 51

- 2.4 The *XMM*-Newton x-ray spectrum for 2dFGRS TGS314Z138. The observations are the black points, while the lines show model fits. The emission is most consistent with a power law model with little intrinsic hydrogen column density. . . . . 52
- 2.5 Radio light curves (lines) and typical durations/luminosities (squares) for classes of radio transients. The squares are retrieved from (218) and are measured at 1.4 GHz. The TDE lightcurves are from (150, 219, 220), and references therein, and are largely at 5 GHz. The SN lightcurves are at 5 – 8 GHz, are from (221–224). The lightcurve for VT J1548 is measured at 3 GHz (163). For comparison, the 5 GHz lightcurve of VT J0243 is shown in red, assuming the flare was launched around MJD 56000. This source is of comparable brightness to jetted TDEs, but is still rising whereas previous events began fading by  $\sim 1,000$  days post-event. It is also at a comparable luminosity to the newly radio loud AGN from (157), shown as orange circles, and the radio variable AGN from (154), which are shown as orange dot-dashed light curves. The triangles in the light curves denote upper limits. We have arbitrarily chosen the start date of these AGN flares for ease of comparison to VT J0243. . . . . 52
- 3.1 *zrg* image of SDSS J1548, the host galaxy of the radio transient VT J1548. The optical nucleus is shown as a small red circle and the radio transient position is shown as small black circle. The circle radii show approximate  $3\sigma$  statistical uncertainties. Systematic reference-frame uncertainties are not included. The radio transient is consistent with being nuclear. The blue rectangles show the slit positions for LRIS follow up and the orange rectangles shows that for ESI follow up. Image from the Legacy Survey (7). . . . . 61
- 3.2 Five variations of the BPT diagram (4–6), following Figure 13 from (199). The SDSS measurements of SDSS J1548 are shown as a black square, while the LRIS measurements are shown as a reddish cross. Where possible, we include the changing look LINERs from (199) and the ECLEs from (14) for comparison. SDSS J1548 has weak or no AGN activity. . . . . 62

- 3.3 A summary of the observations of SDSS J1548. (*top*) The optical and IR light curves for SDSS J1548. IR magnitudes are in their native Vega system, whereas optical magnitudes are in their native AB system. The IR light curve flares by  $\sim 2 - 3$  mag beginning around MJD 58100. There is no obvious optical flare, although gaps in survey coverage mean that we cannot rule one out. The optical upper limits are consistent with the tail of the best-fit blackbody to the IR emission. We overplot the range of fluxes expected in different bands (as denoted by the color of the band) from typical optical TDEs as shaded regions. We have adopted the models of ZTF optical TDE light curves from Table 6 of (128) with the appropriate distance for SDSS J1548 and extinction  $E(B-V)_{\text{nuc}} \sim 1$ . We plot the central  $\pm 1\sigma$  range of fluxes expected from these models. We shift the start date of the each band to be within the coverage of the corresponding survey but still consistent with the start of the WISE flare. (*middle*) The 3 GHz radio (black squares) and 0.2 – 10 keV X-ray light curves. Solid lines show power law fits to the radio light curve, with the launch date in each case noted in the legend. (*bottom*) The optical spectrum evolution. The late-time LRIS optical spectra show transient broad Balmer and coronal line emission. We highlight regions impacted by reduction problems in red. . . . . 64
- 3.4 Line profiles for selected lines from the ESI observations of SDSS J1548. The *top left* panel shows the  $H\alpha$  narrow component and [O III] line profiles. The faint lines show the observations and the solid lines show Gaussian fits, where we include two Gaussian components in each case to match the coronal line profiles. The *top right* and *bottom* panels show the coronal line profiles, which all clearly contain two Gaussian components separated by  $215 - 240 \text{ km s}^{-1}$ . The solid lines in between each pair of lines indicates the average of the two peak wavelengths. . . . . 70

- 3.5 Balmer line profiles from the second epoch of LRIS observations of SDSS J1548. The *left* panel shows the  $H\alpha$  and N II line profiles. The faint lines show the observations and the solid lines show Gaussian fits with uncertainties. A strong, broad  $H\alpha$  component is clearly present. The *right* panel shows the  $H\beta$  profile and fit. We overplot the broad  $H\alpha$  fit scaled down by the expected  $H\alpha/H\beta$  ratio  $\sim 3$  (8). The  $H\beta$  profile is inconsistent with including such a strong, broad component, suggesting that the broad emission must be heavily extinguished. . . . . 71
- 3.6 Late time multiwavelength SED of VT J1548. We show the most recent WISE and ZTF observations, along with the VLA SED and the unabsorbed Swift/XRT best-fit spectrum. We also include the coronal line emission and the best-fit blackbody to the WISE emission. Note that the reported blackbody parameter uncertainties are only due to errors in the NEOWISE flux measurement; differential internal extinction between the WISE W1 and W2 bands could increase the temperature by  $\sim 250$  K for the extreme case  $E(B-V) = 3$ . . . . . 72
- 3.7 The best-fit blackbody parameters for the mid-IR transient associated with VT J1548. The luminosity (*left*), temperature (*middle*), and radius (*right*) evolution are shown with  $1\sigma$  uncertainties. The reported uncertainties are due to errors in the NEOWISE flux measurement. Differential internal extinction between the WISE W1 and W2 bands could increase the temperature by  $\sim 250$  K for the extreme case  $E(B-V) = 3$ . . . . . 74
- 3.8 The observed radio SED and best fit models. The *top* panel show the VLA follow-up observations in black, the VLASS E2 observations in green, and the best fit self absorbed synchrotron and free-free absorbed models, with  $1\sigma$  error bars. In both cases, the models provide extremely poor fits. We also show an extrapolation of a power law fit to the VLASS E2 points in green. The *bottom* panel shows the non-standard synchrotron model fits. The blue band shows the best-fit inhomogeneous model. The top-most orange band shows the best-fit multi-component synchrotron model. Each component is shown as an orange band in the lower part of the panel. The non-standard models both provide substantially better fits. . . . . 76

- 3.9 The *XMM*-Newton spectrum for VT J1548 (black points). The best-fit bremsstrahlung model is shown in solid blue, the best-fit Comptonized blackbody is dashed green, and the best-fit power-law in dot-dashed orange. Residuals are shown in the bottom panel. The Comptonized blackbody provides the best-fit. . . . . 80
- 3.10 (*left*) The radio SED compared with the observed X-ray emission. The inhomogeneous (blue) and multi-component (orange) SSA models both predict an X-ray flux that is many orders of magnitude lower than the observations. We have included a cooling break, and the plausible cooling break frequencies are denoted by the red band. The cooling break would have to be at a frequency orders of magnitude higher than predicted for the X-ray synchrotron to be observable. We conclude that it is unlikely that the synchrotron tail contributes the the X-ray emission. (*right*) The fundamental plane for black hole accretion from (233), with observations of SDSS J1548 overplotted. This source is inconsistent with both the X-ray and radio emission being associated with normal accretion. . . . . 80
- 3.11 A cartoon showing the approximate geometry of SDSS J1548/VT J1548. Some event triggered a flare at the nucleus of the galaxy, which caused the formation of an accretion disk or was associated with enhanced accretion from a pre-existing accretion disk. The broad  $H\alpha$  emission originates from near the accretion disk ( $\sim 1000$  AU), and is extinguished by the dusty torus along the line of sight to the observer. Any optical emission from the transient event is also heavily extinguished. The coronal line-emitting gas, synchrotron-emitting outflow, and MIR emitting dust are all at roughly the same distance ( $\sim 0.4$  pc). The coronal line-emitting clouds are embedded in a radiation-driven wind ( $\sim 100$  km s $^{-1}$ ) off of the torus, which causes the double peaked emission. Alternatively, the clouds may be orbiting the SMBH at  $\sim 0.3$  pc to produce the double peaked lines. IR emission comes from the heated dust in the torus. The radio emitting outflow is shown in blue. . . . . 84

- 4.1 The optical spectra for the radio-selected TDEs in our sample. The observed spectra are shown in black and the best-fit stellar continuum in red (Appendix 4.10). The Balmer, He II, and [Fe X] features observed from J1008 and J2012 are associated with the transient and are discussed in (9). . . . . 111
- 4.2 *Left panel:* Stellar mass distributions for the radio-selected TDE hosts in this work (red line) as compared to the optically-selected TDE hosts from (13) (dashed black line). The radio-selected TDEs tentatively prefer lower mass galaxies. *Middle panel:* Stellar velocity dispersion distributions for the radio-selected TDE hosts in this work (red line) as compared to the optically-selected TDE hosts from (134) (dotted black line). The radio-selected TDEs tentatively prefer lower velocity dispersion galaxies. *Right panel:* SMBH mass distributions for the radio-selected TDE hosts in this work (red line) as compared to the optically-selected TDE hosts from (134) (dotted black line). . . . . 114
- 4.3 Baldwin, Phillips & Terlevich (BPT) and  $W_{\text{H}\alpha}$  versus  $[\text{NII}]/\text{H}\alpha$  (WHAM) diagrams (4–6) for the radio-selected TDEs. The radio-selected TDEs are shown as colored markers with different shapes. Optically-selected TDEs with detected emission lines as reported in Figure 5 of (135) are shown in black in the *top left* panel, for comparison. Note that VT J0813 and VT J1752 are also in the optically-selected sample. . . . . 115
- 4.4 *Left panel:* The rest-frame  $u - r$  color ( $^{0.0}u - r$ ) of the TDE host galaxies vs the host galaxy stellar mass. The radio-selected sample is shown as colored markers, and the optically-selected sample is shown as light blue squares. The region of this plot occupied by galaxies in the green valley is shown as a green shaded region (10). *Right panel:* The  $\text{H}\alpha$  equivalent width versus the Lick  $\text{H}\delta_A$  absorption for the TDE host galaxies. The different TDEs are formatted the same way as in the *left panel*, except upper limits are shown as arrows. . . . . 117
- 4.5 The optical lightcurves for our TDE candidates. Each band is shown in a different color. . . . . 120
- 4.6 The transient optical-IR SED for VT J1356 near optical peak. The observations are shown as black scatter points. The black line and band shows the best-fit blackbody and  $\pm 1\sigma$ . The best-fit parameters are shown in the figure. . . . . 120

- 4.7 *Left panel:* The peak blackbody luminosity vs the blackbody temperature at peak luminosity for the radio-selected TDEs and the optically-selected TDEs, in the same format as other figures. *Right panel:* The rise versus decay times for the optically- and radio-selected events, in the same format as the *left panel*. No obvious trends are present. . . . . 121
- 4.8 Representative radio SEDs for each VLASS TDE candidate. The observations are shown as scatter points, and the best-fit synchrotron  $\pm 1\sigma$  models shown as transparent colored bands. The color of the scatter points and fit bands correspond to the time since optical peak of each radio observation. Note that VT J1752 is an example of a source that is very poorly fit by a simple synchrotron model; we adopt this model despite the inconsistent fit for uniformity. . . . . 122
- 4.9 GHz radio lightcurves for a representative sample of radio-detected TDEs. The solid, blue lines show example jetted TDEs and the dashed, cyan lines show the non-relativistic TDE sample. The thick lines correspond to objects that were found in untargeted radio searches, whereas the thin lines correspond to objects that were selected in other bands (see *11*, and references therein). . . . . 123
- 4.10 The evolution of the equipartition energies (*top*), radii (*middle*), and magnetic fields (*bottom*) for the TDEs in our sample (colored markers) compared to those in the (*149*) sample (blue circles and limits). The objects from the (*149*) with unconstrained peak flux densities/frequencies are shown as limits. Our events tend to occupy a higher energy, lower magnetic field, large radius state than the objects in the (*149*) sample. . . . . 126
- 4.11 Summary of the properties of VT J1356. The *bottom left* panel shows a PANSTARRS image of the host galaxy before the flare. The *top left* panel shows a Legacy survey (*7*) image of the host galaxy and transient during the flare. The transient is visible as a blue nucleus in the galaxy. The *right* panels summarize the transient emission associated with the event. The *top right* panel shows the 3 GHz and 887.5 MHz radio lightcurves. Example power law fits to the 3 GHz lightcurve are overlaid in black. The *middle right* panel shows the ASASSN lightcurve of this source. The *bottom right* panel shows the WISE infrared lightcurve of this source (*12*). . . . . 130

- 5.1 Summary plot for VT J1008. Panel a shows an image of the host galaxy. Panel b shows an example optical spectrum. The observed spectrum is shown on top in black, and the best-fit stellar emission model is shown in red. The observed spectrum with the stellar continuum subtracted is shown on the bottom in black, with the transient emission lines clearly visible. Panel c shows multiwavelength light curves for VT J1008. Panel c1 shows the radio light curve in blue and the X-ray light curve in black. Upper limits are shown as triangles. Panel c2 shows the ATLAS *co* and ZTF *gr* optical lightcurve. Panel c3 shows the WISE MIR lightcurve, with no obvious flare detected. Panel d shows the radio observations of this source. The radio SED is consistent with a wide-angle, non-relativistic outflow. . . . . 144
- 5.2 Summary plot for VT J2012, in the same format as Figure 5.1. . . . . 147
- 5.3 Zoom-ins on select optical lines from the low resolution LRIS observations of VT J1008. Each row shows a different observation epoch. The observations are shown in black, and the best-fit models are shown as colored lines. The colored bands denote  $1\sigma$  uncertainties. The blue fits correspond to the first observation epochs, and the orange fits correspond to the second epochs. The features blueward of  $H\alpha$  are caused by telluric features . . . . . 151
- 5.4 Zoom-ins on select optical lines from the low resolution LRIS observations of VT J2012. Each row shows a different observation epoch. The observations are shown in black, and the best-fit models are shown as colored lines. The colored bands denote  $1\sigma$  uncertainties. The blue fits correspond to the first observation epochs, and the orange fits correspond to the second epochs. . . . . 151
- 5.5  $H\alpha$  spectral profiles from the medium resolution ESI observations. The observations of VT J1008 are in the *left* panel, and those of VT J2012 are in the *right* panel. The blue line shows the first epoch of observations and the orange line shows the second epoch. The flux for each epoch is normalized to the local continuum, which is not expected to be the same in both observations. In the *right* panel, regions particularly impacted by strong sky lines are shown in red. . . . . 154

- 5.6 Comparison of the  $H\alpha$  emission line from VT J1008 and VT J2012 to optically-selected TDEs ((3, 13), E. Hammerstein, private communication) and ECLEs (14). In the *left* panel, we show  $H\alpha$  luminosity lightcurves for VT J1008 (red crosses), VT J2012 (magenta X's), ECLEs (blue stars), and optically-selected TDEs (black circles). The  $H\alpha$  luminosities of VT J1008 and VT J2012 are much brighter at late times than those of optically-selected TDEs. They are more comparable to the ECLEs. In the *right* panel, we show the distance of the emitting region from the central SMBH,  $r$ , implied from the  $H\alpha$  width. The radio-selected TDEs are at larger radii than almost every TDE and ECLE. . . . . 159
- 5.7 An example cartoon geometry that could produce either redshifted emission without a blueshifted counterpart, or non-shifted emission. We invoke a dusty torus that is misaligned from the TDE-produced accretion disk. The blue clouds represent accretion disk winds, the black clouds represent dense gas in the torus, and the grey clouds represent less dense gas at larger distances. When the disk winds slam into the dense torus, radiative shocks are produced. The radio emission, which is not shown here, could also be produced by a subset of these disk winds that travel fast and shock against the more extended material at  $\sim 0.1$ pc. The resulting free-free emission photoionizes gas in the vicinity, including outflow gas launched from the disk, producing the observed emission lines. In the *left* panel, the blueshifted component is obscured from the observer by the dusty torus. In the *right* panel, no redshifted or blueshifted components are produced. . . . . 166
- 6.1 The full optical lightcurve showing the first and second flares from AT 2020vdq. Observations are shown as scattered points. . . . . 178
- 6.2 The optical and UV lightcurves for the first (. *top*) and second (. *bottom*) flares from AT 2020vdq. Observations are shown as scattered points. The best-fit parametric, evolving black body models, as described in Section 6.3 are shown as solid lines. . . . . 179

- 6.3 The radio evolution of AT 2020vdq. The black scatter points show a VLA observation from 500 days after the initial flare, or equivalently 470 days before the second flare. The red scatter points show a VLA observations from eight days after the rebrightening. The green upper limit shows a NOEMA observation from two weeks after the rebrightening. Both SEDs can be fit with spherical, non-relativistic synchrotron models. No young emitting component is required in the SED from shortly after the rebrightening. VLASS epoch 3 observations from  $\sim 400$  days after the rebrightening (light blue square) are consistent with our second epoch within  $1.5\sigma$  and show no evidence for a young outflow. . . . . 181
- 6.4 A comparison of the parametric, evolving, blackbody fit parameters for AT 2020vdq (black) to those of the TDEs from (134) (blue). The initial flare from AT 2020vdq is denoted with open markers while the rebrightening is denoted with filled markers. The pTDE candidate has a lightcurve that is generally consistent with the broader TDE population, although the rebrightening is luminous and fast evolving. 184
- 6.5 Non-parametric temperature, radius, and luminosity evolution for those TDEs and pTDEs that have available multi-epoch UV and optical data. Data from the rebrightening of AT 2020vdq is shown as black circles. The required multi-epoch UV data is not available for the initial flare, so only the rebrightening is shown. The candidate pTDEs AT 2018fyk and ASASSN-14ko are shown as colored stars, while normal TDEs are shown as open black circles. The data is retrieved from (329, 430, 444–448). AT 2020vdq shows a significant initial cooling and a rapid luminosity evolution. Otherwise, this pTDE candidate is generally consistent with the normal TDEs. . . . 185
- 6.6 Example non-parametric SED fits to three epochs of observations of AT 2020vdq, highlighting the observed cooling. . . . . 186
- 6.7 The total emitted optical/UV energy inferred from the pTDE candidate optical/UV flares, in the same format as Figure 6.4. The left axis shows the emitted energy while the right axis shows the equivalent stellar mass, assuming an accretion efficiency of 10%. . . . . 187

- 6.8 Summary of post-rebrightening UV/optical spectra of AT 2020vdq. Red regions are contaminated by sky background or telluric lines. In all spectra, a variety of strong broad, intermediate width, and narrow features are visible on top of a blue continuum. . . . . 188
- 6.9 Best-fit models of the broad emission lines from the post-rebrightening, AT 2020vdq optical spectra. The observed spectra are shown in black. The best-fit models are shown in blue and the best-fit continuum is shown in orange. Regions highlighted in gray are excluded from the fit due to strong sky/telluric line features that render the reduction uncertain. . . . . 190
- 6.10 Best-fit models of the broad emission lines from the post-rebrightening, AT 2020vdq optical spectra, in the same format as Figure 6.9. For visualization, we have subtracted out the normalization in this figure and show the best-fit model subcomponents are shown in red. Broad Balmer, intermediate width Balmer, and Helium lines are detected. The Balmer lines fade slightly between the two spectra while the He II line brightens and the He I line fades dramatically, suggesting that these lines all originate from different locations in the source. . . 190
- 6.11 The evolution of the intermediate Balmer lines observed from AT 2020vdq, with the best fit host stellar population subtracted.  $H\beta$  is shown in the left panel while  $H\alpha$  is shown in the right. Data is shown as lines with errorbars while Gaussian model fits are shown as lines. The Balmer lines were brightening by  $\sim 2$  years after the first flare, but faded and became slightly blueshifted by the rebrightening. A few weeks post-rebrightening, the Balmer lines began brightening while remaining blueshifted. . . . . 191
- 6.12 Fit to the  $Ly\alpha$  region and a continuum region of the *HST* spectrum, in the same format as Figure 6.10. Note that we are not showing the full spectrum, which can be seen in Figure 6.8, but just the fit regions. The spectrum is well-modelled as two broad lines ( $Ly\alpha$  and an ambiguous line near  $Si\ IV\ \lambda 1394$ ), one intermediate line ( $Ly\alpha$ ), two narrow emission lines ( $Ly\alpha$  and  $N\ V$ ), and one narrow absorption line ( $Ly\alpha$ ). The broad  $Ly\alpha$  line is redshifted by  $\sim 7600\text{ km s}^{-1}$  relative to the host rest-frame, which is in strong contrast to the optical spectral features. . . . . 193

- 6.13 . *XMM-Newton* spectrum of AT 2020vdq, observed +2 days post the peak of the rebrightening. The data is shown as black points while the best-fit  $\text{TBabs} \times \text{zshift} \times (\text{simpl} \otimes \text{diskbb})$  model is shown as a blue line. . . . . 197
- 6.14 Historical lightcurves for AT 2020vdq. The lightcurves for each survey/ band have been binned in 3 days bins. For clarity, we distinguish data from different surveys with different colors, but do not show different colors for each band (e.g., the ZTF lightcurve includes *gri* observations). We find no evidence for earlier flares in any of the data. ATLAS data rule out similar-brightness flares in the last  $\sim 10$  years. . . . . 199
- 6.15 The full optical lightcurve showing the first and second flares from AT 2021mhg. Observations are shown as scattered points. . . . . 209
- 6.16 Spectral evolution of AT 2021mhg. The grey spectrum was observed 60 days after the first flare and the black spectrum was observed 36 days after the second flare. The gap in the grey spectrum masks a region that is strongly contaminated by poorly subtracted telluric features. . . . . 210
- 7.1 Summary of emission from 24puz. The *left* panel shows the ZTF lightcurve on the *top* panel, the radio/millimeter upper limits in the *middle* panel, and the 0.3 – 10 keV Swift/XRT and XMM-Newton lightcurves in the *bottom* panel. The X-ray fluxes are computed as the unabsorbed flux assuming a  $\Gamma = 1.77$  power-law. The two Swift/XRT observations that are joined together by a line were individually non-detections, so we show the flux measured by stacking the two observations, which is significant. Dates of Keck I/LRIS spectroscopy are shown as dashed lines. The *top right* panels shows the optical spectral sequence, which no significant features detected. The solid lines are smoothed by a Gaussian with width of 5 pix. The faded lines show the unsmoothed spectra. Commonly detected transient lines are shown as dashed red lines, none are detected. The apparent line in the red, MJD 60520 spectrum near 4000 is a poorly subtracted sky line. The *bottom right* panel shows a zoom-in on the detected absorption lines, with the lines labeled in grey. . . . . 217

- 7.2 Comparison between the optical/UV emission from 24puz and LFBOTs/TDEs from (134, 490, 492, 502). In all panels, LFBOTs are shown in orange, TDEs are shown in blue, and 24puz in red. The *left* panel shows the black body luminosity evolution. LFBOTs show rapid fading with a similar late-time power-law decay as 24puz, but on overall slower timescales and typically with fainter luminosities. TDEs show a range of lightcurve shapes, which generally evolve slower than that of 24puz. Some TDEs show a rapid fade like 24puz, but these are all at least one order of magnitude fainter than 24puz. These trends are highlighted in the *right* panel, which shows the peak *g*-band luminosity versus time above half-peak luminosity. We also include fast blue optical transients (FBOTs) as faint diamonds. TDEs are divided into featureless TDEs (F-TDEs, circles), which show featureless spectra like 24puz, and those that have transient spectral features (diamonds). 24puz is intermediate to LFBOTs and TDEs, and is notably more luminous than all events at a similar timescale and is much faster evolving than F-TDEs. . . . . 218
- 7.3 Position angle of the Keck I/LRIS longslit for each observation, overlaid on the *HST*/WFC3 F105W observation. 24puz is towards the bottom right corner of the image whereas the galaxy is in the center. The MJD 60590 observation longslit was positioned to include the nearby galaxy and 24puz. . . . . 221
- 7.4 Fits to the absorption lines Fe II  $\lambda\lambda$ 2586, 2600, Mg II  $\lambda\lambda$ 2796, 2803, and Mg I  $\lambda$ 2852. The spectra are fit as linear continuum components and Gaussian lines, as described in Section 7.4. The Gaussian widths and redshifts are fixed to the same value for all lines. The best fit redshift is  $z = 0.35614 \pm 0.00009$ . The Mg II absorption is consistent with a strong-absorber ( $EW_{2796} = 0.753 \pm 0.104 \text{ \AA} > 0.3 \text{ \AA}$ ), suggesting that this absorption is more likely occurring within the nearest galaxy to 24puz (G1) or a nearby group/cluster. . . . . 224

- 7.5 Morphology of the nearest galaxy to 24puz, which we name G1. We show *HST*/WFC3 imaging of G1 in the F606W (*left*), F105W (*middle*), and F160W (*right*) bands. These images were taken 56 rest-days post-discovery. We have reprojected all images to the F606W pixel scale for ease of comparison, but this means that the F105W and F160W have been resampled to a smaller pixel scale than the original images. G1 and 24puz are labeled. The white lines show contours, which highlight the morphology of G1. In all bands, there is an extended tidal tail or other irregular component towards the top left of G1. The contour levels are shown for visualization but are not intended to represent sigma levels. . . . . 227
- 7.6 Constraints on the stellar population of G1. We assume a simple stellar population, due to a lack of constraints on the galaxy emission. The corner plot shows the distribution of possible stellar ages ( $t_{\text{age}}$ ), metallicities  $Z$ , and stellar masses  $M_*$  with grey contours overlaid. The mass-metallicity relation from (527) is shown in dark purple. We find that G1 is a dwarf galaxy with  $M_* \lesssim 10^{8.75} M_\odot$ . If it lies on the mass-metallicity relation, then the mass is  $10^{7.75} \lesssim M_*/M_\odot \lesssim 10^{8.25}$  and the age  $t_{\text{age}}/\text{Myr} \sim 100$  Myr. . . . . 229
- 7.7 Emission line fits to the optical spectrum of 24puz from MJD 60590.2, or 61.4 rest-days post-discovery. Fits to  $\text{H}\beta$ ,  $\text{H}\alpha$  and the  $[\text{O II}] \lambda\lambda 3726, 3729$  doublet are shown in the *left*, *middle*, and *right* panels respectively. The data is shown in black. The amplitudes of the Balmer lines are tied to the expected ratio for star formation and the ratio of the  $[\text{O II}]$  doublet amplitudes are likewise tied. The apparent line at the location of  $\text{H}\beta$  is a sky subtraction artifact — re-reducing the spectrum with different sky subtraction algorithms removes this feature. The  $[\text{O II}]$  line, on the other hand, is robust to sky subtraction. Blue lines show samples from our Gaussian `emcee` fits. . . . . 231

- 7.8 *Left:* Star-formation vs stellar mass of G1 relative to other galaxy populations. Constraints from the optical spectroscopy of G1 are shown in red. LFBOT hosts from (487, 489, 491, 495, 528, 529) are shown in orange and TDE hosts from (134) in blue. The core-collapse supernova host galaxy sample from (530) is shown in grey. Lines of constant specific star formation rate (sSFR) are shown in grey dashed. 24puz lies below the star forming main sequence. Its location is consistent with LFBOT host galaxies, but is at a low sSFR and stellar mass relative to core-collapse supernova hosts and a low stellar mass relative to TDE hosts. *Right:* Star-formation vs physical offset from host galaxy of 24puz relative to other populations. The format is the same as in the *left* panel, except that we have colored the points by their stellar mass but left the marker outline colors the same as in the *left* panel. For TDEs, we assume a host galaxy offset  $< 0.6''$ . The LFBOT AT2020xnd does not have a reported offset so we assume that it is  $\lesssim 1''$ , based on a by-eye approximation from images in (528). 24puz is at a larger offset than expected from its host galaxy mass, if it is associated with a star-forming region. . . . 231
- 7.9 The evolution of the best-fit blackbody parameters to the optical/UV photometry of 24puz. The blackbody luminosity, radius, and temperature are shown in the *top*, *middle*, and *bottom* panels, respectively. The luminosity rapidly rises over a few days, then slowly rises/plateaus before rapidly decaying. The radius expands at a velocity of  $0.1c$  or a powerlaw  $\sim t^{0.4}$  and then decays as  $t^{-1.3}$  after a  $\sim$ week. The temperature is largely constant and the weighted-mean value is  $\log T_{\text{bb}}/\text{K} = 4.32 \pm 0.14$ . . . . . 233
- 7.10 *Left:* the MJD 60536 (21.4 rest-days) *XMM-Newton* spectrum of 24puz (blue scatter) with the best-fit power-law model overlaid. *Right:* corner plot showing the best-fit power-law parameters. The host galaxy absorption is negligible ( $n_H \lesssim 3 \times 10^{21} \text{ cm}^{-2}$ ). The power-law index is  $\Gamma = 1.73^{+0.10}_{-0.09}$ . . . . . 235

- 7.11 Constraints on the physical parameters of any synchrotron-emitting region from our radio/millimeter observations. The *left* panel shows the ambient medium density  $n$  at outflow radius  $R$  for a spherical, non-relativistic outflow. The dashed lines mark the boundary between physical parameters excluded and allowed by a model that includes free-free absorption where the absorbing medium density is assumed to be the same as the emitting region. The grey region is allowed by all models. Each line corresponds to a different observation and the color scales with the time since discovery. The solid lines do not include free-free emission. Regions to the left of these lines are allowed while regions to the right are excluded. The LFBOT AT2018cow is shown in stars for comparison (15, 16). The *right* panel is in the same format as the *left* but is shows physical parameters appropriate for a stellar-wind like circum-transient medium. The x-axis shows velocity  $v$  and the y-axis the mass-loss rate  $\dot{M}$ . . . . . 237
- 7.12 Summary of results from the MOSFIT TDE modeling. Realizations from the MCMC samples are overlaid on select observations in the *left* panel. We only include observations in representative bands for clarity, but perform the fit with all data. The constraints on black hole ( $M_{\text{BH}}$ ) and disrupted star mass ( $M_s$ ) are shown in the *right* panel. 242

- 7.13 Constraints on a shock breakout model for the optical/UV emission from 24puz, assuming that the ejecta mass ( $M_{\text{ej}}$ ) is much larger than the circum-transient medium mass ( $M_{\text{ctm}}$ ) and the circum-transient medium has a power-law density profile with slope  $s = 1$ . The optical/UV blackbody luminosity is shown as a function of time in black in both panels. The red points show the luminosity obtained from early  $g$ -band-only detections of 24puz, for which we could not fully constrain the luminosity. We assume the temperature is the average of the over the first  $\sim 5$  days. We show the case of small  $t_{\text{bo}}$  for illustration. The shock emergence is assumed to occur on the same day in both panels, corresponding to the time at which the luminosity begins to decrease. The blue solid line shows the expected power-law evolution of the lightcurve within the shock breakout model, from equation 7.9. The resulting inferred physical parameters (circum-transient medium radius  $R_{\text{ctm}}$  and mass  $M_{\text{ctm}}$ ) are listed on the bottom, including a range of possible shock velocities inferred from the assumption that  $M_{\text{ej}} \gg M_{\text{ctm}}$  and the ejecta mass is reasonably small  $\lesssim 10^2 M_{\odot}$ . . . . 245
- 7.14 Constraints on the origin of the red excess from 24puz. The *left* panel shows the *HST* spectral energy distribution of 24puz in black and, for comparison, an epoch of observations of the red excess from AT2018cow in red. A best-fit hot blackbody is shown in brown. The dashed lines show the hot blackbody with potential red excess emission added on. These are not fits but are meant to guide the eye. In orange, a  $\lambda^{-1}$  power-law was added to represent reprocessing in a shallow medium; in green, a  $\lambda^{-3/2}$  power-law is summed to represent reprocessing in a wind-like medium. In blue, we add a dust blackbody to show that this model peaks redward of the excess. The *right* panel shows our radio upper limits as black triangles. The grey band shows an extrapolation of a power-law fit to the *HST* data to radio frequencies. Considering that the *HST* data is taken at later-times than the radio, so we would expect it to have faded with time, the power-law extrapolation over-predicts the radio limits. . . . . 248

7.15	X-ray lightcurve comparison, adapted from (529). 24puz is shown in red and LFBOTs in orange. For completeness, a population of gamma-ray bursts (GRBs) is shown in light blue, as these are common comparison points for X-ray transient emission. The jetted TDE SwJ1644 is shown in blue. 24puz is among the most X-ray luminous LFBOTs. It shows a variability and evolution timescale comparable to both LFBOTs and the jetted TDE. . . . .	255
7.16	Blackbody fits to each epoch of UV/optical imaging of 24puz, as described in Section 7.4. The fits are shown as colored bands and the data as black scatter points. . . . .	266
7.17	Spectral constraints from the MJD 60558 (37.6 rest-days) <i>XMM-Newton</i> observations, in the same format as Figure 7.10 We assume no absorption in this fit, based on the results from the higher signal-to-noise MJD 60536 observations. The photon index from the first epoch is shown in blue. The photon index has tentatively softened: the probability that the photon-index is consistent with the first epoch is $P(\Gamma \leq 1.73) = 1\%$ . . . . .	268
7.18	Corner plot showing the full MOSFIT parameter set. . . . .	270

## LIST OF TABLES

<i>Number</i>	<i>Page</i>
2.1 Radio Observations . . . . .	23
2.2 Host Galaxy, 2dFGRS TGS314Z138 . . . . .	28
2.3 Synchrotron Analysis Results . . . . .	33
3.1 Host Galaxy . . . . .	63
3.2 Optical Emission Line Strengths . . . . .	66
3.3 Best-fit Radio SED Parameters . . . . .	75
3.4 Results of the synchrotron equipartition analysis . . . . .	75
3.5 Best-fit X-ray Model Parameters . . . . .	81
3.6 Comparison to select published transients . . . . .	87
4.1 Properties of our TDE sample . . . . .	103
4.2 Summary of VLA follow-up . . . . .	107
4.3 Host Galaxy . . . . .	111
4.4 Optical light curve parameters . . . . .	119
4.5 Radio emitting region parameters for radio-selected, optically-detected TDEs . . . . .	138
5.1 Properties of our TDEs . . . . .	142
5.2 Summary of optical spectra . . . . .	150
5.3 Emission line fit parameters . . . . .	174
6.1 Basic properties of the host galaxy of AT 2020vdq. . . . .	179
6.2 Best-fit evolving blackbody parameters for the optical flares from AT 2020vdq, including results from both the parametric and non- parametric fits to flare II. We report the energy from the non-parametric fit as a lower limit. We define the equivalent mass as $M_{\text{bb}} = 10E/c^2$ , where we have assumed an accretion efficiency of 10%. . . . .	182
6.3 Broad line fit parameters, with uncertainties as reported by our least squares fit. We caution against directly interpreting the reported luminosities as our fit makes many simplified assumptions and does not fully account for the strong degeneracies between the line fluxes and the continuum level/shape. . . . .	189
6.4 Intermediate Balmer line properties and evolution . . . . .	192
6.5 UV spectral features . . . . .	194
6.6 Swift/XRT $5\sigma$ upper limits . . . . .	196
6.7 Best-fitted parameters for <i>XMM-Newton</i> spectrum. . . . .	199

6.8	Summary of observations of AT 2020vdq . . . . .	200
6.9	Summary of published repeating pTDEs . . . . .	204
7.1	Absorption line equivalent widths . . . . .	224
7.2	Emission line fluxes . . . . .	230
7.3	Intermediate width Balmer line constraints . . . . .	234
7.4	P60/SEDM Observation Summary . . . . .	262
7.5	Lowell Discovery Telescope Observations . . . . .	262
7.6	Liverpool Telescope Observations . . . . .	263
7.7	Swift/UVOT Observations . . . . .	264
7.8	Swift/XRT Observations . . . . .	264
7.9	<i>XMM-Newton</i> Observations . . . . .	265
7.10	<i>NuSTAR</i> Observations . . . . .	265
7.11	Keck I/LRIS observations . . . . .	265
7.12	<i>HST</i> /WFC3 Observation summary . . . . .	266
7.13	UVOIR blackbody modeling . . . . .	267

## *Chapter 1*

### INTRODUCTION

In 1964, a bright X-ray source, now named Cygnus X-1, was discovered in the constellation Cygnus using Geiger counters attached to an unguided rocket (17). Follow-up observations showed peculiar properties relative to all previous sources. Of particular note, Cygnus X-1 was detected out to 100 keV, was X-ray variable on timescales as short as milliseconds (18), and had correlated radio flaring (19). It was associated with a supergiant star in a binary (20), and the binary motion suggested a massive companion  $\gtrsim 3 M_{\odot}$ . Cygnus X-1 was identified as a likely black hole (BH), as no other massive object was capable of producing such luminous and variable multiwavelength emission (21). It is now confirmed to be a  $\sim 21 M_{\odot}$  BH accreting from the stellar winds of its companion (22).

A year before the discovery of Cygnus X-1, Maarten Schmidt obtained an optical spectrum of the luminous radio source 3C 273, thought to be an unusual star and called a quasi-stellar object, or quasar. He showed that it was located far beyond our Galaxy at a redshift  $z = 0.158$  (23). Other quasars were soon shown to also be extragalactic. Like Cygnus X-1, quasars were variable, with optical flaring on timescales shorter than months, as well as variability on years timescales (24). This variability, combined with the massive amounts of emitted energy and evidence for superluminal motion from radio observations, led to the association of these objects with hugely massive  $\sim 10^8 M_{\odot}$  BHs at the centers of galaxies (25–27). This also led to the first prediction of a massive, but largely quiescent, BH at the center of the Milky Way Galaxy (28). The existence of these supermassive BHs (SMBHs) was not confirmed until high resolution observations unambiguously showed that the central compact objects were too compact to be explained as anything other than a BH (by (29) for NGC 4258 and (30, 31) for the Milky Way; see (32) for a review of earlier efforts).

We now know of *populations* of BHs from stellar mass to supermassive scales, and they play a foundational role in astrophysics. The most massive black holes are critical in shaping galaxy evolution (33). The lower mass subset of these objects, the elusive intermediate mass black holes may play a critical role in reionization (34) and shaping dwarf galaxies through feedback (35). The SMBHs profoundly

affect the star formation histories and gas cycles in massive galaxies (36). In this introduction, I will begin with a review of BH astrophysics and outstanding open questions, with a focus on those topics addressed in this thesis. Then, I will discuss probes of both accreting and non-accreting BHs. I will provide a detailed theoretical and observational review of tidal disruption events, which are fundamental to my work, and conclude with a brief summary of my thesis.

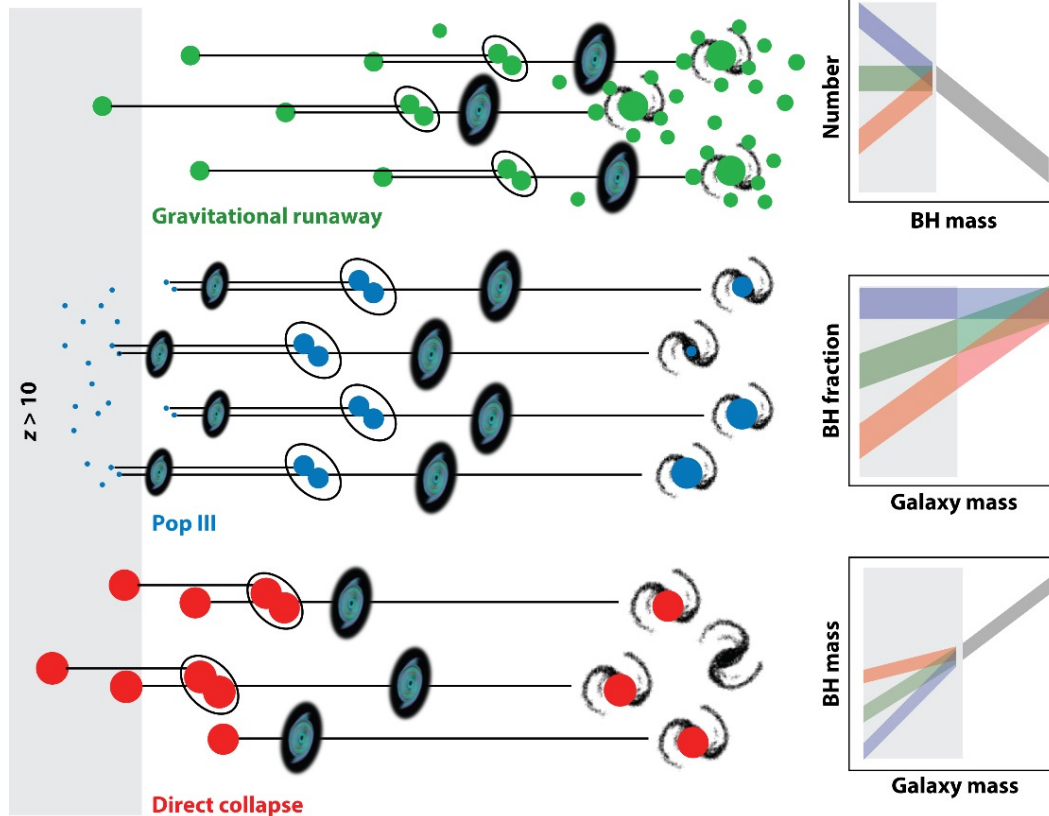
### 1.1 The astrophysics of black holes and open questions

Throughout this thesis, I will divide BHs into three classes by their masses. I will define stellar mass black holes, such as Cygnus X-1, as those with BH masses  $M_{\text{BH}} \approx 1 - 100 M_{\odot}$ . Supermassive BHs, like the BH at the center of the Milky Way (Sagittarius A\*, or Sgr A\*), have  $M_{\text{BH}} \gtrsim 10^5 M_{\odot}$ , with the most massive known SMBHs at  $M_{\text{BH}} \approx 10^{10} M_{\odot}$  (e.g. 37). The class of intermediate mass BHs (IMBHs) spans the mass range between stellar mass and supermassive BHs  $M_{\text{BH}} \approx 10^{2-5} M_{\odot}$ . IMBHs and SMBHs together are sometimes called massive BHs (MBHs): this MBH regime is the focus of my thesis. This section will review the formation, growth, and open questions surrounding BHs. I will focus on MBHs, but, as much BH theory was developed for stellar mass BHs and later applied to MBHs, I will discuss stellar mass BHs as necessary.

#### The origins of black holes and their role within astrophysics as a whole

I begin with a basic summary of each BH class. I do not describe BH growth processes in detail, as they are the focus of the next section.

1. *Stellar mass BHs* are formed in the final phases of massive star evolution. Stars with initial masses  $\sim 25 - 60 M_{\odot}$  form BHs, while those between  $\sim 8 - 25 M_{\odot}$  form neutron stars and those between  $\sim 0.08 - 8 M_{\odot}$  form white dwarfs (39). These mass boundaries are approximate. The boundary between neutron star and BH formation can be changed with, e.g., differing models of stellar mass loss (e.g. 40). Stars with initial masses above  $\sim 60 - 100 M_{\odot}$  are theorized to trigger pair-instability supernovae (41), where electron-positron pair production reduces the pressure support inside the stellar core, causing an implosion (pair-instability supernova). The most massive stars are completely destroyed, but stars with helium cores  $\sim 45 - 65 M_{\odot}$  will undergo thermonuclear burning during the contraction that counters the collapse, triggering a series of pulsations until the mass has reduced enough to enable normal stellar evolution (pulsational pair-instability supernova). This process, combined with the



AR Greene JE, et al. 2020.  
*Annu. Rev. Astron. Astrophys.* 58:257–312

Figure 1.1: Summary of SMBH formation models and resulting observable properties of IMBHs in the local universe, reproduced from (38).

boundary between neutron star and BH formation, leave stark imprints on the stellar mass black hole mass function: a lower-mass gap  $M_{\text{BH}} \approx 2.2 - 5 M_{\odot}$  and the upper-mass gap  $M_{\text{BH}} \approx 40 - 120 M_{\odot}$ , where BHs are not expected to form as the remnants of single-star evolution. Gravitational wave searches have uncovered BHs in these mass gaps, however, posing a problem for stellar evolution models. These gaps can be filled through, e.g., mergers and accretion in dense environments (42, 43). Stellar mass black holes have proven critical for our understanding of general relativity (44) and massive star evolution (45), among other subjects.

2. *Supermassive BHs* occupy the centers of nearly every massive galaxy in the local universe (46), and the masses of these SMBHs correlate strongly with their host galaxy properties, including velocity dispersions and stellar masses (47). This correlation is unexpected as SMBHs can only directly influence

objects in the innermost regions of galaxies<sup>1</sup>; for example, Sgr A\* only affects the dynamics of objects to  $\sim 0.1$  pc. Nevertheless, SMBHs significantly affect the large-scale structure and evolution of their host galaxy, largely through feedback processes tied to their accretion and growth that enable the injection of energy into their hosts on large scales through the launch of winds and jets (48). The formation of SMBHs remains an open question (38, 49, 50). The detection of SMBHs in the earliest epochs of the universe with telescopes such as the *James Webb Space Telescope* necessitates models wherein BHs with masses  $\gtrsim 10^7 M_{\odot}$  can form within  $\sim 100$ s of Myrs (e.g. 51). SMBHs are expected to grow from the intermediate mass seeds via a combination of mergers and accretion (52–56). Thus, IMBHs are a key diagnostic of SMBH formation models.

Models to form these seed BHs are split into two classes: light and heavy seed models. Light seed models propose that SMBHs began as  $\sim 100 M_{\odot}$  BHs formed as the stellar remnants of the first stars at high-redshift (Population III stars; (50, 57)). These BHs are the high redshift analogues of the stellar mass BHs described earlier, but at higher masses due to the extremely high masses but low metallicities of their progenitor stars. Some models invoke extremely high accretion rates to grow these BHs to supermassive sizes. The require accretion rates are well above the Eddington limit, which, as I will discuss in detail in the next section, is a theoretical limit on the accretion rate, above which radiation pressure will overcome the gravitational force and the accreted material will be blown away. Alternatively, if the seed BHs form in dense environments (e.g., nuclear star clusters), some of the BH growth may occur via mergers. In heavy seed models, gas clouds of  $\gtrsim 10^4 M_{\odot}$  directly collapse into SMBHs in the early universe (52, 53). These models predict distinct, observable properties for the present day IMBH populations, as seen in Figure 1.1 (38).

3. *Intermediate mass* black holes, despite being key to constraining SMBH formation are the least well understood class of BHs. Dwarf galaxies may host IMBHs, analogous to SMBHs occupying massive galaxy centers. Just as SMBHs affect their host galaxies evolution, IMBHs will influence their dwarf hosts. In the early universe, these IMBHs may contribute to reionization (34).

---

<sup>1</sup>The radius out to which a SMBH affects the dynamics of material in its host galaxy is defined as the radius of influence  $r_{\text{inf}} = GM_{\text{BH}}/\sigma^2$ , where  $G$  is the gravitational constant and  $\sigma$  is the velocity dispersion in the central regions of the galaxy.

Unlike SMBHs, IMBHs need not reside in the center of their host galaxy: dwarf galaxies may not have well-defined nuclei or gravitational potential minima (58). Moreover, within the hierarchical structure build up within the  $\Lambda$  Cold Dark Matter ( $\Lambda$ CDM) paradigm, IMBHs are predicted to exist in the outskirts of massive galaxies due to mergers (59) or they may be hosted by globular clusters (60).

### **The growth of black holes**

After the formation of a BH in any of these mass classes, growth occurs through two processes: mergers and accretion. I focus on accretion processes here, which are of most relevance to my thesis. Mergers contribute particularly to the growth of massive SMBHs at low redshift.

#### *Black hole accretion: a basic theoretical background*

BHs are well established to grow via accretion of nearby matter, as they can be extremely luminous during such events. As I will discuss, non-accreting BHs are difficult or impossible to identify observationally, while highly accreting BHs can be some of the brightest sources in the sky. Accreting MBHs in the centers of galaxies are termed active galactic nuclei (AGN). The demographics of the most luminous AGN, or quasars, were an early piece of evidence that all massive galaxies must host SMBHs (46). Accretion also enables the connection between MBHs and their host galaxies. During accretion, the BHs can launch relativistic, collimated jets and powerful winds that propagate to galaxy scales, injecting energy throughout the host (48). At stellar mass scales, the most commonly observed accreting BHs are X-ray binaries (XRBs), where the stellar mass BH is consuming a stellar companion. When XRBs launch relativistic, collimated jets, they are termed microquasars.

At the most basic level, BHs accrete from a disk of material. For many of the observed accreting black holes, friction efficiently dissipates energy from the material, but angular momentum is only slowly removed, leading to a disk-like structure. The disk assumption breaks down for the lowest and highest accretion rates, as I will touch on shortly.

The accretion state of a BH is largely encapsulated in its Eddington ratio  $\lambda_{\text{Edd}}$ , which is defined as the accretion luminosity  $L_{\text{acc}}$  in units of the theoretical maximum accretion luminosity, or the Eddington luminosity  $L_{\text{Edd}}$ :  $\lambda_{\text{Edd}} = L_{\text{acc}}/L_{\text{Edd}}$ . This is typically converted to a mass accretion rate  $\dot{M}_{\text{BH}}$  by assuming that 10% of the accreted energy is emitted as radiation, or  $L_{\text{acc}} = \eta \dot{M}_{\text{BH}} c^2$  for  $\eta = 0.1$ . The

Eddington luminosity is calculated such that the radiation pressure on a particle in the accretion disk is equal to the gravitational force from the BH, or

$$L_{\text{Edd}} = \frac{4\pi G M_{\text{BH}} m_p c}{\sigma_T} = 1.26 \times 10^{38} \left( \frac{M_{\text{BH}}}{M_{\odot}} \right) \text{erg s}^{-1}. \quad (1.1)$$

We have defined the proton mass  $m_p$ , the speed of light  $c$  and the Thomson scattering cross section  $\sigma_T = 6.65 \times 10^{-25} \text{cm}^2$ . Sgr A\*, with its mass  $M_{\text{BH}} \approx 10^6 M_{\odot}$ , has  $L_{\text{Edd}} \approx 10^{44} \text{erg s}^{-1}$ .

Most well-studied AGN are in the regime  $\lambda_{\text{Edd}} \lesssim 1$ , where the accretion disk structure is well-approximated as a thin disk, which is defined as  $h/R \ll 1$  for scale height  $h$  and disk size  $R$ . The (61) model is the most common prescription for such a disk. It models a stationary, axially symmetric disk for a cooling dominated flow. The key assumption is that the angular momentum transport is dominated by a turbulent viscosity that is proportional to the disk sound speed and height. The proportionality constant is typically assumed to be constant.

The disk spectrum can be approximated as a sum of blackbodies over the disk. The blackbody temperature is given by

$$T_{\text{eff}}(R) = \left[ \frac{3GM_{\text{BH}}\dot{M}_{\text{BH}}}{8\pi\sigma_{\text{SB}}} \left( 1 - \sqrt{\frac{R_{\text{in}}}{R}} \right) \right]^{\frac{1}{4}} R^{-3/4} \\ \approx 8.6 \times 10^7 \text{K} \left( \frac{M_{\text{BH}}}{10^6 M_{\odot}} \right)^{-\frac{1}{2}} \left( \frac{\dot{M}_{\text{BH}}}{1 M_{\odot} \text{yr}^{-1}} \right)^{\frac{1}{4}} \left( 1 - \sqrt{\frac{R_{\text{in}}}{R}} \right)^{\frac{1}{4}} \frac{R}{R_{\text{in}}}^{-3/4}, \quad (1.2)$$

where, to compute the numbers in the second equality, we have assumed that the disk inner radius  $R_{\text{in}} \approx R_g = GM_{\text{BH}}/c^2$ . The accretion rate is given by  $\dot{M}_{\text{BH}}$ , the radius within the disk  $R$ , and the Stefan-Boltzmann constant is  $\sigma_{\text{SB}}$ . The spectrum is then the sum of a series of blackbody-emitting rings with this temperature distribution.

A key assumption of the (61) model is that the disk cooling is advection dominated. For low accretion rates ( $\lambda_{\text{Edd}} \lesssim 0.01$ ), the viscous energy cannot be efficiently radiated and is instead advected towards the BH. This form of accretion is termed an advection dominated accretion flow (ADAF; (62–65)). This model can only occur if the accretion timescale is much faster than the Coulomb coupling timescale, such that the electrons are much cooler than the protons so radiation is inefficient: this timescale requirement is why ADAFs occur for low accretion rates. The disk becomes geometrically thick ( $h/R \sim 1$ ) and has a low luminosity. ADAFs are predicted to commonly launch outflows and jets, which we will discuss in more detail later. ADAFs formed a key test of general relativity, as accreting BHs can

absorb the advected energy within the event horizon, whereas neutron stars must radiate the energy from their surface.

For high accretion rates ( $\lambda_{\text{Edd}} \gtrsim 1$ ), like in the lowest accretion states, the thin disk model breaks down. The accretion disk becomes radiation pressure dominated, as is clear from the definition of the Eddington limit, but the emitting energy is limited to the Eddington luminosity (66). Like in the ADAF model, all remaining energy is carried inwards by advection and the disk is geometrically thick. As in ADAFs, slim disks are expected to launch significant outflows. These outflows, as well as patchy and non-spherical geometries, can enable super-Eddington luminosities. Many open questions remain about super-Eddington accretion, including the long-timescale stability, the accretion and radiative efficiency (i.e., what fraction of the energy is consumed, radiated, or blown away in outflows), and what super-Eddington luminosities are feasible.

### *Jets and outflows*

Early observations of accreting SMBHs detected significant radio emission from these sources, consistent with highly relativistic beams of emission shocking against surrounding gas. Ultraviolet and X-ray spectroscopy has suggested the presence of fast outflows (67–70). These jets and outflows enable the BHs to inject energy on the scale of their host galaxies, rather than only affecting their host within the radius of influence (48). I will briefly review processes by which accreting BHs launch outflows.

I first consider non-relativistic, wide-angle winds. There are three basic mechanisms that can drive a wind from an accretion disk: thermal pressure, radiation pressure, or magnetic fields (see 71, for a review). Thermally launched winds occur when X-rays from the central accretion flow heat low density gas to  $\sim 10^7$  K, which can accelerate winds up to  $\sim 2000$  km s<sup>-1</sup> (72, 73). These are thought to be responsible for narrow absorption lines observed in X-ray spectra (e.g. 74).

Radiation pressure-driven winds can occur in super-Eddington sources, where radiation pressure is dominant. For BHs with lower accretion rates, these winds must be line-driven. Such a model is borne out observationally: quasars are often observed to have ultraviolet spectra with complex emission and absorption features superimposed on a strong continuum suggestive of moderately ionized, high velocity gas illuminated by a luminous ultraviolet source (75). This mechanism is only efficient, however, if the wind is shielded from the luminous X-rays produced by the inner

disk, so that it does not become fully ionized. There has been debate over whether shielding is efficient in typical AGN with strong winds (76).

Magnetically-driven winds can be launched by the magnetocentrifugal force or magnetic pressure (71). The former occurs in the case where this a a strong poloidal component to the magnetic field and the field lines have an angle  $> 30$  deg relative to the disk rotation axis (77). In the latter case, a strong toroidal field creates magnetic pressure and launches the wind, but these winds may be transitory (78).

The (77) mechanism may also play a role in the launching of highly collimated, relativistic jets. Alternatively, the jet energy may be extracted from the rotation of the BH itself via the (79) mechanism, or the jet may be the result of a combination of these processes. High resolution imaging with the Event Horizon Telescope (EHT; (80)) is proving key to test these mechanisms. As I will discuss in the next section, there appears to be a strong connection between the accretion disk and the jet, at least in XRBs. Steady jets are only detected in certain accretion states: at the highest and lowest accretion states. Geometrically thick disks may help collimate the jet, or retain the requisite large scale magnetic flux to launch the jet. As in the case of accretion disk models, it is unclear whether the jet-disk connection is the same in XRBs and AGN. This is a topic that my thesis will briefly address.

### **Observations of BHs**

Observations of BHs have tested formation, evolution, and growth models. I will highlight results that are of particular relevance to this thesis.

*BH number density:* The number density of SMBHs in the local universe has been constrained using the luminosity function of quasars, as well as mass-estimates based on scaling relations with host galaxies, to be  $\sim 4 \times 10^5 M_{\odot} \text{cMpc}^3$  (81–84). At higher redshift, the quasar luminosity function provides a lower limit, but whether, e.g., the quasar radiative efficiency and active fraction evolve with redshift is unknown (85). Results with the *James Webb Space Telescope* are suggesting that some SMBHs may have established their masses at high-redshift (86).

*AGN duty cycle:* Comparisons of the local quasar luminosity function to the number density of BHs established via, e.g., host galaxy correlations, as well as case studies of AGN with age estimates, suggest that local AGN spend  $\sim 10^7$  yr in an active state (81, 87). The fraction of active AGN may increase with redshift for high mass SMBHs (88), although it may be lower for smaller SMBHs (89).

*Super-Eddington accretion:* The detection of massive SMBHs in the early universe

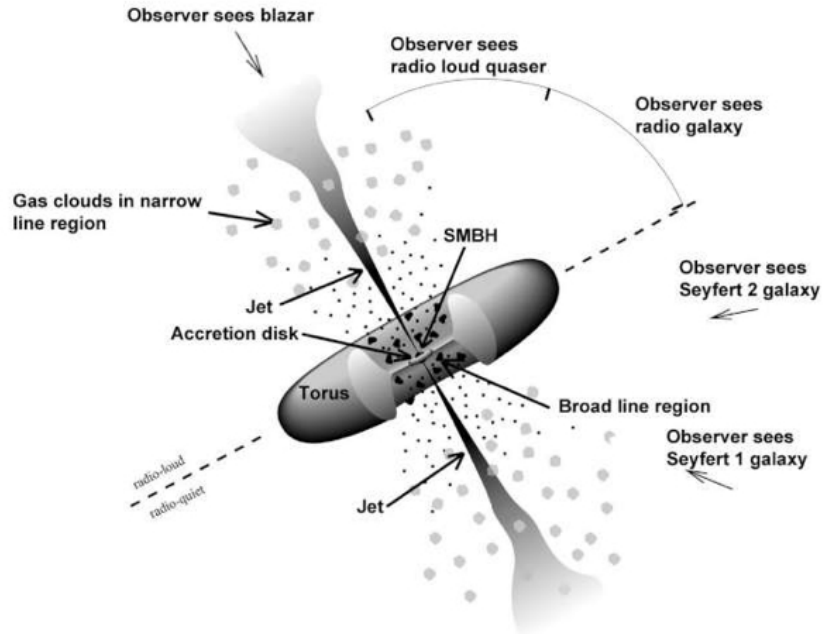


Figure 1.2: The structure of an AGN, from <https://fermi.gsfc.nasa.gov/science/eteu/agn/>, with the type of source perceived by the observer along different lines-of-sight noted.

suggests that, within light seed models for SMBH formation, very super-Eddington accretion must be sustainable (51). Observations of candidate super-Eddington quasars in the local (90) and high-redshift universe (91) suggest that such accretion is possible, but how abundant such objects are, the observable characteristics of super-Eddington events, and the stability of such accretion remain unclear (92).

*Simple disk models fail:* AGN are observed to undergo many types of behavior that are not explained within the standard model, such as luminous outbursts over long timescales (93, 94). X-ray binaries, for which many of the simple disk models were developed, show clear correlations between the disk state and jet/wind launching, where in the lowest and highest accretion states, steady jets are launched. It is unclear whether AGN have similar behavior (95). These observations may suggest that AGN disk models are insufficient. Some success has been found explaining AGN flaring as the result of stars embedded in the AGN disk (96).

*The environment around an SMBH:* AGN show a dichotomy in observable emission, where in some sources, emission associated from close to the SMBH (highly broadened lines; strong, unabsorbed X-rays) are detected. In others, this emission cannot be seen. In all AGN, narrow line emission suggestive of gas up to  $\sim 100$  pc in

size is observable. These observations are thought to be the result of a characteristic structure (Figure 1.2), where AGN have a central SMHB with an accretion disk, surrounded by clouds of high-velocity gas, potentially launched as winds from the accretion (97). Surrounding this interior structure on  $\sim$ pc-scales is a donut-like, dusty torus, and, on the largest scales, a cloud of gas forming the narrow line region (98). The origin of the broad line region and dusty torus remain open questions (99), as well as whether such gas and dust exists in non-accreting SMBH systems.

*IMBHs are hard to find:* There have been numerous efforts to search for signatures of IMBHs via accretion or dynamics (100–103), with limited success. The faintness of these sources, as well as the lack of prior on their locations, render them difficult to conclusively identify (see 38, for a review).

### **Key outstanding questions**

Many open questions about MBHs and their growth/evolution remain. In particular, I will focus on the following four points, the first two of which are directly connected to accretion physics while the final two are focused on demographics of SMBHs:

1. *How does SMBH accretion differ from stellar mass BH accretion?* XRBs show distinct accretion states that have been extensively considered within the ADAF-thin disk-slim disk framework. They show strong connections between the accretion state and jet launching properties. AGN show some evidence for similar behavior, but they do not seem to produce state transitions analogous to XRBs.
2. *What are the properties of super-Eddington accretion onto MBHs?* While some super-Eddington events are known, we still do not fully understand the detailed physics. In particular, if SMBHs can stay in highly super-Eddington states for long timescales, this will be significant for SMBH formation models.
3. *Do quiescent BHs or low accretion rate AGN have the same properties as AGN?* Our knowledge of SMBH demographics are largely based on the most highly accreting objects, but most will not be in this state. How do their demographics and environments differ from the accreting BHs? Why are only certain BHs accreting?
4. *What are the demographics of IMBHs?* Searches for IMBHs have proven challenging. How can we identify a population of bona-fide IMBHs?

Key to answering these questions is expanding our studies of MBHs beyond the most highly luminous objects. Efforts to do this include using gravitational waves (e.g. *104, 105*), gravitational lensing (e.g. *106*), direct imaging (*80, 107*), and dynamics (e.g. *108*). In my thesis, I focus on transient accretion as a probe of otherwise hidden BHs. In particular, if a star ventures close to a MBH, it will be shredded in a dramatic, electromagnetic transient. This is called a tidal disruption event (TDE).

## 1.2 Tidal disruption events

Tidal disruption events (TDEs) were originally predicted in the 1980s, when astronomers were hotly debating the existence of a black hole in the Milky Way center (*109–111*). If the Milky Way has a MBH, then, in all probability, nuclear MBHs are ubiquitous. Eventually, stars in galactic nuclei will be scattered onto plunging orbits to these MBH two-body interactions, allowing tidal forces from the MBH to violently shred the star. If such a process can efficiently convert the stellar mass to radiation, these TDEs could temporarily light up otherwise quiescent black holes. They would provide a smoking gun of the presence of MBHs, possibly in galaxies out to large distances if the emission is sufficiently luminous. Depending on the details of the radiation mechanism, they could be used to measure the mass and other properties of the MBH, as well as to study the structure (both gas and stellar) of the nuclear environment.

In this section, I provide key theoretical and observational background on TDEs, following (*111, 112*).

### Basic theory

TDEs occur when a star is on an orbit with a pericenter  $R_p$  smaller than the tidal radius  $R_T$ , given by

$$R_T \approx R_* \left( \frac{M_{\text{BH}}}{M_*} \right)^{1/3} \approx 0.5 \text{ AU} \left( \frac{R_*}{1 R_\odot} \right) \left( \frac{M_*}{1 M_\odot} \right)^{-1/3} \left( \frac{M_{\text{BH}}}{1 M_\odot} \right)^{1/3}, \quad (1.3)$$

where the stellar radius is  $R_*$ , the stellar mass is  $M_*$ , and the BH mass is  $M_{\text{BH}}$ . The tidal radius scales as  $R_T \propto M_{\text{BH}}^{1/3}$ , whereas the gravitational radius  $R_g = GM_{\text{BH}}/c^2 \propto M_{\text{BH}}$ , so there is a maximum mass where TDEs can occur. Assuming the event horizon is given by  $2R_g$ , the maximum BH mass is given by

$$M_{\text{BH, max}} = \left( \frac{c^2}{2G} \right)^{3/2} M_*^{-1/2} R_*^{3/2} \approx 10^8 M_\odot \left( \frac{M_*}{M_\odot} \right)^{-1/2} \left( \frac{R_*}{M_\odot} \right)^{3/2}. \quad (1.4)$$

Note that accounting for BH spin modifies this limit.

Upon reaching  $R_T$ , the star will be disrupted. The binding energy of the star will have a spread

$$\Delta\epsilon = \frac{GM_*}{R_*} \left( \frac{M_{\text{BH}}}{M_*} \right)^{\frac{1}{3}}, \quad (1.5)$$

such that roughly half the matter is bound to the BH ( $\Delta\epsilon < 0$ ) and half is unbound. The bound portion will, eventually, be accreted onto the BH, while the unbound will be ejected in an outflow. The bound material will return to the BH on the fallback timescale, or the orbit period of the most bound debris,

$$t_{\text{fb}} = 2\pi \frac{GM_{\text{BH}}}{(2\epsilon)^{\frac{3}{2}}} = 2\pi \left( \frac{GM_*}{2} \frac{M_*}{M_{\text{BH}} R_*^3} \right)^{-\frac{1}{2}} = 0.1 \text{ yr} \left( \frac{R_*}{R_\odot} \right)^{\frac{3}{2}} \left( \frac{M_*}{M_\odot} \right)^{-1} \left( \frac{M_{\text{BH}}}{M_\odot} \right)^{\frac{1}{2}}. \quad (1.6)$$

The fallback rate as a function of time is given by

$$\frac{dM}{dt} = \frac{dM}{d\epsilon} \frac{d\epsilon}{dt} = \frac{(2\pi GM_{\text{BH}})^{2/3}}{3} \frac{dM}{d\epsilon} t^{-\frac{5}{3}} = \frac{1}{3} \frac{M_*}{t_{\text{fb}}} \left( \frac{t}{t_{\text{fb}}} \right)^{-\frac{5}{3}}. \quad (1.7)$$

A common assumption is that  $dM/d\epsilon$  is roughly constant, so  $\dot{M} \propto t^{-5/3}$ . The stellar parameters (density structure and spin), the stellar orbit, and the BH spin will affect this result.

The peak fallback rate is thus

$$\dot{M}(t_{\text{fb}}) = \frac{M_*}{3t_{\text{fb}}} = 133 \dot{M}_{\text{Edd}} \left( \frac{\eta}{0.1} \right) \left( \frac{M_{\text{BH}}}{10^6 M_\odot} \right)^{-\frac{3}{2}} \left( \frac{M_*}{1 M_\odot} \right)^{\frac{4}{5}}. \quad (1.8)$$

If the accretion rate tracks the fallback rate, then the accretion rate is highly super-Eddington for solar-type stars and  $M_{\text{BH}} \lesssim 2 \times 10^7 M_\odot$ . For smaller BH masses, the Eddington ratio is higher: this fact makes TDEs powerful probes of the lowest mass BHs.

The accretion disk will be compact (size  $\sim R_T$ ). The temperature can be estimated by treating the disk as a spherical blackbody:  $T \approx 3.6 \times 10^6 \beta^{3/4} M_6^{-7/24} m_*^{1/3} r_*^{-7/8}$ . The emission will thus peak in the X-ray/EUV. If the disk is in a super-Eddington state, it will be puffy and able to launch significant winds, producing a cloud of debris. Alternatively, the unbound stellar debris may also form a cloud, or an outflow may be launched from shocked, bound stellar debris (113). This cloud can absorb and reprocess the hot,  $T \sim 10^6$  K emission into a  $T \sim 10^4$  K blackbody, which emits in the optical/UV.

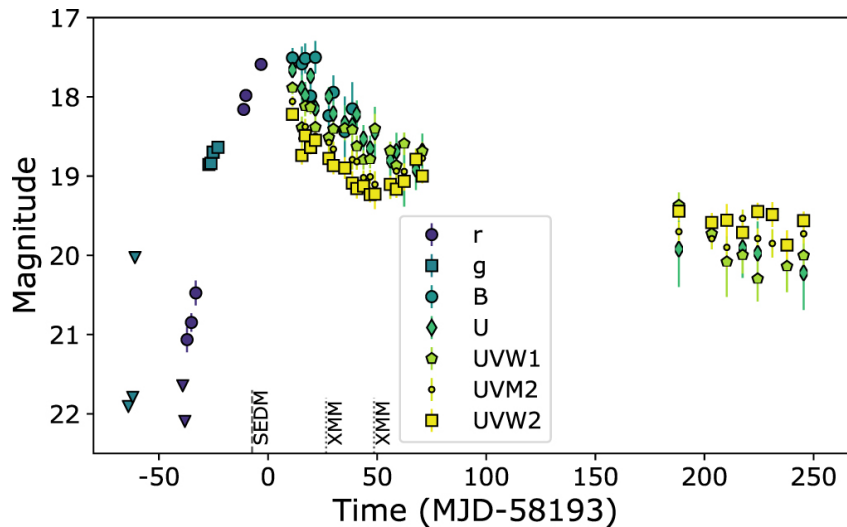


Figure 1.3: The optical lightcurve of the first TDE discovered by the Zwicky Transient Facility, reproduced from (116). Each color denotes a different band. The flare has a constant, blue color and evolves on month timescales.

The accretion rate declines as  $t^{-5/3}$  after the fallback time and will drop below the Eddington rate after

$$t_{\text{Edd}} = 1.1 \text{ yr} \beta^{-6/5} \left( \frac{M_{\text{BH}}}{10^6 M_{\odot}} \right)^{-2/5} \left( \frac{M_*}{1 M_{\odot}} \right)^{1/5} r_*^{-3/5}.$$

Lower mass black holes spend longer in a super-Eddington accretion state. If this super-Eddington accretion state is conducive to collimating jets and launching fast winds, radio emission may be produced. Alternatively, the unbound half of the stellar debris may shock against the circumnuclear medium (CNM), producing synchrotron emission, or jets/winds may be launched through other processes (e.g., analogously to X-ray binaries). The CNM itself may also emit in the IR, if it is heated by UV photons produced during the TDE (114, 115).

From these considerations, we see that TDEs may produce optical/UV/X-ray emission that peaks on  $\sim$ week timescales and decays over  $\sim$ months–years. The emission may correspond to super-Eddington accretion, and thus be quite luminous. They may also emit in the radio and infrared.

## Observations

TDE search efforts began in the 1990s with the launch of the ROentgen SATellite (ROSAT), which monitored the full sky in the soft X-rays. At that point, TDE emission was expected to be dominated by that from the hot accretion disk, so

ROSAT provided an ideal dataset to search for events (117–120). In the early 2000s, the GALEX UV and the SDSS optical photometric surveys enabled the discovery of the first optical/UV TDEs (121–123).

In 2019, the Zwicky Transient Facility (ZTF; (124–127)) turned on and revolutionized the study of TDEs with the first quasi-uniformly selected samples (128) (see Figure 1.3 for the lightcurve of the first TDE discovered by ZTF). The extended ROentgen Survey with an Imaging Telescope Array (eROSITA; (129)) instrument on the Spectrum-Roentgen-Gamma (SRG) telescope has enabled the same in the soft X-ray (130). Mid-infrared selected TDE samples have been produced using data from the Wide-field Infrared Survey Explorer (WISE) mission (131, 132), and upcoming UV missions will enable sample searches in that band. This thesis will produce radio-selected TDE samples using the Jansky Very Large Array (JVLA) and its 3 GHz, wide-field survey, the VLA Sky Survey (VLASS; (133)), as well as optically-selected events that are beyond the selection bounds of previous searches.

Throughout the rest of this section, I will discuss the results of these searches in more detail. I will begin by summarizing the methodology used to identify TDEs in each survey. I will focus on the ZTF TDE samples, as I will heavily rely on the optical results and methodology throughout this thesis.

For the ZTF TDE sample, we focus on the selection from (134), which is relatively representative of the criteria used from other ZTF TDE papers (e.g., (13)). In brief, TDEs are selected as blue transients in the nuclei of (mostly) quiescent galaxies that rise of a timescale of  $\sim$ weeks and fade over  $\sim$ months. In more detail, (134) identified TDEs as transients that are offset by  $< 0.6''$  from the nearest object and where the nearest object must have a galaxy-like (i.e. extended) morphology. The peak  $g$ - and  $r$ -band magnitudes must both be brighter than 19.5 mag, although this constraint is loosened in other ZTF TDE searches. The source must not be classified as a quasar or star in a number of catalogs and the mid-infrared lightcurve from WISE must not show variability. The flare must have a mean color  $g - r < 0.2$  mag, i.e., it must be blue. The color must evolve at  $< 0.02$  mag day $^{-1}$  post-peak. The resulting sources are then all examined visually and followed up spectroscopically to confirm their TDE classifications.

The SRG/eROSITA team identified TDEs as X-ray transients in the nuclei of a quiescent galaxy (130). They followed up all these nuclear transients with optical spectroscopy and excluded sources with AGN signatures in their spectra. The resulting sample consisted of thirteen events. Mid-infrared TDE searches identify

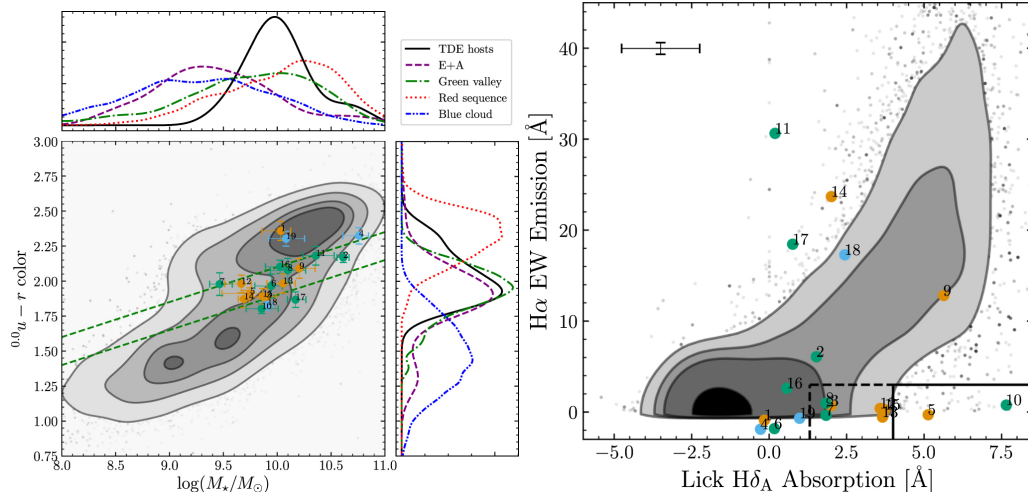


Figure 1.4: The preferred host galaxies of optically-selected TDEs, reproduced from (135). The *left* panel shows that the TDE hosts are over-abundant in the green valley (colored points) relative to a background sample (contours). The *right* panel shows that TDE hosts tend to be hosted by E+A galaxies, with  $\sim 1$  Gyr old stellar populations.

TDEs as luminous, long-lived infrared flares in the nuclei of relatively quiescent galaxies (132).

There have been a few key takeaways (for the purposes of this thesis) from these, and other, TDE searches:

*The typical host galaxies of TDEs:* Optically-selected TDEs tend to be hosted by centrally concentrated, post-starburst galaxies that are located in the green valley (135–139). They are relatively low mass ( $\lesssim 10^{10-11} M_{\odot}$ ; (140)), as is expected given that solar mass stars cannot be disrupted by large SMBHs ( $\gtrsim 10^8 M_{\odot}$ ). X-ray selected TDEs may tend to prefer higher mass galaxies than optically-selected TDEs (130). There is some suggestion that infrared-selected TDEs prefer different, although equally unusual, host galaxies to optically-selected events (132)

*Characteristics of broadband optical emission from TDEs:* Even within the bounds of the optical flare selection criteria, the broadband optical lightcurves from TDEs show a range of behavior (13, 134). The observed peak luminosity range is  $\sim 10^{42-45} \text{ erg s}^{-1}$ . Some of the lightcurves plateau near peak, while others briefly rebrighten a single time in the  $\sim 10$ s of days post-peak. Others plateau at late times and remain detectable for  $\sim 100$ s of days. There are a few TDEs with well-characterized (i.e., deep, high cadenced follow-up beyond survey data) optical/UV

emission near peak, and many of these show a temperature evolution involving an initial, rapid cooling following by a stabilization, although this behavior has not been discussed. A few TDEs show 2+ rebrightenings on  $\sim$ year timescales: these are likely repeating partial TDEs (141).

*Characteristics of X-ray emission from TDEs:* The X-ray emission from TDEs, both as observed in the X-ray selected sample and in follow-up of optically-selected TDEs, tends to be extremely soft (photon index  $\Gamma \sim 4 - 11$ ; (130, 142)). The X-ray lightcurves show a range of properties, including rapid variability, late-time turn ons, and long timescale emission in various cases (143).

*Infrared emission from optically-selected TDEs:* There have been detailed studies of the infrared lightcurves from the WISE survey for some of the optically-selected TDEs. Broadly, optically-selected TDEs tend to produce little infrared emission, corresponding to dust covering fractions  $\lesssim 1\%$  (144). Of course, this is likely in part a selection bias: dust will redden the optical flares and optical TDE selection require a blue flare color (13, 134). If there is sufficient dust, the optical flare may not be detectable at all. More and more TDEs are being discovered with extremely bright infrared flares, including a few unusual optically-selected events, although many are selected in different wavebands (e.g. (131, 132, 145)).

*Optical/UV spectral features produced by optically-selected TDEs:* Some optically-selected TDEs are observed to have broad emission lines in their optical and UV spectra, with widths  $\sim 10^4$  km s $^{-1}$  (128). From the optical spectra, these events can be classified into four categories: (1) H-TDEs, which only show Balmer lines; (2) H+He-TDEs, which show Helium lines in addition to the Balmer lines; (3) He-TDEs, which show only Helium lines and Bowen fluorescence features; and (4) featureless TDEs, which show no spectral features (13). These lines typically fade within a year of the TDE turning on. The width of the lines may suggest that they originate in a fast outflow or in gas where electron scattering plays a strong role (146, 147). At late times ( $\sim$ years), some TDEs are observed to produce coronal line emission (e.g., [Fe X]; (148)), suggesting that dense gas formed from sublimated dust is being irradiated by a strong X-ray source. Prior to the detection of these lines from definitive TDEs, strong, evolving coronal line emission was known to be produced by a subset of galaxies called the extreme coronal line emitters (ECLEs), which are now suggested to be old TDEs (14).

*Radio emission from optically-selected TDEs:* Over the last few years, there have been extensive efforts to follow-up optically-selected TDEs in the radio (150). Few

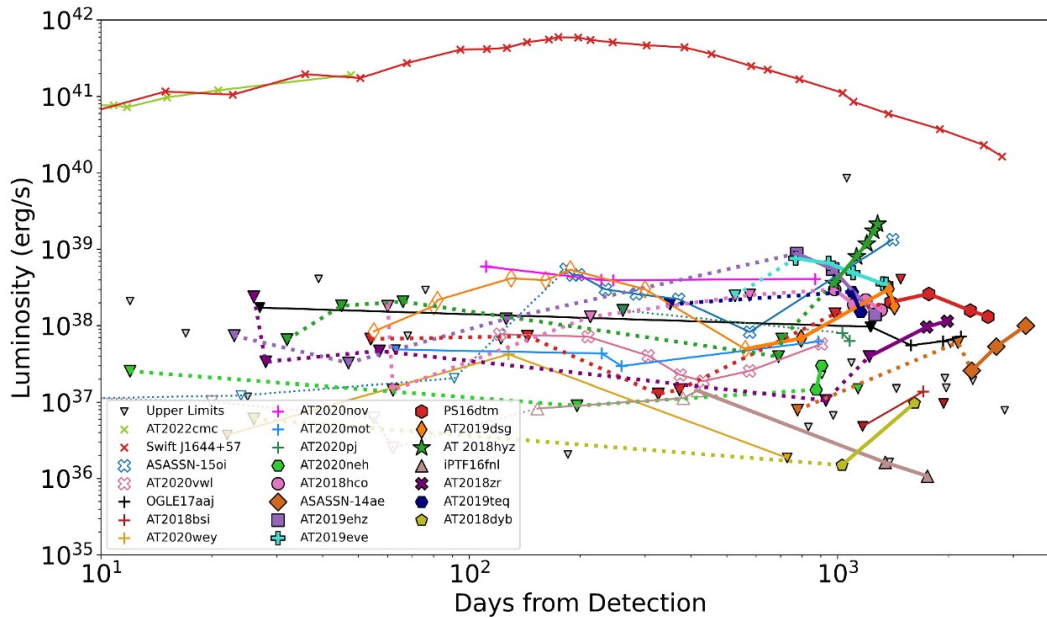


Figure 1.5: Radio evolution of TDEs at GHz frequencies, reproduced from (149). TDEs show a range of evolution. The on-axis, jetted TDEs are the luminous events at the top of the figure.

optically-selected TDEs produce radio emission at early times ( $\lesssim 100$  days post-optical peak). A growing sample of events ( $\gtrsim 30\%$  of optically-selected TDEs) have been detected to turn on at late-times (years post-optical peak) and some of those with early time emission rebrighten at late times, possibly suggesting the launch of a new outflow/jet (149, 151–153), as shown in Figure 1.5. The origin of this radio emission, and in particular whether it originates from a collimated jet or wide-angle outflow, are hotly debated.

*Correlations between multiwavelength emission from TDEs selected in different bands:* X-ray selected TDEs are infrequently observed to be optically bright, and vice versa ((130, 143), although see (142)). This could occur if the optical emission is produced when the accretion disk is obscured by stellar debris. Likewise, IR selected TDEs have distinct host galaxies and do not show optical flares, although this may be because the events are too old for good optical survey coverage (132). These results suggest that TDEs selected in different bands may be fundamentally different events.

*The TDE black hole mass function and rate:* The X-ray selected TDE rate was measured to be  $(1.1 \pm 0.5) \times 10^{-5}$  galaxy $^{-1}$  year $^{-1}$  (130). The optically-selected TDE rate was measured to be  $\approx 3.2 \times 10^{-5}$  galaxy $^{-1}$  yr $^{-1}$  (134). The IR-selected TDE rate

is comparable to that of optically-selected events. Of course, these measurements may be underestimated if many TDEs are being missed by current selections. The optically-selected TDE blackhole mass function was found to be consistent with a flat local BH mass function, and was consistent at the high mass end with predictions of direct capture rather than disruption for large SMBHs (134).

### 1.3 This thesis

Despite these monumental advances in our understanding of TDEs, many open questions remain, which directly connect to the open questions around BH and AGN noted above. Of most relevance to this work,

1. *What TDEs are we missing?* The current TDE samples are biased towards a certain subset of events (e.g., optically-selected TDEs must be blue). It is possible that many TDEs are being missed by these selections, affecting both rate calculations and the general landscape of TDE emission. The host galaxy preference of optically-selected TDEs has been suggested to arise from these selection effects.
2. *Where are the IMBH TDEs?* Connecting to the previous issue, few, if any, bona-fide TDEs with masses  $M_{\text{BH}} \lesssim 10^5 M_{\odot}$  are known, but they are predicted to exist. Are we missing these because of selection effects, such as the host galaxy requirements? Or are they not optically bright?
3. *What produces the observed radio emission?* The observed radio emission from TDEs spans a diverse range of luminosities and behaviors. Some proportion of these are likely produced by jets, while some may be disk outflows or outflowing stellar debris. It is unknown how this connects to the accretion disk state, as with AGN, but, because of the younger age of the system, TDEs may pose a simpler test case. We require an unbiased census of radio emission.

These are the questions that my thesis aims to address. In the rest of this work, I present attempts to identify and characterize TDEs at novel wavelengths and with new selection criteria, with the aim of identifying new populations of TDEs or showing that the current events are representative. In Chapters 2–5 of my thesis, I will use radio survey data to produce a sample of radio-selected TDEs, which I will compare to optical populations and use to constrain TDE outflow launching and host galaxy properties. In Chapters 6–7, I will discuss results from efforts to reduce

and modify the selection effects in optical TDE searches. Finally, in Chapter 8, I will conclude and highlight future directions for studies of MBHs.

*Chapter 2*

## A CANDIDATE RELATIVISTIC TIDAL DISRUPTION EVENT AT 340 MPC

Somalwar, J. J. et al. (Mar. 2023). In: ApJ 945, 142. doi: 10.3847/1538-4357/acbafc

Jean J. Somalwar<sup>1</sup>, Vikram Ravi<sup>1</sup>, Dillon Z. Dong<sup>1</sup>, Yuyang Chen<sup>2,3</sup>, Shari Breen<sup>4</sup>, Poonam Chandra<sup>5</sup>, Tracy Clarke<sup>6</sup>, Kishalay De<sup>7</sup>, B. M. Gaensler<sup>3,2</sup>, Gregg Hallinan<sup>1</sup>, Sibasish Laha<sup>8,9,10</sup>, Casey Law<sup>1</sup>, Steven T. Myers<sup>11</sup>, Tyler Parsotan<sup>8,9,10</sup>, Wendy Peters<sup>6</sup>, and Emil Polisensky<sup>6</sup>

<sup>1</sup>Cahill Center for Astronomy and Astrophysics, MC 249-17 California Institute of Technology, Pasadena CA 91125, USA.

<sup>2</sup>David A. Dunlap Department of Astronomy and Astrophysics, University of Toronto, 50 St. George Street, Toronto M5S 3H4, Canada

<sup>3</sup>Dunlap Institute for Astronomy and Astrophysics, University of Toronto, 50 St. George Street, Toronto M5S 3H4, Canada

<sup>4</sup>SKA Observatory, Jodrell Bank, Lower Withington, Macclesfield, SK11 9FT, UK

<sup>5</sup>National Radio Astronomy Observatory, 520 Edgemont Road, Charlottesville VA 22903, USA

<sup>6</sup>Naval Research Laboratory, 4555 Overlook Ave SW, Washington, DC 20375, USA.

<sup>7</sup>MIT-Kavli Institute for Astrophysics and Space Research, 77 Massachusetts Ave., Cambridge, MA 02139, USA

<sup>8</sup>Center for Space Science and Technology, University of Maryland Baltimore County, 1000 Hilltop Circle, Baltimore, MD 21250, USA.

<sup>9</sup>Astrophysics Science Division, NASA Goddard Space Flight Center, Greenbelt, MD 20771, USA.

<sup>10</sup>Center for Research and Exploration in Space Science and Technology, NASA/GSFC, Greenbelt, Maryland 20771, USA

<sup>11</sup>National Radio Astronomy Observatory, P.O. Box O, Socorro, NM 87801, USA

### **Abstract**

We present observations of an extreme radio flare, VT J024345.70-284040.08, hereafter VT J0243, from the nucleus of a galaxy with evidence for historic Seyfert activity at redshift  $z = 0.074$ . Between NRAO VLA Sky Survey observations in 1993 to VLA Sky Survey observations in 2018, VT J0243 rose from a  $\sim$ GHz radio luminosity of  $\nu L_\nu \lesssim 10^{38}$  erg s<sup>-1</sup> to  $\nu L_\nu \sim 10^{40}$  erg s<sup>-1</sup>, and still continues to brighten. The radio spectral energy distribution (SED) evolution is consistent with a nascent jet that has slowed over  $\sim 3,000$  days with an average  $0.1 < \langle \beta \rangle < 0.6$ . The jet is

energetic ( $\sim 10^{51-52}$  erg), and had a radius  $\sim 0.7$  pc in Dec. 2021. X-ray observations suggest a persistent or evolving corona, possibly associated with an accretion disk, and IR and optical observations constrain any high-energy counterpart to be sub-Eddington. VT J0243 may be an example of a young, off-axis radio jet from a slowly evolving tidal disruption event. Other more mysterious triggers for the accretion enhancement and jet launching are possible. In either case, VT J0243 is a unique example of a nascent jet, highlighting the unknown connection between supermassive black holes, the properties of their accretion flows, and jet launching.

## 2.1 Introduction

In galactic nuclei, accretion-associated phenomena produce extreme radio variability on timescales of months–years and with flare luminosities covering the full range up to  $\gtrsim 10^{32}$  erg s $^{-1}$  Hz $^{-1}$ . These flares are often associated with tidal disruption events (TDEs; (150)), young radio jets from active galactic nuclei (AGN; (154–157)), or outflows launched from accretion disks (e.g. 158).

The physical mechanisms causing many of these radio flares in galactic nuclei have yet to be understood. For stellar mass black holes, it is well established that there is a strong connection between accretion and the launching of radio-emitting outflows and jets (see 159, for a review). Jet and outflow launching from supermassive black holes (SMBHs) is an unsolved problem, whether we consider those black holes associated with AGN that have been accreting for long timescales or the newly active black holes resulting from stellar disruptions. The conditions under which radio jets launch, the mechanisms through which they emit across the electromagnetic spectrum, and their duty cycle remain open questions (e.g. 160).

Our understanding of accretion-associated radio transients is evolving significantly with the advent of high-resolution, wide-field radio surveys, such as the Very Large Array Sky Survey (VLASS; (133)). In this paper, we present an extraordinarily luminous radio transient discovered with VLASS, VT J024345.70-284040.08, hereafter VT J0243. VT J0243 is located in the nucleus of a nearby galaxy, 2dFGRS TGS314Z138 ( $z = 0.0742$ , Section 2.4). We identified VT J0243 as a radio transient between the NRAO VLA Sky Survey (NVSS; (161)) and VLASS. VT J0243 has risen to  $\sim 10^{40}$  erg s $^{-1}$  over  $\sim 5$  years, and continues to brighten. As we will show, VT J0243 is likely a nascent radio jet, yet no other event observed to date has shown its multiwavelength signatures, including a radio luminosity that continues to rise more than 1,000 days after the jet turned on. In Section 2.2, we

describe our selection criteria that led to the discovery of VT J0243. In Section 2.3, we describe our multiwavelength archival searches and follow-up observations. In Section 2.4, we present our analysis of the observations, and in Section 2.5, we discuss the interpretation of VT J0243.

We adopt the (162) cosmology with  $H_0 = 67.7 \text{ km s}^{-1} \text{ Mpc}^{-1}$ .

## 2.2 Target Selection

VT J0243 was detected as part of our transient search using the 1.4 GHz NRAO VLA Sky Survey in the 1990s (161) and the 3 GHz VLA Sky Survey (133), observing from 2017 to today. These surveys provide a unique opportunity to identify slowly evolving radio transients. NVSS has an rms noise 0.45 mJy/beam and a resolution of 45'' FWHM, and VLASS has an rms noise 0.14 mJy/beam and a resolution 1.5'' FWHM. Dong et al., in prep., generated a transient catalog by identifying sources that were detected by pyBDSF at a  $> 7\sigma$  level in VLASS but were not detected ( $< 3\sigma$ ) in NVSS. We refer the reader to that work and Appendix A of (163) for a detailed description of the pipeline used.

VT J0243 was also selected as an evolving source in an independent search (Chen et al., in prep.) that identified young radio transients through VLASS and the VLITE Commensal Sky Survey (VCSS; 164). VCSS is a survey conducted simultaneously with VLASS by VLITE, a commensal instrument on the VLA (165, 166). VCSS covers the same regions of the sky as VLASS and observes at  $\nu \sim 340 \text{ MHz}$  with an angular resolution of  $\theta \sim 20''$  and a median image rms of 3 mJy/beam. Additionally, VT J0243 was identified to be young because of its inverted spectrum between 340 MHz – 3 GHz, suggesting optically thick emission at low frequencies.

Because of the extreme radio luminosity of this source given its history of inactivity and its coincidence with the nucleus of a low-mass galaxy, we initiated an extensive, multi-wavelength follow-up campaign.

## 2.3 Observations and Data Reduction

In this section, we describe our multi-wavelength follow-up of and archival searches for VT J0243 and its host, 2dFGRS TGS314Z138.

### Radio observations

The available archival radio observations and our radio follow-up are summarized in Table 2.1. After a nondetection by NVSS on MJD 49520, VT J0243 was first detected

Table 2.1: Radio Observations

Instrument/Survey	Date	MJD	Frequency [GHz]	Flux Density [mJy]
NVSS <sup>(1)</sup>	Sept. 20 1993	49250	1.4	< 1.3 ( $3\sigma$ )
TGSS <sup>(2)</sup>	Dec. 27 2010	55557	0.15	< 15 ( $3\sigma$ )
VCSS <sup>(3)</sup> Epoch 1	Feb. 17, 2018	58166	0.340	$23 \pm 7$
VLASS <sup>(4)</sup> Epoch 1	Feb. 17, 2018	58166	2.157	$39.14 \pm 0.31$
VLASS Epoch 1	Feb. 17, 2018	58166	2.578	$40.21 \pm 0.26$
VLASS Epoch 1	Feb. 17, 2018	58166	3.048	$41.54 \pm 0.30$
VLASS Epoch 1	Feb. 17, 2018	58166	3.865	$41.39 \pm 0.34$
RACS <sup>(5)</sup>	Apr. 28, 2019	58601	0.8875	$45.81 \pm 0.64$
VCSS Epoch 2	Nov. 1, 2020	59154	0.340	$22 \pm 7$
VLASS Epoch 2	Nov. 1, 2020	59154	2.157	$54.33 \pm 0.48$
VLASS Epoch 2	Nov. 1, 2020	59154	2.579	$53.85 \pm 0.34$
VLASS Epoch 2	Nov. 1, 2020	59154	3.048	$52.84 \pm 0.29$
VLASS Epoch 2	Nov. 1, 2020	59154	3.685	$52.29 \pm 0.34$
ATCA Epoch 1 (PC: CX486)	Jun. 27, 2021	59392	1.877	$68.82 \pm 11.51$
ATCA Epoch 1 (PC: CX486)	Jun. 27, 2021	59392	2.636	$71.26 \pm 12.69$
ATCA Epoch 1 (PC: CX486)	Jun. 27, 2021	59392	4.79	$59.23 \pm 6.59$
ATCA Epoch 1 (PC: CX486)	Jun. 27, 2021	59392	5.779	$55.92 \pm 6.24$
ATCA Epoch 1 (PC: CX486)	Jun. 27, 2021	59392	6.732	$52.48 \pm 5.34$
ATCA Epoch 1 (PC: CX486)	Jun. 27, 2021	59392	7.734	$49.27 \pm 5.22$
ATCA Epoch 1 (PC: CX486)	Jun. 27, 2021	59392	8.706	$46.49 \pm 4.9$
ATCA Epoch 1 (PC: CX486)	Jun. 27, 2021	59392	9.677	$45.08 \pm 4.98$
ATCA Epoch 1 (PC: CX486)	Jun. 27, 2021	59392	10.68	$43.61 \pm 5.56$
ATCA Epoch 2 (PC: CX486)	Aug. 13, 2021	59439	5.25	$57.47 \pm 0.7$
ATCA Epoch 2 (PC: CX486)	Aug. 13, 2021	59439	8.75	$48.74 \pm 0.52$
ATCA Epoch 2 (PC: CX486)	Aug. 13, 2021	59439	18.0	$32.0 \pm 0.66$
ATCA Epoch 2 (PC: CX486)	Aug. 13, 2021	59439	34.0	$21.4 \pm 0.71$
ATCA Epoch 2 (PC: CX486)	Aug. 13, 2021	59439	40.0	$19.82 \pm 0.69$
GMRT (PID: ddtC203)	Aug. 27, 2021	59454	0.402	$32.39 \pm 0.24$
GMRT (PID: ddtC203)	Aug. 29, 2021	59454	0.648	$52.44 \pm 0.26$
GMRT (PID: ddtC203)	Aug. 28, 2021	59454	1.264	$60.88 \pm 0.41$

**Note.** Archival and follow-up radio observations of VT J0243. References: <sup>(1)</sup>(161), <sup>(2)</sup>(167), <sup>(3)</sup>(164), <sup>(4)</sup>(133), <sup>(5)</sup>(168).

on MJD 58166 in the first epoch of the VLASS with a luminosity  $\nu L_\nu(3 \text{ GHz}) \sim 10^{40}$  erg s<sup>-1</sup>. NVSS and VLASS are described at the beginning of Section 2.2. At the same time as the VLASS first epoch observations, VCSS detected the source (see Section 2.2 for details of VCSS). The source was then detected by the Australian SKA Pathfinder (ASKAP) telescope as part of the Rapid ASKAP Continuum Survey (RACS) at 0.9 GHz (*168*). RACS is observing the whole sky visible to ASKAP in the 700–1800 MHz band with 15'' resolution and a sensitivity of  $\sim 0.25$  mJy/beam. The final surveys to detect VT J0243 were the second epochs of VLASS and VCSS. Follow-up observations for this source were obtained using the Australia Telescope Compact Array (ATCA), the upgraded Giant Metrewave Radio Telescope (uGMRT), and the Very Long Baseline Array (VLBA).

Two epochs of ATCA observations were obtained on MJDs 59392 and 59439 with the six 22 m dishes arranged in the extended 6B configuration, providing baselines spanning 214–5969 m.<sup>1</sup> The Compact Array Broadband Backend (CABB; *169*) was used in the CFB-1M mode to simultaneously record full-polarization visibilities in two 2048 MHz bands each split into 2048 1 MHz channels. In the first epoch, by cycling between three different non-standard frequency setups data were obtained in 2048 MHz bands centered on 2.1 GHz, 5.25 GHz, 7 GHz, 8.75 GHz, and 10.25 GHz. Observations in the first epoch totaled two hours. Scans of PKS 1934–638 in each frequency setup were used to set the flux-density scale, and calibrate the complex time-independent bandpasses. Regular observations of the unresolved source PKS 0237–233 were used to calibrate the time-variable complex gains. In the second epoch, data were obtained at 5.25 GHz, 8.75 GHz, 18 GHz, 24 GHz, 34 GHz, and 40 GHz in 2048 MHz bands to further constrain time evolution and spectral shape at high frequencies. For the cm bands, scans of PKS 1934-638 and PKS 0237-233 were again used to calibrate the bandpass, flux density scale, and time-variable gains. For the mm bands, scans of PKS 1921-293 were used instead of PKS 1934-638 for the bandpass and flux calibration.

The data were reduced, edited, calibrated and imaged using standard techniques implemented in the MIRIAD package (*170*). Multi-frequency synthesis images were made in multiple sub-bands, centered on frequencies listed in Table 2.1. VT J0243 was detected in all images; single rounds of phase-only self calibration were applied in each band to improve image quality. Flux densities and their uncertainties were estimated using the MIRIAD task `imfit`.

<sup>1</sup>[https://www.narrabri.atnf.csiro.au/observing/users\\_guide/html/chunked/aph.html](https://www.narrabri.atnf.csiro.au/observing/users_guide/html/chunked/aph.html)

The event VT J0243 was observed with the upgraded Giant Metrewave Radio Telescope (uGMRT) under Director’s Discretionary Time (DDT) proposal DDT C203 on 2021 Aug 27, 28 and 29 in bands 3 (250—500 MHz), 5 (1000– 1450 MHz) and 4 (550—900 MHz), respectively, of the uGMRT. The observations were two hours in duration including overheads using a bandwidth of 400 MHz in bands 4 and 5, whereas the duration was three hours in band 3. The VLA calibrator 3C 147 was used as a flux and a bandpass calibrator and J0240-231 was used as a phase calibrator. We use the Common Astronomy Software Applications (CASA; (171)) for data analysis. The data were analyzed in three major steps, i.e. flagging, calibration and imaging using the procedure laid out in (172). A total of six rounds of phase self-calibrations and two rounds of amplitude & phase self-calibration were performed. A source was clearly detected at the VLASS position. The source flux densities at bands 5, 4, and 3 are mentioned in Table 2.1.

VLBA observations of VT J0243 were conducted on MJD 59569, with 512 MHz of bandwidth centered on 8.368 GHz, and the data were processed using the DiFX correlator (173). All standard VLBA stations were used except for North Liberty. Data were recorded at a rate of 4.096 Gbps at all sites besides North Liberty in four 128 MHz sub-bands, using the Digital Downconverter (DDC) mode of the Roach Digital Backends. Given the high expected flux density of the source, we planned to self-calibrate the observations. The 45 min observation included two 2-min scans of the fringe finder J0555+3948, and two 1-min scans of the check source J0236-2953, and a total of 31.5-min on VT J0243. Calibration and imaging of the observations was carried out using CASA, following procedures outlined in VLBA Memo 38.<sup>2</sup> Following data editing, we performed a global fringe-fit, which was successful for seven antennas (data from Pie Town and St. Croix were substantially lower in sensitivity). We then performed two rounds of phase-only self-calibration on VT J0243, and one round of amplitude+phase self-calibration. This yielded phase variations under  $\pm 5$  deg. The PSF was  $3.5 \times 0.6$  mas at a PA of  $-15^\circ$ . Inspection of visibility amplitudes on VT J0243 revealed a marginally resolved source. We fit the data with an elliptical Gaussian model using the CASA task `uvmodelfit`, and found a flux density of 37 mJy (with  $\sim 10\%$  uncertainty), a major axis of  $1.1 \pm 0.1$  mas, and a minor axis of  $0.5 \pm 0.1$  mas, at a position angle of  $-23$  deg. This corresponds to an outflow radius of  $R = 0.71 \pm 0.02$  pc.

<sup>2</sup>[https://library.nrao.edu/public/memos/vlba/sci/VLBAS\\_38.pdf](https://library.nrao.edu/public/memos/vlba/sci/VLBAS_38.pdf)

### Optical photometry

From the radio observations of VT J0243, we can naively constrain the radio-turn-on time range to 1990 – 2018. The Catalina Realtime Transient Survey (CRTS; (174)) observed the location of VT J0243 between  $\sim$ 2005 and 2013 (MJD 53554 – 56302), the Pan-STARRS  $3\pi$  survey (175) over  $\sim$ 2010–2013 (MJD 55433 – 56970), and the Asteroid Terrestrial-impact Last Alert System (ATLAS; (176)) between  $\sim$ 2015 – 2021 (MJD 57303 – 59097). We retrieve the CRTS photometry for this source from the default `photcat` catalog (174). This photometry is performed on absolute (i.e., not difference) images using `SExtractor` to measure aperture magnitudes. Also note that CRTS does not use a filter, so the absolute calibration of the photometry is uncertain. We retrieved archival optical images of the source from the PanSTARRS1 survey (175). The reduced images were processed through a custom image subtraction pipeline (described in (177)) to remove the host galaxy light using the first epoch of PS1 observations as a template. Point-spread function photometry was performed on the resulting difference images to derive the optical light curve shown in Figure 2.1. We retrieve ATLAS photometry at the position of 2dFGRS TGS314Z138 from their forced photometry server<sup>3</sup> using default settings. Finally, we generated a mid-infrared lightcurve for VT J0243 by performing PSF photometry on single-epoch difference images from the UNWISE reprocessing of observations from the WISE and NEOWISE surveys (12, 178–180). The resulting lightcurves are summarized in Figure 2.1.

### Optical spectroscopy

An optical spectrum of VT J0243 was obtained before 2002 (MJD < 52375) as part of the 2dF Galaxy Redshift Survey (2dFGRS; (181)). The spectrum was taken using a 2.0'' arcsec fiber with the 2dF instrument on the Anglo-Australian Telescope telescope. The wavelength range was 3627 – 8037 Å (observed frame) and the resolution  $R = 648$ . We retrieved the non-flux calibrated spectrum from the NASA/IPAC Extragalactic Database (NED). We observed VT J0243 on the night of Oct. 6 2021 (MJD 59493) using the Low Resolution Image Spectrometer (LRIS; (182)) on the Keck I telescope. We used the 1.0'' slit centered on the galactic nucleus using a parallactic angle ( $-0.035^\circ$ ). We used the 400/3400 grism, the 400/8500 grating with central wavelength 7830, and the 560 dichroic. We observed this source for 20 min. The resulting wavelength range was  $\sim$ 1300–10000 Å and the resolution  $R \sim 700$ . Comparing these spectra, there are no obvious transient features

<sup>3</sup><https://fallingstar-data.com/forcedphot/>

(Figure 2.1). Weak AGN-like emission lines are visible, but no broad emission lines are detected. The spectra are all fully consistent with being host-dominated.

### X-ray/UV observations

VT J0243 was observed in the X-ray band as part of the ROSAT survey on Jan. 6, 1990 (MJD 47897). There is no detection reported in the Second ROSAT All-Sky Survey Point Source Catalog (183, 184). We retrieved the ROSAT image at the location of VT J02438 from the HEASARC archive<sup>4</sup>, and used `ximage` to find a  $3\sigma$  upper limit of the 0.3–10 keV, unabsorbed soft X-ray flux,  $f_X \lesssim 2 \times 10^{-13}$  erg cm<sup>-2</sup> s<sup>-1</sup>, assuming a power law spectrum with  $\Gamma = 3$  and the Milky Way  $N_{H,MW} = 1.51 \times 10^{20}$  cm<sup>-2</sup> (185). VT J0243 was subsequently observed by the *XMM*-Newton Slew Survey on Jul. 30, 2008 (MJD 54677), Dec. 30, 2009 (MJD 55195), Jul. 12, 2012 (MJD 56120), Jan. 26, 2021 (MJD 59240), and Jun. 26, 2021 (MJD 59391). No detection was reported on any of these dates, so we adopt an upper limit corresponding to the flux limit reported by the survey  $f(0.2\text{--}12 \text{ keV}) = 1.3 \times 10^{-12}$  erg s<sup>-1</sup> cm<sup>-2</sup> ( $L \sim 1.67 \times 10^{43}$  erg s<sup>-1</sup>). Finally, VT J0243 was observed by the Monitor of All-sky X-ray Image (MAXI; (186)). We retrieved 2–30 keV photometry for this transient using the on-demand photometry survey provided by the MAXI collaboration<sup>5</sup> for the MJD range 55058.0–58000.0. No significant detection was reported, and the typical upper limit was  $f_X(0.3\text{--}10 \text{ keV}) \lesssim 7.7 \times 10^{-11}$  erg s<sup>-1</sup> cm<sup>-2</sup>. There was also no significant detection by the Swift Burst Area Telescope (BAT) in the transient monitor light curve produced for this source during the MJD range 55798–56961 (187).

We observed VT J0243 using the X-ray Telescope (XRT) on The Neil Gehrels Swift Observatory (Swift XRT; (188)) on MJD 59379 and 59484 for 3 and 5 ks exposures, respectively. A source was detected in both exposures, with 0.3 – 10 keV fluxes of  $0.67 \pm 0.35 \times 10^{-13}$  erg cm<sup>-2</sup> s<sup>-1</sup> and  $1.28 \pm 0.37 \times 10^{-13}$  erg cm<sup>-2</sup> s<sup>-1</sup>, respectively, assuming power-law spectra with  $\Gamma = 3$ . We then obtained a soft X-ray spectrum for VT J0243 on MJD 59391 using the *XMM*-Newton observatory EPIC camera using the thin filters in full frame mode with a 30 ks exposure time. We used the standard analysis pipeline to process the data and extract an X-ray spectrum.

Swift/UVOT observed VT J0243 simultaneously with the Swift/XRT observations in the UVW1 band. We reduced the observations using the standard HEASOFT pipeline and measured the source magnitude using the `uvotsource` tool with a 5''

<sup>4</sup><https://heasarc.gsfc.nasa.gov/docs/archive.html>

<sup>5</sup><http://maxi.riken.jp/mxondem/>

source region and a 15'' background region offset from the source. We found a UVW1 AB magnitude  $20.38 \pm 0.06(\text{stat}) \pm 0.03(\text{sys})$ . This is consistent within  $2\sigma$  with the quiescent-level predictions from our SED fit (see Section 2.4), so there is no detectable transient emission and we do not consider these observations further.

## 2.4 Analysis

In this section, we present our analyses of the archival and follow-up observations of VT J0243. We begin in Section 2.4 with a brief discussion of the host properties. In Section 2.4, we constrain the physical properties of the radio-emitting outflow or jet using the radio observations. In Section 2.4 we constrain the origins of the X-ray emission, and in Section 2.4, we discuss the optical and infrared photometry at the location of VT J0243.

### Host Galaxy

Table 2.2: Host Galaxy, 2dFGRS TGS314Z138

Parameter	Value
R.A. (J2000)	02:43:45.70
Dec. (J2000)	-28:40:40.08
Redshift $z$	0.0742
$d_L$	347.0 Mpc
$\log M_*/M_\odot$	$10.28^{+0.06}_{-0.14}$
$t_{\text{age}}$ [Gyr]	$1.6^{+5.4}_{-0.4}$
$\tau_2$	$0.69^{+0.034}_{-0.028}$
[M/H]	$-1.23^{+0.14}_{-0.16}$
$t_{\text{burst}}$	$0.3^{+5.4}_{-0.2}$
$f_{\text{burst}}$	$0.78^{+0.11}_{-0.34}$
$\log M_{\text{BH}}/M_\odot$ (from $M_{\text{BH}} - M_*$ )	$6.94 \pm 0.82$

**Note.** R.A. and Dec. are from the Legacy imaging survey (189). Redshift is as measured in our work. The parameters below the line are derived from an SED fit using fsp and prospector (190–192). The SMBH mass is measured using the (38)  $M_{\text{BH}} - M_*$  relation.

VT J0243 is offset by 0.2'' ( $1\sigma$  uncertainty  $\sim 0.15''$ ) from the Pan-STARRS centroid of the galaxy 2dFGRS TGS314Z138. 2dFGRS TGS314Z138 is an SA galaxy. We summarize relevant properties of this host in Table 2.2, including its redshift and location. In this section, we will constrain the star formation rate, stellar and black hole mass, and Baldwin, Phillips & Terlevich (BPT) classification of this galaxy. We will use these properties to constrain the origin of the emission associated with VT J0243 and the trigger of VT J0243 later in this work.

To measure the stellar mass and star formation history of the galaxy, we performed an SED fit using the `Prospector` code (190–192) and the WISE, GALEX, and Pan STARRS galaxy photometry following a similar procedure to (163) and references therein. We assume a tau-model star formation history ( $\text{SFR} \propto e^{-t/\tau}$ ), a (193) IMF, and extinction following (194). We use `emcee` (195) to fit the SED, with 100 walkers, 500 burn-in steps, and 50000 steps. The results showed that  $\tau$  was very small, with a posterior distribution rising towards  $\tau < 0.1$  Gyr and flattening for lower values. `prospector` does not support such low values of  $\tau$ , so we reran the fit including a burst component (i.e., a delta function of star formation) and fixing  $\tau = 0.1$  Gyr. We found the fraction of the stellar mass formed in the burst was poorly constrained but peaked towards 1. The age of the burst is also poorly constrained. We report the maximum-a-posteriori estimate and  $1\sigma$  highest posterior density interval for each fit parameter in Table 2.2

First, we consider the star formation rate of this galaxy. The star formation rate is critical for constraining the source of the observed X-ray emission (Section 2.4). Our SED fitting results were consistent with a large fraction of the stellar mass forming in a star formation burst near the lookback time at  $z = 0.0742$ . Hence, the star formation rate could be very high for this source ( $\gtrsim 1 M_{\odot} \text{ yr}^{-1}$ ). However, our constraints are sufficiently loose that the SFR may be  $\ll 1 M_{\odot} \text{ yr}^{-1}$ . For galaxies with star formation that has remained constant for  $\sim 6$  Myrs, the  $\text{H}\alpha$ -SFR relationship can be used to set an upper limit on the SFR as  $\text{SFR} = 5.5 \times 10^{-42} L_{\text{H}\alpha} \sim 0.21 M_{\odot} \text{ yr}^{-1}$ , with  $\sim 15\%$  uncertainty (196). We measured  $L_{\text{H}\alpha} = (3.73 \pm 0.05) \times 10^{40} \text{ erg s}^{-1}$ , before any host extinction corrections. If we use the  $\text{H}\alpha/\text{H}\beta$  ratio to measure the host extinction, we find  $A_{\text{H}\alpha} = (3.33 \pm 0.80) \times 1.97 \log \left( \frac{\text{H}\alpha/\text{H}\beta}{2.86} \right) = 1.09 \pm 0.26$  (197). Then, the extinction corrected  $\text{H}\alpha$  luminosity is  $L_{\text{H}\alpha,0} = (10.2 \pm 2.5) \times 10^{40} \text{ erg s}^{-1}$ . Plugging this luminosity into the  $\text{H}\alpha$ -SFR relationship, we find  $\text{SFR} = 0.56 \pm 0.16 M_{\odot} \text{ yr}^{-1}$ ; in other words  $\text{SFR} < 1 M_{\odot} \text{ yr}^{-1}$  at the  $3\sigma$  level. We find a consistent constraint using the [O II] luminosity and the SFR-[O II] relation from (198):  $\text{SFR} = 0.10 \pm 0.02 M_{\odot} \text{ yr}^{-1}$ . These constraints are robust even if the line emission is not entirely produced by star formation (see the end of this section for a discussion of possible AGN activity in 2dFGRS TGS314Z138). However, the  $\text{H}\alpha$  constraint relies on the assumption that the star formation has been constant for at least 6 Myrs.

Next we use the stellar mass of 2dFGRS TGS314Z138 to constrain the black hole mass of the galaxy. The black hole mass is critical for constraining the origin of

VT J0243, as different types of transients dominate at different masses (e.g., TDEs cannot occur for  $M_{\text{BH}} \gtrsim 10^8 M_{\odot}$ ). The stellar mass of this galaxy is well-constrained at  $\log M_* = 10.06^{+0.12}_{-0.08}$ . Using the black hole-stellar mass relation from (38), we find a black hole mass  $\log M_{\text{BH}}/M_{\odot} = 6.94 \pm 0.82$ .

Finally, we discuss the optical spectral features, and use them to classify 2dFGRS TGS314Z138 as a possible Seyfert galaxy. Both the archival 2dFGRS and the LRIS spectra show narrow line emission associated with AGN, such as [O III]  $\lambda\lambda 4959, 5007$ , H $\beta$ , H $\alpha$ , [N II]  $\lambda\lambda 6548, 6583$ , and [S II]  $\lambda\lambda 6716, 6731$ . We fit the spectra and measure emission line strengths using the same procedures as (163), and we refer the reader to that work for details. There has been no significant evolution in any of the line ratios, so we assume that the recent LRIS spectrum does not include any transient emission associated with VT J2043 and place both spectra on BPT diagrams (4–6), as shown in Figure 2.2. Both spectra are consistent with BPT-weak Seyferts. Likewise, none of the available WISE mid-infrared colors of 2dFGRS TGS314Z138 are consistent with a strong AGN (200). We thus identify this galaxy as a weak Type 2 Seyfert. As we will discuss in Section 2.4, this galaxy may be a *true* Type 2 Seyfert, meaning that the absence of broad lines may be due to the complete lack of a broad line region (BLR). From the ROSAT soft X-ray flux constraints, we can constrain the pre-flare AGN accretion rate. Since  $L_X \lesssim 2.6 \times 10^{42} \text{ erg s}^{-1} \lesssim 10^{-3} L_{\text{edd}}$ , and assuming a bolometric correction  $\sim 20$  (201), we find  $f_{\text{edd}} \lesssim 2\%$ .

### Radio analysis

Typically, radio emission from galactic centers is dominated by synchrotron emission due to particles accelerated within a relativistic, collimated jet (160) or shocks from the collision of a jet and/or non-relativistic, wide-angle outflow with the circumnuclear medium (CNM). This emission can be self-absorbed or free-free absorbed. Because we are observing a transient, the outflow or jet must be expanding. In this section, we combine a fit to our VLBA observations of this source with synchrotron modelling of the observed SED (Figure 2.3) to constrain the physical parameters of the source.

### Synchrotron analysis methods

We constrain the physical properties of the source by assuming equipartition between the energy in electrons and the energy in the magnetic field. We also adopt the

standard assumption that the relativistic electron distribution is a power-law in Lorentz factor (LF) with index  $p$  and normalization  $N_0$  above a minimum LF  $\gamma_m$ :  $N(\gamma)d\gamma = N_0\gamma^{-p}d\gamma$ ,  $\gamma > \gamma_m$ . In this case, the SED is well-modelled by a broken power law (202, 203).

The slopes of the power law segments depend on the ordering of a number of characteristic LFs. The three relevant LFs for this work are (1) the LF of the lowest energy electrons  $\gamma_m$ , (2) the electron energy at which the optical depth to synchrotron self-absorption is one,  $\gamma_{sa}$ , and (3) the energy at which the electron cooling timescale is shorter than the age of the source,  $\gamma_c$ . Each of these corresponds to a characteristic synchrotron frequency  $\nu_x = \gamma_x^2 e B / (m_e c)$ ,  $x \in [m, sa, c]$ , where  $e$  is the electron charge,  $B$  is the magnetic field strength, and  $m_e$  is the electron mass. These characteristic frequencies correspond to the locations of the breaks in a multiply-broken power law model of the synchrotron emission.

Our radio SED at all epochs is best-modelled when  $\nu_{sa} < \nu_m < \nu_c$ . No other orderings can reproduce the observed broad and flat peak. For  $\nu_{sa} < \nu_m < \nu_c$ , the power-law slope in the optically thick regime ( $\nu < \nu_{sa}$ ) is 2, corresponding to the slope of a Rayleigh-Jeans law with constant brightness temperature. For  $\nu_{sa} < \nu < \nu_m$ , the slope is 1/3, which is that of a single electron spectrum at frequencies smaller than the characteristic synchrotron frequency of that electron. For  $\nu_m < \nu$ , the power-law slope is  $\alpha = -(p - 1)/2$ . Since each electron primarily emits at its characteristic synchrotron frequency  $\nu \propto \gamma^2$  and the synchrotron power for a single electron  $-\frac{dE}{dt} \propto \gamma^2$ , we can approximate the flux density  $S_\nu(\nu)d\nu = -\frac{dE}{dt}N(\gamma)d\gamma \propto \gamma^{2-p}d\gamma \propto \nu^{-(p-1)/2}d\nu$ , leading to the slope  $\alpha = -(p - 1)/2$ .

Following (204), we can now derive expressions for the number of electrons in the outflow  $N_e$ , magnetic field  $B$ , and total energy  $E$  as a function of radius  $R$ , bulk Lorentz factor  $\Gamma$ , and radio SED properties. We assume a fraction  $\epsilon_e$  of the total energy is stored in electrons, and a fraction  $\epsilon_B$  is stored in the magnetic field. We nominally assume  $\epsilon_e = \epsilon_B = 0.1$ , although at the end of this section we will vary those values. We assume the outflow has an area  $f_A \pi R^2$  and volume  $f_V \pi R^3$ . As we will discuss, VT J0243 has transitioned to a regime where  $\Gamma \sim 1$ , so the following

equations apply to the nonrelativistic limit.

$$N_e = \frac{9cF_p^3 d_L^6 \eta^{10} \Gamma^2}{2\sqrt{3}\pi^2 e^2 m_e^2 \nu_p^5 (1+z)^8 f_A^2 R^4} \approx 3.1 \times 10^{52} \frac{F_{p,-25}^3 \eta^{10} \Gamma^2}{\nu_{p,9}^5 R_{18}^4 f_A^2}, \quad (2.1)$$

$$B = \frac{8\pi^3 m_e^3 c \nu_p^5 (1+z)^7 f_A^2 R^4}{9eF_p^2 d_L^4 \eta^{10} \Gamma^3} \approx 0.18 \text{ G} \left( \frac{\nu_{p,9}^5 R_{18}^4 f_A^2}{F_{p,-25}^2 \eta^{10} \Gamma^3} \right), \quad (2.2)$$

$$E = \frac{1}{\epsilon_B} \frac{f_V R^3 B^2}{8\Gamma^2} \approx 5.3 \times 10^{51} \text{ erg} \left( \frac{1}{\epsilon_B} \frac{R_{18}^3 B_{-0.74}^2}{\Gamma^2} \frac{f_V}{4/3} \right). \quad (2.3)$$

Here,  $d_L$  is the luminosity distance,  $F_p$  is the peak flux density,  $\nu_p$  is the peak frequency, and  $z$  is redshift. The notation  $Y_x$  denotes quantity  $Y$  in units of  $10^x$  cgs. The variable  $\eta$  is defined as the ratio between the minimum and self-absorption frequencies:  $\eta = \nu_m/\nu_{\text{sa}}$  if  $\nu_a < \nu_m$ ; else 1. Only the final equation for total energy  $E$  assumes equipartition. In the final equalities, we have adopted the luminosity and redshift of VT J0243. We also assume, both in these equalities and henceforth, that  $f_A = 1$  and  $f_V = 4/3$ , appropriate for a spherical, nonrelativistic outflow. For a jet, the appropriate values are  $f_A = f_V = (\theta_j \Gamma)^2$ , where  $\theta_j$  is the jet half-opening angle. For the jetted TDE Sw J1644, assuming  $\theta_j \sim 0.1$ , we have  $f_A, f_V \gtrsim 0.1$  (205). Given that our best-fit VLBA model is non-spherical, we also test  $f_A = f_V = 0.1$  and present the synchrotron parameters in Table 2.3.

We will also require the electron density of the material into which the outflow is expanding. We denote this density  $n_e$ . Note that  $n_e \neq N_e/(4\pi R^3)$ , since  $N_e$  is the electron number *in* the outflow, whereas  $n_e$  is the density of the material *outside* the outflow. We derive this density following (15), who require conservation of momentum across the shock front and find

$$n_e = \frac{B^2}{6\pi\epsilon_B\beta^2 c^2 m_p} \approx 1.1 \text{ cm}^{-3} \left( \frac{\nu_{p,9}^{10} R_{18}^8 f_A^4}{F_{p,-25}^4 \eta^{20} \Gamma^6 \beta^2 \epsilon_B} \right).$$

Here,  $\beta = v/c$ , where  $v$  is the outflow velocity. This equation assumes expansion of a thermal gas ( $\gamma = 5/3$ ) into fully ionized hydrogen. The generalization to a relativistic gas would modify this equation by a factor of order unity, which we neglect as it is significantly smaller than our measurement errors.

To apply these equations, we require a measurement of  $\eta$ . The self-absorption frequency of this system is likely at or below the low frequency end of our observations, so we cannot tightly constrain  $\eta$  by fitting for  $\nu_{\text{sa}}$  and  $\nu_m$ . Instead, we use the outflow size measured using our VLBA observations. Under equipartition, the

Table 2.3: Synchrotron Analysis Results

$f_A, f_V$	$p$	$\frac{R}{\text{pc}}$	$\epsilon_e, \epsilon_B$	$\Gamma, \beta$	$\eta$	$\log \frac{B}{10^{-2}\text{G}}$	$\log \frac{n_e}{\text{cm}^{-3}}$	$\log \frac{E}{\text{erg}}$	$\log \frac{M_{\text{ej}}}{M_\odot}$
1,4/3	$2.2 \pm 0.1$	$0.71 \pm 0.02$	0.1, 0.1	1.005, 0.1	$10 \pm 3$	$-155 \pm 5$	$1.5 \pm 0.1$	$52.2 \pm 0.1$	$-1.8 \pm 0.1$
				1.3, 0.6	$8 \pm 3$	$-152 \pm 6$	$-0.10 \pm 0.12$	$52.0 \pm 0.1$	$-1.9 \pm 0.1$
			0.1, $10^{-3}$	1.005, 0.1	$15 \pm 5$	$-213 \pm 4$	$2.29 \pm 0.08$	$53.01 \pm 0.08$	$-0.94 \pm 0.08$
				1.3, 0.6	$11 \pm 4$	$-211 \pm 5$	$0.72 \pm 0.09$	$52.83 \pm 0.09$	$-1.12 \pm 0.09$
1/3,1.9	$2.2 \pm 0.1$	$0.71 \pm 0.02$	0.1, 0.1	1.005, 0.1	$4.07 \pm 1.34$	$-118 \pm 10$	$2.2 \pm 0.2$	$51.8 \pm 0.2$	$-2.11 \pm 0.19$
				1.3, 0.6	$3 \pm 1$	$-113 \pm 11$	$0.7 \pm 0.2$	$51.7 \pm 0.2$	$-2.2 \pm 0.2$
			0.1, $10^{-3}$	1.005, 0.1	$6.14 \pm 1.97$	$-178 \pm 7$	$3.0 \pm 0.1$	$52.6 \pm 0.1$	$-1.3 \pm 0.1$
				1.3, 0.6	$4.8 \pm 1.6$	$-175 \pm 8$	$1.4 \pm 0.2$	$52.47 \pm 0.17$	$-1.5 \pm 0.2$

outflow radius is related to  $\eta$  as

$$R = \left[ \frac{3^7 c}{32\sqrt{3}\pi^9 m_e^8} \frac{p-1}{p-2} \frac{\epsilon_B}{\epsilon_e} \right]^{\frac{1}{17}} \frac{\Gamma^{\frac{11}{17}} F_p^{\frac{8}{17}} \eta^{\frac{35}{51}} d_L^{\frac{16}{17}}}{f_V^{\frac{1}{17}} (1+z)^{\frac{25}{17}} f_A^{\frac{7}{17}} \nu_p}$$

$$\approx 6.1 \times 10^{17} \text{ cm} \left[ \left( \frac{p-1}{p-2} \frac{\epsilon_B}{\epsilon_e} \frac{4/3}{f_V} \right)^{\frac{1}{17}} \frac{\Gamma^{\frac{11}{17}} F_p^{\frac{8}{17}} \eta^{\frac{35}{51}}}{(1+z)^{\frac{25}{17}} \nu_p, 9 f_A^{\frac{7}{17}}} \right].$$

### Synchrotron analysis results

In this section, we present the physical parameters derived from our synchrotron analysis. First, however, we consider the fact that our observations can only be fit in the regime  $\nu_{\text{sa}} < \nu_m < \nu_c$ . This is unusual — the (203) model for an adiabatically expanding outflow applied to this source suggests that we should observe  $\nu_{\text{sa}} > \nu_m$  given the  $> 1,000$  day age of the outflow. A very high  $\nu_m$  at late times requires a source of energy which keeps the electron population at high  $\gamma$ . Thus, continual energy injection could explain our observation of  $\nu_{\text{sa}} < \nu_m$ . Continual energy injection is also a possible explanation of the unusual, rising late-time radio light curve (Figure 2.1; also see Section 2.5)

To derive the physical parameters, we first constrain  $F_p$  and  $\nu_p$ . We fit a doubly-broken power-law to the most recent observation epochs (GMRT+ATCA 1+ATCA 2) using the *dynesty* software (206). We fix the slopes to the expected values described above, and allow the position of each break and the electron spectral index  $p$  to float. We adopt broad, Heaviside priors on all parameters, except for  $p$ , which we require be in the physically-motivated range  $[2, 5]$ . We use the resulting best-fit model to evaluate the peak flux density and frequency, along with their uncertainties. We find  $F_p = 66.7 \pm 3.1$  mJy,  $\nu_p = 2.28 \pm 0.28$  GHz, and  $p = 2.40 \pm 0.17$ . Note

that the peak frequency is consistent within  $< 2.5\sigma$  with the best-fit characteristic minimum frequency,  $\nu_m = 2.78 \pm 0.35$  GHz. Next, we constrain the bulk Lorentz factor,  $\Gamma$ . The outflow was launched before the first VLASS observation epoch on MJD 58166; hence, it is at least  $\sim 1,400$  days old. It was launched after the NVSS observation, so it is no more than  $\sim 10,000$  days old. Thus, we have  $0.1 < \langle \beta \rangle \lesssim 0.6$  and average bulk Lorentz factor  $1.005 < \Gamma \lesssim 1.3$ .

Next, we calculate  $\eta$  using the outflow size and the equipartition radius equation. As described in Section 2.3, our VLBA observations imply an approximate radius  $R = 0.71 \pm 0.02$  pc. Thus, we have  $\eta = 5.17 \pm 1.13$  ( $\Gamma = 1.005$ ),  $4.05 \pm 0.89$  ( $\Gamma = 1.3$ ). In both cases, the predicted  $\nu_{\text{sa}}$  is consistent with constraints from our doubly-broken power-law fit. We re-ran the doubly-broken power-law fit while requiring  $\eta$  be consistent with the above values and found that  $p$  has not changed significantly from our previous measurement:  $p = 2.20 \pm 0.12$ .

Finally, we constrain the magnetic field, electron number density, and total energy. We also constrain the required ejecta mass  $M_{\text{ej}} = 2E/c^2$  for total energy  $E$ . This mass is a lower limit as the radio energy is only a subset of the energy in the event. The results are tabulated in Table 2.3. The measured densities are consistent with results for other galaxies: at a similar distance (in units of the Schwarzschild radius), typical densities are  $\gtrsim 10^{-1} \text{ cm}^{-3}$  (see Fig. 2 of (150)). The energies are consistent with jetted TDE observations (205).

Our assumption of  $\epsilon_B = 0.1$  has been shown to be incorrect for the jetted TDE Sw J1644+57 (205). If we adopt the preferred value for that event,  $\epsilon_B = 10^{-3}$ , our physical parameters are modified, and the results are listed in Table 2.3. The energy is now higher than measured for previous jetted TDEs (205). A collimated geometry (i.e., smaller  $f_A$  and  $f_V$ ) will tend to decrease the energy ( $E \propto f_V^{3/7}$ ), increase the magnetic field ( $B \propto f_V^{3/7}$ ), and increase  $n_e$  ( $n_e \propto f_V^{6/7}$ ). We report the values for a cone with opening angle  $\theta = 30^\circ$ , for which  $f_V = \tan^2 \theta / 3 = 1/9$  and  $f_A = \tan^2 \theta = 1/3$  in Table 2.3.

The evolution of VT J0243's radio SED is shown in Figure 2.3. The datapoints are colored by the observation MJD. We have overplotted a doubly-broken power law fit to the most recent epoch in purple. We overplot fits to the VLASS/VCSS observations. In these fits,  $p$  is forced to be consistent with the value measured from the most recent observations. The break frequencies and amplitude are allowed to float freely. These observations are not sufficiently well-sampled to provide strong constraints on any physical parameters, but are roughly consistent with expectations

for an expanding outflow.

In summary, VT J0243 is associated with a luminous, energetic outflow. The outflow is currently non-relativistic, but given the high, and still rising, luminosity, we believe it likely that we are observing a relativistic jet, possibly off-axis, that has slowed. This hypothesis is supported by the observed non-spherical geometry from the VLBA (see the end of Section 2.3).

### X-ray analysis

In this section, we discuss our X-ray observations. First, we present constraints on X-ray emission at the time that VT J0243 turned on. Then, we discuss the luminosity and spectrum from our more recent X-ray observations. Finally, we consider three possible origins for this late-time X-ray emission: star formation, an accretion disk, or something associated with the transient event.

Beginning on MJD  $\sim 59375$ , we detected near-constant X-ray emission from the location of VT J0243 with a 0.3 – 10 keV luminosity of  $\log L_{0.3-10\text{keV}}/(\text{erg s}^{-1}) = 42.3 \pm 0.01$  (Figure 2.1), after correcting for Milky Way HI absorption ( $N_{\text{H,MW}} = 1.51 \times 10^{20}$  at the location of VT J0243; (185)). We do not have strong constraints on the X-ray emission before that date, although from the archival MAXI observations (black triangle upper limits) we can rule out X-ray emission with the same luminosity and lightcurve of the jetted TDE Sw J1644 (red line). We cannot rule out a flare with average luminosity over  $\sim 100$  days that is  $\lesssim 2L_{\text{edd}}$ .

The late-time X-ray spectrum is shown in Figure 2.4. We used `xspec` to fit the X-ray emission to an absorbed power law (`cflux*TBabs*zTBabs*powerlaw`) and a blackbody (`cflux*TBabs*zTBabs*body`). In both cases, we include both Milky Way extinction, for which we fix the hydrogen column density to the known value  $N_{\text{H,MW}} = 1.52 \times 10^{20} \text{ cm}^{-2}$  (185), and intrinsic extinction, for which we let the Hydrogen column density float. The best-fit models are shown in Figure 2.4. The pure blackbody cannot fit our observations (`cstat/dof` = 195/32), but power law (`cstat/dof` = 33.7/33) provides a statistically acceptable fit. The best-fit power law parameters are: intrinsic column density  $< 7.7 \times 10^{19} \text{ cm}^{-2}$  ( $5\sigma$ ), photon-index  $\Gamma = 2.98 \pm 0.06$ , and an absorbed 0.3 – 10 keV flux density  $\log \hat{f}_{0.3-10\text{keV}} = -12.86 \pm 0.01$  ( $L_{0.3-10\text{keV}}/(\text{erg s}^{-1}) = 42.3 \pm 0.01$ ). We will discuss the interpretation of these parameters later in this section.

We consider three general categories of X-ray sources: (1) star formation in the host galaxy, (2) an accretion disk with or without a hot electron corona, and (3)

other transient emission associated with VT J2043. We will now discuss the likely contribution of each of these sources in turn.

X-ray photons associated with star formation are predominantly emitted by low- and high-mass X-ray binaries (LMXBs/HMXBs; (207)). The star formation rate is correlated with the 2–10 keV X-ray luminosity as  $\text{SFR} = (1.40 \pm 0.32) \times \frac{L_{2-10\text{keV}}}{10^{40} \text{ erg s}^{-1}} M_{\odot} \text{ yr}^{-1}$  (208). To reproduce the observed 2 – 10 keV luminosity of  $4.7 \times 10^{40} \text{ erg s}^{-1}$ , we require that the  $\text{SFR} = 6.58 \pm 1.5 M_{\odot} \text{ yr}^{-1}$ . This is consistent with our SED fit, but our SED fit provides very weak constraints on the SFR. It is also consistent with our pre-flare radio limits: radio emission due to star formation has been empirically measured to be  $\text{SFR} = 5.52 \times 10^{-22} L_{1.4\text{GHz, SFR}} \text{ for } L_{1.4\text{GHz, SFR}} > 6.4 \times 10^{28} \text{ erg s}^{-1} \text{ Hz}^{-1}$ , which corresponds to  $L_{1.4\text{GHz, SFR}} = 0.83 \pm 0.22 \text{ mJy}$  for  $\text{SFR} = 6.58 \pm 1.5 M_{\odot} \text{ yr}^{-1}$ . This star formation rate is inconsistent with the observed  $\text{H}\alpha$  emission: from Section 2.4, the SFR based on the  $\text{H}\alpha$  emission is  $\text{SFR} = 0.56 \pm 0.16$ . This expression for the SFR- $\text{H}\alpha$  correlation is only valid if the SFR has been  $\sim$  constant for  $> 6 \text{ Myr}$ , but, if the star formation was very recent, we would not expect to see the X-ray emitting LMXBs and HMXBs. Hence, it is unlikely the X-ray emission was produced by star formation. We briefly consider alternative X-ray sources in the rest of this section.

X-ray emission from AGN is dominated by thermal emission from the disk, and inverse Comptonized thermal photons by the hot electron corona (209). Using the observed correlation between narrow  $[\text{O III}]\lambda 5007$  and  $\text{H}\alpha$  with X-ray luminosity (210), an accretion disk can account for all of the observed X-ray flux. Given that the X-ray lightcurve is consistent with a constant luminosity, it is feasible that the X-ray emission is entirely due to an active accretion disk. A  $\Gamma \sim 3$  power law spectrum is consistent with observations of narrow line Seyfert 1 galaxies (211), although radio-loud Seyferts typically have flatter X-ray spectra ( $\Gamma \sim 2$ ; (212)), but with large scatter.

The X-ray emission from 2dFGRS TGS314Z138 is not entirely consistent with “normal” Seyferts. The intrinsic column density is consistent with zero and inconsistent with the  $n_{\text{H}} > 10^{22} \text{ cm}^{-2}$  typically measured in Seyfert 2s (213). For standard AGN, such a low gas column density means that the BLR should be observable (214). However, as discussed in Section 2.4, we do not detect any broad line emission. This low  $n_{\text{H}}$  may support the hypothesis that the X-ray emission is dominated by star formation. If it is not, and the column density is truly near-zero, 2dFGRS TGS314Z138 may be a “true” Seyfert 2, which show small X-ray column densities

but no broad line emission (215).

Finally, we consider the scenario where the observed X-rays are transient, rather than associated with an old accretion disk or star formation, and consider a few of the possible origins. X-rays may be emitted from the forward shock of the outflow, as may have been the case for jetted TDEs like Sw J1644+57 (205). In this case, we expect the X-ray slope to be  $\Gamma = p/2 + 1 = 2.1 \pm 0.05$ , where  $p$  is taken from Table 2.3. This  $\Gamma$  is significantly inconsistent with our measured value. bremsstrahlung associated with the electrons in the radio-emitting outflow and dense clumps of CNM gas could produce X-rays, but we would expect a harder power-law spectrum in this case.

The X-rays may be associated with a new corona and associated accretion disk, formed as a result of, e.g., a stellar disruption. The observed power-law spectrum would be consistent with expectations for a transient corona/disk (216).

In summary, VT J0243 is not associated with an extraordinarily bright X-ray flare as has been observed for the extremely luminous, on-axis, jetted TDEs. We cannot rule out a flare with  $L \lesssim 2L_{\text{edd}}$ . VT J0243 is detected in late-time X-ray observations with a 0.3–10 keV luminosity  $L_X \sim 10^{42.3} \text{ erg s}^{-1}$ , photon index  $\Gamma \sim 3$ , and negligible intrinsic column density. This emission is unlikely to be related to star formation. Instead, it is most likely a transient, or a pre-existing accretion disk.

### **Infrared and optical analysis**

In Figure 2.1, we show the infrared (bottom) and optical (middle) light curves for VT J0243. In this section, we will provide brief analyses of the possible origins of the observed transient emission. Because of the low cadence and insufficient sensitivity of the observations, we will not perform any detailed modelling.

There is a significant flare detected by the PanSTARRS survey near MJD~55895 with  $g$ -band luminosity  $L_g \sim 4 \times 10^{42} \text{ erg s}^{-1}$ . The flare brightened and faded over a timescale smaller than the PanSTARRS cadence ( $\lesssim 400$  days). Given the low cadence, we cannot measure light curve shape in more detail, but it is consistent with optically-detected TDEs, which typically rise over tens of days and fade over  $\sim 60$  days (128). The co-temporal CRTS observations detect the flare at a  $\sim 2\sigma$  level but are not sensitive enough to reliably constrain the lightcurve. They do suggest that the flare peaked around the time of the brightest PanSTARRS observation, so the peak luminosity is likely within a factor of a few of  $L_g \sim 4 \times 10^{42} \text{ erg s}^{-1}$ . This is slightly dimmer than but consistent with typical optically-detected TDEs;

the dimmest TDE from (128) peaked at  $L_g \sim 7 \times 10^{42} \text{ erg s}^{-1}$ . We fit the fluxes to a blackbody assuming no intrinsic extinction, which is reasonable given the low column density measured from the X-ray spectrum (Section 2.4).

The optical fluxes at peak are consistent with a blackbody with no extinction and temperature  $\log T_{\text{bb}}/\text{K} = 4.35 \pm 0.38$  and radius  $\log R_{\text{bb}}/\text{pc} = -3.89 \pm 0.34$ , corresponding to a blackbody luminosity  $\log L_{\text{bb}}/(\text{erg s}^{-1}) = 43.4 \pm 1.7$ . Again, these blackbody parameters are all standard for optically-detected TDEs. We cannot rule out that the flare has repeated. Shortly after the peak, the optical emission rebrightens slightly to  $L_g \sim (6.7 \pm 1) \times 10^{42} \text{ erg s}^{-1}$ . The fluxes at the rebrightening are consistent with a blackbody with no extinction and temperature  $\log T_{\text{bb}}/\text{K} = 3.70 \pm 0.07$  and radius  $\log R_{\text{bb}}/\text{pc} = -3.19 \pm 0.20$ , corresponding to a blackbody luminosity  $\log L_{\text{bb}}/(\text{erg s}^{-1}) = 42.3 \pm 0.5$ . This blackbody luminosity is roughly an order of magnitude fainter than the brighter peak. The temperature is significantly cooler than the first peak, and the emission may come from a larger radius.

Unfortunately, because of the limited cadence of the PanSTARRS observations and the large uncertainties even at the optical peak, we cannot perform detailed modelling to determine the origin of the optical flare. The peak emission can be modelled as a standard accretion disk. It also could be a thermally-emitting outflow, heated by EUV emission from, e.g., an accretion disk, as may be observed in TDEs.

The infrared lightcurve shows variability with an approximate amplitude  $\sim 150 \mu\text{Jy}$  ( $\sim 10^{42} \text{ erg s}^{-1}$ ). The emission appears to redden slightly between the first three epochs and the rest of the MIR observations, which suggests that the MIR-emitting dust was heated when, e.g., the accretion rate increased. Intriguingly, the time period when this change must have occurred is roughly consistent with the range of launch dates constrained by the outflow radius evolution, and the time of the optical flare. The average change in flux density in each band between the first three epochs and the later observations is  $\Delta f_\nu(\text{W1}) = 44.8 \pm 11.1 \mu\text{Jy}$ ,  $\Delta f_\nu(\text{W2}) = 88.5 \pm 17.6 \mu\text{Jy}$ , where the uncertainties are determined through the standard deviation of the observations.

If we assume that the dust started out cold and the entire flux change was due to the dust heating, we can fit the  $\Delta f_\nu$  values during each WISE epoch to a blackbody to estimate the dust temperature and luminosity, albeit with large uncertainties and covariances. The average temperature over all WISE epochs is  $865 \pm 259 \text{ K}$  and the bolometric luminosity  $\log L_{\text{IR}}/(\text{erg s}^{-1}) \sim 41.69 \pm 0.15$ . If we assume dust with a covering fraction  $\sim 1$ , this implies it is located at an unrealistically small radius  $\sim 10^{-2} \text{ pc}$ . Instead, we favor a scenario where more distant dust with a low covering

fraction is located farther away (e.g., a covering fraction  $\sim 1\%$  corresponds to a distance  $\sim 0.1$  pc). Low covering fractions of  $\sim 1\%$  are consistent with measurements from IR flares during TDEs in quiescent galaxies (144). AGN typically have high covering fractions  $\gtrsim 40\%$  due to the dusty torus (e.g. 217). The best fit average dust luminosity suggests that the bolometric luminosity of the EUV flare that heated the dust was  $\log L_{\text{EUV}}/\text{erg s}^{-1} \sim 43.2 - \log\left(\frac{f_{\text{cov, dust}}}{1\%}\right)$ . Unless the dust covering fraction is abnormally small, the EUV flare was sub-Eddington ( $\lesssim 1\% L_{\text{edd}}$ ).

This analysis of the IR flare assumes that there was no emission in between the low cadence WISE observations. A higher Eddington ratio EUV flare could have heated the dust between the IR observations, and we would not observe it. Hence, these constraints should be taken with a large grain of salt.

In conclusion, the low amplitude of the WISE variability suggests that either this galaxy has an extraordinarily low dust covering fraction, even when compared to completely quiescent galaxies, or that any EUV flare in the time period under question was sub-Eddington. There may have been a higher luminosity EUV flare in between the WISE observations. Moreover, this analysis has been subject to many poorly supported-assumptions. For example, if there was pre-existing accretion disk, our assumption that the dust was initially cold would be incorrect.

## 2.5 Discussion

The radio emission associated with VT J0243 is likely caused by the launching of a jet. Sub-relativistic outflows never produce the observed high luminosity radio emission ( $\nu L_\nu(3 \text{ GHz}) > 10^{40} \text{ erg s}^{-1}$ ), nor such high energies ( $E \sim 10^{51} \text{ erg}$ ). Even fast ( $\beta > 0.1$ ), wide angle outflows from AGN are generally associated with radio-quiet sources and are compact ( $\lesssim 0.1$  pc). Such outflows are not expected to be produced by disks with very low accretion rates, and no outflow has ever reproduced the observed outflow velocity, radio luminosity, and radio/X-ray luminosity ratio. Hence, we do not consider wide-angle, non- or semi-relativistic outflows further. Instead, we assume VT J0243 is associated with the launching of a jet. In this section we discuss the answer to the question: why did a jet launch? First, we summarize our observations:

- X-ray emission with  $\log L_X/\text{erg s}^{-1} = 42.3 \pm 0.01$  and a power-law spectrum with index  $\Gamma = 2.98 \pm 0.06$  and a column density consistent with the Milky Way value. The emission is likely associated with a hot accretion disk and electron corona. The emission may have been transient or persistent, and

may have evolved over the last few decades. The peak luminosity was likely  $\lesssim 2L_{\text{edd}}$ .

- Transient radio emission with a current luminosity  $\nu L_\nu(5 \text{ GHz}) = 3.6 \times 10^{40} \text{ erg s}^{-1}$ . The radio-emitting outflow is currently at a radius  $R = 0.71 \pm 0.02 \text{ pc}$ . It has an average velocity  $0.1 < \beta < 0.6$ , or  $1.005 < \Gamma < 1.3$ , and is currently non-relativistic. It has a high equipartition energy  $\sim 10^{52} \text{ erg}$  and a moderate electron density,  $\gtrsim 1 \text{ cm}^{-3}$ , depending on the assumed fraction of the energy stored in the magnetic field. The magnetic field is  $\sim 10^{-2} \text{ G}$ .
- Significant optical variability, peaking at  $L_g = 4 \times 10^{42} \text{ erg s}^{-1}$ . The flare peaks around MJD 56000, and fades over  $\lesssim 400$  days. The peak date is consistent with an extrapolated radio launch date, assuming constant velocity and  $0.1 < \beta < 0.6$ , although the uncertainties are large and the flare may have been launched a few thousand days before or after the optical peak. The peak is consistent with a  $T \sim 2 \times 10^4 \text{ K}$  blackbody with bolometric luminosity  $10^{43.4} \text{ erg s}^{-1}$ . After the flare faded, it rebrightened to a cooler blackbody ( $T \sim 5000 \text{ K}$ ) with a bolometric luminosity an order of magnitude dimmer at  $10^{42.3} \text{ erg s}^{-1}$ .
- Weak MIR variability suggesting that any EUV flare in the last  $\sim 5000$  days was sub-Eddington, unless it occurred between the low cadence IR observations. The MIR variability increased around MJD 56000, which is consistent with the launch date of the radio-emitting outflow if the outflow has travelled at a constant  $\beta$ .
- The host galaxy of VT J0243, 2dFGRS TGS314Z138, shows narrow line emission consistent with historic, weak Seyfert activity. The MIR colors, on the other hand, are consistent with quiescent galaxies.

In the rest of this section, we consider the possibility that this source is caused by a nascent jet associated with an accreting black hole. First, for completeness, we briefly discuss, and rule out, an alternate possibility: a supernova-triggered jet.

### Supernova-triggered jet

Supernovae (SNe) can produce radio emission spanning from  $L_\nu \sim 10^{25-32} \text{ erg s}^{-1} \text{ Hz}^{-1}$  for timescales as long as ten years (155, 225). The emission is often synchrotron emission associated with an outflow/jet colliding with the dense, local

environment or a relativistic jet (e.g. 202, 223). Typical SNe do not remain as bright as VT J0243 for such long periods of time (see Figure 2.5). Moreover, the  $O(\text{pc})$  size of the radio emitting outflow/jet associated with VT J0243 would be highly unusual. A gamma-ray burst (GRB) can produce such an outflow; however, no GRB has been observed with a rising radio luminosity thousands of days post-explosion (e.g. 226). Moreover, the observation of  $v_{\text{sa}} < v_m$  thousands of days post-explosion is inconsistent with models of GRB outflow evolution (203). Hence, VT J0243 is unlikely to be related to a supernova.

### **Black hole accretion-triggered jet**

Accreting black holes, whether stellar mass or supermassive, are well established to be associated with jet activity. The process through which the jet is launched, the connection between the accretion disk and the jet, and the connection between the black hole properties (i.e., spin) and the jet remain open questions. In the following sections, we provide a basic summary of the physics of jets associated with black holes and accretion, and then we compare the properties of VT J0243 to those expected for young jets launched from accreting black holes.

While the stellar mass black hole regime is not relevant to VT J0243, our understanding of jet physics and the disk-jet connection for stellar mass black holes is more sophisticated. We are better able to study these events because of the short timescales associated with the disk and jet evolution, which allow real-time observations of the jet and disk life cycles, and the smaller dynamic ranges of the systems, which allow for more realistic simulations. Ideally, the accretion disk and black hole evolution would be scale-free, so we can apply the same physics to stellar mass black holes and SMBHs. In reality, effects such as the mass-dependence of the inner disk temperature introduce a scale-dependence (e.g. 227). These effects have critical effects on accreting SMBHs, causing them to behave very differently in certain regimes (e.g., at very high accretion rates) from XRBs. Despite this, much of the stellar mass black hole physics is relevant to SMBHs, so we begin with a summary of stellar mass black hole disc/jet evolution. Then, we discuss the SMBH regime, and finally focus the discussion to comparisons with VT J0243.

### **X-ray binary disk-jet connection**

The evolution of accreting stellar-mass black hole systems, X-ray binaries (XRB), is best understood by considering the evolution in X-ray hardness/luminosity space.

When the X-ray binary is extremely sub-Eddington ( $L_X/L_{\text{edd.}} < 0.01$ ), the X-ray emission is low, with a flat spectral slope. Hence, this is called the low-hard state. In this low Eddington ratio regime, the accretion disk is geometrically-thick, optically-thin, and hot. It is radiatively inefficient, so advection dominates and this type of disk is called an advection dominated accretion flow (ADAF; (62)). In the low-hard state, the XRB is typically observed to have a mildly relativistic ( $\Gamma < 2$ ) jet (228).

As the Eddington ratio increases, the X-ray luminosity increases but the spectrum remains hard as the ADAF continues to dominate the disk. The radio luminosity likewise increases. Eventually, the X-ray emission reaches a peak, as the high Eddington ratio has caused the geometrically-thin outer-disk to extend into the inner disk and replace the ADAF. The X-ray spectrum softens, while the luminosity remains roughly constant (159). During this softening, the jet Lorentz factor increases to  $\Gamma > 2$ , and the jet emission becomes intermittent and dominated by discrete blobs (159). Soon after this change in the jet properties, the XRB will pass the “jet line”, which is a characteristic hardness ratio at which the steady jet completely vanishes (229). The XRB is now in the high-soft state. After this stage, the Eddington ratio will drop while the spectrum remains soft. At low Eddington ratios, the ADAF will begin to dominate again and the X-ray hardens. The XRB will cross the jet line again, and a new jet will launch.

The processes through which the jet is quenched and launched are not fully understood. Both likely involve changes in the magnetic field in the accretion disk. The jet is likely collimated by pressure from external material; hence, the prevalence of jets in low Eddington ratio AGN with puffy disks (230). The internal jet magnetic fields are generally unable to collimate more than the extreme base of the jet (231). As we will discuss in Section 2.5, jets are also sustainable near SMBHs accreting at near- or super-Eddington rates, as the disk again becomes puffy and the jet can be collimated.

XRBs largely remain in the quiescent low-hard state, only entering the high-soft state during outbursts that are thought to be triggered by instabilities in the accretion disk (159). There is some evidence that black hole spin is positively correlated with jet power, as would be expected if jets are powered by the (79) mechanism. However, the sample of XRBs with known spins remains small (232).

### The disk-jet connection for supermassive black holes

There is observational evidence that the disk-jet connection for XRBs can be extrapolated to accreting SMBHs. For example, there is a tight, black-hole-mass dependent correlation between the X-ray and radio luminosities of XRBs, and observations of AGN have shown that these SMBHs lie on the same correlation (233). Moreover, a modified version of the X-ray hardness-luminosity diagram, which replaces the X-ray hardness with the relative luminosity in power law and disk blackbody components, shows the same structure for XRBs and AGN (159). It is not clear, however, that AGN follow the same cycle as XRBs in this diagram. The disk instabilities that cause XRB outbursts have not been proven to occur in AGN (234). The relationship between spin and jet power is observationally unclear, as for X-ray binaries. The observed dichotomy between the radio-loud and quiet low-luminosity AGN (LLAGN) populations ( $\sim 10\%$  of LLAGN are radio loud) is plausibly explained if the radio-quiet LLAGN have low SMBH spins while the radio-loud sources have extremal spins (230). AGN simulations unambiguously find a strong, positive correlation between jet power and spin (230).

As with XRBs, AGN with lower Eddington ratios ( $\ll 0.1$ ) often have weak jets (48, 235, 236). As we will discuss in Section 2.5, there is strong evidence that accreting black holes at near- or super-Eddington rates also launch jets. For example, the TDE Sw J1644 launched a powerful jet during a period of near- or super-Eddington accretion. The exact mechanism through which this jet was launched is unconfirmed, but the observation of a jet from such a young accreting system suggests that the accretion disk became strongly magnetized remarkably quickly (237).

In summary, one can draw parallels between the high-soft/low-hard classification for XRBs and the observed states of AGN, although there are many differences. For example, AGN do not cycle between the high-soft/low-hard states during disk instability-driven outbursts like XRBs, and the mechanism that causes AGN to perform this transition (with its associated jet quenching/launch) is unknown. There may be a correlation between SMBH spin and jet power, although this is not observationally confirmed.

With this background in the jet-disk connection and the factors that control the launching of a SMBH jet, we now turn towards VT J0243. We consider two scenarios. First, VT J0243 may be a young jet launched from a system that has been actively accreting since long before the jet was launched, i.e., an AGN. Alternatively, VT J0243 may be a jet launched near the onset of accretion. In this case, much of the

previous discussion must be altered, as the properties of very young accretion disks are distinct from old disks (in particular, the magnetizations). The combination of young accretion and a new jet is expected for TDEs, so we discuss the possibility that VT J0243 is a jetted TDE.

### **VT J0243 as a young jet from an AGN**

First, we consider the possibility that VT J0243 is a young jet from an AGN. We briefly compare the observations to the theory summarized in the previous subsections, and then we perform a detailed comparison of the observations of VT J0243 and known, young AGN jets.

From a theoretical perspective, even if all of the X-ray emission is due to an accretion disk/corona, VT J0243's bolometric luminosity is sufficiently low that it is feasible that we are observing an AGN in the low-hard state that has launched a jet. The lack of dust, based on the infrared colors and X-ray absorption, and the low luminosities inferred from the IR and optical observations support the hypothesis that any pre-existing accretion disk was in a low state. The low average bulk Lorentz factor of the outflow ( $\Gamma < 1.3$ ) is also consistent with the  $\Gamma < 2$  jets typically associated with this state.

Of course, we cannot exclude that this event had an Eddington ratio  $\gtrsim 0.1$  during the jet launching, although the infrared observations and X-ray limits constrain the Eddington ratio to  $\lesssim 1$ . If the Eddington ratio is  $\gtrsim 0.1$  but not near- or super-Eddington, VT J0243 is in a regime where the physics of jet activity is very unclear. As we have discussed, in XRBs these higher Eddington ratios are associated with no jet activity. However, AGN in this regime are observed to be radio loud, and the mechanism through which the radio-emitting jet is produced is not fully understood (see (238) for simulations of a thin accretion disk that can support jet activity).

VT J0243 is consistent with theoretical expectations, albeit with uncertainties due to the unknown Eddington ratio at the time of jet launch. To further constrain the origin of VT J0243, we compare its properties with past observations. First, we compare the properties of VT J0243 and its host to the population of *persistent* radio-loud Seyferts. Later, we will focus back to transient sources and young jets.

Astronomers have discovered jetted Seyfert galaxies, like VT J0243, although they are uncommon. Around  $\sim 15\%$  of broad line AGN are very radio-loud, where radio loudness is measured by the parameter  $R_{\text{RL}} = f_{6\text{ cm}}/f_{4400\text{ \AA}}$  and  $R_{\text{RL}} > 100$  is the

cut for very radio-loud AGN (239). In contrast, only  $\sim 2.5\%$  of Seyfert 1s have  $R_{\text{RL}} > 100$ , so these galaxies tend to be radio quiet (239). Radio loud Seyferts may have high black hole masses  $\sim 10^{7-8} M_{\odot}$  compared to the general Seyfert population, but still much lower masses than general radio-loud AGN ( $\sim 10^9 M_{\odot}$ ) (239). These black hole masses for radio-loud Seyferts are still higher than observed for VT J0243. Radio-loud Seyferts also have flat X-ray spectra ( $\Gamma \sim 2$  for radio-loud Seyferts compared to  $\Gamma \sim 2.9$  for the general Seyfert population) with rapid variability on as short as hour timescales (212). Note that the typical X-ray spectral slopes of radio-loud Seyferts are shallower than that of VT J0243. Radio-loud Seyferts have high Eddington ratios, and show strong Fe II emission, both in contrast. Finally,  $\sim 70\%$  of radio-loud Seyferts show compact, steep radio SEDs, analogous to the more general compact, steep spectrum (CSS) source population. This compact emission suggests an overabundance of young radio-emitting jets, which do not form into  $\sim$ kpc scale structures like observed in FR I/II galaxies (240). In summary, the population of persistent radio-loud Seyferts shows some similarities to VT J0243, but many distinctions.

VT J0243 is not a persistent source, of course. Candidate young radio jets in AGN and Seyferts have become more common in recent years. (155) reported an AGN that switched from radio-quiet to radio-loud on a decade timescale, and more recently, (156) and (157) published the first samples of such objects. We show individual light curves for these turning-on radio AGN in Figure 2.5. VT J0243 has a luminosity and timescale consistent with these events.

Likewise, VT J0243 is consistent with observations of the jet power and bolometric luminosity of young, radio-loud AGN, which occupy specific regions of jet power–bolometric luminosity parameter space (157). Adopting  $P_J = 5 \times 10^{22} (L_{1.4\text{GHz}}/\text{W Hz}^{-1})^{6/7} \text{ erg s}^{-1}$  (241), and using the X-ray luminosity to approximate the bolometric luminosity with a bolometric correction factor  $\sim 20$  (201), we find  $P_J \sim 10^{43.2} \text{ erg s}^{-1}$  and  $L_{\text{bol}} \sim 10^{43.6} \text{ erg s}^{-1} \sim 0.046 L_{\text{edd}}$  for VT J0243. This low Eddington ratio places the source slightly above the border of the radiatively inefficient regime, where most of the AGN energy is channeled into a radio-emitting jet. This regime is typically defined as  $L_{\text{bol}}/L_{\text{edd}} \lesssim 10^{-2}$ . Given the large uncertainties in the bolometric luminosity of VT J0243, as discussed previously, we cannot convincingly place VT J0243 on either side of this dividing line. If we adopt  $L_{\text{bol}}/L_{\text{edd}} \sim 10^{-1.3}$  and  $P_J/L_{\text{bol}} \sim 10^{-0.4}$ , we find VT J0243 is consistent with radio-detected AGN (157).

On the other hand, VT J0243 has a unique radio SED relative to typical young jetted AGN. Young radio jets from AGN are observed to fall on a characteristic line in peak frequency–linear size parameter space (e.g. *154*). VT J0243 has a significantly smaller linear size compared to other young radio-loud AGN with the same peak frequency, which are typically hundreds of parsec in size.

Even if we only consider Seyferts, VT J0243 has unusual radio SED properties. A few examples of bright radio flares from Seyferts have been detected. (*242*) observed 66 radio-quiet, narrow line Seyfert 1 galaxies at 37 GHz, and detected eight. These sources were undetected in archival observations from the VLA Faint Images of the Radio Sky at Twenty-Centimeters (FIRST) survey. They show variability at 37 GHz as large as a Jansky and on month–year timescales. Seyferts can produce bright radio flares. In contrast to VT J0243, the low frequency emission from these Seyferts is weak ( $\sim$ micro-milliJy), suggestive of strong absorption at low frequencies (*240*).

In summary, while VT J0243 may be consistent with expectations for a young jetted AGN from a theoretical perspective, its radio SED is distinct from typical young jetted AGN, it has a soft X-ray spectrum, and its host properties are unusual. For example, it has quiescent host IR colors, a lack of strong evidence for ongoing AGN activity within a few thousand years of the radio flare, and a low black hole mass. Given the large range of properties of young jetted AGN and the large theoretical uncertainties, we do not rule out that we are observing such an event. However, if VT J0243 is a young jetted AGN, it is an extremely unusual member of this class.

### **VT J0243 as a young jet from a TDE**

Tidal disruption events (TDEs) occur when a star ventures within the tidal radius,  $R_T \sim R_*(M_*/M_{\text{BH}})^{1/3}$ , of a nearby SMBH (e.g. *110, 123, 243, 244*). The bulk of TDEs are “thermal” TDEs with  $\nu L_{\nu, \text{GHz}} \lesssim 10^{38} \text{ erg s}^{-1}$ , which are dominated by a thermally-emitting, hot accretion disk in the soft X-ray, and its reprocessed emission at lower energies (*150*). The radio emission mechanism for thermal TDEs is poorly constrained, but may be associated with a disk wind or stellar debris outflow that is colliding with the CNM (*150*). As is clear from Figure 2.5, VT J0243 is much brighter than all known thermal TDEs.

The luminosity of VT J0243 is, however, consistent with the jetted TDE population, which includes the three brightest ( $\nu L_{\nu, \text{GHz}} \gtrsim 10^{40} \text{ erg s}^{-1}$ ) of the  $\sim 20$  radio-detected TDEs (*2, 3, 205, 245–251*). The radio properties of these events are best exemplified

through Sw J1644+57, the earliest example of an on-axis, jetted TDE. Sw J1644+57 was discovered by the *Swift* Burst Alert Telescope in 2011, and was promptly observed by a variety of telescopes across the electromagnetic spectrum. Within a few days, a radio outflow was detected at a luminosity near  $10^{40}$  erg s $^{-1}$  and best-modelled as relativistic ( $\Gamma \sim 3$ ) with  $v_{\text{sa}} < v_m$ . The energy in the outflow increased over  $\sim 300$  days from  $\sim 2 \times 10^{50}$  erg to  $\sim 4 \times 10^{51}$  erg while  $\Gamma$  decreased as  $\sim t^{-0.2}$ .  $\gtrsim 300$  days post-launch, the energy plateaued, the peak flux began decreasing, and the SED transitioned to the regime with  $v_m < v_{\text{sa}}$ . The outflow transitioned to non-relativistic motion  $\sim 700$  days post-launch.

Around the same time as the radio turned-on, Sw J1644+57 exhibited a bright X-ray flare peaking at an isotropic luminosity  $\sim 10^{48}$  erg s $^{-1}$ , which is  $\sim 2 - 3$  orders of magnitude brighter than the Eddington luminosity of the SMBH. The X-ray emission declined as  $\sim t^{-5/3}$ , corresponding to the mass fallback rate during a TDE, and showed strong variability on  $< 1$  day timescales. At 500 days post-launch, the X-ray emission plummeted precipitously to  $L_X \sim 10^{36}$  erg s $^{-1}$ , which has been interpreted as the jet turning off. Because the X-ray luminosity tracks the expected mass fall back rate after a TDE, it is thought to be powered by a mechanism closely tied to the jet. (252) comprehensively surveyed many possible mechanisms, and favored models in which the X-ray photons are produced through either synchrotron emission or inverse-Comptonization of external photons (i.e., off the accretion disk). The emitting electrons are likely accelerated by magnetic reconnection in a Poynting flux-dominated jet. In this case, the fact that the observed jet was on-axis allowed the X-ray emission to be beamed, enabling the extremeley high luminosities observed.

In contrast to Sw J1644+57, and other similar events, VT J0243 is not associated with hugely super-Eddington X-ray flare. Only one other jetted TDE candidate was not detected as a bright X-ray transient, and this event was off-axis and in the highly obscured nucleus of a merging galaxy. VT J0243 may also be an off-axis jetted TDE. If we assume VT J0243 is a jetted TDE, this suggests that there will be a population of such events that cannot be detected via, e.g., X-ray transient surveys, but require wide field, deep radio surveys like VLASS.

VT J0243 also differs from Sw J1644+57-like events in its radio lightcurve. The  $\sim 5$  GHz luminosity is still increasing  $> 1,000$  days post-launch, whereas “typical” jetted TDEs have long since begun fading at similar frequencies. Moreover, at  $> 1,000$  days post-launch the SED is still in the regime where  $v_{\text{sa}} < v_m$ . These observations may suggest that the jet has yet to turn off. Unusually slowly evolving TDEs are not

unprecedented: some observed non-jetted TDEs evolve on much slower timescales than expected (see (163) Section 7.1 and references therein, see also (253)). The timescale of a TDE depends on factors including the stellar orbital parameters, the stellar structure, and the energy dissipation rate of the tidal debris. We may be seeing the jetted analogue of events in a regime with, e.g., a low energy dissipation rate, such that the accretion disk formation is delayed and the evolution slowed. In the case of VT J0243, the jet launch may have been enabled by magnetization provided by a fossil accretion disk, as was proposed in the case of Sw J1644+57 (237).

The X-ray properties of VT J0243 are consistent with, although the luminosity is at the bright end of, late-time ( $\gtrsim 4$  yrs) observations of non-jetted TDEs (254). However, the sample of TDEs with deep, late-time X-ray observations is small, so a detailed interpretation is difficult. The only object with late-time X-ray observations and a luminosity comparable to VT J0243 is PTF09axc, with  $L_X = 10^{42.4}$  erg s $^{-1}$  and  $\Gamma = 2.5$  eight years after optical peak (254). At early times, PTF09axc was detected with  $L_X = 10^{42.8}$  erg s $^{-1}$ , which is constraints on the early-time X-ray emission from VT J0243. This event was interpreted as a TDE with an accretion disk that underwent a change from an early soft state to a late hard state. No late-time radio detection has been reported for this event. A non-detection five-years post-optical flare set a 6.1 (3.5) GHz  $3\sigma$  upper limit of  $5.3 \times 10^{28}$  ( $1.2 \times 10^{29}$  erg s $^{-1}$  Hz $^{-1}$ ) (136), in strong contrast to the bright emission observed from VT J0243, although the first radio detection of VT J0243 was  $\sim 6$  yrs post-optical flare.

If VT J0243 is a jetted PTF09axc, by analogy to the X-ray binary observations described earlier, the jet may have been launched during the state transition. In this case, VT J0243 is a member of the recently discovered and rapidly growing class of delayed radio TDEs (e.g. 151, 153). These events show radio emission that turns on  $\gtrsim 2$  yrs post-TDE. This radio emission is typically fainter than observed from VT J0423 ( $\lesssim 10$ ) $^{39}$  erg s $^{-1}$ ). Some authors have proposed that the late-time radio emission is associated with an accretion-state change (255), although more coordinated X-ray and radio observations of other events are required to test this possibility. In the case of VT J0243, we cannot confirm a delayed launch of a jet associated with an accretion-state change due to the lack of constraints on the radio launch-date and the X-ray evolution, but this possibility cannot be ruled out.

In summary, VT J0243 is plausibly a jetted TDE. However, it differs from known jetted TDEs because of the slow timescale of the radio evolution and lack of a bright X-ray counterpart, the latter of which may support the idea that we are observing an

off-axis jet. VT J0243 may also be an extreme example of the TDEs with late time ( $\gtrsim 3$  yrs post-TDE) radio turn-on, triggered by an accretion state-change.

## 2.6 Conclusion

We have presented an extraordinarily bright and long lasting radio flare in a galactic nucleus detected in the VLA Sky Survey. VT J0243 rose to  $\sim 10^{40}$  erg s $^{-1}$  in a time period of  $\sim 5 - 20$  years. Radio follow-up suggests the presence of a compact, relativistic jet. X-ray emission with a luminosity  $L_X = 10^{42.3}$  erg s $^{-1}$  is observed, which may be associated with a pre-existing or transient corona and accretion disk. Faint IR variability and an  $L_g = 10^{42}$  erg s $^{-1}$  optical flare are observed, both consistent with reprocessed emission from a sub-Eddington EUV flare. VT J0243 is hosted by a weak Seyfert galaxy. A more detailed summary of our observations is provided at the beginning of Section 2.5.

VT J0243 is a unique example of a young radio source. It is likely caused by the launch of a powerful jet, combined with strongly sub-Eddington multiwavelength flares. This is consistent with a tidal disruption event, although the TDE likely evolved very slowly. It may also be an AGN, but the trigger for the abrupt accretion enhancement is unknown. In either case, VT J0243 highlights the complicated connection between SMBH accretion and jet launching. In the near future, radio surveys like VLASS will hopefully uncover large populations of similar, nascent jets, which, combined with extensive multiwavelength follow-up as was performed in this work, will illuminate the true triggers of such dramatic radio flaring and their connection with SMBH activity.

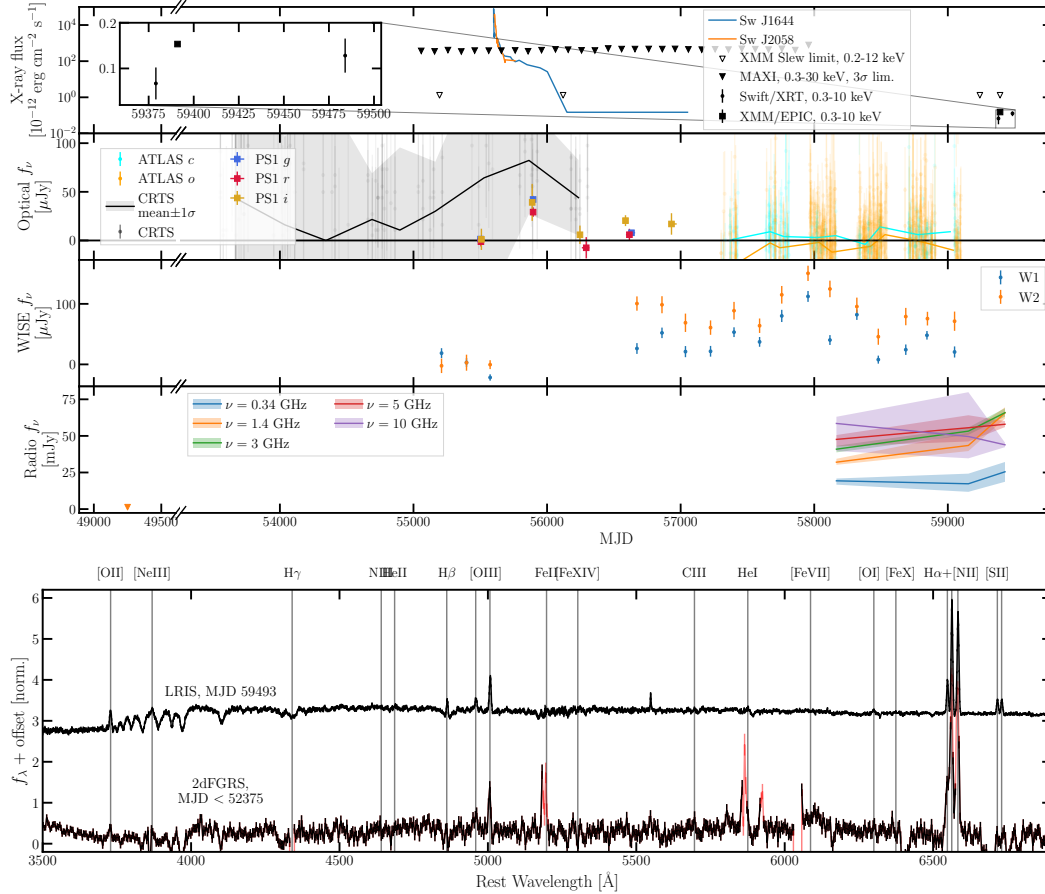


Figure 2.1: (*top*) From top to bottom, X-ray, optical, mid-infrared, and radio lightcurves for VT J0243. In the topmost panel, the black triangles represent three sigma upper limits from the MAXI and XMM slew surveys. The squares and circles show recent detections by Swift/XRT and XMM/EPIC, and the inset axis magnifies this data. The colored lines show the X-ray lightcurves for two of the three X-ray detected jetted TDEs, Sw J1644+57 (1) and Sw J2058+05 (2). We do not show the X-ray lightcurve for the final X-ray detected jetted TDE, Sw J1112-8283 (3), as it largely overlaps with the Sw J1644+57 lightcurve but is poorly sampled in comparison. Regardless of the binning of the MAXI observations, an X-ray flare of the same luminosity as those detected for previous jetted TDEs would have been detected in the first  $\sim 100$  days. An optical flare is detected in PanSTARRS around MJD 56000. The MIR emission is measured using forced photometry on NEOWISE images, and is variable. The MIR color appears to have reddened after the first three epochs. The radio lightcurves are extrapolated from the model fits described in Section 2.4, and the non-detection on the far left of the plot corresponds to the 1990 NVSS observation. (*bottom*) LRIS (*top*) and 2dFGRS (*bottom*) optical spectra, normalized. The red regions of each spectrum show wavelengths flagged by the respective reduction pipelines. No significant transient features are detected. No broad emission lines are significantly detected. The emission line ratios are consistent with weak Seyfert emission on a BPT diagram.

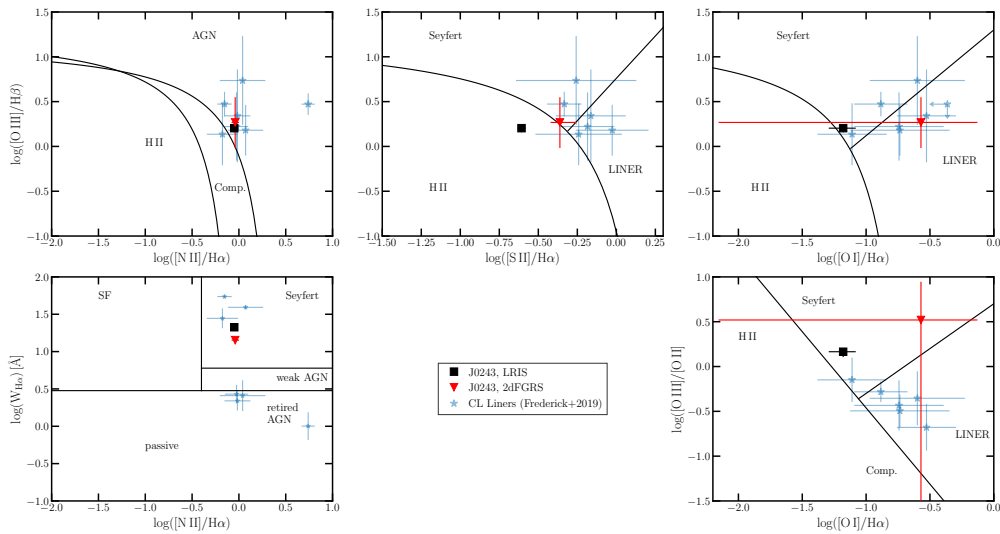


Figure 2.2: Five versions of the BPT diagram (4–6), following Figure 13 from (199). Line ratios measured from the LRIS (2dFGRS) observations of 2dFGRS TGS314Z138 are shown as black squares (red triangles). 2dFGRS TGS314Z138 is consistent with a Seyfert in most of the diagrams.

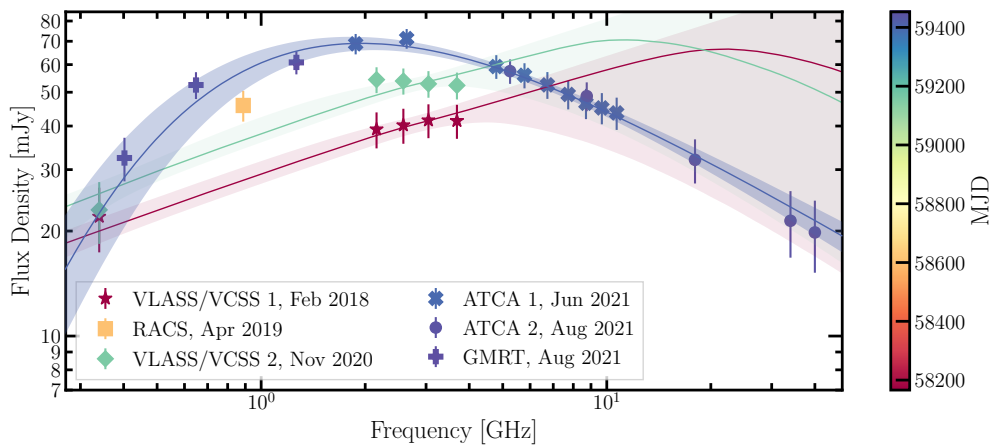


Figure 2.3: The evolution of VT J0243's radio SED. The circles with errorbars correspond to our observations, and are colored with the observation epoch. We fit a synchrotron model to the three main observation epochs (see Section 2.4 for details), and show the best-fit model and  $1\sigma$  errors as lines and bands.

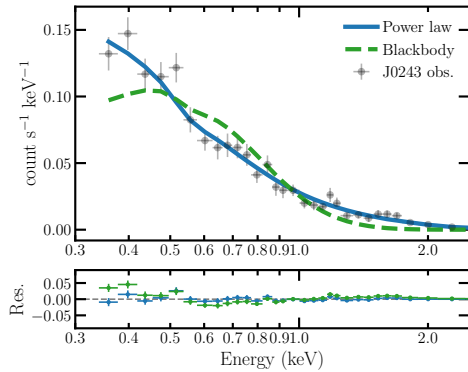


Figure 2.4: The *XMM-Newton* x-ray spectrum for 2dFGRS TGS314Z138. The observations are the black points, while the lines show model fits. The emission is most consistent with a power law model with little intrinsic hydrogen column density.

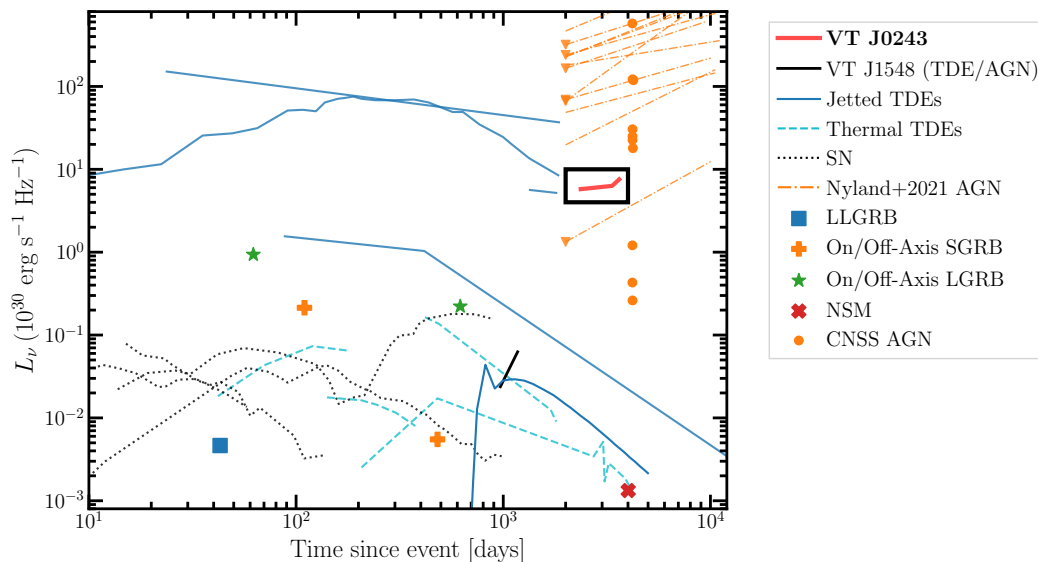


Figure 2.5: Radio light curves (lines) and typical durations/luminosities (squares) for classes of radio transients. The squares are retrieved from (218) and are measured at 1.4 GHz. The TDE lightcurves are from (150, 219, 220), and references therein, and are largely at 5 GHz. The SN lightcurves are at 5 – 8 GHz, are from (221–224). The lightcurve for VT J1548 is measured at 3 GHz (163). For comparison, the 5 GHz lightcurve of VT J0243 is shown in red, assuming the flare was launched around MJD 56000. This source is of comparable brightness to jetted TDEs, but is still rising whereas previous events began fading by  $\sim 1,000$  days post-event. It is also at a comparable luminosity to the newly radio loud AGN from (157), shown as orange circles, and the radio variable AGN from (154), which are shown as orange dot-dashed light curves. The triangles in the light curves denote upper limits. We have arbitrarily chosen the start date of these AGN flares for ease of comparison to VT J0243.

*Chapter 3*

THE NASCENT MILLIQUASAR VT J154843.06+220812.6:  
TIDAL DISRUPTION EVENT OR EXTREME  
ACCRETION-STATE CHANGE?

Somalwar, J. J. et al. (Apr. 2022). In: ApJ 929, 184 doi: 10.3847/1538-4357/ac5e29

Jean J. Somalwar<sup>1</sup>, Vikram Ravi<sup>1</sup>, Dillon Z. Dong<sup>1</sup>, Matthew Graham<sup>1</sup>, Gregg Hallinan<sup>1</sup>, Casey Law<sup>1</sup>, Wenbin Lu<sup>2</sup>, and Steven T. Myers<sup>3</sup>

<sup>1</sup>Cahill Center for Astronomy and Astrophysics, MC 249-17 California Institute of Technology, Pasadena CA 91125, USA.

<sup>2</sup>Department of Astrophysical Sciences, 4 Ivy Lane, Princeton University, Princeton, NJ 08544, USA

<sup>3</sup>National Radio Astronomy Observatory, P.O. Box O, Socorro, NM 87801, USA

**Abstract**

We present detailed multiwavelength follow up of a nuclear radio flare, VT J154843.06+220812.6, hereafter VT J1548. VT J1548 was selected as a  $\sim 1$  mJy radio flare in 3 GHz observations from the VLA Sky Survey (VLASS). It is located in the nucleus of a low mass ( $\log M_{\text{BH}}/M_{\odot} \sim 6$ ) host galaxy with weak or no past AGN activity. VT J1548 is associated with a slow rising (multiple year), bright mid IR flare in the WISE survey, peaking at  $\sim 10\%L_{\text{edd}}$ . No associated optical transient is detected, although we cannot rule out a short, early optical flare given the limited data available. Constant late time ( $\sim 3$  years post-flare) X-ray emission is detected at  $\sim 10^{42}$  erg s<sup>-1</sup>. The radio SED is consistent with synchrotron emission from an outflow incident on an asymmetric medium. A follow-up, optical spectrum shows transient, bright, high-ionization coronal line emission ([Fe X]  $\lambda 6375$ , [Fe XI]  $\lambda 7894$ , [S XII]  $\lambda 7612$ ). Transient broad H $\alpha$  is also detected but without corresponding broad H $\beta$  emission, suggesting high nuclear extinction. We interpret this event as either a tidal disruption event or an extreme flare of an active galactic nucleus, in both cases obscured by a dusty torus. Although these individual properties have been observed in previous transients, the combination is unprecedented. This event highlights the importance of searches across all wave bands for assembling a sample of nuclear flares that spans the range of observable

properties and possible triggers.

### 3.1 Introduction

Supermassive black holes (SMBHs) at the centers of galaxies power myriad observable phenomena across cosmic time. The evolution of galaxies is closely linked to SMBH activity (e.g. 47). Active galactic nuclei (AGN), which have actively accreting SMBHs at their centers, produce bright multiwavelength emission due to the presence of an accretion disk and, in many cases, an associated jet or outflow (256).

Quiescent or only weakly accreting SMBHs are challenging to study because of their dim or nonexistent emission. The recent advent of high cadence photometric and spectroscopic surveys has enabled the discovery of large samples of tidal disruption events (TDEs), which occur when a star is disrupted as it enters the tidal radius of an SMBH, given by  $R_T \sim R_*(M_{\text{BH}}/M_*)^{1/3}$  for a black hole of mass  $M_{\text{BH}}$  and a star of radius (mass)  $R_*(M_*)$  (e.g. 110, 123, 128, 130, 243, 244, 257). TDEs provide a key probe of the SMBHs and nuclear regions in quiescent galaxies: among many insights, they enable measurements of the dust covering factors in quiescent galaxies, the circum-nuclear density profile, and they may provide a new method of measuring the mass of low mass ( $\sim 10^6 M_\odot$ ) SMBHs (e.g. 144, 257–259). They are often observed as  $10^{41-45} \text{ erg s}^{-1}$  X-ray transients, which decay with the mass fallback rate as a  $t^{-5/3}$  power law (e.g. 118, 260, 261). The X-rays may originate directly from an accretion disk or via material forced inward at the nozzle shock close to pericenter (e.g. 118, 262–264).

While the landscape of TDEs in quiescent galaxies is rapidly being mapped out, the evolution of a TDE in a galaxy with a pre-existing accretion disk is poorly understood (although, recent simulations are gaining ground, see 265). Given current knowledge, it is difficult, or in some cases impossible, to observationally differentiate between a nuclear flare caused by a TDE and one caused by an accretion-state change (see 266, for a review of possible distinguishing characteristics). This problem is made particularly challenging because of the many remaining mysteries in accretion disk physics: the magnitude of possible state changes due to accretion disk instabilities, their occurrence rate, and their multiwavelength properties are largely unknown (see 267, and references therein).

Thus, nuclear flares from galaxies with pre-existing accretion disks are particularly challenging to interpret. In galaxies where a pre-existing accretion disk cannot

be ruled out (i.e., those that are either weakly accreting or are quiescent but were accreting in the recent past), several aspects of the central SMBH and the inner few parsecs of the galaxy remain mysterious. For example, it is still not understood if, when, and how a dusty torus can form in a weakly accreting or non-accreting galaxy (e.g. 268, 269).

Progress in observationally mapping out the range and properties of nuclear flares from weakly accreting or recently accreting galaxies is advancing. For example, searches for transient line emission in the Sloan Digital Sky Survey (SDSS) spectroscopic survey (270) have unveiled a class dubbed the extreme coronal line emitters (ECLEs), which show bright, high ionization ( $\gtrsim 100$  eV) coronal emission lines (e.g., [Fe X]  $\lambda 6375$ , [Fe XIV]  $\lambda 5303$ ) (e.g. 271). These lines are excited by a transient, high-energy, photoionizing continuum and fade on  $\sim 3\text{--}5$  yr timescales (272).

Although most of the  $\sim 20$  known ECLEs are in quiescent galaxies (e.g. 14, 199, 271, 273, 274), an increasingly large subset are hosted by galaxies which lie in the grey area between strongly accreting AGN and quiescent galaxies. For example, ASASSN-18jld was a nuclear transient in a host galaxy with no clear evidence for AGN activity (275). Although this event had a TDE-like blue continuum and a high ratio of [Fe X] to [O III], it showed a non-monotonically declining optical light curve and a harder-while-fading X-ray spectrum that are both more typical of AGN activity. Likewise, the transient AT 2019avd showed strong coronal line emission alongside TDE-like transient features (e.g., soft X-ray emission, Bowen fluorescence lines, broad Balmer emission), and is located in an inactive galaxy (274). Its double peaked optical light curve is characteristic of AGN activity, although some exotic TDE models could predict similar behavior (274).

Originally, ECLEs were thought to be associated with TDEs, which can produce the requisite high energy continuum that would only illuminate the coronal line emitting region but not excite [O III] immediately because of light travel time effects (14). However, it is well known that AGN-like continua can produce coronal line emission since, before the discovery of ECLEs, coronal lines were most often observed from Seyfert galaxies of all types (e.g. 276–278).  $\sim 2/3$  of AGN across the range of activity levels show at least one coronal line in the near-infrared (NIR) (279). This fraction is poorly constrained in the optical because optical coronal lines are dim in most AGN, with the brightest [Fe VII]  $\lambda 6086$  lines no more than  $\sim 10\%$  of the [O III]  $\lambda 5007$  flux (280). An accretion state change could well replicate the ECLE phenomena.

Key evidence in understanding the possible triggers of ECLEs lies in their *multiwavelength* emission. ECLEs sometimes show transient, broad lines (FWHM $\sim$ 1000–2000 km s $^{-1}$ ), including hydrogen Balmer emission (e.g. 14). ECLEs have been associated with optical/UV flares, which begin before the coronal lines appear (199, 281). Many ECLEs have been associated with IR flares with luminosities  $\sim 10^{42-43}$  erg s $^{-1}$ , consistent with emission from dust (e.g. 282). The IR emission can fade on timescales as long as  $\sim 10$  years (e.g. 282). The radio emission from ECLEs, which can constrain the presence of a nascent jet or outflow, is practically unconstrained. Note that the relative frequency of the different multi-wavelength signatures in galaxies that may have pre-existing accretion disks and those that are quiescent is unknown.

More conclusive constraints on the trigger(s) of ECLEs require a large sample of events with minimal selection biases. Searches based on evolving optical spectral features may miss objects similar to the ECLEs but with dimmer coronal line emission. The multi-wavelength, transient emission from ECLEs will allow us to understand the full range of possible triggers and host properties.

In this work, we present the first radio selected ECLE, SDSS J154843.06+220812.6, hereafter SDSS J1548. SDSS J1548 shows weak or no evidence for accretion, so we cannot confirm or exclude the presence of a pre-existing accretion disk. SDSS J1548 was identified by (131) as the host of a bright nuclear MIR flare. Independently, we selected SDSS J1548 as part of our ongoing effort to compile a sample of radio-selected TDE candidates using the VLA Sky Survey (VLASS; (133)). We performed an extensive follow up campaign, during which we identified this object as an ECLE with additional broad Balmer features. It is X-ray bright, although, intriguingly, it shows no optical flare in the available data. The transient emission appears to evolve on long ( $\sim$ year) timescales.

We present multi-wavelength observations of SDSS J1548 and the associated transient, which we label VT J1548+2208 (VT J1548 hereafter). In Section 3.2, we describe our target selection. In Section 3.3, we detail both the archival and follow-up observations and data reduction. In Section 3.4, we describe the non-transient galactic-scale properties of SDSS J1548. In Sections 3.5 and 3.6 we discuss the transient emission associated with VT J1548. Finally, in Section 3.7 we consider the possible origins (i.e., TDE, AGN-related activity) of VT J1548, and in Section 3.8 we conclude.

We adopt a standard flat  $\Lambda$ CDM model with  $H_0 = 70$  km s $^{-1}$  Mpc $^{-1}$  and  $\Omega_m = 0.3$ .

All magnitudes are reported in the AB system unless otherwise specified.

### 3.2 Target Selection

We selected VT J1548 during our search for radio-bright TDE candidates using the Karl G. Jansky Very Large Array (VLA) Sky Survey (VLASS; also see (283) for the first discussion of the possibility of searching for TDEs as radio transients). VLASS is a full-sky, radio survey ( $\delta > -40^\circ$ , 2 – 4 GHz; (133)). Each VLASS pointing will be observed three times. The first epoch (E1) was completed between 2017–2018 and the second (E2) is halfway done ( $\sim 2020$ –present). VLASS is optimal for studies of radio-emitting TDEs because it is sensitive ( $\sim 0.13$  mJy) and has a high angular resolution that allows for source localization to galactic nuclei ( $\sim 2.5''$ , with variations with declination and hour angle).

Dong et al., in prep., developed a pipeline to robustly identify radio transients with VLASS, which we used to select radio TDE candidates. We will describe the source detection and photometry in detail in that work; we provide a brief summary in Appendix 3.9.

We selected TDE candidates as nuclear VLASS transients ( $< 3''$  from the center of a Pan-STARRS source; (175, 284)) with no archival radio detections ( $> 3''$  from a source in the NVSS or FIRST catalogues; (161, 285, 286)). We inspect all crossmatches to ensure that the radio transient is located on a galaxy, rather than a star. After this initial selection, we verified that each source was nuclear using precise positions from VLA follow up. We required the stellar mass of the host galaxy, measured using an SED fit (Section 3.4), to be consistent with  $\log M_{\text{BH}}/M_\odot \lesssim 8$  according to the stellar mass - SMBH mass relation from (38) (i.e.,  $\log M_*/M_\odot \lesssim 12$ ). For SMBH masses  $\log M_{\text{BH}}/M_\odot \gtrsim 8$ , stars will be captured whole rather than be disrupted because the Hill radius is comparable to the tidal radius (110). After this initial selection, we carefully inspected the archival radio images to ensure there are no detections (sub-threshold or otherwise) that are at a position consistent with the VLASS position. We will present the full sample of radio selected TDE candidates in future papers. In this paper, and other in prep. work, we present individual, unique candidates, including VT J1548.

### 3.3 Observations and Data Reduction

After identifying VT J1548 as a promising TDE candidate, we performed extensive, multi-wavelength follow up. In this section, we describe the observations and data reduction. We also present the available archival data. Detailed data analysis

and interpretation will be described in later sections. Figure 3.3 summarizes the observation timeline.

### Radio Observations

SDSS J1548 was undetected in the NVSS and FIRST radio surveys (161, 285, 286). Most recently, it was observed on MJD 58046 (Oct. 15, 2018) during VLASS E1 with a  $3\sigma$  upper limit  $f_\nu(3\text{ GHz}) < 0.36$  mJy. VT J1548 was first detected in the radio during VLASS E2 on MJD 59068 (Aug. 7, 2020) with  $f_\nu(3\text{ GHz}) = 1.12 \pm 0.15$  mJy.

We obtained a broadband (0.3–20 GHz) radio SED for VT J1548 on MJD 59273 (Feb. 28, 2021) as part of program 20B-393 (PI: Dong). We reduced the data using the Common Astronomy Software Applications (CASA) with standard procedures. VT J1548 was detected in the L, S, C, and X bands and undetected in the P band.

### Optical/IR Light Curve

SDSS J1548 is in the survey area of the NEOWISE and Zwicky Transient Facility (ZTF) surveys (124–127). NEOWISE has observed SDSS J1548 in the W1 (3.4  $\mu\text{m}$ ) and W2 (4.6  $\mu\text{m}$ ) bands with a cadence of  $\sim 6$  months since MJD  $\sim 56700$ . Each epoch consists of  $\sim 12$  exposures. We downloaded the NEOWISE photometry from [irsa.ipac.caltech.edu](http://irsa.ipac.caltech.edu). The lightcurve is shown in Figure 3.3. SDSS J1548 flared brightly in NEOWISE beginning on MJD  $\sim 58100$  (Mar. 23 2018). It increased from  $W1/W2 \sim 13.6/13.6$  mag (native Vega system) to  $W1/W2 \sim 11.2/10.3$  mag (native Vega system) in  $\sim 900$  days and had not begun to fade by the most recent observation (MJD 59049; Jul. 19 2020). The peak flux of the flare was  $\gg 5\sigma_{\text{quies.}}$ , where  $\sigma_{\text{quies.}}$  was the root-mean-square variability in the pre-flare NEOWISE data.

ZTF is a high cadence optical transient survey. SDSS J1548 was observed as part of the public MSIP survey (287), which observes the full northern sky every three nights in the  $gr$  filters. We used the IPAC forced photometry service (288) to download the optical light curve, and processed it using the recommended signal-to-noise cuts<sup>1</sup>. No optical transient is detected in the available data, although we may have missed the transient because of poor coverage. MJD 57500–58000 is only covered by the ATLAS survey, but the ATLAS coverage has a gap between MJD 57650–57750, and it is possible that an optical transient would be undetected if it occurred near 57500 and contaminated the ATLAS reference images. Assuming no

<sup>1</sup><http://web.ipac.caltech.edu/staff/fmasci/ztf/forcedphot.pdf>

systematic problems in the photometry that may mask a flare, we can exclude an optical transient that peaks during the ATLAS coverage with a flux density brighter than  $\sim 0.6$  mJy ( $L \lesssim 6 \times 10^{42}$  erg s $^{-1}$ ) at the  $5\sigma$  level in the ATLAS  $o$  band. This constraint rules out a flare similar to those in optically-selected TDEs (128), unless it occurred between MJD 57650–57750.

### X-ray Observations

SDSS J1548 is not detected in any archival X-ray catalogs, including the Second ROSAT All-Sky Survey Point Source Catalog (183, 184). The best limit on the host galaxy X-ray flux is from a serendipitous 17.9 ks *XMM-Newton* exposure  $\sim 100$  days before the first VLASS epoch (PI: Seacrest, MJD 57950; Jul. 16 2017). We retrieved the Processing Pipeline System (PPS) products from the *XMM-Newton* archive. The PPS products have already been reduced using standard procedures with the most up-to-date pipeline and calibration files. We used the `ximage sosta` tool to measure the source flux at the location of SDSS J1548 on the EPIC-PN and MOS2 0.2 – 12 keV images (289). (SDSS J1548 was not in the field-of-view of the EPIC-MOS1 image.) We used the recommended source box size. However, SDSS J1548 is near the edge of both images, so the recommended background box sizes extended off the image. We manually drew background boxes of different sizes centered on/near the source and measured the intensity in each case, to verify that our choice did not affect our result. The source was undetected, with a  $3\sigma$  upper limit on the 0.2 – 10 keV flux of  $\sim 10^{-13}$  erg cm $^{-2}$  s $^{-1}$ . We get a similar upper limit using both the PN and MOS1 images, which suggests that our result is not strongly affected by the fact that the source is near the image edge.

SDSS J1548 was observed three times (MJD 59127/Oct. 5 2020, 59281/Mar. 8 2021, 59388/Jun. 23 2021) post-flare with  $\sim 2$  ks exposures by the Swift X-ray Telescope (Swift/XRT; (188)). The final epoch was a target of opportunity (ToO) observation requested by our group. The first two observations are ToOs (PI Dou) that we found during a search of the Swift archive. The data were reduced using the Swift HEASOFT online reduction pipeline<sup>2</sup> with default settings to generate a lightcurve at the position of SDSS J1548 (290). There is no significant evolution between observations.

*XMM-Newton* observed SDSS J1548 on MJD 59457 for a duration of 30 ks with the EPIC camera using the thin filters in full frame mode. We retrieved the Processing

<sup>2</sup>[https://www.swift.ac.uk/user\\_objects/index.php](https://www.swift.ac.uk/user_objects/index.php)

Pipeline Subsystem (PPS) products and extracted a PN spectrum at the location of VT J1548 using standard procedures. The spectrum is shown in Figure 3.9 and we discuss it in Section 3.6.

### Optical Spectroscopy

SDSS J1548 was observed on MJD 53556 (Jul. 5 2005) as part of the SDSS Spectroscopic Survey (270). We retrieved the archival optical spectrum from the SDSS archive. After identifying SDSS J1548 as a transient host, we observed it with the Keck I Low Resolution Image Spectrometer (LRIS; (182)) on MJD 59259 (Feb. 14 2021) and 59348 (May 14 2021) with exposure times of 10 and 30 min. respectively. Because of poor seeing, we used the 1.5'' slit for the first epoch, but we used the 1.0'' slit for the second epoch. The slit positions are shown in Figure 3.1. For both epochs, we used the 400/3400 grism, the 400/8500 grating with central wavelength 7830, and the 560 dichroic. This leads to a usable wavelength range of  $\sim 1300\text{--}10000\text{ \AA}$  and a resolution  $R\sim 700$ .

We reduced the first epoch of observations using the `lpipev2020.09` pipeline with default settings (291). The LRIS red CCD was upgraded before the second epoch of observations and was incompatible with earlier `lpipe` versions, so we reduced this deeper epoch using `lpipev2021.06 $\beta$` .

We observed SDSS J1548 on MJD 59371 (Jun. 6 2021) with the Echellette Spectrograph and Imager (ESI; (292)) on Keck II. ESI is optimal for velocity dispersion measurements because of its resolution, which can be as high as  $R \sim 13000$  ( $22.4\text{ km s}^{-1}$  FWHM) in echellette mode. ESI in echellette mode has a wavelength coverage  $\sim 0.4 - 1.1\text{ }\mu\text{m}$ . We exposed for 25 minutes using the 0.3'' slit. The slit positioning is shown in Figure 3.1. We reduced the observations using the `makee` pipeline with the standard star Feige 34. We used default settings, except to adjust the spectral extraction aperture, as described in Appendix 3.9.

### 3.4 Host Galaxy Analysis

In this section, we describe SDSS J1548, the host galaxy of VT J1548. SDSS J1548 is at redshift  $z \sim 0.031$  ( $d_L \sim 137\text{ Mpc}$ ). Figure 3.1 shows a *zrg* image of SDSS J1548. We have noted the cataloged position of the galaxy nucleus (189) and the radio transient position from our VLA follow up. The radio transient is consistent with being nuclear.

SDSS J1548 is classified as an elliptical or S0 galaxy with a *g*-band semi-major

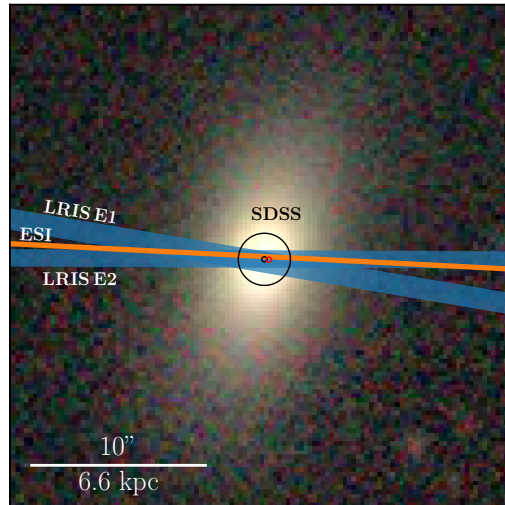


Figure 3.1:  $zrg$  image of SDSS J1548, the host galaxy of the radio transient VT J1548. The optical nucleus is shown as a small red circle and the radio transient position is shown as small black circle. The circle radii show approximate  $3\sigma$  statistical uncertainties. Systematic reference-frame uncertainties are not included. The radio transient is consistent with being nuclear. The blue rectangles show the slit positions for LRIS follow up and the orange rectangles shows that for ESI follow up. Image from the Legacy Survey (7).

half-light axis  $\sim 1.8$  kpc (293, 294). It is bulge-dominated, with a  $g$ - ( $r$ -) band bulge-to-disk ratio  $B/T = 0.7(0.73)$  (294). The bulge-dominated morphology is unusual for ECLEs — the known ECLEs are largely located in intermediate-luminosity disk galaxies with no apparent bulge in SDSS imaging (14).

We measured the galaxy stellar mass using an SED fit following (128) and (295). We retrieved archival photometry from the GALEX (FUV, NUV; (296, 297)), SDSS ( $ugriz$ ; (298)), and WISE ( $W1$ ,  $W2$ ; (12)) surveys. We used `prospector` (190), a Bayesian wrapper for the `fsps` stellar population synthesis tool (191, 192), with a (193) IMF, a  $\tau$ -model star formation history, and the (194) attenuation curve. We fixed the redshift to the best-fit redshift from the LRIS spectrum (0.031; Appendix 3.9). We fit the SED using the `emcee` Monte Carlo Chain Ensemble sampler (195) with 500 (burn-in) + 1000 steps. The best-fit stellar mass is reported in Table 3.1. Our best-fit parameters are consistent with cataloged SED fits of this source from SDSS. We relate the stellar mass to the SMBH mass using the empirically derived  $M_* - M_{\text{BH}}$  relation from (38). We find  $\log M_{\text{BH}} \sim 7.1 \pm 0.79$ , where the uncertainty is dominated by intrinsic scatter in the relation. Alternatively, we can relate the bulge mass to the SMBH mass using the  $M_{\text{bulge}} - M_{\text{BH}}$  relation from

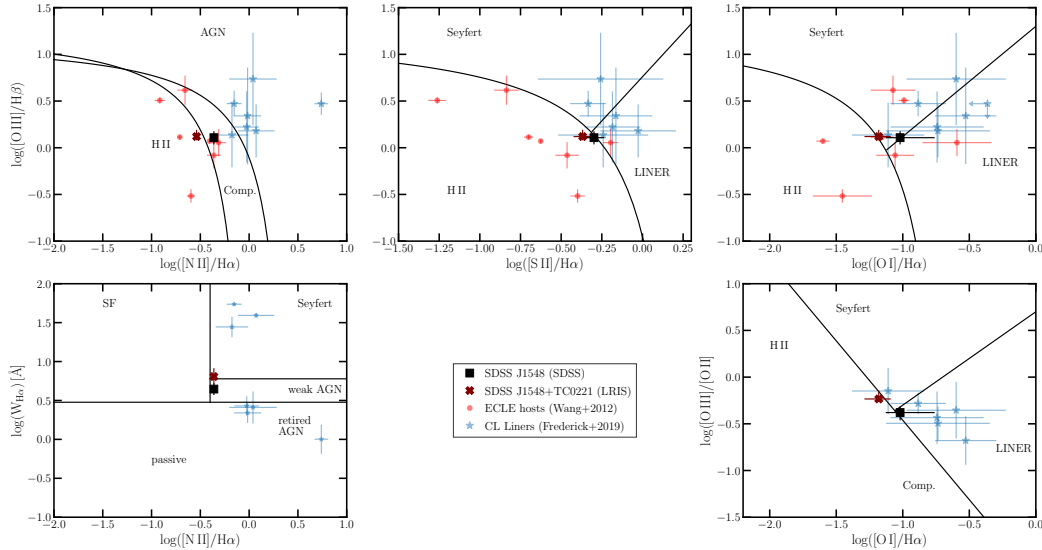


Figure 3.2: Five variations of the BPT diagram (4–6), following Figure 13 from (199). The SDSS measurements of SDSS J1548 are shown as a black square, while the LRIS measurements are shown as a reddish cross. Where possible, we include the changing look LINERs from (199) and the ECLEs from (14) for comparison. SDSS J1548 has weak or no AGN activity.

(47). We estimate the bulge mass using the bulge-to-disk ratio above, and find  $M_{\text{BH}} = 7.51 \pm 0.32$ .

The SMBH mass is more tightly correlated with the bulge velocity dispersion ( $\sigma_*$ ) than  $M_*$ . We measured  $\sigma_*$  from the high resolution ESI spectrum and find an SMBH mass  $\log M_{\text{BH}}/M_{\odot} = 6.48 \pm 0.33$ , as described in Appendix 3.9. The error is dominated by intrinsic uncertainty in the  $M_{\text{BH}} - \sigma_*$  relation. This SMBH mass is consistent with that measured by (131) using the lower resolution archival SDSS spectrum. It corresponds to an Eddington luminosity of  $3 \times 10^{44} \text{ erg s}^{-1}$  (112).

Next, we constrain any prior AGN activity in SDSS J1548. The archival SDSS spectrum is shown in the bottom panel of Figure 3.3. It has many narrow features, including the Balmer series, [O III]  $\lambda 5007$ , [N II]  $\lambda 6548, 6584$ , and [S II]  $\lambda 6713, 6731$ , but no broad emission. We fit the narrow lines following Appendix 3.9 and the fluxes are tabulated in Table 3.2. Figure 3.2 shows five variations of the BPT diagrams, which classify galaxies according to their AGN activity (4–6). We plot the ECLE hosts from (14) and changing look (CL) LINERs from (199), where possible. The CL LINER sample includes one ECLE (see discussion in Section 3.7). SDSS J1548 lies between the ECLE and CL LINER samples. It is consistent with weak or no AGN emission.

The WISE color of a galaxy (pre-transient) provides an additional constraint on its AGN activity (200). The WISE color  $W1-W2= 0.055$  ( $W1/W2 = 13.625 \pm 0.025/13.570 \pm 0.029$ ) is inconsistent with typical AGN, which have  $W1-W2 \gtrsim 0.8$  (200). Hence, SDSS J1548 may be quiescent or weakly active. Note that the current NEOWISE color ( $W1-W2 \sim 0.9$ ) is in the AGN regime.

Table 3.1: Host Galaxy

Parameter	Value
R.A.	15:48:43.06
Dec.	22:08:12.84
Redshift $z$	0.031
$d_L$	137 Mpc
$\log M_*/M_\odot$	$10.15^{+0.07}_{-0.07}$
$\log M_{\text{BH}}/M_\odot$ (from $M_{\text{BH}} - \sigma_*$ )	$6.48 \pm 0.33$

**Notes.** R.A. and Dec. are from the SDSS imaging survey (189). Redshift is as measured in our work. The stellar mass is derived from an SED fit. SMBH mass is measured using the velocity dispersion and the (47)  $M_{\text{BH}} - \sigma_*$  relation.

Finally, SDSS J1548 is within the virial radius of a small group (total halo mass  $\sim 10^{11.5} M_\odot$ ; (299)). SDSS J1548 shows no obvious evidence for a disturbed morphology indicative of a recent interaction or merger.

### 3.5 Analysis of transient spectral features

Next, we consider the transient emission associated with VT J1548, summarized in Figure 3.3. We begin by describing the transient spectral features, which will inform our discussion of the broadband emission in the next section. We identify transient lines as those present in the LRIS spectra but not in the SDSS spectrum.

First, we provide a brief summary of the transient features. The following subsections will analyze specific features in detail. The line fluxes for each observation epoch, measured using the procedure described in Appendix 3.9, are listed in Table 3.2.

VT J1548 was associated with the appearance of strong, high-ionization coronal line emission. We detect [Fe X]  $\lambda 6375$ , [Fe XI]  $\lambda 7892$ , and [S XII]  $\lambda 7611$ . [Fe XIV]  $\lambda 5303$  is marginally detected, and we do not observe any [Fe VII] emission. The coronal lines are all double peaked, with two roughly equal flux components separated by  $\sim 230 \text{ km s}^{-1}$ . We will discuss these lines in detail in Section 3.5. We also detect a broad  $\text{H}\alpha$  component ( $\text{FWHM} \sim 1900 \text{ km s}^{-1}$ ), although we do not

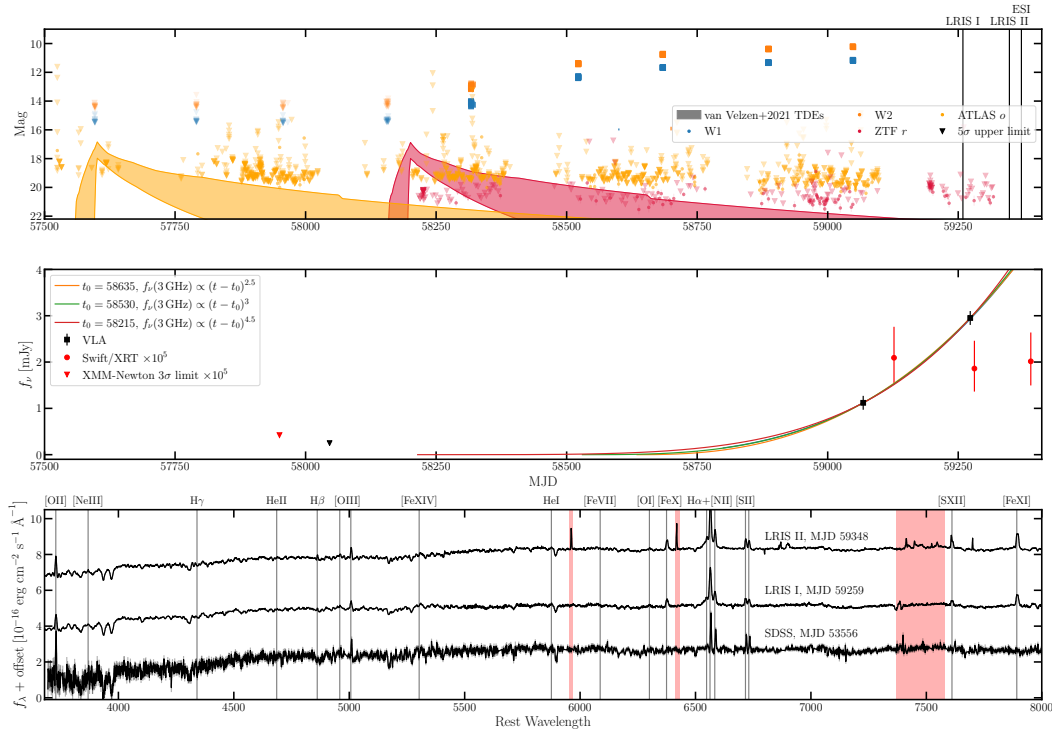


Figure 3.3: A summary of the observations of SDSS J1548. (*top*) The optical and IR light curves for SDSS J1548. IR magnitudes are in their native Vega system, whereas optical magnitudes are in their native AB system. The IR light curve flares by  $\sim 2 - 3$  mag beginning around MJD 58100. There is no obvious optical flare, although gaps in survey coverage mean that we cannot rule one out. The optical upper limits are consistent with the tail of the best-fit blackbody to the IR emission. We overplot the range of fluxes expected in different bands (as denoted by the color of the band) from typical optical TDEs as shaded regions. We have adopted the models of ZTF optical TDE light curves from Table 6 of (128) with the appropriate distance for SDSS J1548 and extinction  $E(B - V)_{\text{nuc}} \sim 1$ . We plot the central  $\pm 1\sigma$  range of fluxes expected from these models. We shift the start date of the each band to be within the coverage of the corresponding survey but still consistent with the start of the WISE flare. (*middle*) The 3 GHz radio (black squares) and 0.2 – 10 keV X-ray light curves. Solid lines show power law fits to the radio light curve, with the launch date in each case noted in the legend. (*bottom*) The optical spectrum evolution. The late-time LRIS optical spectra show transient broad Balmer and coronal line emission. We highlight regions impacted by reduction problems in red.

detect the corresponding  $H\beta$  feature (Section 3.5). We refrain from a detailed line flux evolution analysis because the flux calibration may be imperfect. The transient line fluxes agree within  $2\sigma$  between the LRIS observations. The lines which are present in all observations (SDSS+LRIS) do not evolve between epochs, except that the narrow  $H\alpha$  brightens. This brightening could be caused by the changing slit widths if the  $H\alpha$  is extended, so we do not consider it further.

He II  $\lambda 4686$  is commonly observed in TDE candidates accompanied by N III  $\lambda 4640$  due to the Bowen fluorescence mechanism (112). We do not observe these lines. [Fe II] lines are abundant in Seyferts but are undetected from VT J1548 (300).

### Coronal line emission

The strongest observed coronal lines are [Fe X]  $\lambda 6375$  (ionization potential 262.1 eV), [Fe XI]  $\lambda 7894$  (IP 290.9 eV), and [S XII]  $\lambda 7612$  (IP 564.41 eV) with luminosities  $(1.2, 2.3, 1.3) \times 10^{39}$  erg  $s^{-1}$ , respectively (we have summed over all velocity components, see discussion later in this section). The [O III]  $\lambda 5007$  luminosity is  $\sim 1.2 \times 10^{39}$  erg  $s^{-1}$ . The [Fe X] to [O III] ratio of  $\sim 1$  is unprecedented for “standard” Seyferts, which typically have coronal line luminosities that are a factor of  $\sim 100$  dimmer than [O III] (see Figure 5 of (14)). These fluxes are also marginally dimmer than observed in other ECLEs, which have  $L_{\text{Fe X, lit.}} \gtrsim 3 \times 10^{39}$  erg  $s^{-1}$  despite similarly low SMBH masses (14). Selection effects may explain the brighter coronal lines in many ECLEs. Alternatively, VT J1548 may be more obscured than the (14) ECLEs.

We marginally detect [Fe XIV]  $\lambda 5303$  at  $<2\sigma$  significance. Most ECLEs with [Fe XIV]  $\lambda 5303$  emission have  $L_{\text{[Fe XIV]}} \gtrsim 0.1 L_{\text{[Fe X]}}$  (14). We expect sufficiently high energy photons to ionize [Fe XIV] because it has a lower ionization potential than the bright [S XII] line. Extinction could weaken the [Fe XIV] emission: [Fe XIV] is the bluest of the coronal lines. If the coronal lines are heavily extinguished, like the broad Balmer emission (see next section), the [Fe XIV] line could be extinguished by a factor of  $\sim 1.5 - 2$  relative to [Fe X]. This extinction is unlikely to affect the ECLE classification because reducing the [Fe X] to [O III] ratio by a factor of ten would require  $E(B - V) \gtrsim 5$ .

We do not detect [Fe VII] emission although it has a low ionization potential (14). There are a number of ECLEs with undetected [Fe VII], and most have been attributed to TDEs (14). These ECLEs tend to be galaxies that are less luminous and lower mass than those with detected [Fe VII], which is consistent with the low

Table 3.2: Optical Emission Line Strengths

Line	SDSS	LRIS I	LRIS II
H $\alpha$ (narrow)	15.60 <sup>+0.24</sup> <sub>-0.35</sub>	16.95 <sup>+2.54</sup> <sub>-2.78</sub>	23.34 <sup>+0.09</sup> <sub>-0.15</sub>
H $\alpha$ (2060 km s <sup>-1</sup> )	–	18.09 <sup>+3.84</sup> <sub>-4.22</sub>	26.32 <sup>+1.37</sup> <sub>-1.48</sub>
H $\beta$	4.69 <sup>+0.61</sup> <sub>-0.61</sub>	3.88 <sup>+0.50</sup> <sub>-0.39</sub>	3.84 <sup>+0.35</sup> <sub>-0.31</sub>
[O I] $\lambda$ 6300	1.49 <sup>+0.89</sup> <sub>-0.37</sub>	1.41 <sup>+0.27</sup> <sub>-0.23</sub>	1.54 <sup>+0.32</sup> <sub>-0.38</sub>
[Fe X] $\lambda$ 6375	–	2.31 <sup>+1.10</sup> <sub>-1.36</sub> /2.73 <sup>+0.64</sup> <sub>-1.71</sub>	3.18 <sup>+0.70</sup> <sub>-1.01</sub> /2.56 <sup>+0.62</sup> <sub>-1.97</sub>
[Fe XI] $\lambda$ 7894	–	3.94 <sup>+0.51</sup> <sub>-0.62</sub> /4.60 <sup>+0.40</sup> <sub>-0.52</sub>	5.37 <sup>+0.26</sup> <sub>-0.44</sub> /5.50 <sup>+0.29</sup> <sub>-0.46</sub>
[Fe XIV] $\lambda$ 5303	–	0.65 <sup>+3.31</sup> <sub>-0.42</sub>	0.50 <sup>+0.42</sup> <sub>-0.30</sub>
[S XII] $\lambda$ 7612	–	1.73 <sup>+0.31</sup> <sub>-0.32</sub> /1.55 <sup>+0.26</sup> <sub>-0.42</sub>	2.10 <sup>+0.19</sup> <sub>-0.23</sub> /3.95 <sup>+0.25</sup> <sub>-0.25</sub>
[O II] $\lambda\lambda$ 3726, 3729	14.40 <sup>+1.74</sup> <sub>-2.34</sub>	10.23 <sup>+0.59</sup> <sub>-0.41</sub>	8.67 <sup>+0.36</sup> <sub>-0.43</sub>
[O III] $\lambda$ 4959	2.35 <sup>+0.69</sup> <sub>-0.44</sub>	1.82 <sup>+0.31</sup> <sub>-0.49</sub>	1.66 <sup>+0.31</sup> <sub>-0.24</sub>
[O III] $\lambda$ 5007	6.01 <sup>+0.54</sup> <sub>-0.62</sub>	5.69 <sup>+0.48</sup> <sub>-0.25</sub>	5.06 <sup>+0.25</sup> <sub>-0.25</sub>
[N II] $\lambda$ 6548	2.15 <sup>+0.28</sup> <sub>-0.54</sub>	1.82 <sup>+0.79</sup> <sub>-0.73</sub>	1.34 <sup>+0.48</sup> <sub>-0.43</sub>
[N II] $\lambda$ 6584	6.79 <sup>+0.37</sup> <sub>-0.44</sub>	6.57 <sup>+0.48</sup> <sub>-0.56</sub>	6.75 <sup>+0.42</sup> <sub>-0.39</sub>
[S II] $\lambda$ 6716	3.84 <sup>+0.90</sup> <sub>-0.53</sub>	4.55 <sup>+0.82</sup> <sub>-0.83</sub>	5.39 <sup>+0.43</sup> <sub>-1.22</sub>
[S II] $\lambda$ 6731	4.01 <sup>+0.69</sup> <sub>-0.74</sub>	4.51 <sup>+0.81</sup> <sub>-0.80</sub>	4.61 <sup>+1.21</sup> <sub>-0.38</sub>

**Notes.** Line fluxes are reported in units of  $10^{-16}$  erg cm<sup>-2</sup> s<sup>-1</sup>. While we report absolute fluxes, the flux calibration is likely imperfect. Double-peaked lines (e.g., Fe X) have two reported fluxes which correspond to the blue and red peaks, respectively.

SMBH mass measured for SDSS J1548 (*14*). Moreover, if they are associated with an optical flare, the flare is dimmer than in those galaxies with [Fe VII] detections (*14*). The low statistics in current ECLE samples render these trends inconclusive.

(*14*) suggest that [Fe VII] dim ECLEs can be explained if either the [Fe VII] is collisionally de-excited because of its low critical density ( $10^{6-7}$  cm<sup>-3</sup> compared to  $> 10^9$  cm<sup>-3</sup> for the higher ionization iron lines), or if the X-ray SED is sufficiently bright and peaked above  $\sim 250$  eV so that higher ionization states are favored. The first scenario is disfavored if coronal line emission from ECLEs is produced analogously to that in Seyfert galaxies. In Seyferts, [Fe VII] is expected to be emitted from gas which is lower density and more extended than that which emits the higher ionization Fe lines. For example, (*278*) suggest that the coronal line-emitting gas is embedded in a wind, and the [Fe VII] emitting gas is upstream of the gas which emits the higher ionization Fe lines. If this model also applies to ECLEs, it is unlikely that *all* of the coronal line-emitting gas is above the [Fe VII] critical density.

An excess of soft photons can cause a high [Fe X]/[Fe VII] ratio. (*278*) discuss a few Seyferts with high [Fe X]/[Fe VII] which also have high [Fe X]/[O III] ratios

(although not as extreme as ECLEs) and broad  $H\alpha$  FWHM which are narrower than expected ( $\sim 750 \text{ km s}^{-1}$ ). They argue that these extreme ratios are related to the X-ray SED shape. A soft excess which drops off around 100 eV would cause  $[\text{Fe X}]/[\text{Fe VII}]$  to be high, although it is unclear whether this would explain the extreme ratios observed in  $[\text{Fe VII}]$  dim ECLEs. Alternatively, the soft excess can continue below 100 eV if the  $[\text{Fe VII}]$  emitting gas is obscured from the photoionizing source. As (*14*) discusses in the context of ECLEs, a very bright soft X-ray source that overionizes the coronal line-emitting gas could also explain the  $[\text{Fe VII}]$  non-detections.

Further insight into the origin of the coronal line emission comes from close inspection of the coronal line profiles in the high resolution ESI spectrum (Figure 3.4). Each coronal line contains two velocity components:  $[\text{Fe X}] \lambda 6375$ ,  $[\text{Fe XI}] \lambda 7894$ , and  $[\text{S XII}] \lambda 7612$  have velocity separations of  $215 \pm 8$ ,  $240 \pm 2$ , and  $230 \pm 6 \text{ km s}^{-1}$ , respectively. These velocities are roughly consistent within uncertainties ( $\lesssim 3\sigma$  variation). The individual components all have narrow widths  $50 - 60 \text{ km s}^{-1}$ . From the velocity separation of the velocity components, the coronal line-emitting gas may reside at  $\sim 1 \text{ pc}$  from the SMBH, which is consistent within a factor of a few with the constraints on the position of the MIR emitting dust, as will be described in Section 3.6.

Coronal lines in Seyferts are typically blueshifted (*278*). The blueshift is thought to indicate the ubiquitous presence of radiatively driven outflows from the AGN torus (*278*). In contrast, we observe both a red- and blueshifted component with roughly equal flux. Moreover, the linewidths of coronal lines in Seyferts are often broader than the  $[\text{O III}]$  linewidth, whereas we observe narrower coronal line emission. No other ECLE has a published optical spectrum with sufficiently high resolution to decompose the line profiles, although the coronal lines sometimes appear non-Gaussian in the available, low-resolution spectra (*14*). By eye, the published line profiles seem inconsistent with two, equal-flux peaks.

The coronal line gas could be entrained in and accelerated by the synchrotron emitting outflow (see Section 3.6), but the line widths are too narrow and the velocity difference between the components too small to favor this scenario. Alternatively, we may be observing rotating gas clouds at a radius  $\sim 1 \text{ pc}$ , corresponding to the velocity separation of the two components of the coronal lines, or an obscured, gaseous disk. The coronal line emitting clouds could also be moving in a radiation-driven outflow, as is thought to occur in Seyferts (*278*). We tentatively favor the final scenario

although, as we discussed above, the observed line profiles are different from those in typical Seyferts given that the radiatively driven outflow model has observational support in coronal-line-emitting Seyferts and the different profiles could result from a different geometry. Future observations of the line profile evolution and more detailed modelling, such as was done in (301) using CLOUDY, would constrain this scenario.

Next, we constrain the physical properties of the emitting region. We assume the emission is dominated by photoionized gas. This is a reasonable assumption because shocks only strongly contribute to coronal line emission for shock velocities  $\gtrsim 300$  km s<sup>-1</sup>, which is much larger than the coronal line widths (302). Photoionized gas is expected to be at a temperature  $\sim 10^5$  K (303), so we adopt this as our fiducial value.

First, we roughly estimate the emission measure of the gas following (273). Because the gas is photoionized, it must be optically thin to bound-free absorption of soft X-rays of energy  $\sim 1$  keV. We ignore collisional de-excitation to simplify the calculations. For a uniform emitting region of volume  $V$  with an ion (electron) density  $n_{i(e)}$ , the emission measure is given by  $EM = n_e n_i V$ . For a given ion  $i$ , The emission measure is related to the observed line luminosity  $L_i$ :  $EM = L_i / C_i(T)$ . Here,  $C_i(T)$  is the collisional strength for the relevant ion at the gas temperature  $T \sim 10^5$  K. We retrieve the collision strengths from the CHIANTI archive (304, 305). We find that the emission measures for each strong coronal line are similar, with  $EM_{CL} \sim 10^{58-59}$  cm<sup>-3</sup>. Assuming the gas has solar abundances, the sulfur and iron abundances are both  $n/n_H \sim 10^{-5}$  (306). We assume both sulfur and iron are dominantly in the observed highly ionized states. Then, we can write  $n_e n_H V \sim n_H^2 V \sim 10^{64}$  cm<sup>-3</sup> and

$$V = \frac{4}{3}\pi R^3 = 10^{46} \text{ cm}^3 \left( \frac{n_H}{10^9 \text{ cm}^{-3}} \right)^{-2}, \quad (3.1)$$

$$R = 1.3 \times 10^{15} \text{ cm} \left( \frac{n_H}{10^9 \text{ cm}^{-3}} \right)^{-2/3}, \quad (3.2)$$

$$M = m_H n_H V = 8.4 \times 10^{-3} M_\odot \left( \frac{n_H}{10^9 \text{ cm}^{-3}} \right)^{-1}. \quad (3.3)$$

We adopt a distance  $\sim 0.8$  pc based on the coronal line widths. The coronal line-emitting gas may be at a different distance if it is outflowing, but given the low velocity we do not expect the true distance to be changed by more than a factor of a few. With this assumption, the gas must have  $R \lesssim 0.8$  pc or  $n_H \gtrsim 10^4$  cm<sup>-3</sup>. The

detection of [Fe X] emission requires  $n_H \lesssim 10^9 \text{ cm}^{-3}$ , which is the critical density of that line. This density range corresponds to  $8.4 \times 10^{-3} M_\odot \lesssim M \lesssim 800$ . The large mass at the upper bound leads us to favor a higher density than  $\sim 10^4 \text{ cm}^{-3}$ . The gas column density is  $10^{22} \lesssim N_H/\text{cm}^{-2} \lesssim 10^{24}$ .

For column densities above a few times  $10^{23} \text{ cm}^{-2}$  the gas is optically thick to X-rays. We require optically thin gas. If the gas is clumpy or in a thin shell, the column density will be scaled by a factor of  $\xi^{2/3}$ , where  $\xi = \Delta R/R$  is the relative thickness of the shell or clumps. Likewise, the radius will scale by a factor of  $\xi^{-1/3}$ . If we adopt a column density  $\sim 10^{22} \text{ cm}^{-2}$ , we find  $\xi \sim 10^{-(3-5)}$ . Thus, either the coronal line-emitting gas has a very low density but fills a large volume, which is unlikely given the distinctly double peaked, narrow line profiles, or it is dense with a low covering factor. We favor the latter scenario.

Finally, we can constrain the soft X-ray flux required to power the coronal emission. In coronal line-emitting Seyferts, the coronal line luminosity is correlated with the flux in the soft X-ray photoionizing continuum (278). If we assume that ECLEs lie on this correlation, we can extrapolate to the required soft X-ray flux to power the observed coronal line emission. Given the Seyfert relation  $\log f_{\text{Fe X}}/f_X = -3.43 \pm 0.55$  (278), where  $f_{\text{Fe X}}$  is the flux in the [Fe X] line and  $f_X$  is the X-ray flux, we require a soft X-ray luminosity  $\sim 3 \times 10^{42} \text{ erg s}^{-1}$ . We will discuss the origins of this flare in more detail in Section 3.7.

In summary, we have detected strong, double-peaked coronal line emission (comparable to the [O III] emission). The emission likely comes from clumped gas accelerated by a radiatively driven wind or orbiting the SMBH at  $\sim 0.3 \text{ pc}$ . The coronal lines require an X-ray source with luminosity  $\sim 3 \times 10^{42} \text{ erg s}^{-1}$ , with significant uncertainty.

### **Broad Balmer emission**

VT J1548 is associated with strong, broad  $H\alpha$  emission with luminosity  $\sim 4 \times 10^{39} \text{ erg s}^{-1}$  and width  $\sim 1900 \text{ km s}^{-1}$  (Figure 3.5). The detection of late time broad  $H\alpha$  from an optical TDE is uncommon, but this luminosity and width are both consistent with upper limits on  $\sim 1000$  day  $H\alpha$  emission in optical TDEs (see Figure 7 of (3)). The  $\sim 1900 \text{ km s}^{-1}$  width corresponds to a radius  $\sim 5 \times 10^{-3} \text{ pc} \sim 1000 \text{ AU}$  whether the gas is orbiting the SMBH or driven in an outflow (the correspondence between the expected radius in each case is a coincidence).

The  $H\alpha$  luminosity is dimmer than typical AGN emission. The (307) relationship

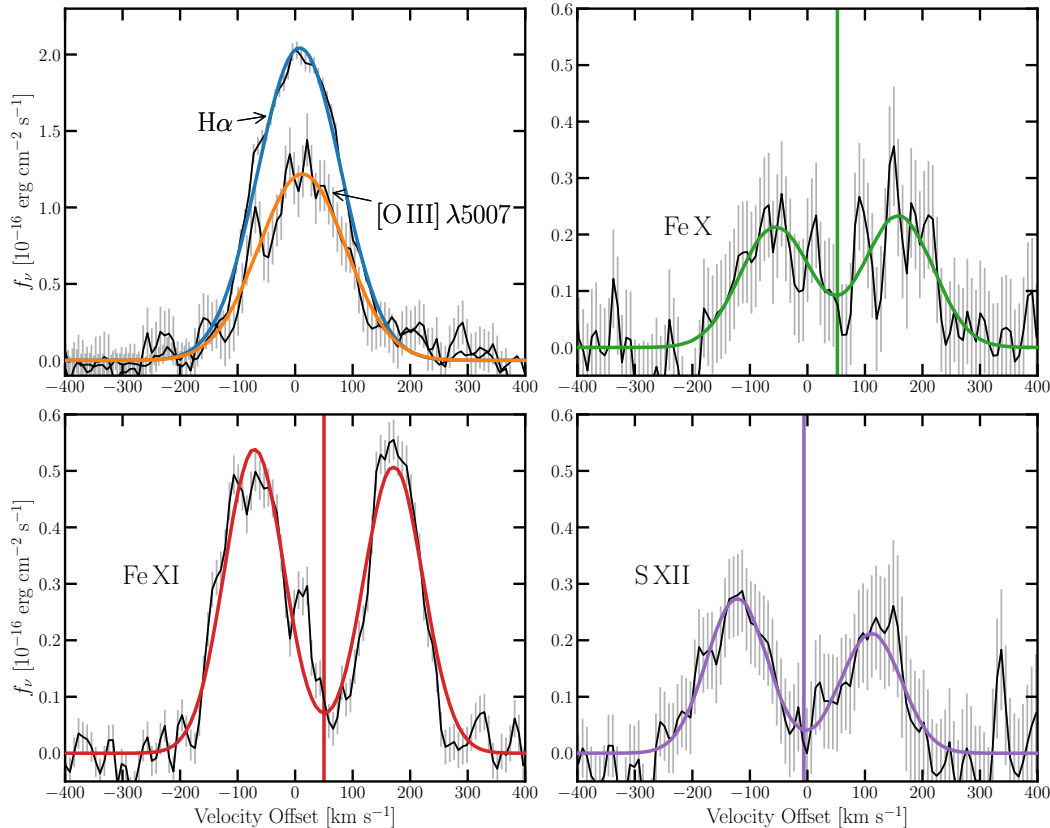


Figure 3.4: Line profiles for selected lines from the ESI observations of SDSS J1548. The *top left* panel shows the H $\alpha$  narrow component and [O III] line profiles. The faint lines show the observations and the solid lines show Gaussian fits, where we include two Gaussian components in each case to match the coronal line profiles. The *top right* and *bottom* panels show the coronal line profiles, which all clearly contain two Gaussian components separated by 215 – 240 km s<sup>-1</sup>. The solid lines in between each pair of lines indicates the average of the two peak wavelengths.

between SMBH mass and the broad H $\alpha$  luminosity/width predicts  $\log M_{\text{BH}}/M_{\odot} \sim 5.3$  from the observed broad H $\alpha$ , which is smaller than the SMBH mass predicted by the  $M_{\text{BH}} - \sigma_*$  relation. The (307) relation was not calibrated to such low mass BHs and this line is heavily extinguished (see next paragraph), so we cannot exclude that the broad emission is consistent with or brighter than that from AGN.

We see no evidence for broad H $\beta$ , which is unusual for optical TDEs. In AGN broad line regions (BLRs), the expected value of the H $\alpha$ /H $\beta$  ratio is universally  $\sim 3$  (8) so we expect an H $\beta$  luminosity  $\sim 2 \times 10^{39}$  erg s<sup>-1</sup>. Possible modifications to account for collisional excitation can increase the ratio to  $\lesssim 5$ , although whether these higher ratios are ever observed is debated (e.g. 308). As shown in Figure 3.5, such a bright

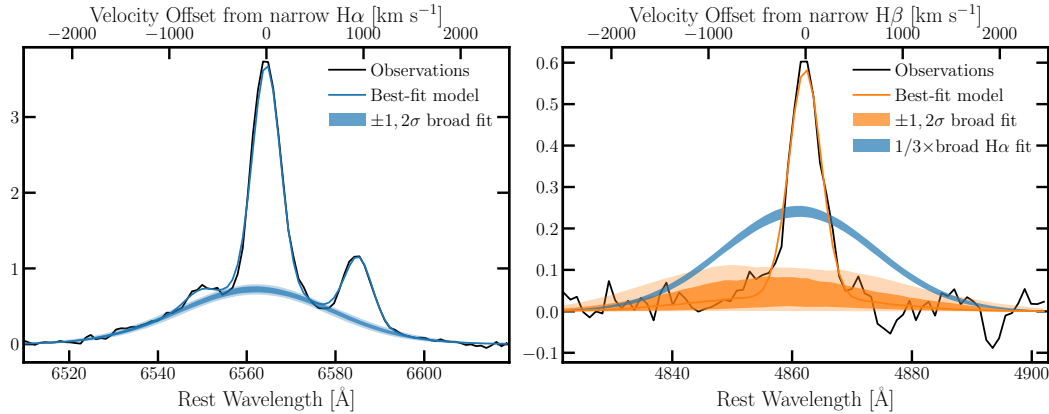


Figure 3.5: Balmer line profiles from the second epoch of LRIS observations of SDSS J1548. The *left* panel shows the H $\alpha$  and N II line profiles. The faint lines show the observations and the solid lines show Gaussian fits with uncertainties. A strong, broad H $\alpha$  component is clearly present. The *right* panel shows the H $\beta$  profile and fit. We overplot the broad H $\alpha$  fit scaled down by the expected H $\alpha$ /H $\beta$  ratio  $\sim 3$  (8). The H $\beta$  profile is inconsistent with including such a strong, broad component, suggesting that the broad emission must be heavily extinguished.

line would be detectable.

Extinction in the galactic nucleus preferentially obscures broad H $\beta$  because it is bluer than H $\alpha$ . Extinction is related to the Balmer line ratio as  $E(B - V)_{\text{nuc}} = 1.97 \log \frac{H\alpha/H\beta}{3}$ . We set an upper limit on the broad H $\beta$  flux by force-fitting a Gaussian profile at the location of H $\beta$  with a FWHM constrained to be within  $1\sigma$  of the broad H $\alpha$  FWHM. The  $3\sigma$  lower limit on the extinction is  $E(B - V)_{\text{nuc}} > 0.7$ . Comparing to measurements of column density and dust extinction in Seyferts BLRs (309), we find that this corresponds to an absorbing column density  $\log N_H/\text{cm}^{-2} \gtrsim 21.5$ .

This extinction is similar to that observed in Seyfert 1.9 galaxies (309). Seyfert 1.9s are an inhomogeneous class (see 310, and references therein). Some fraction likely have a large torus that extinguishes the broad H $\beta$ . Galactic-scale extinction can also play a role in these Seyferts, as well as an abnormal nuclear continuum. As discussed in Section 3.7, we favor a torus as the cause of the high extinction in VT J1548. We cannot exclude the latter two possibilities. For example, a dust lane covering the nucleus could obscure the BLR while remaining consistent with the observed narrow Balmer decrement  $\sim 3.3$  if the narrow H $\alpha$  comes from a very extended region.

In summary, we detect broad H $\alpha$  but no broad H $\beta$ , suggesting we are observing

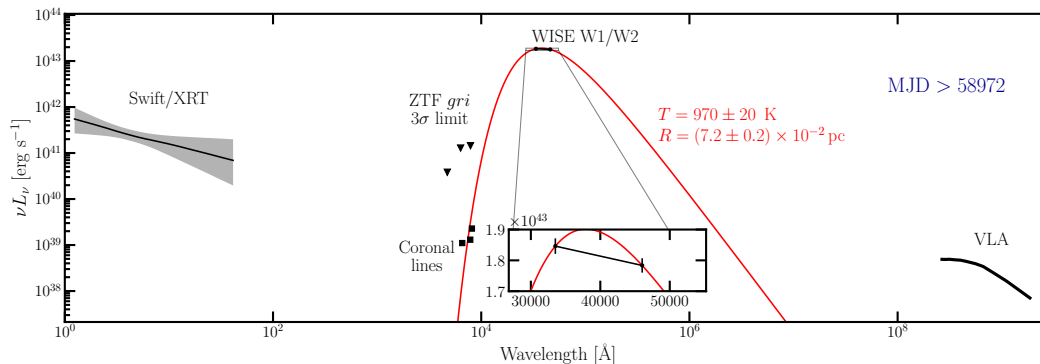


Figure 3.6: Late time multiwavelength SED of VT J1548. We show the most recent WISE and ZTF observations, along with the VLA SED and the unabsorbed Swift/XRT best-fit spectrum. We also include the coronal line emission and the best-fit blackbody to the WISE emission. Note that the reported blackbody parameter uncertainties are only due to errors in the NEOWISE flux measurement; differential internal extinction between the WISE W1 and W2 bands could increase the temperature by  $\sim 250$  K for the extreme case  $E(B-V) = 3$ .

high velocity gas near the SMBH through a screen of obscuring material.

### 3.6 Analysis of transient broadband features

VT J1548 was associated with flares in the infrared (Section 3.6), radio (Section 3.6), and X-ray (Section 3.6). The light curve for each flare is shown in Figure 3.3. VT J1548 was not detected in the optical, and we postpone discussion of the non-detection to Section 3.7.

#### Infrared flare

VT J1548 is associated with a bright ( $\Delta m \sim 2$ ), long lasting ( $\gtrsim 1000$  day) flare in the WISE MIR bands. This flare was  $> 5\times$  brighter than the quiescent state variability. Recent work on IR flares in galactic nuclei has largely argued that the flares can be modeled as “dust echoes” (115). Dust echoes occur when EUV photons are absorbed by circumnuclear dust and reprocessed into IR emission.

Dust echo emission can be fit using detailed models including the dust geometry and emission properties, but they typically agree closely with a blackbody fit (e.g. 311). We fit a blackbody curve to the WISE data points at each epoch. Figure 3.6 shows the WISE SED and blackbody fit in the final epoch. We only report uncertainties due to the flux errors reported by NEOWISE. We emphasize that these uncertainties do not account for internal extinction: while extinction is small in the WISE bands,

differential extinction between the W1 and W2 bands could increase the measured blackbody temperature by as much as  $\sim 250$  K for an extreme  $E(B-V) = 3$ . This shift is sufficiently small that it does not change our conclusions significantly but should be noted.

The emission plateaus at a near constant temperature  $\sim 1000$  K (Figure 3.7). The blackbody radius grows from  $0.7 \times 10^{-2}$  pc to  $7 \times 10^{-2}$  pc (although note that this radius does not correspond to the size of the emitting region but instead encodes information about the dust geometry and properties, see discussion in the rest of this section). The dust luminosity has risen to  $\sim 3 \times 10^{43}$  erg s $^{-1}$   $\sim 0.1 L_{\text{edd}}$ , and has yet to fade.

Integrating the blackbody flux, we find a lower limit on the total emitted energy  $\sim 5 \times 10^{50}$  erg. If we assume that this energy is provided by accretion with an efficiency  $\eta \sim 0.1$ , the accreted mass must be  $\gtrsim 10^{-3} M_{\odot}$ . This is consistent the energy emitted during the first few hundred days of typical TDEs, although a factor of 10 – 100 more energy may be emitted on much longer timescales ( $\gtrsim 5$  years) (see 257, for a review).

A simple explanation of the rising light-curve and nearly constant temperature is a light-travel delay due to dust on different sides of the SMBH. This means that the dust is located at a distance  $\sim 1000 \text{ day} \times c/2 \sim 0.4$  pc from the source. We can determine the bolometric luminosity required to produce the IR radiation using the equilibrium between heating and radiative cooling:

$$e^{-\tau} \frac{L_{\text{bol}}}{4\pi R^2} \pi a^2 Q_{\text{abs}} = \langle Q_{\text{abs}} \rangle_{\text{P}} 4\pi a^2 \sigma T^4. \quad (3.4)$$

$\tau$  is the optical depth for absorption of the heating photons at radii  $< R$ .  $L_{\text{bol}}$  is the bolometric luminosity of the flare.  $R$  is the emitting radius and  $T$  is the emitting temperature.  $a_{\mu}$  is the grain size in units of microns.  $Q_{\text{abs}} \sim 1$  is the absorption efficiency for the incident photons (312), while  $\langle Q_{\text{abs}} \rangle_{\text{P}} \sim a_{\mu}(T/1000\text{K})$  is the Planck-averaged absorption efficiency appropriate for  $a_{\mu} \lesssim 1$  and  $500 \lesssim T/\text{K} \lesssim 1500$  (313). Assuming a negligible optical depth  $\tau$ , we find the bolometric luminosity of the flare is  $L_{\text{bol}} \sim 10^{44}$  erg s $^{-1}$   $\sim L_{\text{edd}}$ , assuming a grain size of 0.1 micron (313). The flare was due to a near- or super-Eddington episode of accretion.

Alternatively, we can estimate the bolometric luminosity required to heat the dust from the total emitted energy and rise time. The rise time of the IR emission sets an upper bound on the length of the flare that heated the dust. Given that the luminosity seemed to near a plateau or peak at MJD  $\sim 59000$  (Figure 3.7), the total length of

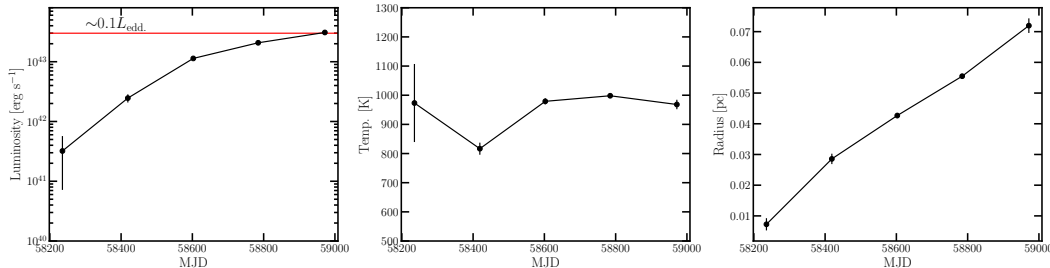


Figure 3.7: The best-fit blackbody parameters for the mid-IR transient associated with VT J1548. The luminosity (*left*), temperature (*middle*), and radius (*right*) evolution are shown with  $1\sigma$  uncertainties. The reported uncertainties are due to errors in the NEOWISE flux measurement. Differential internal extinction between the WISE W1 and W2 bands could increase the temperature by  $\sim 250$  K for the extreme case  $E(B-V) = 3$ .

the ionizing flare is probably  $\lesssim 1000$  days. The total emitted energy is  $\sim 5 \times 10^{50}$  erg  $s^{-1}$ . If we assume a dust covering factor of  $\sim 1\%$ , which is typical of optically selected TDEs (*144, 314*) we find  $L_{\text{bol}} \gtrsim 6 \times 10^{44}$  erg  $s^{-1}$ . If we assume a covering factor  $\sim 10\%$ , which is consistent with an AGN torus (*217*),  $L_{\text{bol}} \gtrsim 6 \times 10^{43}$  erg  $s^{-1}$ . We favor a higher covering factor ( $\gtrsim 10\%$ ) given the high extinction of the broad line region described in Section 3.5. Regardless of the covering factor, the UV flare which heated the dust must have been near- or super-Eddington. If we adopt these estimates for the bolometric luminosity and a flare length of 1000 days, the total emitted energy is  $\sim 5 \times 10^{51-52}$  erg, which is substantially higher than the lower bound discussed earlier. As before, we assume that this energy is provided by accretion with an efficiency  $\eta \sim 0.1$ , so the accreted mass is  $\sim 0.03 - 0.3 M_{\odot}$ . Depending on the dust covering factor, this energy may correspond to a significant fraction of the stellar mass.

In summary, VT J1548 is associated with a  $\sim 10\%$  Eddington MIR flare that has been ongoing for  $\sim 3$  years. The MIR emission is powered by a near- or super-Eddington nuclear flare.

### Radio emission

In this section, we discuss the transient radio emission. First, we consider the rapid light curve evolution. Then, we model the broadband SED.

The radio light curve is shown in Figure 3.3. If the radio emission turned on when the IR emission turned on, the fast rise between the VLASS E2 and VLA follow-up observations requires  $F_{\nu}(3 \text{ GHz}) \propto \Delta t^{4.5}$ . The fastest expected optically thick flux

Table 3.3: Best-fit Radio SED Parameters

Parameter	SSA	FFA	Inhomogeneous SSA	Multi-comp. SSA
$K_1$	$0.46^{+0.02}_{-0.02}$	$9.65^{+0.3}_{-0.3}$	$1.85^{+0.07}_{-0.08}$	$1.68^{+0.28}_{-0.27}, 3.2^{+0.55}_{-0.71}$
$K_2$	$17.5^{+1.2}_{-1.1}$	$4.1^{+0.2}_{-0.2}$	$38.5^{+3.9}_{-3.6}$	$31^{+67}_{-14}, 278^{+165}_{-59}$
$\alpha$	$0.50^{+0.01}_{-0.01}$	$0.56^{+0.02}_{-0.01}$	$0.5^{+0.04}_{-0.04}$	$1.4^{+1.3}_{-0.6}, 1.06^{+0.18}_{-0.05}$
$\alpha'$	–	–	$1.35^{+0.05}_{-0.05}$	–
$\chi^2/\text{dof}$	496/78	458/78	69/77	62/74

**Notes.** All fluxes are assumed to be in mJy and frequencies in GHz.  $1\sigma$  uncertainties are reported. The multi-component SSA model includes a low-frequency pure power-law component that is not included in the reported fits; see text for details of the model.

Table 3.4: Results of the synchrotron equipartition analysis

Parameter	Low freq. Comp.	High freq. Comp.
$p$	$2.28^{+0.37}_{-0.20}$	$3.19^{+0.47}_{-0.35}$
$\log R_p/\text{cm}$	$17.00^{+0.06}_{-0.03}$	$16.68^{+0.04}_{-0.03}$
$\log U_p/\text{erg}$	$48.6^{+0.3}_{-0.08}$	$48.77^{+0.4}_{-0.2}$
$B_p$ [G]	$0.13^{+0.025}_{-0.009}$	$0.469^{+0.13}_{-0.08}$
$\beta$	$0.065^{+0.09}_{-0.005}$	$0.03^{+0.003}_{-0.002}$
$\log n_e/\text{cm}^{-3}$	$2.18^{+0.17}_{-0.08}$	$3.19^{+0.47}_{-0.35}$

**Note.** All parameters are derived assuming equipartition with  $\epsilon_e = \epsilon_B = 0.1$ . We assume that both the low and high frequency components correspond to outflows that launched  $\sim 700$  days after the beginning of the IR flare.

density rise is  $F_\nu(3 \text{ GHz}) \propto \Delta t^3$  for an on-axis, relativistic jet, which is likely an oversimplification (see discussion in *151*). The observed radio emission rises as  $\Delta t^3$  if it turned on  $\sim 400$  days after the IR flare (MJD 58530). The emission is best modeled as sub-relativistic (see discussion at the end of this section), so the light curve should rise more slowly than  $\Delta t^{2.5}$ , which corresponds to an outflow launch date  $\sim 500$  days after the initial IR flare (MJD 58635). These rise times all assume a constant circumnuclear density profile, which is likely incorrect. The launch date need not be delayed if the outflow evolved for  $\sim 700$  days before colliding with a dense shell of material.

The radio SED provides insight into the unusual light curve evolution. The observed SED, shown in Figure 3.8, has evolved significantly between the VLASS E2 observations (green points) and the VLA follow up (black points). The uncertainty on the in-band slope from the VLASS E2 observations is too large to make any conclusive claims, but the 2 – 3 GHz slope has stayed roughly flat.

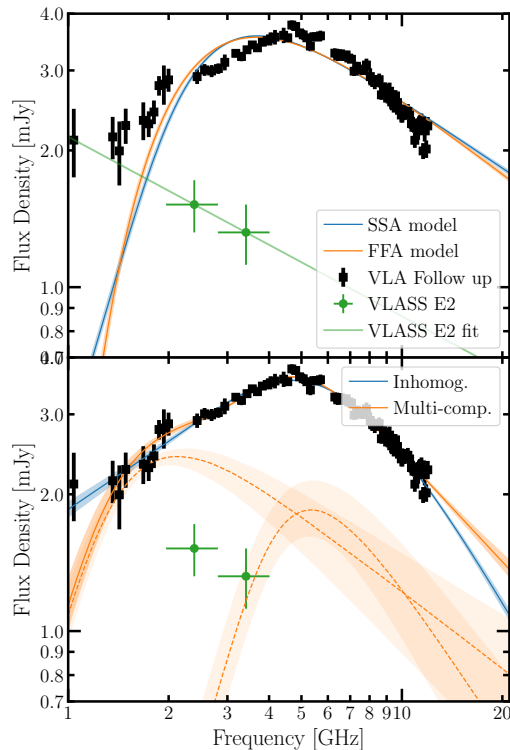


Figure 3.8: The observed radio SED and best fit models. The *top* panel show the VLA follow-up observations in black, the VLASS E2 observations in green, and the best fit self absorbed synchrotron and free-free absorbed models, with  $1\sigma$  error bars. In both cases, the models provide extremely poor fits. We also show an extrapolation of a power law fit to the VLASS E2 points in green. The *bottom* panel shows the non-standard synchrotron model fits. The blue band shows the best-fit inhomogeneous model. The top-most orange band shows the best-fit multi-component synchrotron model. Each component is shown as an orange band in the lower part of the panel. The non-standard models both provide substantially better fits.

Radio emission from a TDE may result from a relativistic or sub-relativistic outflow interacting with the circumnuclear material (CNM) and producing a synchrotron-emitting shockwave. We assume the emission is produced by a population of electrons with a power law energy distribution:

$$\frac{dN(\gamma)}{d\gamma} \propto \gamma^{-p}, \gamma \geq \gamma_m. \quad (3.5)$$

The index  $p$  depends on the acceleration mechanism, with typical mechanisms producing  $2 \lesssim p \lesssim 3$ . The minimum electron Lorentz factor,  $\gamma_m$ , is set by  $\epsilon_e$ , the fraction of the total energy used to accelerate electrons. Equipartition is commonly assumed:  $\epsilon_e = \epsilon_B \sim 0.1$ , where  $\epsilon_B$  is the fraction of the energy density stored in magnetic fields. The SSA model includes characteristic frequencies:  $\nu_m$ ,  $\nu_{sa}$ , and

$\nu_c$ .  $\nu_m$  is the synchrotron frequency of the minimum energy electrons.  $\nu_{sa}$  is the frequency below which emission is optically thick so synchrotron self-absorption (SSA) is important.  $\nu_c$  is the cooling frequency where the electron age is equal to the characteristic cooling time by SSA. We refer the reader to (15) for a concise and clear description of SSA models and the characteristic frequencies.

Typically, the dominant absorption mechanism in TDE-driven outflows is SSA. Then, the radio flux density can be written (315)

$$\frac{F_\nu}{\text{mJy}} = K_1 \left( \frac{\nu}{1 \text{ GHz}} \right)^{2.5} (1 - e^{-\tau_{\text{SSA}}}). \quad (3.6)$$

$$\tau_{\text{SSA}} = K_2 \left( \frac{\nu}{1 \text{ GHz}} \right)^{-(\alpha+2.5)}. \quad (3.7)$$

$K_{1,2}$  are normalizations characterizing the SED flux and optical depth, respectively.  $\alpha$  is the optically thin slope.  $\tau_{\text{SSA}}$  is the optical depth to SSA. We are forcing the optically thick slope to be 5/2, which is expected for optically thick blackbody emission, where the blackbody temperature depends on frequency as  $\nu^{1/2}$ .

We fit this model to the observations using the *dynesty* dynamic nested sampler (206) with uninformative Heaviside priors. The best-fit SED is shown in the top panel of Figure 3.8, and the best-fit parameters are summarized in Table 3.3. The observed optically thick slope is shallower than the canonical 5/2. Variations on this standard SSA model can predict slopes as shallow as 2 (203), which is still inconsistent with our observations.

One possible modification of this model is strong free-free absorption (FFA) rather than SSA. The SED for an FFA dominated model is (202):

$$\frac{F_\nu}{\text{mJy}} = K_1 \left( \frac{\nu}{1 \text{ GHz}} \right)^{-\alpha} e^{-\tau_{\text{FFA}}}. \quad (3.8)$$

$$\tau_{\text{FFA}} = K_2 \left( \frac{\nu}{1 \text{ GHz}} \right)^{-2.1}. \quad (3.9)$$

We fit this FFA model to the observations using the same techniques as for the SSA model. The best fit parameters are tabulated in Table 3.3 and the model is shown in Figure 3.8. The fit is poor with  $\chi^2/dof = 458/78$ .

We may not be in the canonical regime with  $\nu_m < \nu_{sa} < \nu_c$  for which the above parameterizations apply. As we discuss later in this section, the magnetic fields consistent with our SED are  $\sim 0.5$  G. Assuming a  $\gtrsim 500$  day age of the emission, the corresponding cooling frequency is higher than our highest frequency observation,

whereas the other two characteristic frequencies are much smaller. We tested a model with  $\nu_m < \nu_{sa} < \nu_c$ , and found that the resulting  $\chi^2$  was worse at a statistically significant level ( $p < 0.05$ ). Instead, we must consider non-standard emission models. First, we use a model that allows for inhomogeneities in the emitting region. Then, we consider the sum of multiple, independent SSA models.

We model an inhomogenous emitting region following (316–318). The probability of observing a given magnetic field is  $P(B) \propto B^{-a}$ ,  $B_0 < B < B_1$ . When the frequency is below the characteristic synchrotron frequency at  $B_0$ , the SED will have the standard optically thick slope of  $5/2$ . The slope for frequencies above the synchrotron frequency for  $B_1$  is interpreted as the optically thin slope in the standard SSA model. In between, the SED slope is  $\alpha' = (3p + 5\delta' - a(p + 4))/(p + 2(1 + \delta'))$ , where  $0 \leq \delta' \leq 1$  characterizes a correlation between the electron distribution and the magnetic field strength distribution, and all other variables are as defined earlier. We assume the optically thick region with slope  $5/2$  is at frequencies lower than our observations, and adopt the model:

$$\frac{F_\nu}{\text{mJy}} = K_1 \left( \frac{\nu}{1 \text{ GHz}} \right)^{\alpha'} (1 - e^{-\tau_{\text{SSA}}}). \quad (3.10)$$

$$\tau_{\text{SSA}} = K_2 \left( \frac{\nu}{1 \text{ GHz}} \right)^{-[\alpha' + (p-1)/2]}. \quad (3.11)$$

The best fit slopes (Table 3.3) are  $\alpha' = 0.5$  and  $\alpha = (p - 1)/2 = 1.35$ . The value of  $\alpha' = 0.5$  corresponds to  $a = 1.1, 1.6$  for  $\delta' = 0, 1$  respectively. The high frequency spectral slope corresponds to  $p \sim 3.7$ , which is substantially higher than the typical  $p < 3$ . The large  $p$  may be unphysical and suggests the inhomogeneities are more complex than assumed.

We conclude our radio SED modelling by fitting the sum of two independent SSA models. The best-fit parameters for each SSA profile are shown in Table 3.3 and the best fit model is shown in the lower panel of Figure 3.8. The optically thin slopes correspond to  $p \sim 2.3/3.2$  for the low and high frequency components, respectively. Both slopes are consistent with  $2 < p < 3$  within  $1\sigma$ , so we can use a standard equipartition analysis to map the two SSA components to physical parameters of the outflow.

(202) provides a detailed overview of equipartition analyses. In brief, the outer radius of the shock is given by

$$R_p = \left[ \frac{6c_6^{p+5} F_p^{p+6} D^{2p+12}}{(\epsilon_e/\epsilon_B) f(p-2) \pi^{p+5} c_5^{p+6} E_1^{p-2}} \right]^{1/(2p+13)} \left( \frac{\nu_p}{2c_1} \right)^{-1}, \quad (3.12)$$

where the electron rest mass energy  $E_l = 0.51$  MeV,  $f$  is the filling factor, and  $c_1 = 6.27 \times 10^{18}$  (cgs).  $c_5$  and  $c_6$  are both functions of  $p$  (319).  $\nu_p$  is the peak frequency and  $F_p$  is the peak flux density. We have adopted the notation of (15).

Assuming a time  $t_p$  since the initial event, the speed of the shock is given by  $v = \beta c \sim R_p/t_p$ . As discussed at the beginning of this section, the radio light curve for VT J1548 is inconsistent with the dominant synchrotron components corresponding to outflows that are launched with the IR flare. Hence, we calculate the launch date assuming a  $t^{2.5}$  rise, so  $t_p \sim 600$  days. A smaller  $t_p$  would result in a slightly, but not significantly, higher velocity and lower electron density.

Using the same notation, the magnetic field is given by

$$B_p = \left[ \frac{36\pi^3 c_5}{(\epsilon_e/\epsilon_B)^2 f^2 (p-2)^2 c_6^3 E_l^{2(p-2)} F_p D^2} \right]^{\frac{2}{2p+13}} \left( \frac{\nu_p}{2c_1} \right). \quad (3.13)$$

Here,  $D$  is the distance to the source (137 Mpc for SDSS J1548).

Finally, the equipartition energy, which is a lower bound on the true energy, is

$$U = \frac{1}{\epsilon_B} \frac{4\pi}{3} f R^3 \left( \frac{B^2}{8\pi} \right). \quad (3.14)$$

The physical parameters for each component are listed in Table 3.4. Both components are consistent with an energetic, non-relativistic outflow moving through a dense medium. The lower frequency component, which dominates the fast rising light curve, is faster, at slightly larger radius, and is consistent with a lower density than the higher frequency, subdominant component.

These observations might suggest that the outflow is colliding with an asymmetric and/or inhomogeneous medium. We will discuss this interpretation in Section 3.7. In principle, it should be possible to devise a more realistic synchrotron model that includes a physically motivated parameterization of the circumnuclear medium, but such an analysis is beyond the scope of this paper.

To conclude, VT J1548 shows fast-rising, radio emission that is consistent with an outflow at a radius  $\sim 0.1$  pc that is incident on a inhomogenous medium.

### **X-ray emission**

Finally, we consider the X-ray emission associated with VT J1548. First, we discuss the X-ray spectrum and luminosity. Then, we consider the source of the X-ray emission.

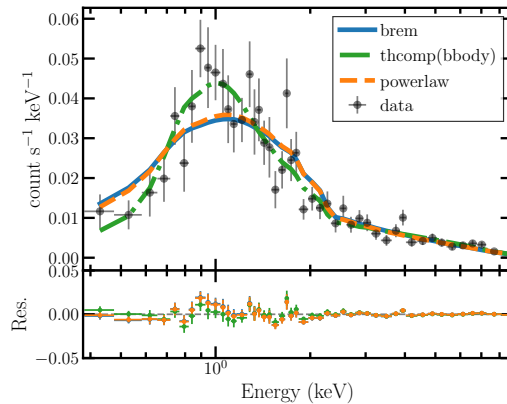


Figure 3.9: The *XMM*-Newton spectrum for VT J1548 (black points). The best-fit bremsstrahlung model is shown in solid blue, the best-fit Comptonized blackbody is dashed green, and the best-fit power-law in dot-dashed orange. Residuals are shown in the bottom panel. The Comptonized blackbody provides the best-fit.

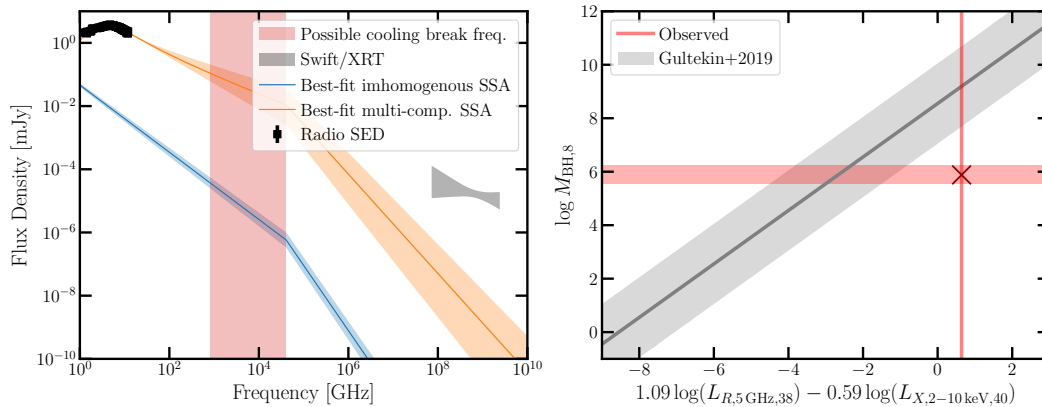


Figure 3.10: (*left*) The radio SED compared with the observed X-ray emission. The inhomogeneous (blue) and multi-component (orange) SSA models both predict an X-ray flux that is many orders of magnitude lower than the observations. We have included a cooling break, and the plausible cooling break frequencies are denoted by the red band. The cooling break would have to be at a frequency orders of magnitude higher than predicted for the X-ray synchrotron to be observable. We conclude that it is unlikely that the synchrotron tail contributes the the X-ray emission. (*right*) The fundamental plane for black hole accretion from (233), with observations of SDSS J1548 overplotted. This source is inconsistent with both the X-ray and radio emission being associated with normal accretion.

Table 3.5: Best-fit X-ray Model Parameters

Model	$kT$ [keV]	$\Gamma$	$n_H$ [ $10^{22}$ cm $^{-2}$ ]	$\log \left( \frac{f_\nu(0.3-10 \text{ keV})}{\text{erg s}^{-1} \text{ cm}^{-2}} \right)$	$\chi^2/\text{dof}$
Bremmstrahlung	$25 \pm 11$	–	$0.177 \pm 0.038$	$-12.396 \pm 0.053$	74/43
Power-law	–	$1.44 \pm 0.082$	$0.226 \pm 0.046$	$-12.394 \pm 0.023$	73/44
Comptonized Blackbody	$0.16 \pm 0.032$	$1.17 \pm 0.16$	$0.58 \pm 0.19$	$-12.392 \pm 0.023$	52/42

**Note.** Best-fit X-ray model parameters. The parameters are as defined in the text.

As shown in the middle panel of Figure 3.3, the X-ray emission from SDSS J1548 is bright, with an *XMM-Newton* flux  $\log f_\nu(0.3-10 \text{ keV})/\text{ergs}^{-1}\text{cm}^{-2} = -12.392 \pm 0.023$ , or  $L_X = (9.5 \pm 0.5) \times 10^{41} \text{ erg s}^{-1}$ , adopting the best-fit model that will be described shortly. This is  $\sim 1\% L_{\text{Edd}}$ , and is bright compared to most late-time ( $\gtrsim 5$  yr) TDE X-ray detections but probably consistent with  $\sim 1000$  day TDE observations provided that there is on-going accretion years to decades after the event (254). The observed luminosity is comparable to that required by the coronal lines, so it likely powers the high ionization emission. Assuming the X-ray flare has lasted for the same duration as the WISE flare, the total energy output is  $\sim 10^{50}$  erg.

X-rays can also be emitted by the tail of the radio synchrotron emission. Given the likely presence of a cooling break between the X-ray and radio frequencies, the synchrotron tail underpredicts the observed X-ray emission by orders of magnitude (left panel of Figure 3.10). Synchrotron emission is not a significant contributor to the X-ray luminosity. The X-ray flare could be related to normal AGN variability, in which case VT J1548 should lie on the fundamental plane for black holes. In the right panel of Figure 3.8, we show the fundamental plane from (233) with our observations overplotted. This source is inconsistent with accretion-related emission. Hence, it is unlikely the result of normal (non-extreme) AGN variability.

Inverse Compton scattering of radiation by electrons in the outflow can produce X-rays. In general, the ratio of synchrotron to inverse Compton power is given by

$$\frac{P_{\text{synch}}}{P_{\text{compt}}} = \frac{U_B}{U_{\text{ph}}}, \quad (3.15)$$

where  $U_{\text{ph}}$  is the photon energy density and  $U_B$  is the magnetic field energy density. The magnetic field in the outflow is  $\sim 0.5$  G, so the magnetic energy density is  $B^2/(8\pi) \sim 0.01 \text{ erg cm}^{-3}$ . The IR luminosity is  $\sim 10^{43} \text{ erg s}^{-1}$  and is emitted from a radius  $\sim 0.4$  pc. Then, we can set a lower limit on the photon energy density of  $\sim 10^{43} \text{ erg s}^{-1} \times (0.4 \text{ pc})/c \times (4/3\pi(0.4 \text{ pc})^3)^{-1} \sim 10^{-4} \text{ erg cm}^{-3}$ . Thus,

we have  $P_{\text{synch}}/P_{\text{compt}} \sim 100$ . The predicted X-ray luminosity from inverse Compton scattering in the outflow is thus  $\sim 10^{36}$  erg s $^{-1}$ . This is  $\sim 6$  orders of magnitude lower than observed.

To tightly constrain the origin of the X-rays, we model the X-ray spectrum. We use `xspec` with (320) statistics and the (321) abundances. We include both external extinction, and internal extinction within the host galaxy. We report the results for three models: bremsstrahlung (`cflux*TBabs*zTBabs*brem`), a power-law (`cflux*TBabs*zTBabs*powerlaw`), and a Comptonized blackbody (`cflux*TBabs*zTBabs*thcomp(bbody)`). We have tested other simple models, including a pure blackbody, and found that they do not provide adequate fits. The bremsstrahlung model has free parameters of total 0.3 – 10 keV flux, internal  $n_H$  and temperature  $kT$ . The power law model has free parameters of total 0.3 – 10 keV flux, internal  $n_H$  and photon index. The Comptonized blackbody model has free parameters of total 0.3 – 10 keV flux, internal  $n_H$ , blackbody temperature  $kT$ , covering fraction  $f_{\text{cov}}$ , which parameterizes the fraction of photons that are Comptonized, and the low-energy power-law photon index  $\Gamma$ . The Comptonized blackbody model also includes a high energy cutoff, parameterized by the electron temperature  $kT_e$ , but our data do not extend to sufficiently high energies to constrain this parameter, so we fix it to the arbitrary high value  $kT_e = 150$  keV. This choice does not affect our results. The results are summarized in Table 3.5, and the models are shown in Figure 3.9.

The Comptonized blackbody model provides a statistically consistent fit that is significantly better than any of the other models tested. The temperature is consistent with X-ray loud TDEs (130). The intrinsic column density is  $n_H \sim 6 \times 10^{21}$  cm $^{-2}$ , similar to the column densities suggested by the coronal lines.

Hence, we conclude that the  $\sim 10^{42}$  erg s $^{-1}$  X-ray emission likely originates from the same source that is causing the coronal line emission and IR flare. As we discuss in the next section, the exact origin of this emission depends on the event that caused the transient. One explanation that could apply in both a TDE scenario or extreme AGN variability is AGN-like soft X-rays from an accretion disk with a hot electron corona, or emission from the base of a nascent jet, and this suggestion is supported by our measurements of the X-ray spectral shape.

### 3.7 Discussion

In this section, we consider models that explain the emission from VT J1548. First, we summarize the observations of SDSS J1548/VT J1548. Then, we compare VT J1548 to published transients. We present a qualitative cartoon model describing the geometry of the system. Finally, we discuss the possible events that triggered the onset of VT J1548, and we finish by describing observations that could distinguish between these properties and/or clarify our physical model.

The observational properties of VT J1548 and its host, SDSS J1548, can be summarized as follows:

- SDSS J1548 is a bulge dominated S0 galaxy. It has line ratios that are marginally consistent with an AGN-like ionizing source. It hosts a low mass black hole, with  $\log M_{\text{BH}}/M_{\odot} = 6.48 \pm 0.33$ .
- VT J1548 is associated with strong ( $[\text{Fe X}]/[\text{O III}] \sim 1$ ), double peaked ( $\Delta v \sim 230 \text{ km s}^{-1}$ ) coronal line emission powered by X-ray emission with a luminosity  $\gtrsim 10^{42} \text{ erg s}^{-1}$ .
- VT J1548 coincided with the onset of broad  $\text{H}\alpha$  emission (FWHM  $\sim 1900 \text{ km s}^{-1}$ ), but no broad  $\text{H}\beta$  emission, suggesting strong internal extinction with  $E(B - V) \gtrsim 0.7$ .
- The transient emission lines commonly associated with optically-selected TDEs (He II, N III) are undetected. We do not detect any of the [Fe II] lines that are abundant in Seyfert spectra.
- VT J1548 is associated with a bright ( $\Delta m \sim 2 - 3$ ) MIR flare. The flare rose over  $\sim 900$  days and had not begun fading from a luminosity of  $\sim 0.1 L_{\text{edd}}$  as of MJD 59000. The flare temperature stayed roughly constant at 1000 K, and the emission is consistent with dust heated by near- or super-Eddington UV flare.
- VT J1548 was undetected in the radio shortly before the beginning of the IR flare, but had turned on within  $\sim 2$  years. The radio emission from VT J1548 is currently consistent with an inhomogeneous SSA model or a two-component SSA model peaking at a frequency of 5 GHz with a flux density 4 mJy, although the best-fit parameters for the two-component model are more consistent with theoretical expectations for synchrotron sources. The best-fit

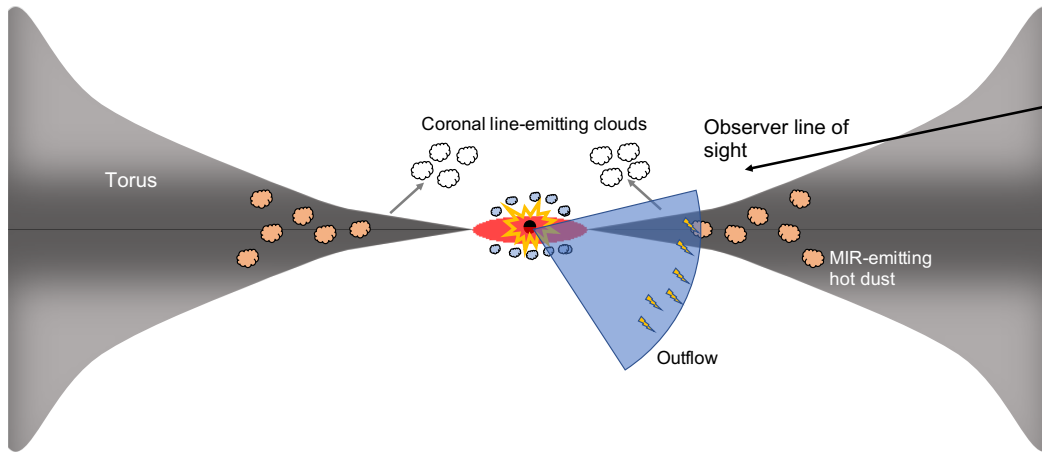


Figure 3.11: A cartoon showing the approximate geometry of SDSS J1548/VT J1548. Some event triggered a flare at the nucleus of the galaxy, which caused the formation of an accretion disk or was associated with enhanced accretion from a pre-existing accretion disk. The broad  $H\alpha$  emission originates from near the accretion disk ( $\sim 1000$  AU), and is extinguished by the dusty torus along the line of sight to the observer. Any optical emission from the transient event is also heavily extinguished. The coronal line-emitting gas, synchrotron-emitting outflow, and MIR emitting dust are all at roughly the same distance ( $\sim 0.4$  pc). The coronal line-emitting clouds are embedded in a radiation-driven wind ( $\sim 100$  km  $s^{-1}$ ) off of the torus, which causes the double peaked emission. Alternatively, the clouds may be orbiting the SMBH at  $\sim 0.3$  pc to produce the double peaked lines. IR emission comes from the heated dust in the torus. The radio emitting outflow is shown in blue.

parameters suggest the components are both non-relativistic outflows, one of which is slightly faster with a lower electron density and magnetic field.

- The transient X-ray emission ( $f_X = (4.1 \pm 0.2) \times 10^{-13}$  erg  $cm^{-2}$   $s^{-1}$ ,  $L_X \sim 10^{42}$  erg  $s^{-1}$ ,  $kT = 0.16 \pm 0.032$  keV) is most likely produced by a Comptonized blackbody, such as would be observed from an AGN.

### Comparison to published transients

These general features have individually been observed in previous transients, but never together. In this section, we compare VT J1548 to select transients from the literature. We refer the reader to (266) for a more comprehensive discussion of unusual TDE candidates. In Table 3.6, we summarize critical properties of VT J1548 and compare them to the “unusual” TDE candidates and two unique changing look AGN that we discuss in Section 3.7. We selected these transients as those that evolve in the optical/IR/X-ray on a timescale slower than the typical TDE ( $\gtrsim 400$

days) or those that initially evolve on shorter timescales but have late-time ( $> 400$  day) X-ray detections. In the rest of this section, we highlight some of the unusual transients.

First, tens of extreme coronal line emitters have been observed with coronal line luminosities that are generally a factor of a few higher than that observed from VT J1548 (e.g. *14, 199, 271, 273*). High extinction in SDSS J1548 could cause the dim emission. The line profiles from ECLEs have not been studied in detail due to a lack of high resolution follow up, but double peaked profiles are not unprecedented for normal AGN and are generally attributed to a partially obscured rotating disk or an outflow (e.g. *278, 322*). It would be unsurprising if high resolution observations of ECLEs uncovered complex line profiles (see *14*, for discussion of possible unusual coronal line profiles in ECLEs).

Most ECLEs are inconsistent with past AGN activity whereas SDSS J1548 has line ratios that could be consistent with weak AGN activity (*14*). One exception is AT2019avd (*93, 274*), which was selected as an X-ray and optical transient in a galaxy with a low SMBH mass  $\log M_{\text{BH}}/M_{\odot} \sim 6.3 \pm 0.3$ . Like VT J1548, the host galaxy was consistent with weak or no AGN activity based on archival X-ray non-detections and BPT line ratios. The optical light curve was initially similar to standard, prompt TDE emission (i.e., it evolved over a timescale of  $\sim 100$  days), but it rebrightened significantly  $\sim 500$  days after the initial peak. Its X-ray emission was very soft ( $\Gamma \sim 5$ ) and the X-ray luminosity  $\sim 600$  days post-optical peak remained at  $\sim 10^{43}$  erg  $\text{s}^{-1}$ , or  $\sim 0.1L_{\text{edd}}$ . It was detected as a WISE flare that turned on after the optical emission. An optical spectrum near the first optical peak showed Fe II emission, and another spectrum taken  $\sim 450$  days post-peak showed He II and Bowen fluorescence lines. It showed broad transient Balmer emission and a Balmer decrement close to the expected value of 3. AT2019avd has been interpreted as either an AGN flare or an unusual TDE. While the high Eddington ratio and MIR detection are similar to our observations of VT J1548, VT J1548 did was highly extinguished and showed slower evolution in the MIR. Both of these difference could be caused by a larger dusty torus in VT1548 if it is undergoing the same type of flare as AT2019avd.

There is a growing population of transients which evolve on longer timescales than the typical TDE. PS1-10adi (*323*) was interpreted as a TDE candidate or highly obscured supernova in a Seyfert galaxy (*323*). This event was notable for its high bolometric luminosity ( $\sim 10^{52}$  erg  $\text{s}^{-1}$ ) and slow evolution: the optical light

curve faded slowly over  $\sim 1000$  days after peaking at the Eddington luminosity. (323) proposed that it is a member of a class of similar transients; here we focus on PS1-10adi for simplicity. PS1-10adi also produced a dust echo, although the dust echo faded more quickly than that of VT J1548 and followed the expected blackbody temperature evolution. It was X-ray dim until  $\sim 1500$  days, at which point it brightened in the X-rays to  $\sim 10^{43}$  erg s $^{-1}$  and rebrightened briefly in the optical/IR. PS1-10adi was not detected in the radio at early times, but without further follow up we cannot exclude late time rebrightening. PS1-10adi also did not show strong coronal lines. Thus, VT J1548 and PS-10adi are similar in their high Eddington ratio, slow timescales, dust echoes, and late time X-ray detections, but there were clearly significant differences between this event and VT J1548. Some, but not all, of the differences can be explained if VT J1548 is observed on a more heavily obscured line of sight.

PS1-10adi shows properties that are similar to the class of slowly-evolving flares reported by (331). That work focused on AT2017bgt, a slowly evolving (timescale  $\gtrsim 14$  months) optical/X-ray transient in an AGN (identified via archival X-ray detections) with  $\log M_{\text{BH}}/M_{\odot} \sim 7$ . It showed strong, broad He II and Bowen fluorescence lines, as well as broad Balmer lines. (331) proposed that this source, along with the similar transients OGLE17aaj and that hosted by the galaxy F01004-2237, form a new class of AGN flares where the UV/optical continuum emission increases by a factor  $\sim 2$  in a few weeks. The flare in F01004-2237 was associated with a bright IR flare with  $\sim$ constant temperature that rose over thousands of days. Given the large number of similarities with VT J1548, it is feasible that VT J1548 is a member of this class but with a larger amount of dust and/or a more extinguished sight line. Radio observations of AT2017bgt and like events are critical for assessing this interpretation.

Every transient discussed thus far has been detected in the optical. On the other hand, the candidate TDE or AGN flare SDSS J1657+2345 was discovered as a MIR flare with no optical counterpart (326). It evolved over  $\sim 1000$  day timescales, like VT J1548. Broad H $\alpha$  is detected in its spectrum, but no broad H $\beta$  is detected. In contrast to VT J1548, no coronal line emission is detected. Follow-up radio and X-ray observations would help determine whether this event is analogous to VT J1548.

Similarly, none of the transients discussed have been reported to have unusual radio emission like that from VT J1548. While the radio luminosity of VT J1548 is typical

Table 3.6: Comparison to select published transients

Name	$\log \frac{M_{\text{BH}}}{M_{\odot}}$	BPT	$\frac{L_{\text{peak}}}{L_{\text{edd.}}}$	Optically dim?	Slow Evol.?	MIR?	Late time X-ray?	Radio?	Delayed radio?	ECLE?	Broad Balmer?	$E(B-V)_{\text{nuc.}} \geq 0.3?$	Trigger
AT2018dyk <sup>1</sup>	5.5	LINER	0.004	✗	✓	✗	?	✗	?	✓	✓	✗	AGN/TDE
PS16dtm <sup>2,3</sup>	6	NLSy1	2.8	✗	✓	✓	?	✗	?	✗	✓	✗	AGN/TDE
SDSS J1657+2345 <sup>4</sup>	6.2	AGN	1.7	✓	✓	✓	?	?	?	✗	✓	✓	AGN/TDE
AT2019avd <sup>5,6</sup>	6.3	Comp.	0.1	✗	Double peaked	✓	?	?	?	✓	✓	✗	AGN/TDE
NGC 3599 <sup>7</sup>	6.4	Sey. 2 LINER	0.004	✓	✓	?	✗	?	?	✗	✗	–	AGN/TDE
<b>VT J1548</b>	<b>6.48</b>	<b>Comp.</b>	<b>0.1</b>	<b>✓</b>	<b>✓</b>	<b>✓</b>	<b>✓</b>	<b>✓</b>	<b>✓</b>	<b>✓</b>	<b>✓</b>	<b>✓</b>	<b>AGN/TDE</b>
PS1-10adi <sup>8,9</sup>	7	H II	~1	✗	✓	✓	✓	?	?	✗	✓	?	TDE/SN
ASASSN-15oi <sup>10–12</sup>	7.1	H II	0.15	✗	✗	✗	✓	✓	✓	✗	✗	–	TDE
IES 1927+654 <sup>13</sup>	7.3	AGN	0.01–0.2	✗	✗	?	✓	?	?	✗	✓	✓	AGN/TDE
AT2017bgt <sup>14</sup>	7.3	Comp.	$\geq 0.1$	✗	✓	?	✓	?	?	✗	✓	?	AGN/TDE
F01004-2237 <sup>15,16</sup>	7.4	H II Sey. 2	0.02–0.7	✗	✓	✓	?	✗	?	✗	✗	–	AGN/TDE
OGLE17aaj <sup>17</sup>	7.4	?	0.01	✗	✓	✓	?	✗	?	✗	✓	?	AGN/TDE
ASASSN-18jd <sup>18</sup>	7.6	Comp.	0.09	✗	✓	✓	✗	?	?	✓	✓	✗	AGN/TDE
XMMSL2 J1446 <sup>19</sup>	7.8	H II	0.02	✓	✓	?	✓	✗	?	✗	✗	–	AGN/TDE
ASASSN-20hx <sup>20</sup>	7.9	LLAGN?	0.003	✗	✓	?	?	?	?	✗	✗	–	AGN/TDE
WISE J1052+1519 <sup>21</sup>	8.6	AGN	0.02	✗	✓	✓	✗	?	?	✗	✓	✗	AGN fading
ASASSN-15lh <sup>11,22,23</sup>	8.7	LINER	0.1	✗	Double peaked	✓	✓	✗	✗	✗	✗	–	SN/TDE
013815+00 <sup>24</sup>	9.3	AGN	0.02	✗	✓	?	?	✓	✗	✗	– (broad Mg II)	–	AGN

**Note.** See text for further description of select transients. Transients are sorted according to SMBH mass. SMBH masses are as reported by the authors, although we prefer to report those measured using the  $M_{\text{BH}}-\sigma_*$  relation. Late time detections refer to detections  $\sim 400$  days after the initial flare. Slow evolution refers to flares that rise over timescales  $\geq 50$  days or fade over a characteristic timescale  $\geq 400$  days in the optical, IR, or X-ray. Eddington ratios are very approximate; they are reported using the peak bolometric luminosity when possible, otherwise using the peak luminosity in any given waveband. The trigger is as given in the relevant reference. Question marks refer to values for which we could not find a reported measurement. Note that WISE J1052+1519 is a fading CL AGN. References: <sup>1</sup>(199), <sup>2</sup>(324), <sup>3</sup>(325), <sup>4</sup>(326), <sup>5</sup>(93), <sup>6</sup>(274), <sup>7</sup>(327), <sup>8</sup>(323), <sup>9</sup>(328), <sup>10</sup>(151), <sup>11</sup>(144), <sup>12</sup>(329), <sup>13</sup>(330), <sup>14</sup>(331), <sup>15</sup>(332), <sup>16</sup>(333), <sup>17</sup>(334), <sup>18</sup>(275), <sup>19</sup>(335), <sup>20</sup>(336), <sup>21</sup>(337), <sup>22</sup>(338), <sup>23</sup>(339), <sup>24</sup>(156).

of non-jetted TDEs (150), the SED and late time detections are atypical. We cannot exclude that most of the aforementioned transients show the same radio light curves as VT J1548: none of these transients have published, late-time, broadband radio follow-up. If the late time emission is caused by an outflow colliding with a dense, torus-like medium, it is particularly important to obtain late-time radio follow-up of transients where there is evidence for large obscuration.

The closest analog in the literature is the delayed radio emission from the TDE ASASSN-15oi reported by (151). ASASSN-15oi rebrightened in the radio  $\sim 1400$  days after its initial flare. This event also rebrightened in the X-ray. The radio light curve evolved at an extremely fast rate, similar to VT J1548, and an inhomogeneous

synchrotron model was required to fit the observations. Apart from this unusual radio emission, ASASSN-15oi was a relatively typical TDE, unlike VT J1548 (*144, 329*).

We conclude that VT J1548 is a unique transient, largely because of its large extinction, slow evolution, and delayed radio flare. While there is no single transient that definitively comes from the same class as VT J1548, by invoking different levels of obscuration it is plausible that the family of transients proposed by (*331*) (AT2017bgt, OGLE17aaj, F01004-2237) and the IR transient SDSS J1657+2345 could form a class of similar objects.

### **A qualitative model for VT J1548**

Next, we present a physical model that can explain all the above observations, and later we constrain the event that triggered VT J1548. In Figure 3.11, we show a very qualitative cartoon model. At the center, we have shown an SMBH with an accretion disk. While we do not have direct evidence for an accretion disk, many of the scenarios we discuss in the rest of this section require a disk. Moreover, emission from an AGN-like disk and its corona could explain some of the observed X-rays. The typical outer radius of an AGN accretion disk is a few light days, or  $\sim 10^{-3}$  pc (*340*).

The clouds surrounding the accretion disk depict the broad line region, which produces the broad  $H\alpha$ . Given the width of the observed broad  $H\alpha$ , we expect that these clouds are located at a distance  $\sim 5 \times 10^{-3}$  pc. The BLR may have existed before the transient, as long as there was no significant ongoing accretion that would have illuminated the BLR and produced observable broad lines in the archival SDSS spectrum. Alternatively, the BLR could have formed via a dusty wind driven from the accretion disk, as has been proposed in some AGN models (*97*).

Outside of the BLR, we show coronal line-emitting clouds orbiting the SMBH, and a large dusty torus. The torus is not depicted as a standard doughnut, which is an oversimplification of the true structure, which fails to predict some observations (e.g. *341, 342*). Instead, we adopt a clumpy, thick, flared, and extended gaseous disk. As discussed by (*269*) and references therein, galactic-scale inflows trigger a series of gravitational instabilities on small scales, which produce a thick, eccentric disk near the SMBH without requiring active accretion. The orientation of the disk may be twisted and misaligned with the inner accretion disk, although we depict it as perfectly aligned for simplicity.

The observer is along a line of sight through the edge of the torus such that there is significant extinction, but the line of sight is not completely obscured as in Type 2 AGN. We expect the line of sight to have a column density  $\log N_{\text{H}}/\text{cm}^{-2} \gtrsim 21.5$  given the constraints on the broad Balmer decrement.

We expect the torus to extend outward from at least  $\sim 0.4$  pc given the constraints from the MIR emission (Section 3.6). At 0.4 pc the temperature of the torus is  $\sim 1000$  K, and the dust interior to this radius is hotter. Dust that has been heated to  $T_{\text{sub}} \sim 1600$  K (115) is sublimated.

The coronal line-emitting gas is represented by clouds at roughly the same distance ( $\sim 0.8$  pc) as the MIR emitting gas and outflow. These clouds form from a hot, dusty wind driven by radiation pressure from the edge of the torus (278, 300, 343). As the dusty clouds are accelerated off of the torus, the dust sublimates and releases the iron that produces the coronal line emission. While similar clouds are likely driven from the lower side of the torus, these would be highly extinguished because they lie on a line of sight through the center of the torus. For simplicity, we do not draw them. While the geometry depicted may not produce the exact coronal line profiles observed, given uncertainties in the torus shape and dusty wind directions and kinematics, we are confident that there is a geometry which could replicate the observations.

Finally, we have drawn an outflow beginning at the accretion disk and that has collided with parts of the torus at a radius  $\sim 0.1$  pc, corresponding to the best-fit radius from our synchrotron model. This radius is roughly consistent with the distance to the MIR emitting dust. A wide angle outflow is required to explain the multiple synchrotron components (see 150, for a discussion of possible origins). We will discuss some of these possibilities in the following sections. While the exact position of this outflow is unknown, we emphasize that it need not be colliding with a uniform medium. Parts of the outflow may be incident on denser parts of the torus, and that could cause the unusual radio SED.

Coronal line emitters are generally interpreted as originating from one of three classes of transients: extreme AGN variability, tidal disruption events, or supernovae. In the following subsections, we discuss each of these possibilities in turn. We expect that our cartoon applies regardless of the exact cause of the flare, unless the flare was triggered by a slightly off-nuclear event (e.g., a supernova). In this case, we are observing the event through some abnormally thick cloud of material. We will discuss this possibility briefly in the following section.

### Is VT J1548 a supernova?

We consider it unlikely that VT J1548 is caused by a supernova because of its luminosity and timescale. The difficulties of interpreting ECLEs as supernova have been discussed in many previous papers (e.g. *14, 199, 273*), so we only briefly consider it here. Only a few Type II<sub>n</sub> supernova are observed to have coronal line emission. One of the SN II<sub>n</sub> with the brightest coronal line emission was SN 2005ip, but by  $\sim 1000$  days the [Fe X] emission was only at  $\sim 10^{37}$  erg s<sup>-1</sup> (*344*), which is a factor of  $\sim 100$  dimmer than we observe. At no point during the evolution of SN 2005ip was the [Fe X] emission within a factor of  $\sim 10$  as bright as observed from VT J1548. Of course, VT J1548 may be the most extreme coronal line-emitting supernova seen to date. The X-ray luminosity  $\sim 10^{42-43}$  erg s<sup>-1</sup> required to produce the coronal lines is unprecedented for supernova — one of the brightest, long-duration X-ray emitting supernova, SN1988Z, was only detected at  $\sim 10^{41}$  erg s<sup>-1</sup> (*345*).

The MIR emission from VT J1548 is difficult to reconcile with a supernova interpretation. Consider the case where the MIR photons are emitted by dust that is ejected by the supernova. The observed MIR emission is consistent with a distance  $\sim 0.4$  pc. To reach this radius within  $\sim 1$  year, the ejecta must have moved at a velocity  $\sim c$ . This is extraordinarily fast, so instead we invoke pre-existing material. The supernova either occurred in the galactic nucleus so that it is obscured by the torus, or the supernova is obscured by a torus-like quantity of dust outside the nucleus. Both of these scenarios are unusual, and combined with the extreme X-ray luminosity required to power the emission, we disfavor the supernova interpretation.

### Is VT J1548 a TDE?

Next, we assess whether VT J1548 is consistent with a TDE. ECLEs are often attributed to TDEs (e.g. *14*), although it is difficult to distinguish between AGN accretion variability (see next section) and TDEs. The observed coronal lines would be excited by the soft X-rays and UV continuum produced by the TDE (e.g. *14*). A complication is that many TDEs show bright optical light curves (e.g. *128*), which we do not observe from VT J1548. However, an increasing number of optically-faint TDEs are being discovered (see *130*, for optically-faint X-ray selected TDEs). The optical emission from TC0221 may be heavily extinguished (see example TDE lightcurves in Figure 3.3). The flare may have occurred during a gap in survey coverage. Alternatively, the TDE may have been optically dim. TDEs associated with SMBHs with masses  $\log M_{\text{BH}}/M_{\odot} < 6$  may lack the optically thick gas layer

which reprocesses higher energy photons and dominates the optical emission (113).

The timescale of VT J1548 may also pose a problem: “standard” TDEs are expected to rise on short ( $\sim 10$ s of days) timescales, and they generally fade according to a canonical  $t^{-5/3}$  power law (see 112, for a review). Example optical light curves are overplotted in Figure 3.3. The IR emission from VT J1548 rises over  $\gtrsim 2$  years. As we discussed in Section 3.6, a prompt, high-energy transient may be able to produce a slowly evolving, MIR flare. Because MIR photons emitted from the far side of the torus have to travel an extra distance  $\sim 2R_{\text{emit}}$  for an emitting radius  $R_{\text{emit}}$ , the flare is smoothed out over a time period  $2R_{\text{emit}}/c$ .

If the observed MIR emission is the echo of a bright, prompt TDE, we have to invoke some delayed X-ray emission to explain our X-ray detections. We might expect dim, late-time X-ray detections from a viscous accretion disk, although whether such disks are expected is uncertain. (257) reported the detection of late-time (5-10 years post-flare) transient UV emission from eight optical TDE hosts which is inconsistent with this late-time models, but could be explained as emission from unobscured accretion disks with long viscous timescales. Similarly, (254) detected late time (5-10 years post-flare) X-ray emission from TDE candidates. Simulations of TDE evolution may have incorrectly predicted the late-time light curve evolution, possibly because of incorrect viscosity assumptions. If a slowly evolving viscous disk is present in SDSS J1548, we would expect the MIR flare to fade extremely slowly (i.e., decades timescale).

Late-time interactions between an outflow launched during the initial TDE and a dusty torus are also able to produced delayed X-ray emission at a luminosity  $\sim 10^{41-42}$  erg  $s^{-1}$  (346). This model can also explain the brightening in the radio via shocks due to the outflow hitting the torus, and predicts that this event should be  $\gamma$ -ray bright (347).

Alternatively, we may be witnessing a TDE that evolves slowly because of delayed accretion disk formation (although see 254, 257). TDE accretion disks may form when stellar debris streams collide because of general relativistic precession, eventually dissipating enough energy to collapse (348). The precession is correlated with the SMBH mass: stellar streams orbiting SMBHs with  $\log M_{\text{BH}}/M_{\odot} \lesssim 6$  may take years for the debris to precess sufficiently to cause collisions (348). The slow disk formation erases information about the mass fallback rate which usually sets the light curve decay time to  $t^{-5/3}$ . TDEs with delayed accretion disks decay following a power law  $\sim t^{-1}$  (348).

This delayed accretion disk model also requires no pre-existing accretion disk. We have invoked a torus to explain the IR emission from VT J1548, but some models predict that tori are only hosted by AGN with sufficiently large luminosities ( $\gtrsim 10^{39}$  erg s $^{-1}$  for a  $\log M_{\text{BH}}/M_{\odot} \sim 6$  SMBH; (268)). As discussed by (269), it is feasible that tori can form in quiescent galaxies if dynamical instabilities reminiscent of the bars-within-bars models drive gas to the galactic center. Regardless, we consider the possibility that SDSS J1548 had a pre-existing accretion disk for completeness.

Like TDEs in quiescent galaxies, it is feasible that TDEs in AGN may produce emission years after the initial flare. However, predictions for the observational characteristics of TDEs in AGN are limited. (265) modeled a TDE in an AGN and predicted light curves that evolve on  $\sim$ month timescales, which is much faster than observed for VT J1548. However, the simulations spanned a very small range of parameter space, so we will have to wait for a more expansive set of models of TDEs in AGN to constrain whether that mechanism could have triggered VT J1548.

In summary, interpreting VT J1548 as a TDE is plausible. In one scenario, the torus geometry and optical depth are such that the long duration MIR brightening can be produced by a short high energy flare. Alternatively, TDEs in AGN may simply be able to evolve on very long timescales.

### **Is VT J1548 an AGN flare?**

VT J1548 may be an extreme AGN event if it is neither a TDE nor a supernova. However, such an event must be unusual. From the low [O III] luminosity  $\sim 10^{39}$  erg s $^{-1}$  and the AGN X-ray/[O III] emission relation from (349), we can constrain the historical X-ray luminosity of this source to be  $\ll 10^{42}$  erg s $^{-1}$ . The light travel time through the narrow line region of an AGN is typically  $10^{2-3}$  years, so we know that the X-ray luminosity from this source over that time period must be  $\ll 10^{42}$  erg s $^{-1}$ . Hence, flares such as that observed must occur infrequently.

Variable obscuration can cause bright flares on the orbital timescale of the obscuring cloud (e.g. 337) but could not explain most all of the other transient emission, such as the broad H $\alpha$ , and we do not consider it further.

Alternatively, VT J1548 may be a changing look AGN (CL AGN; also see (350, 351) for examples of more phenomena that can trigger AGN flares). CL AGN comprise a rapidly growing class of AGN which transition from Type 1, with a weak continuum and narrow line emission, to Type 1.8-2, with broad H $\alpha$  and H $\beta$  alongside a strong continuum, or vice versa. These transitions occur on year-decade timescales, and

the AGN can fade and/or rise (e.g. 352). They are sometimes associated with MIR (337, 352, 353) and X-ray (354) variability and flaring.

If VT J1548 is a CL AGN, it is unprecedented. Unlike most CL AGN, SDSS J1548 showed no strong pre-flare variability or evidence for AGN activity (e.g., see candidates in 355), although this might be a selection effect since CL AGN candidates are often identified by their pre-flare variability. No unambiguous CL AGN with the unusual radio emission and high Eddington ratio of VT J1548 has been observed to date, although radio follow up of CL AGN is limited. The CL AGN 013815+00 is notable because it brightens in both the optical and the radio (356). Similarly, Mrk 590 underwent multiple transitions between Seyfert types in the last thirty years and shows some evidence for radio variability (158, 357). A more complete sample of radio-selected, optical/UV/IR flaring CL AGN, or a comprehensive follow up program to measure the radio light curves of ongoing CL AGN are key to understanding the expected radio signatures.

Flaring galaxies with  $\log M_{\text{BH}}/M_{\odot} \lesssim 8$  are difficult to unambiguously classify as a TDE or AGN flare, in part because AGN accretion disks still present mysteries: observations of large amplitude variability in AGN are becoming common, and most accretion disk models do not predict frequent, large variability, but instead explain these flares by “instabilities” (267). Large uncertainties in the relevant timescales and flare amplitudes renders any comparison to observation difficult.

NGC 3599 exemplifies this difficulty. This galaxy underwent a slow, soft X-ray flare that rose over multiple years (327). It lacked observations between the rise and decay, which complicated the interpretation. However, the slow timescale is atypical of normal, prompt TDEs, although, as we have discussed, it is likely that some TDEs can evolve on much longer timescales and cannot be excluded as a trigger of the flare in NGC 3599. (327) suggested the Lightman-Eardley disk instability as one possible cause of the flare. The instability arises because (61) thin accretion disks become unstable when radiation pressure dominates over thermal pressure. This condition is fulfilled in the inner regions of any disk that is accreting at a near-Eddington luminosity. The instability manifests as a limit-cycle behavior. When the disk is bright and highly accreting, the inner disk is unstable and empties, which reduces the accretion rate. The inner disk slowly refills, eventually returning to the high accretion state and repeating the cycle. The rise time to the high accretion rate state is set by the time required to heat the inner disk, which depends strongly on the

viscosity prescription but must be greater than (327)

$$R_{\text{trunc}}/c_s \sim 1 \text{ month} \left( \frac{R_{\text{trunc}}}{100R_g} \right) \left( \frac{M_{\text{BH}}}{10^6 M_\odot} \right), \quad (3.16)$$

where  $R_{\text{trunc}}$  is the radius at which the disk will become truncated and  $c_s$  is the sound speed.  $R_g$  is the gravitational radius of the SMBH. After the rise, the emission plateaus for an unconstrained time as the inner disk is cleared out. Once the inner disk is empty, the emission will decay to the low state. The decay time is poorly constrained, but it is expected to be faster than the rise time.

Like NGC 3599, VT J1548 evolves on the correct timescales to be explained by the Lightman-Eardley instability. In the future, we can more definitively constrain this possibility by monitoring the evolution of VT J1548 for evidence of (1) a decay time that is much more rapid than the rise time and (2) a repeat flare on a many-decade timescale. Even if such behavior is observed, the interpretation is complicated. The Lightman Eardley instability cannot be considered in isolation: other instabilities are predicted in the inner disk. For example, the ionization instability applies to cool ( $T \sim 6000$  K) regions of the disk and is the result of the strong temperature and density dependence of the opacity of partially ionized hydrogen (356).

Moreover, it is unclear whether the Lightman Eardley instability actually occurs in low mass accreting BHs, let alone AGN (234). The (61) viscosity is an oversimplification, and there is some evidence that a more physical viscosity prescription eliminates the instability (358). Similarly, while the ionization instability is well established for dwarf novae (see 356, for a review), it has not been definitively observed in AGN.

In summary, VT J1548 may be a CL AGN, although its lack of strong AGN signatures and bright radio flare are unusual. Observations of a repeat flare or a fast decay time could support a CL AGN origin.

### **Future work and observations**

It is extremely difficult to unambiguously determine the cause of VT J1548, as is a common issue for like transients. In many cases, extreme AGN variability is as feasible an explanation as a TDE-like transient. In this section, we suggest future observations and theoretical work that could help constrain the origin of VT J1548 and like events. We begin with possible observations.

- *Early time spectroscopic follow up of VT J1548-like transients.* While inapplicable to VT J1548 itself, this follow up could help constrain the presence

of features such as He II and Bowen fluorescence lines that may have faded by the late time observations of VT J1548.

- *Long term NIR/MIR monitoring of VT J1548 (and similar transients).* Knowledge of the IR evolution is essential to constrain the origin of the flare. If this event is triggered by a TDE, we expect the emission to begin fading soon. If VT J1548 is an AGN flare, it could remain bright for decades or longer. Combined with theoretical modelling of AGN flares and TDE in AGN, the fade time of the event may constrain its origin. Some AGN flares may fade more quickly than a typical TDE (327). We are actively monitoring VT J1548 in the NIR. If SDSS J1548 is also monitored in the MIR for multiple decades, we could also constrain the presence of a repeat flare, which may provide a smoking gun for extreme AGN variability.
- *Long term optical spectroscopic monitoring.* We are actively following up VT J1548 with optical spectrographs to determine the evolution of the broad Balmer emission, the coronal lines (both profile and flux), as well as any other features that may begin to evolve.
- *Long term X-ray/Radio (100s of MHz – GHz) monitoring.* Long term X-ray/radio monitoring will allow us to constrain the origin of emission at both wavelengths. As we have mentioned the importance of this follow up throughout the text, we do not discuss it further.
- *Optical IFU follow up.* Optical IFU observations would allow us to constrain whether the pre-existing high ionization emission, such as the [O III] lines, are nuclear or very extended. Then, we could constrain the history of AGN activity.

This list is far from exhaustive (e.g., polarimetric observations and hard X-ray spectra would prove useful).

On the theoretical side, the most critical work is extensive simulations of TDEs in AGN-like environments. In particular, given the difficulty of getting early-time follow up of these events, detailed simulations of the fading of the TDE emission would be valuable. It would also be useful to model the response of an AGN torus to a TDE-like flare accounting for different torus models, inclination angles, and flare durations/shapes. Finally, detailed models of the expected evolution of coronal line

flux and profile during a TDE-like event would prove extremely valuable towards constraining the timescales of ECLEs, and hence their triggers.

### 3.8 Conclusions

We have presented the first radio selected ECLE, VT J1548, and its host, SDSS J1548. This work can be summarized as follows:

1. VT J1548 is associated with a MIR flare that rose in  $\sim 900$  days and has plateaued with a constant color corresponding to a blackbody with  $T \sim 1000$  K and  $L \sim 0.1L_{\text{edd}}$  (Figure 3.3). Radio emission turned on during the WISE flare. The radio SED can be modeled as synchrotron from an outflow incident on an inhomogeneous medium. No optical flare is detected. Transient, X-ray emission with  $L_{0.2-10\text{keV}} \sim 10^{42}$  erg  $\text{s}^{-1}$  was detected  $\sim 1000$  days after the MIR flare began.
2. Transient coronal lines with  $L_{\text{cor.}} \sim L_{[\text{O III}]}$  and broad  $\text{H}\alpha$  emission are detected  $\sim 1000$  days post-flare. The coronal line emission from VT J1548 is double peaked with a velocity separation  $\sim 230$  km  $\text{s}^{-1}$  (Figure 3.4). The broad  $\text{H}\alpha$  emission has FWHM  $\sim 1900$  km  $\text{s}^{-1}$ . No broad  $\text{H}\beta$  is detected, suggesting a high extinction  $E(B-V) \gtrsim 0.7$  (Figure 3.5).
3. SDSS J1548, the host of VT J1548, is an S0 galaxy at  $z = 0.031$  ( $d_L = 137$  Mpc). Its pre-flare line ratios are consistent with no or weak AGN activity (Figure 3.2). Its pre-flare WISE color was inconsistent with typical AGN colors and it showed no significant MIR variability. It hosts a low mass SMBH with  $\log M_{\text{BH}}/M_{\odot} = 6.48 \pm 0.33$ .
4. VT J1548 is unique when compared to other transients, although it shares individual properties with other objects (Table 3.6). It is reminiscent of the class reported by (331) and the MIR flare SDSS J1657+2345 (326), which are all slowly evolving. None of these events emit in the radio like VT J1548, nor do they show coronal line emission. The only transient with radio emission which resembles that from VT J1548 is the TDE candidate ASASSN-15oi, which was detected at late-times in the X-ray and radio with an unusual radio SED, although none of its other properties resemble VT J1548.
5. VT J1548 can be modeled with a broad line region ( $\sim 10^{-3}$  pc) surrounded by a dusty torus (Figure 3.11). At the inner edge of the torus ( $\sim 0.4$  pc),

sublimated dust accelerated in a radiation-driven wind causes the formation of coronal line-emitting clouds. Alternatively, the coronal line-emitting clouds are orbiting the SMBH. Some of the dust in the torus is heated to produce the MIR flare. The synchrotron-emitting outflow is launched near the SMBH and collides with the torus.

6. VT J1548 could plausibly have been triggered by a tidal disruption event or an AGN disk instability. In the TDE scenario, the high observed Eddington ratio, the radio emission, and the slow evolution are unusual. In the AGN scenario, the lack of strong pre-flare AGN activity is uncommon, the high Eddington ratio is unexpected, and the unusual radio emission is unprecedented.

We have emphasized the difficulty of distinguishing between an AGN flare and a TDE in a highly obscured galaxy with evidence for weak AGN activity. Such efforts are particularly complicated because of the freedom in structure and optical depth of a torus, which can eliminate most all timescale information if the inner  $\sim$ pc of the galaxy is too extinguished to be directly visible. Moreover, the uncertainty in the timescale, luminosity, and multiwavelength properties of flares from TDEs (in both AGN and quiescent galaxies) as well as AGN disk instability-driven flares renders it difficult to distinguish between these events even with early time follow up. While it may be difficult to constrain the origins of individual events, population studies are key to characterizing the range and relative frequency of these different flares. The identification of *classes* of transients is likely to be less ambiguous if members are observed from a range of inclination angles over a variety of time baselines in multiple wavebands.

### 3.9 Appendix

#### VLASS Transient Search

We identified transient sources between the VLASS Epoch 2.1 and Epoch 1 observations using the following procedure. First, we run the source extractor PyBDSF (359) on the VLASS Epoch 2.1 quicklook images provided by the National Radio Astronomy Observatory (NRAO) (133), spanning  $\sim 17,000$  deg<sup>2</sup>. We identify point source candidates as regions within the Epoch 2.1 images where contiguous “islands” of  $> 4\sigma$  pixels surrounding a peak pixel of  $> 6\sigma$  can be well described by a single 2D Gaussian. Some of these candidates are due to deconvolution artifacts: typically sidelobes near bright sources or extended stripes. We flag the majority of these artifacts in an automated way using a stripe detection algorithm and by comparing

the pixels near the source to the pixels in the 1 arcminute region around it (Dong et al. in prep). After flagging likely artifacts, we estimate the flux of each point source candidate as its peak pixel value, and the uncertainty as the local value in the quicklook RMS maps provided by the NRAO. We then check the corresponding location in the Epoch 1.1 image data. Based on the local pixel values in each epoch, we estimate the probability of variability by comparison with a grid of Monte Carlo simulations of sources embedded in Gaussian noise (Dong et al. in prep). We create an initial transient catalog in which we retain sources that have (1) no artifact flags, (2) a  $>90\%$  probability of being variable, (3) a peak  $>7\sigma$  in Epoch 2.1, and (4) a peak  $< 3\sigma$  in Epoch 1.1. We visually inspected all transient candidates in the initial catalog, removing the artifacts that were missed by our automated filters. The remaining sources comprise our final transient catalog.

### **Spectral Fitting Methods**

We use a consistent method to fit the optical emission lines in all of our observations. First, we correct the spectrum for Milky Way extinction using  $A_V = 0.1606$  and  $R_V = 3.1$  (360, 361). We remove the stellar continuum using a full spectrum fit with the penalized pixel-fitting (pPXF) method. We use the implementation of pPXF from (362, 363) with the default MILES templates (364). We run the fit using recommended procedures to determine the appropriate regularization error and refer the reader to the pPXF documentation for details. Rather than mask the emission lines during this fit, we include Gaussian components for each emission line, and allow the parameters for narrow forbidden, narrow allowed, and broad lines to float separately. These Gaussian fits are not used to measure the line fluxes; we only include emission line components to prevent the lines from biasing the pPXF fit. Our exact treatment of the emission lines does not affect our results. We also include a multiplicative normalization component that is a degree 10 polynomial.

The MILES templates cover the wavelength range  $3525 - 7500 \text{ \AA}$ , which does not span the full wavelength range of our observations. Hence, we perform an additional median-subtraction to normalize the remaining parts of the spectrum, as well as to correct for any continuum flux that was poorly removed by the pPXF fit. First, we subtract the best-fit stellar continuum and emission lines found by pPXF from our observed spectrum. We subtract the value of the best-fit stellar continuum at the nearest available pixel from the portions of the spectrum not covered by the template fit. From this procedure, we have a preliminary continuum-subtracted spectrum. Next, we median smooth this preliminary continuum-subtracted spectrum

with a kernel of  $\sim 130$  pixels, which we found was sufficient for both the LRIS and SDSS spectra. We identify all points in the spectrum that are  $> 10\sigma$  from the resulting median smoothed continuum and mask them, as well as the  $\sim 10$  pixels neighboring those points. Then, we median smooth the preliminary continuum-subtracted spectrum a second time with these pixels masked. This gives us a correction to the continuum, which we subtract from our preliminary continuum-subtracted spectrum to obtain the final continuum-subtracted spectrum.

Next, we measure the emission line fluxes from the final continuum-subtracted spectrum. We model each line with as many Gaussian profiles as required, and we specify throughout the text any case where multiple components are needed. We let the width of the Gaussians float independently for different lines, and include a broad component if necessary. We also include a linear continuum component to account for any residual flux. We fit each emission line separately unless multiple emission lines are so close that they cannot be fit independently (e.g., the  $H\alpha$  and [N II] lines). We fit a region around each line that includes a  $\sim 10 - 20 \text{ \AA}$  continuum region.

We run the emission line fit using the `dynesty` Nested Sampler (206, 365). Our stopping condition is  $\Delta \log \mathcal{Z} = 5$ , which we verify does not affect our results. Unless otherwise specified, we report  $1\sigma$  errors on all line fluxes.

### Measurement of the Bulge Velocity Dispersion

We measure the bulge velocity dispersion using the  $R \sim 13,000$  ESI spectrum of SDSS J1548 following the methodology in (366). To ensure that we are measuring the *bulge* velocity dispersion, we consider two different methods of extracting the host spectrum: first, we use the spectrum extracted from the full slit; second, we isolate the bulge by using the spectrum extracted from a region centered on the peak galaxy light and with width  $0.5''$ , which roughly corresponds to the seeing during the observation. We find no significant difference in the results.

We use the (363) implementation of `pPXF` to measure the velocity dispersion. First, we mask all emission lines in the spectrum, including the Hydrogen Balmer lines and all TDE features. We fit the spectrum using the (367, 368) high resolution ( $R \sim 10000$ ) template library. We run the fit using the recommended `pPXF` settings. The best fit velocity dispersion is  $\sim 66 \text{ km s}^{-1}$ . Removing the intrinsic resolution ( $\sim 22 \text{ km s}^{-1}$ ) only changes the result by a few  $\text{km s}^{-1}$ . Next, we convert to SMBH mass using the relation from (369). The intrinsic scatter in the  $M_{\text{BH}} - \sigma_*$  relation strongly

dominates our results, although we also propagate through both the uncertainties in the velocity dispersion measurement and assumed uncertainties in the intrinsic resolution. We find an SMBH mass  $\log M_{\text{BH}}/M_{\odot} = 5.98 \pm 0.38$ . Alternatively, the more recent  $M_{\text{BH}} - \sigma_*$  relation from (47) gives  $\log M_{\text{BH}}/M_{\odot} = 6.48 \pm 0.33$ , which is consistent with the (369) within  $1\sigma$ . We adopt the latter calibration because it includes more low mass galaxies.

*Chapter 4*

VLASS TIDAL DISRUPTION EVENTS WITH OPTICAL  
FLARES I: THE SAMPLE AND A COMPARISON TO  
OPTICALLY-SELECTED TDES

Somalwar, J. J. et al. (Apr. 2025). In: ApJ 982, 163. doi: 10.3847/1538-4357/adba4f

Jean J. Somalwar<sup>1</sup>, Vikram Ravi<sup>1</sup>, Dillon Z. Dong<sup>1</sup>, Erica Hammerstein<sup>2</sup>, Gregg Hallinan<sup>1</sup>, Casey Law<sup>1</sup>, Jessie Miller<sup>1</sup>, Steven T. Myers<sup>3</sup>, Yuhan Yao<sup>1</sup>, Richard Dekany<sup>4</sup>, Matthew Graham<sup>1</sup>, Steven L. Groom<sup>5</sup>, Josiah Purdum<sup>1</sup>, and Avery Wold<sup>5</sup>

<sup>1</sup>Cahill Center for Astronomy and Astrophysics, MC 249-17 California Institute of Technology, Pasadena CA 91125, USA.

<sup>2</sup>Department of Astronomy, University of Maryland, College Park, MD 20742, USA

<sup>3</sup>National Radio Astronomy Observatory, P.O. Box O, Socorro, NM 87801, USA

<sup>4</sup>Caltech Optical Observatories, California Institute of Technology, Pasadena, CA 91125

<sup>5</sup>IPAC, California Institute of Technology, 1200 E. California Blvd, Pasadena, CA 91125, USA

### **Abstract**

In this work, we use the Jansky VLA Sky Survey (VLASS) to compile the first sample of six radio-selected tidal disruption events (TDEs) with transient optical counterparts. While we still lack the statistics to do detailed population studies of radio-selected TDEs, we use these events to suggest trends in host galaxy and optical light curve properties that may correlate with the presence of radio emission, and hence can inform optically-selected TDE radio follow-up campaigns. We find tentative trends that radio-selected TDEs tend to have faint and cool optical flares, as well as host galaxies with low SMBH masses, although larger samples are required to establish these trends as statistically significant. Our radio-selected TDEs also tend to have more energetic, larger radio emitting regions than radio-detected, optically-selected TDEs. We consider possible explanations for these trends, including by invoking super-Eddington accretion and enhanced circumnuclear media. Finally, we constrain the radio-emitting TDE rate to be  $\gtrsim 10 \text{ Gpc}^{-3} \text{ yr}^{-1}$ .

### **4.1 Introduction**

Extragalactic radio-synchrotron transients open a novel window onto some of the most extreme activity in the universe. These transients are typically associated

with dramatic accretion events and stellar explosions, among a multitude of other possibilities. Until recently, it was impossible to obtain a uniform census of the transient radio sky due to the difficulty of performing a multi-epoch, full sky radio survey. The advent of surveys like the Caltech-NRAO Stripe 82 Survey (CNSS; (155)), the Jansky Very Large Array Sky Survey (VLASS; (133)), the Australian Square Kilometre Array Pathfinder Variables and Slow Transients (ASKAP VAST; (370)) survey have transformed our understanding by enabling the compilation of samples of radio transients that are assembled with a known selection function.

Despite this progress, many open questions remain. In particular, the relationship between radio transients and higher wavelength flares remains poorly understood, despite providing significant insight into the underlying physical processes. Tidal disruption events (TDEs) provide a quintessential example of this. TDEs occur when a star strays within the tidal radius<sup>1</sup> of a supermassive black hole (SMBH) (e.g. 110, 111, 371). TDEs were originally theorized to produce X-ray emission, so many of the early searches for these events focused on this waveband using the ROSAT All Sky Survey (RASS; e.g., (372)). Soon, UV and optical searches using GALEX and SDSS began producing TDE candidates (e.g. 122).

Throughout this effort, the question of radio emission from TDEs remained unconstrained. (283) first suggested that a radio transient could be produced if TDEs can launch relativistic, highly collimated jets, and the first detection of a candidate jetted TDE followed shortly (373). Efforts to follow-up TDEs in the radio followed, but these tended to involve one or a few observations shortly after the higher wavelength flare and few detections resulted (see 150, for a review). Recently, the detection rate has increased through long-timescale follow-up of optically-selected TDEs (e.g. 149, 151, 153, 253, 374). Still, without a better understanding of the mechanisms that produce TDE radio emission and how they may be related to the multiwavelength properties of the events, it is difficult to identify the optimal candidates for follow-up, the optimal follow-up cadence, and the optimal follow-up sensitivity.

Moreover, even if radio instruments could be used to comprehensively follow up all TDEs, the resulting radio-detected samples will be biased. Any radio-emitting TDEs discovered through follow-up of, e.g., optically-selected events, will be biased towards those TDEs that produce optical emission, and it has already been established that not all TDEs do so (e.g. 130, 163). This renders it near impossible to

---

<sup>1</sup>The tidal radius  $R_T$  where the tidal forces from a SMBH overpower the internal gravity of a star is given by  $R_T \approx R_*(M_{\text{BH}}/M_*)^{-1/3}$  for a non-spinning black hole of mass  $M_{\text{BH}}$  and a star of mass  $M_*$  and radius  $R_*$ .

compile a view of the complete landscape of radio emission through follow-up of known TDEs: if there is a correlation between optical emission and radio emission, selecting on optically-emitting TDEs will bias the expected types of radio emission.

Table 4.1: Properties of our TDE sample

Name	AT Name	R.A.	Dec.	$\Delta d$ ["]	$z$	$f_{\nu, E2}$ [mJy]
VT J0813 <sup>1,2,3</sup>	AT 2019azh	08 <sup>h</sup> 13 <sup>m</sup> 17.0 <sup>s</sup>	+22°38′54.0″	0.0	0.022	1.0
VT J1008 <sup>4,5,6</sup>	AT 2020vdq	10 <sup>h</sup> 08 <sup>m</sup> 53.4 <sup>s</sup>	+42°43′00.2″	0.18	0.045	1.5
VT J1356		13 <sup>h</sup> 56 <sup>m</sup> 12.1 <sup>s</sup>	−26°58′50.7″	0.54	0.018	2.5
VT J1752 <sup>4,6</sup>	AT 2019baf	17 <sup>h</sup> 52 <sup>m</sup> 00.1 <sup>s</sup>	+65°37′36.0″	0.13	0.089	1.4
VT J2012		20 <sup>h</sup> 12 <sup>m</sup> 29.9 <sup>s</sup>	−17°05′56.3″	0.2	0.053	1.1
VT J2030		20 <sup>h</sup> 30 <sup>m</sup> 47.3 <sup>s</sup>	+04°13′31.0″	0.19	0.061	1.4

**Notes.** Redshifts are measured from our follow-up optical spectroscopy as described in Appendix 4.10. References: <sup>1</sup>(128), <sup>2</sup>(253), <sup>3</sup>(255), <sup>4</sup>(134), <sup>5</sup>(375), <sup>6</sup>(9)

A radio-selected TDE sample is key to constraining these many unknowns, and the 3 GHz Jansky Very Large Array Sky Survey (VLASS; (133)) is ideal for such an effort: predictions have estimated that  $\sim 100$  TDEs could be detectable using that survey (376). The first candidates detected in this survey have already been published (11, 163, 219), and compilation of the first VLASS-selected TDE sample, regardless of multiwavelength counterpart, is underway (Somalwar et al., in prep.).

With this VLASS TDE sample, we can begin answering some of the questions posed earlier about the range of radio emission and the emission mechanisms, as well as the relationship between the radio emission and multiwavelength emission. In this paper, we focus on the latter questions: we present the first sample of radio-selected, optically-detected TDEs.

For clarity, we have divided our analysis into three papers. In this paper (Paper I), we present our full radio-selected, optically-detected TDE sample and perform observational comparisons between radio-selected, optically-detected TDEs and optically-selected TDEs, with the aim of identifying those factors that distinguish between radio-emitting TDEs and radio-quiet TDEs. We also discuss the rate of radio-bright, optically-bright TDEs. We will briefly speculate on the physical mechanisms at play. We defer detailed discussion of both the multiwavelength properties and physical interpretations of each event to the companion papers. (9) discusses late-time, transient, optical spectral features detected from two of the events. (377) discusses evidence for and implications of jet launching from three of the events.

## 4.2 Sample Selection

We compile our radio-selected TDE sample using data from the Very Large Array Sky Survey (VLASS; (133)). VLASS is an ongoing effort to observe the entire sky with  $\delta > -40^\circ$  at 3 GHz for three epochs with a cadence of  $\sim 2$  years. VLASS has a  $1\sigma$  sensitivity of  $\sim 0.13$  mJy/beam and a spatial resolution of  $\sim 2.5''$ . Each epoch is divided into two halves. The first half of epoch one, which we denote E1.1, was observed in 2017. The second half of epoch one (E1.2) was observed 2018. E2.1 was observed in 2020, and E2.2 was observed from 2021. E3.1 is ongoing (Jan 2023-present).

We identified TDE candidates using the transient catalog of Dong et al., in prep., who identified all sources that were detected at  $> 7\sigma$  in E2 but not significantly detected ( $< 3\sigma$ ) in E1; i.e., this catalog contains all transients that are rising between E1 and E2. Details about the transient detection algorithm are described in (163) and Dong et al., in prep. We select TDE candidates from this catalog using the following criteria:

1. the transient is within  $1''$  of the position of a source in the PanSTARRS catalog (175, 284);
2. the associated source is a galaxy; i.e., it is inconsistent with being a star using all public catalogs, including GAIA (to remove all objects with significant parallax; (378, 379)) and the PanSTARRS star-galaxy classifier (380);
3. the host galaxy must show no evidence for strong AGN activity. Among the criteria used to identify AGN, we consider: the position of the source on the WISE W1-W2 and W2-W3 color diagram (381) and rule out sources within the AGN region defined by (382); any evidence for past optical, X-ray, or radio variability/detections that could indicate AGN activity; and any public optical spectra with broad or narrow line emission that indicate strong AGN activity. We have found that this criteria rules out strong AGN, but some weak AGN remain, as evidenced by the narrow line emission in our optical spectra, discussed in Section 4.3. In this paper, we include these objects and will discuss the implications of their AGN activity primarily in (377);
4. the host galaxy must have a PanSTARRS photometric redshift  $z_{\text{phot}} < 0.25$  (380). When PanSTARRS photometric redshifts are unavailable, we inspect catalog data for the galaxy to identify the redshift. If no redshift information

is available, we measure a redshift using an SED fit to the galaxy photometry, following the procedure discussed in Appendix 4.10. We include this redshift cut to ensure that we can obtain multiwavelength follow-up to detect counterparts and classify the host galaxies with reasonable exposure times. This redshift cut will bias us against rare TDEs; e.g., we are not sensitive to most on-axis jetted TDEs, which are generally found at  $z \gtrsim 0.3$ . Future work will consider the higher-redshift transients.

In summary, this selection criteria will identify nuclear radio flares in nearby non- or weakly-active galaxies. We obtained optical spectroscopy for all events to measure spectroscopic redshifts, and do not consider any source with  $z_{\text{spec}} > 0.25$ . The resulting sample has  $\sim 100$  objects. We will perform a detailed analysis of the completeness of this selection in future work, when we present the full VLASS TDE sample.

In this paper, we only consider transients with associated optical flares. We obtained forced-photometry at the position of each transient from the Zwicky Transient Facility (ZTF; *gri* bands; (124–127)) and the Asteroid Terrestrial-impact Last Alert System (ATLAS; *co* bands; (176)) using recommended procedures. Our sample includes every transient with an optical lightcurve with at least three  $5\sigma$  detections and at least one  $10\sigma$  in any bands. We chose this criteria to ensure that the flare is significantly detected, and thus amenable to quantitative analysis of the flare evolution. Note that we have already ruled out events with long-term, AGN-like variability in our TDE candidate selection. While we do not do a detailed search of optical lightcurves from the All-Sky Automated Survey for Supernovae (ASASSN; (383)) because of limited optical color information and sensitivity, our final sample includes one source that has an ASASSN flare with simultaneous MIR observations, and thus more constraints on the physical properties of the optical flare (Appendix 4.10).

The resulting sample has six objects, the properties of which are summarized in Table 4.1. These sources are named using our VLASS transient naming convention: VT J081316.97+223853.99 (henceforth VT J0813), VT J100853.44+424300.22 (VT J1008), VT J135612.14-265850.71 (VT J1356), VT J175200.13+653736.04 (J1752), VT J201229.90-170556.32 (VT J2012), and VT J203057.34+041330.97 (VT J2030). We refer to the host galaxies of these objects using the coordinates prefixed with HG (host galaxy; e.g., HG J1356, HG J1008, etc.). In plots, we often

label the individual transients or host galaxies without the prefixes (e.g., J1356, J1008), except when the prefixes are necessary for clarity.

### **The optically-selected TDE sample**

A key aspect of this paper is our comparison of radio-selected and optically-selected TDEs; hence, here we present our chosen optically-selected comparison samples. We consider two different samples: the (134) and (13) samples. The (13) sample includes all classified TDEs discovered in the first  $\sim 3$  years of ZTF. (134) presents a complete sample of TDEs with peak  $g$ -band mag  $\lesssim 19$  during the first three years of ZTF.

We largely compare to the (134) sample. However, when considering host galaxy stellar masses, colors, or star-formation rates, or Baldwin, Phillips & Terlevich (BPT;(4)) classifications, we adopt the (13) sample, because our methods better align with theirs.

In both cases, we restrict our comparison to events at redshifts  $z < 0.1$ . We apply this cut to ensure that redshift evolution doesn't bias our results: the highest redshift object in our sample is at  $z = 0.089$ , whereas the optically-selected TDEs range to much larger redshifts.

Note that there are known radio-emitting TDEs in the optically-selected sample that were not detected in our sample, either because they were below the sensitivity of VLASS or were already detectable in the first epoch of VLASS.

### **4.3 Observations and Data Reduction**

We have performed an extensive multi-wavelength follow-up campaign for all of our TDE candidates. We present a relevant subset of that data here; the full dataset for each TDE candidate is presented in the corresponding companion paper. In this section, we describe our observations and data reduction procedures.

#### **Radio observations**

Each TDE candidate has one or more multi-frequency radio observations from the Jansky Very Large Array. We summarize the observations for all sources except J0813 in Table 4.2. All observations used flux and phase calibrators recommended by the VLA<sup>2</sup> and typical exposure times were  $\sim 5$  min. on source in each band. The reduced VLA SEDs for J0813 were published in (253), so we adopt the spectra

<sup>2</sup><https://science.nrao.edu/facilities/vla/observing/callist>

Table 4.2: Summary of VLA follow-up

Name	MJD	Configuration	Freq. range [GHz]	Program (PI)
VT J1008	59612	B→BnA	1–12	21B-322 (G. Hallinan)
VT J1356	59626	BnA	1–12	21B-322 (G. Hallinan)
VT J1752	59273	A	1–12	20B-393 (D. Dong)
	59632	BnA	1–12	21B-322 (G. Hallinan)
VT J2012	59257	A	1–12	20B-393 (D. Dong)
	59271	A	1–12	20B-393 (D. Dong)
VT J2030	58881	C	1–18	19A-013 (PI: K. Alexander)
	59130	C	1–18	20A-372 (PI: K. Alexander)
	59257	C	1–12	20B-393 (PI: D. Dong)

tabulated in that work. We reduced all other observations using the VLA Calibration Pipeline 2022.2.0.64 and CASA version 6.4.1 (384). We imaged the data using standard CASA recipes, and measured the flux density of each source as the flux density of the peak pixel in a  $50 \times 50$  pixel box centered on the source location. All sources were consistent with point sources.

### Optical transient photometry

We retrieve forced, difference photometry from the Asteroid Terrestrial-impact Last Alert System (ATLAS; (176)) and Zwicky Transient Facility (ZTF; (124–127)) using the recommended procedures and automated pipelines for each survey. We use public data from the ATLAS survey, and both public and partnership data from ZTF. We load the data from both surveys using the Hybrid Analytic Flux Fitter (HAFFET; (385)) code, and then bin each lightcurve with a binsize of one day. The ATLAS photometry of J0813 use different baselines for  $\text{MJD} > 58895$ , leading to zeropoint offsets for this MJD range. We correct for the zeropoint offset by estimating the median non-transient flux in each filter from those data points at  $\text{MJD} > 59200$  in each and subtract that median flux from the lightcurve for  $\text{MJD} > 58895$ . Similarly, the ZTF host reference image of J2030 was taken while the transient was active, so it overestimates the baseline flux, and we correct for this by calculating the median flux in each band for  $\text{MJD} > 58500$  and subtracting this flux from the entire lightcurve.

We treat J1356 separately because it is the oldest transient and is not detected by ATLAS or ZTF. It is, however, detected by the All-Sky Automated Survey for Supernovae (ASASSN; (383)). We retrieved and processed the lightcurve using the recommended ASASSN tools (386, 387). Like for the other events, we binned the

lightcurve in one day bins.

### Host photometry

We retrieve host photometry for each TDE using the same methods as (13), to enable a like-to-like comparison with the results from that work. We refer the reader to (13) for a detailed description of the adopted methods. In brief, we retrieve SDSS or PanSTARRS, where SDSS is unavailable, Kron magnitudes. We also retrieve GALEX NUV and FUV photometry using recommended methods.

### Optical spectroscopy

HG J0813 was previously observed as part of the Sloan Digital Sky Survey (SDSS; (388)) Spectroscopic survey (270) on MJD 52943. We retrieved the spectrum of this source from the SDSS DR17 website.

We obtained optical spectra for the all our TDE candidates except VT J0813 using the Low Resolution Imaging Spectrometer (LRIS) on the Keck I telescope. In all cases, we centered the observation on the galactic nucleus using a parallactic angle. We used the 400/3400 grism, the 400/8500 grating with central wavelength 7830, and the 560 dichroic. The resulting wavelength range was  $\sim 1300\text{--}10000 \text{ \AA}$  and the resolution  $R \sim 700$ . We observed VT J1008 on MJD 59676 for 20 min using the 1'' slit with the standard star Feige 34. We observed VT J1356 on MJD 59616 for 10 min using the 1'' slit with the standard star Feige 34. We observed VT J1752 on MJD 59260 for 10 min using the 1.5'' slit with the standard star Feige 34. We observed VT J2012 on MJD 59464 for 10 min using the 1.5'' slit with the standard star BD+28. We observed VT J2030 on MJD 59464 for 10 min using the 1.5'' slit with the standard star Feige 34. We reduced the observations using the `lpipe` code with standard settings (291).

We obtained high-resolution optical spectra for a subset of the TDE candidates using the Echellette Spectrograph and Imager (ESI) on the Keck II telescope. We used the Echelle mode for all observations. We observed VT J0813 on MJD 59874 for 20 minutes using the 0.5'' arcsec slit. We observed VT J1008 on MJD 59908 for 22.5 min using the 0.3'' slit. We observed VT J2012 on MJD 59876 for 20 min using the 0.5'' arcsec slit. We observed VT J2030 on MJD 59874 for 20 min using the 0.5'' arcsec slit. The 0.5'' (0.3'') slit leads to an instrumental broadening of  $\sigma_{\text{inst}} = 15.8(9.5) \text{ km s}^{-1}$ . We reduced the spectra using the `makee` software following the default, recommended procedures for ESI data reduction.

#### 4.4 Summary of detailed transient properties

In this paper, we focus on the properties of the radio-selected, optically-bright TDE *population*, rather than the individual characteristics of each source. Hence, we will primarily discuss observations that are available for our full sample and for comparison optical TDE samples; namely, the optical lightcurves and spectra, host galaxy observations from public survey data, and the radio observations. Context about the individual transients is, however, useful for interpreting the results of this paper. Thus, we begin our paper with a brief review of the properties of each transient detailed in papers II/III and other sources.

**VT J0813** ((128, 253, 255, 377)): VT J0813 (otherwise known as ASASSN-19dj or AT2019azh) was first discovered as an optical transient by the ASASSN survey on Feb. 22 2019 (389). It was also detected by the ZTF and ATLAS surveys. The optical lightcurve is typical of TDEs. Transient Balmer and Helium lines were detected in follow-up optical spectra, leading to the classification of this source as a TDE-H+He (13, 128). In addition to the optical flare, this source was detected as an X-ray transient with peak luminosity  $L_X = 10^{43}$  erg s<sup>-1</sup> that brightened  $\sim 7$  months after the optical peak (128). The host galaxy shows a disturbed morphology, characteristic of a recent merger or interaction (377).

This source was first detected as a GHz radio transient by (390) with the e-MERLIN telescope and was then observed by numerous radio telescopes, notably by (253), who obtained multi-epoch radio SEDs and argued that the radio-emitting outflow was non-relativistic and had a very optically-thin spectral index. (255) further observed this source with a high cadence and argued that the radio variability was correlated with the X-ray spectral variability and luminosity in a manner similar to that observed from X-ray binaries. They used this to argue for the presence of a jet subject to the accretion state changes in the accretion disk.

**VT J1008** (9, 134, 375): VT J1008 (AT 2020vdq) was first detected as an optical transient by ZTF on Oct. 4 2020. There is no prompt follow-up for this source, so the early time radio and X-ray behavior is unknown. It was not reported as an X-ray transient in any public X-ray surveys. Late-time ( $\sim 2$  years post-optical peak) Neil Gehrels Swift Observatory X-ray Telescope (Swift/XRT; (188)) follow-up  $\sim 2$  years post-TDE did not detect any significant X-ray emission ( $3\sigma$  upper limit  $< 10^{41.8}$  erg s<sup>-1</sup>). In an optical spectrum  $\sim 2$  years post-optical-peak, transient Balmer lines and He II lines are detected with widths  $\sim 1000$  km s<sup>-1</sup> and luminosities  $\sim 10^{40}$  erg s<sup>-1</sup>. These lines are commonly detected from TDEs, but they are typically much broader

( $\sim 10^4$  km s $^{-1}$ ) and fade within a year. The origin of these lines is considered in detail by (9). Roughly three years after the initial optical flare, this source re-brightened in the optical. (375) constrain the origin of the rebrightening and suggest that this event is a repeating, partial tidal disruption event. No new radio emission was detected post-rebrightening.

**VT J1356** (Appendix 4.10): VT J1356 is detected as a transient in ASASSN forced photometry. It is simultaneously detected as a NIR transient in NEOWISE photometry. It is the oldest of our TDE sample, with the ASASSN detections occurring  $\sim 8$  years ago. The NIR flare is double peaked, with an initial, hot ( $T \sim 10^4$  K) flare followed by a  $\gtrsim 5$  year cool flare ( $T \sim 10^3$  K), consistent with blackbody emission from dust at  $\sim 0.5$  pc that has been heated by the high energy emission produced during the transient. This source is not discussed in either of the companion papers, so we describe its properties in detail in Appendix 4.10.

**VT J1752** ((377), simultaneously reported by (134)): VT J1752 (AT2019baf) was first reported as a transient by ZTF on Jan. 9 2019. The optical lightcurve showed an unusual double peaked structure. There was no prompt multiwavelength follow-up for this source, so the early time radio and X-ray behavior is unknown. It was not reported as an X-ray transient in any public X-ray surveys. Late-time ( $\sim 2$  years post-optical peak) Swift/XRT follow-up detected an X-ray source with  $L_X = 10^{42.4}$  erg s $^{-1}$ . No transient optical spectral features were detected in follow-up optical spectra. The host galaxy shows a disturbed morphology, characteristic of a recent merger or interaction. The radio SED is best-fit by a multi-component synchrotron model, suggesting the presence of multiple outflows or a structured outflow. The outflows have high luminosities and energies, suggestive of the presence of a jet.

**VT J2012** ((9)): VT J2012 was first detected as a transient by the ATLAS survey on 58772. It has multiwavelength properties that are very similar to those of VT J1008. The only major differences between these two events is that no transient Helium lines are detected from VT J2012, and the transient Balmer lines are redshifted by  $\sim 700$  km s $^{-1}$ . There is no blueshifted component.

**VT J2030** ((377)): VT J2030 was first detected as transient by the XMM-Newton Slew Survey team, who undertook an X-ray and radio follow-up campaign. The X-ray emission from this source has an peak luminosity  $\sim 10^{43.8}$  erg s $^{-1}$ , but with strong variability of a factor of a few on  $\sim$ week timescales. The radio emission also shows non-monotonic evolution. Both of these properties are consistent with the presence of a young jet.

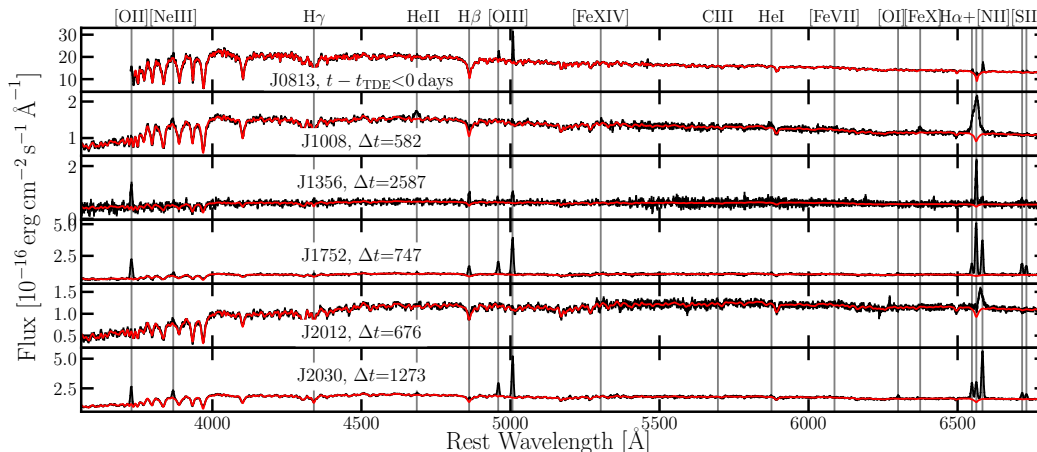


Figure 4.1: The optical spectra for the radio-selected TDEs in our sample. The observed spectra are shown in black and the best-fit stellar continuum in red (Appendix 4.10). The Balmer, He II, and [Fe X] features observed from J1008 and J2012 are associated with the transient and are discussed in (9).

VT J2030 was detected as an optical transient by the ZTF survey. However, the transient occurred during the start of ZTF, so it was present in the reference images and the transient appeared as a negative flux in the ZTF photometry. VT J2030 was also detected as a transient by the ATLAS survey. In this survey, it appeared like a typical TDE, with a positive rise and then decay.

#### 4.5 Host galaxies

Table 4.3: Host Galaxy

Name	$z$	$\log \frac{M_*}{M_\odot}$	$\log \frac{\sigma_*}{\text{km s}^{-1}}$	$\log \frac{M_{\text{BH}}(M_*)}{M_\odot}$	$\log \frac{M_{\text{BH}}(\sigma_*)}{M_\odot}$	BPT	$\log \frac{\text{SFR}_{\text{SED}}}{(M_\odot/\text{yr})}$	$A_V$	$(u-r)_0$
J0813	0.022	$9.79^{0.00}_{0.00}$	$68 \pm 2$	$6.99^{+0.19}_{-0.21}$	$6.44 \pm 0.29$	Sey.	$0.27^{0.04}_{0.04}$	$0.12^{+0.08}_{-0.10}$	$1.77^{0.01}_{0.00}$
J1008	0.045	$9.16^{0.30}_{0.10}$	$44 \pm 3$	$4.81^{+0.40}_{-0.32}$	$5.59 \pm 0.29$	Q?	$0.07^{0.03}_{0.06}$	$0.18^{+0.14}_{-0.13}$	$1.86^{0.15}_{0.11}$
J1356	0.018	$8.94^{0.39}_{0.09}$	—	$5.08^{+0.28}_{-0.30}$	—	SF	$0.08^{0.07}_{0.08}$	$0.08^{+0.05}_{-0.23}$	$1.63^{0.25}_{0.24}$
J1752	0.089	$10.07^{0.32}_{0.07}$	—	$6.91^{+0.28}_{-0.31}$	—	Sey.	$2.41^{3.70}_{0.78}$	$1.10^{+0.35}_{-0.30}$	$1.93^{0.15}_{0.15}$
J2012	0.053	$9.90^{0.32}_{0.09}$	$59 \pm 2$	$6.55^{+0.24}_{-0.32}$	$6.17 \pm 0.31$	Q?	$0.00^{0.06}_{0.00}$	$0.32^{+0.23}_{-0.28}$	$2.34^{0.08}_{0.10}$
J2030	0.061	$9.79^{0.26}_{0.01}$	$62 \pm 5$	$6.37^{+0.22}_{-0.23}$	$6.25 \pm 0.31$	SF	$0.50^{0.10}_{0.07}$	$0.14^{+0.09}_{-0.13}$	$1.84^{0.09}_{0.07}$

**Notes.** The host galaxy properties of our radio-selected TDE sample. The methods of measuring these properties are described in Section 4.5.

In the rest of this paper, our primary goal is to constrain the physical properties that distinguish between radio-selected, optically-bright and optically-selected TDEs. This will rely on observations that are uniformly available for both the radio and optically selected samples; namely, host galaxy photometry and spectroscopy and

optical light curves.

We begin by considering the properties of the host galaxies. The properties of host galaxy directly affect the environment in which the transient occurs and the properties of the astrophysical objects that produced the transient; for example, the presence of long-lived ionized emission lines in the optical spectra can suggest the presence of an AGN, or the morphology and color of the host can suggest that the galaxy recently underwent a merger or interaction. The differences in the host galaxies of these radio-selected, optically-detected transients will inform our understanding of the parameters that control radio emission from TDEs.

Each of the following sections considers one or a subset of the host galaxy properties. We begin by describing the relevance of each property, then discuss our methodology for constraining it, and finally compare the radio-selected host properties to those of the optically-selected sample. The host galaxy properties of our sample, constrained as described in the following sections, are summarized in Table 4.3.

### **Black hole and stellar mass**

SMBHs are central to TDEs and the TDE evolution is certainly affected by the black hole mass. For SMBH masses  $M_{\text{BH}} \gtrsim 10^8 M_{\odot}$  the tidal radius  $R_T \sim R_*(M_{\text{BH}}/M_*)^{2/3}$  is smaller than the Schwarzschild radius  $R_s \sim 2GM_{\text{BH}}/c^2$ , so any star on an orbit that reaches  $R < R_T$  is swallowed whole rather than disrupted. This limit assumes a non-spinning SMBH: if the SMBH has a high spin, the event horizon is smaller and thus TDEs can occur. SMBH mass may also affect the efficiency with which the TDE accretion disk forms. In some models of TDE evolution, an accretion disk forms when the stellar tidal stream precesses due to Lense–Thirring precession and collides with itself, dissipating energy (348). The rate of Lense-Thirring precession is  $\dot{\Omega} \sim M_{\text{BH}}^2$ , so these collisions will occur less frequently, if at all, for TDEs by low mass SMBHs (113). This might reduce the high energy (X-ray, UV) emission, if that emission is partly produced during these shocks. Lower precession could also reduce optical emission, if optical emission is produced when outflowing material that becomes unbound during the shocks reprocesses the higher energy emission (113). Radio emission may also be affected; for example, if radio emission is produced from accretion disk winds, as delayed accretion disk formation could produce delayed winds.

We constrain the SMBH mass using two methods. First, the SMBH mass is tightly connected to the stellar mass (47). Thus, we begin by simply considering the stellar

mass distributions of our galaxies as compared to that of the optically-selected sample. We measure the stellar masses using fits to the UV/optical/IR spectral energy distributions with the `prospector` SED fitting code (190), following the exact methods of (13). The SMBH mass is also tightly connected to the stellar velocity dispersion, which we measure from our high resolution ESI spectra following the same methodology used by (163).

We can then measure SMBH mass distribution in two ways: (1) using SMBH masses from the host galaxy stellar mass-black hole mass relation from (134):

$$\log M_{\text{BH},9} = -(1.83 \pm 0.15) + (1.64 \pm 0.27) \times \log \left( \frac{M_*}{3 \times 10^{10} M_\odot} \right); \text{ intrinsic scatter}=0.18, \quad (4.1)$$

where  $M_{\text{BH},9}$  is the SMBH mass in units of  $10^9 M_\odot$ ; (2) for those sources with high-resolution optical spectra, we use SMBH masses measured using the stellar velocity dispersion-black hole mass relation. We adopt the  $M_{\text{BH}} - \sigma_*$  relation from (47), to match that used by (134):

$$\log \frac{M_{\text{BH}}}{10^9 M_\odot} = -(0.509 \pm 0.049) + (4.384 \pm 0.287) \times \log \left( \frac{\sigma_*}{200 \text{ km s}^{-1}} \right). \quad (4.2)$$

The intrinsic scatter in this relation is 0.29 dex.

We consider the relative black hole masses of the optically-selected and radio-selected samples using three different methods. First, we compare the stellar mass distributions of the two samples, with the caveat that differences in stellar mass can suggest different SMBH masses, or the same SMBH mass but different galactic formation pathways. Then, we compare the stellar velocity dispersion for those objects with stellar velocity measurements, which is a more direct probe of SMBH mass, but is limited by statistics. Finally, we compare the SMBH mass distributions directly, where the masses are inferred from the stellar velocity dispersions and stellar masses.

In Figure 4.2, we show histograms of each of these quantities for the radio-selected sample and the optically-selected sample. In the leftmost panel, we show the stellar mass distribution. In the middle panel, we show the stellar velocity dispersion distribution. In the rightmost panel, we show the black hole mass distribution. In all cases, we have chosen the bin size to be larger than the typical measurement

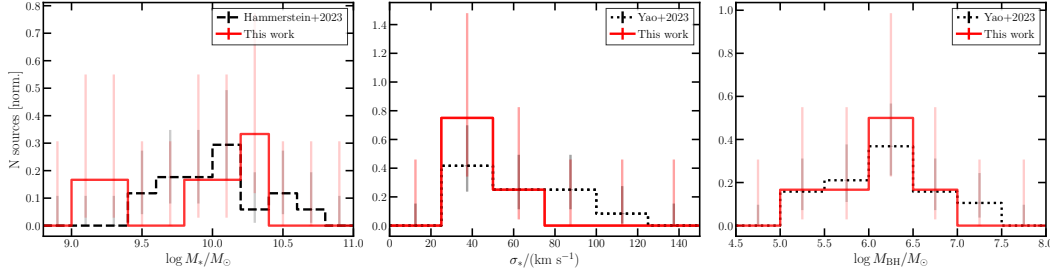


Figure 4.2: *Left panel:* Stellar mass distributions for the radio-selected TDE hosts in this work (red line) as compared to the optically-selected TDE hosts from (13) (dashed black line). The radio-selected TDEs tentatively prefer lower mass galaxies. *Middle panel:* Stellar velocity dispersion distributions for the radio-selected TDE hosts in this work (red line) as compared to the optically-selected TDE hosts from (134) (dotted black line). The radio-selected TDEs tentatively prefer lower velocity dispersion galaxies. *Right panel:* SMBH mass distributions for the radio-selected TDE hosts in this work (red line) as compared to the optically-selected TDE hosts from (134) (dotted black line).

uncertainty. There is a hint of a trend in both the stellar mass and velocity dispersion panels, the radio-selected TDEs appear to prefer lower values than those of the optically-selected TDEs. The mean velocity dispersion for the radio-selected TDE hosts is  $62 \pm 2 \text{ km s}^{-1}$  whereas that for the optically-selected hosts is  $82 \pm 3 \text{ km s}^{-1}$ , which are significantly offset from each other. Note that there are small statistics in both samples, but there has recently been a similar claim that those TDEs that can launch relativistic jets tend to have low black hole masses (391).

This trend towards lower SMBH masses is not present in the rightmost panel of Figure 4.2; however, we urge caution in interpreting this result. While our velocity dispersion measurements agree with (134), to which work we are comparing in this figure, our stellar mass measurements follow the methods of (13) and are consistently larger than those of (134) (see Figure 24 of (134)), which biases our SMBH mass distribution towards higher values. Hence, despite the apparent agreement, we believe there is a tentative trend towards lower SMBH masses for radio-selected TDEs.

### SMBH activity

TDEs by SMBHs that were actively accreting in the years prior to the event may have substantially altered local environments compared to disruptions by non-accreting SMBHs. AGN tend to have more dust and gas in the nuclei, which will obscure optical emission but can enhance radio and infrared emission. Moreover, a pre-

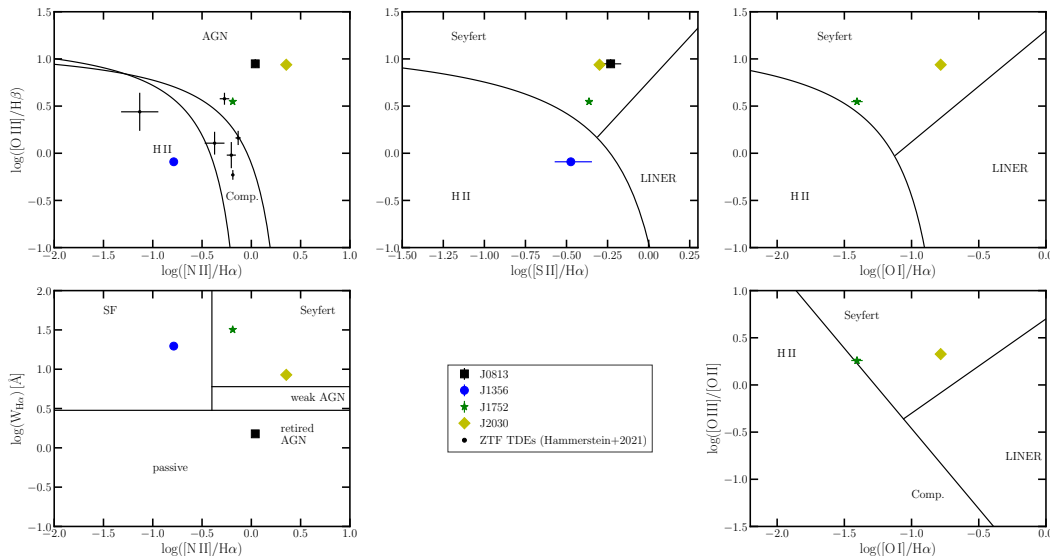


Figure 4.3: Baldwin, Phillips & Terlevich (BPT) and  $W_{H\alpha}$  versus  $[N II]/H\alpha$  (WHAM) diagrams (4–6) for the radio-selected TDEs. The radio-selected TDEs are shown as colored markers with different shapes. Optically-selected TDEs with detected emission lines as reported in Figure 5 of (135) are shown in black in the *top left* panel, for comparison. Note that VT J0813 and VT J1752 are also in the optically-selected sample.

existing accretion disk will alter the properties of the TDE accretion disk; for example, a fossil disk can provide a seed magnetic field that may enable jet launching (237). While our selection criteria excludes strong AGN, weak Seyferts or retired AGN are included in our sample.

We constrain the SMBH activity in each host using Baldwin, Phillips & Terlevich (BPT) and  $W_{H\alpha}$  versus  $[N II]/H\alpha$  (WHAM) diagrams (4–6). We place the host galaxies on BPT and WHAM diagrams using fits to the narrow emission lines in stellar-continuum-subtracted optical spectra. We use the lower resolution LRIS and SDSS spectra for this fit; these are shown in Figure 4.1. We model the spectral continua and emission lines as described in Appendix 4.10. The stellar continuum model is shown in red in Figure 4.1. Because most of our spectra are taken post TDE, it is possible that there is contamination from transient emission lines. In our analysis, we have assumed that the narrow ( $\sim 100$  km s $^{-1}$ ) emission line components are uncontaminated by the TDE, as was also done for the optically-selected TDEs in (135).

The resulting emission line ratios are shown on the BPT and WHAM diagrams in Figure 4.3. In the top left panel, we have overlaid the BPT classifications of

the subset of optically-selected TDEs with host galaxy spectral information (135). Seven of the nineteen ( $(37 \pm 13)\%$ , adopting hereafter Poisson frequentist-confidence uncertainties, (392)) optically-selected TDEs considered in that work show strong nebular emission lines, and can thus be placed on a BPT diagram. In contrast, four out of our six events ( $(67 \pm 25)\%$ ) have nebular emission lines. These fractions are consistent within statistical uncertainties.

A larger fraction of our sample lies in the AGN region than found for the optically-selected events: 2/19 ( $(11 \pm 9)\%$ ) of the optically-selected events are classified as AGN, whereas 3/6 ( $(50 \pm 26)\%$ ) of the radio-selected events are classified as AGN, where we have identified AGN as those host galaxies that are classified as an AGN or Seyfert in the BPT diagrams. We note that VT J0813 is classified as a retired galaxy in the WHAM diagram, suggesting that some of the emission line flux is contributed by an old stellar population. However, the classification of this object as a Seyfert in the BPT diagrams, rather than a LINER, suggests that there may be some emission component resulting from AGN activity: AGN-free, retired galaxies are typically BPT liners (6). 4/19 ( $(21 \pm 12)\%$ ) of the optically-selected events are classified as composite, whereas none of the radio-selected events are classified as such. Finally, 1/19 ( $(5 \pm 8)\%$ ) of the optically-selected events are classified as star-forming, whereas 1/6 ( $(17 \pm 21)\%$ ) of the radio-selected events are classified as such. These results suggest that radio-selected TDEs may prefer galaxies with more recent or stronger AGN activity, and they may prefer star-forming hosts more than optically-selected TDEs. These trends are not statistically significant, however.

Note that if this AGN activity trend is real (as we do not have the statistics to determine), it may be induced by different selection criteria between the samples — while both samples exclude strong AGN, the treatment of weak AGN, like those discussed here, is ambiguous. We include those sources that may have had a recent AGN, but are not necessarily still active. The optical selection may be different, leading to some of these trends. The trend with star-forming hosts should be more robust to selection effects.

The presence of recent AGN activity in the hosts of VT J1752, J2030, and likely J0813 may call into question their TDE classification. Low luminosity AGN can produce flares through mechanisms other than stellar disruption, such as accretion disk instabilities, and distinguishing between TDEs and AGN flares is notoriously difficult (e.g. 163). We cannot rule out that these three events are caused by AGN variability. However, in this paper, we have empirically classified these events as

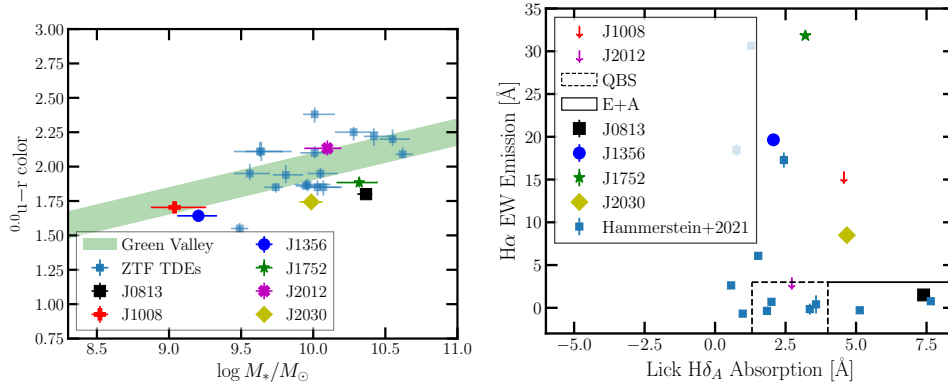


Figure 4.4: *Left panel:* The rest-frame  $u-r$  color ( $^{0.0}u-r$ ) of the TDE host galaxies vs the host galaxy stellar mass. The radio-selected sample is shown as colored markers, and the optically-selected sample is shown as light blue squares. The region of this plot occupied by galaxies in the green valley is shown as a green shaded region (10). *Right panel:* The H $\alpha$  equivalent width versus the Lick H $\delta_A$  absorption for the TDE host galaxies. The different TDEs are formatted the same way as in the *left panel*, except upper limits are shown as arrows.

TDEs for consistency with the optical selection: all of these events would pass the typical optical TDE selection cuts (such as those used in 134), and both VT J0813 and VT J1752 are, in fact, included in optical TDE samples. We consider these events to be TDEs for the rest of this work given the consistency with typical optically-selected events and the fact that the AGN are very low luminosity, if on at all. We urge further research on distinguishing between AGN flares and TDEs.

### Stellar population and star-formation

Galactic star-formation histories, and thus stellar populations, are tightly connected to the galaxy evolution. They may reflect processes that can drive stars to the galactic nucleus; for example, mergers can trigger starbursts and may enhance the TDE rate, so recent bursts of star-formation and young ( $\lesssim 1$  Gyr) stellar populations may correlate TDE rate. Optically-selected TDE hosts also tend to reside in the green valley, which includes the population of galaxies transitioning from the starforming state (blue cloud) to a non-starforming (red-and-dead) state or vice versa (e.g. 393). They are well established to predominantly reside in E+A galaxies (135, 140), which are galaxies that have undergone a recent ( $\lesssim 1$  Gyr) starburst.

Because indicators of the presence of an E+A and/or green valley galaxy have been studied in detail for optically-selected TDEs, we focus on those same indicators for our galaxies (135). We discuss the star formation histories of the individual VLASS

transients in more detail in the companion papers and Appendix 4.10.

We determine whether a galaxy is in the green valley by comparing its MW extinction and redshift-corrected  $u - r$  color, which we denote  $^{0.0}u - r$ , and stellar mass to those for green valley galaxies, as shown in the left panel of Figure 4.4. We adopt the same definition of green valley as (13) and overplot the  $^{0.0}u - r$  colors and stellar masses for their optically-selected sample as blue squares. Qualitatively, all the radio-selected TDE hosts are towards the edges of or outside the green valley, with a preference towards bluer hosts, whereas the optically-selected TDE hosts span it. Quantitatively, two of the six ( $(33 \pm 25)\%$ ) radio-selected TDEs fall within the green valley, which is consistent with the eight of the seventeen ( $(47 \pm 14)\%$ ) optically-selected TDEs in the same region.

We also constrain the stellar populations using the optical spectra. In particular, we identify E+A galaxies using the Lick  $H\delta_A$  absorption index and  $H\alpha$  equivalent width, as shown in the right panel of Figure 4.4. The E+A region is shown in black solid lines. We have adopted the same E+A galaxy definition as (13). We also show the quiescent balmer strong (QBS) region is dashed black lines. Up to 2/6 ( $(33 \pm 25\%)$ ) of the VLASS TDE hosts are consistent with E+A galaxies, although a quiescent  $H\alpha$  luminosity for J1008 is required to confirm that result. This fraction is consistent with the 2/12 ( $(16 \pm 14\%)$ ) of the optically-selected TDEs that satisfy the E+A definition.

## Summary

Our host galaxy analysis can be summarized as follows:

1. Radio-selected, optically-bright TDEs tend to lie at lower stellar masses and SMBH masses than optically-selected TDEs, as determined by a significantly lower mean velocity dispersion among the radio-selected TDEs. Larger samples sizes are needed to evaluate this trend in detail.
2. Radio-selected TDEs occur at a slightly higher rate in galaxies with detectable nebular emission relative to optically-selected TDEs. A larger fraction of these radio-selected events with nebular emission lie in AGN hosts, whereas optically-selected events tend to prefer composite hosts, although this trend may be in part due to different treatments of transients in AGN between the samples.

3. Radio-selected, optically-bright TDEs occupy green valley galaxies and E+A galaxies at approximately the same rate as the optically-selected TDEs.

Future studies with larger radio-selected TDE samples will test whether these correlations are real.

#### 4.6 Optical transient broadband emission analysis

Informed by the discussion of the host emission from the last section, we begin our analysis of the multiwavelength transient emission. We first consider the optical broadband emission for two reasons: (1) the optical emission from TDEs probes the evolution of the TDE debris and the accretion flow at *early* times ( $\sim$ months). Later, we will consider the radio emission, which can be delayed and long-lived. (2) A key datum is the MJD on which the TDE began; VLASS alone is not sufficiently high-cadence to constrain this date. The optical light curves set the strongest constraints because they have long baselines and high cadences. In this section, we present the optical light-curves of our events (Figure 4.5) and perform a basic analysis of their evolution.

#### Methodology

Table 4.4: Optical light curve parameters

Name	$L_{\text{bb}}$	$T_{\text{bb}}$	$R_{\text{bb}}$	$t_{1/2,\text{decay}}$	$t_{1/2,\text{rise}}$	Ref.
VT J0813	44.30	4.46	14.80	$45.4^{+1.0}_{-0.9}$	$24.1^{+1.1}_{-0.9}$	(134)
VT J1008	42.98	4.15	14.76	$23.1^{+1.8}_{-1.2}$	$11.8^{+1.5}_{-1.3}$	(134)
VT J1356	42.64	3.73	15.44	$21.2^{+2.7}_{-2.2}$	$2.6^{+1.4}_{-0.7}$	This work
VT J1752	43.81	4.10	15.28	$27.4^{+0.7}_{-0.7}$	$23.1^{+0.9}_{-0.9}$	(134)
VT J2012	43.07	3.93	15.26	$26.2^{+5.4}_{-5.1}$	$10.2^{+1.5}_{-1.1}$	This work
VT J2030	43.09	3.88	15.36	$66.6^{+2.0}_{-4.4}$	$15^{+14}_{-10}$	This work

TDE optical lightcurves are typically modelled as evolving blackbodies. We aim to constrain four basic parameters of our lightcurves: the peak luminosity  $L_{\text{bb}}$ , the blackbody temperature at the time of the peak luminosity  $T_{\text{bb}}$ , the rise time from half-max-luminosity to max-luminosity  $t_{1/2,\text{rise}}$ , and the decay time from max-luminosity to half-max luminosity  $t_{1/2,\text{decay}}$ . These parameters have already been constrained for J0813, J1008, and J1752 by (134) and we refer the reader to that work for details.

In the case of J1356 (described in detail in Appendix 4.10), we only have one band in the optical, so we do not have enough information to simultaneously fit the

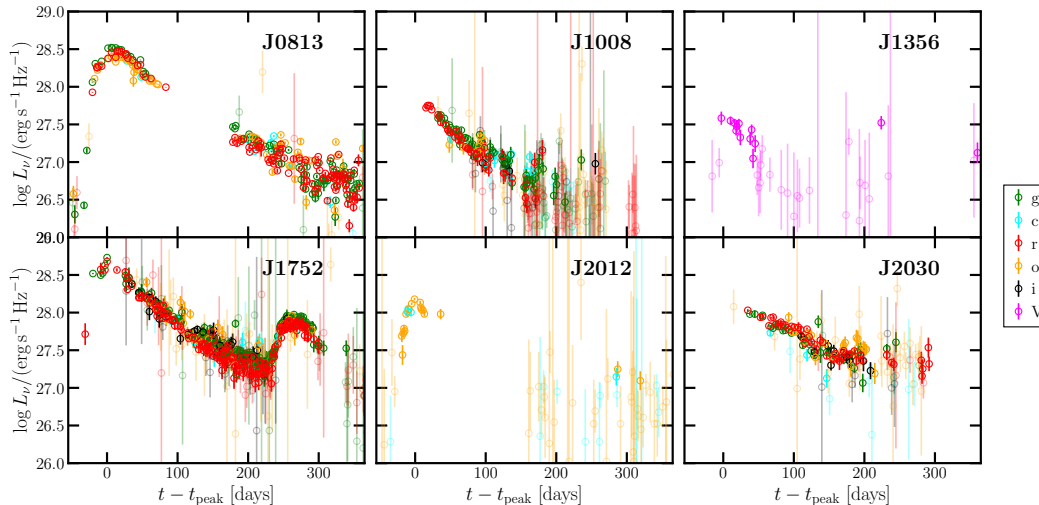


Figure 4.5: The optical lightcurves for our TDE candidates. Each band is shown in a different color.

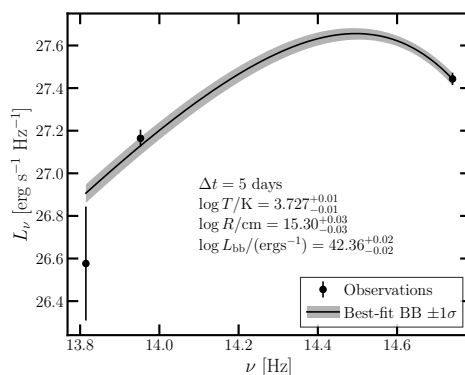


Figure 4.6: The transient optical-IR SED for VT J1356 near optical peak. The observations are shown as black scatter points. The black line and band shows the best-fit blackbody and  $\pm 1\sigma$ . The best-fit parameters are shown in the figure.

blackbody temperature and luminosity from that data alone. Fortunately, J1356 was observed near the optical peak in the IR, and the resulting IR and optical SED is shown in Figure 4.6. We fit this SED to a blackbody and found a best-fit temperature of  $\log T/K = 3.73^{+0.01}_{-0.01}$ . Errors are statistical. We then fit the optical lightcurve to a Gaussian rise and exponential decay model, which is commonly adopted for TDEs. We used the `dynesty` dynamic nested sampling software.

In the case of J2012, the sparse optical observations preclude any detailed constraints on the optical evolution. We fit the optical lightcurve at  $t < 1$  year to a Gaussian rise and exponential decay model with a fixed temperature, but urge caution in

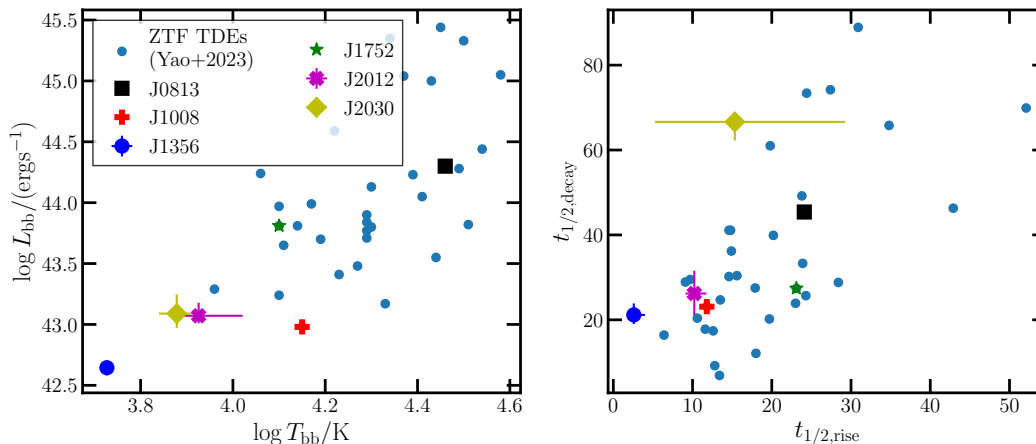


Figure 4.7: *Left panel:* The peak blackbody luminosity vs the blackbody temperature at peak luminosity for the radio-selected TDEs and the optically-selected TDEs, in the same format as other figures. *Right panel:* The rise versus decay times for the optically- and radio-selected events, in the same format as the *left panel*. No obvious trends are present.

interpreting the results.

For J2030, there are no optical observations during the rise or peak of the source, so we can only set a limit on the blackbody temperature and luminosity, and we have no constraints on the rise time. We fit the decay to an exponential model with a fixed blackbody temperature and set a lower limit on the peak luminosity based on the luminosity during the first detection of the source.

The adopted optical lightcurve parameters for each source are summarized in Table 4.4.

## Results

In the rest of this section, we compare the optical lightcurve parameters for our radio-selected, optically-detected TDEs to those for the optically-selected TDE sample from (134).

In Figure 4.7, we show the distribution of blackbody temperature and luminosity in the left panel and  $t_{1/2,\text{rise}}$  vs  $t_{1/2,\text{decay}}$  in the right panel. We see no obvious correlations in the rise/decay times of the lightcurves. Radio-selected TDEs seem to lie towards lower temperature and luminosities than the optically-selected sample, although the bulk of those events at extreme temperatures/luminosities are those without well-sampled data, suggesting this correlation may be an artifact of our analysis methods or data quality. Ignoring those sources (J1356, J2012, J2030), two

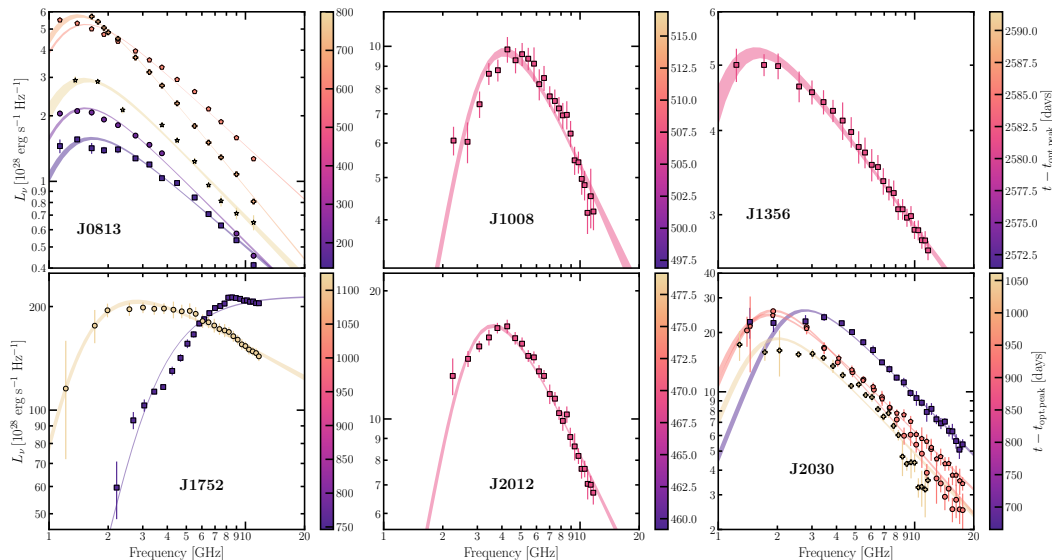


Figure 4.8: Representative radio SEDs for each VLASS TDE candidate. The observations are shown as scatter points, and the best-fit synchrotron  $\pm 1\sigma$  models shown as transparent colored bands. The color of the scatter points and fit bands correspond to the time since optical peak of each radio observation. Note that VT J1752 is an example of a source that is very poorly fit by a simple synchrotron model; we adopt this model despite the inconsistent fit for uniformity.

out of three of the remaining events do lie at low temperatures and luminosities. With such low number statistics, it is impossible to determine if this trend is real, but future work on radio-selected TDEs with deeper surveys (e.g., the Deep Synoptic Array 2000) and radio follow-up of optically-selected TDEs will test any correlations between optical and radio properties.

#### 4.7 Radio emission properties and mechanism

Next, we consider the radio emission mechanisms for our sample and compare to published radio follow-up of optically-selected TDEs. A small but growing sample of TDEs have radio detections; the brightest four of which comprise the on-axis, jetted TDE population (11, 219, 220, 245, 246, 373, 394–397). Most TDEs with radio detections have non-relativistic, wide-angle outflows. The non-relativistic TDEs were largely selected in the optical and followed up in the radio, with a few exceptions. In the following sections, we first consider the radio lightcurves of our events in the context of published TDE radio lightcurves. Then, we constrain the physical parameters of the emitting region and compare these to those of optically-selected, radio-detected TDEs.

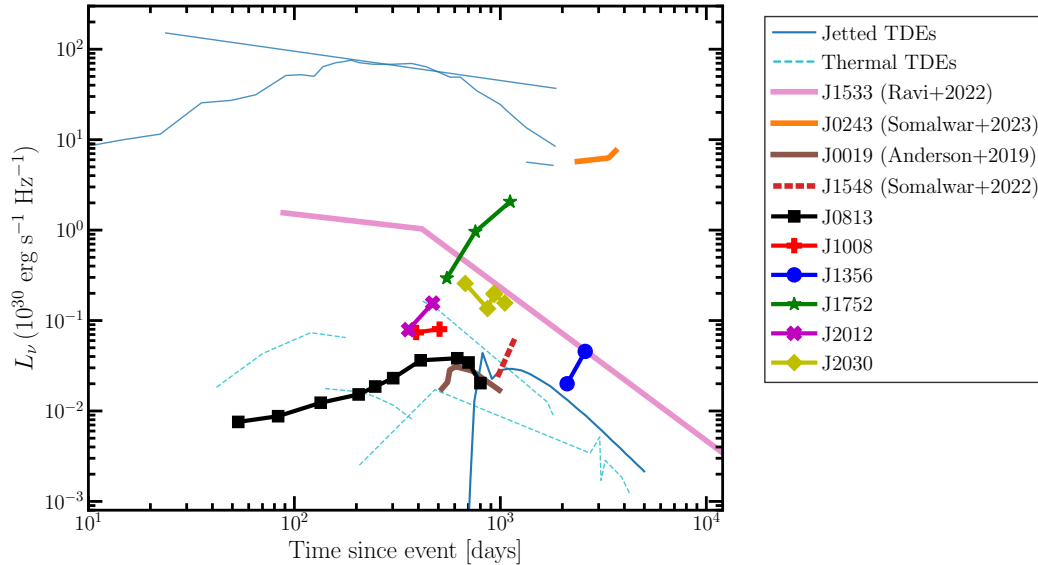


Figure 4.9: GHz radio lightcurves for a representative sample of radio-detected TDEs. The solid, blue lines show example jetted TDEs and the dashed, cyan lines show the non-relativistic TDE sample. The thick lines correspond to objects that were found in untargted radio searches, whereas the thin lines correspond to objects that were selected in other bands (see *11*, and references therein).

### The radio lightcurves of TDEs

First, we show the radio lightcurves for our TDEs and representative sub-sample of all radio-detected TDEs in Figure 4.9. The jetted and non-jetted TDEs are denoted with different line styles and colors. The radio-selected TDEs all have thicker lines than those selected in other bands. The TDEs presented in this paper are demarcated with unique colors and markers.

There are a number of key takeaways from this plot. From the non-radio-selected TDEs alone, there was an apparent bifurcation of the events into those with luminosities  $\gtrsim 10^{31} \text{ erg s}^{-1} \text{ Hz}^{-1}$  and those with luminosities  $\lesssim 10^{29} \text{ erg s}^{-1} \text{ Hz}^{-1}$ . This split approximately mapped onto the type of outflow: relativistic, collimated jet, or non-relativistic, wide-angle outflow. The radio-selected TDEs, as well as increased follow-up efforts of the optically-selected TDEs (e.g. *153*), we have begun spanning the gap between these two outflow classes. For example, we see evidence for jetted sources at luminosities  $\lesssim 10^{30} \text{ erg s}^{-1} \text{ Hz}^{-1}$ , like J1533 from (*219*) and J2030 from this work. The radio-selected TDEs alone span a luminosity range  $10^{28-31} \text{ erg s}^{-1} \text{ Hz}^{-1}$ , with no clear division into separate classes.

We also see a wide range of lightcurve shapes. Until recently, TDE radio lightcurves

were expected to follow gamma-ray burst models, with a power law rise and decay. This paradigm shifted with the discovery of  $\gtrsim 5$ -year-old radio-selected TDEs (e.g. 11, 219) and the discovery of radio rebrightening and other late-time radio emission from optically-selected TDEs (e.g. 151). We see a wide range of light curve shapes, including multiple examples that show late-time rise or rebrightenings. Some of the rises and rebrightenings occur remarkably long after the initial TDE. VT J2030 declines and then brightens  $\sim 3$  years post-optical flare, while VT J1752 is still rising at that time. VT J1356 is still rising after  $\sim 8$  years, making this one of the oldest known radio-emitting TDEs, and the first known in a non-active galaxy. We also see examples like VT J1008 and VT J2012, which show similar multiwavelength properties and are at similar epochs post-TDE, but the 3 GHz luminosities are rising at significantly different rates.

Of course, these single frequency lightcurves cannot provide a complete view of the physical properties of the radio-emitting outflows. Instead, we require multi-frequency radio SEDs (i.e., near-simultaneous observations at multiple frequencies, spanning a few GHz range) spanning multiple epochs, which we can fit to radio outflow models. Hence, for the rest of this section, we analyze the radio SEDs of our events and briefly compare them to published results for optically-selected, radio-detected TDEs.

### **Analysis of the TDE radio spectral energy distributions**

We modelled the SED of each of the TDEs presented in this work uniformly. A detailed model description is provided in Appendix 4.10, which we briefly summarize here. We assume all TDE radio emission is produced by the synchrotron mechanism. We model each radio SED as a spherical outflow of radius  $R$  expanding into a medium with uniform density and magnetic field  $B$ . We assume a single power-law electron population with density  $N_0$ , minimum Lorentz factor  $\gamma = \gamma_{\min}$  and spectral index  $p$ :

$$N(\gamma) \propto \gamma^{-p}, \gamma_{\min} < \gamma. \quad (4.3)$$

With these definitions, the synchrotron flux density can be calculated as a function of frequency, with free parameters  $R$ ,  $B$ ,  $n$ ,  $N_0$ , and  $\gamma_{\min}$ . We assume equipartition with  $\epsilon_e = 0.1$  and  $\epsilon_B = 0.1$ , as is standard in TDE modelling. This assumption allows us to eliminate one parameter from our fit. We fit the synchrotron flux density to each radio SED independently (i.e., assuming no model for time evolution) using the `dynesty` dynamic nested sampler.

In the case of J1752, the radio emission model required with two components. Our methodology was otherwise identical to that used when modelling the rest of the sample.

The best-fit synchrotron parameters for each source at each epoch are summarized in Table 4.5. We additionally include the total energy in the outflow  $E$ , the equivalent ejecta mass  $M_{\text{ej}} = 2E/c^2$ , and the average  $\beta$  factor of the ejecta ( $\beta = v/c$ , for velocity  $v$ ) assuming the first optical detection is the launch date of the outflow. For illustration, we show a representative sample of the radio SEDs for the six TDEs published in this paper in Figure 4.8, with the fits overlaid.

### **Comparison to optically-selected, radio-detected TDEs**

In the rest of this section, we discuss the radio emission observed from both our sample and place it in the context of the general radio-detected TDE population. As a comparison, we primarily rely on (149), who presented radio follow-up of 23 optically-selected TDEs, although without a well-defined selection function. Radio emission was detected from 15 of the sources, although the transient nature of the emission could only be confirmed for 9 sources. Thus at least 40% of the optically-selected TDEs that were considered were radio emitting.

(149) obtained multi-frequency SEDs for their sample and constrained the radii, magnetic field, and energies using methods similar to ours although using a broken power-law fit to measure the peak flux/frequency of the radio SEDs; we refer the reader to that work for details. In the rest of this section we will compare these physical parameters between our sample and that in (149), while keeping in mind that the differences in SED fitting methods may result in small offsets in the measured outflow physical parameters.

In Figure 4.10, we show the radius, energy, and magnetic field evolution as a function of time. For consistency with our methods, we recompute these parameters using the Newtonian prescription from (202). The clearest discrepancy between our sources and the sources from (149) is that the latter are detected in the radio at later times than our sources. Our sources also tend to reside at the upper end of the energy and radius range observed by (149), and the lower end of the magnetic field range. Given the longer timescales of the (149) events, for a fixed velocity outflows one would expect that their events should have larger radii.

These differences between our sample and the (149) sample show that radio and optical searches for TDEs are currently finding different events, even when only

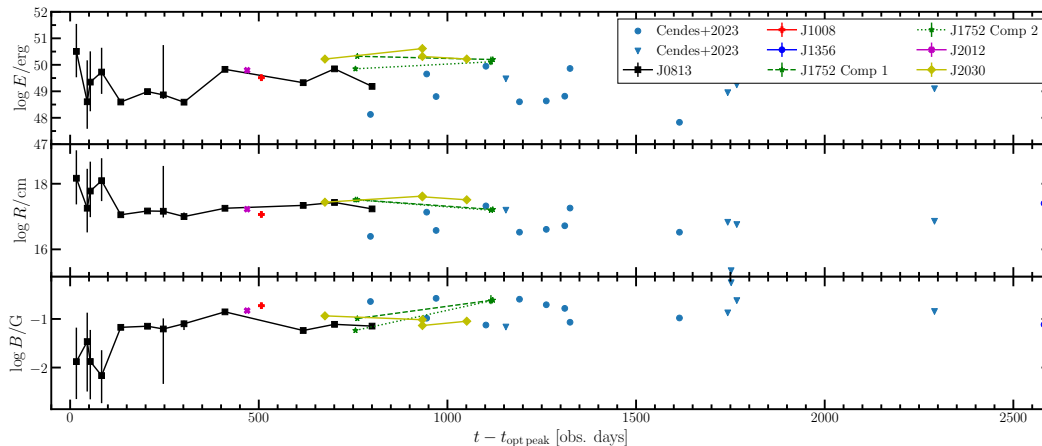


Figure 4.10: The evolution of the equipartition energies (*top*), radii (*middle*), and magnetic fields (*bottom*) for the TDEs in our sample (colored markers) compared to those in the (*I49*) sample (blue circles and limits). The objects from the (*I49*) with unconstrained peak flux densities/frequencies are shown as limits. Our events tend to occupy a higher energy, lower magnetic field, large radius state than the objects in the (*I49*) sample.

considering those TDEs that emit in both bands. Our selection criteria, combined with the flux-limited nature of VLASS and the timeline between the start of ZTF and VLASS E1/2 will tend to produce events that brighten within  $\sim 3$  years post-optical flare and that are intrinsically luminous. The (*I49*), which is based on optically-discovered TDEs and will be biased towards objects with brighter optical flares given the magnitude limited nature of optical TDE searches (whereas we use forced photometry, which is slightly more sensitive), but is sensitive to fainter and older ( $>3$  years) radio emission, since the radio observations used are deeper and later-time than those from VLASS.

#### 4.8 Discussion

In the following sections, we briefly comment on physical explanations for the tentative trends observed in this work and we constrain the rate of radio-emitting, optically-bright TDEs. First, we recapitulate the results of the following sections. We include a few of the hypothesized differences between the radio- and optically-selected TDEs, although with the strong caveat that there were no trends that were significant. Overall, the radio and optical transient and host galaxy properties of radio-selected and optically-selected TDEs are consistent, within the limitations of our statistics, which may suggest that optical and radio TDE searches are subject to similar selection biases.

- The radio-selected TDEs show a tentative preference for lower stellar mass and velocity dispersion galaxies, suggesting that radio-selected TDEs may prefer low SMBH masses, although we lack the statistics to confirm this result.
- Radio-selected TDEs occur slightly more frequently in galaxies with nebular emission lines than optically-selected TDEs. The radio-selected TDE hosts with nebular emission lines are predominantly Seyferts, whereas the optically-selected TDE hosts with nebular emission lines are predominantly composite galaxies, although this result is subject to low number statistics.
- Radio-selected TDE hosts occupy E+A galaxies and green valley galaxies at a consistent rate to that of optically-selected TDE hosts.
- We find a slight overabundance of radio-selected TDEs that peak at lower blackbody temperatures and luminosities than those of the optically-selected TDEs, although this difference could be caused by the difference in available optical datasets for these sources.
- TDEs show a wide-range of radio emission. In our sample, alone, we have TDEs that, at  $\sim 3$ -years post-first-detection, are both rising and fading at 3 GHz. We have TDEs with strongly non-monotonic evolution, and some with brightening 3 GHz emission almost a decade post-event. The radio luminosities of the radio-selected TDEs alone span the range  $10^{28-31}$  erg s $^{-1}$  Hz $^{-1}$ , with no obvious division into subclasses.
- Our radio-selected TDEs tend to have emitting regions with larger energies and radii and smaller magnetic fields than optically-selected/radio-detected TDEs, despite the fact that the radio-selected TDE radio emission turns on at earlier times.

### **Physical explanations for the observed differences between radio- and optically-selected TDEs**

With these observations in mind, we briefly hypothesize physical explanations for the observed trends. A comprehensive review of possible models is beyond the scope of this paper.

If we adopt the model for TDE evolution where radio emission from TDEs may be produced when a wind or jet is launched from near an accretion disk, it is possible to unify the observed trends. First, we consider the low SMBH masses. TDEs with

lower black hole masses spend more time in a near- to super-Eddington state (398). Super-Eddington accretion disks have a puffy structure, with significant unbound material, that may be conducive to launching winds and/or aiding in collimating jets (399). Hence, one might expect that radio emitting TDEs tend to occur when the SMBH mass is lower because of the puffier accretion disk structure.

Of course, the wind and/or jet cannot necessarily be detected unless it shocks against the circumnuclear material (CNM). Then, events with more material in the vicinity of the SMBH will be more likely to produce detectable radio emission. The densities implied by the best-fit synchrotron models to the radio-selected TDEs are comparable to those of the (149) sample, despite the fact that the radio-selected TDE outflows are probing a larger radius and density is expected to decrease as a power law with radius. It is well established that AGN tend to have a significant CNM relative to completely quiescent galaxies (144), so a TDE in a galaxy with a weak or retired AGN may be more likely to produce synchrotron-emitting shocks. This would then explain the prevalence of galaxies with strong nebular emission in our sample.

The faint and cool optical flares may also be explained by the enhanced circumnuclear material, combined with the low black hole masses. Lower black hole masses produce fainter optical flares (400). Moreover, the presence of enhanced circumnuclear material will tend to obscure emission from the nucleus. Then, before correcting for this obscuration, any detected optical flare will appear fainter and cooler. If we had higher quality optical observations, it is plausible that we could constrain the amount of extinction caused by the CNM, although this is not possible with the current data. Another possible method of constraining increased CNM in radio-selected TDE hosts is through MIR studies: we would have direct evidence for the presence of enhanced circumnuclear dust if radio-selected TDEs are more likely than optically-selected events to have a MIR flare, which in TDEs is associated with thermally-emitting dust in the vicinity of the SMBH (401).

Thus, by invoking super-Eddington accretion around low mass SMBHs and enhanced circumnuclear material, we can reconcile most of our observations. Of course, there are significant uncertainties given our small sample size, so other models will be consistent with our results. For example, the collision induced outflow model for TDEs (113) predicts the launch of a wide-angle, non-relativistic wind that emits on  $\sim$ year timescales, as observed from some of our events (e.g., VT J356, J1008, J2012). It is less likely that this model can reproduce the observed emission

from, e.g., VT J1752, which shows a more complex outflow configuration. Also note that (113) expect that super-Eddington winds would likely produce brighter emission than the wind launched as a result of the collision induced outflow. Unbound stellar debris can also produce radio emission in TDEs when it collides with the CNM (264), but cannot explain some of the more complex, multi-component emission observed. Future samples of radio-selected TDEs with larger statistics and improved multiwavelength coverage will be able to probe these possibilities.

### **The rate of radio-emitting, optically-bright TDEs**

One of the key benefits of performing an untargeted search for optically- and radio-detected TDEs is that we can set limits on the rate of such events. Hence, we conclude our discussion by considering the rate of GHz-emitting, optically-bright TDEs on  $\sim 3$  year timescales.

Because the GHz lightcurve evolution of TDEs is poorly understood, we cannot robustly estimate the incompleteness of VLASS to radio-emitting, optically-detected TDEs. Instead, we simply set a lower limit, which acknowledges that fact that there may be some optically-detected, radio-bright TDEs that did not make it into our sample because of, e.g., the cadence or sensitivity of VLASS. Of the 33 ZTF TDEs presented in (134), three are in our sample. Hence, with 90% confidence,  $> 3\%$  of optically-selected TDEs are radio-emitting. The integrated volumetric TDE rate from (134) is  $2.9^{+0.6}_{-1.3} \times 10^{-7} \text{ Mpc}^{-3} \text{ yr}^{-1}$ , leading to a volumetric radio-emitting, optically-bright TDE rate of  $\gtrsim 10 \text{ Gpc}^{-3} \text{ yr}^{-1}$ .

We defer discussion of the luminosity function of radio-selected TDEs, as well as predictions for future surveys, to future work on the full VLASS-selected TDE sample.

## **4.9 Conclusions**

We have presented the first sample of radio-selected TDEs. We selected six radio transients in the VLASS with multiwavelength emission consistent with TDEs; in particular, we require the detection of an optical counterpart. We have compared the properties of these events to optically-selected TDE samples. We tentatively suggest that radio-selected, optically-bright TDEs occur at a higher rate in galaxies with low stellar/black hole masses. They also tend to have cooler and fainter optical emission than optically-selected TDEs. We compare to the results of radio follow-up campaigns of optical TDE samples and find slightly larger energies and radii in our sample, as well as earlier outflow launch times relative to the initial TDE. We

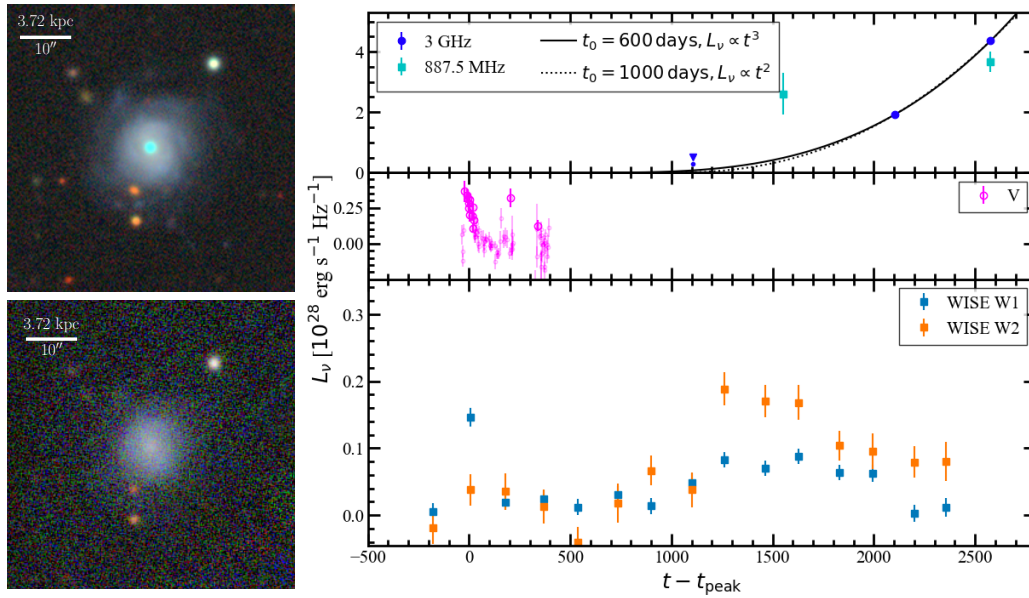


Figure 4.11: Summary of the properties of VT J1356. The *bottom left* panel shows a PANSTARRS image of the host galaxy before the flare. The *top left* panel shows a Legacy survey (7) image of the host galaxy and transient during the flare. The transient is visible as a blue nucleus in the galaxy. The *right* panels summarize the transient emission associated with the event. The *top right* panel shows the 3 GHz and 887.5 MHz radio lightcurves. Example power law fits to the 3 GHz lightcurve are overlaid in black. The *middle right* panel shows the ASASSN lightcurve of this source. The *bottom right* panel shows the WISE infrared lightcurve of this source (12).

constrain the rate of radio-emitting, optically-bright TDEs to be  $> 3\%$  of the optical TDE rate, or  $\gtrsim 10 \text{ Gpc}^{-3} \text{ yr}^{-1}$ .

In future work, we will use VLASS to extend this sample to include those events without multiwavelength counterparts. VLASS, of course, is limited by the observation cadence: it will only be able to identify TDEs with radio emission that lasts for  $\sim 3$  years. By combining VLASS with past radio surveys like FIRST or NVSS, we can probe long timescales. Current and planned radio surveys and instruments, including ASKAP (402), the ngVLA (403) and the DSA 2000 (404), will probe different timescales. The combined radio TDE samples from these surveys will revolutionize our understanding of the landscape of TDE radio emission.

## 4.10 Appendix

### The multi-wavelength properties of VT J1356

In this appendix, we discuss the multiwavelength properties of VT J1356 in detail because this source is not discussed in either of the companion papers.

#### Discovery and host galaxy

We first identified VT J1356 as a radio flare with an unusual MIR counterpart in data from the WISE survey, shown in the right panel of Figure 4.11. The IR flare showed a double peaked structure, with an initial, blue peak, and then a secondary, long-lived, red flare. We obtained optical lightcurves from public, high cadence optical surveys, including ZTF, ASASSN, and ATLAS, and found an optical transient detected in ASASSN data  $\sim 8$  years before the VLASS detection. This transient coincided with the first IR transient peak.

The host galaxy of this transient is shown in the left panel of Figure 4.11. Note that this image was taken during the transient, so the bright nucleus is the optical emission associated with the TDE. We obtained an optical spectrum of the host galaxy, which is described in Section 4.3. The spectrum is that of a star-forming galaxy. There are no obvious transient spectral features. There is no optical spectrum available at times closer to the optical peak.

#### Optical and IR analysis

We analyzed the optical flare as described in Section 4.6. We fit the combined optical-IR SED at the peak of the IR flare to a blackbody and found a temperature  $\sim 10^4$  K (Figure 4.6), consistent with an optically-flaring TDE. The shape of the optical flare is also consistent with TDE observations (see Section 4.6).

The secondary IR peak is reminiscent of the “dust echoes” occasionally seen from TDEs (401). Dust echoes are produced by thermally emitting dust in the vicinity of the SMBH, which is heated by UV emission from the TDE. The temperature of the emission is generally  $\sim 1000$  K, i.e., close to but below the sublimation temperature of the dust. To test this hypothesis and constrain the physical properties of the transient, we perform a detailed analysis of this secondary IR flare. We began by fitting blackbody models to each epoch of the secondary flare with  $> 3\sigma$  detections in both the W1 and W2 bands.

If this flare is a dust echo, the luminosity and timescale of the IR flare is set by the UV lightcurve and the geometry of the dust. Applying simple assumptions, we can set constraints on the dust structure. The secondary IR flare from VT J1356 rose to a peak  $\sim 1200$  days post-optical peak. Assuming the UV flare traces the optical flare and that the dust is in a spherical or torus-like geometry with radius  $R_{\text{dust}}$ , this then constrains  $R_{\text{dust}}$ : the rise time  $t_{\text{IR,rise}}$  is given by  $t_{\text{IR,rise}} \sim 2R_{\text{dust}}/c$ . Then, we have  $R_{\text{dust}} \sim 0.5$  pc, which is comparable to values found for similar sources (e.g. 163).

### Radio and X-ray observations and analysis

We searched for archival X-ray flares using the ESA high energy lightcurve tool. We obtained X-ray follow-up of this source  $\sim 3000$  days post-peak using the Swift/XRT telescope. We reduced the observations using the online Swift/XRT data analysis tool. No emission was detected ( $L_X \lesssim 6 \times 10^{41}$  erg s $^{-1}$ ).

In addition to the VLASS observations of this source, we crossmatched against the Rapid ASKAP Continuum Survey (RACS) catalog (405). The source was detected on MJD 58600 with a 887.5 MHz flux density of  $3.5 \pm 0.9$  mJy. We also obtained a follow-up radio SED, as described in Section 4.3. We fit it to a synchrotron emission model as described in Appendix 4.10.

We begin by discussing the radio lightcurve. We combined the VLASS, RACS, and follow-up data to construct 887.5 MHz and 3 GHz radio lightcurves, as shown in the top left panel of Figure 4.11.

### The origin of VT J1356

In this section, we constrain the origin of VT J1356: is it in fact a TDE? We consider three plausible origins to explain these observations: (1) an AGN flare, (2) a supernova (SN), or (3) a TDE. While exotic models may be able to replicate the data, constraining them is beyond the scope of this work.

We immediately exclude the possibility that we are observing an AGN flare. HG J1356 shows no evidence for AGN activity, either in the form of AGN-like infrared colors nor strong forbidden line emission. If we are observing an AGN flare, it is from an extraordinarily weak AGN, so we consider this scenario unlikely.

Next, we consider a supernova origin. HG J1356 is an actively star forming galaxy, so this possibility is more feasible. Our main evidence against a SN origin comes from the MIR emission. (326) analyzed NEOWISE lightcurves (406) for 2812

SNe from the Open Catalogue of Supernovae (348) and found that (1) the MIR variability typically occurred on a  $\sim 6$  month timescale and (2) SNe MIR lightcurves tend to show a bluer-when-brighter behavior. Our source is variable on many year timescales, and the MIR color becomes redder when the flare is more luminous. As in the AGN flare case, if this event is an SN, it is a very unusual example of such, so we do not prefer this possibility.

We are left with a TDE origin for VT J1356. The optical flare, IR flare, and energetics are consistent with a TDE.

### **Optical spectrum fitting methods**

We fit the stellar continua of the spectra using the `ppxf` code (362, 363) with the MILES templates (364) following the method detailed in Appendix B of (163). The best fit stellar continua are overlaid on Figure 4.1. We then subtracted the stellar continuum from each spectrum and fit the individual emission lines to measure the fluxes. We jointly model lines that are closer together than a few times the instrument resolution to ensure reliable fits, such as the [N II]+H $\alpha$  complex. We assumed each line could be modelled by a Gaussian. We allowed the amplitude, width, and centroid of each line to float, although when simultaneously modelling multiple lines, we assumed the widths were the same for every line. We included a linear component to account for any residual continuum. For each line or line complex, we ran `emcee` for 2000 steps with 200 walkers and discarded the first 1000 steps as burn-in.

### **Synchrotron analysis methodology**

We model our synchrotron spectra using non-standard methodology, although note that the results are identical to, e.g., analyses using (202) and (203). There has been some confusion in the literature among how to use the standard broken power-law parameterizations of synchrotron emission. This particularly arises in cases where the break frequencies are close to each other or in non-standard orders, and various parameterizations have been used to connect the different regimes of synchrotron spectra (e.g., (203)), or if the spectrum is not well modelled as a homogeneous, simple synchrotron emitting region. As part of an effort to improve and clarify synchrotron modelling techniques, we present here a formalism which allows spectra to be fit with a synchrotron model without adopting a broken power-law parameterization, but instead fitting directly for the physical parameters of the system. While our methodology suffers from limitations (e.g., we have not fully

included relativistic effects or consistent cooling), we hope to expand it in future work and present a code that can be used to easily and consistently model synchrotron emission.

We consider an electron in a homogeneous region at redshift  $z$  and luminosity distance  $d_L$ . The rest-frame frequency  $\nu$  is related to the observed frequency as  $\nu = (1+z)\nu_{\text{obs}}$ . We will perform most calculations using rest-frame frequency, and transform to observer frequency before comparing to observations. The magnetic field is given by  $B$ . Consider a single electron with Lorentz factor (LF)  $\gamma$ . The pitch angle, or the angle between the electron's velocity and the magnetic field, is  $\theta$ . The rest-frame synchrotron frequency is

$$\nu_s = \frac{eB\gamma^2}{2\pi m_e c}. \quad (4.4)$$

The synchrotron power for a single electron at rest-frame frequency  $\nu$  is given by

$$P_s(\nu | B, \gamma, \theta) = \frac{\sqrt{3}e^3 B \sin \theta}{m_e c^2} F(\nu/\nu_c), \nu_c = \frac{3}{2}\nu_s \sin \theta. \quad (4.5)$$

The function  $F(\nu/\nu_c)$  encapsulates the frequency dependence of the spectrum. It is defined as

$$F(x) = x \int_x^\infty K_{5/3}(y) dy. \quad (4.6)$$

$K_{5/3}(y)$  is the modified Bessel function of order 5/3.

At low and high frequencies,  $F(x)$  is well approximated by

$$F(x) \longrightarrow F_1(x) = \frac{4\pi}{\sqrt{3}\Gamma(1/3)} \left(\frac{x}{2}\right)^{1/3}, x \rightarrow 0; \quad (4.7)$$

$$F(x) \longrightarrow F_2(x) = \sqrt{\frac{\pi}{2}} x^{1/2} e^{-x}, x \rightarrow \infty. \quad (4.8)$$

Here,  $\Gamma$  is the Gamma function, rather than bulk Lorentz factor. For all equations hereafter, an expression of the form  $\Gamma(x)$  refers to the Gamma function, an expression of the form  $\Gamma(s, x)$  refers to the upper incomplete Gamma function, and the character  $\Gamma$  with no argument refers to the bulk Lorentz factor. For  $x \leq 10^{-5}$  and  $x \geq 10^3$ , these formulae give relative errors  $< 0.1\%$ . For the regime  $10^{-5} < x < 10^3$ ,  $F(x)$  is well approximated (relative error  $< 0.8\%$ ) as

$$F(x) \approx F^{(1)}(x) = F_1(x) \frac{\sum_{i=0}^{14} n_{1i} e^{-\alpha_{1i} x}}{\sum_{i=0}^{14} n_{1i}} + F_2(x) \left(1 - \frac{\sum_{i=0}^{14} n_{2i} e^{-\alpha_{2i} x}}{\sum_{i=0}^{14} n_{2i}}\right). \quad (4.9)$$

Note that the factor  $\sum_{i=0}^{14} n_{1i}$  in the denominator of the final term is *not* a typo. Because we use the sum over  $n_{1i}$  in the denominator,  $F^{(1)}(x)$  does not approach  $F(x)$  exactly as  $x$  goes to infinity. However, as we will show, the difference does not affect our results: for all upcoming calculations, this error will prove insignificant.

The single electron synchrotron spectrum, Equation 4.5, is only valid when the emitting energy during a single orbit is smaller than the energy of the particle, in which regime quantum effects are negligible. The condition corresponds to

$$B < \frac{e/\sigma_T}{\gamma^2 \sin^2 \theta} \sim \frac{7.22 \times 10^{14}}{\gamma^2 \sin^2 \theta} \text{ G}, \quad (4.10)$$

where  $\sigma_T$  is the Thomson cross section.

To compute the synchrotron spectrum for a population of electrons, we must assume an electron energy distribution. We adopt the standard assumption that the electron Lorentz factors are drawn from a cut-off power-law with index  $-p$

$$N(\gamma)d\gamma = N_0\gamma^{-p}d\gamma \quad (\gamma_{\min} < \gamma < \gamma_{\max}) \quad (4.11)$$

$$= N_{\text{tot}} \frac{1-p}{\gamma_{\max}^{1-p} - \gamma_{\min}^{1-p}} \gamma^{-p} d\gamma \quad (\gamma_{\min} < \gamma < \gamma_{\max}) \quad (4.12)$$

$$= \frac{E_e}{m_e c^2} \frac{2-p}{\gamma_{\max}^{2-p} - \gamma_{\min}^{2-p}} \gamma^{-p} d\gamma \quad (\gamma_{\min} < \gamma < \gamma_{\max}). \quad (4.13)$$

$\gamma_{\min}$  ( $\gamma_{\max}$ ) is the minimum (maximum) electron Lorentz factor. A common assumption is  $\gamma_{\max} = \infty$ . Throughout the rest of this work, we assume  $\gamma_{\max} = 10^9$ , which is roughly equivalent to  $\gamma_{\max} = \infty$ , although all derivations are generalized to arbitrary  $\gamma_{\max}$ .  $N_0$  is the normalization of the electron distribution, and is related to both the total number of electrons  $N_{\text{tot}} = \int_{\gamma_{\min}}^{\gamma_{\max}} N(\gamma)d\gamma$  and the total energy stored in the electrons  $E_e = \int_{\gamma_{\min}}^{\gamma_{\max}} \gamma m_e c^2 N(\gamma)d\gamma$ .

Using this energy distribution, the synchrotron emissivity (cgs units  $\text{erg s}^{-1} \text{cm}^{-3} \text{sterad}^{-1}$ ) is given by

$$\epsilon_s(\nu) = \frac{1}{4\pi} \int_{\gamma_{\min}}^{\gamma_{\max}} d\gamma N(\gamma) P(\nu | B, \gamma, \theta) \quad (4.14)$$

$$= \frac{\sqrt{3}}{8\pi} \frac{e^3 N_0 B \sin \theta}{m_e c^2} \left( \frac{\nu}{\nu_0} \right)^{\frac{1-p}{2}} \int_{x_{\max}}^{x_{\min}} x^{(p-3)/2} F(x) dx. \quad (4.15)$$

Here, we have defined the variable  $\nu_0 = \frac{3eB \sin \theta \Gamma}{4\pi m_e c(1+z)}$ , so that  $\nu_c = \gamma^2 \nu_0$ . We have also defined  $x_{\min} = \nu/(\nu_0 \gamma_{\min}^2)$  and  $x_{\max} = \nu/(\nu_0 \gamma_{\max}^2)$ ; note that, despite the subscripts,

$x_{\min} > x_{\max}$ . In the limit  $x_{\min} \rightarrow \infty$  and  $x_{\max} \rightarrow 0$ , we find the expected frequency dependence  $\epsilon_s(\nu) \propto (\nu/\nu_0)^{(1-p)/2}$ .

The approximation for  $F(x)$  described above allows this integral to be analytically evaluated. We find

$$\epsilon_s^{(2)}(\nu) = \frac{\sqrt{3} e^3 N_0 B \sin \theta}{8\pi m_e c^2} \left( \frac{\nu}{\nu_0} \right)^{\frac{1-p}{2}} \left\{ \frac{2^{5/3} \pi}{\sqrt{3} \Gamma(1/3)} \frac{\sum_{i=0}^{14} n_{1i} \alpha_{1i}^{-z_1} (\Gamma(z_1, \alpha_{1i} x_{\min}) - \Gamma(z_1, \alpha_{1i} x_{\max}))}{\sum_{i=0}^{14} n_{1i}} + \sqrt{\frac{\pi}{2}} \left[ (\Gamma(z_2, x_{\min}) - \Gamma(z_2, x_{\max})) - \frac{\sum_{i=0}^{14} n_{2i} (\alpha_{2i} + 1)^{-z_2} (\Gamma(z_2, (\alpha_{2i} + 1) x_{\min}) - \Gamma(z_2, (\alpha_{2i} + 1) x_{\max}))}{\sum_{i=0}^{14} n_{1i}} \right] \right\}; \quad (4.16)$$

$$z_1 = \frac{3p-1}{6}, z_2 = \frac{p}{2}.$$

The relative error of this expression is  $< 0.1\%$  across the full parameter range.

With these expressions for the emissivity, we can readily calculate the synchrotron spectrum for any *optically thin* emission region. In many cases, however, we must consider absorption processes. First, we consider synchrotron self-absorption. The synchrotron self-absorption coefficient is given by

$$\alpha_\nu = \frac{1}{8\pi m_e \nu^2} \int_{\gamma_{\min}}^{\gamma_{\max}} d\gamma P_s(\nu) \gamma^2 \frac{\partial}{\partial \gamma} \left[ \frac{N(\gamma)}{\gamma^2} \right] = \frac{1}{8\pi m_e \nu^2} \int_{\gamma_{\min}}^{\gamma_{\max}} d\gamma \frac{N(\gamma)}{\gamma^2} \frac{\partial}{\partial \gamma} \left[ \gamma^2 P_s(\nu, \theta) \right], \quad (4.17)$$

where the second expression uses the fact that  $N(\gamma_{\min}) = N(\gamma_{\max}) = 0$ , and is particularly relevant in cases where the derivative of  $N(\gamma)$  is not well-defined. Using our power-law expression for  $N(\gamma)$ , we find

$$\alpha_\nu = \frac{(p+2)\sqrt{3}e^3 N_0 B \sin \theta}{16\pi \nu^2 m_e^2 c^2} \left( \frac{\nu}{\nu_0} \right)^{-\frac{p}{2}} \int_{x_{\min}}^{x_{\max}} dx x^{p/2-1} F(x). \quad (4.18)$$

In the limit  $x_{\min} \rightarrow \infty$  and  $x_{\max} \rightarrow 0$ , we find  $\alpha_\nu \propto \nu^{-(p+4)/2}$ , as expected.

As before, we can analytically evaluate this expression using our approximations. Evaluating for  $F^{(1)}(x)$ , we find

$$\alpha_\nu^{(1)} = \frac{(p+2)\sqrt{3}e^3 N_0 B \sin \theta}{16\pi \nu^2 m_e^2 c^2} \left( \frac{\nu}{\nu_0} \right)^{-\frac{p}{2}} \left\{ F_1 \frac{\sum_{i=0}^{14} n_{1i} \alpha_{1i}^{-z_1} (\Gamma(z_1, \alpha_{1i} x_{\min}) - \Gamma(z_1, \alpha_{1i} x_{\max}))}{\sum_{i=0}^{14} n_{1i}} + F_2 \left[ (\Gamma(z_2, x_{\min}) - \Gamma(z_2, x_{\max})) - \frac{\sum_{i=0}^{14} n_{2i} (\alpha_{2i} + 1)^{-z_2} (\Gamma(z_2, (\alpha_{2i} + 1) x_{\min}) - \Gamma(z_2, (\alpha_{2i} + 1) x_{\max}))}{\sum_{i=0}^{14} n_{1i}} \right] \right\}; \quad (4.19)$$

$$z_3 = \frac{2-p}{2} + \frac{1}{3} + 1, z_4 = \frac{2-p}{2} + \frac{1}{2} + 1.$$

The relative error in this expression is  $< 0.1\%$  across the full parameter space.

We are now in a position to solve the radiative transfer equation to calculate the observed spectrum for an arbitrary source. For reference, we restate the radiative transfer equation here:

$$\frac{dI_\nu}{ds} = \alpha_\nu I_\nu + \epsilon_s. \quad (4.20)$$

Here,  $I_\nu$  is the specific intensity [ $\text{erg cm}^{-2} \text{s}^{-1} \text{Hz}^{-1} \text{sterad}^{-1}$ ] and  $s$  is the path length.  $\alpha_\nu$  and  $\epsilon_s$  are still, respectively, the absorption coefficient [ $\text{cm}^{-1}$ ] and emissivity [ $\text{erg cm}^{-3} \text{s}^{-1} \text{sterad}^{-1}$ ]. For a sphere with radius  $R$  ( $A = \pi R^2$ ,  $s = 2R$ ), the flux density is given by

$$F_{\nu, \text{sphere}} = \frac{f_A A}{d_L^2} \frac{\epsilon_s(\nu)}{\alpha_\nu(\nu)} \left[ 1 - \frac{2}{\tau_\nu^2} \left( 1 - (1 + \tau_\nu) e^{-\tau_\nu} \right) \right]; \quad \tau_{\text{sa}}(\nu) = s \alpha_\nu(\nu). \quad (4.21)$$

We adopt this approximation for the synchrotron SED for all the analysis in this work. As is commonly done, we remove degeneracies between parameters by assuming equipartition. We assume that the fraction of energy stored in electrons is  $\epsilon_e = 0.1$  and that in the magnetic field is  $\epsilon_B = 0.1$ . We assume that the emitting region occupies a volume of  $f_V \pi R^3$ , where  $f_V = 4/3$  corresponds to a spherical region. We choose  $f_V = 0.36$ , which is appropriate for an emitting shell of width  $0.1R$ . We adopt these parameters to be consistent with the (149) analysis of radio-emitting TDEs.

Table 4.5: Radio emitting region parameters for radio-selected, optically-detected TDEs

Name	$t_{\text{obs}} - t_{\text{opt. peak}}$	$\log R/\text{cm}$	$\log B/\text{G}$	$\log N_0/\text{cm}^{-3}$	$p$	$\log \beta$	$\log E$	$\log M_{\text{ej}}/M_{\odot}$
VT J0813	17	$18.2^{+0.8}_{-0.9}$	$-2.0^{+0.8}_{-0.7}$	$-2^{+1}_{-1}$	$1.69^{+0.06}_{-0.05}$	$-0.03^{+0.03}_{-0.16}$	$50.4^{+1.0}_{-1.0}$	$-3.5^{+1.0}_{-1.0}$
	45	$17.2^{+1.2}_{-0.7}$	$-1.4^{+0.6}_{-1.0}$	$1^{+2}_{-2}$	$2.08^{+0.13}_{-0.08}$	$-0.4^{+0.3}_{-0.5}$	$48.4^{+1.6}_{-1.0}$	$-5.5^{+1.6}_{-1.0}$
	53	$17.7^{+0.9}_{-0.8}$	$-1.8^{+0.6}_{-0.8}$	$0^{+1}_{-2}$	$2.06^{+0.11}_{-0.10}$	$-0.2^{+0.1}_{-0.4}$	$49^{+1}_{-1}$	$-5^{+1}_{-1}$
	83	$18.1^{+0.7}_{-0.6}$	$-2.2^{+0.5}_{-0.6}$	$-0^{+1}_{-1}$	$2.20^{+0.03}_{-0.03}$	$-0.09^{+0.07}_{-0.22}$	$49.6^{+0.9}_{-0.8}$	$-4.3^{+0.9}_{-0.8}$
	134	$17.05^{+0.01}_{-0.01}$	$-1.17^{+0.02}_{-0.02}$	$2.35^{+0.06}_{-0.06}$	$2.55^{+0.03}_{-0.03}$	$-0.68^{+0.01}_{-0.01}$	$48.49^{+0.03}_{-0.02}$	$-5.46^{+0.03}_{-0.02}$
	205	$17.169^{+0.007}_{-0.006}$	$-1.15^{+0.01}_{-0.01}$	$2.56^{+0.03}_{-0.04}$	$2.81^{+0.02}_{-0.03}$	$-0.712^{+0.006}_{-0.005}$	$48.88^{+0.02}_{-0.02}$	$-5.07^{+0.02}_{-0.02}$
	247	$17.2^{+1.4}_{-0.2}$	$-1.3^{+0.3}_{-1.1}$	$2.2^{+0.6}_{-2.3}$	$2.57^{+0.16}_{-0.09}$	$-0.7^{+0.7}_{-0.2}$	$48.8^{+1.9}_{-0.2}$	$-5.1^{+1.9}_{-0.2}$
	302	$17.00^{+0.11}_{-0.05}$	$-1.10^{+0.06}_{-0.11}$	$2.3^{+0.2}_{-0.3}$	$2.38^{+0.08}_{-0.10}$	$-0.98^{+0.10}_{-0.04}$	$48.48^{+0.10}_{-0.04}$	$-5.47^{+0.10}_{-0.04}$
	410	$17.25^{+0.02}_{-0.01}$	$-0.86^{+0.02}_{-0.02}$	$3.42^{+0.05}_{-0.05}$	$3.51^{+0.03}_{-0.03}$	$-0.86^{+0.01}_{-0.01}$	$49.73^{+0.02}_{-0.02}$	$-4.23^{+0.02}_{-0.02}$
	618	$17.341^{+0.005}_{-0.005}$	$-1.237^{+0.008}_{-0.008}$	$2.29^{+0.02}_{-0.02}$	$2.65^{+0.01}_{-0.01}$	$-0.933^{+0.005}_{-0.005}$	$49.221^{+0.008}_{-0.008}$	$-4.730^{+0.008}_{-0.008}$
	701	$17.43^{+0.01}_{-0.01}$	$-1.11^{+0.01}_{-0.02}$	$2.80^{+0.03}_{-0.04}$	$3.19^{+0.02}_{-0.02}$	$-0.90^{+0.01}_{-0.01}$	$49.74^{+0.01}_{-0.01}$	$-4.21^{+0.01}_{-0.01}$
	800	$17.23^{+0.02}_{-0.02}$	$-1.15^{+0.04}_{-0.04}$	$2.6^{+0.1}_{-0.1}$	$2.85^{+0.07}_{-0.06}$	$-1.13^{+0.02}_{-0.02}$	$49.08^{+0.05}_{-0.04}$	$-4.87^{+0.05}_{-0.04}$
VT J1008	507	$17.06^{+0.01}_{-0.01}$	$-0.73^{+0.05}_{-0.04}$	$3.5^{+0.2}_{-0.1}$	$3.0^{+0.1}_{-0.1}$	$-1.37^{+0.01}_{-0.01}$	$49.4^{+0.1}_{-0.1}$	$-4.5^{+0.1}_{-0.1}$
VT J1356	2581	$17.40^{+0.04}_{-0.04}$	$-1.12^{+0.03}_{-0.03}$	$0.2^{+0.2}_{-0.2}$	$1.80^{+0.04}_{-0.04}$	$-1.73^{+0.04}_{-0.04}$	$49.7^{+0.1}_{-0.1}$	$-4.3^{+0.1}_{-0.1}$
VT J1752	756	$17.814^{+0.003}_{-0.004}$	$0.629^{+0.007}_{-0.013}$	$-2.75^{+0.03}_{-0.02}$	$1.004^{+0.007}_{-0.003}$	$-0.819^{+0.003}_{-0.003}$	$54.38^{+0.02}_{-0.04}$	$0.43^{+0.02}_{-0.04}$
	1115	$17.99^{+0.02}_{-0.02}$	$-0.87^{+0.05}_{-0.05}$	$-0.5^{+0.2}_{-0.2}$	$1.64^{+0.04}_{-0.04}$	$-0.75^{+0.02}_{-0.02}$	$51.9^{+0.1}_{-0.1}$	$-2.0^{+0.1}_{-0.1}$
VT J2012	469	$17.225^{+0.006}_{-0.006}$	$-0.83^{+0.02}_{-0.02}$	$3.27^{+0.08}_{-0.08}$	$2.95^{+0.07}_{-0.06}$	$-1.178^{+0.006}_{-0.006}$	$49.69^{+0.05}_{-0.05}$	$-4.26^{+0.05}_{-0.05}$
VT J2030	675	$17.44^{+0.01}_{-0.01}$	$-0.94^{+0.02}_{-0.02}$	$3.09^{+0.06}_{-0.06}$	$3.03^{+0.04}_{-0.04}$	$-1.122^{+0.011}_{-0.010}$	$50.11^{+0.03}_{-0.03}$	$-3.84^{+0.03}_{-0.03}$
	934	$17.622^{+0.009}_{-0.009}$	$-1.02^{+0.02}_{-0.02}$	$3.04^{+0.04}_{-0.04}$	$3.31^{+0.03}_{-0.03}$	$-1.021^{+0.008}_{-0.008}$	$50.51^{+0.03}_{-0.03}$	$-3.44^{+0.03}_{-0.03}$
	1051	$17.51^{+0.01}_{-0.01}$	$-1.05^{+0.03}_{-0.03}$	$2.89^{+0.08}_{-0.07}$	$3.07^{+0.06}_{-0.06}$	$-1.15^{+0.01}_{-0.01}$	$50.11^{+0.04}_{-0.04}$	$-3.84^{+0.04}_{-0.04}$

**Notes.** The physical parameters of the radio emission regions for our TDE candidates.

*Chapter 5*

VLASS TIDAL DISRUPTION EVENTS WITH OPTICAL  
FLARES II: DISCOVERY OF TWO TDES WITH  
INTERMEDIATE WIDTH BALMER EMISSION LINES AND  
CONNECTIONS TO THE AMBIGUOUS EXTREME CORONAL  
LINE EMITTERS

Somalwar, J. J. et al. (Apr. 2025). In: ApJ 983, 159 doi: 10.3847/1538-4357/adc002

Jean J. Somalwar<sup>1</sup>, Vikram Ravi<sup>1</sup>, and Wenbin Lu<sup>2</sup>,

<sup>1</sup>Cahill Center for Astronomy and Astrophysics, MC 249-17 California Institute of Technology,  
Pasadena CA 91125, USA.

<sup>2</sup>Department of Astronomy and Theoretical Astrophysics Center, University of California, Berkeley,  
CA 94720, USA

**Abstract**

The multiwavelength properties of radio-emitting tidal disruption events (TDEs) are poorly understood. In a previous paper, we presented the first sample of radio-selected, optically-detected TDEs, which included two events (VT J1008 and VT J2012) associated with late-time ( $\sim 2$  years post-optical flare) intermediate width emission lines that are largely unprecedented from TDEs. In this paper, we investigate these two events in detail. The multiwavelength properties of these events are otherwise consistent with optically-selected TDEs. They are hosted by green valley, E+A/Balmer dominated galaxies with low star formation rates and black holes masses  $M_{\text{BH}} \approx 10^{5-6} M_{\odot}$ . The optical flare shapes are fully consistent with those of optically-selected TDEs, although they are slightly faint and cool at peak. The radio emission from both events is consistent with wide-angle, non-relativistic outflows with  $L_R(\text{GHz}) \sim 10^{38} \text{ erg s}^{-1}$ . Balmer and Helium emission lines are detected from both events with full-width-half-maxima  $\sim 700 \text{ km s}^{-1}$  and asymmetric line profiles. VT J1008 additionally shows coronal line emission with a similar width. The lines from VT J2012 are redshifted by  $\sim 700 \text{ km s}^{-1}$  relative to the host galaxy. We show that these events share many characteristics in common with the ambiguous class of extreme coronal line emitters. We argue that the lines are likely associated with a radiative shock or dense, photoionized clumps of outflowing gas

in the circumnuclear medium.

## 5.1 Introduction

Tidal disruption events occur when a star ventures within the tidal radius of a supermassive black hole (SMBH; (243)). In the last decades, our observational and theoretical understanding of TDEs has dramatically improved, largely thanks to the advent of wide field, time-resolved surveys in the optical and X-ray (13, 123, 134, 314, 407). Now,  $\sim 100$  optically-selected TDEs have been discovered, as well as 10s of TDEs identified at other wavelengths.

The large sample of optically-select events have enabled studies of black hole demographics (134) and accretion physics (e.g. 254). Of key relevance to this work, they have also constrained jet/outflow launching (150) and the circumnuclear media (CNM) of non-active galaxies (149, 150).  $\gtrsim 30\%$  of optically-selected TDEs produce radio flares consistent with wide-angle outflows or weak jets (the mechanism is still debated) colliding with the host galaxy's CNM (149, 151). The outflows are, in some cases, consistent with unbound stellar debris (264). In most cases, the outflow evolution is more consistent with an accretion disk wind or weak/off-axis jet (408). In particular, many outflows turn on  $\gtrsim 3$  years post-disruption, and some flare rise-times are too fast to be consistent with a single gamma-ray burst-like outflow (149, 153, 408).  $\sim 1\%$  of TDEs launch energetic, collimated jets (245, 394). These are typically discovered by their non-thermal emission, rather than by the thermal optical emission by which most TDEs are identified. How these jets are launched, and why so few TDEs are able to launch jets, remains an open question (150). Constraints on the rates, dynamics, energetics, and structures of TDE-launched outflows will narrow down the launching mechanisms.

Even without knowledge of the precise jet/outflow launching physics, the radio evolution diagnoses the structure of the gas and dust in the vicinity of the black hole (150). These constraints are largely on the CNM, rather than outflowing stellar debris (although see 264). The CNM density profile has been measured for a handful of events this way (149, 150). It is generally decreasing with radius, analogous to that of the Milky Way, for events without evidence for recent active galactic nuclei. Events in hosts that were recently active galactic nuclei show a shallow, dense inner region, followed by a steeper drop-off in density relative to the non-active host galaxies.

In addition to these radio constraints, infrared (IR) continuum emission and optical spectroscopic emission are sensitive to the CNM structure. Some TDEs produce IR flares on months-years timescales following the disruption (132, 144, 314). The flares are thought to be thermal emission from dust in the CNM that is heated by ultraviolet (UV) photons from the TDE (115). The flare luminosity and evolution depend on the lightcurve of the UV flare and the dust geometry and composition. Most optically-selected TDEs have faint, short-lived IR flares, if any IR emission is detected, which has been used to infer dust covering fractions  $\lesssim 1\%$  (144). These low covering fractions may be in part a selection effect: events with large dust covering fractions can be impossible to detect in the optical due to extinction of the optical flare. Efforts to identify TDEs in the IR show that TDE-like events with larger dust covering fractions may exist (131, 132).

Transient optical line emission is sensitive to the gas structure near the black hole, and in particular the stellar debris. At early times, optically-selected TDEs often produce  $\sim 10^4 \text{ km s}^{-1}$  Hydrogen, Helium, and Bowen Fluorescence lines (13). Which lines are produced, as well as their relative strengths, has been argued to be the result of the composition of the stellar debris and/or the shape of the ionizing continuum (146). The lines last for  $\lesssim 1$  year and show complex line profiles (13, 409). The line profile, which tends to be blueshifted with a red wing, is thought to result from strong electron scattering rather than complex gas kinematics (146). In some cases, the line emission is double-peaked. In these cases, the line profiles are well-modelled as originating from an elliptical, rotating region, i.e., an accretion disk/wind (410).

The late times ( $\sim$ years) transient line from TDEs emission is unclear, largely due to a lack of systematic, late-time, deep spectroscopic follow-up campaigns. It is thought that the class of extreme coronal line emitters (ECLEs), which were originally discovered in the Sloan Digital Sky Survey, are late-time TDEs (14, 271). ECLEs show strong emission from coronal lines, which have ionization potentials  $\gtrsim 100 \text{ eV}$  (e.g.,  $[\text{Fe X}]\lambda 6375$ ). While active galactic nuclei (AGN) also show such emission, ECLEs are defined such that the coronal lines are significantly stronger relative to  $[\text{O III}]\lambda 5007$  than is typical in AGN, which have  $[\text{Fe X}]/[\text{O III}] \ll 1$  (14). ECLEs show line evolution on  $\gtrsim$ year timescales (411). TDEs produce luminous EUV-soft X-ray continua and are transient, and thus are strong candidates to explain the evolving, luminous coronal line emission from ECLEs (14, 411). There is growing evidence that ECLEs are TDEs from similarities between host galaxies to the direct detection of strong coronal line emission from optically-selected TDEs (148, 412).

Like the early-time emission, the coronal line emission luminosities and line profiles are sensitive to the structure of gas in the vicinity of the black hole, as well as the shape of the ionizing continuum. In particular, the optical coronal lines have been used to argue for the presence of dense, cool gas (possible sublimated dust) and strong soft X-ray emission (e.g. *163*).

In this paper, we discuss two TDEs with  $\sim 1000 \text{ km s}^{-1}$ , late-time Balmer and coronal emission lines. These TDEs are part of the first sample of radio-selected TDEs, which is subject to different selection biases from the optically-selected TDEs, and in particular will include TDEs with more gas and dust in the circumnuclear medium. This sample included all TDE-like radio transient in VLASS with optical counterparts and we presented it in (*413*) (hereafter Paper I). One of the most intriguing discoveries from our sample was the detection of intermediate width Balmer emission from the only two events in our sample in quiescent galaxies. Such emission has not been reported for uniformly selected, bona-fide TDEs before (see (*134*) for an event discovered simultaneous with our work): the only previous reports of similar emission are from SDSS-selected ECLEs.

In Paper I, we presented our full sample. In this paper, we delve into the multiwavelength properties and the interpretation of the two events with intermediate width Balmer emission lines. We adopt the (*414*) cosmology throughout.

## 5.2 Sample Selection

Table 5.1: Properties of our TDEs

	VT J1008	VT J2012
R.A.	$10^{\text{h}}08^{\text{m}}53.44^{\text{s}} 20^{\text{h}}12^{\text{m}}29.90^{\text{s}}$	
Dec.	$+42^{\circ}43'00.22'' - 17^{\circ}05'56.32''$	
$\Delta d$ ["]	0.18	0.2
$z$	0.045	0.053
$d_L$ [Mpc]	205	244
$\log M_{\text{BH}}/M_{\odot}$	$4.81^{+0.40}_{-0.32}$	$6.17 \pm 0.31$
SFR [ $M_{\odot} \text{ yr}^{-1}$ ]	$< 1.47$	$< 1$
$L_{\nu}$ (VLASS) [ $10^{28} \text{ erg s}^{-1} \text{ Hz}^{-1}$ ]	$9.6 \pm 0.3$	$9.9 \pm 0.9$

Our sample selection is described in detail in Paper I; we discuss it briefly here. We identified the two objects described in this work as members of a broader sample of radio-selected TDEs. We compiled this TDE sample from the Very Large Array Sky Survey (VLASS; (*133*)). VLASS is observing the sky with  $\delta > -40^{\circ}$  at 3 GHz for three epochs with a cadence of  $\sim 2$  years, a per-epoch sensitivity of  $\sim 0.13 \text{ mJy}$

and a spatial resolution of  $\sim 2.5''$ . The first two epochs were completed in 2017/2018 and 2020/2021. The third epoch is ongoing at the time of writing.

We identified TDE candidates using the transient catalog of Dong et al., in prep., who identified all sources that were detected at  $> 7\sigma$  in E2 but not significantly detected ( $< 3\sigma$ ) in E1; i.e., this catalog contains all transients that are rising between E1 and E2. Details about the transient detection algorithm are described in (163) and Dong et al., in prep. We select TDE candidates from this catalog as sources coincident with PanSTARRS-detected galaxies. The galaxies must show no evidence for strong AGN activity in any public archival data. Among the criteria used to identify AGN, we consider: the position of the source on the WISE W1-W2 and W2-W3 color diagram; any evidence for past optical, X-ray, or radio variability/detections that could indicate AGN activity (based on a cone search of catalogues in the Vizier database at the location of each source). The host galaxy must also have a photometric redshift  $z_{\text{phot}} < 0.25$ , at which redshifts multiwavelength counterparts and host galaxies are more readily detected with reasonable exposure times. The resulting sample has  $\sim 100$  objects.

In Paper I, we focus on the subset of this sample with associated optical flares in data from the Zwicky Transient Facility (ZTF; *gri* bands) and the Asteroid Terrestrial-impact Last Alert System (ATLAS; *co* bands). The resulting sample has six objects, three of which are hosted by weak Seyferts, one by a starforming galaxy, and two by quiescent galaxies. The two objects in quiescent galaxies were also detected to have unusual, intermediate width Balmer lines, and thus are the focus of this work. Details of the rest of the sample are presented in Paper I.

The two sources are named using our VLASS transient naming convention: VT J100853.44+424300.22 (VT J1008) and VT J201229.90-170556.32 (VT J2012). We refer to the host galaxies of these objects using the coordinates prefixed with HG (host galaxy; e.g., HG J1008). In plots, we often label the individual transients or host galaxies without the prefixes (e.g., J1008), except when the prefixes are necessary for clarity.

### 5.3 Summary of transient properties

In this section, we present observations of VT J1008 and J2012 and briefly summarize the multiwavelength properties of each source. We defer discussion of the optical spectral features, which are the main focus of this paper, to the following section.

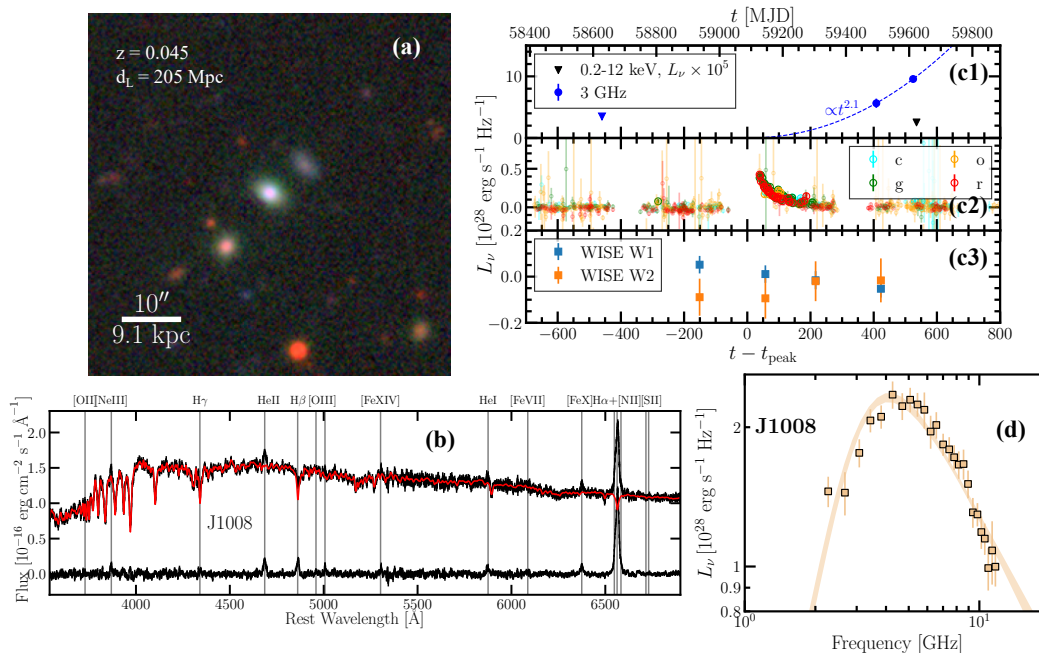


Figure 5.1: Summary plot for VT J1008. Panel a shows an image of the host galaxy. Panel b shows an example optical spectrum. The observed spectrum is shown on top in black, and the best-fit stellar emission model is shown in red. The observed spectrum with the stellar continuum subtracted is shown on the bottom in black, with the transient emission lines clearly visible. Panel c shows multiwavelength light curves for VT J1008. Panel c1 shows the radio light curve in blue and the X-ray light curve in black. Upper limits are shown as triangles. Panel c2 shows the ATLAS *co* and ZTF *gr* optical lightcurve. Panel c3 shows the WISE MIR lightcurve, with no obvious flare detected. Panel d shows the radio observations of this source. The radio SED is consistent with a wide-angle, non-relativistic outflow.

## VT J1008

We begin our discussion with VT J1008, the multiwavelength properties of which are summarize in Figure 5.1. In the following subsections, we break down each panel of Figure 5.1.

### Host galaxy properties

A PanSTARRS optical image of the host galaxy of VT J1008, HG J1008, is shown in the panel a of Figure 5.1. It is at a redshift  $z = 0.045$ , or a luminosity distance  $d_L = 205$  Mpc. The host galaxy spectrum is shown in panel b. Note that this spectrum is contaminated by transient features. Based on the  $H\delta_A$  absorption ( $H\delta_A = 4.5 \pm 0.1$ ) and an upper limit on the  $H\alpha$  EW ( $EW_{H\alpha} < 14.4$ ) we cannot constrain the  $H\alpha$  EW exactly because of the transient emission), this galaxy is

consistent with being an E+A; i.e., it underwent a starburst in the last  $\sim$ Gyr. There is no strong indication of an AGN, although the faint [Ne III] and [O III] emission lines could be produced by a weak AGN. These lines could also be produced by star formation, however.

We performed an SED fit for HG J1008 in Paper I using public survey data spanning the ultraviolet to mid-infrared. We briefly review the results here, but refer the reader to Paper I for a detailed description of our methodology. The host galaxy has a stellar mass  $\log M_*/M_\odot = 9.04^{+0.22}_{-0.16}$ , and the  $3\sigma$  upper limit on the star formation rate is  $\log \text{SFR}/(M_\odot \text{ yr}^{-1}) < 1.47$ . This photometry of the host places it within the green valley defined by (10) (see Figure 4 of Paper I).

These SED fit parameters also set constraints on the SMBH masses. From the stellar mass, we can infer a SMBH mass using the (134) relation constrained using optical TDE host galaxies:

$$\log \frac{M_{\text{BH}}}{10^9 M_\odot} = (-1.75 \pm 0.13) + (1.73 \pm 0.23) \log \frac{M_{\text{gal}}}{3 \times 10^{10} M_\odot},$$

which as an intrinsic scatter of 0.17. We find  $M_{\text{BH}}(M_*) = 4.81^{+0.40}_{-0.32}$ . Alternatively, (134) measured a stellar velocity dispersion for this source  $\sigma_* = 44 \pm 3$ . Using the  $M_{\text{BH}} - \sigma_*$  relation from (47), we find  $M_{\text{BH}}(\sigma_*) = 5.59 \pm 0.29$ , which is consistent with the value measured from the stellar mass within  $1.5\sigma$ . The SMBH mass determined from the velocity dispersion is small relative to the SMBH masses measured from TDEs by (134): VT J1008 has a smaller SMBH mass than 27/32 ( $(84 \pm 8)\%$ ) of their TDEs. The SMBH mass from the stellar mass is even lower than that from the velocity dispersion.

### Optical and IR broadband transient emission

In panel c2 of Figure 5.1, we show the optical lightcurve for VT J1008. This lightcurve was created using the ATLAS<sup>1</sup> and ZTF<sup>2</sup> forced photometry retrieved using recommended procedures. Both surveys detected an optical flare from this source starting on MJD $\sim$ 59100. The flare rise was missed, but the decay was well-sampled. (134) fit this lightcurve as an evolving blackbody with the temperature fixed to that at peak luminosity. They found a peak blackbody luminosity of  $\log L_{\text{bb}}/(\text{erg s}^{-1}) = 42.98$  and peak temperature  $\log T_{\text{bb}}/\text{K} = 4.15$ . The radius

<sup>1</sup><https://fallingstar-data.com/forcedphot/>

<sup>2</sup>[https://irsa.ipac.caltech.edu/data/ZTF/docs/ztf\\_forced\\_photometry.pdf](https://irsa.ipac.caltech.edu/data/ZTF/docs/ztf_forced_photometry.pdf)

at peak luminosity was  $\log R_{\text{bb}}/\text{cm} = 14.76$ . The time to rise from half-max-luminosity to max-luminosity was  $t_{\text{rise},1/2} = 11.8^{+1.5}_{-1.3}$  days, and the time to decay from max to half-max was  $t_{\text{decay},1/2} = 23.1^{+1.8}_{-1.2}$  days. This peak temperature is cool for a typical optically-selected TDE: it is cooler than 25/32 ((78 ± 9)%) of the optical TDEs in (134). The peak luminosity is lower than every TDE in the (134) sample. The rise and decay times are typical of optically-selected TDEs.

During the writing of this work, VT J1008 rebrightened in the optical on MJD 60073 and has been identified as a repeating partial TDE (415). Although it is plausible that the repeating nature of this source has affected the emission, we do not consider the rebrightening here and refer the reader to (375) for details.

In panel c3, we show the IR lightcurve for this source from the NEOWISE survey, processed using the methods described in (11). We do not see any significant IR variability.

### **X-ray emission**

We checked public X-ray survey data, including the XMM Newton Slew Survey, etc, for archival detections of VT J1008. No detections were reported. The pre-optical-flare X-ray upper limit was  $10^{42.9}$  erg s<sup>-1</sup>. The tightest post-optical flare limit is from our Swift/XRT ToO. We obtained X-ray observations of VT J1008 on MJD 59638 using a 3.5 ks exposure with the Swift/XRT telescope (PI Somalwar). The source was not detected, with a  $3\sigma$  luminosity upper limit of  $10^{41.8}$  erg s<sup>-1</sup>. This upper limit is shown in panel c1 of Figure 5.1.

### **Radio emission**

The radio lightcurve for VT J1008 is shown in panel c1. VT J1008 was first observed by VLASS on MJD 58628; this nondetection was ~460 days before the optical peak. It was observed again on MJD 59496 (524 days post-optical peak) and was detected as a  $1.13 \pm 0.15$  mJy source, corresponding to a 3 GHz luminosity of  $L_{\nu} = (5.6 \pm 0.7) \times 10^{28}$  erg s<sup>-1</sup> Hz<sup>-1</sup>. We observed the source with the VLA on MJD 59612 (525 days post-peak) in the CLSX bands. The 3 GHz radio luminosity from this SED had risen since to VLASS observation to  $(9.6 \pm 0.3) \times 10^{28}$  erg s<sup>-1</sup> Hz<sup>-1</sup>. If we assume that the radio-emitting outflow was launched at optical peak, this rise corresponds to a  $L_{\nu} \propto t^{2.1^{+0.6}_{-0.5}}$  power-law evolution, which is consistent with expectations for a constant velocity outflow.

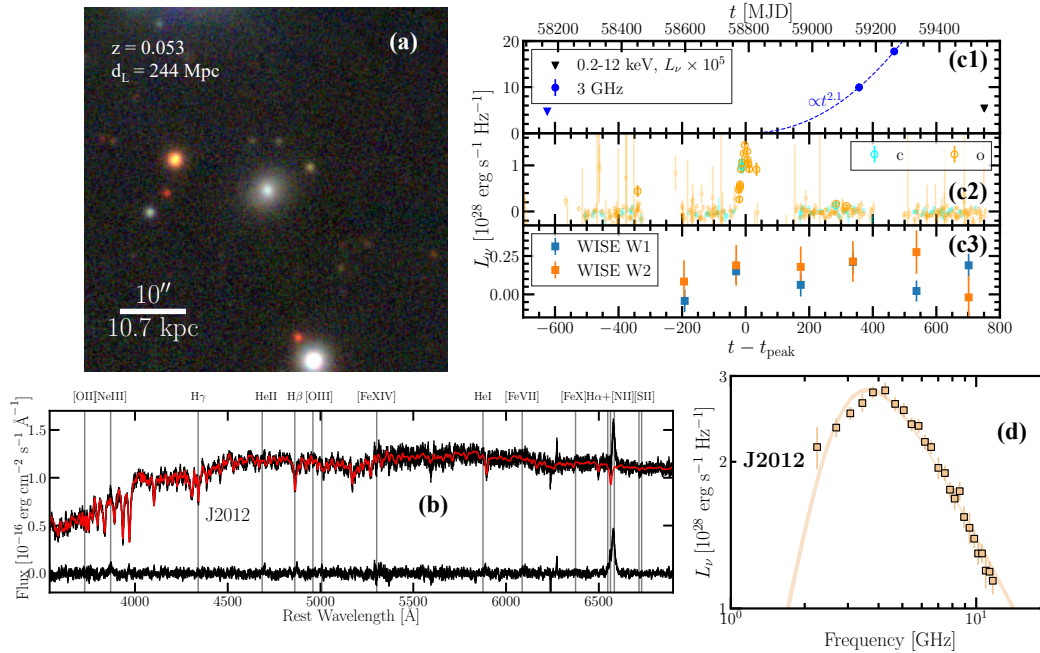


Figure 5.2: Summary plot for VT J2012, in the same format as Figure 5.1.

The VLA radio SED is shown in panel d. We modelled the SED as a synchrotron outflow following the methodology described in Appendix E of Paper I, where we assume a spherically symmetric outflow with magnetic field  $B$ , electron density  $N_0$ , and radius  $R$ . We assume the electrons have a power-law energy distribution with index  $\gamma$ . We assume equipartition with  $\epsilon_E = 11/17$  and  $\epsilon_B = 6/17$ , corresponding to the minimum energy solution. The total energy in the outflow is given by  $E$ . We find a radius  $\log R/\text{cm} = 17.06^{+0.01}_{-0.01}$ , a magnetic field  $\log B/\text{G} = -0.73^{+0.05}_{-0.04}$ , an electron density  $\log N_0/\text{cm}^{-3} = 3.5^{+0.2}_{-0.1}$ , and an energy  $\log E/\text{erg} = 49.4^{+0.1}_{-0.1}$ . Assuming the outflow was launched at the optical peak with velocity  $v$ , the best-fit radius gives  $\log \beta = \log v/c = -1.37^{+0.1}_{-0.1}$ , or  $v \approx 1.3 \times 10^3 \text{ km s}^{-1}$ .

The radio SED is thus consistent with a non-relativistic, wide-angle outflow launched near optical peak.

## VT J2012

### Host galaxy properties

An optical image from the DECam Legacy Survey of HG J2012 is shown in the panel (a) of Figure 5.2. It is at a redshift  $z = 0.053$ , or a luminosity distance  $d_L = 244$  Mpc. The host galaxy spectrum (contaminated by transient features) is shown in panel (b). From the  $H\delta_A$  absorption ( $H\delta_A = 2.7 \pm 0.2$ ) and an upper limit on the  $H\alpha$

EW ( $EW_{H\alpha} < 5$ ), this galaxy is a balmer strong galaxy, which have slightly older stellar population than E+A galaxies. There is no indication of an AGN, although faint [Ne III] emission may be present.

From an SED fit performed in Paper I, the host galaxy has a stellar mass  $\log M_*/M_\odot = 9.90_{0.09}^{0.32}$ . The  $3\sigma$  upper limit on the star-formation rate is  $\log \text{SFR}/(M_\odot \text{ yr}^{-1}) < 1$ . This photometry of the host places it within the green valley defined by (10) (see Figure 4 of Paper I).

From the stellar mass, we can infer a SMBH mass using the (134) relation for optical TDE hosts:  $M_{\text{BH}}(M_*) = 6.55_{-0.32}^{+0.24}$ . In paper I, we measured a stellar velocity dispersion for this source  $\sigma_* = 59 \pm 2$ . Using the  $M_{\text{BH}} - \sigma_*$  relation from (47), we find  $M_{\text{BH}}(\sigma_*) = 6.17 \pm 0.31$ , which is consistent with the value measured from the stellar mass. This SMBH mass is near the median of the SMBH masses from (134)

### Optical and IR broadband transient emission

The optical lightcurve for VT J2012 is shown in panel c2 of Figure 5.2. This source was only detected by the ATLAS survey, and the lightcurve was created using recommended procedures. The flare was first detected on MJD~58800. Paper I fit this lightcurve to the same model as used for VT J1008, and found a peak blackbody luminosity of  $\log L_{\text{bb}}/(\text{erg s}^{-1}) = 43.07$  and peak temperature  $\log T_{\text{bb}}/\text{K} = 3.93$ . The radius at peak luminosity was  $\log R_{\text{bb}}/\text{cm} = 15.26$ . The time to rise from half-max-luminosity to max-luminosity was  $t_{\text{rise},1/2} = 10.2_{-1.1}^{+1.5}$  days, and the time to decay from max to half-max was  $t_{\text{decay},1/2} = 15_{-10}^{+14}$  days. Like VT J1008, this source shows a remarkably cool, faint flare relative to the (134) sample.

In panel c3, we show the IR lightcurve for this source from the NEOWISE survey, processed using the methods described in (11). Like for VT J1008, we do not see any significant IR variability.

### X-ray emission

We checked public X-ray survey data, including the XMM Newton Slew Survey, etc, for archival detections of VT J1008. No detections were reported. The pre-optical-flare X-ray upper limit was  $10^{43.1} \text{ erg s}^{-1}$ . The tightest post-optical flare limit is from our Swift/XRT ToO. We obtained X-ray observations of VT J2012 on MJD 59536 using a 1.6 ks exposure with the Swift/XRT telescope (PI Somalwar).

The source was not detected, with a  $3\sigma$  luminosity upper limit of  $10^{42.1}$  erg s<sup>-1</sup>. This upper limit is shown in panel c1 of Figure 5.1.

### Radio emission

The radio lightcurve for VT J2012 is shown in panel c1. VT J2012 was first observed by VLASS on MJD 58166 (~624 days pre-peak) and the luminosity upper limit was  $L_\nu = 4.7 \times 10^{28}$  erg s<sup>-1</sup> Hz<sup>-1</sup>. It was observed again on MJD 59147 (357 days post-optical peak) and was detected as a  $(9.9 \pm 0.9) \times 10^{28}$  erg s<sup>-1</sup> Hz<sup>-1</sup> source ( $1.48 \pm 0.13$ ). We observed the source with the VLA on MJD 59258 (467 days post-peak) in the CLSX bands, and the 3 GHz radio luminosity had risen to  $(14.9 \pm 0.2) \times 10^{28}$  erg s<sup>-1</sup> Hz<sup>-1</sup>. This corresponds to a  $L_\nu \propto t^{2.14^{+0.32}_{-0.33}}$  power-law, which is consistent with a constant velocity.

The VLA radio SED is shown in panel d. We modelled the SED as a synchrotron outflow following the same methodology used for VT J1008. We find a radius  $\log R/\text{cm} = 17.225^{+0.006}_{-0.006}$ , a magnetic field  $\log B/\text{G} = -0.83^{+0.02}_{-0.02}$ , an electron density  $\log N_0/\text{cm}^{-3} = 3.27^{+0.08}_{-0.08}$ , and an energy  $\log E/\text{erg} = 49.69^{+0.05}_{-0.05}$ . Assuming the outflow was launched at the optical peak with velocity  $v$ , the best-fit radius gives  $\log \beta = \log v/c = -1.178^{+0.006}_{-0.006}$ , or  $v \approx 2 \times 10^4$  km s<sup>-1</sup>.

Like that of VT J1008, this radio SED is consistent with a non-relativistic, wide-angle outflow launched near optical peak.

### Summary

We conclude with a brief summary of the results from this section:

- VT J1008 and VT J2012 are hosted by quiescent galaxies with no evidence for strong AGN activity. The galaxies are both E+A or Balmer-strong galaxies in the green valley. Both galaxies have SMBH masses  $M_{\text{BH}} \approx 10^{5-6} M_\odot$ .
- VT J1008 and VT J2012 have optical counterparts with peak blackbody luminosities  $L_{\text{bb}} \approx 10^{43}$  erg s<sup>-1</sup> and temperature at peak  $T_{\text{bb}} \approx 10^4$  K, which are cooler and fainter than those of typical optically-selected TDEs. The rise and decay times of the optical flares are typical of optically-selected TDEs.
- Neither VT J1008 or VT J2012 have IR or X-ray counterparts.
- VT J1008 and VT J1008 both are associated with radio transients that turned on  $\sim 1 - 2$  years post-optical peak. They both have 3 GHz luminosities  $\sim 10^{29}$

erg s<sup>-1</sup> Hz<sup>-1</sup>, which is a typical luminosity for optically-selected, radio-detected TDEs (see Figure 9 of Paper I). The radio SEDs of both sources are consistent with low velocity  $\sim 10^{-1}c$ , wide angle outflows with energies  $\sim 10^{49.5}$  erg.

#### 5.4 The transient optical spectral features

Table 5.2: Summary of optical spectra

Source	MJD	$t - t_{\text{peak}}$ [days]	Telescope/Instrument	Slit width	Exposure Time [s]	Wavelength Range [Å]	Resolution
VT J1008	59616.4	529	Keck I/LRIS	1''	600	3200–10250	700
	59676.4	589	Keck I/LRIS	1''	1200	3200–10250	700
	59908.5	821	Keck II/ESI	0.3''	1350	4000 – 11000	13000
	60029.3	941	Keck II/ESI	0.5''	2700	4000 – 11000	10000
VT J2012	59464.4	674	Keck I/LRIS	1''	600	3200–10250	700
	59676.4	886	Keck I/LRIS	1''	1800	3200–10250	700
	59876.2	1086	Keck II/ESI	0.5''	1200	4000 – 11000	10000

While keeping the broader picture of the multiwavelength properties of our two radio TDEs in mind, we now delve into the intermediate width transient lines, which are the focus of this work. The optical spectra that we analyze are summarized in Table 5.2. Zoom-ins on these transient features are shown in Figure 5.3 (VT J1008) and Figure 5.4 (VT J2012). In this section, we present our methodology for constraining the emission line properties and present the results. We then briefly compare the observed lines to other transient observations, but defer a detailed discussion of the origins of the lines to Section 5.5.

#### Methodology

We first constrain the properties of the transient spectral lines. We use two sets of observations, which we process separately.

First, we considered low resolution but flux calibrated observations with the Low Resolution Imaging Spectrometer (LRIS) on the Keck I telescope. We observed VT J1008 on MJD 59676 for 20 min. using the 1'' slit with the standard star Feige 34 and on MJD 59616 for 10 min. using the standard star G191-B2B. We centered all observations on the galactic nuclei using a parallactic angle. We used the 400/3400 grism, the 400/8500 grating with central wavelength 7830, and the 560 dichroic. The resulting wavelength range was  $\sim 3200\text{--}10250$  and the resolution  $R\sim 700$ . We observed VT J2012 on MJD 59464 for 10 min using the 1.0'' slit with the standard

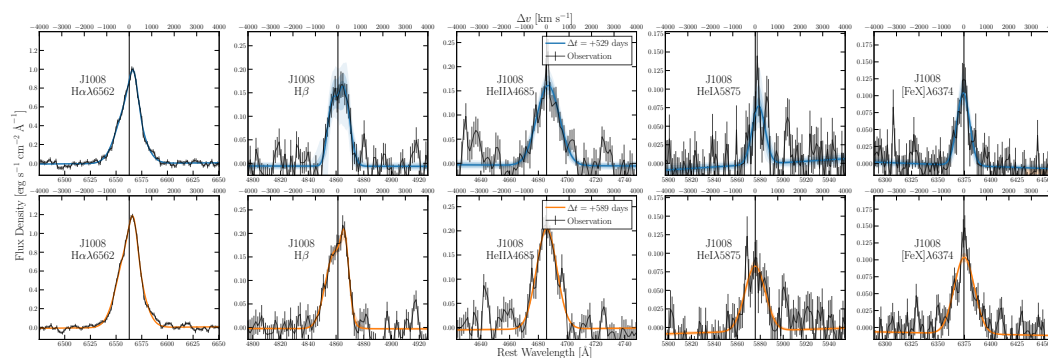


Figure 5.3: Zoom-ins on select optical lines from the low resolution LRIS observations of VT J1008. Each row shows a different observation epoch. The observations are shown in black, and the best-fit models are shown as colored lines. The colored bands denote  $1\sigma$  uncertainties. The blue fits correspond to the first observation epochs, and the orange fits correspond to the second epochs. The features blueward of  $H\alpha$  are caused by telluric features

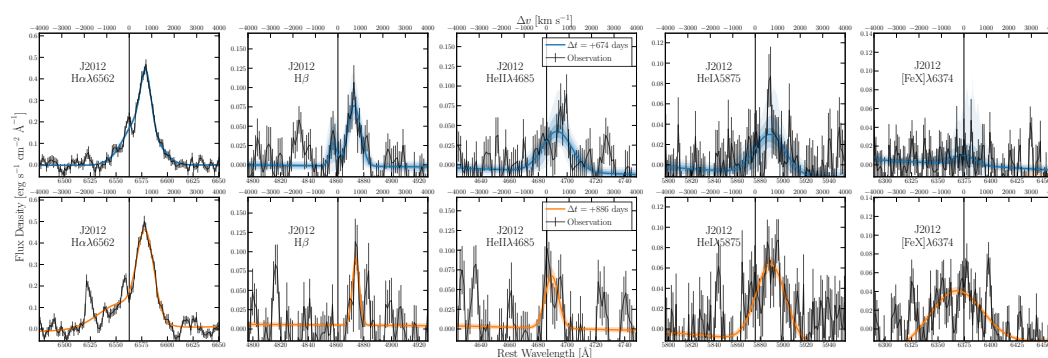


Figure 5.4: Zoom-ins on select optical lines from the low resolution LRIS observations of VT J2012. Each row shows a different observation epoch. The observations are shown in black, and the best-fit models are shown as colored lines. The colored bands denote  $1\sigma$  uncertainties. The blue fits correspond to the first observation epochs, and the orange fits correspond to the second epochs.

stars BD+28 and G191-B2B for the blue/red sides, respectively, and on MJD 59678 using the standard star Feige 34. We reduced all spectra using the `lpipe` code with standard settings. These spectra are summarized in Table 5.2.

To constrain the properties of the transient spectral lines, we first must remove the host galaxy stellar emission from all the spectra. We fit each spectrum with the `ppxf` full spectrum fitting tool using the MILES templates (364) following the method detailed in Appendix B of (163). The resulting best-fit stellar component is shown, for each source, in red in the panel b's of Figure 5.1 and Figure 5.2. We then create a nebular spectrum by subtracting the stellar component from the galaxy spectrum, and the result is shown at the bottom of the panel b's of Figure 5.1 and Figure 5.2.

With these low resolution emission line spectra in hand, we now can fit the line profiles. We consider the following lines, for reasons that will become clear later in this work:  $H\alpha$ ,  $H\beta$ ,  $[\text{O III}]\lambda 5007$ ,  $[\text{O III}]\lambda 4959$ ,  $[\text{O II}]\lambda\lambda 3727, 3729$ , and  $\text{He II}\lambda 4686$ . We first fit each line to a Gaussian with free centroid, width, and flux. We require the centroid be within  $2000 \text{ km s}^{-1}$  of the expected wavelength given the host redshift. We set the lower bound of the width to be such that the line FWHM is greater than 6, corresponding to a rough lower limit on the LRIS resolution. The width upper bound is  $2000 \text{ km s}^{-1}$ , which does not affect the fits. We adopt broad, uninformative priors for the flux:  $f \in [0, 10^{-13}] \text{ erg cm}^{-2} \text{ s}^{-1}$ . For the  $[\text{O II}]\lambda\lambda 3727, 3729$  complex, we fit a single Gaussian rather than two because we do not expect the doublet to be resolvable given the large LRIS FWHM.

For some of the Balmer lines, this single Gaussian fit produces a statistically inconsistent  $\chi^2$ . In those cases, we run a fit with two Gaussian components, each with independent widths, amplitudes, and centroids. For J2012, we fix the centroid of one component at the host redshift. The resulting fit better captures the structure of the emission lines

From both events, the  $[\text{O II}]$  doublet is not significantly detected, and the  $[\text{O III}]$  line is detected with a narrow width  $\sim 100 \text{ km s}^{-1}$ . Given the narrow widths of the  $[\text{O III}]$  emission, we do not believe it is coming from the same location as the Balmer and Helium emission. Instead, it is consistent with being stable host galaxy emission. To constrain the presence of intermediate width, transient emission at the location of these oxygen lines, we repeat the Gaussian fit but fix the width to  $\text{FWHM} \approx 700 \text{ km s}^{-1}$ . In the case of  $[\text{O III}] \lambda 5007$ , we do not subtract out the narrow line component before this fit, so the broad fit absorbs the flux from this narrow line. We choose to do this because it produces the most conservative upper limit on the broad line flux

for this emission line, even though the resulting fit has a high  $\chi^2$ . Subtracting out the narrow component would not affect our conclusions; it would simply tighten the bound on the presence of transient [O III]  $\lambda$ 5007 emission.

The resulting best-fit parameters of the lines from the low resolution spectra are listed in Table 5.3, and the fits are shown in Figure 5.3 for VT J1008 and Figure 5.4 for VT J2012.

In addition to these low resolution spectra, we use high resolution spectra that are not flux calibrated. The high resolution spectra are taken at later times than the low resolution spectra, so they provide constraints on the line profiles over a longer timescale. Moreover, while we cannot set luminosity constraints using the high resolution spectra, we can study the line profiles in detail; in particular, we can distinguish between multiple, blended lines or a single line with a broad profile. We obtained spectra of these objects with the Echellette Spectrograph and Imager (ESI) on the Keck II telescope. We used the Echelle mode for all observations. We observed VT J1008 on MJD 59908 for 22.5 min using the 0.3'' slit and the standard BD+28, and on MJD 60029 for 45 min using the 0.5'' slit and the standard BD+33. We observed VT J2012 on MJD 59876 for 20 min using the 0.5'' arcsec slit and the standard BD+28. We reduced the observations using the `makee` code with standard settings, and removed telluric lines using recommended procedures. These spectra are not flux calibrated because the instrument response function varies with telescope position and we do not have a standard star at a close telescope position. For both objects, the  $H\alpha$  lines fall in a region with strong telluric absorption and bright sky lines. Fortunately, the spectra are of sufficiently high resolution that we can still study the smooth line profiles, but all spikes and other unusual features in the data are due to this contamination.

Zoom-ins on the resulting  $H\alpha$  line profiles are shown in Figure 5.5. While other lines are detected (VT J1008: [O III] $\lambda$ 5007, He II $\lambda$ 4686), no other line is detected at a sufficiently high signal-to-noise to allow detailed constraints on its profile.

Because the line profiles observed cannot be well-modelled as Gaussians, we constrain the line profiles using a different methodology from that used for the LRIS data. We aim to constrain the velocity offset of the line peak, the upper FWHM, and the lower FWHM. Here, we define the upper FWHM as twice the width of the line above peak and the lower FWHM as the twice the width of the line below peak. This definition quantifies the lines asymmetry. We first estimate the peak wavelength as the wavelength of the pixel with the maximum flux. We then fit a

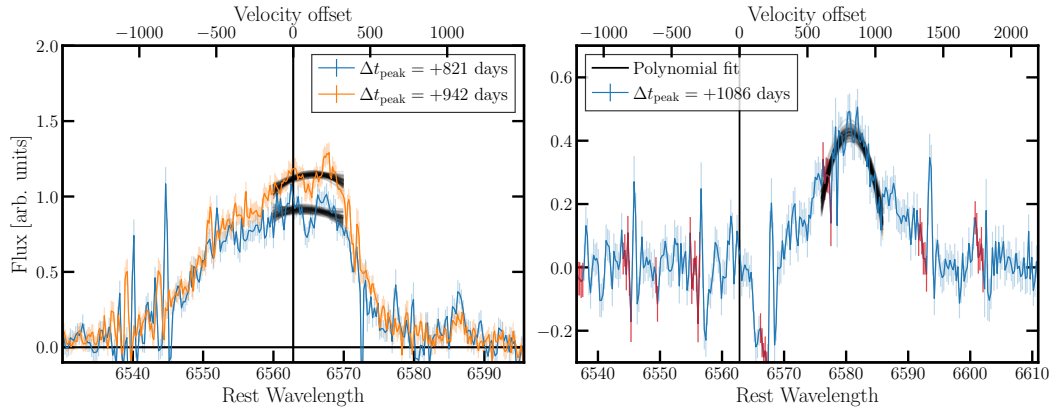


Figure 5.5:  $H\alpha$  spectral profiles from the medium resolution ESI observations. The observations of VT J1008 are in the *left* panel, and those of VT J2012 are in the *right* panel. The blue line shows the first epoch of observations and the orange line shows the second epoch. The flux for each epoch is normalized to the local continuum, which is not expected to be the same in both observations. In the *right* panel, regions particularly impacted by strong sky lines are shown in red.

small region ( $\pm 5$ ) around this estimate of the peak with a second degree polynomial and measure the peak wavelength of that polynomial. We repeat this process 1000 times, where each time we randomize the spectrum based on the observed errors. We show example polynomial fits in Figure 5.5. The reported peak is the median peak of the polynomial and the error is the standard deviation of the polynomial peaks. This method of finding the line centroid is approximate: the centroid is not well defined for the unusual profiles observed here. We then measure the upper and lower FWHM as the distance to the pixels on either side of the peak at which the flux levels drop below half of the peak flux. The results are reported in Table 5.3.

## Results

In this section, we briefly summarize the results from our emission line analysis. We also perform some basic analysis to constrain the parameters of the emitting region, which uses simple approximations for the emission line parameters. While we do not expect the results of this analysis to be exact, we use them to gain a rough understanding of the physical conditions in the emitting region. We adopt critical densities and other atomic data from (304).

We first consider the recombination lines: the Balmer and Helium emission. Both  $H\alpha$  and  $H\beta$  are detected from VT J1008 and VT J2012 in all observations. The  $H\alpha$  lines from both objects have luminosities of  $\sim 10^{40}$  erg  $s^{-1}$  and they are brightening

with time. The  $H\beta$  lines are fainter, at  $\sim 10^{39}$  erg  $s^{-1}$  and are (insignificantly) fading for VT J2012 and brightening for VT J1008. We will discuss the line profiles in more detail later in this section, but note here that the Balmer lines from both objects have widths  $\sim 1000$  km  $s^{-1}$ .

He II  $\lambda 4685$ , and He I  $\lambda 5875$  lines are strongly detected from VT J1008, and all have luminosities  $\sim 10^{39}$  erg  $s^{-1}$  and FWHM  $\sim 700$  km  $s^{-1}$ . The lines are brightening with time. The He II line is faintly detected from VT J2012 at a similar width and with a redshift consistent with that of the Balmer emission, although such a component is not detected in the second observation epoch. He I lines are not detected from VT J2012.

Let us assume that these luminosities are entirely produced by recombination in a spherical region, with a density sufficiently low that case B recombination is valid. We will use the analysis, along with a consideration of the Balmer decrement later in this section, to argue that we are in a high density regime where case B recombination cannot be considered. We will also discuss a wider range of models in Section 5.5. With the case B assumption, we can approximately estimate the mass and volume of the recombining material, following the methodology described in Chapter 13 of (416). The ionized mass  $M_{\text{ion}}$  is given by

$$M_{\text{ion}} = \frac{1.4L_{H\alpha}m_p}{1.15n_p\alpha_{H\alpha}h\nu_{H\alpha}}, \quad (5.1)$$

where we have assumed a pure Hydrogen and Helium gas where the Helium density is a tenth of the Hydrogen density and the Helium is equally divided between its two ionization states. The proton density is denoted  $n_p$  and is related to the electron density as  $n_e = 1.15n_p$  and the proton mass is  $m_p$ . Assuming the  $H\alpha$  luminosity is  $L_{H\alpha} = 10^{40}$  erg  $s^{-1}$  and the recombination coefficient  $\alpha_{H\alpha} \sim 10^{-14}$   $\text{cm}^3$   $s^{-1}$ , appropriate for case B recombination, we find an ionized gas mass  $M_{\text{ion}} \sim 3000 M_{\odot} (10^4 \text{ cm}^{-3}/n_p) \sim 0.3 M_{\odot} (10^9 \text{ cm}^{-3}/n_p)$ . These mass constraints corresponds to radii  $R = (\frac{3M}{4\pi m_p n_p})^{1/3} \sim 10^{18} \text{ cm} (10^4 \text{ cm}^{-3}/n_p)^{2/3} \sim 10^{15} \text{ cm} (10^9 \text{ cm}^{-3}/n_p)^{2/3}$ , assuming a filling factor  $\sim 1$ . Based on the observed variation in the line luminosities and profiles on timescales  $\lesssim 60$  days, we expect that the emitting region has a size  $\lesssim 60 \text{ days} \times c \approx 10^{17}$  cm, implying  $n_p \gtrsim 10^5 \text{ cm}^{-3}$ . As we will discuss in detail later, if this gas is stellar debris from a TDE with a  $\sim 1 M_{\odot}$  star, we require a high density  $n_p \gtrsim 10^9 \text{ cm}^{-3}$  in order that the ionized gas mass be smaller than the stellar mass. Even with that requirement, a large fraction of the stellar debris must be contained in this dense emitting region. A density  $n_p \gtrsim 10^9 \text{ cm}^{-3}$

corresponds to an emitting radius  $\lesssim 10^{15}$  cm, as derived in our radius calculation above. We see that, if the gas mass is to be a fraction of a solar mass, the densities must be high (and, in fact, so high that case B recombination is no longer valid). If the gas is not stellar debris, it could be from the galaxy circumnuclear medium, in which case lower densities are possible.

We can further constrain the physical parameters of the Balmer emitting region using the Balmer decrement. These observed luminosities imply that the Balmer decrements from both transients are remarkably high and are increasing: that of VT J1008 is  $\sim 9$  during the both epochs and that of VT J2012 is 14.5 in the first epoch and 25 in the second epoch. Typical Balmer decrements from unextincted, low density, photoionized gas are  $\sim 3$ . If we assume the Balmer emission is produced by recombination in a low density gas (e.g.,  $n \approx 10^{2-4}$  cm $^{-3}$ ), the high Balmer decrement implies strong extinction. Assuming photoionized gas with  $T = 10^4$  K and a low density  $n \approx 10^2$  cm $^{-3}$ , the color excess is related to the Balmer decrement as

$$E(B - V) = 1.97 \log \left[ \frac{H\alpha/H\beta}{2.86} \right]. \quad (5.2)$$

For VT J1008 (VT J2012), this implies  $E(B - V) \approx 1(1.5)$  mag.

Adopting high extinction with a densities  $\lesssim 10^5$  cm $^{-3}$  would lead to a larger ionized gas mass than computed above ( $\gtrsim 3000 M_{\odot}$ ). While we cannot rule out a very large amount of diffuse, ionized gas surrounding the black holes of both sources, if we instead assume a high density, we can reduce the ionized gas mass (as described above) and increase the Balmer decrement without requiring large extinction. High densities and radiative transfer effects can increase the Balmer decrement, although considering the latter is beyond the scope of this work. In AGN broad line regions, which have densities  $\gtrsim 10^9$  cm $^{-3}$  the decrement is often observed to reach values  $\sim 6$ .

In the case of VT J1008, the detection of coronal lines provides additional evidence of dense gas. Coronal lines are emission lines with extremely high ionization potentials  $> 100$  eV, and they are most often observed from AGN. However, coronal lines from AGN always have [Fe X] $\lambda 6375$  to [O III] $\lambda 5007$  ratios  $\ll 1$  (14). We observe a ratio  $> 2$ , which is unprecedented for AGN. This high ratio places VT J1008 in the class of extreme coronal line emitters, which we will discuss in the next section. Here, we use the detection of [Fe X] to constrain the physical parameters of the emitting region. Because the width of the [Fe X] line is similar to the Balmer widths, within a factor of a few, we expect that they are coming from  $\sim$ the same distance from the

central SMBH, so it is plausible that the conditions of the coronal line emitting gas are similar to those of the Balmer emitting gas. We can constrain the density of the coronal line emitting gas using the lack of an [Fe VII] detection. Generally, the [Fe X] coronal line is accompanied by the detection of [Fe VII] transitions, which have a lower ionization potential, and so would be expected to be stronger. One way to suppress [Fe VII] is to invoke high density gas: the [Fe VII] critical density is  $\sim 10^7 \text{ cm}^{-3}$ , whereas the [Fe X] critical density is  $\sim 10^{10} \text{ cm}^{-3}$ . Alternatively, the [Fe VII] could be suppressed if the ionizing SED is peaked above 250 eV, although we disfavor this possibility given the detection of low ionization potential lines like  $H\alpha$  and He II with similar FWHM. Thus, the detection of [Fe X] without [Fe VII] suggests that there is high density gas in the intermediate-line emitting region. Since we now are confident that there is  $\gtrsim 10^7 \text{ cm}^{-3}$  gas in the vicinity of the Balmer line emitting region, given the similar line widths of the Balmer and coronal lines, it is plausible that the Balmer emitting region is similarly dense.

A high density would also explain the lack of intermediate width Oxygen lines. We detect neither intermediate width [O II] nor [O III] lines from VT J1008. Given that the ionizing source is such that we observe both Balmer and [Fe X] lines, we would expect Oxygen lines to be detectable, given the intermediate ionization potentials of these transitions. The [O III] line has a critical density  $\sim 10^7 \text{ cm}^{-3}$ ; thus, high densities would explain the lack of a detection.

Coronal lines are not detected from VT J2012, which could be caused by a lack of high density gas or a lack of ionizing photons. We favor the latter, although deep, soft X-ray observations would be required to confirm it. The similarity of observed lines to broad line regions in AGN supports the hypothesis of a high density emitting region. AGN broad line regions show Balmer emission but no [O III] emission due to the critical density  $\sim 10^7 \text{ cm}^{-3}$ . AGN narrow line regions, on the other hand, have strong [O III] emission due to lower densities, with typical [O III]- $H\beta$  ratios  $\sim 1$ . We do not detect intermediate width [O III], however, which favors a density  $\gtrsim 10^7 \text{ cm}^{-3}$ . It is possible that the lack of detection could also be explained by an ionizing continuum that lacks [O III] ionizing photons, but TDEs ubiquitously produce strong UV-continua, so we disfavor this possibility. If another VT J2012-like source is discovered (i.e., a TDE with intermediate width Balmer but lacking coronal lines), deep soft X-ray constraints would be definitively determine if insufficient X-ray luminosity is causing the lack of coronal lines.

Based on the previous arguments, we consider it very likely that the intermediate

line emitting regions from both sources have densities  $\gtrsim 10^7 \text{ cm}^{-3}$ .

We can further constrain the conditions of the line emitting region using the line profiles. We primarily consider the Balmer line profiles, because these lines are among the brightest. The Balmer line profiles from both objects are asymmetric. The Balmer emission from VT J1008 shows a slightly redshifted peak a long blue tail. VT J2012 shows similarly asymmetric  $H\alpha$  emission. The observed  $H\beta$  emission is narrower and more symmetric, although  $H\beta$  is quite faint from VT J2012, so it is possible that the signal-to-noise is affecting our result. In contrast to the Balmer lines from VT J1008, those from VT J2012 are redshifted by  $\sim 700 \text{ km s}^{-1}$ , with no significant evolution in line centroid between epochs.

From the later-time, high resolution spectra, we see that the line profile for VT J1008 shows a broad, flat top, with a long blue tail. In the  $\sim 120$  days between ESI observations, the line profile became slightly more peaked towards the red side. Note that the apparent brightening may not be real — the flux is continuum-normalized, but the continuum level is expected to be different in the two observations because the slit orientations were different. In contrast to that of VT J1008, the line profile for VT J2012 is peaked and symmetric.

Based on these line profiles, the emitting region must be aspherical and, in the case of VT J2012, flowing away from the observer.

In summary, VT J1008 and VT J2012 show transient, intermediate width ( $\sim 700 - 1000 \text{ km s}^{-1}$ ) Balmer emission. VT J1008 additionally shows He II, He I, and [Fe X] emission. VT J2012 has weak He II and He I emission. Based on the observed luminosities and line profiles, we consider it likely that the emission is arising from a dense ( $\gtrsim 10^7 \text{ cm}^{-3}$ ), compact ( $\lesssim 10^{16} \text{ cm}$ ), aspherical, outflowing emitting region.

### **Comparison to published TDE observations**

In the rest of this section, we compare the observed emission lines to observations of published transients. We first compare these objects to TDEs. In the next section, we discuss coronal-line emitting transients, some of which are TDEs and some of which are of ambiguous origin. Then, we compare to non-TDE transients. In this section, because we aim to compare to previous TDEs, we will focus on those lines that have been studied in published TDEs; namely, we focus on the Hydrogen and Helium lines.

We begin by discussing the Hydrogen and Helium lines. Optically-detected TDEs are well-established to produce these transient spectral features (13, 409, 417). These

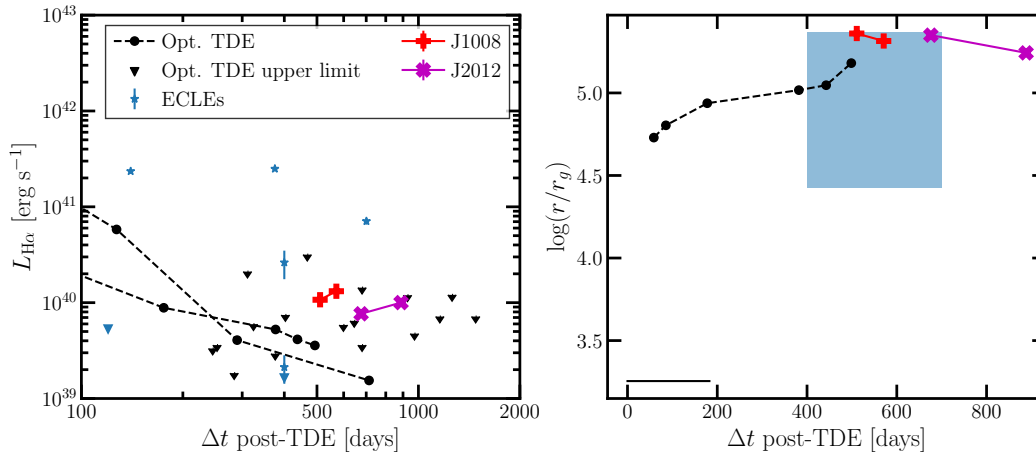


Figure 5.6: Comparison of the H $\alpha$  emission line from VT J1008 and VT J2012 to optically-selected TDEs ((3, 13), E. Hammerstein, private communication) and ECLEs (14). In the *left* panel, we show H $\alpha$  luminosity lightcurves for VT J1008 (red crosses), VT J2012 (magenta X's), ECLEs (blue stars), and optically-selected TDEs (black circles). The H $\alpha$  luminosities of VT J1008 and VT J2012 are much brighter at late times than those of optically-selected TDEs. They are more comparable to the ECLEs. In the *right* panel, we show the distance of the emitting region from the central SMBH,  $r$ , implied from the H $\alpha$  width. The radio-selected TDEs are at larger radii than almost every TDE and ECLE.

TDEs can be divided into four classes based on their early time ( $\lesssim 6$  month post-optical flare): (1) Hydrogen rich TDEs, which should broad  $\sim 10^4$  km s $^{-1}$  Balmer features; (2) Hydrogen and Helium TDEs, which show  $\sim 10^4$  km s $^{-1}$  Balmer features and a complex of emission lines near He II  $\lambda 4686$ , typically including N III  $\lambda 4640$  and N III  $\lambda 4100$ ; (3) Helium TDEs, which show only a broad ( $\sim 10^4$  km s $^{-1}$ ) He II  $\lambda 4686$  line; and (4) featureless TDEs, which show no transient spectral features and have brighter optical flares and, typically, higher redshift host galaxies relative to those of the former three TDE classes (13, 128).

Our events would appear to most closely resemble the Hydrogen and Helium TDEs based on the detection of both Balmer and He II lines. However, there are many differences between our observed lines and those observed from Hydrogen and Helium TDEs. First, we do not observe N III lines. The N III lines are expected to be produced by the Bowen fluorescence mechanism, which only operates under specific physical conditions (147). It is feasible that, at late times, it is not able to operate.

Our observed lines also differ from typical TDEs because of their high luminosities

and narrow widths. These are highlighted in Figure 5.6. The left panel of this figure shows the evolution of H $\alpha$  width and luminosity for a sample of optically-selected TDEs (3, 13). The luminosities of our lines are both  $\gtrsim 10^{40}$  erg s $^{-1}$ , and are brightening with time  $\sim 2$  years post-TDE. Very few other optically-detected TDEs have detectable H $\alpha$  at such late times: most of the available  $3\sigma$  upper limits are at or below the luminosity detected from our events. The TDEs ASASSN 14li and ASASSN 14ae both have H $\alpha$  detections  $\gtrsim 500$  days post-TDE (3), but the observed luminosities are at least a factor of a few fainter than those from our TDEs, and they both show declining H $\alpha$  luminosities whereas our events are brightening.

The right panel of Figure 5.6 shows the gravitational radius in units of Schwarzschild radii  $r_g$  of the H $\alpha$  emitting region for our TDEs, ASASSN-14li, and the typical early-time optically-selected TDE. We calculate this radius from the FWHM of the lines  $v$  as  $r/r_g = 2(v/c)^2$ . For the typical early-time optically-selected TDE, we assume  $v \sim 10^4$  km s $^{-1}$ . The H $\alpha$  lines from our TDE are much broader than those from ASASSN 14li and those from early-time observations of optically-selected TDEs. Our TDEs have  $\log r/r_g \sim 5.5$ , and the radius is decreasing. The typical optically-selected TDE has  $\log r/r_g \sim 3$ . ASASSN 14li has  $\log r/r_g \sim 5$  at  $\sim 500$  days post-TDE, although the radius is increasing and it is possible it evolved to match our events after the last observations.

In summary, the lines from our TDEs most closely match those from the Hydrogen+Helium TDE class. However, they are significantly brighter and narrower than any previously observed TDE.

### **Comparison to coronal-line emitting transients**

There have been a few bona-fide TDEs and a growing sample of ambiguous transients with strong coronal line emission, like that observed from VT J1008. These objects are typically referred to as the extreme coronal line emitters (ECLEs). The first known ECLE, SDSS J0952+2143, was discovered by (114, 271) in a search for galaxies in SDSS with evolving spectral features. This source was associated with X-ray, optical, IR, and UV flares. There is no radio detection reported, although extensive radio follow-up was not performed. The source showed many transient emission lines, including bright coronal, He II and Balmer features. The coronal lines and He II lines are broad, with FWHM  $\sim 800$  km s $^{-1}$ . The Balmer lines were decomposed into multiple components: a narrow component consistent with the host galaxy dispersion and redshift, a redshifted broad component, and two

unresolved horns on either side of the rest-frame component. The redshifted, broad  $H\alpha$  component had a velocity offset of  $\sim 560 \text{ km s}^{-1}$ , a  $\text{FWHM} \sim 1930 \text{ km s}^{-1}$ , and a luminosity  $\sim 10^{41} \text{ erg s}^{-1}$ . The redshifted, broad  $H\beta$  component had similar parameters, but with a luminosity implying a Balmer decrement  $\sim 9$ . Both Balmer lines were first detected  $\sim 1$  year after the associated optical flare and remained bright  $\sim 3$ -post optical flare, although they faded in that time.

The cause of this transient emission is unknown. The event could be a TDE, but it is also consistent with a supernova with extreme coronal line emission. AGN-like emission lines are detected from the host galaxy, so the emission could also be associated with a flaring AGN. If the source is caused by a TDE, (114) argues that the broad lines are likely produced by photoionized stellar debris that has become unbound and forms eccentric streams surrounding the SMBH. They argue that the unresolved, narrow horns are produced by shocks in a neutral medium, but (418) shows that such a mechanism would require an unreasonable Hydrogen density.

The emission lines from SDSS J0952+2143 are remarkably similar to those observed from VT J1008 and VT J2012 (although VT J2012 does not show the coronal lines), although we do not detect narrow emission at the location of the Balmer lines and the Oxygen lines detected from our sources are much fainter than those from SDSS J0952+2143. We also do not detect multiwavelength flares analogous to those from SDSS J0952+2143. However, it is plausible that some of the differences between our sources and SDSS J0952+2143 could be reconciled by invoking a TDE in a galaxy with pre-existing accretion disk and/or a different line-of-sight.

After the discovery of SDSS J0952+2143, (14) performed a search for transient coronal-line emitting galaxies in SDSS. They identified a sample of seven non-active galaxies with strong coronal line emission. The host galaxies all had narrow line emission, with six qualifying as BPT H II galaxies and one bordering the LINER and H II regions. Four of the objects showed  $\geq 3\sigma$  variations in their optical continua in the  $\sim$ months–years before the spectroscopic observations, measured by comparing their SDSS spectral and fiber magnitudes. In five of the seven sources, intermediate width emission lines are detected with  $\text{FWHM} \sim 880\text{--}2600 \text{ km s}^{-1}$ . The lines were fading in all objects. Broad He II  $\lambda 4686$  is detected in three objects.

We overlay the luminosities and widths of the  $H\alpha$  from these ECLEs on the panels in Figure 5.6. Note that the time since optical flare is very uncertain for these events. We adopted the time between the SDSS spectroscopic and photometric observations for those objects with detected optical flares, and 400 days for those

objects without detected optical flares. The broad emission from these events much more closely resembles that from VT J1008 and VT J2012. The primary differences between these ECLEs and our events come from their host galaxies: the (14) ECLEs and SDSS J0852+2143 show strong nebular emission, whereas our events are in quiescent galaxies. Recent work, however, has suggested that, when considering the full ECLE population, they do tend to have TDE-like host galaxies; i.e., host galaxies that more closely resemble those of VT J1008 and VT J2012.

There is growing evidence that ECLEs are definitive TDEs, primarily based on arguments about the required ionizing flux, the optical light curve shapes for those few events with well-sampled light curves, and the similarities of TDE and ECLE host galaxies (412). However, most of the known ECLEs are in galaxies with nebular emission lines from the host galaxies, rendering this conclusion uncertain: it is impossible to exclude an AGN origin for these events. We still lack a large sample of bona-fide TDEs with coronal line detections. It is, then, intriguing how closely the multiwavelength, transient properties of ECLEs resemble VT J1008 and VTJ2012, both of which have quiescent hosts, well-sampled optical light curves, and other multiwavelength data that allow us to argue that they are in fact bona-fide TDEs (see Section 5.5).

### **Comparison to ambiguous and non-TDE transients**

In addition to TDEs and ECLEs, other transients can produce lines similar to those observed here. In particular, our objects resemble some supernovae. In particular, type IIn supernovae have been detected with similar line profiles. For example, SN2012ab is an optically-flaring Type IIn supernovae hosted near the nucleus a spiral galaxy that was discovered by (419). SN2012ab is associated with an intermediate width H $\alpha$  component of width  $\sim 4500 \text{ km s}^{-1}$  that is redshifted by  $\sim 800 \text{ km s}^{-1}$ . The intermediate width component was first detected  $\sim 7$  days after the optical flare, alongside a broad H $\alpha$  component with FWHM  $\sim 20000 \text{ km s}^{-1}$ . The intermediate width component is still detected  $\sim 1200$  days post-event. The late-time spectrum is not of sufficiently high signal-to-noise to constrain the presence of a late-time broad component. (419) argues that SN2012ab is a type IIn supernova based on the observed spectral features and the optical light curve. The unusual H $\alpha$  emission is caused by interaction with an aspherical circumstellar material. They note that they cannot rule out a TDE origin; however, if the event is a TDE, it would be highly unusual because of the asymmetric material needed to produce the observed emission lines.

Based on the emission lines produced by VT J1008 and VT J2012, we see similar evidence for asphericities as observed for SN 2012ab. In contrast to SN 2012ab, VT J1008 and VT J2012 are hosted by quiescent galaxies. Moreover, no broad H $\alpha$  component is detected from our events, although our spectra were taken  $> 500$  days post-optical flare, and it is possible that a broad component was present at early times.

### Summary

VT J1008 and VT J2012 are associated with Balmer, Helium, and (for VT J1008) coronal line emission. The line widths are  $\sim 1000 \text{ km s}^{-1}$ , which is much narrower than typical lines detected from optically-selected TDEs. Based on the line parameters, we suggested that the emission comes from a dense  $\gtrsim 10^7 \text{ cm}^{-3}$  region. The mass of the ionized, recombination line-emitting gas is likely  $\gtrsim 0.03 - 0.3 M_{\odot}$ ; i.e., the mass is a large fraction of a solar mass. These emission lines do not resemble those detected from the optically-selected TDE sample. Instead, the observed emission lines most closely resemble those observed from the ambiguous class of ECLEs, which have been proposed, though not confirmed, to be TDEs.

## 5.5 Discussion

### Summary

- VT J1008 and VT J2012 are radio-selected transients in the nuclei quiescent, green valley host galaxies. The host galaxies have SMBHs with masses  $M_{\text{BH}} \sim 10^{5-6} M_{\odot}$ .
- VT J1008 and VT J2012 have optical counterparts, with lightcurves typical of optically-selected TDEs except that they are slightly fainter and cooler at peak. They do not have detectable X-ray or IR counterparts.
- VT J1008 and VT J2012 have radio counterparts with GHz luminosities  $\sim 10^{38} \text{ erg s}^{-1}$  that have SEDs consistent with wide-angle, low velocity  $\beta \lesssim 0.1$  outflows at radii  $\sim 0.1 \text{ pc}$ .
- VT J1008 and VT J2012 both have transient, intermediate-width Balmer and He II emission detected  $\sim 2$  years post-TDE. Their H $\alpha$  luminosities are  $\sim 10^{40} \text{ erg s}^{-1}$  and are likely increasing. All the lines have FWHM  $\sim 700 - 1000 \text{ km s}^{-1}$ , and may be broadening slightly with time. VT J1008 also has strong He I and [Fe X] emission with similar line widths.

- The observed transient lines detected from these radio-selected events are reminiscent of Hydrogen+Helium TDEs. However, the lines are much more luminous at late-times than other optically-detected TDEs, and they are narrower than is typically observed from optically-selected TDEs.
- Instead, the observed spectral features more closely resemble the emission lines associated with some extreme coronal line emitters. A subset of these objects are known to have intermediate width lines, in some cases with centroids that are redshifted relative to the host (e.g., J0952+2143).

### **Are VT J1008 and VT J2012 tidal disruption events?**

Before delving into the origin of the transient emission lines, we briefly consider and rule out the possibility that VT J1008 and VT J2012 are not tidal disruption events. The three most likely origins for these events are: stellar explosions, active galactic nuclei flares, or TDEs. In the following, we consider each of these possibilities. We assume both events are caused by the same type of event, which is justified given the strong similarities in their multiwavelength properties and host galaxies.

#### **Stellar explosions.**

We first consider the possibility that these events are stellar explosions. Supernovae can produce radio-loud events with optical flares and transient optical spectral lines. However, the only type of supernovae that has been observed to produce radio outflows with velocities  $\sim 0.1c$ , as observed for our events, are SN Ic-BL, so we only consider this type of event to be possible. There are a number of factors that make VT J1008 and VT J2012 unusual for SNe Ic-BLs. First, these events are in the nuclei of their host galaxies: their offsets in units of the host half-light radii are consistent with zero. SNe Ic-BLs tend to lie in the outskirts of their host galaxies, with a median offset relative to host half-light radius of  $0.7 \pm 0.2$  (420). Second, our events are hosted by non-star forming galaxies, whereas SNe Ic-BL hosts tend to be star-forming (0.3% of core-collapse supernovae hosts are quiescent).

The observed optical light curve is very unusual for SN Ic-BL: these SN often, though not always, show rapid post-peak cooling, which is not present for our events (421). While the late time spectra of SN Ic-BL are not well constrained, intermediate width features such as we see are unprecedented (S. Anand, private communication).

While we cannot definitively rule out a SN Ic-BL origin, there are many factors that would make our events extremely unusual. Hence, we do not believe our events are

associated with stellar explosions.

### **Active galactic nuclei flares.**

We next consider active galactic nuclei flares. AGN can produce variability and flaring across the electromagnetic timescale and over a wide range of timescales. The main evidence against an AGN origin for VT J1008 and VT J2012 is the lack of any evidence that there was active accretion prior to the optical flare. The optical spectra do not show any evidence for strong AGN emission. It is possible that the weak [O III] detections are caused with an AGN, but it would imply a very weak AGN. Moreover, that line could also be caused by weak star formation. The IR colors of the host galaxy also show no evidence for AGN activity; likewise, the lack of an X-ray detection and the lack of optical variability support the hypothesis that these are quiescent galaxies.

From the above evidence, we disfavor an AGN origin. Of course, none of these arguments completely rule out the possibility of a very weak, flaring AGN. In this case, some trigger has caused a large amount of mass to be dumped on the central SMBH. Such events are extremely poorly understood: it is not clear whether such events could even happen without a discrete object like a star venturing near the SMBH. However, given the broad consistency of our events with TDEs and the large complications associated with interpreting low luminosity AGN flares, we do not consider this possibility further.

### **Tidal disruption event.**

After ruling out AGN flares and stellar explosions, we are left with TDEs. As we have discussed in this work and in Paper I, the host galaxy, optical lightcurves, and radio emission of VT J1008 and VT J2012 are broadly consistent with optically-selected TDEs. Henceforth, we consider these events to be definitive TDEs.

### **The origin of the transient spectral features**

In the rest of this paper, we discuss the origin of the transient spectral features. We make the strong but necessary assumptions that (1) the ionization source producing the Balmer emission is the same that produces the higher ionization lines and (2) the same emission mechanism is active in both VT J1008 and VT J2012.

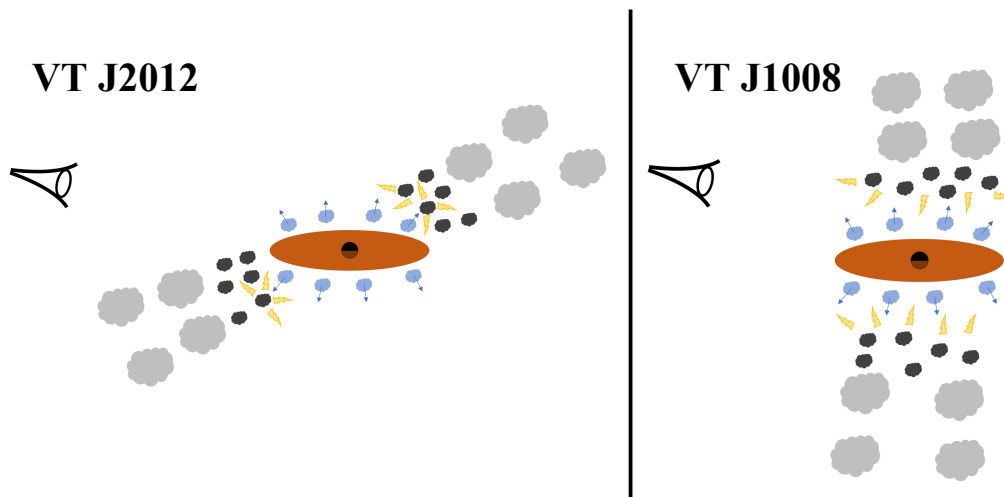


Figure 5.7: An example cartoon geometry that could produce either redshifted emission without a blueshifted counterpart, or non-shifted emission. We invoke a dusty torus that is misaligned from the TDE-produced accretion disk. The blue clouds represent accretion disk winds, the black clouds represent dense gas in the torus, and the grey clouds represent less dense gas at larger distances. When the disk winds slam into the dense torus, radiative shocks are produced. The radio emission, which is not shown here, could also be produced by a subset of these disk winds that travel fast and shock against the more extended material at  $\sim 0.1$  pc. The resulting free-free emission photoionizes gas in the vicinity, including outflow gas launched from the disk, producing the observed emission lines. In the *left* panel, the blueshifted component is obscured from the observer by the dusty torus. In the *right* panel, no redshifted or blueshifted components are produced.

### Are the lines associated with a shock?

In both VT J1008 and VT J2012, we know that fast outflows exist given the observed radio emission. It is not a far stretch to imagine that the transient emission lines are also associated with a shocking outflow. Shocks can produce emission lines in multiple ways, depending on the shock velocity and medium density. If the shocked gas can cool efficiently, it will produce strong free-free emission that can photoionize the surrounding medium. Otherwise, the shock is “nonradiative” and primarily emits through collisional ionization.

We can determine if a shock is radiative by comparing the age to the cooling time. To compute the cooling time, we need to know the density  $n$  and the shock velocity  $v_s$ . From the shock velocity, we first must compute the shock temperature  $T_s$ :

$$T_s = \frac{2(\gamma - 1)}{(\gamma + 1)^2} \frac{m_p}{k_B} v_s^2 = 2.2 \times 10^7 \text{ K} \left( \frac{v_s}{10^3 \text{ km s}^{-1}} \right)^2, \quad (5.3)$$

where  $\gamma$  is the adiabatic index and we adopt  $\gamma = 5/3$ . We consider shock velocities in the range  $\sim 500 - 10^4 \text{ km s}^{-1}$ , which approximately match the observed line widths. Slow shocks  $v_s \lesssim 100 \text{ km s}^{-1}$  do not produce  $\sim 1000 \text{ km s}^{-1}$  emission lines.

Then, we must compute the cooling rate  $\Lambda(T)$ , which, following (306), we approximate as

$$\frac{\Lambda(T)}{\text{erg cm}^3 \text{ s}^{-1}} = \begin{cases} 2.3 \times 10^{-24} \left(\frac{T_s}{10^6 \text{ K}}\right)^{0.5}, & T_s > 10^{7.3} \text{ K} \\ 1.1 \times 10^{-22} \left(\frac{T_s}{10^6 \text{ K}}\right)^{-0.7}, & 10^5 \text{ K} < T_s \leq 10^{7.3} \text{ K}. \end{cases} \quad (5.4)$$

At high densities, such as those we will consider, the cooling rate can be suppressed because collisional de-excitation reduces cooling through heavy elements. However, at the high temperatures we are consider  $\gtrsim 10^7 \text{ K}$ , cooling through heavy elements in subdominant and this suppression is minimal (422), so we do not consider it further.

With these definitions, the cooling time is given by

$$\begin{aligned} t_{\text{cool}} &= \frac{3k_B T_s}{n\Lambda(T)} \\ &= 1.3 \text{ years} \left(\frac{T_s}{10^7 \text{ K}}\right) \left(\frac{n}{10^6 \text{ cm}^{-3}}\right)^{-1} \left(\frac{\Lambda(T)}{10^{-22} \text{ erg cm}^3 \text{ s}^{-1}}\right)^{-1}. \end{aligned} \quad (5.5)$$

If the shock has  $t_{\text{age}} \approx 1 \text{ year}$ , then the shock is non-radiative if the density  $n \lesssim 10^7 \text{ cm}^{-3}$  and  $v_s \sim 10^3 \text{ km s}^{-1}$ , or if the shock is near-relativistic and has  $10^7 \lesssim n/\text{cm}^{-3} \lesssim 10^8$ .

With these constraints on the parameter space, we now explore possible emission mechanisms for both radiative and non-radiative shocks. First, we consider a non-radiative shock. In this case, we know that the density is relatively low ( $n \lesssim 10^7 \text{ cm}^{-3}$ ) if the shock is non-relativistic. One possible emission mechanism comes from an analogy to type II supernova, which produce similar velocity shocks but in such low density material ( $n \sim 0.1 - 10 \text{ cm}^{-3}$ ). In these events, Balmer emission resembling that which we observe is produce from Balmer dominated shocks, which occur when the pre-shock material is partly neutral. In this case, we can approximate the mass of  $\text{H}\alpha$  emitting atoms as

$$\begin{aligned} M_{\text{H}\alpha} &= \frac{L_{\text{H}\alpha} t_{\text{H}\alpha} m_{\text{H}}}{E_{\text{H}\alpha} \epsilon_{\text{H}\alpha}} \\ &= 438 M_{\odot} \frac{L_{\text{H}\alpha}}{10^{40} \text{ erg s}^{-1}} \frac{t_{\text{H}\alpha}}{1 \text{ year}}. \end{aligned} \quad (5.6)$$

Here,  $L_{H\alpha}$  is the average  $H\alpha$  luminosity and  $t_{H\alpha}$  is the duration of the  $H\alpha$  emission. We adopted fiducial values  $L_{H\alpha} \sim 10^{39}$  erg s $^{-1}$  and  $t_{H\alpha} \sim 1$  year, which are likely correct to within an order of magnitude.  $m_H$  is the mass of a neutral Hydrogen atom,  $E_{H\alpha} \sim 2$  eV is the energy of an  $H\alpha$  photon, and  $\epsilon_{H\alpha} \sim 0.2$  is the fraction of excited Hydrogen atom that undergo the  $H\alpha$  transition. If the density of the emitting region is  $\lesssim 10^8$  cm $^{-3}$ , then the size of the emitting region must be  $\gtrsim 0.03$  pc. Assuming a source age of  $\sim 3$  years, the outflow that produced the Balmer dominated shocks must have a velocity  $v \gtrsim 10^5$  km s $^{-1}$ . This value is inconsistent with the width of the observed lines, which is expected to correspond to roughly the velocity of the shock for Balmer dominated shocks. Because of this inconsistency, we do not consider a Balmer dominated shock a feasible cause of the observed emission. However, most modelling of Balmer dominated shocks, on which we base our discussion, assumes low densities applicable to supernova remnants. It is possible that similar shocks in high density environments could have different properties, in which case something similar to a Balmer dominated shock could produce the observed emission. Further exploration of this is beyond the scope of this work.

We now move to the possibility of a radiative shock. In this case, the shock has caused surrounding gas to heat up to  $\sim 10^7$  K as described earlier, which is cooling quickly via free-free emission. This emission ionizes the surrounding gas, which is likely at a similar density to the shocked, cooling gas ( $n \gtrsim 10^8$  cm $^{-3}$ ). From Equation 5.4, the cooling rate for gas at a temperature  $\gtrsim 2 \times 10^7$  K is  $\Gamma(T) \gtrsim 10^{-23}$  erg cm $^3$  s $^{-1}$ . Assuming  $n_e \gtrsim 10^7$  cm $^{-3}$  in a region of radius  $r \sim 0.01$  pc, we have a total luminosity of  $\gtrsim 10^{41}$  erg s $^{-1}$ . Most of these photons will be Hydrogen- and Helium-ionizing given the high temperature of the free-free emitting region.

In typical models of the emission lines produced by radiative shocks, Oxygen lines (e.g., (423)) are produced. In this case, we would not expect to see Oxygen lines given the high density of the material and the low critical densities of the typical lines. Instead, we would only expect to see recombination lines, such as the observed Balmer and Helium emission, and lines with very high critical densities, such as [Fe X]. The detailed modelling required to constrain this possibility quantitatively is beyond the scope of this paper, but from this qualitative discussion we believe it feasible that the observed emission could be produced by a radiative shock.

Now that we have established that the observed lines could be produced by a radiative shock, we must consider the centroid offsets from the host redshifts. Discussion of the line profiles is beyond the scope of this work. The intermediate width lines

from VT J2012 are redshifted relative to the host galaxy, whereas the lines from VT J1008 are near the host redshift. There are two possible explanations for the line offsets: (1) the SMBH that produces VT J2012 is moving or (2) the emitting gas is outflowing. We are pursuing follow-up to constrain (1) and will consider it in a future paper; here, we consider (2). While it is possible that we do not detect a blueshifted event by chance, with a shock model it is feasible to produce a geometry where only redshifted velocities are possible.

In Figure 5.7, we show a cartoon of one model that can produce the observed lines (not to scale). First, we suppose that the TDE has produced an accretion disk that is producing disk winds (see 71, for possible disk wind launch models). These winds are outflowing, and collide with the CNM of the galaxy to produce the radiative shocks. A fast component of these winds colliding with material at  $\sim 0.1$  pc could explain the radio observations. While the structure of the CNM is poorly constrained, it is feasible that it is in a torus (or some extended, axisymmetric) structure, as is known to exist in AGN host galaxies. There is no a priori reason that this axisymmetric dust structure need be aligned with the TDE accretion disk: if the torus orientation is set by the SMBH spin direction, while the disk orientation is related to the orbit of the disrupted star, it will be independent of the torus orientation (424). Lense-Thirring precession can bring the TDE disk orientation into alignment with the black hole spin, but this process is very slow for moderate to low spins (424). In Figure 5.7, we show two possible orientations. In the left panel, the torus is inclined relative to the disk, and in the right panel, the disk and torus orientation are perpendicular to each other. In the left panel, the disk wind clouds will tend to collide with the edge of the dusty structure. The clouds that are outflowing away from the observer (redshifted) will be visible, but those flowing towards the observer (blueshifted) are seen through a large column of dust. In the right panel, all of the clouds are visible, but no blueshift or redshift is expected. A prediction of this model is that disk emission should be detectable, at least at late-times when any reprocessing wind is gone. Such emission is expected in the ultraviolet and X-ray (400) While this is a cartoon model, and it is unclear whether this dust structure is expected, it could reproduce the observed geometry.

One potential issue with invoking a gas-rich environment is the lack of a mid-infrared flare, which have been detected for many previous coronal line emitters (411, 412). The early-time, ultraviolet emission is expected to be luminous enough to heat surrounding dust and produce thermal emission. Our preferred explanation

is that the WISE limits are too weak. The upper limit for both events is near  $L_{\text{IR}} \lesssim 5 \times 10^{41} \text{ erg s}^{-1}$  (computed as approximately  $\nu L_\nu$  from the W1 upper limit). Dividing by the peak blackbody luminosity measured from the optical, we find a ratio  $\lesssim 5\%$ : this is still much higher than typical covering fractions of optically-selected TDEs, which are  $< 1\%$  (*144*). We then predict that deeper mid-infrared observations of events like VT J2012 and VT J1008 should discover dust echoes, and we encourage such future follow-up of new events.

In summary, a radiative shock model invoking an axisymmetric dusty structure misaligned with the TDE accretion disk could reproduce the observed lines, including their widths and offset from host redshift.

### **Are the lines photoionized by a central source?**

If the lines are not associated with the shock, they are likely photoionized by a central source associated with the accretion induced by the TDE, as is observed at early times. The observed lines would thus be the evolved version of the early time lines observed from optically-selected TDEs. This leads to two questions: (1) can the models that produce the early time TDE emission also explain the late-time emission, and (2) why do we detect these lines in these radio-detected, optically-selected TDEs, when they do not seem to be present in most optically-selected TDEs?

The evolution of early-time TDE transient lines is not well explored, but available observations suggest that they tend to fade within  $\sim 1$  year. Before this work, none had been detected above  $10^{40} \text{ erg s}^{-1}$  at times  $\gtrsim 1$  year post-optical peak. The only strong detection was from the extensively studied radio-emitting TDE ASASSN 14li, which had an  $\text{H}\alpha$  detection  $\sim 1.5$  years post-optical peak at a luminosity  $7 \times 10^{38} \text{ erg s}^{-1}$ .

The origin of these early-time lines is still debated. (*146*) presented a model where the lines originate from an extended, optically thick envelope surrounding the SMBH. The envelope reprocesses soft X-ray photons emitted during the accretion of the stellar debris. A percentage of the reprocessed emission produces an optical continuum, corresponding to the observed optical flares. Hydrogen and helium in the envelope become ionized and produce the observed emission lines, but because the envelope is optically thick, the Balmer lines are suppressed relative to the Helium emission. The resulting line profiles were analyzed by (*146*), who show that an optically-thick envelope will produce  $\sim 10^4 \text{ km s}^{-1}$  emission lines due to electron

scattering, without requiring high velocity dispersion gas. If the optically-thick envelope is outflowing, the line profile will not be Gaussian but instead will have a blueshifted peak with an extended red wing. With time, the emission lines will narrow as the density decreases and electron scattering reduces. The time evolution of the line luminosities relative to the optical continuum level has not been explored in depth.

Narrower lines may be expected at late times, if the (146) model is correct. The line profiles that we observe, however, do not match those predicted by (146). In the case of stationary gas a symmetric line profile is expected whereas outflowing gas would produce a blueshifted peak with a redshifted tail. In the observations of both VT J1008 and VT J2012, we see a redshifted peak with a blueshifted tail. It is possible that altering the geometry of the envelope could produce the observed emission, but the required modelling is beyond the scope of this work.

Another challenging aspect of a model where the lines are produced by photoionization from a central source is the association with radio emission. There is no reason, a-priori, that we would expect the intermediate width lines to preferentially occur in radio-emitting systems if they are produced by photoionization. One possible explanation is that both these lines and radio-emitting shocks are produced by TDEs with slow accretion rate decays, in which case the photoionizing continuum can remain sufficiently strong at late times to produce the observed emission lines. This explanation is subject to significant theoretical uncertainties; in particular, there is no expectation that events with slower accretion rate decays will tend to cause radio-emission. We also have no direct observational evidence that long-lived TDEs tend to produce radio emission. In Paper I, we saw no significant correlation between the decay of the optical light curve and the presence of radio emission. We do not detect any remarkable X-ray emission from these sources.

Alternatively, we can invoke a gas-rich environment to explain both the radio emission and the spectral features. Such an environment has been invoked for coronal line emitters in the past (336). Then, the radio detections are caused by shocks in the gas. While this is plausible, it is unclear why this would produce the unusual line profiles that are observed, nor why the emission would be entirely redshifted in the case of VT J2012. Unlike in the case of shock ionization, there is no clear geometry that could produce the observed redshift, unless the SMBH is recoiling or in a binary, which we will constrain in a future paper. This tension becomes stronger if we include events like J0952+2143, which also shows redshifted inter-

mediate width emission. It seems improbable, though not impossible, both of these are TDEs by recoiling or binary SMBHs. Instead, we require dense, rapidly outflowing, asymmetrically-distributed photoionized gas. The gas could be the outflowing stellar debris, but, as we discussed in Section 5.4, the mass of the ionized gas is a large fraction of a solar mass. Unless these events were caused by the discussion of high mass ( $\gtrsim$  a few solar mass) stars, we require that most of the unbound debris remains in a compact region. This is not expected based on current TDE theory.

In summary, while photoionization from a central source is a feasible model, we prefer a shock ionized model. It is possible that detailed models of the evolution of the transient emission lines from TDEs and the dust geometry and kinematics in the circumnuclear medium could reproduce the observed emission, but we do not currently have strong evidence to favor this model.

## 5.6 Conclusions

We have presented the multiwavelength properties of two radio-selected TDEs. The TDEs were selected from our sample of six radio-selected, optically-detected TDEs from the VLA Sky Survey. They were the only two TDEs in quiescent galaxies, and they showed unusual, intermediate-width Balmer and Helium emission. These events were otherwise fully consistent with optically-selected TDEs. We discussed the origin of the intermediate width emission lines in detail, and argued that they likely originate from a radiative shock. Alternatively, the lines could originate from outflowing, asymmetric, dense gas in the circumnuclear medium that is photoionized by the TDE, but we marginally disfavor this model.

One of the most intriguing findings in this work is that the transient spectral features observed from these two radio-selected TDEs share many characteristics with those from the ambiguous class of coronal line emitting transients, the ECLEs: both VT J1008 and VT J2012 show intermediate width Balmer lines, which have previously only been reported for members of the ECLE class, and VT J1008 shows extreme coronal line emission. This connection provides yet more evidence that ECLEs are caused by TDEs. Moreover, just as early time transient spectral features from TDEs allow the events to be subdivided into classes with different properties, these late-time spectral features may allow for a new TDE classification system: featureless late-time spectra, the extreme coronal line emitters with intermediate width recombination lines, and the extreme coronal line emitters without intermediate width recombination lines. These different classes likely correspond to physically

different events; e.g., events with an abundance of optical coronal line-ionizing soft X-ray photons and those without. Mid-infrared spectroscopy to constrain the relative strength of coronal lines that are ionized by extreme UV photons can help probe the shape of the ionizing spectral energy distribution. In future work, we hope to obtain late-time spectra for a large sample of TDEs, with the aim of further developing classification system and pinning down the physical causes of the late-time emission.

Table 5.3: Emission line fit parameters

Name	MJD	Line Name	$\Delta\nu$	FWHM, upper		FWHM, lower	$f_{\text{line}}$	$L_{\text{line}}$	
			$\text{km s}^{-1}$	$\text{km s}^{-1}$	$\text{km s}^{-1}$	$10^{-16} \text{ erg cm}^{-2} \text{ s}^{-1}$	$10^{39} \text{ erg s}^{-1}$		
VT J1008	59676	[OII] $\lambda\lambda$ 3726, 3728	$99.9 \pm 42.3$	$86.4 \pm 32.9$	–		$0.18 \pm 0.07$	$0.09 \pm 0.03$	
		HeII $\lambda$ 4685	$-18.6 \pm 21.7$	$379.3 \pm 18.3$	–		$3.6 \pm 0.2$	$1.7 \pm 0.1$	
		H $\beta$	$205 \pm 36$	$583 \pm 119$	$1041 \pm 184$		$3.1 \pm 0.9$	$1.5 \pm 0.4$	
		[OIII] $\lambda$ 5006	$30.2 \pm 19.5$	$126.6 \pm 17.7$	–		$0.84 \pm 0.09$	$0.40 \pm 0.05$	
		HeI $\lambda$ 5875	$-72.5 \pm 45.4$	$352.4 \pm 45.3$	–		$1.8 \pm 0.2$	$0.8 \pm 0.1$	
		[FeX] $\lambda$ 6374	$16.2 \pm 25.1$	$342.9 \pm 27.0$	–		$2.6 \pm 0.2$	$1.2 \pm 0.1$	
		H $\alpha$	$140 \pm 6$	$732 \pm 18$	$1135 \pm 22$		$27.7 \pm 0.5$	$13.2 \pm 0.2$	
	59616	[OII] $\lambda\lambda$ 3726, 3728	$242.9 \pm 34.6$	$99.1 \pm 25.1$	–		$0.31 \pm 0.08$	$0.15 \pm 0.04$	
		HeII $\lambda$ 4685	$52.0 \pm 34.5$	$406.0 \pm 32.1$	–		$3.0 \pm 0.2$	$1.4 \pm 0.1$	
		H $\beta$	$115 \pm 3$	$779 \pm 4$	$779 \pm 4$		$2.5 \pm 0.0$	$1.19 \pm 0.01$	
		[OIII] $\lambda$ 5006	$128.3 \pm 17.6$	$114.8 \pm 18.2$	–		$0.8 \pm 0.1$	$0.4 \pm 0.1$	
		HeI $\lambda$ 5875	$130.5 \pm 59.0$	$277.3 \pm 45.6$	–		$1.1 \pm 0.2$	$0.5 \pm 0.1$	
		[FeX] $\lambda$ 6374	$-29.6 \pm 29.4$	$239.8 \pm 28.3$	–		$1.6 \pm 0.2$	$0.8 \pm 0.1$	
	59909	H $\alpha$	$1466.23 \pm 0.00$	$7.09 \pm 0.00$	$4.47 \pm 0.00$		–	–	
	60029	H $\alpha$	$25.69 \pm 0.00$	$372.28 \pm 0.00$	$535.05 \pm 0.00$		–	–	
	VT J2012	59464	[OII] $\lambda\lambda$ 3726, 3728	$-786.9 \pm 516.9$	$821.8 \pm 486.9$	–		$0.5 \pm 0.3$	$0.4 \pm 0.2$
			HeII $\lambda$ 4685	$531.3 \pm 92.6$	$464.8 \pm 106.6$	–		$1.2 \pm 0.2$	$0.8 \pm 0.1$
			H $\beta$	$694 \pm 39$	$605 \pm 120$	$607 \pm 120$		$0.8 \pm 0.2$	$0.6 \pm 0.1$
[OIII] $\lambda$ 5006			$43.9 \pm 29.3$	$106.3 \pm 20.9$	–		$0.41 \pm 0.08$	$0.28 \pm 0.05$	
HeI $\lambda$ 5875			$694.9 \pm 69.1$	$121.7 \pm 63.3$	–		$0.5 \pm 0.2$	$0.4 \pm 0.1$	
[FeX] $\lambda$ 6374			$-120.0 \pm 370.1$	$472.1 \pm 219.7$	–		$0.3 \pm 0.2$	$0.2 \pm 0.1$	
H $\alpha$			$718 \pm 12$	$729 \pm 33$	$1083 \pm 79$		$11.6 \pm 0.4$	$7.8 \pm 0.3$	
59677		[OII] $\lambda\lambda$ 3726, 3728	$-871.1 \pm 62.5$	$133.1 \pm 51.0$	–		$0.4 \pm 0.2$	$0.3 \pm 0.1$	
		HeII $\lambda$ 4685	$196.1 \pm 72.2$	$241.3 \pm 40.3$	–		$0.9 \pm 0.2$	$0.6 \pm 0.1$	
		H $\beta$	$804 \pm 169$	$370 \pm 1067$	$370 \pm 252$		$0.6 \pm 0.1$	$0.4 \pm 0.1$	
		[OIII] $\lambda$ 5006	$35.4 \pm 63.7$	$92.2 \pm 50.8$	–		$0.4 \pm 0.1$	$0.3 \pm 0.1$	
		HeI $\lambda$ 5875	$707.2 \pm 84.8$	$557.7 \pm 83.2$	–		$2.2 \pm 0.3$	$1.5 \pm 0.2$	
59909	[FeX] $\lambda$ 6374	$-337.0 \pm 105.2$	$907.3 \pm 72.1$	–		$3.2 \pm 0.3$	$2.1 \pm 0.2$		
59909	H $\alpha$	$687 \pm 9$	$958 \pm 28$	$1075 \pm 32$		$15.0 \pm 0.7$	$10.1 \pm 0.5$		
59909	H $\alpha$	$814.88 \pm 7.82$	$187.75 \pm 25.62$	$218.94 \pm 56.37$		–	–		

**Notes.** Line parameters are defined in Section 5.4. For the Balmer lines, which are asymmetric, we have defined an upper and lower FWHM, which are defined as twice the width of the line above/below the peak. For all other lines, we report the standard FWHM but put this value in the “FWHM, upper” column.

*Chapter 6*

THE FIRST SYSTEMATICALLY IDENTIFIED REPEATING  
PARTIAL TIDAL DISRUPTION EVENT

Somalwar, J. J. et al. (May. 2025). In: ApJ. doi: 10.3847/1538-4357/adcc19

Jean J. Somalwar<sup>1</sup>, Vikram Ravi<sup>1</sup>, Yuhan Yao<sup>2,3</sup>, Muryel Guolo<sup>4</sup>, Matthew Graham<sup>1</sup>, Erica Hammerstein<sup>5</sup>, Wenbin Lu<sup>6</sup>, Matt Nicholl<sup>7</sup>, Yashvi Sharma<sup>1</sup>, Robert Stein<sup>1</sup>, Sjoert van Velzen<sup>8</sup>, Eric C. Bellm<sup>9</sup>, Michael W. Coughlin<sup>10</sup>, Steven L. Groom<sup>11</sup>, Frank J. Masci<sup>11</sup>, and Reed Riddle<sup>12</sup>

<sup>1</sup>Cahill Center for Astronomy and Astrophysics, MC 249-17 California Institute of Technology, Pasadena CA 91125, USA.

<sup>2</sup>Miller Institute for Basic Research in Science, 468 Donner Lab, Berkeley, CA 94720, USA

<sup>3</sup>Department of Astronomy, University of California, Berkeley, CA 94720, USA

<sup>4</sup>Bloomberg Center for Physics and Astronomy, Johns Hopkins University, 3400 N. Charles St., Baltimore, MD 21218, USA

<sup>5</sup>Department of Astronomy, University of Maryland, College Park, MD 20742, USA

<sup>6</sup>Department of Astronomy and Theoretical Astrophysics Center, University of California, Berkeley, CA 94720, USA

<sup>7</sup>Astrophysics Research Centre, School of Mathematics and Physics, Queens University Belfast, Belfast BT7 1NN, UK

<sup>8</sup>Leiden Observatory, Leiden University, Postbus 9513, 2300 RA, Leiden, The Netherlands

<sup>9</sup>DIRAC Institute, Department of Astronomy, University of Washington, 3910 15th Avenue NE, Seattle, WA 98195, USA

<sup>10</sup>School of Physics and Astronomy, University of Minnesota, Minneapolis, Minnesota 55455, USA

<sup>11</sup>IPAC, California Institute of Technology, 1200 E. California Blvd, Pasadena, CA 91125, USA

<sup>12</sup>Caltech Optical Observatories, California Institute of Technology, Pasadena, CA 91125, USA

### Abstract

Tidal disruption events (TDEs) occur when a star enters the tidal radius of a supermassive black hole (SMBH). If the star only grazes the tidal radius, a fraction of the stellar mass will be accreted in a partial TDE (pTDE). The remainder can continue orbiting and may re-disrupted at pericenter, causing a repeating pTDE. pTDEs may be as or more common than full TDEs (fTDEs), yet few are known. In this work, we present the discovery of the first repeating pTDE from a systematically-selected sample, AT 2020vdq. AT 2020vdq was originally identified as an optically- and radio-flaring TDE. Around 947 days after its discovery, it rebrightened dramatically

in the optical. The optical flare was remarkably fast and luminous given its black hole mass compared to previous TDEs. It was accompanied by extremely broad ( $\sim 0.1c$ ) optical/UV spectral features and faint X-ray emission ( $L_X \sim 3 \times 10^{41} \text{ erg s}^{-1}$ ), but no new radio-emitting component. Based on the transient optical/UV spectral features and the broadband light curve, we show that AT 2020vdq is a repeating pTDE. We then use it to constrain TDE models; in particular, we favor a star originally in a very tight binary system that is tidally broken apart by the Hills mechanism. We also constrain the repeating pTDE rate to be  $10^{-6}$  to  $10^{-5} \text{ yr}^{-1} \text{ galaxy}^{-1}$ , with uncertainties dominated by the unknown distribution of pTDE repeat timescales. In the Hills framework, this means the binary fraction in the galactic nucleus is of the order few percent.

## 6.1 Introduction

Much about supermassive black holes (SMBHs) remains enigmatic, including their formation pathways, typical growth histories, and effects on their hosts (e.g. 47). Much of the reason for our lack of knowledge about SMBHs is their inherent faintness: if the SMBH is not actively accreting as an active galactic nucleus (AGN), it can only be detected if it is in a very nearby galaxy. Even if it is accreting, the accretion process is poorly understood, so inferring physical properties of the SMBH and its environment from the observed emission is nontrivial (see 33, for a review).

In the last few decades, tidal disruption events (TDEs) have become key probes of SMBH physics (see 112, for a review). TDEs occur when a star ventures within the tidal radius of an SMBH:  $R_T \approx R_*(M_{\text{BH}}/M_*)^{1/3}$ , where  $R_T$  is the tidal radius,  $M_{\text{BH}}$  is the SMBH mass,  $R_*$  is the stellar radius, and  $M_*$  is the stellar mass (110, 111, 371). Tidal forces shred the star and, eventually, the stellar debris is accreted, producing a bright multiwavelength flare. The development of high cadence, wide field optical, radio, and X-ray surveys has enabled the discovery of  $\gtrsim 100$  candidate events (e.g. 130, 134).

To produce a TDE, a star must enter into a plunging orbit with a pericenter that is within the tidal radius of the SMBH but outside the Schwarzschild radius. This occurs only once every  $\sim 10^{4-5}$  years in galaxies with  $M_{\text{BH}} \lesssim 10^8 M_\odot$  (134, 425, 426). In contrast, if the star is on a grazing orbit, but still reaches the vicinity of the tidal radius, it can be partially disrupted, and only a fraction of the stellar mass will be deposited on the SMBH (427, 428). Theoretical work has suggested that

the pTDE rate could be orders of magnitude higher than the full TDE (fTDE) rate and may contribute significantly to the growth of SMBHs (429). They also provide a unique avenue to test/improve our TDE theory. The structure of the star (as it is tidally perturbed during each partial disruption), the amount of mass joining the accretion flow, and the circumnuclear medium (CNM; if the previous disruptions launched outflows) may change between disruptions. The black hole mass and spin, however, should remain roughly constant, allowing us to assess the relative effects of the black hole parameters and the changing system parameters in the flare emission. An accretion disk may also form after the first disruptions, so subsequent disruptions can be used to assess the role that the disk plays in the TDE behavior.

Few candidate pTDEs are confidently identified, despite the high rate estimates. Given our insufficient understanding of TDE physics, one of the best ways to confirm a candidate pTDE is if it repeats; i.e. if the star is on a bound orbit. If the orbital period is  $P \simeq 10^5 \text{ yr } (a/\text{pc})^{3/2} (M/10^6 M_\odot)^{-1/2}$  ( $a$  being the orbital semi-major axis and  $M$  being the SMBH mass), as expected for isolated stars in a nuclear star cluster slowly migrating onto grazing orbits due to orbital relaxation, we will not detect a repeat. It is possible that some or most of the known TDEs are this type of pTDE, but we require a better understanding of pTDE and fTDE physics to be able to accurately classify such sources.

Indeed, the pTDE candidates that are known were discovered because they repeated within  $\lesssim 10$  years (ASASSN 14ko (141, 430, 431); eRASSt J045650.3-203750 (431); AT 2018fyk (141, 432); RX J133157.6-324319.7 (433, 434); AT 2022dbl (435, 436); Swift J0230 (437, 438); AT 2021aeuk (439, 440)). Such tightly bound stars are difficult to reproduce with orbital relaxation alone (441). The most likely mechanism for such objects invokes Hills break-up of a tight binary, resulting in one bound object and one ejected object. If the binary is tight enough (inner semi-major axis  $\lesssim 0.01$  AU, with dependence on the SMBH mass), dynamical arguments predict that the bound star will have a period from  $O(10^2)$  days to a few years (442). The binary fraction in galactic nuclei is not well known, but could be sufficiently high to explain the rate of these events.

These pTDE candidates are an inhomogeneous group, however, with some selected in the X-ray, some in the optical, and none as part of a uniform search. Hence, the pTDE rate and the differences in their multiwavelength properties relative to fTDEs are still unconstrained. Fortunately, over the last few years, the Zwicky Transient Facility (ZTF; (124–127)) has enabled systematic searches for optically-

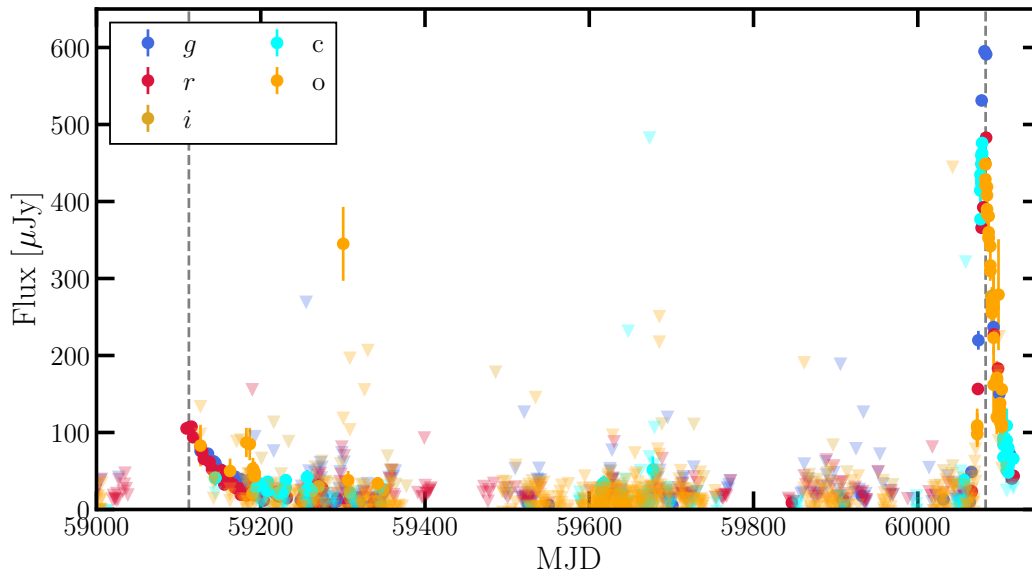


Figure 6.1: The full optical lightcurve showing the first and second flares from AT 2020vdq. Observations are shown as scattered points.

flaring TDEs. It has produced the first uniformly-selected samples of TDEs (13, 128, 134). In May 2023, one of the ZTF TDEs, AT 2020vdq, rebrightened (415) (see optical lightcurve in Figure 6.1). We commenced follow-up efforts and classified it as a repeating pTDE.

In this work, we will present observations and analysis of AT 2020vdq. Until Section 6.5, we will assume that this source is a pTDE and later justify this assumption. We describe the detection and properties of the first flare from AT 2020vdq in Section 6.2 and we detail the second flare in Section 6.3. We constrain past flares from this source in Section 6.4. In Section 6.5, we summarize key results, show that AT 2020vdq is consistent with being a pTDE, compare it to published observations of pTDEs, and use our observations to constrain both TDE and pTDE models. In particular, we constrain key aspects of TDE radio, optical, and spectral line emission, and we constrain the pTDE rate and typical number of repetitions. We also discuss possible contributions of pTDEs to solving the missing energy problem. Finally, we conclude in Section 6.6.

## 6.2 Observation of the initial flare

We begin by describing the multiwavelength properties of the first flare from AT 2020vdq. These properties are described in detail by (9, 134, 413).

Table 6.1: Basic properties of the host galaxy of AT 2020vdq.

Parameter	AT 2020vdq
R.A.	$10^{\text{h}}08^{\text{m}}53.50^{\text{s}}$
Dec.	$+42^{\text{d}}43^{\text{m}}00.40^{\text{s}}$
Redshift	0.045
$d_L$ [Mpc]	206

**Notes.** Basic properties of the host galaxy of AT 2020vdq.

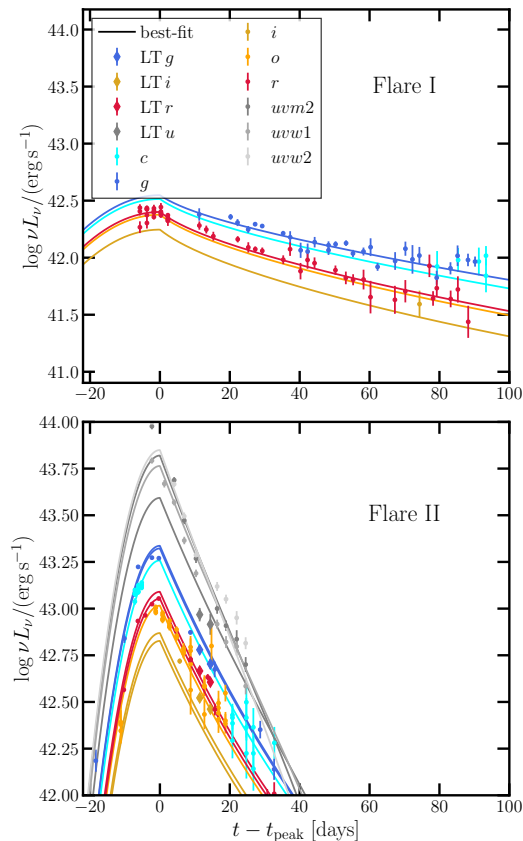


Figure 6.2: The optical and UV lightcurves for the first (. *top*) and second (. *bottom*) flares from AT 2020vdq. Observations are shown as scattered points. The best-fit parametric, evolving black body models, as described in Section 6.3 are shown as solid lines.

AT 2020vdq was first detected as an optical transient by the Zwicky Transient Facility (ZTF) on Oct. 4 2020 (MJD 59126) using the selection described in (134) implemented using the AMPEL filter (443). It was located at the nucleus of a dwarf galaxy at  $z = 0.045$  with  $\log M_*/M_\odot = 9.16 \pm 0.2$ . The stellar velocity dispersion of the nucleus host galaxy was measured to be  $\sigma_* = 44 \pm 3 \text{ km s}^{-1}$  from

a high resolution spectrum obtained with ESI on the Keck II telescope (134). This dispersion corresponds to a black hole mass of  $\log M_{\text{BH},\sigma_*}/M_\odot = 5.59 \pm 0.29$  using the  $M_{\text{BH}} - \sigma_*$  relation from (47). We refer the reader to (9, 134, 413) for more details of the host observations and analysis.

The first optical flare from AT2020vdq is shown in the top panel of Figure 6.2. The optical flare was first detected at 18.8 mag in the  $r$ -band near Sept. 23 2020 (MJD 59115). The rise was not strongly detected, although (134) provide a constraint on the rise time from the slight increase in luminosity over the first few days of evolution, which may have shown a slight rise. We fiducially assume that the resulting rise time and peak luminosity are correct. However, it is possible there was a true peak before the first detection that was brighter, but the source was not observed at this time. Comparison between the lightcurve of AT 2020vdq in Fig. 9 of (134) and the other TDEs in this sample shows that this behavior would be unusual, but not completely unheard of. We will nominally assume that the peak and rise time constrained by (134) is the true peak, but, where relevant, include a discussion of the implications if this assumption is wrong. This peak was fit to a blackbody by (134), who found that the peak is consistent with a blackbody with temperature  $\log T_{\text{bb}}/\text{K} = 4.16$  and luminosity  $\log L_{\text{bb}}/(\text{erg s}^{-1}) = 42.99$ . Note that this measurement is based on observations in only the  $g$  and  $r$  bands, so unknown systematic errors render the results uncertain. Stronger constraints are not possible because no UV observations were obtained at peak. This luminosity makes AT 2020vdq the lowest luminosity TDE in the (134) sample, even relative to events with lower black hole masses, although note that, if the assumed peak is not the true peak, the luminosity may be higher. The flare temperature is also in the coolest 20% quantile of the sample.

AT 2020vdq was detected as a radio source in 3 GHz observations from the VLA Sky Survey (VLASS; (133)) on Oct. 9 2021 (MJD 59496), or 383 days after the first optical peak. It had a flux of  $f_{\nu,3\text{GHz}} = 1.48 \pm 0.14$  mJy or  $\nu L_\nu = (2.3 \pm 0.2) \times 10^{38}$  erg s $^{-1}$ . The transient location had been previously observed by VLASS on May 25, 2019 (MJD 58628), or 485 days before the optical peak. No emission was detected, with a  $3\sigma$  upper limit  $f_{\nu,3\text{GHz}} < 0.7$  mJy or  $\nu L_\nu < 10^{38}$  erg s $^{-1}$ . We obtained follow-up radio observations with the VLA on Feb. 2, 2022 (MJD 59612), or 499 days after the optical peak. The radio SED, shown in Figure 6.3 was consistent with a non-relativistic, spherical synchrotron source with equipartition radius  $\log R_{\text{eq}}/\text{cm} = 17.07^{+0.01}_{-0.01}$  and magnetic field  $\log B_{\text{eq}}/\text{G} = -0.59^{+0.05}_{-0.04}$  (note the one discrepant point at low frequencies in the  $\Delta t_i = +500$  days observations is

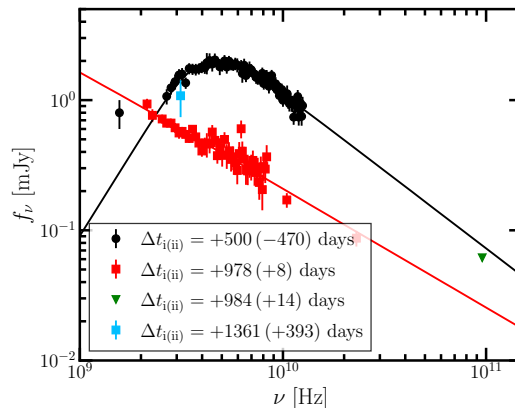


Figure 6.3: The radio evolution of AT 2020vdq. The black scatter points show a VLA observation from 500 days after the initial flare, or equivalently 470 days before the second flare. The red scatter points show a VLA observations from eight days after the rebrightening. The green upper limit shows a NOEMA observation from two weeks after the rebrightening. Both SEDs can be fit with spherical, non-relativistic synchrotron models. No young emitting component is required in the SED from shortly after the rebrightening. VLASS epoch 3 observations from  $\sim 400$  days after the rebrightening (light blue square) are consistent with our second epoch within  $1.5\sigma$  and show no evidence for a young outflow.

severely contaminated by radio frequency interference and can safely be ignored. We attempted to manually re-reduce this data point and found a flux  $0.8 \pm 0.2$  mJy, which is consistent with the fit at a  $\sim 2\sigma$  level, but we show the pipeline reduction in Figure 6.3 for consistency with the rest of the SED.). Assuming the radio-emitting outflow was launched near optical peak, this radius corresponds to an average velocity  $v \approx 2.7 \times 10^4$  km s $^{-1}$ , or  $\beta = v/c \approx 0.09$ . The energy in the outflow is  $\log E_{\text{eq}}/\text{erg} = 49.7^{+0.01}_{-0.01}$ . The power-law index of the electron energy distribution was consistent with  $p = 3.4^{+0.1}_{-0.1}$ . We refer the reader to (9, 413) for more details of the radio modeling and observations.

AT 2020vdq was not detected as an X-ray transient in observations with the Swift/XRT telescope on Feb. 28, 2022; the  $3\sigma$  upper limit on the 0.2 – 10 keV flux was  $L_X \lesssim 3 \times 10^{42}$  erg s $^{-1}$ . No significant transient UV emission was detected by Swift/UVOT on the same date.

We obtained optical spectra of AT 2020vdq on Feb. 6 and Apr. 7, 2022 (MJDs 59616, 59676), or 503/563 days post-optical peak using the LRIS spectrograph on the Keck I telescope (for reference, the source repeated after 947 days). The observation and reduction details are described in (9, 413). The spectra are shown

and discussed in detail in (9). Multiple transient spectral features are visible, as described in detail in (9): intermediate width Balmer, He II $\lambda$ 4685, He I $\lambda$ 5875, and [Fe X] $\lambda$ 6374 features. The Balmer features have asymmetric profiles with a slightly redshifted peak and a blue tail with average FWHM $\sim$ 900 km s $^{-1}$ . The Balmer emission is consistent with being produced by dense  $n_e \gtrsim 10^5$  cm $^{-3}$ , compact  $R \lesssim 10^{17}$  cm gas using standard recombination theory. The Balmer decrement of these lines is high:  $H\alpha/H\beta = 9$ , suggesting that the emission is heavily extinguished or produced by a non-standard ionization mechanism. The Balmer features brightened between the two spectra. The other transient features have narrower, symmetric profiles with FWHM $\sim$ 300 km s $^{-1}$ .

### 6.3 Observations of the rebrightening

#### Broadband transient optical/UV emission

Table 6.2: Best-fit evolving blackbody parameters for the optical flares from AT 2020vdq, including results from both the parametric and non-parametric fits to flare II. We report the energy from the non-parametric fit as a lower limit. We define the equivalent mass as  $M_{\text{bb}} = 10E/c^2$ , where we have assumed an accretion efficiency of 10%.

	$t_{\text{peak}}$	$\log \frac{L_{\text{bb}}}{\text{erg s}^{-1}}$	$\log \lambda_{\text{Edd}}$	$\log \frac{T_{\text{bb}}}{\text{K}}$	$\frac{dT}{dt}$	$t_{1/2,\text{rise}}$	$t_{1/2,\text{decay}}$	$t_0$
<b>Flare I</b>	$59115 \pm 1$	$42.73 \pm 0.08$	$-0.89 \pm 0.14$	$0.00 \pm 0.05$	$87 \pm 20$	$12 \pm 13$	$71 \pm 4$	$7 \pm 8$
<b>Flare II (par.)</b>	$60083.5 \pm 0.3$	$43.99 \pm 0.03$	$0.3 \pm 0.3$	$4.30 \pm 0.01$	$-212 \pm 33$	$4.9 \pm 0.1$	$5.8 \pm 4$	$91 \pm 42$
<b>Flare II (nonpar.)</b>	–	$44.2 \pm 0.06$	$0.3 \pm 0.3$	$4.45 \pm 0.03$	–	–	–	–

**Notes.** Best-fit evolving blackbody parameters for the optical flares from AT 2020vdq, including results from both the parametric and non-parametric fits to flare II. We report the energy from the non-parametric fit as a lower limit. We define the equivalent mass as  $M_{\text{bb}} = 10E/c^2$ , where we have assumed an accretion efficiency of 10%.

The rebrightening of AT 2020vdq was first detected by optical surveys: ZTF detected the rebrightening on May 9, 2023 (MJD 60073), 947 days after the first optical peak. The mean position of the rebrightening photometry was fully consistent with the original position with an separation of  $(0.14 \pm 0.07)''$ . This optical flare (from ZTF forced PSF photometry on difference images) is shown in the bottom panel of Figure 6.2. UV observations with Swift/UVOT were triggered shortly after (PIs: Lin, Leloudas, Guolo). We processed this data using the same methods as (13, 128); i.e., we reduced the Swift/UVOT data using recommended procedures, measured the source flux using aperture photometry, and subtracted the host contribution in a matched aperture using the results from spectral energy distribution fits to the host galaxy from (413). The UV lightcurve is overlaid on Figure 6.2. Optical

(*ugri*) observations with the Liverpool telescope observations were also triggered (PI: Nicholl). The observations were reduced using standard methods and the host component was subtracted using SDSS photometry. PSF photometry was performed on the difference images. The resulting difference photometry is overlaid on Figure 6.2. The evolution of this optical/UV rebrightening is notably different from that of the first flare. The emission peaks at a *g*-band luminosity a factor  $\sim 5$  higher than that of the original flare, assuming that the assumed first peak is the true luminosity peak. The decay time of the rebrightening is significantly faster than that of the original flare. The rebrightening also cools significantly within  $\sim 10$  days post-peak. Similar cooling is not obviously visible at  $\sim > 10$  days post-peak during the first flare, during which period we have color constraints.

We quantify these differences by modelling the optical/UV emission with two methods. First, we fit the UV/optical lightcurves with a parametric model, following (134). We assume the lightcurve can be modeled as an evolving blackbody. The blackbody luminosity rises as a Gaussian and decays as a power law and the temperature is constant pre-peak and evolves linearly post-peak:

$$L_{\text{bb}} = L_{\text{peak}} \begin{cases} e^{-\frac{1}{2} \left( \frac{t-t_{\text{peak}}}{\sigma_{\text{rise}}} \right)^2}, & t < t_{\text{peak}} \\ \left( \frac{t-t_{\text{peak}}+t_0}{t_0} \right)^p, & \text{otherwise.} \end{cases} \quad (6.1)$$

$$T_{\text{bb}} = T_0 + \begin{cases} 0, & t < t_{\text{peak}} \\ \frac{dT}{dt} \times (t - t_{\text{peak}}), & \text{otherwise.} \end{cases} \quad (6.2)$$

The time of luminosity peak is given by  $t_{\text{peak}}$ ,  $t_0$  and  $p$  control the luminosity decay shape,  $\sigma_{\text{rise}}$  controls the rate of the rise, and  $\frac{dT}{dt}$  controls the rate at which the temperature evolves.

We fit both the initial and second flares using this model so that we can compare the temperature evolution. We perform a least-squares fit with bounds  $t_{\text{peak}} \in [-100, 100]$ ,  $t_0 \in [0.1, 10^6]$ ,  $L_{\text{peak}} \in [38, 50]$ ,  $\sigma_{\text{rise}} \in [0.1, 1e2]$ ,  $p \in [-1000, 0]$ ,  $\frac{dT}{dt} \in [-1000, 1000]$ ,  $T_0 \in [3, 6]$ . The resulting best-fit parameters are shown in Table 6.2. We also report the rise time from half-peak to peak luminosity,  $t_{1/2,\text{rise}}$ , and the corresponding value for the decay ( $t_{1/2,\text{decay}}$ ). The best-fit models are shown in Figure 6.2; note that the parametric model is significantly discrepant from, in particular, the data near peak. To remain consistent with other work, we will use the model regardless, but discuss results from a non-parametric model that gives a better fit later. Note

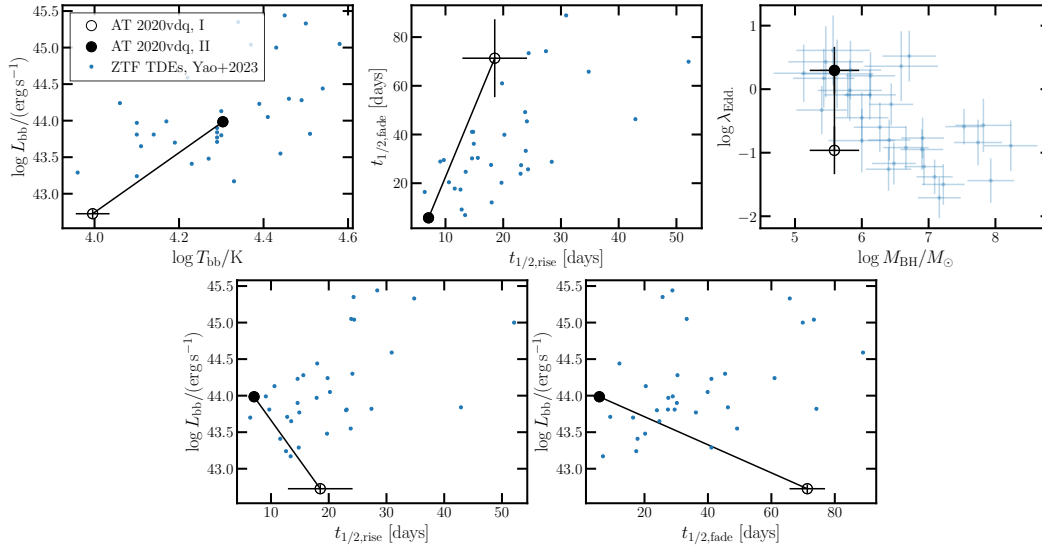


Figure 6.4: A comparison of the parametric, evolving, blackbody fit parameters for AT 2020vdq (black) to those of the TDEs from (134) (blue). The initial flare from AT 2020vdq is denoted with open markers while the rebrightening is denoted with filled markers. The pTDE candidate has a lightcurve that is generally consistent with the broader TDE population, although the rebrightening is luminous and fast evolving.

that the combination of the large best-fit  $t_0$  and high  $p$  place this source in a linear rather than power-law regime, unlike many other TDEs.

The peak luminosity of the rebrightening is 1.2 dex brighter than that of the initial flare, assuming that there is no luminosity peak that was missed before the first detection of AT 2020vdq. The optical/UV Eddington ratio  $\lambda = L_{\text{peak}} / L_{\text{Edd}}$  is correspondingly higher, such that the rebrightening corresponds to super-Eddington emission. The blackbody temperature of the rebrightening is 0.3 dex higher than that of the first flare, although we caution that the lack of UV observations of the first flare render this measurement uncertain. The rebrightening shows significant cooling, whereas the first flare shows little temperature evolution. The fade time of the rebrightening is also significantly faster than those of the first flare.

We compare these best-fit parameters to the ZTF-selected TDEs from (134) in Figure 6.4. In the top left panel, we show the evolution of the pTDE candidate in blackbody luminosity/temperature space. The initial flare is remarkably faint and cool, whereas the rebrightening is relatively typical. In the top middle panel, we show the evolution of the rise/decay times. Both the initial and second flares have short rise times relative to the ZTF TDE sample, although the uncertainties on the

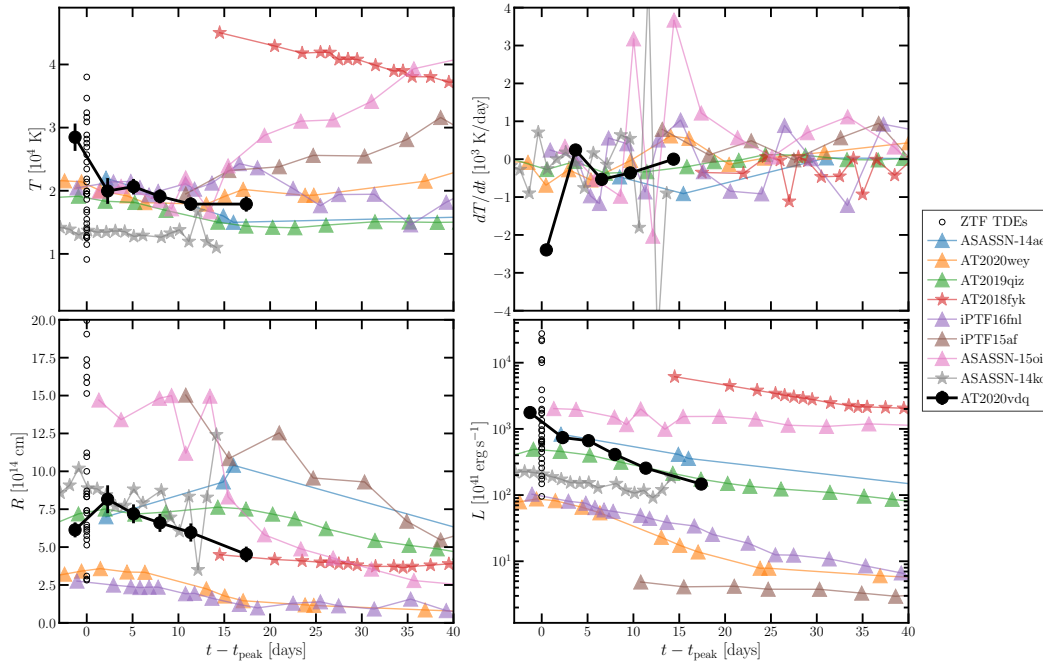


Figure 6.5: Non-parametric temperature, radius, and luminosity evolution for those TDEs and pTDEs that have available multi-epoch UV and optical data. Data from the rebrightening of AT 2020vdq is shown as black circles. The required multi-epoch UV data is not available for the initial flare, so only the rebrightening is shown. The candidate pTDEs AT 2018fyk and ASASSN-14ko are shown as colored stars, while normal TDEs are shown as open black circles. The data is retrieved from (329, 430, 444–448). AT 2020vdq shows a significant initial cooling and a rapid luminosity evolution. Otherwise, this pTDE candidate is generally consistent with the normal TDEs.

rise time of the initial flare are large. The second flare, in contrast, is the fastest rising TDE observed by ZTF and it has one of the fastest decay times. In the top right panel, we show the evolution of the flare Eddington ratio. The peak Eddington ratio of the first flare is significantly lower than that of the ZTF TDEs at similar black hole masses, assuming that the assumed peak is the true luminosity peak. The second flare, on the other hand, is at the upper end of the Eddington ratio distribution: there are only four ZTF TDEs with more super-Eddington emission, placing it in the upper 90% percentile of TDEs. In the bottom left panel, we show the rise time versus peak luminosity. In this parameter space, it is clear that AT 2020vdq is both fast-rising and the rebrightening is very luminous for this fast rise. Likewise, the bottom right panel shows that the TDE is fast-decaying and luminous.

We can improve upon the parametric model fits, which do not provide a good fit

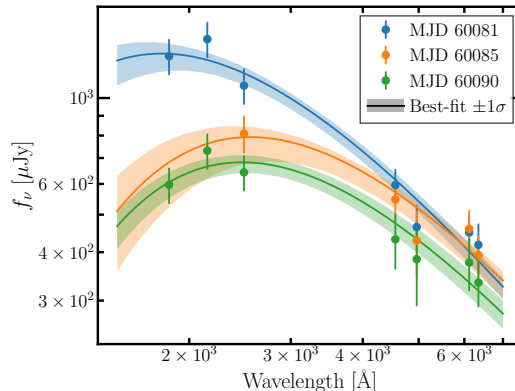


Figure 6.6: Example non-parametric SED fits to three epochs of observations of AT 2020vdq, highlighting the observed cooling.

near the peak of the rebrightening, by fitting independent blackbodies to the observations at multiple epochs. This is possible because we have multiple epochs of UV observations for the rebrightening, so we can tightly constrain the blackbody parameters for those epochs without relying on a parametric model. We first interpolate the optical lightcurves to the UV observation epochs using a Gaussian process model with a Matern kernel, as implemented in the `sklearn` package. We then fit the UV+optical for each epoch with a blackbody curve. The resulting temperature, radius, and luminosity evolution is shown in Figure 6.5. Example SED first are shown in Figure 6.6. As expected given the poor fit near peak from the parametric model, the peak luminosity and temperature from these single-epochs fits are significantly altered. The peak luminosity is  $\log L_{\text{bb}}/(\text{erg s}^{-1}) = 44.2 \pm 0.06$ , corresponding to an Eddington ratio  $\log \lambda = 0.3 \pm 0.3$ . The temperature at peak is  $\log T_{\text{bb}}/\text{K} = 4.45 \pm 0.03$ . The temperature cools dramatically at  $\sim -2300$  K/day in the first few days of the flare, and then stabilizes to  $\sim -200$  K/day.

We integrate this non-parametric bolometric luminosity post-flare to calculate the total energy released during the event. This energy is a lower limit as the non-parametric luminosity of the second flare from AT 2020vdq was only able to be estimated to  $\sim 20$  days. We estimate an upper limit by integrating the parametric light curve fit to 100 days, although note that this parametric fit did not model the data well and was extrapolated well past the edge of the data. We include it to show that it is not hugely different from our non-parametric energy and does not significantly affect our conclusions. We integrate the reported best-fit parametric models from the (134) lightcurves to 100 days to compile a comparison bolometric energy sample. We do the same for the first flare from AT 2020vdq. For the first

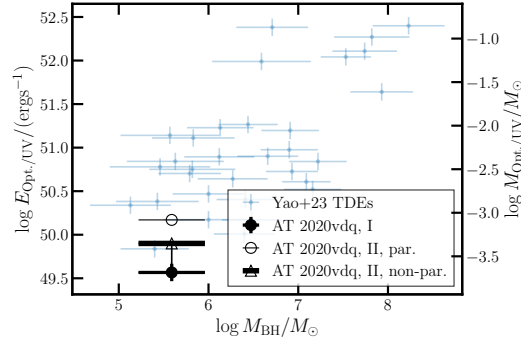


Figure 6.7: The total emitted optical/UV energy inferred from the pTDE candidate optical/UV flares, in the same format as Figure 6.4. The left axis shows the emitted energy while the right axis shows the equivalent stellar mass, assuming an accretion efficiency of 10%.

flare, this energy is a lower limit if observations missed the true luminosity peak. The resulting bolometric energies emitted during the first and second flares are shown in Figure 6.7 and the first flare energy and the second flare non-parametric energy limit are tabulated in Table 6.2. We also compute the equivalent stellar mass assuming an accretion efficiency of 10%. We computed that bolometric energies for the (134) following the same procedures. The energy released during both flares of AT 2020vdq is comparable to that from the (134). The second flare releases a factor of a few more energy than the first (pending constraints on the late-time evolution).

We searched the literature for other TDEs with published non-parametric fits and overlay the results from these similar analyses of other fTDEs and pTDEs in Figure 6.5. Candidate pTDEs are distinguished by star markers, while fTDEs are circle markers. Because this comparison sample of TDEs with non-parametric fits is highly heterogeneous as few events have such data published, for illustration we also show the best-fit values at peak for all ZTF TDEs, although we note that these values are measured using parametric fits that do not all include UV observations and so may not be directly comparable. The initial temperature evolution of AT 2020vdq is significantly faster than that of all other TDEs, although this trend is entirely governed by a single data point. Many other TDEs do, however, show some initial cooling within the first  $\sim 20$  days post-peak. The typical cooling rate in these  $\sim 20$  days is comparable to that of AT 2020vdq if we ignore the first observation. In particular, the temperature evolution from days  $\sim 5 - 15$  resembles that of AT 2020wey. The temperature is significantly hotter than that observed from the partial TDE ASASSN-14ko. The radius evolution is generally similar to other TDEs.

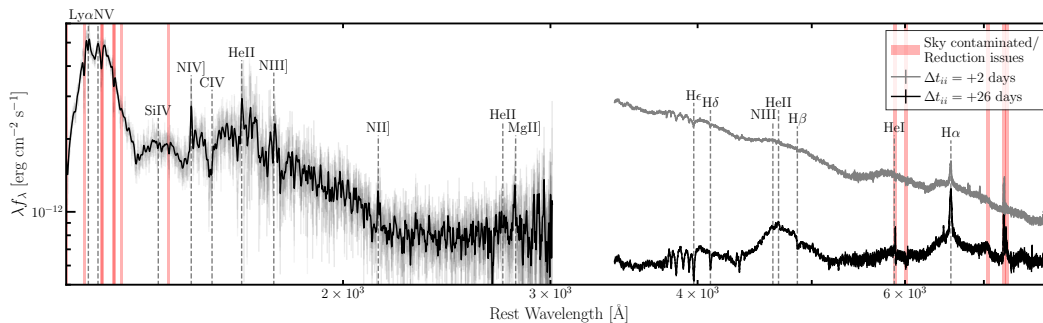


Figure 6.8: Summary of post-rebrightening UV/optical spectra of AT 2020vdq. Red regions are contaminated by sky background or telluric lines. In all spectra, a variety of strong broad, intermediate width, and narrow features are visible on top of a blue continuum.

The luminosity evolution, however, is remarkably rapid. This luminosity fades on a timescale comparable to the “fast and faint” TDEs AT2020wey and iPTF16fnl despite being an order of magnitude brighter than these events.

We conclude by briefly considering the flux level between the two flares. We calculated the average flux between  $\sim 300$  days after the first flare to  $\sim 100$  days before the second flare. We found a quiescent  $g$ -band luminosity  $L_g \approx 4 \times 10^{37} \text{ erg s}^{-1}$  ( $14.5\sigma$  significance) and an  $r$ -band luminosity  $L_r \approx 2 \times 10^{37} \text{ erg s}^{-1}$  ( $7\sigma$  significance).

### Transient spectral optical emission

We obtained optical spectra of AT 2020vdq with the LRIS/Keck I telescope using the same settings as (9). These spectra were observed 3 and 27 days post-optical peak (May 21 and Jun. 14 2023; MJDs 60085, 60109). These LRIS spectra are shown in Figure 6.8 along with a UV spectrum that will be discussed in the next section. All spectra were reduced following standard procedures.

In both LRIS spectra, the host galaxy features, a blue continuum, and transient spectral features are significantly detected. In particular, we see clear evidence for a broad He II  $\lambda 4686$ /H $\beta$  blend, broad He I  $\lambda 5876$ , and both broad and intermediate-width H $\alpha$ . Unfortunately, measuring the broad line fluxes in the spectra is complicated by strong degeneracies between the broad lines and the continuum. We attempt to model the spectra as the sum of broad Gaussian components near the expected wavelengths of He II  $\lambda 4686$ , H $\beta$ , He I  $\lambda 5876$ , and H $\alpha$  in addition to a fifth degree Legendre polynomial continuum component. We also require an intermediate width H $\alpha$  component, although we postpone detailed discussion of that line to later in this section, and a

Gaussian absorption line near the  $H\beta$  wavelength.

Table 6.3: Broad line fit parameters, with uncertainties as reported by our least squares fit. We caution against directly interpreting the reported luminosities as our fit makes many simplified assumptions and does not fully account for the strong degeneracies between the line fluxes and the continuum level/shape.

<b>Param.</b>		<b>MJD 60085</b>	<b>MJD 60109</b>
$\text{FWHM}_b$	$\text{km s}^{-1}$	$25260 \pm 110$	$19949 \pm 111$
$\frac{\text{FWHM}_b}{c}$		$0.0843 \pm 0.0004$	$0.0665 \pm 0.0004$
$\Delta v$	$\text{km s}^{-1}$	$-148 \pm 51$	$-1122 \pm 51$
$L_{H\alpha}$	$10^{40} \text{ erg s}^{-1}$	$9.22 \pm 0.08$	$5.71 \pm 0.08$
$L_{H\beta}$	$10^{40} \text{ erg s}^{-1}$	$4.41 \pm 0.06$	$2.38 \pm 0.06$
$L_{\text{He II}\lambda 4686}$	$10^{40} \text{ erg s}^{-1}$	$3.02 \pm 0.06$	$6.99 \pm 0.06$
$L_{\text{He I}\lambda 5876}$	$10^{40} \text{ erg s}^{-1}$	$7.68 \pm 0.05$	$1.33 \pm 0.05$

**Notes.** Broad line fit parameters, with uncertainties as reported by our least squares fit. We caution against directly interpreting the reported luminosities as our fit makes many simplified assumptions and does not fully account for the strong degeneracies between the line fluxes and the continuum level/shape.

In Figure 6.9, we show the spectra with the best-fit model and continuum model overlaid. In Figure 6.10, we subtract the continuum and overlay the individual best-fit line models. The best-fit optical broad line parameters are shown in Table 6.3. Unfortunately, the continuum level, which is the sum of galactic emission and the TDE continuum emission, is highly degenerate with the line fluxes (and, to a lesser extent, the line widths) and rendered uncertain by imperfections in the flux calibration due to unknown slit losses, which are different for the host galaxy and transient emission. Moreover, we have fixed the FWHM and velocity offsets of all the broad lines to a single value to remove degeneracies between the broad He II and  $H\beta$  emission; however, these assumptions are not physically motivated and likely cause erroneous flux measurements. Hence, we caution against detailed interpretation of the line luminosities. The FWHM measurement is likely more reliable, although it is still subject to significant degeneracies. Given the aforementioned uncertainties, we will not discuss and interpret the line fluxes in detail, other than to note that the Balmer decrement may be tantalizingly flat ( $H\alpha/H\beta \approx 2$ ), as has been observed for previous TDEs (449).

The line FWHM are nearly  $\sim 0.1c$  with small blueshifts. The line width narrows slightly with time, while the blueshift increases. The  $H\alpha$ ,  $H\beta$ , and He I lines evolve similarly: they begin bright and broad, but fade by the second observation. The He II line, in contrast, appears to brighten between the two observations, suggesting

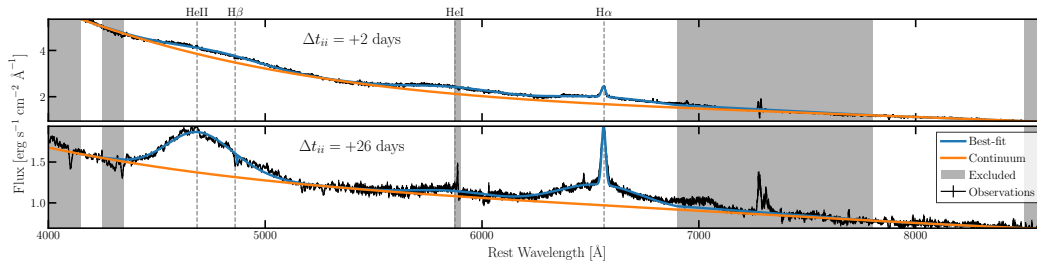


Figure 6.9: Best-fit models of the broad emission lines from the post-rebrightening, AT 2020vdq optical spectra. The observed spectra are shown in black. The best-fit models are shown in blue and the best-fit continuum is shown in orange. Regions highlighted in gray are excluded from the fit due to strong sky/telluric line features that render the reduction uncertain.

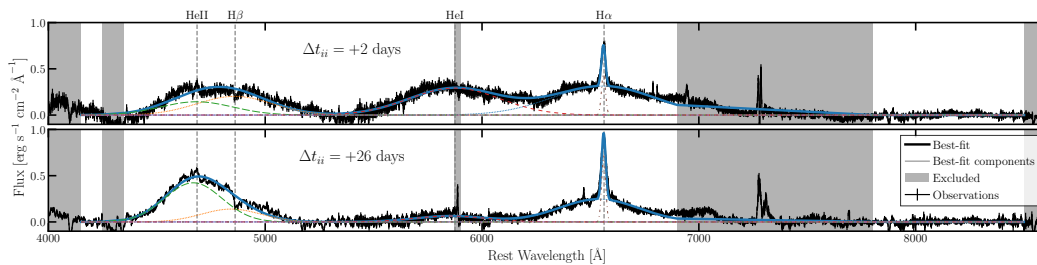


Figure 6.10: Best-fit models of the broad emission lines from the post-rebrightening, AT 2020vdq optical spectra, in the same format as Figure 6.9. For visualization, we have subtracted out the normalization in this figure and show the best-fit model subcomponents are shown in red. Broad Balmer, intermediate width Balmer, and Helium lines are detected. The Balmer lines fade slightly between the two spectra while the He II line brightens and the He I line fades dramatically, suggesting that these lines all originate from different locations in the source.

an alternate origin of the line. Similar behavior has been reported from the TDE candidate AT 2018hyz (449).

If the electron scattering optical depth is large, line broadening in TDEs may instead be dominated by electron scattering (146). For a moderate optical depth, a narrow line is produced by the unscattered photons and a broad base is visible due to the scatter photons. While we do observe both broad and narrow line emission in our spectra, it seems unlikely that the narrow line emission is the unscattered component of the emission: He I and  $H\alpha$  are at similar wavelength and have similar broad line fluxes in the early spectrum, yet  $H\alpha$  shows a strong narrow line and no detectable narrow He I line is present. Unless the He I emission region has a substantially higher optical depth than the  $H\alpha$  emitting region, the narrow lines

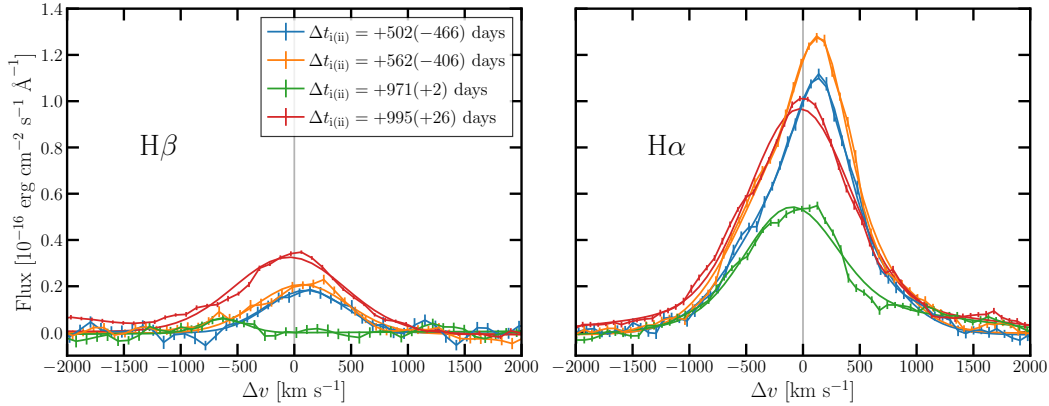


Figure 6.11: The evolution of the intermediate Balmer lines observed from AT2020vdq, with the best fit host stellar population subtracted.  $H\beta$  is shown in the left panel while  $H\alpha$  is shown in the right. Data is shown as lines with errorbars while Gaussian model fits are shown as lines. The Balmer lines were brightening by  $\sim 2$  years after the first flare, but faded and became slightly blueshifted by the rebrightening. A few weeks post-rebrightening, the Balmer lines began brightening while remaining blueshifted.

cannot be produced by the same mechanism as the broad lines. Hence, we assume that no significant unscattered component is detectable, so the emitting regions all have large electron scattering optical depths. It is beyond the scope of this work to calculate the exact optical depth required to produce the line widths observed, although we note that none of the line profiles presented by (146) are as broad as the lines observed here. We urge attempts to reproduce the spectrum observed with this source with electron scattering models to determine if it is possible to match our observations. Based on Figure 3 of (146), symmetric broad lines similar if not as broad as those produced by AT2020vdq are emitted by static or near-static gas with  $\tau_{\text{es}} \gtrsim 8$ . Adopting  $R \sim 10^{14.8}$  cm as before, this corresponds to a gas density  $\rho \gtrsim 4 \times 10^{-15}$  g cm $^{-3}$  or a number density  $n \gtrsim 10^9$  cm $^{-3}$ . The total mass in this outflowing gas is thus  $0.002 M_{\odot}$ .

In addition to these broad lines, we observe strong intermediate-width Balmer emission, similar to that observed following the first flare. These lines are treated in detail in (9), so we only briefly discuss the properties and interpretation here. The evolution of these intermediate width lines from before to after the rebrightening is shown in Figure 6.11. We have removed the stellar continuum using a fit with the ppxf software. While this subtraction may affect the core of the intermediate width lines, from higher resolution observations of the early time lines in (9), we do not

Table 6.4: Intermediate Balmer line properties and evolution

Parameter	Unit	$\Delta t_{ii} = -466$ days	$\Delta t_{ii} = -406$ days	$\Delta t_{ii} = +2$ days	$\Delta t_{ii} = +26$ days
$L_\alpha$	$10^{40}$ erg s $^{-1}$	$1.231 \pm 0.013$	$1.452 \pm 0.011$	$0.874 \pm 0.022$	$1.69 \pm 0.05$
$\text{FWHM}_\alpha$	km s $^{-1}$	$855 \pm 18$	$892 \pm 12$	$1077 \pm 18$	$1152 \pm 10$
$\Delta v_\alpha$	km s $^{-1}$	$128 \pm 6$	$128 \pm 5$	$-94 \pm 6$	$-26 \pm 2$
$L_\beta$	$10^{40}$ erg s $^{-1}$	$0.128 \pm 0.009$	$0.171 \pm 0.008$	$0.025 \pm 0.005$	$0.323 \pm 0.004$
$\text{FWHM}_\beta$	km s $^{-1}$	$807 \pm 57$	$932 \pm 47$	$464 \pm 99$	$1145 \pm 14$
$\Delta v_\beta$	km s $^{-1}$	$-104 \pm 22$	$-70 \pm 19$	$630 \pm 42$	$42 \pm 6$
$L_\alpha/L_\beta$		$9.6 \pm 0.7$	$8.5 \pm 0.4$	$35 \pm 8$	$5.22 \pm 0.17$

**Notes.** Best-fit Gaussian model parameters to the intermediate width Balmer lines, as described in Section 6.3.

see strong evidence for a dominant host component. Since the host has not changed between observations and the intermediate width lines have brightened at the host redshift, this will remain true. Following (9), we found that the  $H\alpha$  lines could be well modeled as the sum of two Gaussians. The  $H\beta$  lines are well-modeled as single Gaussians. Those fits are overlaid in Figure 6.11 and the best-fit parameters are summarized in Table 6.4.

Before the rebrightening, the emission lines were peaked near the host redshift and were brightening. They began fading at some point in the  $\sim 400$  days before the source rebrightened. In the earliest spectrum post-rebrightening, the lines were slightly blueshifted relative to the host. The lines had brightened by the next spectrum,  $\sim 24$  later or 27 days post-peak, suggesting that the emitting material is located  $\lesssim 7 \times 10^{16}$  cm from the SMBH. In all spectra, the Balmer decrement was  $> 5$ , suggesting extreme extinction or non-standard ionization, as photoionization of low density gas predicts a Balmer decrement  $\sim 3$  (see 9, for a detailed discussion). This is different from the very broad Balmer lines, which have a flat Balmer decrement, and suggests distinct emitting regions (the very different line widths also support this hypothesis). Following (9), we assume that the intermediate width emission is produced via recombination and use the distance limit from the variability timescale as an upper limit on the size of the emitting region. We find that the gas density is  $\gtrsim 10^5$  cm $^{-3}$ . Such a high density suggests that we are seeing emission from very compact clumps of outflowing gas.

We note that, after the first flare, we also detected emission from the coronal line [Fe X]  $\lambda 6375$ , signifying the presence of a strong soft X-ray continuum. That line is faintly present in the post-flare spectrum and shows fading from  $(1.6 \pm$

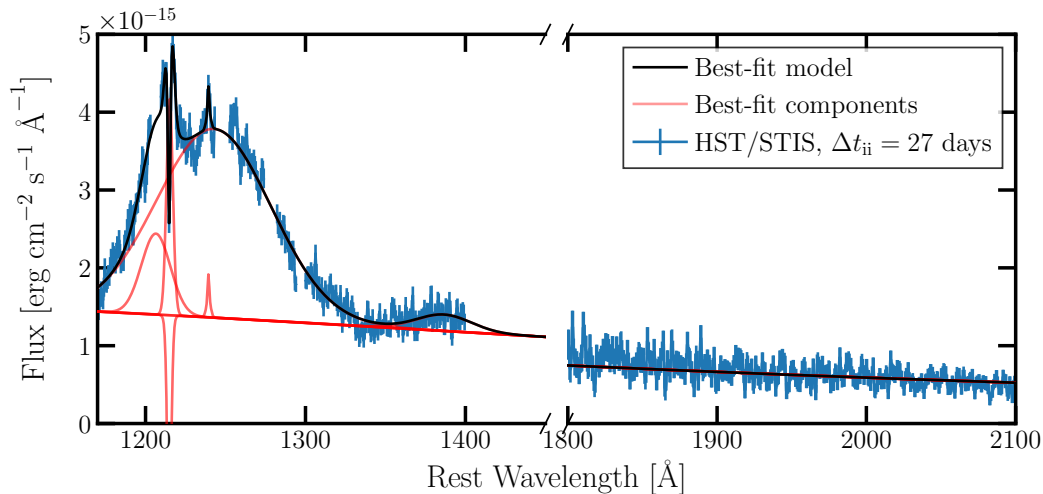


Figure 6.12: Fit to the  $\text{Ly}\alpha$  region and a continuum region of the . *HST* spectrum, in the same format as Figure 6.10. Note that we are not showing the full spectrum, which can be seen in Figure 6.8, but just the fit regions. The spectrum is well-modelled as two broad lines ( $\text{Ly}\alpha$  and an ambiguous line near  $\text{Si IV}\lambda 1394$ ), one intermediate line ( $\text{Ly}\alpha$ ), two narrow emission lines ( $\text{Ly}\alpha$  and  $\text{N V}$ ), and one narrow absorption line ( $\text{Ly}\alpha$ ). The broad  $\text{Ly}\alpha$  line is redshifted by  $\sim 7600 \text{ km s}^{-1}$  relative to the host rest-frame, which is in strong contrast to the optical spectral features.

$0.2) \times 10^{-16} \text{ erg cm}^{-2} \text{ s}^{-1}$  pre-rebrightening to  $(0.47 \pm 0.08) \times 10^{-16} \text{ erg cm}^{-2} \text{ s}^{-1}$ . This suggests that either the coronal line emitting gas is too distant for the bright continuum to have reached it yet, or the soft X-rays are not present. Given that the previous detection of  $[\text{Fe X}]$  was narrower than that of  $\text{H}\alpha$ , which suggests it may lie at larger distances and thus may turn on at late times, further late-time follow-up will be required to constrain this.

### UV spectrum

We obtained a UV spectrum on June 14, 2023 (MJD 60109) using the Space Telescope Imaging Spectrograph (STIS) on the . *Hubble Space Telescope* (. *HST*). We observed AT 2020vdq with the G140L grating and the FUV-MAMA detector for 3560 seconds and with the G230L grating and the NUV-MAMA detector for 1082 seconds, for a total of two orbits. All observations used the  $52 \times 0.2''$  aperture. The resulting UV spectrum is shown in Figure 6.8.

We begin with a qualitative description of the spectrum. Strong, hot blackbody emission (consistent with the transient photometry) is detected in the continuum of the UV spectrum. On top of this continuum, a number of emission lines are

detected. First, an extremely broad Ly $\alpha$  and/or N V $\lambda$ 1239 emission line is present. Superposed on the broad line(s) is an intermediate width Ly $\alpha$  emission line with a narrow absorption component. There are other broad features near the wavelengths of Si IV $\lambda$ 1394, N IV]  $\lambda$ 1486, and C IV  $\lambda$ 1548, 1551. Near but blueshifted relative to the wavelength of C IV, two narrow absorption lines are present. A number of narrow emission lines are also detected at a  $> 3\sigma$  significance (assuming Gaussian models) and with widths consistent with the instrumental resolution: N IV]  $\lambda$ 1486, Mg II]  $\lambda$ 2796, 2803, He II  $\lambda$ 1640, and N II]  $\lambda$ 2143. These lines are often detected in galaxies, so we assume they are associated with the host. We do not have sufficient signal-to-noise to perform a detailed analysis of the line emitting regions, so we do not discuss these lines further.

In the rest of this section, we attempt to quantitatively analyze and interpret these features. We focus on the broad Ly $\alpha$ + N V $\lambda$ 1239 complex. While the other broad emission lines may be present, our spectrum is not of sufficiently high signal-to-noise to characterize them.

Table 6.5: UV spectral features

<b>Name</b>	<b>Lum.</b> $10^{40} \text{ erg s}^{-1}$	<b>FWHM</b> $\text{km s}^{-1}$	$\Delta v$ $\text{km s}^{-1}$
Ly $\alpha_1$ + N V $\lambda$ 1239	$95 \pm 5$	$18747 \pm 646$	$7556 \pm 344$
Ly $\alpha_2$	$16 \pm 3$	$7290 \pm 650$	$-2883 \pm 252$
Si IV	$3 \pm 1$	$7830 \pm 2086$	$-1401 \pm 758$

We fit this region by modelling the range from 1200–1400 as the sum of Gaussians and a blackbody. We also include the continuum-dominated region from 1800–2100 in the fit to help constrain the blackbody parameters. While redder regions of the spectra also are continuum-dominated, we exclude them because the galaxy contribution is expected to be larger and potentially dominant. Seven Gaussians are required for a statistically consistent fit: (1) a broad component near Ly $\alpha$  and N V $\lambda$ 1239, (2) an intermediate-width Ly $\alpha$  component, (3) a broad component near 1400 (possible Si IV $\lambda$ 1394) (4) a narrow Ly $\alpha$  absorption line, and (5-6) two narrow Ly $\alpha$  and N V $\lambda$ 1239 emission components. We generally adopt broad bounds for the parameters in this fit, including for the blackbody temperature and radius. The best fit with subcomponents is shown in Figure 6.12 and the best-fit broad/intermediate line parameters are tabulated in Table 6.5.

The first broad component may not be entirely Ly $\alpha$  may be a blend of Ly $\alpha$  and N V $\lambda$ 1239. We tested adding a separate Gaussian for each separate these lines but

found that the fit did not improve, so we are unable to separate the contributions of these lines. Fitting a single component, we find that this blend is well-modelled as a Gaussian redshifted by  $\sim 7600 \text{ km s}^{-1}$  and with a FWHM  $\sim 19000 \text{ km s}^{-1} = 0.06c$ . This FWHM is consistent with those of the optical broad lines; however, the optical lines are slightly blueshifted whereas this line is redshifted relative to the expected Ly $\alpha$  wavelength. A strong NV component could play a role in this, but it would have to dominate over the Ly $\alpha$  emission. It is possible that a Gaussian is not the correct parameterization for these lines, which could also affect the velocity offset. If this line is, e.g., flat-topped or has multiple components (both of which can be produced by accretion disks and have been observed from past TDEs; (449)), the redshift and relative contribution from NV may be lessened. The total luminosity of this component is a factor  $\sim 10$  higher than that of the broad H $\alpha$  line, which is comparable to the expected ratio of 8.7 from case B recombination, although it is unclear whether case B recombination will apply in this extreme emitting material. The origin of this luminous, broad emission remains a mystery.

We require a second, intermediate component in our Ly $\alpha$  model that has a FWHM  $\sim 7000 \text{ km s}^{-1}$  and a blueshift of  $\Delta v \sim 3000 \text{ km s}^{-1}$ . This line is broader than the intermediate width components observed in the optical. If the broad Ly $\alpha$  component discussed above is not well-modelled by a Gaussian but is instead, e.g., flat-topped, we expect that the parameters of the intermediate component could vary substantially. Without a physically motivated model, we cannot constraint this. We note that we might expect an analogue to the intermediate width optical lines, which could be contributing here.

A few past TDEs (both fTDEs and pTDEs) have UV spectroscopy; a good summary of observations is provided by Figure 11 of (450). Broad Ly $\alpha$  lines, like that observed here, are detected in most near-peak TDE UV spectra (450–454), although the emission from AT 2020vdq appears significantly broader than typically observed (note that few authors provide fits to the broad emission, so a quantitative comparison is not possible). iPTF 15af shows a similarly broad line, although with strong absorption features superimposed that we do not see here (448). The broad Si IV and CIV are also frequently observed (e.g. 450). Intermediate width emission from Ly $\alpha$  has not been reported before, to our knowledge. Thus, other than the intermediate width components and the extreme width of the broad emission, the UV spectrum of AT 2020vdq resembles those of past TDEs.

### Radio emission

We obtained radio follow-up shortly after the rebrightening of AT 2020vdq using the VLA telescope ( $\sim 1 - 20$  GHz; Proposal AS1800, PI Somalwar) and the NOEMA telescope (mm; proposal E22AH, PI Somalwar). All observations used standard configurations. We observed AT 2020vdq with the VLA in the S, C, X, K, and Ku bands on May 26, 2023 (MJD 60090), or 7 days after the peak of the optical/UV rebrightening. The VLA observations were reduced using the most recent CASA VLA pipeline (2022.2.0.64). The source was detected in all bands and was sufficiently bright in S, C, and X to image individual spectral windows. The signal-to-noise was lower in the K and Ku bands, so we imaged all spectral windows together.

We observed AT 2020vdq at 95.7 GHz with the NOEMA telescope on June 1, 2023 (MJD 60096), or 14 days after the rebrightening peak. The observations were reduced using recommended pipeline procedures. The source was not detected, with a  $5\sigma$  flux limit of  $< 0.06$  mJy.

The resulting fluxes and upper limits are shown in Figure 6.3. The fluxes can be well-modeled as a single power-law, consistent with expansion of the early-time component. A new outflow component would appear as a second broken power-law component.

After the initial writing of this paper, VLASS re-observed AT 2020vdq as part of their epoch 3. We show the detection in blue in Figure 6.3. It is consistent within  $1.5\sigma$  with our second VLA epoch.

Table 6.6: Swift/XRT  $5\sigma$  upper limits

MJD	AT 2020vdq [ $10^{40}$ erg s $^{-1}$ ]
59638.2	$<34.6$
60081.2	$<6.2$
60084.8	$<11.4$
60087.3	$<96.5$
60090.5	$<90.8$
60093.8	$<90.8$
60099.8	$<4.4$
60102.2	$<147.6$
60105.5	$<170.3$
60108.1	$<4.0$

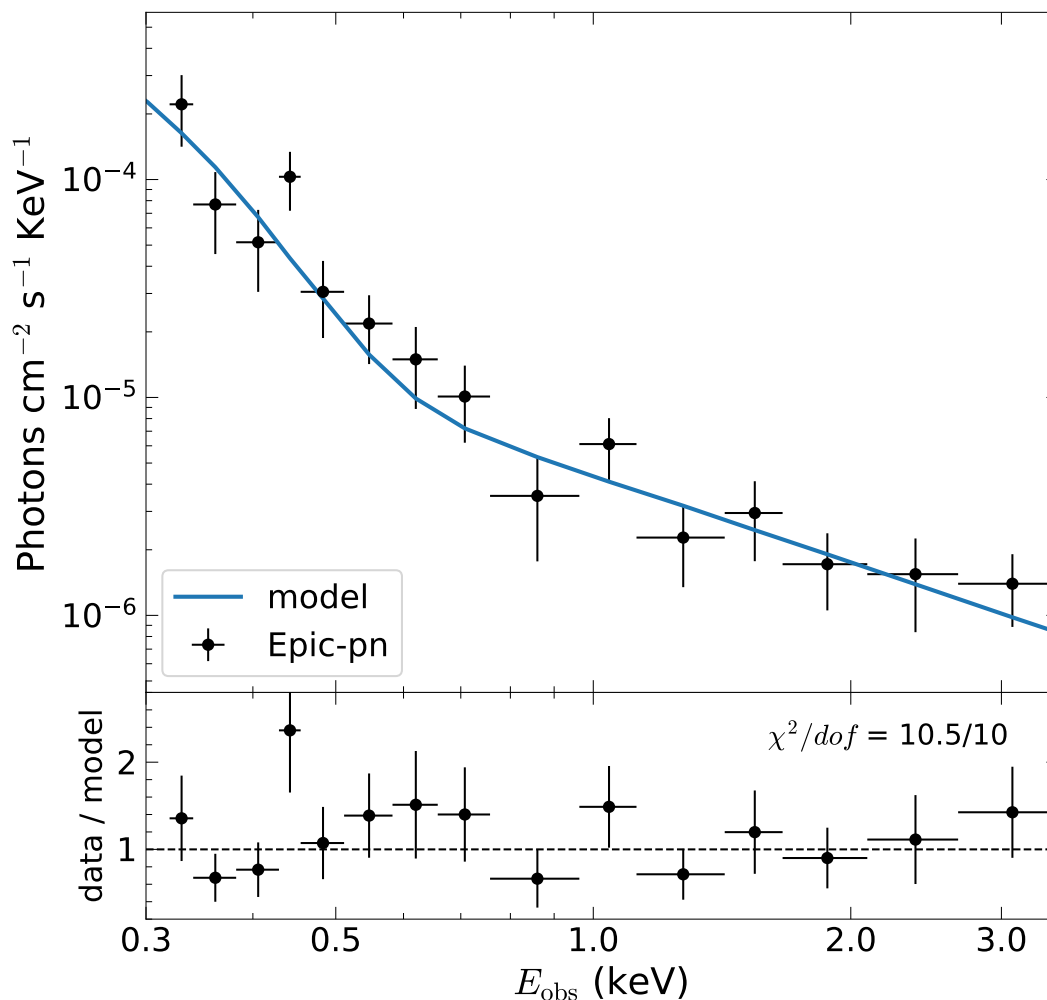


Figure 6.13: . *XMM-Newton* spectrum of AT 2020vdq, observed +2 days post the peak of the rebrightening. The data is shown as black points while the best-fit TBabs×zshift×(simpl⊗diskbb) model is shown as as a blue line.

### X-ray emission

We (among other groups) obtained X-ray follow-up of AT 2020vdq during the rebrightening using Swift/XRT (PIs: Lin, Leloudas, Guolo) and XMM-Newton (PI Somalwar). The Swift/XRT observations were performed in photon counting mode and reduced using standard `heasoft` procedures. We used the `sosta` function to perform forced photometry at the location of the source using default parameters. The source was not detected in any single Swift/XRT epoch; upper limits on shown in Table 6.6.

AT 2020vdq was observed and detected by XMM-Newton in  $\sim 10$  ks on MJD 60085 (+2 days post peak; May 21, 2023). The observation data files (ODFs) were reduced

using the *XMM-Newton* Standard Analysis Software (SAS; 455), and the detailed reduction processes as described in Guolo, Gezari, Yao, van Velzen, Hammerstein, Cenko, and Tokayer (142) were followed. The source spectrum, shown in Figure 6.13, is detected above the background up to  $\sim 3.0$  keV. The following spectral fitting procedures were done using the python version of *xspec* (456), *pyxspec*<sup>1</sup>. For all spectral models described below, we included the Galactic absorption using the TBabs model (321), with the hydrogen-equivalent neutral column density  $N_H$  fixed at the galactic value  $N_H = 1.38 \times 10^{20} \text{ cm}^{-2}$ . We shifted the TDE emission using the convolution model *zshift*. We start by trying to model the spectrum with a phenomenological powerlaw (TBabs $\times$ *zshift* $\times$ *powerflaw*), as expected (142), the powerlaw model is an inadequate model for TDE X-ray emission, the resulting  $\chi^2/\text{degrees of freedom (dof)} = 20/12$ . Alternatively, we also employ a purely thermal model (TBabs $\times$ *zshift* $\times$ *diskbb*), which also results in a poor fit  $\chi^2/\text{dof} = 30/12$ , from a strong residual at energies higher than 1.0 keV.

Finally, based on Guolo, Gezari, Yao, van Velzen, Hammerstein, Cenko, and Tokayer (142), we combined the thermal model with a convolution model (*simpl*, (457)) that emulates the comptonization process to create a powerlaw. With two free parameters:  $f_{\text{sc}}$ , the fraction of comptonized photons, and  $\Gamma$ , the resulting powerlaw photon index. Our final model TBabs $\times$ *zshift* $\times$ (*simpl* $\otimes$ *diskbb*), results in a great fit  $\chi^2/\text{dof} = 10.3/10$ , the best-fitted parameters are shown Table 6.7. The unabsorbed 0.3–10 keV flux was  $\log f_X/(\text{erg cm}^{-2} \text{ s}^{-1}) = -12.95 \pm 0.05$ , or  $\log L_X/(\text{erg s}^{-1}) = 41.4 \pm 0.05$  ( $L_X = 0.005L_{\text{edd}}$ .)

This X-ray emission is consistent with both observations of X-ray faint TDEs shortly post-peak (142, 143) and late-time X-ray observations of TDEs (142, 254), so it could be associated with the new flare or it could be relic emission from the accretion disk created during the first flare. The temperature of the thermal component is consistent with other optically selected TDEs (142), and the faint powerlaw emission ( $f_{\text{sc}} = 0.03_{-0.01}^{+0.01}$ ), could originate both from the reprocessing layer that produces the bright UV/optical, or a nascent corona (142, 458), late time observations may be able to distinguish them.

#### 6.4 Constraints on previous flares from AT 2020vdq

In this section, we search for past flares from AT 2020vdq. We retrieve photometry of this source from the ZTF, the Catalina Real Time Transient Survey (CRTS; (174)),

<sup>1</sup><https://heasarc.gsfc.nasa.gov/xanadu/xspec/python>

Table 6.7: Best-fitted parameters for *XMM-Newton* spectrum.

Model	Component	Value
TBabs	$N_{\text{H}}$	$1.38 \times 10^{20} \text{ cm}^{-2}$ (fixed)
zashift	$z$	0.045 (fixed)
simpl	$f_{\text{sc}}$	$0.03^{+0.01}_{-0.01}$
	$\Gamma$	$1.35^{+0.31}_{-0.25}$
diskbb	$T_{\text{in}}$	$58^{+4}_{-6} \text{ eV}$
	norm	$816^{+706}_{-270}$

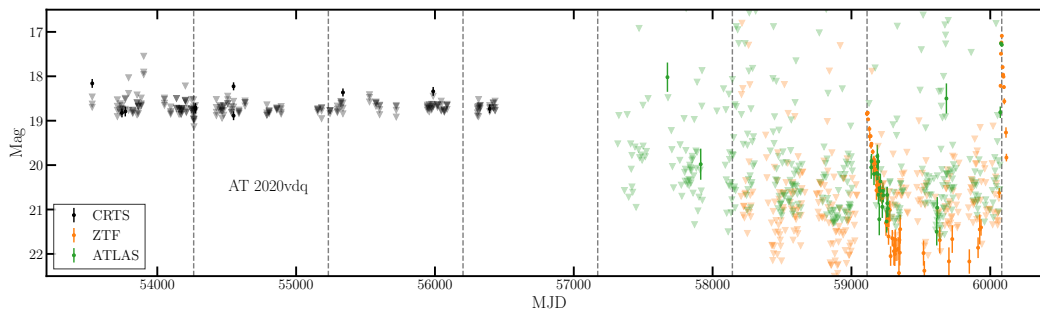


Figure 6.14: Historical lightcurves for AT 2020vdq. The lightcurves for each survey/band have been binned in 3 days bins. For clarity, we distinguish data from different surveys with different colors, but do not show different colors for each band (e.g., the ZTF lightcurve includes *gri* observations). We find no evidence for earlier flares in any of the data. ATLAS data rule out similar-brightness flares in the last  $\sim 10$  years.

and Asteroid Terrestrial-impact Last Alert System (ATLAS; (176)). As shown in Figure 6.14, no significant flare is detected by any survey. In both cases, ATLAS coverage is sufficient to rule out previous flares as bright or brighter than the detected flares. We cannot, however, rule out previous flares that had peak magnitudes that were fainter by  $\sim 1$  mag.

## 6.5 Discussion

We have presented the ZTF-discovered partial TDE candidate AT 2020vdq. Key properties of this event is summarized in Table 6.8.

In this section, we will first argue that AT 2020vdq is caused by a pTDE rather than a different type of activity. Then, we will discuss AT 2020vdq in the context of other pTDEs and we will use it to constrain both TDE and pTDE models.

Table 6.8: Summary of observations of AT 2020vdq

Parameter	Flare I	Flare II
Host galaxy	post-starburst, green-valley; $M_{\text{BH}} = 10^{5.6} M_{\odot}$	
Optical/UV flare	$L_{\text{bb}} = 10^{42.8} \text{ erg s}^{-1} = 0.1 L_{\text{edd}}$ $T_{\text{bb}} = 10^4 \text{ K}$ rose over $\sim 8$ days decayed over $\sim 60$ days	$L_{\text{bb}} = 10^{44} \text{ erg s}^{-1} = 2 L_{\text{edd}}$ $T_{\text{bb}} = 10^{4.3} \text{ K}$ rose over $\sim 5$ days decayed over $\sim 6$ days (one of the fastest evolving TDE flares)
Broad lines	no early time spectra	extremely broad ( $\sim 0.1c$ ), mildly blueshifted Balmer, He I, He II, and Ly $\alpha$ lines (H+He TDE)
Narrow lines	$\sim 1000 \text{ km s}^{-1}$ , slightly redshifted ( $\sim 100 \text{ km s}^{-1}$ ) Balmer (with large decrement), He I, He II, and [Fe X] detected	$\sim 1000 \text{ km s}^{-1}$ lines detected that brightened over the first few weeks, high but variable Balmer decrement. [Fe X] detected but no brightening yet.
X-ray	No early-time X-ray observations, $L_X \sim$ within 2 weeks post-peak $L_X \lesssim 3 \times 10^{41} \text{ erg s}^{-1} \sim 1.4$ years post-flare	
Radio	Detected as a $L_R \approx 10^{38} \text{ erg s}^{-1}$ radio transient $\sim 1.4$ years after the initial flare. The radio-rebrightening emitting region was consistent with a non-relativistic ( $\beta \sim 0.1$ ), wide-angle outflow.	

### The cause of AT 2020vdq

We first argue that AT 2020vdq is a pTDE. We consider four possible origins of this event (1) a TDE followed by a supernova, (2) AGN variability, (3) a TDE by a SMBH binary, (4) two independent TDEs, or (5) a repeating partial TDE.

The first scenario is disfavored by many pieces of evidence. First, the intermediate width Balmer lines were initially caused by a TDE (Paper II). They began evolving after the second flare, which would not be expected if the second flare is caused by a SN rather than an event directly in the vicinity of the SMBH. In addition, the broad optical spectral features are well-modelled as a TDE, but are less typical for SN. In the case of a Type II SN, the lack of star-formation provides additional evidence against a SN flare origin. Hence, we do not believe that the second flare from AT 2020vdq could be caused by a SN.

Instead, it is possible that both flares from AT 2020vdq are related to a flaring AGN.

As we argue in (9), the lack of any signatures of AGN activity from this source render this hypothesis unlikely: the WISE W1-W2 color is 0.088 mag, which is outside of the AGN regime (381, 459), and we do not see significant infrared variability pre-flaring. We do not see evidence for strong narrow Balmer on top of the intermediate width transient lines and only weak, narrow [O III] is detected. There are also no archival radio nor X-ray detections. AT 2020vdq could, at most, be an extremely low luminosity AGN.

A TDE by a SMBH in a binary is expected to have an accretion rate that initially follows standard predictions for TDE evolution. The accretion rate will then cut off after a fraction of the period of the SMBH binary, but it eventually may increase again (460, 461). In no model of such events, however, is the accretion rate expected to be increase after the first flare. Hence, we would not expect a flare such as that observed from AT 2020vdq, which is more energetic during the rebrightening.

We next consider the possibility that AT 2020vdq is two independent TDEs in a single galaxy. The TDE rate has been measured to be  $\sim 3.2 \times 10^{-5} \text{ yr}^{-1} \text{ galaxy}^{-1}$  using 33 ZTF TDEs. After monitoring these TDEs for  $\sim 3$  years post-discovery, we would expect to detect a mean of  $\sim 3.2 \times 10^{-5} \text{ yr}^{-1} \text{ Galaxy}^{-1} \times 33 \text{ Galaxies} \times 3 \text{ years} = 0.003$  additional TDEs. Thus, the probability of observing one or more additional, independent TDE from these 33 TDE hosts is 0.3%. While this probability is not negligible, it suggests that it is unlikely that we have observed two independent TDEs. However, we urge careful consideration of this possibility in future repeating pTDE analyses, as the probability of observing two independent events in a single galaxy will only increase with time and as TDE samples grow.

Considering that post-starburst galaxies have elevated TDE rates (by a factor of 10 to 100) as compared to other types of galaxies, the time interval between two independent TDEs may be as short as a few hundred years (135–137, 139). For the case of an average rate of  $3 \times 10^{-3} \text{ yr}^{-1} \text{ galaxy}^{-1}$ , the probability of detecting two independent TDEs from 33 TDE hosts in 3 years is as large as 30%. This possibility can be tested by future monitoring of AT 2020vdq; (not) detecting another flare from AT 2020vdq in the near future will constrain this possibility.

We conclude that AT 2020vdq is most likely a pTDE.

### **AT 2020vdq in the context of published repeating pTDE candidates**

There are a handful of published partial TDE candidates. We only consider those that flared at least twice. There have been optical/UV pTDE candidates identified

based on their low-luminosity and/or fast-evolving flares (e.g. 462); however, non-repeating pTDEs are very difficult to confirm as it may be possible to generate low-luminosity/fast flares through additional mechanisms (e.g., intermediate mass black hole disruptions; (463)). The repeating pTDEs that we consider to be reliable candidates are summarized as follows.

*ASASSN-14ko* (430, 450, 464): ASASSN-14ko is one of the most well-studied pTDE candidates discovered to date. It is a nuclear transient in an AGN that was discovered by the ASASSN survey. It flared seventeen times between 2014 and 2020 in the optical, with a period of 114.2 days. The optical flaring was accompanied by UV flaring and the best-fit flare blackbody parameters and evolution are consistent with typical TDEs (grey stars in Figure 6.5). At least a subset of the optical flares are accompanied by X-ray variability. The optical spectra for this source show possible evidence for broad Balmer features.

*eRASSt J045650.3–203750* (431, 465): eRASSt J045650.3–203750 (J0456) was first discovered as a repeating, nuclear, X-ray transient by eROSITA. The X-ray lightcurve is characterized by a rise followed by a  $\sim$ months-long plateau that rapidly fades. This flare profile repeats every  $\sim$ 223 days and has repeated three times. The host galaxy has no detectable optical broad or narrow spectral features, suggesting that it is quiescent in all senses. UV follow-up detected moderate variability, but no optical variability is detected. Radio emission was detected during the X-ray plateau.

*AT 2018fyk* (141, 432): AT 2018fyk was first detected as a nuclear optical transient by the ASASSN survey. Optical spectra taken post-flare detected broad He, He, and Bowen lines, along with narrow Fe II features. AT 2018fyk was detected as both a UV and X-ray transient in follow-up ( $L_X \approx 10^{43}$  erg s $^{-1}$ ,  $L_{UV,peak} = 10^{44}$  erg s $^{-1}$ ) and the UV/X-ray emission remained bright for  $\sim$ 600 days. After this period, the UV and X-ray emission plummeted, although remained detectable (plausibly due to a disk state change).  $\sim$ 1200 days after the first flare, the UV and X-ray rebrightened, with  $L_X \approx 8 \times 10^{42}$  erg s $^{-1}$  and  $L_{UV} \approx 10^{43}$  erg s $^{-1}$ . The host galaxy is classified as a retired galaxy based on its narrow optical emission lines. There is no evidence for AGN activity from infrared observations. It has a massive blackhole, with  $M_{BH} \approx 10^{7.7} M_{\odot}$ .

*RX J133157.6–324319.7* (433, 434): RX J133157.6–324319.7 (RX J1331) was detected as an ultra-soft X-ray transient with  $L_X \approx 10^{43}$  erg s $^{-1}$  by ROSAT in 1993 (433). The transient evolved rapidly, with a factor of eight luminosity increase within  $\sim$ 8 days. The host galaxy is non-active and non-star forming. It was not

detected in sparse, survey observations until  $\sim 30$  years later, when it flared back to  $\sim 10^{43}$  erg s $^{-1}$  during eROSITA observations. The X-ray spectrum during this flare was ultra-soft, like the first flare. It was not detected in follow-up observations  $\sim 20$ – $100$  days post-peak.

*AT 2022dbl* (435, 436): AT 2022dbl is a repeating partial TDE detected in optical surveys. It flared twice with a period of  $720 \pm 4.7$  days (436). The optical flares had similar peak temperatures, but second flare was a factor  $\sim 2$  slower than the first and a factor  $\sim 2.6$  less luminous (435). The optical spectra taken near peak of both flares show very similar Balmer, Helium, and N III features (435). No X-ray emission was detected during either flare, but faint emission with a luminosity  $L_X = 3 \times 10^{41}$  erg s $^{-1}$  was detected between flares. The host galaxy is classified as passive and Balmer strong.

*IRAS F01004-2237* (466): F01004-2237 flared in the optical twice, separated by  $\sim 10$  years. The first flare was detected in 2010 and was argued to be associated with a TDE based on a broad He II line in an optical spectrum  $\sim 5$  years post-event. The second flare was detected in 2021 with a peak luminosity  $\sim 10^{44}$  erg s $^{-1}$ , which is brighter than the first flare at  $\sim 4 \times 10^{43}$  erg s $^{-1}$ . The flare evolution was slow ( $\sim 50$  day rise to peak) and produced soft X-ray flares with a photon index  $\Gamma = 4.4$ .

We also briefly mention two proposed repeating partial TDE candidates that we do not include because there are alternate mechanisms that could explain their emission, rendering the partial TDE association uncertain:

*Swift J0230* (437, 438): Swift J0230 was detected as an X-ray transient by the Swift telescope. It outbursted ten times with a peak luminosity  $\sim 4 \times 10^{42}$  erg s $^{-1}$ . The outbursts were not perfectly periodic but showed a  $\sim 22$  day period (437, 438). No optical/UV flaring was detected, but transient radio emission was detected (437, 438). This event was proposed to be the repeated tidal disruption of a main-sequence star by a lower mass massive black hole  $\sim 4 \times 10^5 M_\odot$  (437), but this explanation was disfavored by (438) because the stellar orbit must be highly fine-tuned to reproduce the observations and the lightcurve evolution does not match expectations from fallback accretion. This work instead favors a model invoking an extreme mass ratio inspiral. Because of the uncertainty in the origin of this event, we will not further consider it in our analysis.

*AT 2021aeuk* (439, 440): AT 2021aeuk is a radio-loud, narrow-line Seyfert 1 galaxy that flared three times in the optical over a period of five years. The flares showed irregular spacing and luminosity, and the final two flares were both slower-evolving

than typical TDE flares. Because this event had a host galaxy with strong indications of AGN activity (red mid-infrared colors, radio emission) and the flare evolution are reminiscent of the ambiguous nuclear transients (275, 330, 336, 467), which are not necessarily caused by TDEs, we do not consider this source further.

Table 6.9: Summary of published repeating pTDEs

Name	Band	Period [years]	$\log M_{\text{BH}}/M_{\odot}$	N. flares
ASASSN-14ko <sup>1,2,3</sup>	Optical/UV/X-ray	0.3	7.9	$\gtrsim 20$
eRASSt J045650.3–203750 <sup>4,5</sup>	X-ray/UV	0.61	7.0	5
AT 2022dbl <sup>6,7</sup>	Optical/UV	2.0	6.4	2
AT 2020vdq <sup>8</sup>	Optical/UV	2.7	6.1	2
AT 2018fyk <sup>9,10</sup>	UV/X-ray	3.3	7.7	2
F01004-2237 <sup>11</sup>	Optical/UV	10.3	7.4	2
RX J133157.6–324319.7 <sup>12,13</sup>	X-ray	$\lesssim 30$	6.5	2

**Notes.** Summary of published repeating pTDE candidates, sorted by flare period. The bands listed are those in which the rebrightening was detected. <sup>1</sup>(430), <sup>2</sup>(464), <sup>3</sup>(450), <sup>4</sup>(431), <sup>5</sup>(465), <sup>6</sup>(435), <sup>7</sup>(436), <sup>8</sup>This work, <sup>9</sup>(432), <sup>10</sup>(141), <sup>11</sup>(466), <sup>12</sup>(433), <sup>13</sup>(434)

In Table 6.9, we tabulate the bands in which these TDEs were detected, their periods, and their black hole masses. While it is difficult to draw conclusions about trends among candidates due to the small sample size and inhomogeneous selection, there are a number of key facts to note about this sample:

*Flare periods:* The flare period distribution ranges from  $\sim 20$  days to  $\sim 2$ –10 years. All but two of the observed flares have periods  $\lesssim 3$  years. As has been detailed in other work (e.g. 468), placing stars on such short period orbits requires Hills capture of a binary. In this scenario, a binary is destroyed by the SMBH tidal forces, leading to one object being captured into a tight orbit around the SMBH and the other ejected. The typical binaries that will undergo this process will be on tight orbits themselves, as is required for them to survive the high velocity dispersion environment near the SMBH. These orbits are sufficiently tight as to require either two low mass stars or one star and one compact object. We will discuss the consequences of this fact further in Section 6.5.

*Multiwavelength properties:* The multiwavelength properties of the known pTDEs are very inhomogeneous. RX J1331 and J0456 are both primarily detected in the X-rays, with possible UV variability in the case of J0456. AT 2020vdq and AT 2022dbl, in contrast, show little X-ray emission. Even when only comparing the optical/UV properties of ASASSN-14ko, AT 2020vdq, and AT 2018fyk, we see a wide range of evolution and blackbody fit parameters, as is highlighted in Figure 6.5.

### Constraints on TDE models from AT 2020vdq

Partial TDEs provide a unique opportunity to constrain both pTDE, but also fTDE models: the only aspects of the system we expect to change between disruptions are the stellar structure and, possibly, the CNM. With this in mind, we use the changes in the emission between flares from AT 2020vdq to constrain both pTDE and fTDE models. There are four key takeaways from the observations of AT 2020vdq:

#### *1. Launching a radio-emitting outflow may require a sub-Eddington state*

AT 2020vdq launched a radio outflow in the  $\sim 2$  years following its initial flare. Launching such an outflow requires an accretion disk. AT 2020vdq thus likely had a pre-existing accretion disk during its rebrightening, and that this disk was, at one point, capable of launching radio-emitting outflows. Despite this, no new radio component was detected in the weeks following the rebrightening, when the event was in a relatively high accretion rate state. There are three possible explanations for the lack of radio emission: (1) AT 2020vdq cannot launch radio-emitting outflows except in a sub-Eddington state; (2) this TDE cleared out the circumnuclear material in a region around the SMBH, so no material was present during AT 2020vdq's rebrightening against which the outflow could shock; (3) the change in stellar structure affected the disk's ability to launch an outflow. Cadenced radio observations of radio-emitting partial TDEs will be valuable for constraining the outflow-launch mechanisms in these events.

#### *2. Bright and fast rebrightening*

The rebrightening of AT 2020vdq was rapidly evolving relative to most TDEs. It has the fastest rise time and one of the fastest decay times of all TDEs. When controlling for rise time, it is also luminous pTDE models predict that these events should evolve more rapidly than fTDEs: the fallback rate of stellar debris from fTDE decays is expected to follow a  $\sim t^{-5/3}$  power-law, whereas pTDE decays are expected to follow a  $\sim t^{-9/4}$  power-law due to the gravitational pull of the surviving stellar core. Intriguingly, however, the first flare from AT 2020vdq was less extreme: the decay time was among the longest for the (134) sample. It is possible that the fast evolution of the rebrightening is tied to the change in the stellar structure, rather than the pTDE nature of the event. However, (469) simulated the fallback rate for stellar disruptions with a range of polytropic indices and did not predict any early time fallback rates that were significantly steeper than the standard  $\sim t^{-5/3}$ . Instead, maybe the rapid evolution is due to a pre-existing accretion disk: the first pTDE episode likely created a disk with a size  $\sim R_T$ , and the interaction between a disk and stellar debris can cause rapid circularization and accretion (470).

### 3. Initial cooling of the optical flare

The temperature evolution of AT 2020vdq, while not unusual, deserves note. TDEs are often assumed to not cool. However, multiple TDEs show initial cooling near-peak, followed by  $\sim 10$ s of days in a  $\sim$ constant temperature state. This has been noted by previous authors (e.g. 446, 463), although models do not exist to explain the evolution to our knowledge. This evolution is particularly apparent from AT 2020vdq: Near-peak, the temperature cools dramatically. It then hovers near a zero-cooling state.

### 4. Otherwise, AT 2020vdq is a fairly normal event

The final point worth noting about AT 2020vdq is that, like some of the other published pTDEs, it is a relatively normal TDE. While it shows some unusual features (fast evolution, broad emission lines), it is not massively outside the typical TDE parameter space in any case. Both flares from this source would pass the “normal” TDE cuts used in (134). This suggests that some of the known TDEs could well be pTDEs.

## Partial TDE rates and the missing energy problem

We conclude by discussing the rate of partial TDEs. We then apply this discussion to the enigmatic missing energy problem of TDEs.

We first consider the rate of pTDEs, where each pTDE, regardless of the number of flares, is counted as a single event. Because AT 2020vdq was drawn from the (134) sample, we begin with the TDE rate measured in that work and scale it to estimate the pTDE rate. We first searched that sample for other pTDEs. One other transient, AT 2021mhg, showed a rebrightening. However, as we show in Appendix 6.7, this source is a TDE followed by a Type Ia supernova, so we do not consider it further.

(134) measured a TDE rate of  $\sim 3.2 \times 10^{-5} \text{ yr}^{-1} \text{ galaxy}^{-1}$  using 33 ZTF TDEs. Note that this rate is an average over the population, but the rate depends on luminosity and increases for lower luminosities. Moreover, it is enhanced for certain galaxy types. In particular, AT 2020vdq is hosted by E+A, which may have an enhanced TDE rate (135). Assuming that none of the other TDEs in this sample will rebrighten, the rate of partial TDEs on  $\sim 3$  year timescales is  $\approx 1/33 \times \sim 3.2 \times 10^{-5} \text{ yr}^{-1} \text{ Galaxy}^{-1} \approx 10^{-6} \text{ yr}^{-1} \text{ galaxy}^{-1}$ . This is a lower limit on the rate, as more rebrightening TDEs and accounting for the E+A nature of the AT 2020vdq host will increase the value, as will accounting for the luminosity dependence of the ZTF TDE rate and the ASASSN-14ko-like events that would not make it into the (134) sample.

Instead of assuming that no more TDEs are hidden pTDEs, we now constrain the fraction of the (134) that could be pTDEs. We assume that the pTDE flare period distribution is a uniform distribution ranging from 0.3–2.7 years (i.e., all flares periods are between that of ASASSN-14ko and AT2022vdq). This flare period distribution was chosen arbitrarily and could affect our results: further theoretical studies are needed to motivate the correct form of this distribution. We also assume that, if one flare from a PTDE was detectable, any other flare should be detectable as long as it occurs while ZTF is online. Given that AT 2020vdq showed large luminosity differences between flares, this could affect our results; once more repeating PTDEs are found, the luminosity distribution can be constrained. Assume the fraction of pTDEs in the (134) sample is  $f_{\text{pTDE}}$ . We assign each TDE in the (134) sample to be a pTDE or fTDE according to this fraction. For those assigned as pTDEs, we randomly generate a flare period and count the number of pTDEs that would repeat before June 2023 (approximately when we last searched for ZTF pTDEs). We repeat this process  $10^6$  times and calculate the fraction of trials where one or fewer objects are observed to repeat, which we call  $P(N_{\text{pTDE}} \leq 1)$ . We find that  $P(N_{\text{pTDE}} \leq 1) < 10^{-3}$  for  $f_{\text{pTDE}} \geq 0.3$ ; i.e., we have constrained the fraction of pTDEs in the (134) to be  $\lesssim 30\%$  at the  $3\sigma$  level. Thus, we can once more constrain the repeating pTDE rate for  $\sim 0.3 - 2.7$  year timescales to be  $\lesssim 46\%$  of the TDE rate, or  $\lesssim 10^{-5} \text{ yr}^{-1} \text{ galaxy}^{-1}$ . Combining this result with the lower limit on the rate computed by assuming that AT 2020vdq is the only pTDE in the (134) sample, we find that the repeating pTDE rate for  $\sim 0.3 - 2.7$  year timescales is in the range  $10^{-(5-6)} \text{ yr}^{-1} \text{ galaxy}^{-1}$ .

Note that this result is strongly dependent on the assumed flare period distribution. Decreasing the lower limit on this distribution or having it peak towards smaller values tightens our constraints. However, if maximum allowed flare period is larger, a larger pTDE fraction is allowed. For example, if we assume the flare periods are drawn from a uniform distribution ranging from 0.3–5 years, we can only say that is the pTDE fraction  $\lesssim 40\%$  at the  $3\sigma$  level. One way to constrain the potential for longer timescale pTDEs is to look at older TDE samples, although no uniformly selected such sample exists. Regardless, we checked all the older optical/UV TDEs listed in (112) for rebrightenings in ZTF or ATLAS data and do not find any detections. This suggests that TDEs do not frequently brighten on longer timescales, although this sample is small and inhomogeneous, so we do not attempt to set any detailed constraints on the longest allowed flare periods. We suggest, however, that at least some of the known TDEs are true, full TDEs rather than pTDEs.

In the theoretical frame work of Hills mechanism (442), the rate of repeating pTDEs depends on the rate at which stars migrate into deeply penetrating orbits and the binary fraction of stars in the galactic nucleus. From the above discussion, we can conclude that the ratio of the number of Hills-captured, partially disrupted stars to tidally disrupted single stars is  $\lesssim 40\%$ . This fraction is less than unity mainly because few binaries can survive in galactic nuclei with semi-major axes that would produce a  $\sim$ -year period pTDE. Simulations of this process assuming different binary fractions and semi-major axis distributions would provide valuable information for interpreting the observed rate.

This measured rate, which suggests that pTDEs may not dominate the TDE rate, as well as the discussion in the previous parts of this work, have implications for the long-standing “missing energy problem” of TDEs: the total energy observed to be emitted during TDEs is always  $\sim 2$  orders of magnitude lower than expected from the accretion of a  $\sim$ solar mass star. A number of possible explanations abound; for example, the bolometric corrections adopted to convert the observed luminosity into the total luminosity may be hugely overestimated (e.g. 142, 143, 471–473), more energy may be input into winds and/or jets than is currently expected (e.g. 471, 474), or the energy may be trapped in a disk with high optical depth (475). Alternatively, if all or most of the known TDEs are in fact pTDEs, the low detected energies would be expected because only a small fraction of the star need be accreted during each disruption. Our suggestion above that at least some of the known TDEs are true full TDEs refutes this hypothesis. Of course, if longer period ( $\sim$ decade) pTDEs are common, it is still possible that pTDEs can aid the missing energy problems. Intriguingly, this pTDE hypothesis is supported by the fact that the original flare from AT 2020vdq was originally identified as relatively typical TDEs, with no extremely unusual features that could have hinted at the fact that they would rebrighten, supports this possibility: the multiwavelength properties of the known pTDEs are so similar to the known TDEs that we can not rule out that any given event is instead a partial disruption. Future work on the long-term lightcurves of known TDEs will thus be critical for constraining the contribution of pTDEs to the missing energy problem.

## 6.6 Conclusions

In this work, we have presented observations and analysis of the partial tidal disruption event, AT 2020vdq. AT 2020vdq is the first pTDE identified from a well-characterized TDE sample, allowing us to constrain the pTDE rate to  $\approx 10^{-(5-6)}$

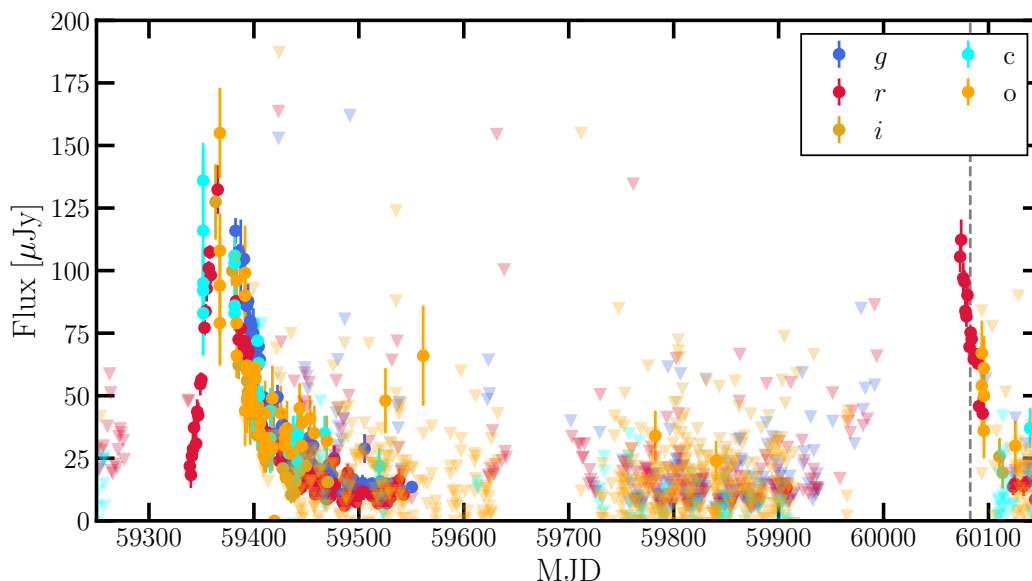


Figure 6.15: The full optical lightcurve showing the first and second flares from AT 2021mhg. Observations are shown as scattered points.

galaxy<sup>-1</sup> yr<sup>-1</sup>, subject to uncertainties in the flare rate of pTDEs. We have used the properties of AT 2020vdq to constrain TDE and pTDE models. Of note, the lack of a launch of a radio-emitting outflow shortly after the second disruption despite the launch of such an outflow after the first disruption may suggest that some TDEs must be in a low accretion state to launch such outflows.

Intriguingly, and unlike previous pTDEs, the multiwavelength properties of AT 2020vdq are generally characteristic of “typical” TDEs; for example, it has a low black hole mass and its optical flares are not hugely divergent from those observed from other TDEs (it was first identified as part of a standard TDE sample). This suggests that some of the known TDEs may in fact be pTDEs in disguise, so we urge careful monitoring of all events. However, we also urge caution when classifying repeating nuclear transients. As in the case of AT 2021mhg (Appendix 6.7), large TDE samples combined with many-year monitoring campaigns leads to a high probability of chance detections of multiple, independent transients in a single host.

## 6.7 Appendix

### The second repeating ZTF transient, AT 2021mhg: a TDE and SN Ia in the same galaxy

After the discovery of AT 2020vdq, we performed forced photometry for all ZTF

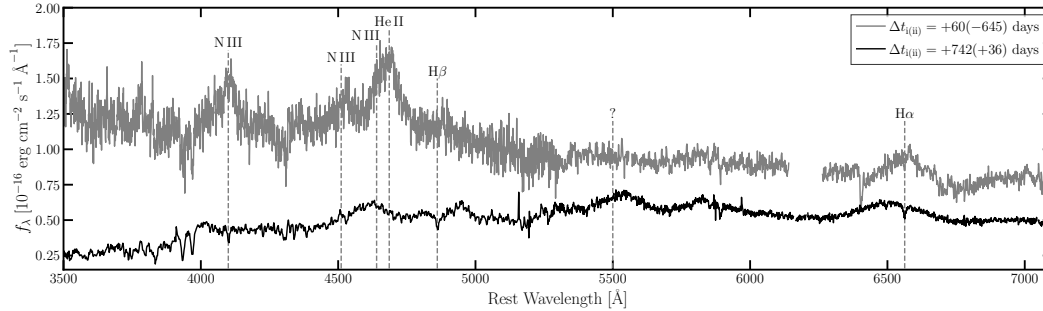


Figure 6.16: Spectral evolution of AT 2021mhg. The grey spectrum was observed 60 days after the first flare and the black spectrum was observed 36 days after the second flare. The gap in the grey spectrum masks a region that is strongly contaminated by poorly subtracted telluric features.

TDEs to search for any other rebrightenings on  $\sim$ year timescales. Coincidentally, AT 2021mhg had rebrightened in the  $r$ -band shortly before AT 2020vdq (476) (see lightcurve in Figure 6.15). The time delay between flares is 705 days. The mean position of the rebrightening photometry was fully consistent with the original position with an separation of  $(0.2 \pm 0.1)''$ . Upon discovery, we and other groups triggered multiwavelength follow-up.

AT 2021mhg is hosted by a Balmer-strong, blue galaxy with a black hole mass  $\log M_{\text{BH}}/M_{\odot} = 6.1 \pm 0.37$  (134). No narrow emission lines are detected in the host spectra, although no host galaxy spectra without any transient emission are available. Strong host absorption lines are detected, in contrast. We tentatively identify this galaxy as quiescent, both in terms of star formation and AGN activity.

In Figure 6.16, we show one spectrum of AT 2020vdq observed with P200/DBSP (PI: Kulkarni; (134))  $\sim$ 70 days after the first flare (grey) and one spectrum observed  $\sim$ 35 days after the rebrightening with Keck I/LRIS (black). These spectra look markedly different. Broad Balmer, He II, and N III are detected after the first flare. The detection of these lines places AT 2021mhg in the H+He TDE class. The presence of N III places AT 2021mhg in the class of Bowen TDEs, which show Bowen fluorescence lines. The detected lines do not show significant velocity offsets and have widths  $\sim 8000 \text{ km s}^{-1} = 0.03c$ . These line widths are typical for H+He TDEs that are observed  $\sim$ 50 days post-peak.

The post-rebrightening spectrum is extremely unusual for a TDE. We detect the typical broad lines He II  $\lambda 4686$ , possible H  $\beta$  and He I  $\lambda 5876$ , and H  $\alpha$ . However, there are also broad features near 5000 and 5500 that, to our knowledge, have

not been seen from a TDE before and that we cannot identify. N III  $\lambda$ 4100 is not obviously present.

While the first flare from AT 2021mhg is a typical TDE, the second flare is highly unusual because of the broad features in the spectrum. We use the Supernova Identification (snid) tool to model the post-rebrightening optical spectrum from this source. The spectrum is well-modeled (87% match) as a type Ia supernova observed  $\sim 30$  days post-peak. The mysterious broad features near 5000 are perfectly modeled in this scenario.

We conclude that AT 2021mhg is a galaxy where a TDE occurred, followed by a Type Ia SN after  $\sim 2$  years. The probability of observing a scenario like this is non-negligible, and must be considered in future searches for pTDEs. A Type Ia SN in a  $\sim$ Milky Way-like galaxy once every  $\sim 500$  years. Assuming this rate is uniform throughout the galaxy, the typical TDE host has a radius of  $\sim 3''$  and we define the nucleus as the central  $\sim 1''$ , a Type Ia SN will occur in a galaxy nucleus every  $2 \times 10^4$  years.

We have searched a sample of 33 galaxies (i.e., the (134) sample) for flares over a period of  $\sim 3$  years (i.e., the time since the first TDE flares in each). Thus, the probability of detecting a Type Ia SN from one of these galaxies in this time period is  $33 \times 3 \text{ years} / 2 \times 10^4 \text{ years} = 0.02$ . The probability of detecting one or more events given that this expected probability is  $\sim 2\%$ . In other words, the detection of AT 2021mhg source is only a  $\sim 2\sigma$  fluctuation.

As we continue monitoring TDEs for rebrightenings, the probability of detecting both a TDE and another transient in the same galaxy will continue increasing. We strongly urge the careful consideration of this scenario when future pTDE candidates are detected.

*Chapter 7*

## A LUMINOUS AND HOT INFRARED THROUGH X-RAY TRANSIENT AT A 5 KPC OFFSET FROM A DWARF GALAXY

Jean J. Somalwar<sup>1</sup>, Vikram Ravi<sup>1</sup>, Raffaella Margutti<sup>2,3</sup>, Ryan Chornock<sup>2</sup>, Priyamvada Natarajan<sup>4,5,6</sup>, Wenbin Lu<sup>2,7</sup>, Charlotte Angus<sup>8</sup>, Matthew J. Graham<sup>1</sup>, Erica Hammerstein<sup>2</sup>, Edward Nathan<sup>1</sup>, Matt Nicholl<sup>8</sup>, Kritti Sharma<sup>1</sup>, Robert Stein<sup>9,10,11</sup>, Frank Verdi<sup>1</sup>, Yuhan Yao<sup>2,12</sup>, Eric C. Bellm<sup>13</sup>, Tracy X. Chen<sup>14</sup>, Michael W. Coughlin<sup>15</sup>, David Hale<sup>16</sup>, Mansi M. Kasliwal<sup>1</sup>, Russ R. Laher<sup>14</sup>, Reed Riddle<sup>16</sup>, and Jesper Sollerman<sup>17</sup>

<sup>1</sup>Cahill Center for Astronomy and Astrophysics, MC 249-17 California Institute of Technology, Pasadena CA 91125, USA.

<sup>2</sup>Department of Astronomy, University of California, Berkeley, CA 94720-3411, USA

<sup>3</sup>Department of Physics, University of California, 366 Physics North MC 7300, Berkeley, CA 94720, USA

<sup>4</sup>Department of Astronomy, Yale University, P.O. Box 208101, New Haven, CT 06520, USA

<sup>5</sup>Black Hole Initiative, Harvard University, Cambridge, MA 02138, USA

<sup>6</sup>Department of Physics, Yale University, P.O. Box 208121, New Haven, CT 06520, USA

<sup>7</sup>Theoretical Astrophysics Center, University of California, Berkeley, CA 94720, USA

<sup>8</sup>Astrophysics Research Centre, School of Mathematics and Physics, Queens University Belfast, Belfast BT7 1NN, UK

<sup>9</sup>Department of Astronomy, University of Maryland, College Park, MD 20742, USA

<sup>10</sup>Joint Space-Science Institute, University of Maryland, College Park, MD 20742, USA

<sup>11</sup>Astrophysics Science Division, NASA Goddard Space Flight Center, Mail Code 661, Greenbelt, MD 20771, USA

<sup>12</sup>Miller Institute for Basic Research in Science, 468 Donner Lab, Berkeley, CA 94720, USA

<sup>13</sup>DIRAC Institute, Department of Astronomy, University of Washington, 3910 15th Avenue NE, Seattle, WA 98195, USA

<sup>14</sup>IPAC, California Institute of Technology, 1200 E. California Blvd, Pasadena, CA 91125, USA

<sup>15</sup>School of Physics and Astronomy, University of Minnesota, Minneapolis, MN 55455, USA

<sup>16</sup>Caltech Optical Observatories, California Institute of Technology, Pasadena, CA 91125

<sup>17</sup>Department of Astronomy, The Oskar Klein Center, Stockholm University, AlbaNova University Center, SE 106 91 Stockholm, Sweden

### **Abstract**

We are searching for hot, constant-color, offset optical flares in the Zwicky Transient Facility (ZTF) data stream that are  $>10''$  from any galaxy in public imaging data

from the PanSTARRS survey. Here, we present the first discovery from this search: AT 2024puz, a luminous multiwavelength transient offset by 5 kpc from a  $\sim 10^8 M_\odot$  galaxy at  $z = 0.356$  with a low-moderate star formation rate. It produced luminous  $10^{44.79 \pm 0.04} \text{ erg s}^{-1}$  optical/UV emission that evolved on a  $\sim 20$  day timescale, as well as  $10^{44.12 \pm 0.03} \text{ erg s}^{-1}$  X-ray emission with a photon-index  $\Gamma = 1.7$ . No associated radio or millimeter emission was detected. We show that the early-time optical emission is likely powered by reprocessing of high-energy, accretion-powered radiation, with a possible contribution from a shock in a dense circum-transient medium. If the shock is dominant at early-times, the circum-transient medium has a mass  $\sim 0.1 - 1 M_\odot$ , radius  $10^{15}$  cm, and a density profile shallower than  $\sim r^{-1}$ . A near-infrared excess appears at late-times and is suggestive of reprocessing within a wind or other circum-transient medium. The X-rays are most consistent with a central engine. We suggest that AT 2024puz may be associated with an accretion event onto a  $50 - 10^5 M_\odot$  BH, where the lower masses are preferred based on the large projected offset from the host galaxy. AT2024puz exhibits properties similar to both luminous fast blue optical transients (LFBOTs) and tidal disruption events (TDEs), but is intermediate between them in its energetics and evolution timescale. This highlights the need for broader exploration of the landscape of hot optical transients to trace their origins.

## 7.1 Introduction

Many open questions surround the formation and demographics of black holes (BHs) with masses  $10^{2-5} M_\odot$ . The mass function of stellar mass BHs informs models of stellar evolution. The “upper mass gap” of stellar mass black holes, near  $\sim 50 M_\odot$ , is thought to be the result of implosion of more massive stars in pulsational pair instability supernovae (SNe), but gravitational wave searches have begun detecting objects above this limit (41, 477), possibly due to mergers of massive stellar BHs in dense environments (42).

These massive stellar-mass BHs may be the local universe analogues of the seeds of SMBHs (BH mass  $M_{\text{BH}} > 10^6 M_\odot$ ). SMBH seeding and growth is one of the biggest open problems in astrophysics (49, 50). If BHs with masses  $\sim 100 M_\odot$ , formed from the stellar remnants of the first stars at high redshift, can grow rapidly through super-Eddington accretion, they may be able to form SMBHs detected at both high and low redshifts as proposed by the light seed models of SMBH growth (50, 57). Additionally, amplified growth of light seeds might be incubated in nuclear star clusters that might operate throughout cosmic time leading to the formation of

IMBHs even in the nearby universe (478). Heavy seed models invoke  $\sim 10^4 M_{\odot}$  gas clouds that directly collapse into BHs in the early universe (52, 53) or stellar mass black holes that rapidly accrete through runaway mergers and/or rapid accretion in dense environments (54–56). The resulting massive BHs may subsequently grow through Eddington-limited accretion to SMBH masses over time. These models produce distinct, observable predictions for the present-day demographics, occupation fraction, and locations of intermediate mass BHs (IMBHs;  $M_{\text{BH}} \sim 10^{2-5} M_{\odot}$ ) (38).

To solve these challenging open problems, we must discover more massive stellar and supermassive BHs. Transient emission is proving to be the most promising method of doing so as they uncover both active and quiescent BHs. In particular, transient optical flaring is enabling us to discover *populations* of time-domain varying events associated with compact objects and pushing to new regimes of their physics. Accretion flares from low mass SMBHs and IMBHs form a clear example of this, which we briefly outline here.

Tidal disruption events (TDEs) occur when a massive black hole (MBH,  $M_{\text{BH}} \sim 10^{2-9} M_{\odot}$ ) tidally shreds a nearby star (110, 111, 371). TDEs produce luminous electromagnetic flares and illuminate otherwise non-accreting and unobservable MBHs. To date  $\sim 100$  TDEs have been discovered, largely thanks to wide-field, cadenced, optical surveys, like the Zwicky Transient Facility (ZTF; (124–127)), All Sky Automated Survey for SuperNovae (ASASSN; (383, 387)), Panoramic Survey Telescope and Rapid Response System (Pan-STARRS1; PS1; (175)), and Asteroid Terrestrial-impact Last Alert System (ATLAS). These have contributed  $\gtrsim 100$  events in the last decade (e.g. 13, 116, 128, 134, 389, 479–482). TDEs produce blue, hot ( $T \sim 10^{4-5}$  K) optical flares that show minimal cooling and evolve over weeks-months.

TDE discoveries are beginning to push down to the lowest mass SMBHs known ( $\sim 10^5 M_{\odot}$ ; (e.g. 463, 483)), providing unique access and potential for discovering the elusive population of bona-fide IMBHs. Selection effects, however, may be preventing discoveries of a population of IMBH TDEs. In ZTF, TDEs are typically identified as blue ( $g - r < 0.2$  mag), constant color ( $d(g - r)/dt < 0.02$  mag/day) coincident with the location of a galactic nucleus, defined by pre-TDE images from public survey data (typically Pan-STARRS; (116, 134, 175)). The last host galaxy cut is particularly significant for ZTF IMBH TDE sensitivity. First, many IMBHs are expected to be hosted by dwarf galaxies, which are not detectable to large comoving

volumes in typical survey data (e.g., a  $10^8 M_\odot$  galaxy can be detected to  $z \approx 0.1$  in Pan-STARRS). Requiring a detectable host galaxy typically rules out these sources. Likewise, dwarf galaxies may not have well-defined nuclei, or gravitational potential minima (58), but TDEs are required to reside in their hosts' nuclei. Off-center TDEs are expected to be more numerous in more massive galaxies from wandering IMBHs in the hierarchical build up of structure in the standard  $\Lambda$  cold dark matter paradigm via mergers of galaxies and the BHs hosted by them (59). These will likewise be excluded from current searches (but see 484).

Searches of optical transient surveys that focus on non-TDE phenomena do not suffer from the same selection effects, and so may be more sensitive to IMBHs. One candidate for an IMBH-triggered transient is the luminous fast blue optical transient (LFBOT; (16, 485–488)). LFBOTs have optical evolution similar to TDEs (blue, constant color), but vary on much faster timescales  $\lesssim 1$  week and always offset from their host galaxy center (e.g. 15, 487–497). They are produced by a compact object of an as yet unknown nature: stellar mass BHs, IMBHs, and neutron stars (NSs) have all been proposed as potential sources (16, 485, 498–500). Like TDE searches, LFBOT searches may be limited by other selection effects: events are typically required to rise and fade on a  $\lesssim$  week timescale (490), which is significantly faster than almost all SMBH TDEs (134), leaving a gap between these populations. If LFBOTs are not TDEs, they are likely triggered by accretion onto a NS or stellar mass BH, or spindown of a young magnetar (see 16, and references therein).

If we want to identify the nature of the compact object that triggers LFBOTs, or find definitive accreting IMBHs, we must extend optical transient searches to span the parameter space intermediate to TDEs and LFBOTs. In other words, we need to map out the full range of these extreme, energetic, hot optical transients, regardless of timescale or host galaxy. This will allow us to conclusively connect these populations, or show that they are distinct and that LFBOTs are more likely associated with stellar mass compact objects, as well as potentially identify new types of transients.

This paper presents the first discovery of our ongoing effort to explore the full landscape of energetic, hot optical transients with ZTF. Here, we present AT 2024puz (hereafter 24puz), a luminous, multiwavelength transient in a dwarf galaxy that may be associated with an extreme compact object accretion event. We favor models with an accreting BH ranging in mass  $50 - 10^5 M_\odot$ . In Section 7.2, we present the parameters of the search in which we discovered 24puz. In Section 7.3, we detail

our extensive multiwavelength follow-up effort and data reduction. In Section 7.4, we analyze our observations to constrain the basic physical parameters of 24puz. In Section 7.5, we constrain the emission mechanisms and sizes of the emitting regions. In Section 7.6, we compare 24puz to similar transient classes, constrain the rate of 24puz-like events, and comment on the most likely kind of compact object powering the event. Finally, we present our conclusions and future prospects in Section 7.7.

We adopt the Planck2015 (414) cosmology with  $H_0 = 67.7 \text{ km s}^{-1}$  and  $\Omega_M = 0.3075$ . We correct for Milky Way extinction using the (361) extinction law with  $A_V = 0.1 \text{ mag}$  and  $R_V = 3.1$  (501).

## 7.2 Discovery

AT 2024puz was the first discovery from an ongoing, real-time search for hostless or highly offset, consistently blue, optical transients with ZTF ((124–127)). ZTF conducts several public and private surveys using the Palomar 48-inch Schmidt telescope (287). The public survey covers the northern sky once every 2 days in the g and r bands, while private surveys include i-band as well as high cadence observations of smaller areas. We identify candidates in ZTF alert photometry from the kowalski broker (503, 504). Our cuts are identical to those for the TDE sample in (134) (see Section 2.2), except that we require a significant offset from the nearest PanSTARRS source ( $>10''$ ). The goal of this search is to identify TDE-like events that are either at higher redshift or in low mass galaxies.

We manually scan through the resulting candidates on a  $\sim$ weekly basis using the `fritz.science` instance of the SkyPortal platform (503, 504). We identify sources that have lightcurves that are inconsistent with a Cataclysmic Variable, which form our main background. We do this by rejecting sources that have no observations during the flare rise and a perfectly linear decay (by eye) in magnitude space, with no color evolution. We obtain rapid follow-up with the Spectral Energy Distribution Machine (SEDM) on the Palomar 60-inch telescope (505, 506) and/or the Low Resolution Imaging Spectrometer (LRIS) on the Keck I telescope (182), with some dependence on our telescope allocations. We rule out any objects with spectra that have features that are well-modelled as a supernova or that are at  $z \approx 0$ . We continue to follow-up any remaining sources.

24puz was first reported on the Transient Name Survey by (507) on 2024-07-20 or MJD 60511 and was the first source to pass all these cuts, a few months after we began

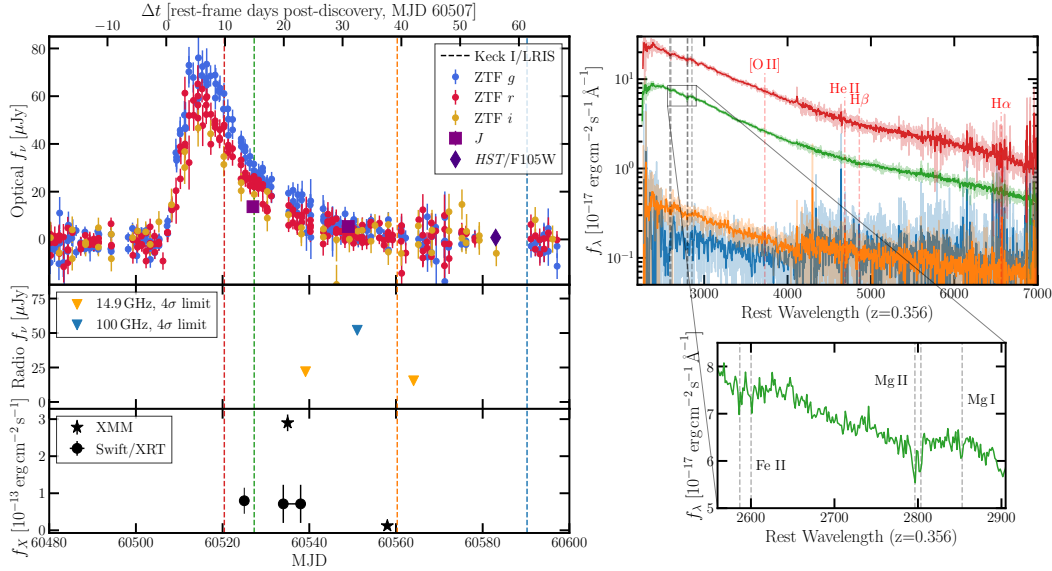


Figure 7.1: Summary of emission from 24puz. The *left* panel shows the ZTF lightcurve on the *top* panel, the radio/millimeter upper limits in the *middle* panel, and the 0.3 – 10 keV Swift/XRT and XMM-Newton lightcurves in the *bottom* panel. The X-ray fluxes are computed as the unabsorbed flux assuming a  $\Gamma = 1.77$  power-law. The two Swift/XRT observations that are joined together by a line were individually non-detections, so we show the flux measured by stacking the two observations, which is significant. Dates of Keck I/LRIS spectroscopy are shown as dashed lines. The *top right* panels shows the optical spectral sequence, which no significant features detected. The solid lines are smoothed by a Gaussian with width of 5 pix. The faded lines show the unsmoothed spectra. Commonly detected transient lines are shown as dashed red lines, none are detected. The apparent line in the red, MJD 60520 spectrum near 4000 is a poorly subtracted sky line. The *bottom right* panel shows a zoom-in on the detected absorption lines, with the lines labeled in grey.

our search. The ZTF lightcurve for this source (described in detail below) is shown in the top left panel of Figure 7.1. We initiated an expansive multiwavelength follow-up for 24puz upon obtaining a Keck I/LRIS spectrum that showed a featureless spectrum with galaxy ISM absorption features at  $z = 0.356$ . Figure 7.2 compares the optical properties of 24puz to other classes of featureless, blue transients (LFBOTs and TDEs), we will discuss this figure in detail in Section 7.6, but include it here for context.

The first ZTF forced-photometry detection ( $>3\sigma$ ) of 24puz occurred on MJD 60507, or 2024-07-16. We adopt this MJD as the discovery date  $t_0$  throughout this work.

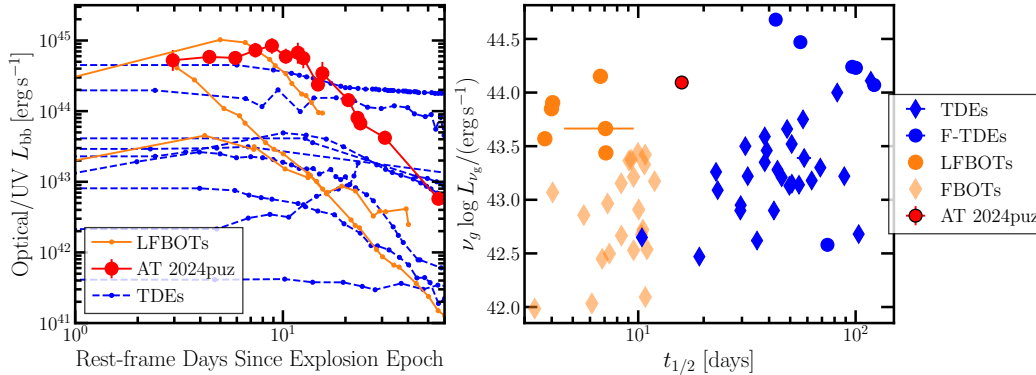


Figure 7.2: Comparison between the optical/UV emission from 24puz and LFBOTs/TDEs from (134, 490, 492, 502). In all panels, LFBOTs are shown in orange, TDEs are shown in blue, and 24puz in red. The *left* panel shows the black body luminosity evolution. LFBOTs show rapid fading with a similar late-time power-law decay as 24puz, but on overall slower timescales and typically with fainter luminosities. TDEs show a range of lightcurve shapes, which generally evolve slower than that of 24puz. Some TDEs show a rapid fade like 24puz, but these are all at least one order of magnitude fainter than 24puz. These trends are highlighted in the *right* panel, which shows the peak  $g$ -band luminosity versus time above half-peak luminosity. We also include fast blue optical transients (FBOTs) as faint diamonds. TDEs are divided into featureless TDEs (F-TDEs, circles), which show featureless spectra like 24puz, and those that have transient spectral features (diamonds). 24puz is intermediate to LFBOTs and TDEs, and is notably more luminous than all events at a similar timescale and is much faster evolving than F-TDEs.

### 7.3 Multiwavelength Observations and Data Reduction

In this section, we summarize archival and follow-up observations and our data reduction procedures.

#### Zwicky Transient Facility

While we discovered 24puz in alert photometry from ZTF, we perform all analysis using forced photometry from the IPAC ZTF forced photometry server (288) in the  $gri$  bands. This server performs point spread function photometry on ZTF difference images. We processed the resulting lightcurve following recommended procedures<sup>1</sup> and it is shown in Figure 7.1.

#### Palomar 60in. Rainbow Camera

We obtained optical  $ugri$  photometry of 24puz with the Spectral Energy Distribution Machine rainbow imager on the Palomar 60in. telescope (PI: R. Stein; (505)). The

<sup>1</sup>[https://irsa.ipac.caltech.edu/data/ZTF/docs/ztf\\_forced\\_photometry.pdf](https://irsa.ipac.caltech.edu/data/ZTF/docs/ztf_forced_photometry.pdf)

observations are summarized in Table 7.4. We reduce the data using the automated pipeline<sup>2</sup>.

### **Palomar 200in. Wide Field Infrared Camera**

We observed 24puz with the Wide Field Infrared Camera (WIRC) on the Palomar 200 inch (P200) telescope on MJDs 60526 (2024-08-04; PI S. Ocker) and 60546 (2024-08-24; PI V. Ravi). We used the *J*-band and exposure times of 1620 and 6525 sec, respectively. We reduced both epochs using the `irImagePipe` code (508) using default settings, including flux calibration against sources from the Two Micron All Sky Survey (2MASS) catalog (509). We measured the source flux in an aperture of radius 7 pix. and subtracted the median background in an annulus of [10, 50] pix. The source was detected at *J*-band flux densities of  $14.2 \pm 1.6$  and  $5.9 \pm 1.2 \mu\text{Jy}$  in each epoch.

### **The Neil Gehrels Swift Observatory**

We obtained observations of 24puz with the Neil Gehrels Swift Observatory (Swift; (510)) through ToOs 20912 and 20962 (PI Somalwar, object ID 16746). The observations are summarize in Table 7.8 and Table 7.7. The X-Ray Telescope (XRT) was used in photon counting mode and the Ultra-violet Optical Telescope (UVOT) observations used the `u`, `uvm2`, `uvw1`, and `uvw2` filters.

We first describe the UVOT data reduction and then the XRT. For UVOT, we used the default data reduction provided by the observatory. We measured the source flux in all bands using an aperture centered on the position of 24puz with radius 5'' and a background region offset from the source region with radius 20''. We used the `uvotsource` tool in `heasoft` (v6.34) to perform the photometry. We used the `ssstype=high` flag to reject observations where the transient was located in a low sensitivity region. The measured fluxes for all good observations are detailed in Table 7.7.

We processed the XRT data using the online Swift/XRT data products tool<sup>3</sup>. We used the `lightcurve` tool to measure the count rate in each observation, adopting the ZTF coordinates of 24puz and a  $3\sigma$  detection threshold. We used default settings and binned by observation ID. We converted counts to fluxes assuming a power-law spectrum with photon-index  $\Gamma = 1.7$ , motivated by our X-ray spectral modeling in Section 7.5, and Milky-Way absorption with  $n_H = 2.88 \times 10^{20} \text{ cm}^{-2}$  (185). The

<sup>2</sup><https://sites.astro.caltech.edu/sedm/Pipeline.html>

<sup>3</sup>[https://www.swift.ac.uk/user\\_objects/](https://www.swift.ac.uk/user_objects/)

resulting count rates and upper limits are shown in Table 7.8.

### **The XMM-Newton Telescope**

We observed 24puz with the XMM-Newton telescope on the dates and with the exposure times listed in Table 7.9. We used the thin filters for all observations. We retrieved the PPS data for each observation from the XMM-Newton archive. For each epoch, we extracted a spectrum of 24puz following recommended procedures<sup>4</sup>, including flagging bad time intervals using the `tabtigen` command with a rate upper limit found by manual inspection of the lightcurve. We process the data from all three EPIC cameras and perform all fitting to the data from the three detectors together. We centered the source apertures on the ZTF position of 24puz and used radii of 20'' to avoid contamination from a nearby source. We used 30'' background regions close to the source but uncontaminated by any nearby sources. Our first EPIC-PN exposure had the strongest contamination and so the effective exposure time quoted in Table 7.9 is lower than the on-source time as observed by the telescope.

### **The Nuclear Spectroscopic Telescope Array**

The *Nuclear Spectroscopic Telescope Array* (*NuSTAR*) is a hard X-ray telescope, with two independent detectors known as Focal Plane Module (FPM) A and B, observing between 3–79 keV (511). We obtained two observations approximately a day apart, details in Table 7.10. We reduced the observations with the data reduction software *NuSTARDAS* v2.1.2, with *CALDB* v20240520. For each observation, we used the *NUPIPELINE* task to produce a cleaned event list from each detector. From these event lists, we extract events from a 60'' circular region around the expected source location, and also from a 60'' circular background region located close to the source region on the detector. We report the observed count rates from each region on each detector in Table 7.10. As none of the detectors showed a clear detection, we use the method of (512) to estimate the 90% upper confidence limit for the number of counts seen by each *NuSTAR* detector.

### **The Low Resolution Imaging Spectrometer**

We obtained both optical spectra and photometry for 24puz with the Low Resolution Imaging Spectrometer (LRIS) on the Keck I telescope (182) (PI: V. Ravi). The observations are summarized in Table 7.11.

---

<sup>4</sup><https://www.cosmos.esa.int/web/xmm-newton/sas-threads>

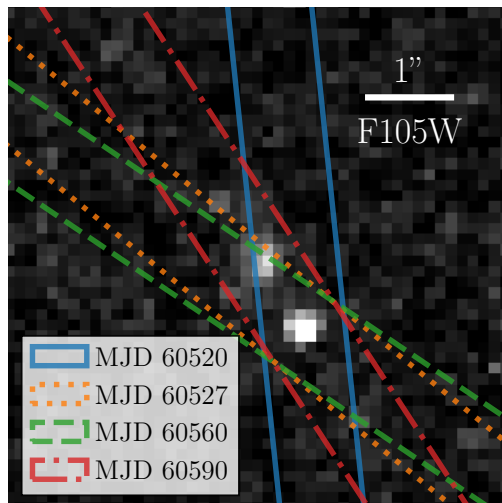


Figure 7.3: Position angle of the Keck I/LRIS longslit for each observation, overlaid on the *HST*/WFC3 F105W observation. 24puz is towards the bottom right corner of the image whereas the galaxy is in the center. The MJD 60590 observation longslit was positioned to include the nearby galaxy and 24puz.

We centered all observations on the transient location as measured by ZTF. The slit angle was set to parallactic for all observations except MJD 60590, for which we set the angle to  $337.18^\circ$  to include the closest galaxy to 24puz that is detected in our *Hubble Space Telescope* (*HST*) observations, described later in this section. The slit positions are shown in Figure 7.3. We used the 400/3400 grism, the 400/8500 grating with central wavelength 7830, and the 560 dichroic. We reduced the observations using the `lpipe` data reduction pipeline (291) with default settings.

The resulting wavelength range from  $\sim 3100 - 10000 \text{ \AA}$  and the resolution  $R \approx 700$ . Our spectroscopic observations are summarized in Table 7.11. The slit positions are overlaid on a *Hubble Space Telescope* image of the transient in Figure 7.3.

### The Lowell Discovery Telescope

We obtained observations of 24puz with the Large Monolithic Imager (LMI) mounted on the 4.3-m Lowell Discovery Telescope (LDT; PI E. Hammerstein) on 2024-08-27. We reduced the LDT data using standard data reduction techniques, including bias subtraction, flat-fielding, and cosmic ray rejection. We used the `Scamp` code to align frames and the `Swarnp` code to combine. We flux calibrate using the PanSTARRS DR2 catalog. The data is summarized in Table 7.5.

### **The Liverpool Telescope**

We obtained imaging of 24puz in the  $u$ ,  $g$ ,  $r$ , and  $i$  bands with the Liverpool Telescope (LT; PI C. Angus) between Aug. 5 2024 and Aug. 20 2024. All raw LT images were reduced using standard reduction techniques, and aperture photometry was performed using the ‘Photometry Sans Frustration’ pipeline (PSF; 513), using a PSF optimized aperture and archival images from the Sloan Digital Sky Survey (SDSS; 514) for template subtraction. The observations are summarized in Table 7.6.

### **The Hubble Space Telescope**

We observed 24puz for two orbits with four bands using the Wide Field Camera 3 on the *Hubble Space Telescope* on Sept. 30, 2024 (PID 17854, PI Somalwar). The data is summarized in Table 7.12. We retrieved the reduced data from the mast archive. From some basic data quality checks, we concluded that all the default data was sufficient for our analysis, except the IR/F160W image. This image suffered from scattered light, so we followed recommended procedures to manually flag the individual reads that were most affected and then redrizzled the data using recommended parameters <sup>5</sup>.

The transient was significantly detected ( $> 5\sigma$ ) in all images, alongside many other sources. We performed aperture photometry for both the transient and all other sources in the image using the *sep* package (515, 516). We first background subtract each image using background boxes of size  $32 \times 32 \text{ pix}^2$  and a smoothing kernel of  $3 \times 3 \text{ pix}^2$ . We also measure the uncertainty in the images using these parameters. We detect sources on the F606W image, because of its combination of resolution and sensitivity. We verify by eye that we are not missing any IR or UV-bright sources because of this choice. We extract sources within  $200''$  of the transient (1 Mpc at  $z = 0.356$ ) using a  $3 \times 3$  smoothing kernel and requiring at least 5 pixels above  $1.5\sigma$ . We measure elliptical kron radii using *sep*. We then perform aperture photometry using the *photutils* package. We use elliptical apertures scaled to twice the kron radii, which should include  $\sim 90\%$  of the enclosed flux for typical galaxies. For the IR images, which have poorer spatial resolutions, we increase the aperture radii by the quadrature difference of the IR and F606W PSFs. We measure the background around each source and the local flux uncertainty using the mean and root-mean-squared error in a circular aperture from  $1.8'' - 3''$ , centered on each source. We reject any source that is not detected at a  $3\sigma$  level in at least 3

<sup>5</sup>see [https://github.com/spacetelescope/WFC3Library/tree/main/notebooks/ir\\_scattered\\_light\\_calwf3\\_corrections](https://github.com/spacetelescope/WFC3Library/tree/main/notebooks/ir_scattered_light_calwf3_corrections) for details

bands.

For most of the sources in the images, our goal is to measure approximate stellar masses (to be described in Section 7.4) and half-light radii. We measure half-light radii using the `sep_flux_radius` function. For the transient, we modify our photometry slightly. We adopt a circular aperture with radius twice the kron radius. We then correct the photometry in each band for the encircled energy curves provided by *MAST*.

### **The Very Large Array**

We observed 24puz with the Jansky Very Large Array (VLA) on MJDs 60539 (2024-08-17; PI Somalwar, Project 24B-456) and 60564 (2024-09-11; PI J. Somalwar, Project 24B-456). The VLA was in B configuration and we observed in the Ku band. We used J1740+5211 as a gain calibrator and 3C286 as a flux calibrator. We followed recommended procedures for high frequency observations. We manually reduced each epoch using the `casa` package (384) version 6.5.3.28 following recommended procedures. No source was detected in a 5'' box around the known transient location in either observation. The root-mean-square (RMS) uncertainties were 5.5, 3.8  $\mu\text{Jy}$ , respectively. We set  $4\sigma$  upper limits of  $< 22, 15.2 \mu\text{Jy}$  respectively, where we adopt the rms measured in a 30'' box.

### **The Northern Extended Millimetre Array**

We observed 24puz with the Northern Extended Millimetre Array (NOEMA) on MJD 60551 (2024-08-29) at 100 GHz with proposal D24AB (PI: V. Ravi), using a standard continuum setup. We used MWC349 as the flux calibrator, and 1739+522 as the gain calibrator. The observations were reduced using the standard NOEMA pipeline. No source was detected in a 5'' box around the known transient location in either observation, with an RMS of 13  $\mu\text{Jy}$ . We set a  $3\sigma$  upper limit of  $< 52, \mu\text{Jy}$ , where we adopt the rms measured in a 20'' box.

## **7.4 Data Analysis**

In this section, we describe the physical properties of 24puz and its environment that can be inferred from our observations. We begin with constraints on the redshift and host galaxy of 24puz. Then, we consider the transient emission. We first discuss the ultraviolet-infrared lightcurve, followed by the limits on transient optical spectral features, the X-ray lightcurve and spectral evolution, and finally the implications of the radio limits.

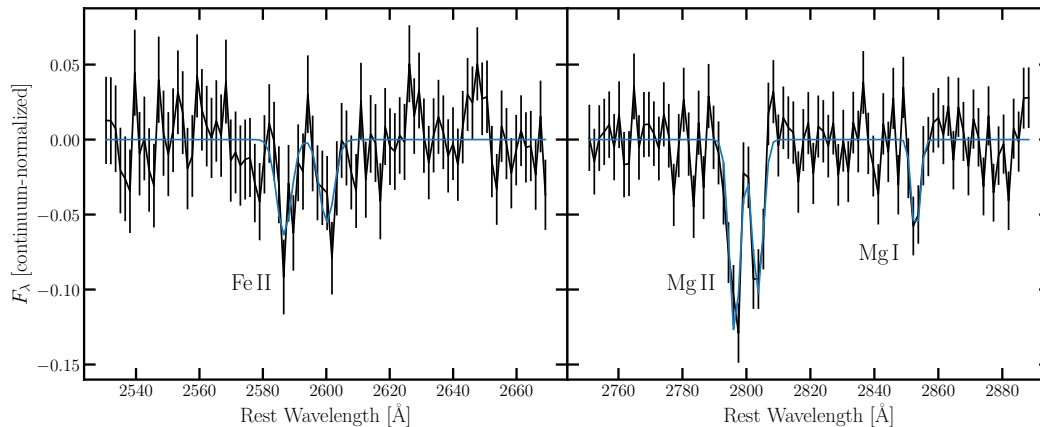


Figure 7.4: Fits to the absorption lines Fe II  $\lambda\lambda$ 2586, 2600, Mg II  $\lambda\lambda$ 2796, 2803, and Mg I  $\lambda$ 2852. The spectra are fit as linear continuum components and Gaussian lines, as described in Section 7.4. The Gaussian widths and redshifts are fixed to the same value for all lines. The best fit redshift is  $z = 0.35614 \pm 0.00009$ . The Mg II absorption is consistent with a strong-absorber ( $EW_{2796} = 0.753 \pm 0.104 \text{ \AA} > 0.3 \text{ \AA}$ ), suggesting that this absorption is more likely occurring within the nearest galaxy to 24puz (G1) or a nearby group/cluster.

### Host galaxy and environment

In this section, we identify possible host galaxies of 24puz. We first constrain the redshift of 24puz using the detected ISM absorption lines. Then we consider whether 24puz is associated with a galaxy (or galaxy overdensity) that is detected in imaging of the field. We finally constrain the possibility that 24puz is associated with an undetected (i.e., faint and/or compact and obscured by the transient) host galaxy.

### Optical spectroscopy: ISM Absorption and redshift constraints

Table 7.1: Absorption line equivalent widths

Line	Equivalent Width [ $\text{\AA}$ ]
Fe II $\lambda$ 2586	$0.502 \pm 0.148$
Fe II $\lambda$ 2600	$0.438 \pm 0.14$
Mg II $\lambda$ 2796	$0.753 \pm 0.104$
Mg II $\lambda$ 2803	$0.599 \pm 0.099$
Mg I $\lambda$ 2852	$0.286 \pm 0.098$

**Notes.** The line redshifts were tied together in fitting. The line widths were tied together for doublets, but were otherwise allowed to float freely. The best-fit redshift was  $z = 0.35614 \pm 0.00009$ .

In this section, we measure the redshift and equivalent widths of the ISM absorption lines detected in the spectra of 24puz, as shown in Figure 7.4. We consider the Fe II  $\lambda\lambda$ 2586, 2600, Mg II  $\lambda\lambda$ 2796, 2803, and the Mg I  $\lambda$ 2852 lines. We do not detect any Ca absorption. We measure these lines using our spectrum from MJD 60527.3, which is the deepest spectrum we obtained that includes bright transient emission (as required to detect the absorption lines). We fit the spectrum in the regions [2630 Å, 2670 Å] and [2760 Å, 2880 Å], which include sufficient continuum to perform a local continuum fit around each line. We model the continuum in each region separately as first degree polynomials. We chose these continuum models as the lowest degree polynomials required such that the  $\chi^2/\text{dof}$  was consistent in each region with a p-value  $> 10\%$ . We fit each absorption line as a Gaussian. The Gaussian amplitudes were independent. The widths were tied for lines within doublets but were otherwise free. We perform the fit using the `scipy` least-squares function and report best-fit equivalent widths and  $1\sigma$  uncertainties in Table 7.1. The fit is shown in Figure 7.4. The best-fit redshift was  $z = 0.35614 \pm 0.00009$ . The lines are largely unresolved. The  $\chi^2/\text{dof}$  of the final fit was 140/167, for a fully consistent p-value of 0.94.

The Mg II  $\lambda$ 2796 equivalent width is  $\text{EW}_{2796} = 0.753 \pm 0.104 \text{ \AA}$ , placing the absorber in the class of strong absorbers ( $W_{2796} \gtrsim 0.3 \text{ \AA}$ ; (517)). This gas could originate from the host galaxy of 24puz or from the extended circumgalactic medium of a nearby galaxy/galaxy group. We will discuss these possibilities in the following section.

### ***HST* imaging: nearby galaxies and probability of association**

We next consider the galaxies detected in our deep *HST* imaging of the field of 24puz (zoom-in in Figure 7.5). We will show that 24puz is likely associated with a detected galaxy, and in the following sections we will identify and characterize the galaxy that is the most likely host. Henceforth, we will call the nearest galaxy to 24puz in projected distance “G1”.

In Appendix 7.8, we show that the probability of 24puz randomly lying at its location relative the G1 is  $p_1 = 3 \times 10^{-4}$ . We also show that the probability that all the second through tenth-nearest neighbors are closer than those observed for 24puz is small:  $p_{2-10} = 1.3 \times 10^{-3}$ . It is thus  $\gtrsim 3\sigma$  unlikely both that 24puz lies close to the observed galaxies by chance.

Given that the probability of 24puz randomly lying near both the nearest and the

second-tenth nearest neighbors is low, 24puz is likely part of a galaxy group or cluster. The closest cataloged galaxy group is centered at a  $5.89'$  offset and at spectroscopic redshift  $z = 0.354$ , corresponding to a 1.8 Mpc projected distance (518, 519). This redshift is fully consistent ( $<1\sigma$ ) with the ISM/CGM absorption lines in the spectrum of 24puz at  $z = 0.35614 \pm 0.00009$ . The reported mass and radius of this structure are  $M_{500} = 8.5 \times 10^{13} M_{\odot}$  and  $r_{500} = 0.612$  Mpc (519). The projected offset between 24puz and this group is large: 1.8 Mpc corresponds to  $2.9r_{500}$ . 24puz is well outside the virial radius of the group (note that  $r_{200} \approx (1.4 - 2)r_{500}$ , so the offset is  $\sim(1.5 - 2)r_{200}$ ). 24puz may be associated with a structure that is infalling into this group, or it may be unassociated and instead part of a smaller, nearby group that is undetectable in X-ray or spectroscopic group catalogs.

Even though 24puz may not be associated with this group, the Mg II absorber that is detected in our optical spectroscopy could be associated with the group at 1.8 Mpc. If the Mg II absorber is associated with the group, it is possible that we are simply unlucky and 24puz is a background source at  $z \gtrsim 0.356$  that happens to lie along the line-of-sight of this group. At a 1.8 Mpc =  $2.9r_{500}$  projected offset from a low-mass cluster, the covering fraction of Mg II absorbers is low:  $<1\%$  (520). It is unlikely that 24puz would happen to lie along such a line of sight, unless it is associated with a structure (e.g., a galaxy) that hosts Mg II absorbers. As we will discuss, 24puz is coincident with a galaxy, so it is feasible that the absorber is within this galaxy (521).

Thus, regardless of the precise large-scale structure that 24puz is associated with, we can come to some reasonable conclusions. First, 24puz is unlikely to be randomly associated with the galaxies in the field. Second, the ISM/CGM absorption lines at  $z = 0.35614 \pm 0.00009$  are unlikely to be associated with an absorber in the nearby group given the large projected offset, and instead are probably associated with a galaxy or galaxy group closer to 24puz. We can then reasonably assume that 24puz is located within a more nearby galaxy or group, and is thus also at  $z = 0.35614 \pm 0.00009$ . We adopt the assumption that 24puz is at this redshift for the rest of this work.

### Host Galaxy Candidates

From the previous section, we have concluded that 24puz is likely hosted by a large-scale structure at  $z = 0.35614 \pm 0.00009$ . Now, we narrow down the association:

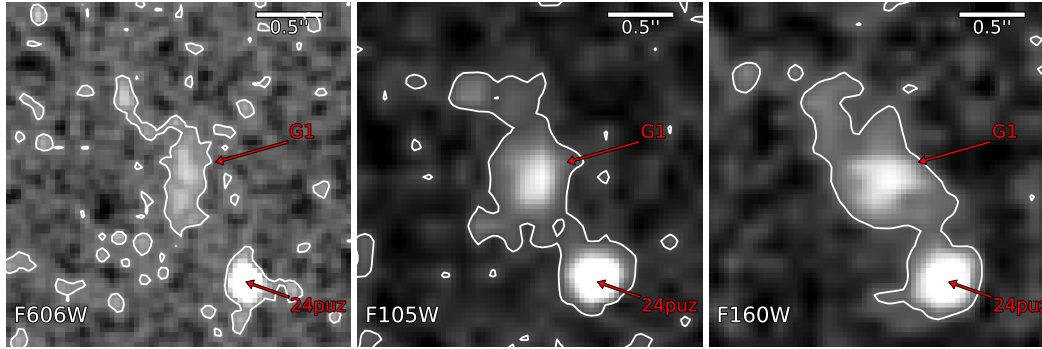


Figure 7.5: Morphology of the nearest galaxy to 24puz, which we name G1. We show *HST*/WFC3 imaging of G1 in the F606W (*left*), F105W (*middle*), and F160W (*right*) bands. These images were taken 56 rest-days post-discovery. We have reprojected all images to the F606W pixel scale for ease of comparison, but this means that the F105W and F160W have been resampled to a smaller pixel scale than the original images. G1 and 24puz are labeled. The white lines show contours, which highlight the morphology of G1. In all bands, there is an extended tidal tail or other irregular component towards the top left of G1. The contour levels are shown for visualization but are not intended to represent sigma levels.

24puz is either an object that (1) is gravitationally bound to a galaxy, like a star or stationary BH; or, (2) ejected, like a recoiling BH or NS. In the former case, we expect 24puz to be within, roughly, the virial radius of its host. In the latter, 24puz may be offset from its host galaxy.

We first consider the case where 24puz is bound to a galaxy. We have named the closest galaxy (in projected distance) to 24puz “G1”. 24puz is at a  $\sim 5$  kpc offset from G1, assuming  $z = 0.356$ . We model our *HST*/F606W image of G1 with a Sersic profile, in addition to a Moffat profile to represent 24puz. 24puz is located at  $\sim 3$  projected half-light radii from G1.

In the previous section, we showed that the random association probability with G1 is low ( $p_1 = 3 \times 10^{-4}$ ), assuming a uniform probability of 24puz occurring at any point in the field. The galaxy with the second-lowest chance association probability has  $p_2 = 0.02$ , a factor  $\sim 70\times$  higher. If 24puz has a higher probability of occurring within the virial radius of the other galaxies in the field, the probability of chance association with G1 would *decrease*. Thus, even though there are many galaxies within a virial radius of 24puz, G1 is the most likely host.

We next consider the case that 24puz is produced by an astrophysical object that has received a kick velocity after a dynamical event (a merger, binary/triple inter-

actions (e.g. 522, 523)). In this case, the offset distribution depends on the type of astrophysical object and the process that caused the kick. If 24puz is kicked but it still associated with G1, we require a low velocity kick  $\lesssim 100 \text{ km s}^{-1}$ : the observed offset is 5 kpc, so for a mean kick velocity  $v_k$ , we have a mean delay time  $\sim 60 \text{ Myr} \times \frac{v_k}{100 \text{ km s}^{-1}}$ . Note that G1 is a dwarf galaxy with low escape velocity  $\lesssim 150 \text{ km/s}$ . If the kick velocities are  $v_k \gg 100 \text{ km s}^{-1}$  or the delay times  $\sim$ giga-years, then 24puz cannot be associated with G1. While we cannot exclude this case, the problem of the low probability of chance association with G1 remains. Thus, we still prefer a physical association with G1, and thus small kick velocity and delay time.

Based on these arguments, we will cautiously associate 24puz with G1 for the rest of this work.

### Host Galaxy Physical Properties

In this section, we analyze the photometric properties of G1. For completeness, we also constrain the presence of a stellar overdensity (e.g., a stellar cluster) at the location of 24puz, but the luminous emission from 24puz precludes any strong photometric constraints on the overdensity.

We first consider the morphology of G1. In Figure 7.5, we show zoom-ins of G1 in the F606W, F105W, and F160W bands. The F606W image is smoothed with a Gaussian kernel of width 0.9 pix for visualization. All images have been reprojected onto the frame of the F606W image. Contours are overlaid on each image to guide the eye. While the low signal-to-noise of the G1 detection combined with the insufficient resolution in the redder bands preclude quantitative modelling of the structure of G1, the images suggest a faint source detected near G1, which may be connected to G1 via a low surface brightness tail. We cannot confirm this, however, due to the low signal-to-noise of the image: we require deep, space-based follow-up. G1 may be in an interacting pair, have tidal tails, or simply be near a background galaxy. We favor one of the former two scenarios, particularly given the evidence that 24puz is in a galaxy group. The chance association probability of a background galaxy with G1 is even lower than that of 24puz, given the proximity of the candidate background galaxy.

Next, we consider the stellar mass and age of G1. We model the *HST* photometry of G1, including an upper limit from the F336W band, as a simple stellar population. The lack of wavelength coverage and high signal-to-noise observations prevents

more detailed modeling. We use the `prospector` code (190, 524, 525). We set a normal redshift prior at  $z = 0.35614 \pm 0.00009$ . We do not include host galaxy extinction, given the lack of photometric constraints on G1 and the low extinction level implied by the UV/optical SED of 24puz, but we do include Milky Way extinction with  $A_V = 0.1$  mag and  $E(B - V) = 0.03$  mag (501). We allow the redshift, galaxy age, galaxy metallicity, and galaxy mass to float. We require that the galaxy age is smaller than the age of the universe at each redshift. We fit the data using the `dynesty` code using the random walk sampling, 400 initial live points and 200 live points per batch (206, 365, 526).

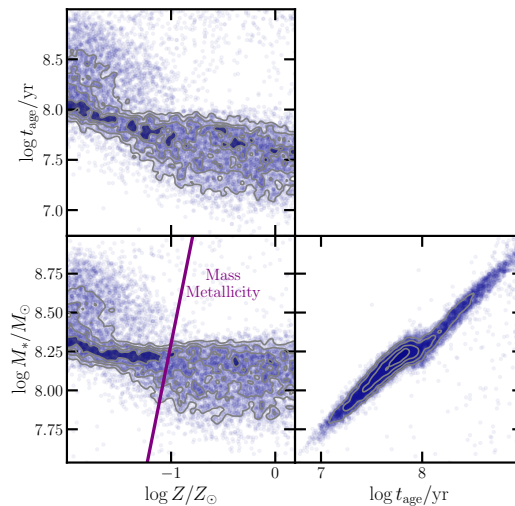


Figure 7.6: Constraints on the stellar population of G1. We assume a simple stellar population, due to a lack of constraints on the galaxy emission. The corner plot shows the distribution of possible stellar ages ( $t_{\text{age}}$ ), metallicities  $Z$ , and stellar masses  $M_*$  with grey contours overlaid. The mass-metallicity relation from (527) is shown in dark purple. We find that G1 is a dwarf galaxy with  $M_* \lesssim 10^{8.75} M_\odot$ . If it lies on the mass-metallicity relation, then the mass is  $10^{7.75} \lesssim M_*/M_\odot \lesssim 10^{8.25}$  and the age  $t_{\text{age}}/\text{Myr} \sim 100$  Myr.

The results are shown in Figure 7.6. There are strong degeneracies between the stellar mass, age, and metallicity, but we can draw some conclusions. First, G1 is a dwarf galaxy, with a stellar mass  $M_* \lesssim 10^{8.75} M_\odot$ . If G1 lies on the mass-metallicity relation from (527), then the stellar mass is  $10^{7.75} \lesssim M_*/M_\odot \lesssim 10^{8.25}$ . In this case, the stellar population age is  $10 \lesssim t_{\text{age}}/\text{Myr} \lesssim 100$  Myr, although the upper end of this range is preferred.

We briefly consider a stellar population that is hidden beneath the transient emission from 24puz. Because 24puz was still luminous during our *HST* observations, our

constraints are weak. As we will discuss in Section 7.4, however, 24puz shows an evolving red excess. A component, however, could also be produced by a stellar population. We model this by assuming that all the emission in the F105W and F160W bands is produced by stars, with no transient component. This will give us a rough estimate on the maximum mass expected. We use the F336W and F606W constraints on the transient emission as upper limits. We find a 99% mass upper limit  $M_* < 10^{8.9} M_\odot$ ; i.e., a compact dwarf galaxy or stellar cluster could be present. Deep, space-based follow-up once the transient emission has faded will be critical for constraining the stellar population at the location of 24puz.

We conclude that G1 is a low mass dwarf galaxy with a moderately young stellar population. Current constraints on any stars hidden underneath the transient emission allow for a compact dwarf galaxy or stellar cluster, with a mass upper limit  $M_* < 10^{8.9} M_\odot$ .

### Star formation rate constraints

Table 7.2: Emission line fluxes

Date	$\Delta t$ [days]	$L_{H\alpha}$ [ $10^{40} \text{ erg s}^{-1}$ ]	$\text{SFR}_{H\alpha}$ [ $M_\odot \text{ yr}^{-1}$ ]	$L_{[\text{O II}]}$ [ $10^{40} \text{ erg s}^{-1}$ ]	$\text{SFR}_{[\text{O II}]}$ [ $M_\odot \text{ yr}^{-1}$ ]
2024-07-29	60520.4	< 3.04	< 0.09	< 2.62	< 0.17
2024-08-05	60527.3	< 1.44	< 0.04	< 1.0	< 0.07
2024-09-07	60560.3	< 0.65	< 0.02	< 0.19	< 0.01
2024-10-07	60590.2	< 1.56	< 0.05	$0.15^{+0.05}_{-0.05}$	$0.01^{+0.003}_{-0.003}$

**Notes.** Line emission and star formation rate constraints. All luminosities are in units of  $10^{40} \text{ erg s}^{-1}$  and star formation rates in units of  $M_\odot \text{ yr}^{-1}$ .  $\Delta t$  gives rest-frame days post-discovery.

We constrain the star formation rate at the location of 24puz by constraining the  $H\alpha$ ,  $H\beta$ , and  $[\text{O II}] \lambda\lambda 3726, 3729$  luminosities from our LRIS spectra. Note that the slits for each spectrum were positioned differently. All the spectra were centered on 24puz and contained fractions of G1. The MJD 60590 (61.4 rest-days) spectrum was positioned to fully cover both 24puz and G1. We will consider each spectrum separately, given the different fractions of G1 included in the slit.

We fit each spectrum after continuum subtraction. We model the continuum by convolving each spectrum with a Gaussian kernel of width 50 pixels and subtracting this from the spectrum. We fit  $H\alpha$  and  $H\beta$  simultaneously because they are expected to have correlated luminosities: we fit for the  $H\alpha$  luminosity, denoted  $L_\alpha$  and fix the  $H\beta$  luminosity  $L_\beta = L_\alpha/2.86$ , where we have adopted the theoretical Balmer

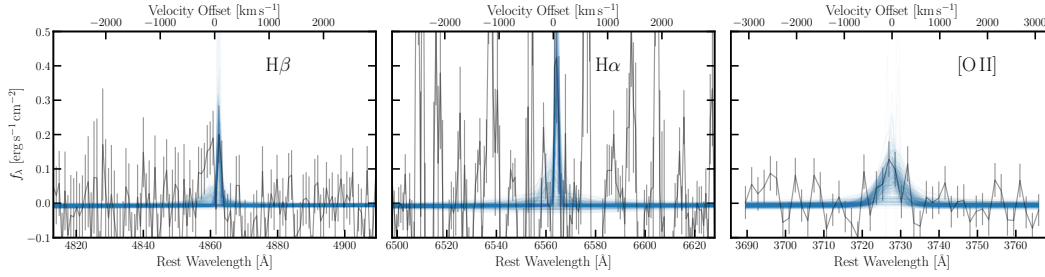


Figure 7.7: Emission line fits to the optical spectrum of 24puz from MJD 60590.2, or 61.4 rest-days post-discovery. Fits to  $H\beta$ ,  $H\alpha$  and the  $[O II] \lambda\lambda 3726, 3729$  doublet are shown in the *left*, *middle*, and *right* panels respectively. The data is shown in black. The amplitudes of the Balmer lines are tied to the expected ratio for star formation and the ratio of the  $[O II]$  doublet amplitudes are likewise tied. The apparent line at the location of  $H\beta$  is a sky subtraction artifact — re-reducing the spectrum with different sky subtraction algorithms removes this feature. The  $[O II]$  line, on the other hand, is robust to sky subtraction. Blue lines show samples from our Gaussian emcee fits.

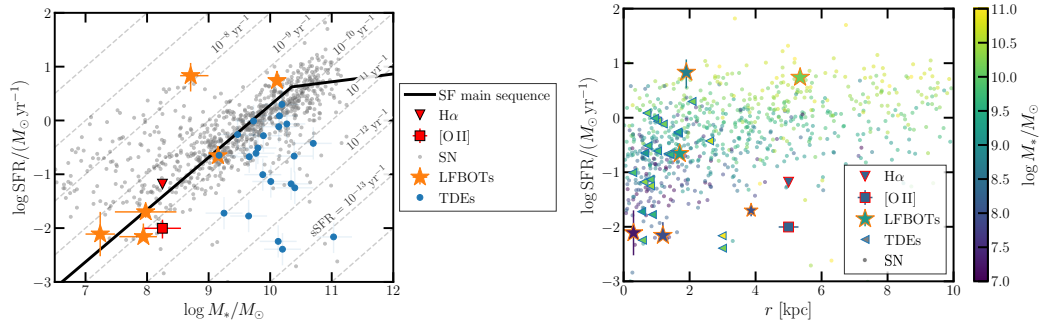


Figure 7.8: *Left*: Star-formation vs stellar mass of G1 relative to other galaxy populations. Constraints from the optical spectroscopy of G1 are shown in red. LFBOT hosts from (487, 489, 491, 495, 528, 529) are shown in orange and TDE hosts from (134) in blue. The core-collapse supernova host galaxy sample from (530) is shown in grey. Lines of constant specific star formation rate (sSFR) are shown in grey dashed. 24puz lies below the star forming main sequence. Its location is consistent with LFBOT host galaxies, but is at a low sSFR and stellar mass relative to core-collapse supernova hosts and a low stellar mass relative to TDE hosts. *Right*: Star-formation vs physical offset from host galaxy of 24puz relative to other populations. The format is the same as in the *left* panel, except that we have colored the points by their stellar mass but left the marker outline colors the same as in the *left* panel. For TDEs, we assume a host galaxy offset  $< 0.6''$ . The LFBOT AT 2020xnd does not have a reported offset so we assume that it is  $\lesssim 1''$ , based on a by-eye approximation from images in (528). 24puz is at a larger offset than expected from its host galaxy mass, if it is associated with a star-forming region.

decrement commonly assumed for star-formation (computed assuming photoionized gas at temperature  $10^4$  K; (416)). This Balmer decrement assumes no host galaxy extinction. We separately fit a Gaussian at the locations of [O II]  $\lambda\lambda 3726, 3729$  and we tie the doublet ratio to be  $L_{3726}/L_{3729} = 0.35$  (416). We allow the widths of the lines to vary between  $\sigma_v \in [90, 600]$  km s $^{-1}$ . We assume a redshift  $z = 0.356$  but allow the line centroids to vary by  $\Delta_v \in [-150, 150]$  km s $^{-1}$ . These velocities are assumed to be the same for the Balmer lines but are allowed to be different for [O II]  $\lambda\lambda 3726, 3729$ . We adopt a linear model to absorb any residual continuum. We fit regions of each spectra corresponding to  $10^4$  km s $^{-1}$  around each relevant line. We use the emcee sampler with default settings to perform the fit independently for each spectrum (195). We used 200 walkers and 7000 burn-in steps, followed by an additional 5000 steps. We thinned the resulting chains by a factor of thirteen.

The fit results are summarized in Table 7.2. The only  $3\sigma$  line detection was [O II]  $\lambda\lambda 3726, 3729$  in the MJD 60590 (61.4 rest-days) spectrum. Assuming that the [O II] luminosity correlates with star formation rate as  $\text{SFR} = 6.58 \times 10^{-42} L([\text{O II}]) / (\text{erg s}^{-1})$  (198), we find that this detection corresponds to a star formation rate  $\text{SFR} = 0.01_{-0.003}^{+0.003} M_{\odot} \text{ yr}^{-1}$ , or a specific star formation rate  $\text{sSFR} \approx 10^{-10} \text{ yr}^{-1}$ . This detection is consistent with the Balmer upper limit and the upper limits from every other spectrum. Extrapolating to low stellar masses from the star-forming main sequence at  $z = 0.356$  measured by (531), we find that this emission is below the star forming main sequence (see the right panel of Fig 7.8), although it is within  $\sim 2\sigma$  of the measured spread (extrapolated by eye from Fig. 3 of (531)).

Note that the significance of the [O II]  $\lambda\lambda 3726, 3729$  detection is somewhat sensitive to the prior on the line width. We tested increasing the prior to a maximum of  $3000$  km s $^{-1}$  (which is unphysically broad), the significant decreases to  $\sim 2.5\sigma$ , so we consider this line a marginal detection. The conclusion that the star formation late is below the star-forming main sequence is still robust.

We conclude that G1 is located below the star forming main sequence, and there is no evidence for strong star formation at the location of 24puz.

### **Broadband UVOIR Lightcurve**

We modeled the broadband transient emission from ultraviolet through infrared (UVOIR) wavelengths as evolving blackbodies. We find a statistically consistent fit at all epochs without including extinction within the host galaxy. We use the dynesty nested sampler with default settings (206). We adopt uninformative Heaviside

priors on the temperature  $T_{bb}$  and radius  $R_{bb}$ :  $\log T_{bb}/\text{K} \in [3, 5]$  and  $\log R_{bb}/\text{cm} \in [12, 17]$ . We report the best-fit parameters and computed luminosities  $L_{bb}$  and absolute  $g$ -band magnitudes  $M_g$  in Table 7.13.

The final two epochs of observations showed an infrared excess above a single blackbody fit, so we require a second component. We consider three models: (1) a second blackbody (e.g., warm gas), (2) an absorbed, dusty blackbody, where the absorption is assumed to be caused by graphite grains, and (3) a power-law, defined as  $f_\nu \propto \nu^{-\Gamma}$ . As we will discuss, these choices are motivated by similar excesses in observations of luminous fast blue optical transients and tidal disruption events (16, 489, 532, 533). For the blackbody models, we report infrared luminosities integrated across all wavelengths. For the power-law model, we integrate from  $2000 - 10^7 \text{ \AA}$  to compute the luminosity, to match previous work (532). We will discuss the red excess and these models in more detail in Section 7.5.

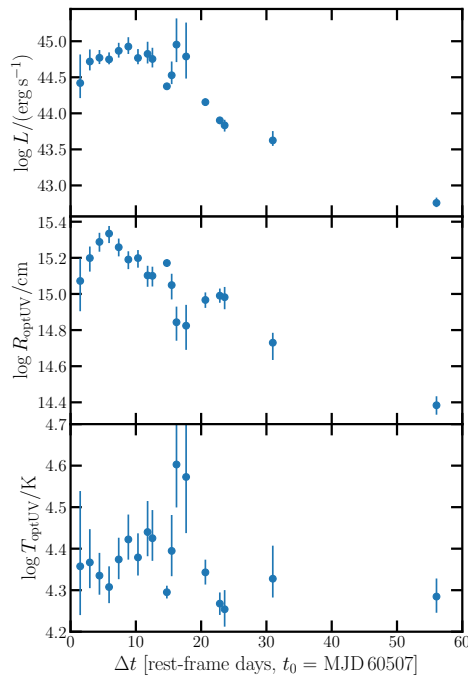


Figure 7.9: The evolution of the best-fit blackbody parameters to the optical/UV photometry of 24puz. The blackbody luminosity, radius, and temperature are shown in the *top*, *middle*, and *bottom* panels, respectively. The luminosity rapidly rises over a few days, then slowly rises/plateaus before rapidly decaying. The radius expands at a velocity of  $0.1c$  or a powerlaw  $\sim t^{0.4}$  and then decays as  $t^{-1.3}$  after a  $\sim$ week. The temperature is largely constant and the weighted-mean value is  $\log T_{bb}/\text{K} = 4.32 \pm 0.14$ .

All fits are shown in Figure 7.16 and best-fit parameters in Table 7.13. The luminos-

ity, radius, and temperature evolution are shown in Figure 7.9. The luminosity rises over a  $\sim$ day timescale and then approximately plateaus or slowly rises, with a mean value of  $\log L_{\text{peak, OptUV}} = 10^{44.79 \pm 0.04} \text{ erg s}^{-1}$ . After a  $\sim 12$  days (rest-frame), the luminosity drops as  $t^{-3}$ , although note that this slope is sensitive to the best-fit luminosity from our *HST* observations, which showed a significant red excess for which the appropriate model is uncertain, as we will discuss. The radius is consistent with expanding at  $v = (0.082 \pm 0.02)c$  to a peak of  $\log R_{\text{OptUV}}/\text{cm} = 15.33 \pm 0.04$  at 5.9 rest-days post-discovery. Alternatively, the radius expansion may be a power-law  $\log R_{\text{OptUV}}/\text{cm} \propto t^{0.4}$ . The temperature shows slight evolution, but is relatively constant at  $\log T_{\text{OptUV}}/\text{K} = 4.32 \pm 0.14$ . The error is driven by the standard deviation of the measured temperatures around the mean rather than measured error bars, implying that the temperature does evolve slightly.

### Transient spectral features

Table 7.3: Intermediate width Balmer line constraints

Date	MJD	$L_{\text{H}\alpha}$ [ $10^{40} \text{ erg s}^{-1}$ ]	$L_{\text{H}\beta}$ [ $10^{40} \text{ erg s}^{-1}$ ]
2024-07-29	60520.4	< 4.28	< 4.53
2024-08-05	60527.3	< 2.26	< 3.64
2024-09-07	60560.3	< 1.3	< 0.12
2024-10-07	60590.2	< 2.85	< 2.34

**Note.** All luminosities are in units of  $10^{40} \text{ erg s}^{-1}$ .

We constrain narrow ( $\lesssim 3000 \text{ km s}^{-1}$ ) transient features. We do not consider broad spectral features other than to note that none are apparent by eye in any of our optical spectral (top right panel of Figure 7.1). We focus on narrow, transient Balmer  $\text{H}\alpha$  and  $\text{H}\beta$  lines, as these are sometimes observed at late-times from optical transients, as we will discuss later. These constraints are identical to those from our star-formation constraints on these lines in Section 7.4, but we allow the line widths to range from  $\sigma_v \in [0, 0.01c]$ . We also fit  $\text{H}\alpha$  and  $\text{H}\beta$  independently, as transient spectral features need not be photoionized and so the Balmer decrement can vary from the nominal value  $\sim 3$ . The resulting luminosity constraints are shown in Table 7.3. No significant emission is detected.

### X-ray lightcurve and spectrum

We constrained the X-ray evolution of 24puz using our Swift/XRT, XMM-Newton, and *NuSTAR* observations. We adopt a Milky-Way Hydrogen density  $n_H = 2.88 \times$

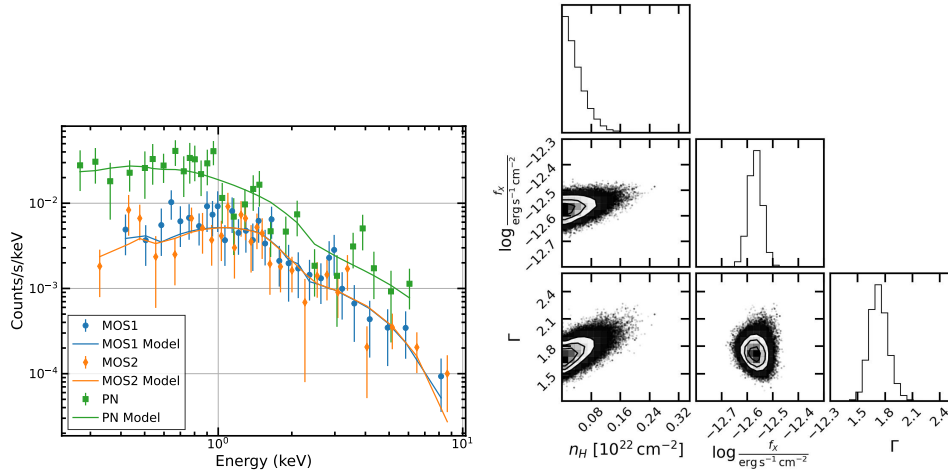


Figure 7.10: *Left:* the MJD 60536 (21.4 rest-days) *XMM-Newton* spectrum of 24puz (blue scatter) with the best-fit power-law model overlaid. *Right:* corner plot showing the best-fit power-law parameters. The host galaxy absorption is negligible ( $n_H \lesssim 3 \times 10^{21} \text{ cm}^{-2}$ ). The power-law index is  $\Gamma = 1.73^{+0.10}_{-0.09}$ .

$10^{20} \text{ cm}^{-2}$  and report integrated fluxes in the energy band 0.3 – 10 keV everywhere (185). We first constrained the spectral shape using our first *XMM-Newton*/epic-PN observation (MJD 60536, 21.4 rest-days). We modeled the spectrum using the *xspec* tool with Wilm abundances (321), Vern cross sections (534), and W statistics (320). The spectrum was best modeled as a power-law (`tbabs*zashift*tbabs*cflux*powerlaw`, total W statistic 67.87 for 88 degrees of freedom) rather than a blackbody (`tbabs*zashift*cflux*body`, total W statistic 146.92 for 88 degrees of freedom), so we adopt the power-law model for all epochs. We run a length 300000 Monte Carlo Markov Chain using *xspec* and the Metropolis-Hastings algorithm with a temperature of 50 to fully sample the parameter space. The best-fit power-law and a corner plot showing the best-fit parameter range are shown in the top panels of Figure 7.10.

The best-fit power-law index is  $\Gamma = 1.73^{+0.10}_{-0.09}$ . The spectral modeling prefers no intrinsic absorption, with a  $3\sigma$  upper limit  $n_H \lesssim 2 \times 10^{21} \text{ cm}^{-2}$ .

We also tested a Bremsstrahlung model and note that it is consistent with our spectrum (`tbabs*apec`, cash statistic 77.63 for 88 degrees-of-freedom), but not preferred over the power-law model. The best-fit temperature is  $7.0 \pm 1.5 \text{ keV}$ . This temperature is low for typical interactions, which produce a forward shock at  $\sim 10^9 \text{ K}$ , or 100 keV (535). This temperature may be consistent with emission from the reverse shock, but the reverse shock is expected to be highly absorbed due to rapid (sub-day) cooling in the post-shock region (see Table 1 of 535), and so will

not dominate the emission. The best-fit normalization corresponds to a volume emission measure  $\int n_e n_H dV = (3.29 \pm 0.17) \times 10^{66} \text{ cm}^{-3}$ . Assuming a spherical emitting region with radius  $\sim 10^{15} \text{ cm}$ , this corresponds to a high average density  $\sim 10^{10} \text{ cm}^{-3}$ . This analysis will become relevant when we discuss possible shock origins of the X-ray emission in Section 7.5.

Our second epoch of *XMM-Newton* observations ( $\Delta t = 37.6$  rest-days) are tentatively softer than the first epoch. We model this epoch as an unabsorbed power-law (tbabs\*zashift\*cflux\*powerlaw, W statistic 28.31 for 26 degrees of freedom), given the lack of evidence for absorption in the first epoch. The results are shown in Appendix Figure 7.17, and we find a 1% chance that the photon index is consistent with the first epoch  $\Gamma \leq 1.73$ . This tentatively suggests that the photon index softened with time. Following the same procedure, the final *XMM-Newton* observation was best modeled with  $\Gamma = 1.5 \pm 0.3$ , which is consistent with both the first and second epochs.

Given that the evidence for evolution in the photon index is tentative, we construct a lightcurve with better constrained fluxes by simultaneously fitting all epochs together with a constant photon index, following the same procedure as above in *xspec*. Likewise, we convert the *NuSTAR* and Swift/XRT observations into X-ray fluxes, assuming that the underlying spectrum is an unabsorbed power-law with a photon index of 1.7. The resulting lightcurve is shown in the bottom left panel of Figure 7.1. We verify that our conclusions do not change if we separately fit the photon indices.

The soft X-ray emission is luminous and highly variable. The peak luminosity detected was in the 21.4 rest-days post-discovery *XMM-Newton* observation, with  $L_X = 10^{44.12 \pm 0.034} \text{ erg s}^{-1}$ . By stacking the Swift/XRT observations at 20.6 and 23.2 rest-days, we obtain a  $3\sigma$  upper limit of luminosity  $L_X < 10^{43.8} \text{ erg s}^{-1}$ . Our most luminous detection at 21.4 rest-days (i.e., in between the Swift data points) is  $6\sigma$  higher than the Swift upper limit. 24puz was variable at a factor of  $3.8^{+5.5}_{-1.5}$  assuming normally distributed fluxes ( $3\sigma$  limit  $> 1.3$ ) on  $\sim 3$  day timescales in the soft X-ray. The *NuSTAR* upper limits exclude any luminous hard emission component.

### Radio-mm emission

24puz was not detected in any of our radio or millimeter observations. Motivated by radio observations of similar transients, as we will discuss in the following section, we constrain the circum-transient medium under the assumption that any radio emission is produced by a non-relativistic, wide-angle outflow colliding with

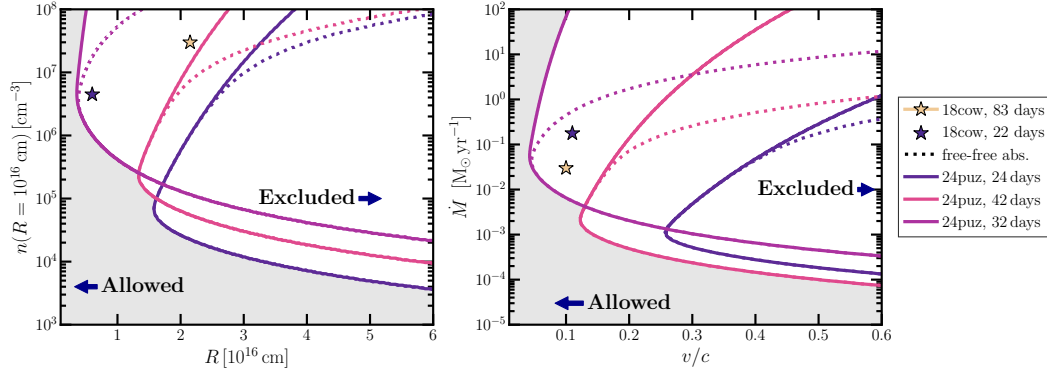


Figure 7.11: Constraints on the physical parameters of any synchrotron-emitting region from our radio/millimeter observations. The *left* panel shows the ambient medium density  $n$  at outflow radius  $R$  for a spherical, non-relativistic outflow. The dashed lines mark the boundary between physical parameters excluded and allowed by a model that includes free-free absorption where the absorbing medium density is assumed to be the same as the emitting region. The grey region is allowed by all models. Each line corresponds to a different observation and the color scales with the time since discovery. The solid lines do not include free-free emission. Regions to the left of these lines are allowed while regions to the right are excluded. The LFBOT AT 2018cow is shown in stars for comparison (15, 16). The *right* panel is in the same format as the *left* but is shows physical parameters appropriate for a stellar-wind like circum-transient medium. The x-axis shows velocity  $v$  and the y-axis the mass-loss rate  $\dot{M}$ .

a dense medium. Radio emission in this scenario is generally produced by the synchrotron mechanism, with possible contributions from bremsstrahlung. We follow (536) closely in this section.

We consider an electron with Lorentz factor  $\gamma$  and pitch angle  $\theta$  in a region of uniform density ( $n$ ) and magnetic field ( $B$ ). The synchrotron frequency of this electron is  $\nu_s = \frac{eB\gamma^2}{2\pi m_e c}$ , where  $e$  is the electron charge,  $m_e$  is the electron mass, and  $c$  is the speed of light. The synchrotron power for this electron is given by

$$P_s(\nu | B, \gamma, \theta) = \frac{\sqrt{3}e^3 B \sin \theta}{m_e c^2} = F(\nu/\nu_c), \quad (7.1)$$

where  $\nu_c = 3/2\nu_s \sin \theta$ ,  $F(x) = x \int_x^\infty K_{5/3}(y) dy$ , and  $K_{5/3}(y)$  is the modified Bessel function of order  $5/3$ .

For a population of electrons, the synchrotron spectrum is computed by summing Equation 7.1 over all electrons. We adopt the standard assumption of a population of electrons with Lorentz factors drawn from a power law with index  $p$ :

$N(\gamma)d\gamma = N_0\gamma^{-p}d\gamma$ . We adopt the approximation of  $F(x)$  used in (413), which allows Equation 7.1 to be analytically integrated for a power-law electron distribution with small errors relative to numerically integrating  $K_{5/3}(y)$ .

Let the system volume be given by  $V$ , where for a spherical region of radius  $R$  and filling factor  $f_V$  we have  $V = 4/3\pi f_V R^3$ . The total energy in the system is given by  $E$ . Then, the total energy stored in the magnetic field is  $E_B = \frac{B^2 V}{8\pi}$ . We adopt the equipartition assumption, such that the total energy stored in the magnetic field  $E_B$  is a fixed fraction of the total energy of the system:  $\epsilon_B = E_B/E$ . Likewise, the total energy stored in the electrons,  $E_e = \frac{N_0 m_e c^2}{(p-2)\epsilon_e}$  is a fixed fraction of the total energy  $\epsilon_e = E_e/E$ . This assumption allows us to reduce the number of free parameters in the system. We adopt the common assumption that  $\epsilon_B = 0.01$  and  $\epsilon_e = 0.1$  (16).

Thus, given a magnetic field, radius, and electron energy distribution index  $p$ , we can compute the expected synchrotron luminosity at each frequency. The post-shock density, in the strong shock regime, is given by

$$n_e = \frac{B^2}{6\pi\epsilon_B m_p v^2}, \quad (7.2)$$

where we have defined the shock velocity  $v$ , which we assume is the average velocity  $v = R/t$  given a radius  $R$  and a time since launch  $t$ . Whenever we discuss density in the rest of this section, we refer to this post-shock density.

In some cases, we must also include free-free absorption. The free-free optical depth is given by (306, Eq. 10.13)

$$\tau_{ff} = \sqrt{\frac{2\pi}{3m_e^3 k_B T_e}} \frac{4e^6}{3hc\nu^3} \times (1 - e^{-\frac{h\nu}{k_B T_e}}) Z_i^2 g_{ff}(\nu, T_e, Z_i) \int n_i n_e dl. \quad (7.3)$$

We have defined the electron temperature  $T_e$ , the number of electrons per ion  $Z_i$ , frequency  $\nu$ , the ion density  $n_i$  and the electron density  $n_e$ , and the Gaunt factor  $g_{ff}(\nu, T_e, Z_i)$ . We approximate the Gaunt factor following Section 10.2 of (306). All other variables follow common notation for constants (e.g., electron mass  $m_e$ ). The final integral is over the line-of-sight and is the emission measure  $EM = \int n_i n_e dl$ . We adopt the common assumptions  $Z_i = 1$  and  $n_i = n_e$ . We adopt a temperature of  $T_e = 10^5$  K, which is higher than the standard photoionization equilibrium temperature due to Compton heating by hard X-ray photons. This is justified in Appendix 7.9.

We assume the density profile is  $\sim r^{-2}$ , such that the emission measure is  $EM = \int_R^\infty n_e n_i dl = n_e^2 R/3$ . As we will discuss in Section 7.5, our modeling of the optical/UV emission as a shock prefers a shallower density profile  $\sim r^{-1}$  in the inner regions of the circum-transient medium ( $R \lesssim 10^{15}$  cm). If the outer density profile is similarly shallow, the emission measure will increase by a factor of  $\sim 3$  (assuming the outer radius is large enough that integrating to infinity causes minimal errors). This does not change our conclusions.

In Figure 7.11, we show the post-shock density from the 24puz upper limits. We treat each observation independently. In the left panel of this figure, we show, the upper limit on radius (x-axis) for a range of assumed densities. The dashed lines include free-free absorption, while the solid lines only include synchrotron self-absorption. The shaded region is allowed by all observations. The right panel shows the same results but in variables appropriate for stellar winds. We assume a wind-like density profile  $\rho = \dot{M}/(4\pi v r^2)$ . We convert radius to average velocity for each epoch. The plot is otherwise formatted the same as the left panel.

The observations allow for a non-relativistic outflow colliding with a dense medium. A faster outflow is allowed for low densities  $\lesssim 10^4 \text{ cm}^{-3}$  or very high densities  $\gtrsim 10^9 \text{ cm}^{-3}$ , although note that we are not consistently treating relativistic effects.

## 7.5 Results

As detailed in the previous section, our observations have shown:

- 24puz is most likely associated with G1, a dwarf galaxy ( $10^{7.74} \lesssim M_*/M_\odot < 10^{8.25}$ ) that is located slightly below ( $\lesssim 1$  dex) the star forming main sequence. 24puz is 5 kpc offset from G1 and shows no evidence for star formation or a massive stellar structure ( $\lesssim 10^9 M_\odot$ ) at its location, although space-based follow-up once 24puz has faded is critical for tighter constraints. Both 24puz and G1 are most likely at  $z = 0.35614 \pm 0.00009$ , based on the detection of ISM or CGM absorption lines, and may be bound to or infalling into a galaxy group. G1 shows tentative evidence for irregularities that could suggest a merger or environmental stripping, but deep imaging is required to confirm that the irregularities are not a background galaxy.
- 24puz produced a luminous UVOIR flare. The flare is well-modelled as a single blackbody in observations from 1.5 – 27 rest-days post-discovery. The emission peaks at a luminosity  $L_{\text{OptUV}} = 10^{44.79 \pm 0.04} \text{ erg s}^{-1}$  after a short,

day-timescale rise. The luminosity stays near this value for  $\sim 12$  days and then decreases rapidly, as  $\sim t^{-3}$ . The emitting region radius initially expands rapidly as a power-law or constant velocity ( $v = (0.082 \pm 0.02)c$ ) to a maximum radius of  $R_{\text{OptUV}} = 10^{15.33 \pm 0.04}$  cm. The temperature of the emitting region is relatively constant at  $T_{\text{OptUV}} = 10^{4.3 \pm 0.1}$  K. At 31 rest-days, a near-infrared excess is detected, which is more significantly detected at 56 rest-days. A similar excess could have been present on earlier times, but the hot optical/UV emission dominate.

- 24puz is a luminous, highly variable, soft X-ray source. The peak X-ray luminosity observed was  $L_X = 10^{44.12 \pm 0.034}$  erg s $^{-1}$  at 21.4 rest-days. At this time, the photon index was  $\Gamma = 1.73^{+0.10}_{-0.09}$  with low intrinsic absorption  $n_H \lesssim 3 \times 10^{21}$  cm $^{-2}$ . There is tentative evidence for a softer photon-index in the 37.6 rest-days spectrum, with a p-value  $\sim 1\%$  that this spectrum has the same photon-index as at peak. The X-ray emission is variable on  $\sim 3$  day timescales by a factor of  $3.8^{+5.5}_{-1.5}$  ( $3\sigma$  limits  $> 1.3$ ). For the spectrum at peak, a power-law model is preferred over a blackbody or Bremsstrahlung. Bremsstrahlung emission can fit the observations, but the implied temperature ( $7 \pm 1.5$  keV) is too low for typical emission from a forward shock.
- 24puz is non-detected at 15 GHz and 100 GHz (observer frame). If an outflow was launched, the circum-transient material must have a density either below  $\sim 10^5$  cm $^{-3}$  if the average velocity is  $\gtrsim 0.1c$  or a higher density but an average velocity  $\lesssim 0.1c$ .

In the rest of this section, we discuss the structure, physics, and energetics of the emitting regions and compare to published classes of transients.

### **Energetics and emitting region scales**

The optical/UV photosphere is observed at radii from  $(0.25 - 1.6) \times 10^{15}$  cm. Numerically integrating the blackbody luminosity over time, we find a total emitted energy from 0-55 rest-frame days post-discovery of  $1.4^{+0.7}_{-0.2} \times 10^{51}$  erg. In the case where this is an accretion energy, which we will consider, the accreted mass is  $7.7 \times 10^{-3} M_\odot$  for a radiative efficiency of 10% (note that this efficiency is often lower for super-Eddington accretion, as will become relevant later; (537–540)). This energy does not include contributions from the red excess observed in later epochs, but total energy emitting in this red excess is small relative to that emitting in the

optical/UV. If we assume that the red excess luminosity traces the optical/UV (as we have the best evolution constraints in this band), then the excess energy emitting at redder wavelengths is  $\sim 10\%$  of that at optical/UV wavelengths.

The variability of the X-ray emission sets a weak limit on the size of the emitting region  $\lesssim 3$  light days  $= 8 \times 10^{15}$  cm. It is plausible that the X-ray emitting region is much more compact and associated with the central engine that is ionizing the UV-infrared emitting regions, in which case the emitting region size must be smaller than that of the optical emitting region. The total energy detected in the X-rays is  $\gtrsim 4 \times 10^{49}$  erg. We computed this value by fitting a power-law in time to the first and last X-ray detections and integrating. This is a lower limit because of the high variability, which is not included in this estimate, and because we integrate over the 0.3 – 10 keV range. From the variability alone, the real energy could be a factor  $\sim 4$  higher. We estimate the energy in the X-rays to be  $\sim 4 - 16\%$  of the optical/UV energy.

The lack of transient optical spectra features implies that the optical-infrared emitting region is fully ionized, or that the emitting region density profile rapidly steepens above the photosphere so that the line-forming region is small. Given the luminous UV emission and the sizes of the regions stated above, either is feasible.

### The optical/UV emission

We first consider the origin of the optical/UV flare. We rule out a transient powered by  $^{56}\text{Ni}$  decay, following the same logic as (16) used for the LFBOT AT2018cow. The  $^{56}\text{Ni}$  mass can be constrained in two ways. First, from the optical/UV peak luminosity and, second, from the rise time. From (541), the rise time  $t_{\text{rise}}$  can be approximated as the diffusion time  $t_{\text{dif}}$

$$t_{\text{rise}} \approx t_{\text{dif}} \approx \left( \frac{M_{\text{ej}} K}{4\pi v_{\text{ej}} c} \right)^{1/2} = 10 \text{ days} \left( \frac{M_{\text{ej}}}{4.3 M_{\odot}} \right)^{1/2} \left( \frac{v_{\text{ej}}}{0.1c} \right)^{-1/2}, \quad (7.4)$$

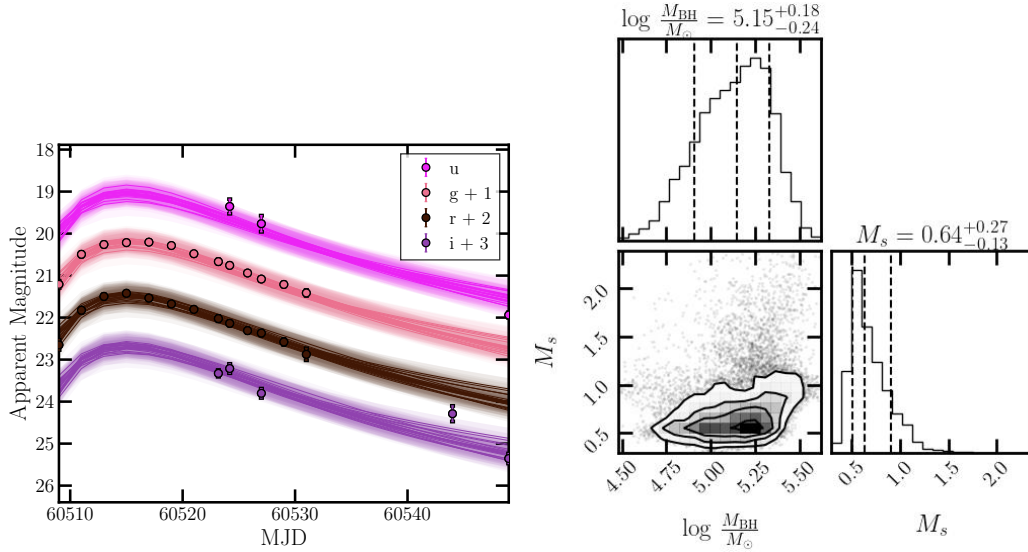


Figure 7.12: Summary of results from the MOSFIT TDE modeling. Realizations from the MCMC samples are overlaid on select observations in the *left* panel. We only include observations in representative bands for clarity, but perform the fit with all data. The constraints on black hole ( $M_{\text{BH}}$ ) and disrupted star mass ( $M_s$ ) are shown in the *right* panel.

where  $\kappa = 0.1 \text{ cm}^2 \text{ g}^{-1}$  is the effective opacity,  $v_{\text{ej}}$  is the ejecta velocity, and  $M_{\text{ej}}$  is the ejecta mass. The peak bolometric luminosity is given by (542)

$$\begin{aligned}
 L_{\text{bol}} = & \\
 & \frac{M_{\text{Ni}}}{\tau_{\text{Co}} - \tau_{\text{Ni}}} \left\{ \left( Q_{\text{Ni}} \left( \frac{\tau_{\text{Co}}}{\tau_{\text{Ni}}} - 1 \right) - Q_{\text{Co}} \right) e^{-\frac{t}{\tau_{\text{Ni}}}} + Q_{\text{Co}} e^{-\frac{t}{\tau_{\text{Co}}}} \right\} \\
 & = \frac{M_{\text{Ni}}}{M_{\odot}} \left( 6.45 e^{-\frac{t}{8.8 \text{ days}}} + 1.45 e^{-\frac{t}{111.3 \text{ days}}} \right) 10^{43} \text{ erg s}^{-1}, \quad (7.5)
 \end{aligned}$$

where  $\tau_{\text{Co}} = 111.3$  days is the half-life of  $^{56}\text{Co}$  and  $\tau_{\text{Ni}} = 8.8$  days is the half-life of  $^{56}\text{Ni}$ ,  $Q_{\text{Ni}} = 1.75$  MeV and  $Q_{\text{Co}} = 3.73$  MeV are emitted energies per decay, and  $t$  is the time since the initial event.  $M_{\text{Ni}}$  is the Nickel mass. To reproduce the peak optical/UV luminosity of 24puz, we thus require a large  $^{56}\text{Ni}$  mass of  $\sim 30 M_{\odot}$ . This contradicts constraints from the lightcurve rise time, which would correspond to the diffusion time. The ejecta mass required for a  $\lesssim 10$  day rise with an ejecta velocity of  $0.1c$ , as implied by the optical/UV photosphere, is  $\lesssim 4 M_{\odot}$ . The kinetic energy of this ejecta mass is large at  $4 \times 10^{52}$  erg. We disfavor a  $^{56}\text{Ni}$ -powered model.

We next consider an accretion-powered flare, where gas surrounding a central source reprocesses high-energy emission to produce the optical/UV flare. Motivated by the

similarity of this transient to TDEs that we present in Section 7.6, we first tested this origin using the MOSFIT code to model the optical/UV emission from 24puz as a TDE-like accretion flare (258, 543). MOSFIT is based on a grid of hydrodynamical simulations of simulated disruptions of a  $1 M_{\odot}$  star by a  $10^6 M_{\odot}$  SMBH, which are then scaled to other stellar and blackhole parameters using analytic relations. The luminosity is assumed to trace the fallback rate measured from these simulations, but with delays from the time for the debris to circularize into an accretion disk, as well as viscosity in that accretion disk. The accretion power is then reprocessed into a blackbody by a reprocessing layer with power-law evolution in the photospheric radius.

By default, MOSFIT requires sub-Eddington luminosities, but we turned off the Eddington accretion limit as 24puz requires super-Eddington accretion for reasonable BH masses, as we will discuss further. We otherwise ran with default settings. We used the *dynesty* sampler and the default priors for the TDE model, except that we set the black hole mass lower limit to  $50 M_{\odot}$ . The results are shown in Figure 7.12. A full corner plot with the results is shown in Appendix Figure 7.18. The best-fit model invokes a black hole with  $\log M_{\text{BH}}/M_{\odot} = 5.15^{+0.18}_{-0.24}$  that is fully disrupting a relatively low mass star  $M_* = 0.64^{+0.27}_{-0.13} M_{\odot}$ . As we discuss in Section 7.6, such a high BH mass is unlikely for this system, although we cannot exclude it. We disfavor this model.

Regardless of the exact mechanism powering the emission, the peak optical/UV luminosity is likely highly super-Eddington. As we will show in Section 7.6, we favor a model with accretion onto a BH of mass  $M_{\text{BH}}/M_{\odot} \lesssim 10^5$ , corresponding to a radiation Eddington ratio  $10^2 \lesssim \lambda_{\text{Edd}}$ . Simulations are increasingly suggesting that super-Eddington radiation and accretion are feasible (537–540). The accretion power may be in the form of mechanical energy carried by optically thick outflows which then convert the kinetic energy into radiation. Observations of ultraluminous X-ray sources (ULXs) find luminosities up to  $10^{42} \text{ erg s}^{-1}$ , corresponding to Eddington ratios  $10^{2-3}$  (544).

If we are observing emission from gas that is photoionized by an accretion source, then we must consider the lightcurve shape, which begins with a  $\sim$ days rapid rise. The lightcurve then shows a slow rise or a plateau for  $\sim 10$  days before rapidly decaying. The initial turn-on may correspond to accretion beginning. The slow rise/plateau could be explained as a super-Eddington cap (or see 485, for an accretion-powered model that could produce similar emission. We will discuss this

model in more detail shortly.). If 24puz has reached the limit of super-Eddington radiation, the observed radiation may appear as a plateau until the accretion rate has dropped to sufficiently low values that the radiation begins to trace the accretion rate. Extrapolating from the power-law decay to early times, this implies a remarkable peak accretion rate of  $\gtrsim 10^{46}$  erg s $^{-1}$ . Alternatively, the central source may have a plateau in its accretion rate.

We conclude that an accretion powered model may be able to explain our observations, although with significant uncertainties. The standard modeling code MOSFIT can reproduce our observations, but only with a black-hole mass that is slightly higher than our preferred range, as we will discuss in Section 7.6.

We next consider a shock breakout. This discussion closely follows (545). Let us define  $M_{\text{ctm}} = M_{\text{ctm},\odot} M_{\odot}$  as the mass of the circum-transient material,  $R_{\text{ctm}} = R_{\text{ctm},16} \times 10^{16}$  cm as the edge of the circum-transient material,  $M_{\text{ej}}$  as the ejecta mass, and  $v_{\text{ej}} = \beta_{\text{ej}} c$  as the ejecta velocity. Define  $\eta = M_{\text{ctm}}/M_{\text{ej}}$ . The shock velocity at  $R_{\text{ctm}}$  is related to the ejecta velocity as  $v_{\text{sh}} = \beta_{\text{sh}} c = v_{\text{ej}} \eta^{-\alpha}$ .

As discussed in detail in (545), there are four regimes that produce separate lightcurve behavior, determined by (1) whether the shock breakout occurs within or at the edge of the circum-transient medium and (2) whether  $\eta$  is large ( $\gtrsim 1$ ) or small ( $\ll 1$ ). The optical emission from the LFBOT AT2018cow was reproduced by a shock model for the case of edge shock breakout with a small circum-transient medium ( $\eta \ll 1$ ). 24puz rises rapidly in the optical for a few days, and then the rise rate slows for  $\sim 1$  week. The luminosity then rapidly drops. Unlike AT2018cow, the behavior of 24puz is expected in a model where the shock breakout occurs inside the circum-transient material, but still with a light circum-transient medium ( $\eta \ll 1$ ). In this case, the initial, rapid rise corresponds to the shock breakout. The slow rise traces the shock kinetic luminosity and, as we will show, implies a shallow circum-transient medium density profile. The rapid drop begins once the shock reaches  $R_{\text{ctm}}$ . At this point, we would expect to detect some cooling of the emission, which is not the case for 24puz, so we would require a secondary component to heat the ejecta at late-times. We will discuss this later in this section.

We assume a slope  $s = 1$  fiducially. To reproduce the slope of the slow luminosity rise, we require an ejecta profile  $\rho_{\text{ej}} = r^{-n}$  with  $n = 12$ . A shallower slope  $s$  is also allowed, in which case the ejecta profile will also be slightly shallower (e.g., for  $s = 0$ , we have  $n = 10$ ). We tested values of  $s = 0$  and  $s = 1$  and our general conclusions do not change. We do not perform any quantitative fitting and instead attempt to

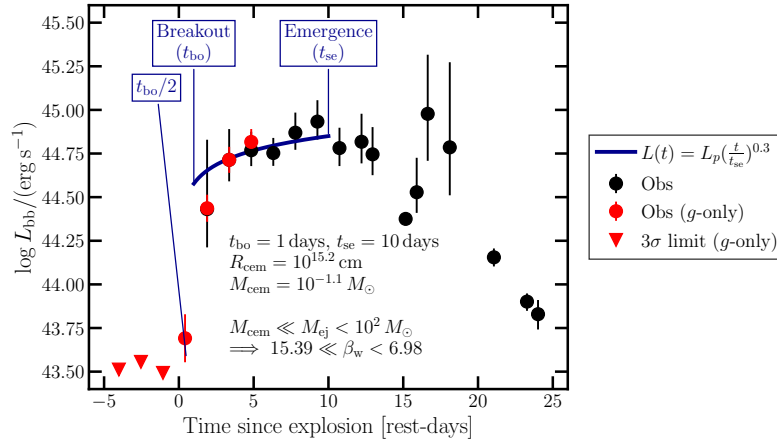


Figure 7.13: Constraints on a shock breakout model for the optical/UV emission from 24puz, assuming that the ejecta mass ( $M_{\text{ej}}$ ) is much larger than the circum-transient medium mass ( $M_{\text{ctm}}$ ) and the circum-transient medium has a power-law density profile with slope  $s = 1$ . The optical/UV blackbody luminosity is shown as a function of time in black in both panels. The red points show the luminosity obtained from early  $g$ -band-only detections of 24puz, for which we could not fully constrain the luminosity. We assume the temperature is the average of the over the first  $\sim 5$  days. We show the case of small  $t_{\text{bo}}$  for illustration. The shock emergence is assumed to occur on the same day in both panels, corresponding to the time at which the luminosity begins to decrease. The blue solid line shows the expected power-law evolution of the lightcurve within the shock breakout model, from equation 7.9. The resulting inferred physical parameters (circum-transient medium radius  $R_{\text{ctm}}$  and mass  $M_{\text{ctm}}$ ) are listed on the bottom, including a range of possible shock velocities inferred from the assumption that  $M_{\text{ej}} \gg M_{\text{ctm}}$  and the ejecta mass is reasonably small  $\lesssim 10^2 M_{\odot}$ .

roughly reproduce the lightcurve using analytic estimates from (545); we encourage work quantitatively fitting the lightcurve to light, interior shock interaction models.

The start date is not directly observable, so we constrain it (and thus  $t_{\text{bo}}$  and  $t_{\text{se}}$ ) as follows. This procedure is imperfect, and constraining the physical parameter using a simulated model grid instead would be ideal. First, we use the analytic expression in (545) to solve for the ejecta velocity  $v_{\text{ej}} = \beta_{\text{ej}}c$ , the circum-transient medium mass  $M_{\text{ctm}}$ , the outer radius of the circum-transient medium  $R_{\text{ctm}}$ , and the breakout luminosity  $L_{\text{bo}}$  as a function of breakout time  $t_{\text{bo}}$ , shock emergence time  $t_{\text{se}}$ , and  $\eta$ .

We find

$$v_{\text{ej}} = \eta^\alpha \left( \frac{\kappa L_p}{4\pi c t_{\text{bo}}} \right)^{1/3}; \quad (7.6)$$

$$M_{\text{ctm}} = L_p t_{\text{se}} \left( \frac{4\pi c t_{\text{bo}}}{\kappa L_p} \right)^{2/3}; \quad (7.7)$$

$$R_{\text{ctm}} = \left( \frac{\kappa L_p t_{\text{se}}^3}{4\pi c t_{\text{bo}}} \right)^{1/3}; \quad (7.8)$$

$$L_{\text{bo}} = L_p \left( \frac{t_{\text{bo}}}{t_{\text{se}}} \right)^{\frac{(5-s)(n-3)}{n-s}-3}. \quad (7.9)$$

Here, we have defined  $\alpha = \frac{1}{n-3}$  and the electron scattering absorption coefficient  $\kappa = 0.34 \text{ cm}^2 \text{ g}^{-1}$ . We pick combinations of  $t_{\text{bo}}$  and  $t_{\text{se}}$  such that (1)  $t_{\text{se}}$  corresponds to 9.6 rest-days post-discovery, which is when the luminosity began to decay and (2) the luminosity at time  $t_{\text{bo}}/2$  is approximately equal to  $0.1 L_{\text{bo}}$ . We consider two extreme values of  $t_{\text{bo}}$  and  $t_{\text{se}}$ , corresponding to early and late start dates to highlight the range of possible parameters. Earlier start times relative to the detection epoch will bring the ratio of  $t_{\text{se}}$  and  $t_{\text{bo}}$  close to one to satisfy condition (2), while later start times would always overproduce the  $t_{\text{bo}}/2$  luminosity.

The corresponding circum-transient medium parameters are  $R_{\text{ctm}} \approx 10^{15} \text{ cm}$ , which roughly matches the maximum measured blackbody radius, and  $M_{\text{ctm}} \approx 0.1 - 1 M_\odot$ . We cannot tightly constrain the ejecta mass without a direct observation of the wind velocity. We have assumed  $\eta \ll 1$ , so we have  $M_{\text{ej}} \gg 0.1 M_\odot$ . This corresponds to a shock velocity  $\beta_{\text{sh}} \gg 0.06$  at  $R_{\text{ctm}}$ , implying a fast shock. If we assume the ejecta mass is not huge, which we will define as  $\lesssim 100 M_\odot$ , we can set a lower limit on the shock velocity  $\beta_{\text{sh}} \gg 0.03$ . The limits for the case of small  $t_{\text{bo}}$  are shown in Figure 7.13. Note that these parameters are consistent with the radio upper limits: the implied densities are sufficiently high ( $\sim 10^{10} \text{ cm}^{-2}$ ) that free-free absorption will prevent detection of synchrotron emission, or the density may fall as a steeper power-law outside  $R_{\text{ctm}}$ .

The shock breakout model explains the optical/UV lightcurve shape at early-times, and such a model has been used for events with similar lightcurve evolution, although generally on much longer timescales and with lower luminosities (e.g. 546). We encounter two problems at later times: the lack of cooling and transient spectral features. The lack of cooling may require an additional ionizing source that dominates by  $\sim 20$  days (16, 547), but we may expect a contribution from reprocessing of a central source given the luminous X-rays detected (e.g. 16, 113, 485). The

lack of lines could also be explained by an additional ionizing source, if it is sufficient to keep the emitting region fully ionized, or if the circum-transient medium has a rapid density drop-off at the photosphere so that the line-emitting region is small. Full radiative transfer simulations of the shock model with similar physical parameters to those of 24puz would determine whether the lack of cooling and lines are prohibitive.

In summary, the early time optical/UV lightcurve could be explained using both accretion-powered and shock breakout models. At late times, the shock breakout model does not naturally explain the lack of cooling and spectral features, but detailed simulations are required to assess the significance of this problem. The late-time emission likely requires additional accretion power, regardless of the origin of the early-time emission.

### **The red excess**

In addition to the optical/UV flare, 24puz showed a red excess above a single blackbody fit in the final two epochs of observations (31 – 56 rest-days post-discovery). There are a few models that are typically considered for similar sources: thermally emitting gas/dust, re-processing of high energy emission by gas, gamma-ray burst-like nonthermal emission, and radioactive decay. We consider the agreement with each of these models with our *HST* observations, which have the best coverage of the red excess.

We begin with a thermally emitting region. We first modeled the UVOIR emission as two blackbodies. The temperature of the cooler blackbody was  $\log T_r \approx 3600$  K, which is above the sublimation of all dust grains, but too cool to be consistent with photoionized gas. If the red excess is produced by dust, the temperature inconsistency can be improved by modeling the emission as a hot blackbody and a modified blackbody that accounts for dust absorption (533, 548). We test both the graphite and silicate models from (549) and report the results for the more conservative graphite model in Table 7.13. The temperature is still  $\sim 3500$  K, i.e., significantly above the sublimation temperature of graphite grains ( $\sim 2000$  K). This discrepancy is highlighted in Figure 7.14, where we show our *HST* observations in black and an example spectral energy distribution for a hot blackbody with additional graphite thermal emission in dashed blue. The model shown is not fit to the data, but demonstrates that graphite emission causes a peak redward of the observed red excess (near  $2 \mu\text{m}$ ), whereas the observed red excess is present by  $9000 \text{ \AA}$ . We thus

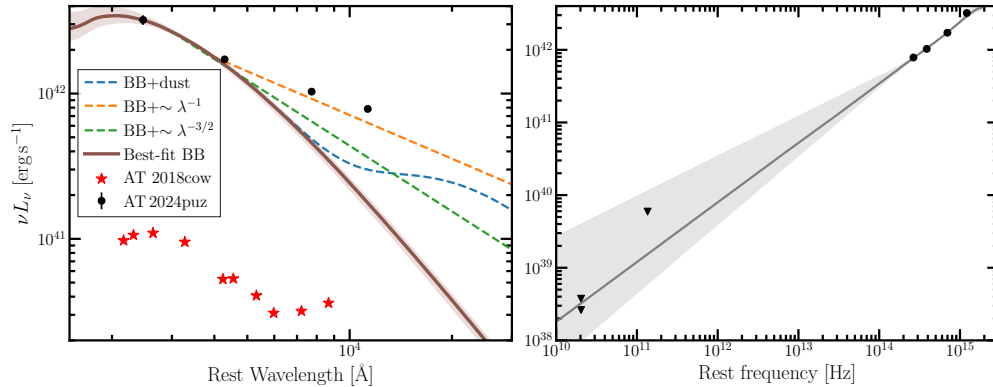


Figure 7.14: Constraints on the origin of the red excess from 24puz. The *left* panel shows the *HST* spectral energy distribution of 24puz in black and, for comparison, an epoch of observations of the red excess from AT2018cow in red. A best-fit hot blackbody is shown in brown. The dashed lines show the hot blackbody with potential red excess emission added on. These are not fits but are meant to guide the eye. In orange, a  $\lambda^{-1}$  power-law was added to represent reprocessing in a shallow medium; in green, a  $\lambda^{-3/2}$  power-law is summed to represent reprocessing in a wind-like medium. In blue, we add a dust blackbody to show that this model peaks redward of the excess. The *right* panel shows our radio upper limits as black triangles. The grey band shows an extrapolation of a power-law fit to the *HST* data to radio frequencies. Considering that the *HST* data is taken at later-times than the radio, so we would expect it to have faded with time, the power-law extrapolation over-predicts the radio limits.

exclude dust as the main source of the red excess.

We next consider gamma-ray burst-like non-thermal emission. This model is immediately disfavored by the long timescale of the emission, which is much slower evolving than gamma-ray burst-like afterglows. Moreover, a power-law + hot blackbody fit provides a poor model of the *HST* data, as seen in the bottom right panel of Figure 7.16. In the right panel of Figure 7.14, the best-fit power-law+blackbody to the *HST* data predicts a radio luminosity that is comparable to our  $4\sigma$  upper limits, which are described in Section 7.4. However, our *HST* data was obtained  $\sim 40$ – $60$  rest-days after the *HST* observations. If the emission is caused by an on-axis jet, then the jet emission should be brighter at earlier times: this is ruled out by the luminous radio emission predicted at late-times by the power-law extrapolation from the *HST* data. If the emission is caused by an off-axis jet that is now wide-angle and non-relativistic, allowing us to view its emission, it is feasible for the radio emission to be brighter at  $\sim 80$  days than at early times. The shallow observed slope disfavors this scenario. As discussed, we have  $\nu F_\nu \sim \nu$ , or  $F_\nu \sim \text{const}$ . This slope

is inconsistent with typical gamma-ray burst synchrotron frameworks. Because of the poor fit, the lack of a radio detection, and the shallow observed slope, we rule out this model.

We next consider high-energy emission that has been reprocessed by gas in the circum-transient medium. We will leave detailed models of this reprocessing to future work, but use simple estimates to assess agreement with our observations. We follow (550) and (113).

In this model, the red excess is caused by a change in the dominant opacity at longer wavelengths, as detailed in (113). At near-infrared wavelengths, free-free absorption dominates. This absorption coefficient is given by

$$\kappa_{ff} = 0.018T^{-3/2}\nu^{-2}\rho^2m_p^{-2} [\text{cm}^2 \text{g}^{-1}], \quad (7.10)$$

where  $T$  is the temperature of the emitting region,  $\nu$  is the frequency under consideration,  $\rho$  is the density, and  $m_p$  is the proton mass. We have assumed that we are in the Rayleigh-Jeans limit and neglected the Gaunt factor.

We assume a power-law density profile

$$\rho = \rho_0 \left( \frac{r}{r_0} \right)^{-s}. \quad (7.11)$$

In the near-infrared, free-free absorption dominates the opacity, so the thermalization radius is given by the radius at which the effective optical depth, or the product of the free-free optical depth ( $\tau_{ff} \approx \kappa_{ff}\rho r$ ) and electron-scattering optical depth ( $\tau_{es} \approx \kappa_{es}\rho r$ ), is one. Quantitatively,

$$\tau_{ff}\tau_{es} \approx \kappa_{ff}\kappa_{es}\rho^2r_{th,\nu}^2 \approx 1. \quad (7.12)$$

Here,  $\kappa_{es} = 0.34 \text{ cm}^2 \text{ g}^{-1}$  is the electron scattering opacity. The luminosity is then given by

$$\nu L_\nu = 4\pi r_{th,\nu}^2 \frac{4\pi\nu B_\nu(T(r_{th,\nu}))}{\kappa_{es}\rho(r_{th,\nu})r_{th,\nu}(s-1)}. \quad (7.13)$$

Combining these four equations, we find

$$\nu L_\nu = \frac{32\pi^2 k_B}{\kappa_{es} c^2 (s-1)} \left( \frac{0.018 \kappa_{es}}{m_p} \right)^{\frac{1+s}{3s-2}} T^{\frac{7-3s}{4-6s}} (\rho_0 r^s)^{\frac{5}{3s-2}} \left( \frac{c}{\lambda} \right)^{\frac{7s-8}{3s-2}}. \quad (7.14)$$

For a wind-like density profile ( $s = 2$ ), we have  $\lambda L_\lambda \sim \lambda^{-3/2}$ . As shown by the dashed green line in Figure 7.14, this slope is steeper than the observed red excess, although note that our transition from the hot blackbody to a slope  $-3/2$  power-law is ad-hoc and not quantitatively accurate. For a shallow density profile  $\rho \sim r^{-1}$ , we have  $\lambda L_\lambda \sim \lambda^{-1}$ , which is closer to the observed slope and is consistent with our optical/UV shock interaction analysis. Many of the approximations quoted above, however, break down for slopes that are much shallower than  $s = 2$ . We will thus adopt an intermediate slope  $s = 1.5$  for the following analysis to prevent divergences, but urge simulations of the  $s = 1$  case to test if our conclusions hold.

We can evaluate the required density by matching the red excess luminosity to that predicted by Equation 7.14. For a luminosity  $\nu L_\nu \sim 10^{42} \text{ erg s}^{-1}$  at  $\sim 7000$  and  $s = 1.5$ , we find that the density is  $10^{10.5} \text{ cm}^{-3}$  at  $10^{15} \text{ cm}$  and the total mass must be  $\sim 0.2 M_\odot (R_{\text{out}}/10^{15.1} \text{ cm})$ . This is consistent with the circum-transient medium mass that was inferred in our shock interaction analysis  $M_{\text{ctm}} \lesssim 1 M_\odot$  for  $R_{\text{ctm}} \approx 10^{15} \text{ cm}$ . If this density profile extends farther out, our radio analysis may pose a problem as we find  $\rho(R = 10^{16} \text{ cm}) \approx 10^9 \text{ cm}^{-3}$ , which is on the border of our excluded region in Figure 7.11 unless the outflow velocity is  $\lesssim 0.1c$ . Free-free absorption would remove this limit. Alternatively, if the density profile drops rapidly at  $10^{15} \text{ cm}$ , then the allowed outflow velocity is higher. Given that the implied mass if this profile extends to  $10^{16} \text{ cm}$  is  $\sim 20 M_\odot$ , which is very large, we believe this latter explanation is likely.

The lack of any significant absorption in the X-ray spectrum poses a problem: the implied column density is  $\gtrsim 10^{25} \text{ cm}^{-2}$  for an outer radius  $R_{\text{ctm}} \sim 10^{15.1} \text{ cm}$  and an inner radius corresponding to the smallest radius measured from our blackbody fitting in Table 7.13,  $R_{\text{in}} \sim 10^{14.4} \text{ cm}$ . A smaller  $R_{\text{in}}$  corresponds to a larger column density. We can alleviate this discrepancy if the emitting region is aspherical. If we are viewing the system along a line-of-sight without significant gas/dust, then the X-rays would appear unabsorbed, as is observed. Alternatively, if the emitting region is fully ionized, it is effectively transparent to X-rays.

There are a number of key caveats to this analysis. First, we adopted common approximations to the photon diffusion time and optical depth that break as the density profile becomes shallower. Moreover, this analysis assumes a spherical, homogeneous medium. If the material is anisotropic or clumpy, then the total mass will be reduced by the volume filling factor (550). Finally, we have adopted an outer radius based on our optical/UV shock analysis, but accretion-power likely

contributes to this emission and this was not included in our modeling.

### The X-ray emission

We next consider the origin of the X-ray emission. The X-ray spectrum, luminosity evolution, and variability are both very similar to that of the soft component of AT 2018cow. The X-rays from AT 2018cow are considered to be associated with a shock or central engine (16).

We first consider a central engine model. In this case, the rapid variability is expected given the small scales of an accretion disk. The implied X-rays are highly super-Eddington. Note, however, that with the exception of the luminous *XMM-Newton* observation, the typical X-ray luminosity is  $\sim 3 \times 10^{43}$  erg s<sup>-1</sup>, which is  $\lesssim 10^3$  Eddington for the compact object masses we will favor in the following section. As discussed earlier, this Eddington ratio is feasible (544). The luminous optical/UV emission suggests that most of the X-rays, in a central engine model, are reprocessed. A fraction escape either due to inhomogeneities in the surrounding medium or because they have ionized the ejecta along our line-of-sight.

We next consider a shock origin of the X-rays. This model faces two problems. First, as discussed in Section 7.4, our Bremsstrahlung modeling suggests a best-fit temperature of  $7 \pm 1.5$  keV, which is lower than typical X-ray emission from shocks (535). It is also challenging for a shock to produce the  $\sim$ day timescale variability observed from 24puz: this would require significant density variations in the circum-transient medium. Variability on a timescale of days for a shock traveling at  $0.1c$  implies spatial variability scales of  $\sim 10^{14}$  cm. Some circumstellar media do show such variability, but it is not clear whether this is natural for a system like 24puz (e.g., see similar discussion for the LFBOT AT 2018cow in (551)). We encourage simultaneous modeling of the optical/UV and X-ray emission within a shock framework to assess whether shocks can dominate the observed emission, but we currently disfavor shocks as the dominant source of X-ray emission.

We conclude that a central engine model for 24puz can explain the observed X-rays. A shock model may be feasible, but faces significant challenges (low best-fit temperature and rapid variability).

## 7.6 Discussion

### Comparison with known transients

The persistently blue optical colors and featureless spectra place 24puz in the section of optical transient parameter space occupied by two observational classes: LFBOTs (485, 486) and TDEs (111, 552, 553). Supernovae are excluded by the rapid evolution and persistently featureless spectra, with a lack of interaction signatures and the high radiated energy ( $>10^{51}$  erg). The luminous, fast-cooling transients presented by (513) occupy a similar location in luminosity-timescale space, but show rapid cooling that is excluded for 24puz. They are also not X-ray and radio bright.

TDEs occur when a star is disrupted by a massive black hole (MBH; (110, 371, 554)). Like LFBOTs, TDEs typically produce blue, constant color optical lightcurves, but they evolve more slowly, rising over few-week timescales and fading over months (116, 121, 128, 136). Most TDEs produce broad ( $\sim 10^4$  km s $^{-1}$ ) Balmer and Helium spectroscopic features (13, 128, 134), but two, possibly connected subclasses of TDEs produce featureless spectra: featureless TDEs (F-TDEs; (13)) and jetted TDEs (394). F-TDEs have spectra that are featureless for months post-TDE (13, 134). Jetted TDEs are best known for launching collimated, relativistic jets (245, 373, 395–397), and there is some evidence that they also produce featureless spectra and blue, constant color thermal emission (in addition to luminous, nonthermal emission from the jet; (394)). By selection, TDEs are traditionally detected in the nuclei of their host galaxies (typically within 1''; (13, 116, 128, 134)).

LFBOTs rise on few-day timescales and fade over  $\sim 1$  week (487, 490–492, 494, 528, 529, 555). LFBOTs produce hot ( $\sim 10^{4-5}$  K) optical flares without substantial cooling and absolute magnitudes brighter than approximately  $-20.5$  mag. They evolve fast ( $\lesssim$  week timescale), with no detectable optical spectral lines at early times. LFBOTs never show nebular features, and instead have Hydrogen and Helium features, unlike stellar explosions. They are luminous in the millimeter, suggestive of outflows into dense media ( $\sim 10^5$  cm $^{-3}$ ). LFBOTs have hard X-rays ( $\nu F_\nu \sim \nu^{-0.5}$ ) likely from the central engine that is also responsible for powering the transients, which could be explained by invoking an asymmetric circum-transient medium and a weak, decelerating jet. They often have a Compton hump feature detected in the hard X-ray, which is common among accretors like X-ray binaries and AGN, and is associated with cold, optically-thick gas (556). The X-ray spectra have been detected to soften at late-times (497). LFBOTs are hosted in a range of environments,

although most have been offset within galaxies near the star forming main sequence. LFBOTs have featureless blue optical spectra that, in some cases, develop broad ( $\sim 10^4 \text{ km s}^{-1}$ ) hydrogen/helium emission after  $\sim 10$ s of days and intermediate width ( $\sim 10^3 \text{ km s}^{-1}$ ) lines after  $\sim 1$  month. *Hubble Space Telescope* observations of one LFBOT, AT 2018cow, show a late-time (years) plateau in the UV and soft X-ray (496, 497, 557, 558). The most offset LFBOT detected thus far is at  $1 \text{ kpc} \approx 3.5r_e$  from its host galaxy, where  $r_e$  is galaxy half-light radius (495).

The physical origin of LFBOTs is unknown. The late-time UV and possible X-ray plateau detected for AT 2018cow is reminiscent of late-time emission from the compact accretion disks produced during TDEs (496, 497, 557, 558), suggesting that LFBOTs may be TDEs. The faintness of the plateau, combined with the off-nuclear location of the transients, requires TDEs by IMBHs. LFBOTs may alternatively be extreme stellar explosions/mergers. Models are typically required to produce an extended, dense, aspherical medium and a highly energetic and compact central engine. (485) proposes the delayed merger of a black hole and a Wolf-Rayet star. (16) consider a failed explosion of a blue supergiant star, resulting in a stellar-mass BH surrounded by the remains of the star, although (497) revise this model to prefer a super-Eddington accreting source. Both models require the presence of massive stars ( $\gtrsim 20 M_\odot$ ). A millisecond magnetar formed after the electron capture supernova of a  $\sim 8\text{--}10 M_\odot$  star is consistent with observations, but still invokes a relatively massive star. Attempts to model the LFBOT AT 2018cow as a magnetar require neutron stars with near maximal masses and may not be able to explain the multiwavelength emission (e.g., fast X-ray variability, late-time UV plateau) (498).

24puz has multiwavelength properties that are consistent with both TDEs and LFBOTs. In Figure 7.2, we compare the optical/UV blackbody luminosity evolution of 24puz, TDEs, and LFBOTs. The left panel shows the blackbody luminosity as a function of time for these objects. 24puz has a lightcurve evolution that is generally consistent with LFBOTs, with a rapid rise followed by a power-law decay. 24puz peaks at a later time relative to other LFBOTs and has a slower rise. This is highlighted in the right panel, which shows the time above half peak luminosity on the x-axis and the peak  $g$ -band luminosity on the y-axis. 24puz is slower than all LFBOTs. Selection effects likely play a role in this trend: LFBOTs are selected to be fast-evolving, with generally faster than  $\sim 1$  week timescales (e.g. 490). 24puz may be a slow evolving LFBOT, suggesting that LFBOT searches should be performed with looser timescale cuts.

The lightcurve shape of 24puz is also consistent with TDEs, although these events show more variation in their blackbody luminosity evolution relative to LFBOTs. The location of 24puz in luminosity-timescale space is unprecedented for TDEs, which generally show a positive correlation between luminosity and timescale. F-TDEs break this correlation, but have long timescales ( $\gtrsim 30$  days). There are no obvious selection effects that would prevent events like 24puz from being discovered in TDEs searches, if 24puz-like objects can occur in galactic nuclei, suggesting that such events are rare.

The featureless optical spectra detected from 24puz are consistent with both early time LFBOT observations and with F-TDEs and jetted TDEs. LFBOTs generally produce some spectral features at late times (both broad and narrow interaction lines). If 24puz is an LFBOT, the lack of lines could be consistent with the high luminosity, as discussed above, but this would be unprecedented for this class. F-TDEs remain featureless at all times, consistent with 24puz.

A red excess like that from 24puz has been detected for the LFBOT AT 2018cow (489). The origin of this excess is also unknown, although similar models were proposed as we have explored for 24puz. The optical-IR SED of AT 2018cow is shown as red stars in Figure 7.14. The peak of the AT 2018cow excess is redder than that of 24puz, and so a thermally-emitting dust origin is still consistent with the observations (533). Reprocessing can also reproduce the red excess, but requires  $\gtrsim 5 M_{\odot}$  of material (550). TDEs have been theorized to produce near-infrared excesses due to reprocessing (113), with one known example that showed a red excess likely due to reprocessing by a disk-like structure (559). Thermally emitting dust has been detected for multiple TDEs, but this emission peaks in the mid-infrared and on year-long timescales and is inconsistent with the observations of 24puz.

The radio and millimeter limits from 24puz are consistent with both TDEs and LFBOTs.  $\gtrsim 30\%$  of optically-selected TDEs produce radio emission at  $\gtrsim 3$  yrs post-disruption. The fraction detected at early times is lower, suggesting that most TDEs do not produce luminous radio emission at this point ( $\lesssim 10^{38}$  erg  $s^{-1}$ ). This is consistent with the 24puz limits. It is also important to note that most radio-observed TDEs are not F-TDEs, which are generally at higher redshifts. A more detailed study of the early-time radio properties of these events would be required to compare to 24puz.

LFBOTs ubiquitously produce radio and millimeter emission. As shown by the stars in Figure 7.11, the parameter space occupied by the radio/mm luminous LFBOT

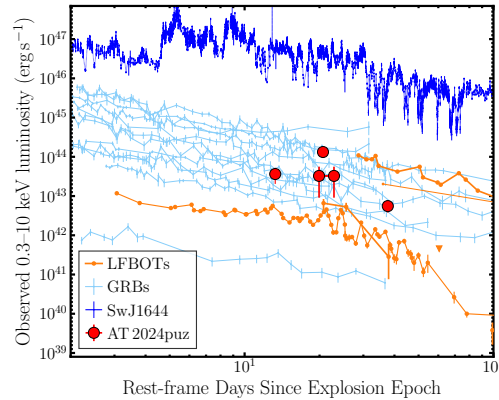


Figure 7.15: X-ray lightcurve comparison, adapted from (529). 24puz is shown in red and LFBOTs in orange. For completeness, a population of gamma-ray bursts (GRBs) is shown in light blue, as these are common comparison points for X-ray transient emission. The jetted TDE SwJ1644 is shown in blue. 24puz is among the most X-ray luminous LFBOTs. It shows a variability and evolution timescale comparable to both LFBOTs and the jetted TDE.

AT 2018cow is excluded for 24puz, but if 24puz has a moderately less dense ambient medium relative to AT 2018cow, the lack of radio/mm is expected. The lack of transient spectral features would also be expected in this case.

The X-ray lightcurve from 24puz is fully consistent with LFBOTs, as shown in Figure 7.15. The high variability and rapid decline have been observed for multiple LFBOTs. 24puz is among the most X-ray luminous LFBOTs. The hard spectral index  $\Gamma = 1.7$  is also consistent with observations of X-rays from LFBOTs. The rapid evolution and hardness of LFBOT X-rays have been used to argue for the presence of a compact central engine from these sources.

The X-ray properties of TDEs are much more heterogeneous than those of LFBOTs. Most X-ray detected TDEs have soft spectra  $\Gamma \gtrsim 3$ , although exceptions do exist (142, 560, 561). There are also X-ray detected TDEs that show rapid variability and fading (142), although this behaviour is not as ubiquitous as for LFBOTs. Jetted TDEs, in particular, show hard, variable X-rays like 24puz (373, 394, 396). As shown by the blue lightcurve in Figure 7.15, the X-ray luminosities of these events are much higher than that from 24puz due to beaming effects, but the lightcurve evolution is otherwise similar. X-ray constraints on F-TDEs are weak.

The host galaxy of 24puz is also fully consistent with LFBOT hosts in terms of stellar mass, star formation rate, and offset from the transient. LFBOT host galaxy are shown relative to that of 24puz and the star forming main sequences in Figure 7.8.

While the LFBOT hosts show a range of stellar masses, they tend to lie near the star forming main sequence and, there are three events at comparable host galaxy masses to that of 24puz. As shown in the right panel of Figure 7.8, 24puz would be among the most offset LFBOTs relative to its host, but the LFBOT AT 2023fhn is at a similarly large offset (492, 495). 24puz and AT 2023fhn both have large offsets given expectations based on their stellar mass, if they are associated with star formation, as is seen when comparing to the core-collapse supernovae shown in Figure 7.8.

TDE host galaxies, in contrast, are inconsistent with the 24puz host. TDE hosts are shown as blue scatter in Figure 7.8. These hosts are generally more massive than that of 24puz and lie below the star forming main sequence (134, 135). Selection effects likely play a role here. TDEs are required to be nuclear, whereas massive black holes in dwarf galaxies are often wandering due to a poorly defined gravitational potential. If TDEs from low mass galaxies tend to be off-nuclear, like 24puz, they will not be included in current selections. F-TDE host galaxies are the most discrepant from that of 24puz, as they tend to be the reddest and most massive ( $M_* \gtrsim 10^{10} M_\odot$ ) of the TDE hosts (13)

We conclude that 24puz closely resembles LFBOTs, except that it is more luminous in the X-ray through optical, slower evolving, and has no spectral features at late times. 24puz is similar to TDEs in many ways, but that it is fast and luminous in the optical/UV, off-nuclear from a low-mass galaxy, and has harder, faster-evolving X-ray emission than most TDEs.

### **The rate of 24puz-like transients**

Our search that produced 24puz was incomplete, and a sample size of one leads to large statistical uncertainties in a rate estimate. However, we can set an upper limit on the rate using the ZTF bright transient survey (BTS; (562, 563)), which has produced complete samples of transients above  $m < 18.5$  mag. No sources have been reported with blue, constant colors, extragalactic redshifts, and a timescale of  $\sim 10$  days. We thus use the lack of 24puz-like objects reported in the BTS sample to constrain the rate of such events. Given the peak magnitude of 24puz ( $m_g = 19.2$  mag), the magnitude limit of BTS, and the completeness reported by (562), we find a  $3\sigma$  upper limit on the rate of 24puz-like objects of  $< 4.6 f_c^{-1} \text{ Gpc}^{-3} \text{ yr}^{-1}$ . Here  $f_c$  is the completeness fraction.

The optical TDE rate is  $310_{-100}^{+60} \text{ Gpc}^{-3} \text{ yr}^{-1}$  (134), which is higher than the 24puz

rate, but is consistent if 24puz-like objects are a subset of TDEs. The jetted TDE rate is  $2_{-1}^{+4} (f_b/1\%)^{-1} \text{Gpc}^{-3} \text{yr}^{-1}$  for a beaming fraction  $f_b = 1\%$  (394), which is consistent with the rate of 24puz-like objects. The rate of LFBOTs has been estimated as  $0.3\text{--}420 \text{yr}^{-1} \text{Gpc}^{-3}$  (490),  $< 300 \text{yr}^{-1} \text{Gpc}^{-3}$  (487, extrapolated from Palomar Transient Factory data), and  $700\text{--}1400 \text{yr}^{-1} \text{Gpc}^{-3}$  (487, extrapolated from Pan-STARRS1 Medium-Deep Survey data). These are generally consistent with the rate of 24puz-like objects, although the LFBOT rate from the Pan-STARRS1 Medium-Deep Survey is higher.

### **Nature of the powering source**

We next consider possible explanations to account for nature of the source powering 24puz. We require a system that can produce  $\gtrsim 10^{51}$  erg of radiated energy, largely in a  $\sim 2$  week span. In the shock model, this energy could be produced in a shorter,  $\sim$ day time-span ( $\sim 10^5$  s), corresponding to the light-curve rise time. The source is surrounded by a dense  $\sim 10^{10} \text{cm}^{-3}$  medium extending to at least  $10^{15}$  cm, with a shallow density profile scaling as  $\sim r^{-1}$ . The source produces hard ( $\Gamma = 1.7$ ) X-ray emission that is variable on short,  $\sim 3$  day timescales. We conclude that 24puz has a compact central engine, as has been argued for LFBOTs and given the concordance with the observed properties.

In the next portion of this discussion, we will speculate from the host galaxy properties of 24puz. With a sample size of one, such a procedure is poorly justified. Our goal is not to definitely exclude models or declare a specific model correct. Even if we favor a model, we note that this will always be riddled with uncertainty as we are extrapolating from a single observed source at this time.

The host galaxy of 24puz has a low star-formation rate and stellar mass. The lack of strong star formation is in contrast to expectations from models invoking massive stars or magnetars for the origin of a source like 24puz. The low mass is unexpected for models that invoke neutron stars, which should be more abundant in galaxies with higher stellar masses. Selection effects may of course play a role as we required a faint host galaxy. Star-forming galaxies are detectable to higher redshifts than quiescent galaxies, due to their higher luminosities. If this selection effect is the reason that we have not detected star formation, then the lack of 24puz-like transients identified thus far in, e.g., the BTS sample or supernovae searches is a puzzle. These events should be orders of magnitude more common in star-forming and massive galaxies. Alternatively, we may be simply fortunate to have detected

24puz in a galaxy with very few massive stars. The only way to test this explanation is to continue searching for such events and discovering a sample. Instead, for the rest of this section, we will assume that 24puz is not produced by a massive star. A similar argument holds if 24puz is associated with a globular cluster or a NS, which should be more common in massive galaxies, so we do not consider these scenarios either. Note that this does not rule out a *nuclear* stellar cluster as a putative host.

Instead, we consider accreting black holes. If 24puz is associated with a  $< 50 M_{\odot}$  stellar mass black hole, such events should be orders of magnitude more abundant in massive galaxies  $\sim 10^{11} M_{\odot}$  (564, 565). If 24puz is associated with SMBHs  $> 10^6 M_{\odot}$ , TDE searches should have discovered analogous events, although they have not been focused on off-center events. Moreover, the proximity of a putative dwarf galaxy host and the empirically derived local scaling relations between central black hole mass and stellar mass of galaxies suggests that the BH mass in 24puz is firmly in the IMBH mass range (566). Hence, if 24puz is associated with a black hole, it must be associated with a black hole of mass  $M_{\text{BH}}$  such that  $50 \lesssim M_{\text{BH}}/M_{\odot} \lesssim 10^5 M_{\odot}$ .

We conclude that 24puz is most likely produced by a moderately massive black hole. From the energy budget point of view, accretion events onto massive BHs can readily produce the amount of energy observed, and accreting BHs are known to be able to launch winds/jets, so our shock models are feasible. However, in the context of this explanation, we must contend with two points. First, the transient is highly offset. Second, the shock breakout analysis of the optical emission suggests a dense ( $\sim 10^{10} \text{ cm}^{-3}$ ), extended ( $10^{15} \text{ cm} \approx 10^4 \text{ AU}$ ) medium surrounding the transient. This is much denser than typical environments around nuclear supermassive black holes (see Fig. 2 of (150)). Feasible scenarios to produce 24puz must produce this medium, regardless of BH mass.

The high offset from the host galaxy is feasible if the black hole is recoiling and/or has been ejected. At the lower end of this mass range, a recoil is fairly plausibly expected: BHs formed from stellar deaths are expected to have a natal kick similar to that of a neutron star (567). If the BH is formed at the time that most of the stars in the galaxy formed ( $\sim 100 \text{ Myr}$  ago, based on our host stellar population modeling) and receives a kick of  $\sim 100 \text{ km s}^{-1}$ , it will travel 10 kpc by the time of our observation. Thus, the projected offset observed of 5 kpc is feasible.

At the higher end of this mass range, we are met with a challenge. IMBHs, if formed via direct collapse of a gas cloud in-situ, should not necessarily have an associated kick. They are however expected to wander throughout their host galaxy (59, 568),

particularly if the host is a dwarf galaxy with a poorly defined gravitational potential (58). This BH is very offset from any light from the host galaxy, which depending on the simulation suite analyzed may or may not be expected frequently, the predictions from the ROMULUS simulation (59) are different from those from the ASTRID simulation wherein wanderer off-set distributions are shorter (58). Assuming the dark matter traces the stellar matter, it is unlikely that the BH is close to even a local minimum in the gravitational potential. This model is currently unsettled. Instead, the IMBH could recoil if it has undergone a merger with another IMBH (569), which is feasible if the disturbed morphology of G1 indicates a merger. Deep follow-up imaging can confirm or exclude evidence of a merger, but note that the galaxies of stellar mass  $10^8 M_{\odot}$  are not expected to undergo many mergers specially at late times, with an expected rate of  $<0.01 \text{ Gyr}^{-1}$  (570). The ejection of an IMBH that has formed and grown in a dense nuclear star cluster (478) that has been ejected as a result of a merger is yet another possibility. In that case, we favor the tidal disruption of a white dwarf (571) over the case of main-sequence disruption, because the circularization (or disk formation) timescale for main-sequence TDEs may be much longer for IMBHs due to weak apsidal precession (572). Another challenge of the IMBH-TDE picture is the need of a dense circum-transient medium, which is not generally available before the disruption.

The high circum-transient medium density and energetics of the event can be accommodated by the model from (485). This model nominally invokes a black hole or neutron star in a binary with a massive, Wolf-Rayet star. The compact object enters into a common envelope phase with the massive star and begins inspiraling until it disrupts the stellar core. The lack of star formation from 24puz disfavors a massive star companion, but an main-sequence or evolved stellar companion should produce a similar signal. If the evolved star is a (sub)giant with a large radius, then the timescale may be too long to produce the very short rise time of 24puz. A tidally disrupted main-sequence star may better match the timescale (573). We encourage efforts to simulate the emission from 24puz within this model, in particular, taking into account the requirements of an evolved or main sequence stellar companion and a low binary mass ratio.

We finally consider the case that our assumption that the source cannot be produced by an NS or low-mass, stellar-mass BH due to the host galaxy stellar mass does not hold up to continued searches for 24puz-like sources. Another possible scenario is that the event comes from the explosion of a low-mass helium star with a main-

sequence companion star and that the newly born neutron star happens to tidally disrupt the companion star (499). The low-mass helium star undergoes extreme mass loss before the SN explosion (574), creating the dense circum-transient medium. Such an explosion may be produced after a delay up to 50 Myrs that is consistent with the stellar population age in G1.

## 7.7 Conclusions

In this paper, we have presented AT 2024puz, a luminous, multiwavelength transient associated with a dwarf galaxy. 24puz was discovered as a hostless, blue optical flare by the ZTF survey. Deep imaging and spectroscopy showed that it is associated with a dwarf galaxy of mass  $\sim 10^8 M_\odot$  at  $z = 0.35614 \pm 0.00009$  that lies below the star-formation main sequence. The spectra show no features associated with the transient.

The optical transient was accompanied by luminous UV, IR, and X-ray emission. The early-time optical/UV emission is consistent with either an accretion flare that produces highly super-Eddington radiation, or with a shock that is breaking out within the circum-transient medium. In the latter case, the circum-transient medium mass is  $\lesssim 1 M_\odot$  and it extends to a radius  $\sim 10^{15}$  cm with a shallow density profile. The shock breakout model may not explain the lack of late-time cooling and line emission, and so would require an additional ionizing source, such as accretion, at  $\sim 20$  days. A near-infrared excess is seen at late-times  $\sim 80$  days that may be consistent with a re-processing layer. The X-ray emission could be produced by a shock or a compact central engine, but the rapid evolution and variability is challenging to accommodate within a shock model.

Based on the lack of star formation and low stellar mass in the host galaxy, we favor a model invoking an BH with mass  $\gtrsim 50 M_\odot$  (i.e., high mass stellar mass BH or IMBH), although we mildly prefer a BH formed in a stellar explosion to accommodate the high observed offset from the host galaxy. A similar model has been proposed by (485), who postulate a stellar mass black hole consuming a massive star. Given the low star formation rate of G1, we prefer a main sequence or evolved companion, and we encourage more detailed consideration of this model. However, models that involve ejected IMBHs also remain plausible, in which case we favor the tidal disruption of a white dwarf to match the observed timescale of 24puz.

Pinning down the trigger of 24puz requires a sample of similar sources. The portion of parameter space occupied by this transient has, to our knowledge, barely been

explored, and opens up a new section of the landscape of hot, blue transients. These objects are proving to offer a powerful probe of discovering massive stellar mass BHs, IMBHs, and NSs. Instruments and telescopes such as the upcoming Rubin Observatory, the Einstein Probe, and the Ultraviolet Explorer should be sensitive to thousands of these hot blue transients. However, archival searches in ZTF show great promise for identifying and characterizing such previously unexplored transient classes.

In addition to identifying a sample of 24puz-like events, deep late-time follow-up may be able to pin down the event trigger. In particular, deep, multi-band imaging would enable detailed constraints on the star-formation history both of G1 and at the location of 24puz, strengthening our arguments against massive star and NS progenitors. Late-time radio constraints would exclude the late-time emergence of any collimated jet, as is sometimes observed for TDEs and thus may favor an IMBH progenitor (149). Deep space-based spectroscopy can rule out any late-time interaction features, which would provide an additional handle on the circum-transient medium spectrum.

We conclude by briefly considering implications for LFBOT searches and models, if 24puz is a member of this population and our analysis of the likely progenitor is correct (accreting,  $\gtrsim 50 M_{\odot}$  stellar mass BH in a binary). 24puz adds to the increasing fraction of LFBOTs detected in low mass galaxies near the star-forming main sequence, and is the second LFBOT with a very high offset. Models that implicate massive stars in LFBOT models should be reassessed. 24puz suggests that LFBOTs need not be as fast evolving as previously found, and they can be even more luminous than thought. If this high luminosity is a function of the circum-transient medium parameters, it might suggest that LFBOT luminosity will be correlated with the properties of the companion star from which the BH is accreting. While the radio/millimeter constraints from 24puz offer poor constraints at present, they do suggest that, despite the high optical/UV and X-ray luminosities from this event, the radio/millimeter luminosity was not correspondingly high. LFBOTs may not be ubiquitously associated with luminous emission at these frequencies, as was once thought.

## 7.8 Appendix

### Details of observations

In Tables 7.4, 7.6, 7.7, 7.8, 7.9, 7.10, 7.11, and 7.12, we provide the details of our observations, as described in Section 7.5.

Table 7.4: P60/SEDM Observation Summary

Date	MJD	Filter	Mag	Mag Error	Limiting Mag
2024-08-01	60523.2	<i>u</i>	19.58	0.13	20.14
		<i>u</i>	19.58	0.45	18.78
		<i>r</i>	20.066	0.0485	21.69
		<i>i</i>	20.391	0.0769	21.52
2024-08-02	60524.2	<i>u</i>	19.51	0.16	19.87
		<i>u</i>	19.51	0.18	19.75
		<i>r</i>	20.152	0.063	21.49
		<i>i</i>	20.28	0.11	21.03
2024-08-14	60536.2	<i>g</i>	21.16	0.19	21.32
	60543.2	<i>g</i>	21.52	0.20	21.61
2024-08-22	60544.2	<i>g</i>	21.78	0.22	21.75
		<i>i</i>	21.35	0.18	21.55

**Note.** Summary of P60/SEDM Observations.

Table 7.5: Lowell Discovery Telescope Observations

Filter	Mag	Mag Error
<i>u</i>	22.101	0.068
<i>g</i>	22.220	0.054
<i>r</i>	22.417	0.062
<i>i</i>	22.425	0.117
<i>z</i>	21.935	0.314

**Note.** Summary of Lowell Discovery Telescope observations on 2024-08-27 (MJD 60549).

### Chance association probability

In this section, we compute the probability that 24puz randomly lies at its location with respect to nearby galaxies. If 24puz were associated with an unrelated background source, it would have a uniform probability of lying at any location in the field. We assess the probability that 24puz, if unassociated with any detected galaxy, would be located at the observed position with respect to the detected galaxies. Because of the limited field-of-view of our *HST* observation, we perform this

Table 7.6: Liverpool Telescope Observations

Date	MJD	Filter	Mag	Mag Error	Limiting Mag
2024-08-05	60527.97	<i>u</i>	19.85	0.15	19.27
		<i>g</i>	20.27	0.08	20.71
		<i>r</i>	20.53	0.08	21.15
		<i>i</i>	20.9	0.10	21.26
2024-08-06	60528.96	<i>u</i>	19.92	0.11	19.98
		<i>g</i>	20.33	0.05	21.30
		<i>r</i>	20.91	0.07	21.61
		<i>i</i>	21.04	0.06	21.98
2024-08-08	60530.96	<i>u</i>	20.20	0.13	20.07
		<i>g</i>	20.61	0.06	21.36
		<i>r</i>	21.15	0.09	21.63
		<i>i</i>	21.09	0.07	21.86
2024-08-15	60537.89	<i>u</i>	20.84	0.31	19.59
		<i>g</i>	21.83	0.29	20.86
		<i>r</i>	21.58	0.20	21.17
		<i>i</i>	21.32	0.13	21.50
2024-08-16	60538.96	<i>u</i>	19.97	0.26	18.53
		<i>g</i>	20.78	0.19	20.20
		<i>r</i>	21.60	0.32	20.36
		<i>i</i>	21.62	0.28	20.54
2024-08-18	60540.87	<i>g</i>	20.41	0.22	20.10
		<i>r</i>	21.45	1.07	20.40
		<i>i</i>	22.52	0.92	20.87
2024-08-19	60541.87	<i>u</i>	20.34	0.45	25.93
		<i>g</i>	21.10	0.51	27.14
		<i>i</i>	21.33	0.54	27.84
2024-08-20	60542.88	<i>i</i>	21.43	0.22	19.16

**Note.** Summary of Liverpool Telescope observations.

experiment using observations of the Cosmological Evolution Survey (COSMOS; (575)) field as part of the Cosmic Assembly Near-infrared Deep Extragalactic Legacy Survey (CANDELS; (576, 577)), which were performed with the *HST* ACS/WFC instrument and include F606W measurements. While the filter throughputs and pixel scales are slightly different for ACS/WFC F606W and WFC3/UVIS F606W images, we estimate that they cause percent-level changes in the measured fluxes and Kron radii, which are negligible for our purposes. We retrieved *sextractor* catalogs for the CANDELS field from (578).

Table 7.7: Swift/UVOT Observations

Date	MJD	ObsID	Band	Exposure [sec]	Flux [ $\mu$ Jy]
2024-08-03	60525.8001	16746001	<i>u</i>	165.1	$39.7 \pm 6.2$
–	–	–	<i>u</i>	165.2	$46.1 \pm 6.4$
–	–	–	<i>m2</i>	495.8	$20.5 \pm 3.7$
–	–	–	<i>w2</i>	601.5	$16.9 \pm 2.2$
2024-08-12	60535.0001	16746002	<i>u</i>	148.4	$27.2 \pm 6.0$
–	–	–	<i>m2</i>	444.7	$13.0 \pm 5.0$
–	–	–	<i>w1</i>	296.0	$19.3 \pm 4.1$
–	–	–	<i>w2</i>	544.8	$9.9 \pm 1.9$
2024-08-16	60538.5001	16746003	<i>m2</i>	323.6	$5.6 \pm 3.6$
–	–	–	<i>w2</i>	403.0	$3.9 \pm 1.8$

**Note.** Summary of Swift/UVOT Observations.

Table 7.8: Swift/XRT Observations

Date	MJD	ObsID	Exposure [sec]	Counts $\text{sec}^{-1}$	Flux [ $10^{-13} \text{ erg cm}^{-2} \text{ s}^{-1}$ ]
2024-08-03	60525.816746001	3671.3	0.0019 <sup>+0.0011</sup> <sub>-0.0008</sub>	$0.8^{+0.5}_{-0.4}$	
2024-08-12	60535.016746002	1476.8	0.001 <sup>+0.0019</sup> <sub>-0.001</sub>	< 4.1	
2024-08-16	60538.516746003	2783.2	0.0023 <sup>+0.0017</sup> <sub>-0.0012</sub>	< 3.8	
2024-08-20	60542.616746004	2482.2	0.0005 <sup>+0.001</sup> <sub>-0.0005</sub>	< 2.2	
2024-10-30	60613.016746005	2061.1	0.0009 <sup>+0.0012</sup> <sub>-0.0007</sub>	< 2.7	
2024-11-02	60616.216746006	2805.7	0.0006 <sup>+0.0008</sup> <sub>-0.0005</sub>	< 1.9	
2024-11-05	60619.016746007	2657.9	0.0 <sup>+0.0009</sup> <sub>0.0</sub>	< 1.6	
2024-11-08	60622.416746008	2710.4	0.0034 <sup>+0.0024</sup> <sub>-0.0017</sub>	< 5.5	

**Note.** Summary of Swift/XRT Observations. Fluxes are computed assuming  $\Gamma = 1.7$ . Upper limits are  $3\sigma$ .

We compute the random association probability as follows. First, we correct for the increased depth of the CANDELS image. We randomly assign each COSMOS source a per-pixel rms noise from the observed per-pixel noises in our observations and define detectable sources as those with a total signal-to-noise (i.e., integrated over the entire source rather than per-pixel) larger than three, which is our detection threshold.

We treat the undetected sources as a random sample of background sources and compute the distances from each to the  $n^{\text{th}}$  nearest-neighbors, in units of Kron radii, for  $n = 1 - 10$ . We only consider galaxies within  $20''$  given the distance from 24puz to the edge of the observation field. We use these distances to compute

Table 7.9: *XMM-Newton* Observations

Date	MJD	ObsID	Instrument	Exposure [s]	Count Rate [ $10^{-2}$ ct s $^{-1}$ ]	$\log\left(\frac{\text{Flux}}{\text{erg cm}^{-2} \text{ s}^{-1}}\right)$
2024-08-14	60536	0953011201	EPIC-PN	3873	$4.04 \pm 0.35$	$-12.577 \pm 0.024$
–	–	–	EPIC-MOS1	12370	$1.19 \pm 0.12$	–
–	–	–	EPIC-MOS2	13660	$0.98 \pm 0.09$	–
2024-09-05	60558	0953011301	EPIC-PN	12940	$0.34 \pm 0.12$	$-13.92 \pm 0.15$
–	–	–	EPIC-MOS1	23700	$0.033 \pm 0.033$	–
–	–	–	EPIC-MOS2	27790	$0.017 \pm 0.042$	–
2024-11-30	60644	0953012101	EPIC-PN	27090	$0.175 \pm 0.052$	$-13.91 \pm 0.07$
–	–	–	EPIC-MOS1	37470	$0.045 \pm 0.020$	–
–	–	–	EPIC-MOS2	39130	$0.050 \pm 0.020$	–

**Note.** Summary of *XMM-Newton* Observations. Exposure times are quoted after GTI flagging. Fluxes are computed from 0.3–10 keV using a power-law model with a tied photon index.

Table 7.10: *NuSTAR* Observations

Date	MJD	ObsID	FPM	Exposure [s]	Counts (src/bkg)	Flux 90% UL [ $10^{-13}$ erg cm $^{-2}$ s $^{-1}$ ]
2024-09-06	60559.29	1001632002	A	24879.3	205 / 207	0.52
–	–	–	B	24622.1	242 / 251	0.57
2024-09-07	60560.79	1001632004	A	37667.2	302 / 294	0.70
–	–	–	B	37284.5	376 / 370	0.73

**Note.** Summary of *NuSTAR* Observations. 90% confidence limits assume an unabsorbed power-law with  $\Gamma = 1.77$  in the 3–79 keV range.

Table 7.11: Keck I/LRIS observations

Date	MJD	Exposure [sec]	Airmass	Standard (spec.)	Slit Width (spec.)
2024-07-29	60520.4	600	1.33	BD+28	1.0''
2024-08-05	60527.3	1800	1.20	BD+28	1.0''
2024-09-07	60560.3	4500	1.42	Feige 110	1.0''
2024-10-07	60590.2	7200	1.82	G191-B2B	1.0''

**Note.** Summary of Keck I/LRIS observations.

two probabilities. First, we consider the nearest galaxy to 24puz, which we will denote “G1” hereafter. We compute the probability of finding the nearest-neighbor closer than the distance G1 for a randomly located sources. We find a probability  $p_1 = 3 \times 10^{-4}$  of the nearest neighbor being closer than G1. Second, we compute the probability that all the second through tenth-nearest neighbors are closer than

Table 7.12: *HST*/WFC3 Observation summary

Date	MJD	Detector	Filter	Exposure [sec]
2024-09-30	60583	UVIS	F606W	994
2024-09-30	60583	UVIS	F336W	1073
2024-09-30	60583	UVIS	F105W	1059
2024-09-30	60583	UVIS	F160W	1059

**Note.** Summary of *HST*/WFC3 observations.

those observed for 24puz:  $p_{2-10} = 1.3 \times 10^{-3}$ . It is thus unlikely both that 24puz lies close to the observed galaxies by chance ( $3\sigma$ ) or that 24puz lies close to G1 by chance ( $3.4\sigma$ ).

### Ultraviolet-infrared spectral energy distributions and best-fit parameters

In Figure 7.16, we show the multi-epoch, best-fit blackbody models. In Table 7.13, we tabulate the best-fit parameters.

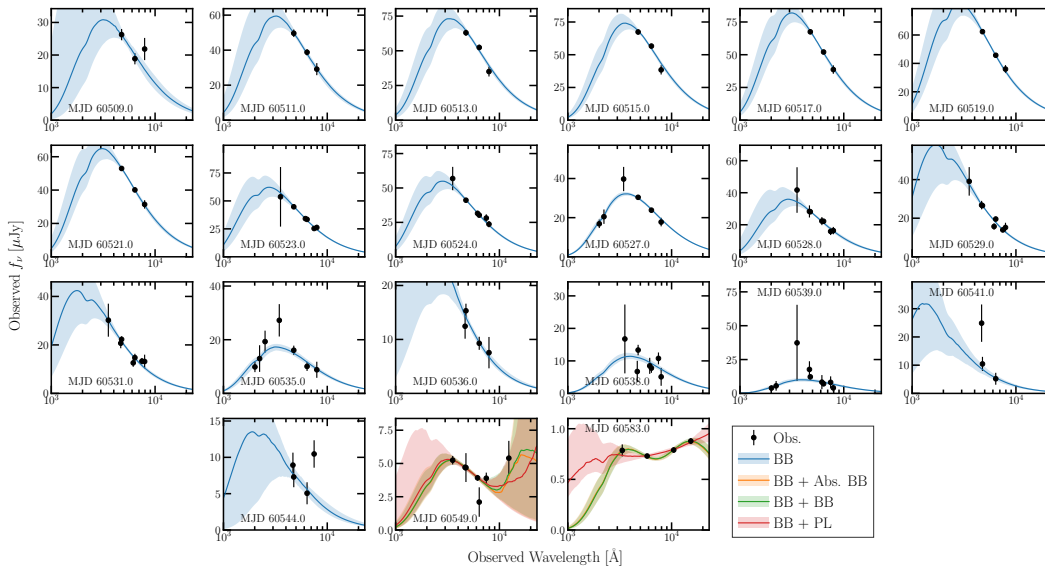


Figure 7.16: Blackbody fits to each epoch of UV/optical imaging of 24puz, as described in Section 7.4. The fits are shown as colored bands and the data as black scatter points.

### X-ray spectral modeling

The best-fit spectral parameters of our MJD 60558 *XMM-Newton* observations are shown in Figure 7.17.

Table 7.13: UVOIR blackbody modeling

Date	MJD	Model	$\log \frac{T_{bb}}{K}$	$\log \frac{R_{bb}}{cm}$	$\log \frac{L_{bb}}{erg\ s^{-1}}$	$M_g$ [mag]	$\log \frac{T_{IR}}{K}$	$\log \frac{R_{IR}}{cm}$	$\Gamma_{IR}$	$\log \frac{L_{IR}}{erg\ s^{-1}}$
2024-07-1860509		BB	4.37 <sup>+0.18</sup> <sub>-0.13</sub>	15.06 <sup>+0.14</sup> <sub>-0.17</sub>	44.44 <sup>+0.4</sup> <sub>-0.24</sub>	-20.56 <sup>+0.101</sup> <sub>-0.069</sub>	—	—	—	—
2024-07-2060511		BB	4.37 <sup>+0.081</sup> <sub>-0.064</sub>	15.197 <sup>+0.066</sup> <sub>-0.074</sub>	44.73 <sup>+0.17</sup> <sub>-0.13</sub>	-21.249 <sup>+0.052</sup> <sub>-0.052</sub>	—	—	—	—
2024-07-2260513		BB	4.336 <sup>+0.055</sup> <sub>-0.046</sub>	15.288 <sup>+0.049</sup> <sub>-0.054</sub>	44.774 <sup>+0.114</sup> <sub>-0.091</sub>	-21.55 <sup>+0.032</sup> <sub>-0.033</sub>	—	—	—	—
2024-07-2460515		BB	4.309 <sup>+0.04</sup> <sub>-0.039</sub>	15.333 <sup>+0.042</sup> <sub>-0.042</sub>	44.751 <sup>+0.08</sup> <sub>-0.067</sub>	-21.646 <sup>+0.035</sup> <sub>-0.033</sub>	—	—	—	—
2024-07-2660517		BB	4.377 <sup>+0.056</sup> <sub>-0.048</sub>	15.257 <sup>+0.046</sup> <sub>-0.054</sub>	44.871 <sup>+0.118</sup> <sub>-0.094</sub>	-21.581 <sup>+0.037</sup> <sub>-0.035</sub>	—	—	—	—
2024-07-2860519		BB	4.425 <sup>+0.056</sup> <sub>-0.051</sub>	15.189 <sup>+0.046</sup> <sub>-0.05</sub>	44.93 <sup>+0.12</sup> <sub>-0.11</sub>	-21.451 <sup>+0.032</sup> <sub>-0.027</sub>	—	—	—	—
2024-07-3060521		BB	4.384 <sup>+0.057</sup> <sub>-0.048</sub>	15.195 <sup>+0.048</sup> <sub>-0.053</sub>	44.775 <sup>+0.124</sup> <sub>-0.095</sub>	-21.295 <sup>+0.032</sup> <sub>-0.031</sub>	—	—	—	—
2024-08-0160523		BB	4.436 <sup>+0.073</sup> <sub>-0.055</sub>	15.106 <sup>+0.05</sup> <sub>-0.063</sub>	44.81 <sup>+0.17</sup> <sub>-0.12</sub>	-21.077 <sup>+0.022</sup> <sub>-0.026</sub>	—	—	—	—
2024-08-0260524		BB	4.423 <sup>+0.068</sup> <sub>-0.055</sub>	15.102 <sup>+0.051</sup> <sub>-0.058</sub>	44.75 <sup>+0.15</sup> <sub>-0.12</sub>	-21.006 <sup>+0.032</sup> <sub>-0.037</sub>	—	—	—	—
2024-08-0560527		BB	4.299 <sup>+0.014</sup> <sub>-0.015</sub>	15.164 <sup>+0.019</sup> <sub>-0.016</sub>	44.377 <sup>+0.029</sup> <sub>-0.027</sub>	-20.751 <sup>+0.028</sup> <sub>-0.039</sub>	—	—	—	—
2024-08-0660528		BB	4.397 <sup>+0.086</sup> <sub>-0.068</sub>	15.046 <sup>+0.069</sup> <sub>-0.078</sub>	44.54 <sup>+0.19</sup> <sub>-0.14</sub>	-20.613 <sup>+0.049</sup> <sub>-0.038</sub>	—	—	—	—
2024-08-0760529		BB	4.61 <sup>+0.15</sup> <sub>-0.11</sub>	14.84 <sup>+0.09</sup> <sub>-0.11</sub>	44.96 <sup>+0.37</sup> <sub>-0.26</sub>	-20.431 <sup>+0.049</sup> <sub>-0.038</sub>	—	—	—	—
2024-08-0960531		BB	4.58 <sup>+0.18</sup> <sub>-0.12</sub>	14.82 <sup>+0.11</sup> <sub>-0.13</sub>	44.8 <sup>+0.46</sup> <sub>-0.29</sub>	-20.205 <sup>+0.055</sup> <sub>-0.061</sub>	—	—	—	—
2024-08-1360535		BB	4.345 <sup>+0.03</sup> <sub>-0.031</sub>	14.966 <sup>+0.041</sup> <sub>-0.046</sub>	44.157 <sup>+0.052</sup> <sub>-0.055</sub>	-19.966 <sup>+0.093</sup> <sub>-0.084</sub>	—	—	—	—
2024-08-1460536		BB	4.66 <sup>+0.23</sup> <sub>-0.21</sub>	14.66 <sup>+0.17</sup> <sub>-0.15</sub>	44.83 <sup>+0.6</sup> <sub>-0.49</sub>	-19.74 <sup>+0.07</sup> <sub>-0.11</sub>	—	—	—	—
2024-08-1660538		BB	4.268 <sup>+0.028</sup> <sub>-0.027</sub>	14.987 <sup>+0.04</sup> <sub>-0.039</sub>	43.903 <sup>+0.047</sup> <sub>-0.049</sub>	-19.708 <sup>+0.11</sup> <sub>-0.073</sub>	—	—	—	—
2024-08-1760539		BB	4.253 <sup>+0.05</sup> <sub>-0.045</sub>	14.982 <sup>+0.059</sup> <sub>-0.075</sub>	43.83 <sup>+0.083</sup> <sub>-0.088</sub>	-19.62 <sup>+0.15</sup> <sub>-0.13</sub>	—	—	—	—
2024-08-1960541		BB	4.78 <sup>+0.17</sup> <sub>-0.25</sub>	14.47 <sup>+0.16</sup> <sub>-0.11</sub>	44.91 <sup>+0.47</sup> <sub>-0.64</sub>	-19.19 <sup>+0.25</sup> <sub>-0.14</sub>	—	—	—	—
2024-08-2260544		BB	4.55 <sup>+0.29</sup> <sub>-0.25</sub>	14.63 <sup>+0.24</sup> <sub>-0.21</sub>	44.3 <sup>+0.74</sup> <sub>-0.55</sub>	-19.15 <sup>+0.14</sup> <sub>-0.15</sub>	—	—	—	—
2024-08-2760549		BB+BB	4.33 <sup>+0.07</sup> <sub>-0.046</sub>	14.728 <sup>+0.055</sup> <sub>-0.083</sub>	43.624 <sup>+0.118</sup> <sub>-0.074</sub>	-18.72 <sup>+0.122</sup> <sub>-0.063</sub>	3.41 <sup>+0.19</sup> <sub>-0.26</sub>	17.6 <sup>+1.0</sup> <sub>-1.4</sub>	42.7 <sup>+0.7</sup> <sub>-5.8</sub>	—
		BB+Dust	4.33 <sup>+0.07</sup> <sub>-0.046</sub>	14.728 <sup>+0.055</sup> <sub>-0.083</sub>	43.624 <sup>+0.118</sup> <sub>-0.074</sub>	-18.72 <sup>+0.122</sup> <sub>-0.063</sub>	3.42 <sup>+0.2</sup> <sub>-0.27</sub>	16.0 <sup>+1.07</sup> <sub>-0.68</sub>	—	42.8 <sup>+0.9</sup> <sub>-1.2</sub>
		BB+PL	4.33 <sup>+0.07</sup> <sub>-0.046</sub>	14.728 <sup>+0.055</sup> <sub>-0.083</sub>	43.624 <sup>+0.118</sup> <sub>-0.074</sub>	-18.72 <sup>+0.122</sup> <sub>-0.063</sub>	—	—	2.3 <sup>+1.7</sup> <sub>-1.4</sub>	44.6 <sup>+4.8</sup> <sub>-7.6</sub>
2024-09-3060583		BB+BB	4.284 <sup>+0.045</sup> <sub>-0.039</sub>	14.385 <sup>+0.051</sup> <sub>-0.054</sub>	42.756 <sup>+0.078</sup> <sub>-0.057</sub>	-16.778 <sup>+0.048</sup> <sub>-0.064</sub>	3.584 <sup>+0.033</sup> <sub>-0.032</sub>	17.075 <sup>+0.058</sup> <sub>-0.055</sub>	41.95 <sup>+0.021</sup> <sub>-0.034</sub>	—
		BB+Dust	4.284 <sup>+0.045</sup> <sub>-0.039</sub>	14.385 <sup>+0.051</sup> <sub>-0.054</sub>	42.756 <sup>+0.078</sup> <sub>-0.057</sub>	-16.778 <sup>+0.048</sup> <sub>-0.064</sub>	3.586 <sup>+0.029</sup> <sub>-0.032</sub>	15.375 <sup>+0.057</sup> <sub>-0.049</sub>	—	41.948 <sup>+0.027</sup> <sub>-0.028</sub>
		BB+PL	4.284 <sup>+0.045</sup> <sub>-0.039</sub>	14.385 <sup>+0.051</sup> <sub>-0.054</sub>	42.756 <sup>+0.078</sup> <sub>-0.057</sub>	-16.778 <sup>+0.048</sup> <sub>-0.064</sub>	—	—	0.23 <sup>+0.24</sup> <sub>-0.17</sub>	42.684 <sup>+0.058</sup> <sub>-0.056</sub>

## 7.9 The Compton equilibrium temperature

Given the strong X-ray source associated with 24puz, the electron temperature may be hotter than the standard photoionization equilibrium temperature  $\sim 10^4$  K due to Compton heating (15). We compute the Compton equilibrium temperature  $T_C$  as follows. The Compton heating rate per unit density is given by (15, 579)

$$H(\nu) = \frac{\sigma_T}{m_e c^2} \int_0^\infty h\nu f_\nu a\left(\frac{h\nu}{m_e c^2}\right) d\nu, \quad (7.15)$$

where  $f_\nu$  is the incident flux density,  $\nu$  is frequency, and all constants are given with standard symbols. The function  $a\left(\frac{h\nu}{m_e c^2}\right)$  accounts for Klein-Nishina corrections

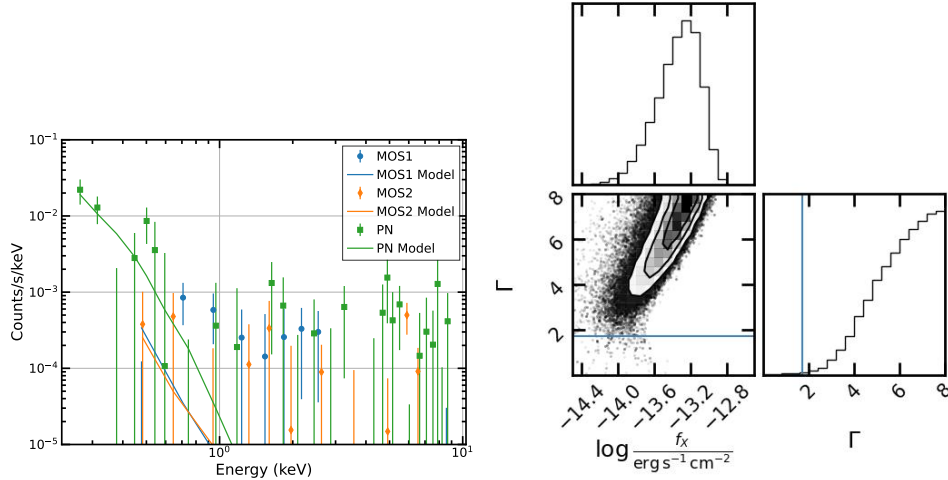


Figure 7.17: Spectral constraints from the MJD 60558 (37.6 rest-days) *XMM-Newton* observations, in the same format as Figure 7.10. We assume no absorption in this fit, based on the results from the higher signal-to-noise MJD 60536 observations. The photon index from the first epoch is shown in blue. The photon index has tentatively softened: the probability that the photon-index is consistent with the first epoch is  $P(\Gamma \leq 1.73) = 1\%$ .

and, for  $k_B T_C \ll m_e c^2$ , is given by

$$\begin{aligned}
 a(x) &= \frac{3}{8x^4} (x-3)(x+1) \ln(2x+1) \\
 &\quad + \frac{-10x^4 + 51x^3 + 93x^2 + 51 + 9}{4x^3(2x+1)^3} \\
 &\approx 1 - \frac{21x}{5} + O(x^2).
 \end{aligned} \tag{7.16}$$

For many astrophysical systems, including 24puz, the heating is dominated by photons with  $h\nu \gtrsim 10$  keV, i.e., hard X-rays.

The cooling rate is given by

$$C(\nu) = \frac{4k_B T \sigma_T}{m_e c^2} \int_0^\infty f_\nu b\left(\frac{h\nu}{m_e c^2}\right) d\nu. \tag{7.17}$$

Here,  $T$  is the temperature of the irradiated region and  $b\left(\frac{h\nu}{m_e c^2}\right)$  accounts for Klein-

Nishina corrections. The latter is given by

$$\begin{aligned}
 b(x) = \frac{1}{4} & \left( \frac{3(3x^2 - 4x - 13)}{16x^3} \ln(2x + 1) + \right. \\
 & \frac{-216x^6 + 476x^5 + 2066x^4}{8x^2(2x + 1)^5} \\
 & \left. + \frac{2429x^3 + 1353x^2 + 363x + 39}{8x^2(2x + 1)^5} \right) \\
 & \approx 1 - \frac{47x}{8} + \mathcal{O}(x^2). \quad (7.18)
 \end{aligned}$$

Once again, this expression is valid for  $k_B T_C \ll m_e c^2$ . Compton cooling is dominated by photons with  $h\nu \lesssim 10$  keV.

The temperature evolution is then given by  $(3/2)k_B dT/dt = H(\nu) - C(\nu)$ . The temperature reaches an equilibrium  $T_C$  when the heating and cooling rates are equal, or

$$T_C = \frac{1}{4k_B} \frac{\int_0^\infty h\nu f_\nu a\left(\frac{h\nu}{m_e c^2}\right) d\nu}{\int_0^\infty f_\nu b\left(\frac{h\nu}{m_e c^2}\right) d\nu}. \quad (7.19)$$

Extrapolating from the optical/UV and X-ray observations of 24puz described in Sections 7.4 and 7.5 to typical values during our radio observation, we assume that  $f_\nu$  is the sum of a blackbody with  $T \approx 10^{4.3}$  K and  $\log L_{\text{OptUV}}/(\text{erg s}^{-1}) \approx 43.5$  and a power-law with  $\Gamma = 1.77$  and  $L_X/(\text{erg s}^{-1}) \approx 42.2$ , where we cut-off the power-law at 0.3 keV. These values are most appropriate during our final epoch of radio observations, but we verified that the equilibrium temperature does not change significantly by adopting values appropriate for earlier observations. We find  $T_C = 4 \times 10^5$  K, and this equilibrium temperature is reached in  $\sim$ days. An increased optical/UV luminosity will decrease the temperature, while an increased X-ray component will increase the temperature. We tested a range of optical/UV and X-ray luminosity and found  $T_C \gtrsim 10^5$  K for most reasonable assumptions. As can be seen from Equation 7.3 (or Eq. 10.16 of 306), in the radio regime, where  $h\nu \ll kT_e$ , increasing the temperature tends to decrease  $\tau_{ff}$ , so we conservatively adopt  $T_e = 10^5$  K.

## 7.10 MOSFIT

In Figure 7.18, we show the full set of best-fit parameters found by MOSFIT. The parameter definitions are detailed in (258).

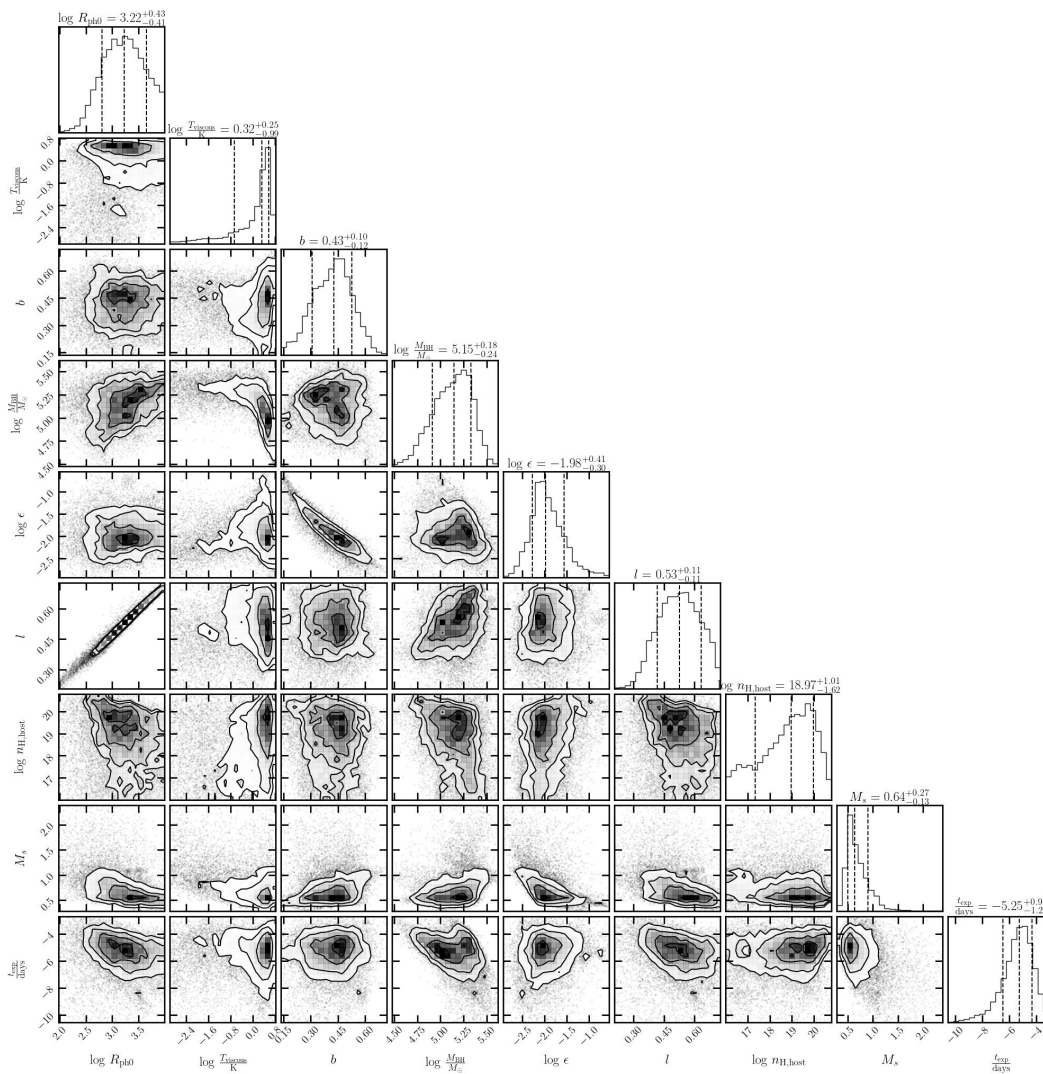


Figure 7.18: Corner plot showing the full MOSFIT parameter set.

## CONCLUSIONS

**8.1 Summary**

My thesis has attempted to expand the selection wavelengths and methodology to answer three key open questions about tidal disruption events, discussed in Chapter 1. I have reproduced these points below, with a discussion of the contribution of my work to each.

1. *What TDEs are we missing?*

In Chapters 2-5, I identified eight radio-selected TDEs and compared their properties to optically-selected events. These events generally had similar host galaxies as the optically-selected TDEs. The events presented in Chapters 3 and 5 showed an increased amount of dust/gas relative to optically-selected TDEs, but I saw no significant evidence that there are TDEs that are radio-bright that substantially differ from the optically-selected events in terms of host galaxies or optical flares. The radio emission from the radio-selected events was more luminous than found from most optically-selected TDEs at the time, but continued follow-up is closing this gap (149). There was a hint in Chapter 4 that radio-selected, optically-detected TDEs may have fainter, cooler optical emission and lower BH masses, but a larger sample is required to test this correlation.

In Chapter 6, I presented a candidate repeating partial TDE, which showed substantial cooling during the second flare. This suggests that TDEs may show early-time cooling, which is currently selected against in typical TDE searches. Likewise, repeating events are excluded in most TDE searches, but recent efforts beyond my own have begun to remedy this issue (e.g. 435, 436).

2. *Where are the IMBH TDEs?*

In Chapter 4, I suggested that radio-selections may be more sensitive to IMBH TDEs as the radio-selected TDEs had tentatively lower BH masses than their optically-selected counterparts. This is theoretically justified because IMBH TDEs are in a super-Eddington state for longer.

In Chapter 7, I presented a candidate flaring IMBH or high mass stellar mass BH that was identified in a search for hostless transients. This event occupied a portion of luminosity-timescale space seemingly unexplored by previous transient searches, and showed the power of new search methodology for identifying unique events.

### 3. *What produces the observed radio emission?*

In Chapter 2, I presented a radio-selected, long-lived jetted TDE. This event was still getting brighter after years, and there was evidence for continual energy injection into the jet. The accretion state was extremely sub-Eddington, providing evidence that TDEs, like X-ray binaries, may power jets when they reach sub-Eddington accretion states. In Chapter 3, I presented a radio-emitting TDE with evidence for inhomogeneities in the synchrotron-emitting medium. Standard outflow modeling techniques fail for this source, so models for outflows from TDEs must be re-assessed to account for such events. In Chapter 4, I presented a sample of radio-selected TDEs with varying radio emission evolution, tentatively suggesting a mix of jets and non-relativistic outflows.

## 8.2 Future prospects

Transients, like those presented in my work, probe the most extreme regimes of BHs and their accretion. In the final sections of my thesis, I would like to briefly discuss ongoing and future efforts to understand these BHs and to answer the fundamental questions stated in Section 1.1. I will address each question individually

### Testing the accretion models for MBHs

There is still significant room to use TDEs as a test of MBH accretion models. In particular, the late-time TDE emission provides a simple starting point. At late-times, the complex details of circularization and re-processing layers do not matter. Instead, (400) predicted that the late-time emission from TDEs should be consistent with a compact, but slowly expanding, accretion disk. Detailed spectral energy distribution modeling of this disk as a function of time can probe the timescale of the expansion and search for any variability that develops. Simultaneous deep radio monitoring will be critical to assess any connection between the disk structure and jet/wind launching in a sub-Eddington state (255).

Recent work has uncovered two classes of nuclear flares in AGN: the ambiguous

nuclear transients (ANTs; (336)) and extreme nuclear transients (ENTs; (580)). Both are remarkably luminous and long-lived. ENTs are particularly energetic and are suggested to be TDEs of intermediate mass stars in AGN (96, 580). Whether all ANTs and ENTs must be associated with some sort of stellar disruption, or if they can be fit within a smooth accretion disk framework, remains to be seen.

Upcoming and recently launched instruments will also provide powerful new constraints on the accretion state of AGN. In particular, the X-ray Imaging and Spectroscopy Mission (XRISM; (581)) was recently launched, and is providing high throughput and high resolution spectroscopy of AGN accretion disks. Early results suggest that these spectra can resolve the dynamics on scales as small as the accretion disk out to the dusty torus (582)

### **Understanding super-Eddington accretion onto MBHs**

Efforts to further probe the limits of super-Eddington accretion are largely coming from three angles. The *James Webb Space Telescope* is discovering candidate highly-super Eddington sources at high-redshift: these are the analogues of SMBH seeds (51, 91, 583).

There is much left to learn about super-Eddington accretion from transient sources. These sources are particularly powerful as they can exist in the local universe and so can often be studied with ground-based telescopes. My discovery in Chapter 6 of a likely super-Eddington source in a little-explored section of optical transient parameter space suggests that further searches for such sources should be fruitful: there are still discoveries to be made in optical transients, without requiring more sensitive surveys. Filling out the parameter space of hot, constant temperature optical transients shows promise for identifying super-Eddington sources. Likewise, continued efforts to searches for TDEs by IMBHs, which are expected to be super-Eddington, will be key.

In the next few years, multiple surveys will turn on that will be invaluable for searches for super-Eddington transients. In particular, as I have discussed, super-Eddington accretion is associated with the launching of jets and winds. Radio surveys, like the Deep Synoptic Array 2000 (DSA-2000; (404)), which will monitor the sky to  $\mu\text{Jy}$  sensitivity levels with  $\sim$ month cadence, will enable blind searches for these outflows. The candidates that are discovered with DSA-2000 can be combined with constraints from the deep, cadenced optical imaging that the Vera Rubin Observatory's Legacy Survey of Space and Time (LSST; (584)) and ultraviolet

constraints from the Ultraviolet Explorer (UVEX; (585)).

### **The demographics and environment of quiescent/low accretion rate BHs**

Multimessenger studies may prove to be a key method to measure the demographics of BHs, regardless of accretion rate (105). The recent detection by pulsar timing arrays of the gravitational wave background from all merging SMBHs in the universe was used by me and other authors to suggest that the SMBH population was established at early redshift (104, 586–588). Soon, missions like the Laser Interferometer Space Antenna (LISA) will push these constraints to lower mass MBHs, including IMBHs (589).

The DSA-2000 may allow modeling of the history of AGN activity in a currently inactive galaxy, using the large scale radio emission to constrain the history of outflows. LSST will enable variability-based searches for the faintest AGN (590). Both instruments can be used to identify TDEs in lower mass and/or more distant galaxies, to provide a more complete census of the BH populations.

TDEs will continue to be key for shining a flashlight on the interior of otherwise quiescent nuclei. We will require systematic, deep optical and infrared spectroscopic follow-up to constrain late-time transient spectral features as the UV emission from the TDE propagates out to the gas in the circumnuclear medium. Infrared follow-up can sensitively probe the dust in these systems (132).

There are also many ongoing searches for nuclear transients beyond a single disrupted star, which open a view into the dynamics and composition of galactic nuclei. Searches for quasi-periodic eruptions in systems with young accretion disk, as well as extreme mass ratio inspirals, and the consumption of objects other than the main sequence stars that are the focus of TDE searches (e.g., massive stars, binary systems) are providing a census of the contents of galactic nuclei (591–594).

### **The demographics of IMBHs**

In my view, IMBH searches are one of the most promising avenues in the next few years. Variability and flaring is proving to be a powerful way to light up undetectable BHs, and thus may be the ideal method to identify IMBHs (38). Archival work will prove key for such searches, as searches for off-nuclear or hostless AGN or TDE-like flaring are minimal. In the case of TDEs, archival multiwavelength searches may prove fruitful, as these events can remain highly super-Eddington for years and then should show signatures of winds and outflows, in addition to optical/UV

radiation. Deep, infrared spectroscopy to search for coronal lines and X-ray imaging can constrain the signatures of accretion.

Upcoming surveys will likely overwhelm us with candidates, which is why the current datasets are a perfect place to start. Once we have a baseline picture of the landscape of variable IMBHs, LSST and DSA-2000 will be powerful discovery machines. XRISM and other X-ray facilities can be used to search for signatures of accretion.

A dramatic change in our understanding of accretion and MBH demographics is likely underway, and, particularly if archival and multiwavelength data is used and combined effectively, transient/variable phenomena will play a central role.

## BIBLIOGRAPHY

1. A. J. Levan *et al.*, *ApJ* **819**, 51, arXiv: 1509.08945 (astro-ph.HE) (Mar. 2016).
2. D. R. Pasham *et al.*, *ApJ* **805**, 68, arXiv: 1502.01345 (astro-ph.HE) (May 2015).
3. J. S. Brown, T. W. Holoiien, K. Auchettl, K. Z. Stanek, C. S. Kochanek, B. J. Shappee, J. L. Prieto, D. Grupe, *MNRAS* **466**, 4904–4916, arXiv: 1609.04403 (astro-ph.HE) (Apr. 2017).
4. J. A. Baldwin, M. M. Phillips, R. Terlevich, *PASP* **93**, 5–19 (Feb. 1981).
5. L. J. Kewley, B. Groves, G. Kauffmann, T. Heckman, *MNRAS* **372**, 961–976, arXiv: astro-ph/0605681 (astro-ph) (Nov. 2006).
6. R. Cid Fernandes, G. Stasińska, A. Mateus, N. Vale Asari, *MNRAS* **413**, 1687–1699, arXiv: 1012.4426 (astro-ph.CO) (May 2011).
7. A. Dey *et al.*, *AJ* **157**, 168, arXiv: 1804.08657 (astro-ph.IM) (May 2019).
8. X. Dong, T. Wang, J. Wang, W. Yuan, H. Zhou, H. Dai, K. Zhang, *MNRAS* **383**, 581–592, arXiv: 0710.1458 (astro-ph) (Jan. 2008).
9. J. Somalwar, V. Ravi (Sept. 2023).
10. K. Schawinski *et al.*, *MNRAS* **440**, 889–907, arXiv: 1402.4814 (astro-ph.GA) (May 2014).
11. J. J. Somalwar *et al.*, *ApJ* **945**, 142, arXiv: 2207.02873 (astro-ph.HE) (Mar. 2023).
12. E. L. Wright *et al.*, *AJ* **140**, 1868–1881, arXiv: 1008.0031 (astro-ph.IM) (Dec. 2010).
13. E. Hammerstein *et al.*, *ApJ* **942**, 9, arXiv: 2203.01461 (astro-ph.HE) (Jan. 2023).
14. T.-G. Wang, H.-Y. Zhou, S. Komossa, H.-Y. Wang, W. Yuan, C. Yang, *ApJ* **749**, 115, arXiv: 1202.1064 (astro-ph.HE) (Apr. 2012).
15. A. Y. Q. Ho *et al.*, *ApJ* **871**, 73, arXiv: 1810.10880 (astro-ph.HE) (Jan. 2019).
16. R. Margutti *et al.*, *ApJ* **872**, 18, arXiv: 1810.10720 (astro-ph.HE) (Feb. 2019).
17. S. Bowyer, E. T. Byram, T. A. Chubb, H. Friedman, S. Bowyer, E. T. Byram, T. A. Chubb, H. Friedman, *Sci* **147**, 394–398, ISSN: 0036-8075, (<https://ui.adsabs.harvard.edu/abs/1965Sci...147..394B/abstract>) (1965).

18. M. Oda *et al.*, *ApJL* **166**, L1, ISSN: 0004-637X, (<https://ui.adsabs.harvard.edu/abs/1971ApJ...166L...10/abstract>) (May 1971).
19. R. M. Hjellming, C. M. Wade, V. A. Hughes, A. Woodsworth, *Natur* **234**, 138, ISSN: 0028-0836, (<https://ui.adsabs.harvard.edu/abs/1971Natur.234..138H/abstract>) (1971).
20. H. E. Smith, B. Margon, P. S. Conti, H. E. Smith, B. Margon, P. S. Conti, *ApJL* **179**, L125, ISSN: 0004-637X, (<https://ui.adsabs.harvard.edu/abs/1973ApJ...179L.125S/abstract>) (Feb. 1973).
21. M. Oda, *SSRv* **20**, 757–813, ISSN: 0038-6308, (<https://ui.adsabs.harvard.edu/abs/1977SSRv...20..757O/abstract>) (Nov. 1977).
22. J. C. Miller-Jones *et al.*, *Science* **371**, 1046–1049, ISSN: 10959203, (<https://ui.adsabs.harvard.edu/abs/2021Sci...371.1046M/abstract>) (Mar. 2021).
23. M. Schmidt, *Nature 1963 197:4872* **197**, 1040–1040, ISSN: 1476-4687, (<https://www.nature.com/articles/1971040a0>) (1963).
24. H. J. Smith, D. Hoffleit, H. J. Smith, D. Hoffleit, *Natur* **198**, 650–651, ISSN: 0028-0836, (<https://ui.adsabs.harvard.edu/abs/1963Natur.198..650S/abstract>) (1963).
25. E. E. Salpeter, *apj* **140**, 796–800 (Aug. 1964).
26. Y. B. Zel'dovich, Zel'dovich, Y. B., *SPhD* **9**, 195, (<https://ui.adsabs.harvard.edu/abs/1964SPhD...9..195Z/abstract>) (1964).
27. D. Lynden-Bell, *Nature 1969 223:5207* **223**, 690–694, ISSN: 1476-4687, (<https://www.nature.com/articles/223690a0>) (1969).
28. D. Lynden-Bell, M. J. Rees, *Monthly Notices of the Royal Astronomical Society* **152**, 461–475, ISSN: 0035-8711, (<https://dx.doi.org/10.1093/mnras/152.4.461>) (July 1971).
29. M. Miyoshi, J. Morant, J. Herrnstein1, N. Nakail, L. Greenhill, P. Dlamond, M. Inouei, *Natur* **373**, 127–129, ISSN: 0028-0836, (<https://ui.adsabs.harvard.edu/abs/1995Natur.373..127M/abstract>) (Jan. 1995).
30. A. M. Ghez *et al.*, *The Astrophysical Journal* **689**, 1044–1062, ISSN: 0004-637X, (<https://ui.adsabs.harvard.edu/abs/2008ApJ...689.1044G/abstract>) (Dec. 2008).
31. R. Schodel *et al.*, *Natur* **419**, 694–696, (<http://arxiv.org/abs/astro-ph/0210426>) (<http://dx.doi.org/10.1038/nature01121>) (Oct. 2002).
32. J. Kormendy, D. Richstone, *Annual Review of Astronomy and Astrophysics* **33**, 581–624, ISSN: 0066-4146, (<http://www.annualreviews.org/doi/10.1146/annurev.aa.33.090195.003053>) (Sept. 1995).

33. T. M. Heckman, P. N. Best, *ARA&A* **52**, 589–660, arXiv: 1403.4620 (astro-ph.GA) (Aug. 2014).
34. P. Madau, M. J. Rees, M. Volonteri, F. Haardt, S. P. Oh, *ApJ* **604**, 484–494, (<http://arxiv.org/abs/astro-ph/0310223><http://dx.doi.org/10.1086/381935>) (Oct. 2003).
35. J. Silk, *ApJL* **839**, L13, arXiv: 1703.08553 (astro-ph.GA) (Apr. 2017).
36. A. King, *ApJL* **596**, L27–L29, arXiv: astro-ph/0308342 (astro-ph) (Oct. 2003).
37. N. J. McConnell, C. P. Ma, K. Gebhardt, S. A. Wright, J. D. Murphy, T. R. Lauer, J. R. Graham, D. O. Richstone, *Nature* 2011 480:7376 **480**, 215–218, ISSN: 1476-4687, (<https://www.nature.com/articles/nature10636>) (Dec. 2011).
38. J. E. Greene, J. Strader, L. C. Ho, *ARA&A* **58**, 257–312, arXiv: 1911.09678 (astro-ph.GA) (Aug. 2020).
39. C. J. Hansen, S. D. Kawaler, V. Trimble, *sipp*, Astronomy and Astrophysics Library, 84, (<https://ui.adsabs.harvard.edu/abs/1994sipp.book.....H/abstract>) (1994).
40. M. Zevin, M. Spera, C. P. L. Berry, V. Kalogera, *The Astrophysical Journal Letters* **899**, L1, ISSN: 2041-8205, (<https://ui.adsabs.harvard.edu/abs/2020ApJ...899L...1Z/abstract>) (Aug. 2020).
41. S. E. Woosley, *The Astrophysical Journal* **836**, 244, ISSN: 0004-637X, (<https://ui.adsabs.harvard.edu/abs/2017ApJ...836..244W/abstract>) (Feb. 2017).
42. K. Kremer, M. Spera, D. Becker, S. Chatterjee, U. N. D. Carlo, G. Fragione, C. L. Rodriguez, C. S. Ye, F. A. Rasio, *The Astrophysical Journal* **903**, 45, ISSN: 0004-637X, (<https://iopscience.iop.org/article/10.3847/1538-4357/abb945><https://iopscience.iop.org/article/10.3847/1538-4357/abb945/meta>) (Oct. 2020).
43. Y. Yang, V. Gayathri, I. Bartos, Z. Haiman, M. Safarzadeh, H. Tagawa, *The Astrophysical Journal Letters* **901**, L34, ISSN: 2041-8205, (<https://ui.adsabs.harvard.edu/abs/2020ApJ...901L..34Y/abstract>) (Oct. 2020).
44. K. Yagi, L. C. Stein, *Classical and Quantum Gravity* **33**, 054001, ISSN: 13616382, (<https://ui.adsabs.harvard.edu/abs/2016CQGra...33e4001Y/abstract>) (Feb. 2016).
45. A. Heger, B. Müller, I. Mandel, A. Heger, B. Müller, I. Mandel, *arXiv*, arXiv:2304.09350, (<https://ui.adsabs.harvard.edu/abs/2023arXiv230409350H/abstract>) (Apr. 2023).

46. Soltan, A., *MNRAS* **200**, 115–122, ISSN: 0035-8711, (<https://ui.adsabs.harvard.edu/abs/1982MNRAS.200..115S/abstract>) (Sept. 1982).
47. J. Kormendy, L. C. Ho, *ARA&A* **51**, 511–653, arXiv: 1304.7762 (astro-ph.CO) (Aug. 2013).
48. A. C. Fabian, *ARA&A* **50**, 455–489, arXiv: 1204.4114 (astro-ph.CO) (Sept. 2012).
49. K. Inayoshi, E. Visbal, Z. Haiman, *Annual Review of Astronomy and Astrophysics* **58**, 27–97, ISSN: 00664146, (<https://ui.adsabs.harvard.edu/abs/2020ARA&A..58...27I/abstract>) (2020).
50. P. Natarajan, *General Relativity and Gravitation* **46**, 1702 (May 2014).
51. A. D. Goulding *et al.*, *The Astrophysical Journal Letters* **955**, L24, ISSN: 2041-8205, (<https://iopscience.iop.org/article/10.3847/2041-8213/acf7c5%20https://iopscience.iop.org/article/10.3847/2041-8213/acf7c5/meta>) (Sept. 2023).
52. A. Loeb, F. A. Rasio, *ApJ* **432**, 52, ISSN: 0004-637X, arXiv: 9401026 (astro-ph), (<https://ui.adsabs.harvard.edu/abs/1994ApJ...432...52L/abstract>) (Sept. 1994).
53. G. Lodato, P. Natarajan, *MNRAS* **371**, 1813–1823, arXiv: astro-ph/0606159 (astro-ph) (Oct. 2006).
54. M. C. Miller, D. P. Hamilton, *The Astrophysical Journal* **576**, 894–898, ISSN: 0004-637X (Sept. 2002).
55. B. Devecchi, M. Volonteri, *ApJ* **694**, 302–313, arXiv: 0810.1057 (astro-ph) (Mar. 2009).
56. T. Alexander, P. Natarajan, *Science* **345**, 1330–1333, arXiv: 1408.1718 (astro-ph.GA) (Sept. 2014).
57. P. Madau, M. J. Rees, *The Astrophysical Journal* **551**, L27–L30, ISSN: 0004637X, (<https://iopscience.iop.org/article/10.1086/319848%20https://iopscience.iop.org/article/10.1086/319848/meta>) (Apr. 2001).
58. E. J. Weller, F. Pacucci, L. Hernquist, S. Bose, *Monthly Notices of the Royal Astronomical Society* **511**, 2229–2238, ISSN: 13652966, (<https://ui.adsabs.harvard.edu/abs/2022MNRAS.511.2229W/abstract>) (Apr. 2022).
59. A. Ricarte, M. Tremmel, P. Natarajan, C. Zimmer, T. Quinn, *MNRAS* **503**, 6098–6111, arXiv: 2103.12124 (astro-ph.GA) (June 2021).
60. M. C. Miller, D. P. Hamilton, *MNRAS* **330**, 232–240, (<http://arxiv.org/abs/astro-ph/0106188%20http://dx.doi.org/10.1046/j.1365-8711.2002.05112.x>) (June 2001).

61. N. I. Shakura, R. A. Sunyaev, *A&A* **500**, 33–51 (June 1973).
62. R. Narayan, I. Yi, *ApJL* **428**, L13, arXiv: astro-ph/9403052 (astro-ph) (June 1994).
63. R. Narayan, I. Yi, *The Astrophysical Journal* **444**, 231, ISSN: 0004-637X, (<https://ui.adsabs.harvard.edu/abs/1995ApJ...444..231N/abstract>) (May 1995).
64. R. Narayan, I. Yi, *The Astrophysical Journal* **452**, 710, ISSN: 0004-637X, (<https://ui.adsabs.harvard.edu/abs/1995ApJ...452..710N/abstract>) (Oct. 1995).
65. M. A. Abramowicz, X. Chen, S. Kato, J.-P. Lasota, O. Regev, *ApJL* **438**, L37, (<http://arxiv.org/abs/astro-ph/9409018>), (<http://dx.doi.org/10.1086/187709>) (Sept. 1994).
66. M. A. Abramowicz, B. Czerny, J. P. Lasota, E. Szuszkiewicz, M. A. Abramowicz, B. Czerny, J. P. Lasota, E. Szuszkiewicz, *ApJ* **332**, 646, ISSN: 0004-637X, (<https://ui.adsabs.harvard.edu/abs/1988ApJ...332..646A/abstract>) (Sept. 1988).
67. C. M. Harrison, T. Costa, C. N. Tadhunter, A. Flütsch, D. Kakkad, M. Perna, G. Vietri, *Nature Astronomy* **2**, 198–205, ISSN: 23973366, (<http://dx.doi.org/10.1038/s41550-018-0403-6>) (2018).
68. N. Arav, B. Borguet, C. Chamberlain, D. Edmonds, C. Danforth, *mnras* **436**, 3286–3305 (Dec. 2013).
69. M. Mehdipour *et al.*, *Astronomy and Astrophysics* **670**, A183, ISSN: 14320746, (<https://ui.adsabs.harvard.edu/abs/2023A&A...670A.183M/abstract>) (Feb. 2023).
70. Y. Xu, C. Pinto, D. Rogantini, D. Barret, S. Bianchi, M. Guainazzi, J. Ebrero, W. Alston, E. Kara, G. Cusumano, *Astronomy & Astrophysics* **687**, A179, ISSN: 0004-6361, ([https://www.aanda.org/articles/aa/full\\_html/2024/07/aa49001-23/aa49001-23.html](https://www.aanda.org/articles/aa/full_html/2024/07/aa49001-23/aa49001-23.html)), (<https://www.aanda.org/articles/aa/abs/2024/07/aa49001-23/aa49001-23.html>) (July 2024).
71. D. Proga, presented at the The Central Engine of Active Galactic Nuclei, ed. by L. C. Ho, J. -. Wang, vol. 373, p. 267, arXiv: astro-ph/0701100 (astro-ph).
72. D. S. Balsara, J. H. Krolik, *ApJ* **402**, 109, ISSN: 0004-637X, (<https://ui.adsabs.harvard.edu/abs/1993ApJ...402..109B/abstract>) (Jan. 1993).
73. D. T. Woods, R. I. Klein, J. I. Castor, C. F. McKee, J. B. Bell, *ApJ* **461**, 767, ISSN: 0004-637X, (<https://ui.adsabs.harvard.edu/abs/1996ApJ...461..767W/abstract>) (Apr. 1996).

74. D. Chelouche, H. Netzer, *ApJ* **625**, 95–107, (<http://arxiv.org/abs/astro-ph/0502272><http://dx.doi.org/10.1086/429580>) (Feb. 2005).
75. D. Proga, J. M. Stone, T. R. Kallman, *The Astrophysical Journal* **543**, 686–696, ISSN: 0004-637X, (<https://iopscience.iop.org/article/10.1086/317154><https://iopscience.iop.org/article/10.1086/317154/meta>) (Nov. 2000).
76. N. Higginbottom, D. Proga, C. Knigge, K. S. Long, J. H. Matthews, S. A. Sim, *Astrophysical Journal* **789**, 19, ISSN: 15384357, (<https://ui.adsabs.harvard.edu/abs/2014ApJ...789...19H/abstract>) (July 2014).
77. R. D. Blandford, D. G. Payne, R. D. Blandford, D. G. Payne, *MNRAS* **199**, 883–903, ISSN: 0035-8711, (<https://ui.adsabs.harvard.edu/abs/1982MNRAS.199..883B/abstract>) (Aug. 1982).
78. J. M. Stone, M. L. Norman, J. M. Stone, M. L. Norman, *ApJ* **433**, 746, ISSN: 0004-637X, (<https://ui.adsabs.harvard.edu/abs/1994ApJ...433..746S/abstract>) (Oct. 1994).
79. R. D. Blandford, R. L. Znajek, *MNRAS* **179**, 433–456 (May 1977).
80. K. Akiyama *et al.*, *The Astrophysical Journal Letters* **875**, L1, ISSN: 2041-8205, (<https://iopscience.iop.org/article/10.3847/2041-8213/ab0ec7><https://iopscience.iop.org/article/10.3847/2041-8213/ab0ec7/meta>) (Apr. 2019).
81. F. Shankar, D. H. Weinberg, J. Miralda-Escudé, *The Astrophysical Journal* **690**, 20, ISSN: 0004-637X, (<https://iopscience.iop.org/article/10.1088/0004-637X/690/1/20><https://iopscience.iop.org/article/10.1088/0004-637X/690/1/20/meta>) (Dec. 2008).
82. F. Shankar, P. Salucci, G. L. Granato, G. De Zotti, L. Danese, *Monthly Notices of the Royal Astronomical Society* **354**, 1020–1030, ISSN: 00358711, (<https://ui.adsabs.harvard.edu/abs/2004MNRAS.354.1020S/abstract>) (Nov. 2004).
83. A. W. Graham, S. P. Driver, *The Astrophysical Journal* **655**, 77–87, ISSN: 0004-637X, (<https://iopscience.iop.org/article/10.1086/509758><https://iopscience.iop.org/article/10.1086/509758/meta>) (Jan. 2007).
84. A. Marconi, G. Risaliti, R. Gilli, L. K. Hunt, R. Maiolino, M. Salvati, *MNRAS* **351**, 169–185, arXiv: astro-ph/0311619 (astro-ph) (June 2004).
85. X. Shen, P. F. Hopkins, C. A. Faucher-Giguère, D. M. Alexander, G. T. Richards, N. P. Ross, R. C. Hickox, *Monthly Notices of the Royal Astronomical Society* **495**, 3252–3275, ISSN: 0035-8711, (<https://dx.doi.org/10.1093/mnras/staa1381>) (July 2020).

86. W. Li, K. Inayoshi, M. Onoue, W. He, Y. Matsuoka, Z. Pan, M. Akiyama, T. Izumi, T. Nagao, *The Astrophysical Journal* **969**, 69, ISSN: 0004-637X, (<https://iopscience.iop.org/article/10.3847/1538-4357/ad46f9><https://iopscience.iop.org/article/10.3847/1538-4357/ad46f9/meta>) (July 2024).
87. A. Shulevski *et al.*, *Astronomy & Astrophysics* **583**, A89, ISSN: 0004-6361, ([https://www.aanda.org/articles/aa/full\\_html/2015/11/aa25632-15/aa25632-15.html](https://www.aanda.org/articles/aa/full_html/2015/11/aa25632-15/aa25632-15.html)<https://www.aanda.org/articles/aa/abs/2015/11/aa25632-15/aa25632-15.html>) (Nov. 2015).
88. I. Delvecchio *et al.*, *The Astrophysical Journal* **892**, 17, ISSN: 0004-637X, (<https://iopscience.iop.org/article/10.3847/1538-4357/ab789c><https://iopscience.iop.org/article/10.3847/1538-4357/ab789c/meta>) (Mar. 2020).
89. F. Pacucci, B. Nguyen, S. Carniani, R. Maiolino, X. Fan, *ApJL* **957**, L3, ISSN: 0004-637X, (<https://ui.adsabs.harvard.edu/abs/2023ApJ...957L...3P/abstract>) (Nov. 2023).
90. M. Kong, L. C. Ho, *The Astrophysical Journal* **859**, 116, ISSN: 0004-637X, (<https://iopscience.iop.org/article/10.3847/1538-4357/aabe2a><https://iopscience.iop.org/article/10.3847/1538-4357/aabe2a/meta>) (May 2018).
91. H. Suh *et al.*, *NatAs* **9**, 271–279, ISSN: 23973366, (<http://arxiv.org/abs/2405.05333>) (May 2024).
92. P. Marziani, K. G. Luna, A. Floris, A. del Olmo, A. Deconto-Machado, T. M. Buendia-Rios, C. A. Negrete, D. Dultzin, *Univ* **11**, 69, ISSN: 22181997, (<http://arxiv.org/abs/2502.14713>) (Feb. 2025).
93. S. Frederick *et al.*, *arXiv e-prints*, arXiv:2010.08554, arXiv: 2010.08554 (astro-ph.HE) (Oct. 2020).
94. M. J. Graham, S. G. Djorgovski, A. J. Drake, D. Stern, A. A. Mahabal, E. Glikman, S. Larson, E. Christensen, *Monthly Notices of the Royal Astronomical Society* **470**, 4112–4132, ISSN: 0035-8711, (<https://dx.doi.org/10.1093/mnras/stx1456>) (Oct. 2017).
95. J. A. Fernández-Ontiveros, T. Muñoz-Darias, *Monthly Notices of the Royal Astronomical Society* **504**, 5726–5740, ISSN: 0035-8711, (<https://dx.doi.org/10.1093/mnras/stab1108>) (June 2021).
96. B. McKernan, K. E. Ford, M. Cantiello, M. Graham, A. S. Jermyn, N. W. Leigh, T. Ryu, D. Stern, *Monthly Notices of the Royal Astronomical Society* **514**, 4102–4110, ISSN: 13652966, (<https://ui.adsabs.harvard.edu/abs/2022MNRAS.514.4102M/abstract>) (Aug. 2022).

97. B. Czerny, K. Hryniewicz, *A&A* **525**, L8, arXiv: 1010.6201 (astro-ph.CO) (Jan. 2011).
98. Osterbrock, D. E., *ApJ* **404**, 551, ISSN: 0004-637X, (<https://ui.adsabs.harvard.edu/abs/1993ApJ...404..551O/abstract>) (Feb. 1993).
99. K. Wada, *ApJ* **758**, 66, (<http://arxiv.org/abs/1208.5272><http://dx.doi.org/10.1088/0004-637X/758/1/66>) (Aug. 2012).
100. C. Ward *et al.*, *The Astrophysical Journal* **936**, 104, ISSN: 0004-637X, (<https://iopscience.iop.org/article/10.3847/1538-4357/ac8666><https://iopscience.iop.org/article/10.3847/1538-4357/ac8666/meta>) (Sept. 2022).
101. M. Mezcuca (2017).
102. F. Koliopanos, B. C. Ciambur, A. W. Graham, N. A. Webb, M. Coriat, B. Mutlu-Pakdil, B. L. Davis, O. Godet, D. Barret, M. S. Seigar, *Astronomy & Astrophysics* **601**, A20, ISSN: 0004-6361, ([https://www.aanda.org/articles/aa/full\\_html/2017/05/aa30061-16/aa30061-16.html](https://www.aanda.org/articles/aa/full_html/2017/05/aa30061-16/aa30061-16.html)<https://www.aanda.org/articles/aa/abs/2017/05/aa30061-16/aa30061-16.html>) (May 2017).
103. A. E. Reines, J. E. Greene, M. Geha, *The Astrophysical Journal* **775**, 116, ISSN: 0004-637X, (<https://iopscience.iop.org/article/10.1088/0004-637X/775/2/116><https://iopscience.iop.org/article/10.1088/0004-637X/775/2/116/meta>) (Sept. 2013).
104. G. Agazie *et al.*, *The Astrophysical Journal Letters* **951**, L8, ISSN: 2041-8205, (<https://iopscience.iop.org/article/10.3847/2041-8213/acdac6><https://iopscience.iop.org/article/10.3847/2041-8213/acdac6/meta>) (June 2023).
105. R. Abbott *et al.*, *A&A* **659**, A84, arXiv: 2105.15120 (astro-ph.HE) (Mar. 2022).
106. J. W. Nightingale *et al.*, *Monthly Notices of the Royal Astronomical Society* **521**, 3298–3322, ISSN: 0035-8711, (<https://dx.doi.org/10.1093/mnras/stad587>) (Mar. 2023).
107. Event Horizon Telescope Collaboration *et al.*, *ApJL* **930**, L12 (May 2022).
108. E. R. Liepold, M. E. Quenneville, C.-P. Ma, J. L. Walsh, N. J. McConnell, J. E. Greene, J. P. Blakeslee, *The Astrophysical Journal* **891**, 4, ISSN: 0004-637X, (<https://ui.adsabs.harvard.edu/abs/2020ApJ...891...4L/abstract>) (Mar. 2020).
109. V. V. Lidskii, L. M. Ozernoi, *Soviet Astronomy Letters* **5**, 16–19 (Jan. 1979).
110. M. J. Rees, *Nature* **333**, 523–528 (June 1988).
111. E. S. Phinney, presented at the The Center of the Galaxy, ed. by M. Morris, vol. 136, p. 543.

112. S. Gezari, *ARA&A* **59**, 21–58, arXiv: 2104.14580 (astro-ph.HE) (Sept. 2021).
113. W. Lu, C. Bonnerot, *MNRAS* **492**, 686–707, arXiv: 1904.12018 (astro-ph.HE) (Feb. 2020).
114. S. Komossa *et al.*, *ApJ* **701**, 105–121, arXiv: 0902.3248 (astro-ph.GA) (Aug. 2009).
115. W. Lu, P. Kumar, N. J. Evans, *MNRAS* **458**, 575–581, arXiv: 1512.00020 (astro-ph.HE) (May 2016).
116. S. van Velzen *et al.*, *ApJ* **872**, 198, arXiv: 1809.02608 (astro-ph.HE) (Feb. 2019).
117. S. Sembay, R. G. West, *MNRAS* **262**, 141–150 (May 1993).
118. S. Komossa, N. Bade, *A&A* **343**, 775–787, arXiv: astro-ph/9901141 (astro-ph) (Mar. 1999).
119. S. Komossa, J. Greiner, *A&A* **349**, L45–L48, arXiv: astro-ph/9908216 (astro-ph) (Sept. 1999).
120. J. Greiner, R. Schwarz, S. Zharikov, M. Orio, *A&A* **362**, L25–L28, arXiv: astro-ph/0009430 (astro-ph) (Oct. 2000).
121. S. Gezari *et al.*, *ApJL* **653**, L25–L28, arXiv: astro-ph/0612069 (astro-ph) (Dec. 2006).
122. S. Gezari *et al.*, *ApJ* **676**, 944–969, arXiv: 0712.4149 (astro-ph) (Apr. 2008).
123. S. van Velzen, G. R. Farrar, S. Gezari, N. Morrell, D. Zaritsky, L. Östman, M. Smith, J. Gelfand, A. J. Drake, *ApJ* **741**, 73, arXiv: 1009.1627 (astro-ph.CO) (Nov. 2011).
124. E. C. Bellm *et al.*, *PASP* **131**, 018002, arXiv: 1902.01932 (astro-ph.IM) (Jan. 2019).
125. M. J. Graham *et al.*, *PASP* **131**, 078001, arXiv: 1902.01945 (astro-ph.IM) (July 2019).
126. R. Dekany *et al.*, *PASP* **132**, 038001, arXiv: 2008.04923 (astro-ph.IM) (Mar. 2020).
127. F. J. Masci *et al.*, *PASP* **131**, 018003, arXiv: 1902.01872 (astro-ph.IM) (Jan. 2019).
128. S. van Velzen *et al.*, *ApJ* **908**, 4, arXiv: 2001.01409 (astro-ph.HE) (Feb. 2021).
129. P. Predehl *et al.*, *A&A* **647**, A1, arXiv: 2010.03477 (astro-ph.HE) (Mar. 2021).

130. S. Sazonov *et al.*, MNRAS **508**, 3820–3847, arXiv: 2108.02449 (astro-ph.HE) (Dec. 2021).
131. N. Jiang *et al.*, ApJS **252**, 32, arXiv: 2012.06806 (astro-ph.GA) (Feb. 2021).
132. M. Masterson *et al.*, ApJ **961**, 211, arXiv: 2401.01403 (astro-ph.HE) (Feb. 2024).
133. M. Lacy *et al.*, PASP **132**, 035001, arXiv: 1907.01981 (astro-ph.IM) (Mar. 2020).
134. Y. Yao *et al.*, ApJL **955**, L6, arXiv: 2303.06523 (astro-ph.HE) (Sept. 2023).
135. E. Hammerstein *et al.*, ApJL **908**, L20, arXiv: 2010.10738 (astro-ph.HE) (Feb. 2021).
136. I. Arcavi *et al.*, ApJ **793**, 38, arXiv: 1405.1415 (astro-ph.HE) (Sept. 2014).
137. K. D. French, I. Arcavi, A. Zabludoff, ApJL **818**, L21, arXiv: 1601.04705 (astro-ph.GA) (Feb. 2016).
138. K. D. French, I. Arcavi, A. Zabludoff, ApJ **835**, 176, arXiv: 1609.04755 (astro-ph.GA) (Feb. 2017).
139. J. Law-Smith, E. Ramirez-Ruiz, S. L. Ellison, R. J. Foley, ApJ **850**, 22, arXiv: 1707.01559 (astro-ph.HE) (Nov. 2017).
140. K. D. French, T. Wevers, J. Law-Smith, O. Graur, A. I. Zabludoff, SSRv **216**, 32, arXiv: 2003.02863 (astro-ph.HE) (Mar. 2020).
141. T. Wevers *et al.*, ApJL **942**, L33, arXiv: 2209.07538 (astro-ph.HE) (Jan. 2023).
142. M. Guolo, S. Gezari, Y. Yao, S. van Velzen, E. Hammerstein, S. B. Cenko, Y. M. Tokayer, ApJ **966**, 160, arXiv: 2308.13019 (astro-ph.HE) (May 2024).
143. R. Saxton, S. Komossa, K. Auchettl, P. G. Jonker, SSRv **216**, 85 (July 2020).
144. N. Jiang, T. Wang, X. Hu, L. Sun, L. Dou, L. Xiao, ApJ **911**, 31, arXiv: 2102.08044 (astro-ph.GA) (Apr. 2021).
145. S. Reusch *et al.*, PhRvL **128**, 221101, arXiv: 2111.09390 (astro-ph.HE) (June 2022).
146. N. Roth, D. Kasen, ApJ **855**, 54, arXiv: 1707.02993 (astro-ph.HE) (Mar. 2018).
147. C. J. Saxton, H. B. Perets, A. Baskin, MNRAS **474**, 3307–3323, arXiv: 1612.08093 (astro-ph.HE) (Mar. 2018).

148. P. Short *et al.*, MNRAS **525**, 1568–1587, arXiv: 2307.13674 (astro-ph.HE) (Oct. 2023).
149. Y. Cendes *et al.*, *The Astrophysical Journal* **971**, 185, ISSN: 0004-637X, (<https://ui.adsabs.harvard.edu/abs/2024ApJ...971..185C/abstract>) (Aug. 2024).
150. K. D. Alexander, S. van Velzen, A. Horesh, B. A. Zauderer, SSRv **216**, 81, arXiv: 2006.01159 (astro-ph.HE) (June 2020).
151. A. Horesh, S. B. Cenko, I. Arcavi, *Nature Astronomy* **5**, 491–497, arXiv: 2102.11290 (astro-ph.HE) (May 2021).
152. A. Horesh, I. Sfaradi, R. Fender, D. A. Green, D. R. A. Williams, J. S. Bright, ApJL **920**, L5, arXiv: 2109.10921 (astro-ph.HE) (Oct. 2021).
153. Y. Cendes *et al.*, ApJ **938**, 28, arXiv: 2206.14297 (astro-ph.HE) (Oct. 2022).
154. K. Nyland *et al.*, ApJ **905**, 74, arXiv: 2011.08872 (astro-ph.GA) (Dec. 2020).
155. K. P. Mooley *et al.*, ApJ **818**, 105, arXiv: 1601.01693 (astro-ph.HE) (Feb. 2016).
156. M. Kunert-Bajraszewska, A. Wołowska, K. Mooley, P. Kharb, G. Hallinan, ApJ **897**, 128, arXiv: 2007.01590 (astro-ph.GA) (July 2020).
157. A. Wołowska, M. Kunert-Bajraszewska, K. P. Mooley, A. Siemiginowska, P. Kharb, C. H. Ishwara-Chandra, G. Hallinan, M. Gromadzki, D. Koziel-Wierzbowska, ApJ **914**, 22, arXiv: 2103.08422 (astro-ph.GA) (June 2021).
158. J. Y. Koay, M. Vestergaard, H. E. Bignall, C. Reynolds, B. M. Peterson, MNRAS **460**, 304–316, arXiv: 1602.07289 (astro-ph.GA) (July 2016).
159. R. Fender, in *Lecture Notes in Physics, Berlin Springer Verlag*, ed. by T. Belloni, vol. 794, p. 115.
160. R. Blandford, D. Meier, A. Readhead, ARA&A **57**, 467–509, arXiv: 1812.06025 (astro-ph.HE) (Aug. 2019).
161. J. J. Condon, W. D. Cotton, E. W. Greisen, Q. F. Yin, R. A. Perley, G. B. Taylor, J. J. Broderick, AJ **115**, 1693–1716 (May 1998).
162. Planck Collaboration *et al.*, A&A **641**, A6, arXiv: 1807.06209 (astro-ph.CO) (Sept. 2020).
163. J. J. Somalwar, V. Ravi, D. Dong, M. Graham, G. Hallinan, C. Law, W. Lu, S. T. Myers, ApJ **929**, 184, arXiv: 2108.12431 (astro-ph.HE) (Apr. 2022).

164. W. Peters, E. Polisensky, W. Brisken, W. Cotton, T. Clarke, S. Giacintucci, N. Kassim, presented at the American Astronomical Society Meeting Abstracts, vol. 53, 211.06, p. 211.06.
165. T. E. Clarke, N. E. Kassim, W. Brisken, J. Helmboldt, W. Peters, P. S. Ray, E. Polisensky, S. Giacintucci, presented at the Ground-based and Airborne Telescopes VI, ed. by H. J. Hall, R. Gilmozzi, H. K. Marshall, vol. 9906, 99065B, 99065B.
166. E. Polisensky, W. M. Lane, S. D. Hyman, N. E. Kassim, S. Giacintucci, T. E. Clarke, W. D. Cotton, E. Cleland, D. A. Frail, *ApJ* **832**, 60, arXiv: 1604.00667 (astro-ph.HE) (Nov. 2016).
167. H. T. Intema, P. Jagannathan, K. P. Mooley, D. A. Frail, *A&A* **598**, A78, arXiv: 1603.04368 (astro-ph.CO) (Feb. 2017).
168. D. McConnell *et al.*, *PASA* **37**, e048, arXiv: 2012.00747 (astro-ph.IM) (Nov. 2020).
169. W. E. Wilson *et al.*, *MNRAS* **416**, 832–856, arXiv: 1105.3532 (astro-ph.IM) (Sept. 2011).
170. R. J. Sault, P. J. Teuben, M. C. H. Wright, presented at the Astronomical Data Analysis Software and Systems IV, ed. by R. A. Shaw, H. E. Payne, J. J. E. Hayes, vol. 77, p. 433, arXiv: astro-ph/0612759 (astro-ph).
171. J. P. McMullin, B. Waters, D. Schiebel, W. Young, K. Golap, presented at the Astronomical Data Analysis Software and Systems XVI, ed. by R. A. Shaw, F. Hill, D. J. Bell, vol. 376, p. 127.
172. B. Maity, P. Chandra, *ApJ* **907**, 60, arXiv: 2012.05166 (astro-ph.HE) (Feb. 2021).
173. A. T. Deller *et al.*, *PASP* **123**, 275, arXiv: 1101.0885 (astro-ph.IM) (Mar. 2011).
174. A. J. Drake *et al.*, *ApJ* **696**, 870–884, arXiv: 0809.1394 (astro-ph) (May 2009).
175. K. C. Chambers *et al.*, *arXiv e-prints*, arXiv:1612.05560, arXiv: 1612.05560 (astro-ph.IM) (Dec. 2016).
176. J. L. Tonry, L. Denneau, A. N. Heinze, B. Stalder, K. W. Smith, S. J. Smartt, C. W. Stubbs, H. J. Weiland, A. Rest, *PASP* **130**, 064505, arXiv: 1802.00879 (astro-ph.IM) (June 2018).
177. K. De *et al.*, *ApJ* **905**, 58, arXiv: 2004.09029 (astro-ph.HE) (Dec. 2020).
178. D. Lang, *AJ* **147**, 108, arXiv: 1405.0308 (astro-ph.IM) (May 2014).
179. A. M. Meisner, D. Lang, D. J. Schlegel, *AJ* **154**, 161, arXiv: 1705.06746 (astro-ph.IM) (Oct. 2017).

180. A. Mainzer *et al.*, *ApJ* **731**, 53, arXiv: 1102.1996 (astro-ph.EP) (Apr. 2011).
181. S. Cole *et al.*, *MNRAS* **362**, 505–534, arXiv: astro-ph/0501174 (astro-ph) (Sept. 2005).
182. J. B. Oke *et al.*, *PASP* **107**, 375 (Apr. 1995).
183. W. Voges, *Advances in Space Research* **13**, 391–397 (Dec. 1993).
184. T. Boller, M. J. Freyberg, J. Truemper, F. Haberl, W. Voges, K. Nandra, *VizieR Online Data Catalog*, J/A+A/588/A103 (Mar. 2016).
185. N. Ben Bekhti *et al.*, *Astronomy and Astrophysics* **594**, A116, ISSN: 14320746, (<https://ui.adsabs.harvard.edu/abs/2016A&A...594A.116H/abstract>) (Oct. 2016).
186. M. Matsuoka *et al.*, *PASJ* **61**, 999, arXiv: 0906.0631 (astro-ph.IM) (Oct. 2009).
187. H. A. Krimm, S. D. Barthelmy, C. B. Markwardt, D. Sanwal, J. Tueller, N. Gehrels, Swift/BAT Team, presented at the AAS/High Energy Astrophysics Division #9, vol. 9, 13.47, p. 13.47.
188. D. N. Burrows *et al.*, *SSRv* **120**, 165–195, arXiv: astro-ph/0508071 (astro-ph) (Oct. 2005).
189. D. G. York *et al.*, *AJ* **120**, 1579–1587, arXiv: astro-ph/0006396 (astro-ph) (Sept. 2000).
190. B. D. Johnson, J. Leja, C. Conroy, J. S. Speagle, *ApJS* **254**, 22, arXiv: 2012.01426 (astro-ph.GA) (June 2021).
191. C. Conroy, J. E. Gunn, M. White, *ApJ* **699**, 486–506, arXiv: 0809.4261 (astro-ph) (July 2009).
192. C. Conroy, J. E. Gunn, *ApJ* **712**, 833–857, arXiv: 0911.3151 (astro-ph.CO) (Apr. 2010).
193. G. Chabrier, *PASP* **115**, 763–795, arXiv: astro-ph/0304382 (astro-ph) (July 2003).
194. D. Calzetti, L. Armus, R. C. Bohlin, A. L. Kinney, J. Koornneef, T. Storchi-Bergmann, *ApJ* **533**, 682–695, arXiv: astro-ph/9911459 (astro-ph) (Apr. 2000).
195. D. Foreman-Mackey, D. W. Hogg, D. Lang, J. Goodman, *Publications of the Astronomical Society of the Pacific* **125**, 306–312, ISSN: 00046280, (<https://ui.adsabs.harvard.edu/abs/2013PASP...125..306F/abstract>) (Mar. 2013).
196. D. Calzetti, in *Secular Evolution of Galaxies*, ed. by J. Falcón-Barroso, J. H. Knapen, p. 419.

197. A. Domínguez *et al.*, ApJ **763**, 145, arXiv: 1206.1867 (astro-ph.CO) (Feb. 2013).
198. L. J. Kewley, M. J. Geller, R. A. Jansen, AJ **127**, 2002–2030, arXiv: astro-ph/0401172 (astro-ph) (Apr. 2004).
199. S. Frederick *et al.*, ApJ **883**, 31, arXiv: 1904.10973 (astro-ph.HE) (Sept. 2019).
200. R. J. Assef, D. Stern, G. Noirot, H. D. Jun, R. M. Cutri, P. R. M. Eisenhardt, ApJS **234**, 23, arXiv: 1706.09901 (astro-ph.GA) (Feb. 2018).
201. E. Lusso *et al.*, MNRAS **425**, 623–640, arXiv: 1206.2642 (astro-ph.CO) (Sept. 2012).
202. R. A. Chevalier, ApJ **499**, 810–819 (May 1998).
203. J. Granot, R. Sari, ApJ **568**, 820–829, arXiv: astro-ph/0108027 (astro-ph) (Apr. 2002).
204. R. Barniol Duran, E. Nakar, T. Piran, ApJ **772**, 78, arXiv: 1301.6759 (astro-ph.HE) (July 2013).
205. T. Eftekhari, E. Berger, B. A. Zauderer, R. Margutti, K. D. Alexander, ApJ **854**, 86, arXiv: 1710.07289 (astro-ph.HE) (Feb. 2018).
206. J. S. Speagle, *Monthly Notices of the Royal Astronomical Society* **493**, 3132–3158, ISSN: 13652966, (<https://ui.adsabs.harvard.edu/abs/2020MNRAS.493.3132S/abstract>) (2020).
207. S. Mineo, M. Gilfanov, B. D. Lehmer, G. E. Morrison, R. Sunyaev, MNRAS **437**, 1698–1707, arXiv: 1207.2157 (astro-ph.HE) (Jan. 2014).
208. S. Vattakunnel *et al.*, MNRAS **420**, 2190–2208, arXiv: 1111.3285 (astro-ph.CO) (Mar. 2012).
209. F. Haardt, L. Maraschi, ApJL **380**, L51 (Oct. 1991).
210. H. Netzer, V. Mainieri, P. Rosati, B. Trakhtenbrot, A&A **453**, 525–533, arXiv: astro-ph/0603712 (astro-ph) (July 2006).
211. D. Grupe, S. Komossa, K. M. Leighly, K. L. Page, ApJS **187**, 64–106, arXiv: 1001.3140 (astro-ph.CO) (Mar. 2010).
212. S. Komossa, presented at the Revisiting Narrow-Line Seyfert 1 Galaxies and their Place in the Universe, 15, p. 15, arXiv: 1807.03666 (astro-ph.GA).
213. G. Risaliti, R. Maiolino, M. Salvati, ApJ **522**, 157–164, arXiv: astro-ph/9902377 (astro-ph) (Sept. 1999).
214. F. Panessa, L. Bassani, A&A **394**, 435–442, arXiv: astro-ph/0208496 (astro-ph) (Nov. 2002).
215. M. R. S. Hawkins, A&A **424**, 519–529, arXiv: astro-ph/0406163 (astro-ph) (Sept. 2004).

216. D. E. Osterbrock, *Reports on Progress in Physics* **54**, 579–633 (Apr. 1991).
217. C. Ricci *et al.*, *Nature* **549**, 488–491, arXiv: 1709.09651 (astro-ph.HE) (Sept. 2017).
218. B. D. Metzger, P. K. G. Williams, E. Berger, *ApJ* **806**, 224, arXiv: 1502.01350 (astro-ph.HE) (June 2015).
219. V. Ravi, H. Dykaar, J. Codd, G. Zaccagnini, D. Dong, M. R. Drout, B. M. Gaensler, G. Hallinan, C. Law, *ApJ* **925**, 220, arXiv: 2102.05795 (astro-ph.HE) (Feb. 2022).
220. S. Mattila *et al.*, *Science* **361**, 482–485, arXiv: 1806.05717 (astro-ph.GA) (Aug. 2018).
221. P. Salas, F. E. Bauer, C. Stockdale, J. L. Prieto, *MNRAS* **428**, 1207–1217, arXiv: 1208.3455 (astro-ph.HE) (Jan. 2013).
222. A. M. Soderberg, R. A. Chevalier, S. R. Kulkarni, D. A. Frail, *ApJ* **651**, 1005–1018, arXiv: astro-ph/0512413 (astro-ph) (Nov. 2006).
223. A. M. Soderberg *et al.*, *Nature* **463**, 513–515, arXiv: 0908.2817 (astro-ph.HE) (Jan. 2010).
224. S. R. Kulkarni, D. A. Frail, M. H. Wieringa, R. D. Ekers, E. M. Sadler, R. M. Wark, J. L. Higdon, E. S. Phinney, J. S. Bloom, *Nature* **395**, 663–669 (Oct. 1998).
225. K. W. Weiler, N. Panagia, M. J. Montes, R. A. Sramek, *ARA&A* **40**, 387–438 (Jan. 2002).
226. T. Kangas, A. S. Fruchter, *ApJ* **911**, 14, arXiv: 1911.01938 (astro-ph.HE) (Apr. 2021).
227. R. Fender, E. Koerding, T. Belloni, P. Uttley, I. McHardy, T. Tzioumis, *arXiv e-prints*, arXiv:0706.3838, arXiv: 0706.3838 (astro-ph) (June 2007).
228. R. P. Fender, T. M. Belloni, E. Gallo, *MNRAS* **355**, 1105–1118, arXiv: astro-ph/0409360 (astro-ph) (Dec. 2004).
229. R. P. Fender, J. Homan, T. M. Belloni, *MNRAS* **396**, 1370–1382, arXiv: 0903.5166 (astro-ph.HE) (July 2009).
230. A. Tchekhovskoy, R. Narayan, J. C. McKinney, *ApJ* **711**, 50–63, arXiv: 0911.2228 (astro-ph.HE) (Mar. 2010).
231. A. Tchekhovskoy, J. C. McKinney, R. Narayan, *ApJ* **699**, 1789–1808, arXiv: 0901.4776 (astro-ph.HE) (July 2009).
232. R. P. Fender, E. Gallo, D. Russell, *MNRAS* **406**, 1425–1434, arXiv: 1003.5516 (astro-ph.HE) (Aug. 2010).
233. K. Gültekin, A. L. King, E. M. Cackett, K. Nyland, J. M. Miller, T. Di Matteo, S. Markoff, M. P. Rupen, *ApJ* **871**, 80, arXiv: 1901.02530 (astro-ph.HE) (Jan. 2019).

234. A. Janiuk, B. Czerny, MNRAS **414**, 2186–2194, arXiv: 1102.3257 (astro-ph.HE) (July 2011).
235. H. Falcke, N. M. Nagar, A. S. Wilson, L. C. Ho, J. S. Ulvestad, presented at the Black Holes in Binaries and Galactic Nuclei, ed. by L. Kaper, E. P. J. V. D. Heuvel, P. A. Woudt, p. 218, arXiv: astro-ph/9912436 (astro-ph).
236. S. Laha, C. S. Reynolds, J. Reeves, G. Kriss, M. Guainazzi, R. Smith, S. Veilleux, D. Proga, *Nature Astronomy* **5**, 13–24, arXiv: 2012.06945 (astro-ph.GA) (Jan. 2021).
237. A. Tchekhovskoy, B. D. Metzger, D. Giannios, L. Z. Kelley, MNRAS **437**, 2744–2760, arXiv: 1301.1982 (astro-ph.HE) (Jan. 2014).
238. M. Liska, C. Hesp, A. Tchekhovskoy, A. Ingram, M. van der Klis, S. B. Markoff, M. Van Moer, MNRAS **507**, 983–990, arXiv: 1904.08428 (astro-ph.HE) (Oct. 2021).
239. S. Komossa, W. Voges, D. Xu, S. Mathur, H.-M. Adorf, G. Lemson, W. J. Duschl, D. Grupe, AJ **132**, 531–545, arXiv: astro-ph/0603680 (astro-ph) (Aug. 2006).
240. M. Berton, E. Järvelä, L. Crepaldi, A. Lähteenmäki, M. Tornikoski, E. Congiu, P. Kharb, G. Terreran, A. Vietri, A&A **636**, A64, arXiv: 2003.02654 (astro-ph.GA) (Apr. 2020).
241. K. Rusinek, M. Sikora, D. Kozieł-Wierzbowska, L. Godfrey, MNRAS **466**, 2294–2301, arXiv: 1612.07392 (astro-ph.GA) (Apr. 2017).
242. A. Lähteenmäki, E. Järvelä, V. Ramakrishnan, M. Tornikoski, J. Tammi, R. J. C. Vera, W. Chamani, A&A **614**, L1, arXiv: 1806.02058 (astro-ph.GA) (June 2018).
243. J. Frank, M. J. Rees, MNRAS **176**, 633–647 (Sept. 1976).
244. J. L. Donley, W. N. Brandt, M. Eracleous, T. Boller, AJ **124**, 1308–1321, arXiv: astro-ph/0206291 (astro-ph) (Sept. 2002).
245. S. B. Cenko *et al.*, ApJ **753**, 77, arXiv: 1107.5307 (astro-ph.HE) (July 2012).
246. B. A. Zauderer *et al.*, Nature **476**, 425–428, arXiv: 1106.3568 (astro-ph.HE) (Aug. 2011).
247. E. Berger, A. Zauderer, G. G. Pooley, A. M. Soderberg, R. Sari, A. Brunthaler, M. F. Bietenholz, ApJ **748**, 36, arXiv: 1112.1697 (astro-ph.HE) (Mar. 2012).
248. K. Wiersema *et al.*, MNRAS **491**, 1771–1776, arXiv: 1910.11624 (astro-ph.HE) (Jan. 2020).
249. B. A. Zauderer, E. Berger, R. Margutti, G. G. Pooley, R. Sari, A. M. Soderberg, A. Brunthaler, M. F. Bietenholz, ApJ **767**, 152, arXiv: 1212.1173 (astro-ph.HE) (Apr. 2013).

250. J. Yang, Z. Paragi, A. J. van der Horst, L. I. Gurvits, R. M. Campbell, D. Giannios, T. An, S. Komossa, *MNRAS* **462**, L66–L70, arXiv: 1605.06461 (astro-ph.HE) (Oct. 2016).
251. Y. Cendes, T. Eftekhari, E. Berger, E. Polisensky, *ApJ* **908**, 125, arXiv: 2011.00074 (astro-ph.HE) (Feb. 2021).
252. P. Crumley, W. Lu, R. Santana, R. A. Hernández, P. Kumar, S. Markoff, *MNRAS* **460**, 396–416, arXiv: 1604.06468 (astro-ph.HE) (July 2016).
253. A. J. Goodwin, S. van Velzen, J. C. A. Miller-Jones, A. Mummery, M. F. Bietenholz, A. Wederfoort, E. Hammerstein, C. Bonnerot, J. Hoffmann, L. Yan, *MNRAS* **511**, 5328–5345, arXiv: 2201.03744 (astro-ph.HE) (Apr. 2022).
254. P. G. Jonker, N. C. Stone, A. Generozov, S. van Velzen, B. Metzger, *ApJ* **889**, 166, arXiv: 1906.12236 (astro-ph.HE) (Feb. 2020).
255. I. Sfaradi, A. Horesh, R. Fender, D. A. Green, D. R. A. Williams, J. Bright, S. Schulze, *ApJ* **933**, 176, arXiv: 2202.00026 (astro-ph.HE) (July 2022).
256. H. Netzer, *ARA&A* **53**, 365–408, arXiv: 1505.00811 (astro-ph.GA) (Aug. 2015).
257. S. van Velzen, N. C. Stone, B. D. Metzger, S. Gezari, T. M. Brown, A. S. Fruchter, *ApJ* **878**, 82, arXiv: 1809.00003 (astro-ph.HE) (June 2019).
258. B. Mockler, J. Guillochon, E. Ramirez-Ruiz, *ApJ* **872**, 151, arXiv: 1801.08221 (astro-ph.HE) (Feb. 2019).
259. B. D. Metzger, D. Giannios, P. Mimica, *MNRAS* **420**, 3528–3537, arXiv: 1110.1111 (astro-ph.HE) (Mar. 2012).
260. N. Bade, S. Komossa, M. Dahlem, *A&A* **309**, L35–L38 (May 1996).
261. P. Esquej, R. D. Saxton, M. J. Freyberg, A. M. Read, B. Altieri, M. Sanchez-Portal, G. Hasinger, *A&A* **462**, L49–L52, arXiv: astro-ph/0612340 (astro-ph) (Feb. 2007).
262. T. Piran, G. Svirski, J. Krolik, R. M. Cheng, H. Shiokawa, *ApJ* **806**, 164, arXiv: 1502.05792 (astro-ph.HE) (June 2015).
263. K. Auchettl, J. Guillochon, E. Ramirez-Ruiz, *ApJ* **838**, 149, arXiv: 1611.02291 (astro-ph.HE) (Apr. 2017).
264. J. Krolik, T. Piran, G. Svirski, R. M. Cheng, *ApJ* **827**, 127, arXiv: 1602.02824 (astro-ph.HE) (Aug. 2016).
265. C.-H. Chan, T. Piran, J. H. Krolik, *ApJ* **903**, 17, arXiv: 2004.06234 (astro-ph.HE) (Nov. 2020).
266. A. Zabludoff *et al.*, *SSRv* **217**, 54, arXiv: 2103.12150 (astro-ph.HE) (June 2021).

267. A. Lawrence, *Nature Astronomy* **2**, 102–103, arXiv: 1802.00408 (astro-ph.HE) (Feb. 2018).
268. S. F. Hönig, T. Beckert, *MNRAS* **380**, 1172–1176 (Sept. 2007).
269. P. F. Hopkins, C. C. Hayward, D. Narayanan, L. Hernquist, *MNRAS* **420**, 320–339, arXiv: 1108.3086 (astro-ph.CO) (Feb. 2012).
270. M. A. Strauss *et al.*, *AJ* **124**, 1810–1824, arXiv: astro-ph/0206225 (astro-ph) (Sept. 2002).
271. S. Komossa *et al.*, *ApJL* **678**, L13, arXiv: 0804.2670 (astro-ph) (May 2008).
272. C.-W. Yang, T.-G. Wang, G. Ferland, W. Yuan, H.-Y. Zhou, P. Jiang, *ApJ* **774**, 46, arXiv: 1307.3313 (astro-ph.CO) (Sept. 2013).
273. T.-G. Wang, H.-Y. Zhou, L.-F. Wang, H.-L. Lu, D. Xu, *ApJ* **740**, 85, arXiv: 1108.2790 (astro-ph.CO) (Oct. 2011).
274. A. Malyali *et al.*, *A&A* **647**, A9, arXiv: 2101.08760 (astro-ph.HE) (Mar. 2021).
275. J. M. M. Neustadt *et al.*, *MNRAS* **494**, 2538–2560, arXiv: 1910.01142 (astro-ph.HE) (May 2020).
276. C. K. Seyfert, *ApJ* **97**, 28 (Jan. 1943).
277. M. V. Penston, R. A. E. Fosbury, A. Boksenberg, M. J. Ward, A. S. Wilson, *MNRAS* **208**, 347–364 (May 1984).
278. J. M. Gelbord, J. R. Mullaney, M. J. Ward, *MNRAS* **397**, 172–189, arXiv: 0904.3156 (astro-ph.GA) (July 2009).
279. R. Riffel, A. Rodríguez-Ardila, M. G. Pastoriza, *A&A* **457**, 61–70, arXiv: astro-ph/0605463 (astro-ph) (Oct. 2006).
280. T. Murayama, Y. Taniguchi, *ApJL* **503**, L115–L118, arXiv: astro-ph/9806287 (astro-ph) (Aug. 1998).
281. L. Palaversa, S. Gezari, B. Sesar, J. S. Stuart, P. Wozniak, B. Holl, Ž. Ivezić, *ApJ* **819**, 151, arXiv: 1512.08614 (astro-ph.GA) (Mar. 2016).
282. L. Dou, T.-g. Wang, N. Jiang, C. Yang, J. Lyu, H. Zhou, *ApJ* **832**, 188, arXiv: 1605.05145 (astro-ph.HE) (Dec. 2016).
283. D. Giannios, B. D. Metzger, *MNRAS* **416**, 2102–2107, arXiv: 1102.1429 (astro-ph.HE) (Sept. 2011).
284. H. A. Flewelling *et al.*, *ApJS* **251**, 7, arXiv: 1612.05243 (astro-ph.IM) (Nov. 2020).
285. D. J. Helfand, R. L. White, R. H. Becker, *ApJ* **801**, 26, arXiv: 1501.01555 (astro-ph.GA) (Mar. 2015).

286. R. L. White, R. H. Becker, D. J. Helfand, M. D. Gregg, *ApJ* **475**, 479–493 (Feb. 1997).
287. E. C. Bellm *et al.*, *PASP* **131**, 068003, arXiv: 1905.02209 (astro-ph.IM) (June 2019).
288. F. J. Masci, R. R. Laher, B. Rusholme, D. Shupe, R. Paladini, S. Groom, A. Wold, A. A. Miller, A. Drake, *arXiv e-prints*, arXiv:2305.16279, arXiv: 2305.16279 (astro-ph.IM) (May 2023).
289. P. Giommi, L. Angelini, P. Jacobs, G. Tagliaferri, presented at the Astronomical Data Analysis Software and Systems I, ed. by D. M. Worrall, C. Biemesderfer, J. Barnes, vol. 25, p. 100.
290. P. A. Evans *et al.*, *A&A* **469**, 379–385, arXiv: 0704.0128 (astro-ph) (July 2007).
291. D. A. Perley, *PASP* **131**, 084503, arXiv: 1903.07629 (astro-ph.IM) (Aug. 2019).
292. A. I. Sheinis, M. Bolte, H. W. Epps, R. I. Kibrick, J. S. Miller, M. V. Radovan, B. C. Bigelow, B. M. Sutin, *PASP* **114**, 851–865, arXiv: astro-ph/0204297 (astro-ph) (Aug. 2002).
293. M. Huertas-Company, J. A. L. Aguerri, M. Bernardi, S. Mei, J. Sánchez Almeida, *A&A* **525**, A157, arXiv: 1010.3018 (astro-ph.CO) (Jan. 2011).
294. L. Simard, J. T. Mendel, D. R. Patton, S. L. Ellison, A. W. McConnachie, *ApJS* **196**, 11, arXiv: 1107.1518 (astro-ph.CO) (Sept. 2011).
295. J. T. Mendel, L. Simard, M. Palmer, S. L. Ellison, D. R. Patton, *ApJS* **210**, 3, arXiv: 1310.8304 (astro-ph.CO) (Jan. 2014).
296. C. Million, S. W. Fleming, B. Shiao, M. Seibert, P. Loyd, M. Tucker, M. Smith, R. Thompson, R. L. White, *ApJ* **833**, 292, arXiv: 1609.09492 (astro-ph.IM) (Dec. 2016).
297. D. C. Martin *et al.*, *ApJL* **619**, L1–L6, arXiv: astro-ph/0411302 (astro-ph) (Jan. 2005).
298. R. Ahumada *et al.*, *ApJS* **249**, 3, arXiv: 1912.02905 (astro-ph.GA) (July 2020).
299. C. Saulder, E. van Kampen, I. V. Chilingarian, S. Mieske, W. W. Zeilinger, *A&A* **596**, A14, arXiv: 1511.05856 (astro-ph.CO) (Nov. 2016).
300. J. R. Mullaney, M. J. Ward, *MNRAS* **385**, 53–74, arXiv: 0711.4604 (astro-ph) (Mar. 2008).
301. J. R. Mullaney, M. J. Ward, C. Done, G. J. Ferland, N. Schurch, *MNRAS* **394**, L16–L20, arXiv: 0811.3204 (astro-ph) (Mar. 2009).
302. S. M. Viegas-Aldrovandi, M. Contini, *A&A* **215**, 253–261 (May 1989).

303. K. T. Korista, G. J. Ferland, ApJ **343**, 678 (Aug. 1989).
304. K. P. Dere, E. Landi, H. E. Mason, B. C. Monsignori Fossi, P. R. Young, A&AS **125**, 149–173 (Oct. 1997).
305. G. Del Zanna, K. P. Dere, P. R. Young, E. Landi, ApJ **909**, 38, arXiv: 2011.05211 (physics.atom-ph) (Mar. 2021).
306. B. T. Draine, *Physics of the Interstellar and Intergalactic Medium*.
307. J. E. Greene, L. C. Ho, ApJ **630**, 122–129, arXiv: astro-ph/0508335 (astro-ph) (Sept. 2005).
308. D. Ilić, L. Č. Popović, G. La Mura, S. Ciroi, P. Rafanelli, A&A **543**, A142, arXiv: 1205.3950 (astro-ph.CO) (July 2012).
309. A. Schnorr-Müller *et al.*, MNRAS **462**, 3570–3590, arXiv: 1607.07308 (astro-ph.GA) (Nov. 2016).
310. L. Hernández-García, J. Masegosa, O. González-Martín, I. Márquez, M. Guainazzi, F. Panessa, A&A **602**, A65, arXiv: 1703.05250 (astro-ph.GA) (June 2017).
311. E. C. Kool *et al.*, MNRAS **498**, 2167–2195, arXiv: 2006.01518 (astro-ph.HE) (Oct. 2020).
312. B. T. Draine, ApJ **732**, 100, arXiv: 1003.0474 (astro-ph.GA) (May 2011).
313. B. T. Draine, H. M. Lee, ApJ **285**, 89 (Oct. 1984).
314. S. van Velzen, A. J. Mendez, J. H. Krolik, V. Gorjian, ApJ **829**, 19, arXiv: 1605.04304 (astro-ph.HE) (Sept. 2016).
315. I. A. G. Snellen, R. T. Schilizzi, G. K. Miley, M. N. Bremer, H. J. A. Röttgering, H. J. van Langevelde, NewAR **43**, 675–679, arXiv: astro-ph/9811453 (astro-ph) (Nov. 1999).
316. C. -. Björnsson, ApJ **769**, 65, arXiv: 1303.4254 (astro-ph.HE) (May 2013).
317. C. -. Björnsson, S. T. Keshavarzi, ApJ **841**, 12, arXiv: 1704.05283 (astro-ph.HE) (May 2017).
318. P. Chandra, A. J. Nayana, C. -. Björnsson, F. Taddia, P. Lundqvist, A. K. Ray, B. J. Shappee, ApJ **877**, 79, arXiv: 1904.06392 (astro-ph.HE) (June 2019).
319. A. G. Pacholczyk, *Radio astrophysics. Nonthermal processes in galactic and extragalactic sources*.
320. W. Cash, ApJ **228**, 939–947 (Mar. 1979).
321. J. Wilms, A. Allen, R. McCray, ApJ **542**, 914–924, arXiv: astro-ph/0008425 (astro-ph) (Oct. 2000).

322. X. Mazzalay, A. Rodríguez-Ardila, S. Komossa, *MNRAS* **405**, 1315–1338, arXiv: 1002.3152 (astro-ph.GA) (June 2010).
323. E. Kankare *et al.*, *Nature Astronomy* **1**, 865–871, arXiv: 1711.04577 (astro-ph.HE) (Nov. 2017).
324. P. K. Blanchard, M. Nicholl, E. Berger, J. Guillochon, R. Margutti, R. Chornock, K. D. Alexander, J. Leja, M. R. Drout, *ApJ* **843**, 106, arXiv: 1703.07816 (astro-ph.HE) (July 2017).
325. N. Jiang, T. Wang, L. Yan, T. Xiao, C. Yang, L. Dou, H. Wang, R. Cutri, A. Mainzer, *ApJ* **850**, 63, arXiv: 1707.09087 (astro-ph.GA) (Nov. 2017).
326. Q. Yang, Y. Shen, X. Liu, X.-B. Wu, L. Jiang, J. Shangguan, M. J. Graham, S. Yao, *ApJ* **885**, 110, arXiv: 1907.12721 (astro-ph.GA) (Nov. 2019).
327. R. D. Saxton, S. E. Motta, S. Komossa, A. M. Read, *MNRAS* **454**, 2798–2803, arXiv: 1509.05193 (astro-ph.GA) (Dec. 2015).
328. N. Jiang, T. Wang, G. Mou, H. Liu, L. Dou, Z. Sheng, Y. Wang, *ApJ* **871**, 15, arXiv: 1812.01295 (astro-ph.GA) (Jan. 2019).
329. T. W. -. Holoien *et al.*, *MNRAS* **463**, 3813–3828, arXiv: 1602.01088 (astro-ph.HE) (Dec. 2016).
330. B. Trakhtenbrot *et al.*, *ApJ* **883**, 94, arXiv: 1903.11084 (astro-ph.GA) (Sept. 2019).
331. B. Trakhtenbrot *et al.*, *Nature Astronomy* **3**, 242–250, arXiv: 1901.03731 (astro-ph.GA) (Jan. 2019).
332. C. Tadhunter, R. Spence, M. Rose, J. Mullaney, P. Crowther, *Nature Astronomy* **1**, 0061, arXiv: 1702.02573 (astro-ph.GA) (Mar. 2017).
333. L. Dou, T. Wang, L. Yan, N. Jiang, C. Yang, R. M. Cutri, A. Mainzer, B. Peng, *ApJL* **841**, L8, arXiv: 1703.05773 (astro-ph.HE) (May 2017).
334. M. Gromadzki *et al.*, *A&A* **622**, L2, arXiv: 1901.03718 (astro-ph.HE) (Feb. 2019).
335. R. D. Saxton, A. M. Read, S. Komossa, P. Lira, K. D. Alexander, I. Steele, F. Ocaña, E. Berger, P. Blanchard, *A&A* **630**, A98, arXiv: 1908.01065 (astro-ph.HE) (Oct. 2019).
336. J. T. Hinkle *et al.*, *ApJ* **930**, 12, arXiv: 2108.03245 (astro-ph.HE) (May 2022).
337. D. Stern *et al.*, *ApJ* **864**, 27, arXiv: 1805.06920 (astro-ph.GA) (Sept. 2018).
338. G. Leloudas *et al.*, *Nature Astronomy* **1**, 0002, arXiv: 1609.02927 (astro-ph.HE) (Dec. 2016).

339. R. Margutti *et al.*, ApJ **836**, 25, arXiv: 1610.01632 (astro-ph.HE) (Feb. 2017).
340. D. Mudd *et al.*, ApJ **862**, 123, arXiv: 1711.11588 (astro-ph.GA) (Aug. 2018).
341. R. E. Mason, T. R. Geballe, C. Packham, N. A. Levenson, M. Elitzur, R. S. Fisher, E. Perlman, ApJ **640**, 612–624, arXiv: astro-ph/0512202 (astro-ph) (Apr. 2006).
342. C. Ramos Almeida, N. A. Levenson, J. M. Rodríguez Espinosa, A. Alonso-Herrero, A. Asensio Ramos, J. T. Radomski, C. Packham, R. S. Fisher, C. M. Telesco, ApJ **702**, 1127–1149, arXiv: 0906.5368 (astro-ph.CO) (Sept. 2009).
343. A. Dorodnitsyn, T. Kallman, ApJ **761**, 70, arXiv: 1211.6402 (astro-ph.CO) (Dec. 2012).
344. N. Smith, J. M. Silverman, R. Chornock, A. V. Filippenko, X. Wang, W. Li, M. Ganeshalingam, R. J. Foley, J. Rex, T. N. Steele, ApJ **695**, 1334–1350, arXiv: 0809.5079 (astro-ph) (Apr. 2009).
345. A. C. Fabian, R. Terlevich, MNRAS **280**, L5–L8 (May 1996).
346. G. Mou *et al.*, ApJ **908**, 197, arXiv: 2009.10420 (astro-ph.HE) (Feb. 2021).
347. G. Mou, W. Wang, MNRAS, arXiv: 2012.02997 (astro-ph.HE) (Aug. 2021).
348. J. Guillochon, E. Ramirez-Ruiz, ApJ **809**, 166, arXiv: 1501.05306 (astro-ph.HE) (Aug. 2015).
349. T. M. Heckman, A. Ptak, A. Hornschemeier, G. Kauffmann, ApJ **634**, 161–168, arXiv: astro-ph/0507674 (astro-ph) (Nov. 2005).
350. G. Miniutti *et al.*, Nature **573**, 381–384, arXiv: 1909.04693 (astro-ph.HE) (Sept. 2019).
351. R. Arcodia *et al.*, Nature **592**, 704–707, arXiv: 2104.13388 (astro-ph.HE) (Apr. 2021).
352. Z. Sheng, T. Wang, N. Jiang, C. Yang, L. Yan, L. Dou, B. Peng, ApJL **846**, L7, arXiv: 1707.02686 (astro-ph.GA) (Sept. 2017).
353. Z. Sheng, T. Wang, N. Jiang, J. Ding, Z. Cai, H. Guo, L. Sun, L. Dou, C. Yang, ApJ **889**, 46, arXiv: 1905.02904 (astro-ph.GA) (Jan. 2020).
354. M. L. Parker *et al.*, MNRAS **461**, 1927–1936, arXiv: 1606.04955 (astro-ph.HE) (Sept. 2016).
355. Q. Yang *et al.*, ApJ **862**, 109, arXiv: 1711.08122 (astro-ph.GA) (Aug. 2018).

356. J. M. Hameury, *Advances in Space Research* **66**, 1004–1024, arXiv: 1910.01852 (astro-ph.SR) (Sept. 2020).
357. J. Yang *et al.*, MNRAS **502**, L61–L65, arXiv: 2101.04629 (astro-ph.HE) (Mar. 2021).
358. O. M. Blaes, S. W. Davis, S. Hirose, J. H. Krolik, J. M. Stone, ApJ **645**, 1402–1407, arXiv: astro-ph/0601380 (astro-ph) (July 2006).
359. N. Mohan, D. Rafferty, *PyBDSF: Python Blob Detection and Source Finder*, Feb. 2015, ascl: 1502.007.
360. E. F. Schlafly, D. P. Finkbeiner, ApJ **737**, 103, arXiv: 1012.4804 (astro-ph.GA) (Aug. 2011).
361. E. L. Fitzpatrick, PASP **111**, 63–75, arXiv: astro-ph/9809387 (astro-ph) (Jan. 1999).
362. M. Cappellari, E. Emsellem, PASP **116**, 138–147, arXiv: astro-ph/0312201 (astro-ph) (Feb. 2004).
363. M. Cappellari, MNRAS **466**, 798–811, arXiv: 1607.08538 (astro-ph.GA) (Apr. 2017).
364. A. Vazdekis, P. Sánchez-Blázquez, J. Falcón-Barroso, A. J. Cenarro, M. A. Beasley, N. Cardiel, J. Gorgas, R. F. Peletier, MNRAS **404**, 1639–1671, arXiv: 1004.4439 (astro-ph.CO) (June 2010).
365. J. Skilling, presented at the Bayesian Inference and Maximum Entropy Methods in Science and Engineering: 24th International Workshop on Bayesian Inference and Maximum Entropy Methods in Science and Engineering, ed. by R. Fischer, R. Preuss, U. V. Toussaint, vol. 735, pp. 395–405.
366. T. Wevers, S. van Velzen, P. G. Jonker, N. C. Stone, T. Hung, F. Onori, S. Gezari, N. Blagorodnova, MNRAS **471**, 1694–1708, arXiv: 1706.08965 (astro-ph.GA) (Oct. 2017).
367. P. Prugniel, C. Soubiran, M. Koleva, D. Le Borgne, *VizieR Online Data Catalog*, III/251 (Apr. 2007).
368. P. Prugniel, C. Soubiran, A&A **369**, 1048–1057, arXiv: astro-ph/0101378 (astro-ph) (Apr. 2001).
369. L. Ferrarese, H. Ford, SSRv **116**, 523–624, arXiv: astro-ph/0411247 (astro-ph) (Feb. 2005).
370. T. Murphy *et al.*, PASA **30**, e006, arXiv: 1207.1528 (astro-ph.IM) (Feb. 2013).
371. C. R. Evans, C. S. Kochanek, ApJL **346**, L13 (Nov. 1989).
372. R. D. Saxton, A. M. Read, P. Esquej, S. Komossa, S. Dougherty, P. Rodríguez-Pascual, D. Barrado, A&A **541**, A106, arXiv: 1202.5900 (astro-ph.CO) (May 2012).

373. J. S. Bloom *et al.*, *Science* **333**, 203, arXiv: 1104.3257 (astro-ph.HE) (July 2011).
374. A. J. Goodwin *et al.*, *MNRAS* **522**, 5084–5097, arXiv: 2304.12661 (astro-ph.HE) (July 2023).
375. J. J. Somalwar *et al.*, *arXiv e-prints*, arXiv:2310.03782, arXiv: 2310.03782 (astro-ph.HE) (Oct. 2023).
376. M. M. Anderson *et al.*, *ApJ* **903**, 116, arXiv: 1910.11912 (astro-ph.HE) (Nov. 2020).
377. J. Somalwar, V. Ravi, *et al.* (in prep.).
378. Gaia Collaboration *et al.*, *arXiv e-prints*, arXiv:2208.00211, arXiv: 2208.00211 (astro-ph.GA) (July 2022).
379. Gaia Collaboration *et al.*, *A&A* **595**, A1, arXiv: 1609.04153 (astro-ph.IM) (Nov. 2016).
380. R. Beck, I. Szapudi, H. Flewelling, C. Holmberg, E. Magnier, K. C. Chambers, *MNRAS* **500**, 1633–1644, arXiv: 1910.10167 (astro-ph.GA) (Jan. 2021).
381. D. Stern *et al.*, *ApJ* **753**, 30, arXiv: 1205.0811 (astro-ph.CO) (July 2012).
382. T. H. Jarrett *et al.*, *ApJ* **735**, 112 (July 2011).
383. C. S. Kochanek *et al.*, *Publications of the Astronomical Society of the Pacific* **129**, 104502, ISSN: 1538-3873, (<https://iopscience.iop.org/article/10.1088/1538-3873/aa80d9%20https://iopscience.iop.org/article/10.1088/1538-3873/aa80d9/meta>) (Aug. 2017).
384. CASA Team *et al.*, *PASP* **134**, 114501, arXiv: 2210.02276 (astro-ph.IM) (Nov. 2022).
385. S. Yang *et al.*, *A&A* **655**, A90, arXiv: 2107.13439 (astro-ph.HE) (Nov. 2021).
386. T. Jayasinghe *et al.*, *MNRAS* **485**, 961–971, arXiv: 1901.00009 (astro-ph.SR) (May 2019).
387. B. J. Shappee *et al.*, *The Astrophysical Journal* **788**, 48, ISSN: 0004-637X, (<https://iopscience.iop.org/article/10.1088/0004-637X/788/1/48%20https://iopscience.iop.org/article/10.1088/0004-637X/788/1/48/meta>) (May 2014).
388. Abdurro'uf *et al.*, *ApJS* **259**, 35, arXiv: 2112.02026 (astro-ph.GA) (Apr. 2022).
389. J. T. Hinkle *et al.*, *Monthly Notices of the Royal Astronomical Society* **500**, 1673–1696, ISSN: 0035-8711, (<https://dx.doi.org/10.1093/mnras/staa3170>) (Dec. 2020).

390. M. Perez-Torres, J. Moldon, S. Mattila, A. Alberdi, R. Beswick, S. Ryder, E. Varenius, M. Fraser, E. Kankare, E. Kool, *The Astronomer's Telegram* **12870**, 1 (June 2019).
391. T. Eftekhari *et al.*, *ApJ* **974**, 149, arXiv: 2404.10036 (astro-ph.HE) (Oct. 2024).
392. E. A. Maxwell, *arXiv e-prints*, arXiv:1102.0822, arXiv: 1102.0822 (math.ST) (Feb. 2011).
393. D. C. Martin *et al.*, *ApJS* **173**, 342–356, arXiv: astro-ph/0703281 (astro-ph) (Dec. 2007).
394. I. Andreoni *et al.*, *Nature* **612**, 430–434, arXiv: 2211.16530 (astro-ph.HE) (Dec. 2022).
395. G. C. Brown, A. J. Levan, E. R. Stanway, N. R. Tanvir, S. B. Cenko, E. Berger, R. Chornock, A. Cucchiaria, *MNRAS* **452**, 4297–4306, arXiv: 1507.03582 (astro-ph.HE) (Oct. 2015).
396. D. N. Burrows *et al.*, *Nature* **476**, 421–424, arXiv: 1104.4787 (astro-ph.HE) (Aug. 2011).
397. D. R. Pasham *et al.*, *Nature Astronomy* **7**, 88–104, arXiv: 2211.16537 (astro-ph.HE) (Jan. 2023).
398. S. Wu, E. R. Coughlin, C. Nixon, *MNRAS* **478**, 3016–3024, arXiv: 1804.06410 (astro-ph.HE) (Aug. 2018).
399. B. Curd, R. Emami, R. Anantua, D. Palumbo, S. Doeleman, R. Narayan, *MNRAS* **519**, 2812–2837, arXiv: 2206.06358 (astro-ph.HE) (Feb. 2023).
400. A. Mummery, S. van Velzen, E. Nathan, A. Ingram, E. Hammerstein, L. Fraser-Taliente, S. Balbus, *MNRAS* **527**, 2452–2489, arXiv: 2308.08255 (astro-ph.HE) (Jan. 2024).
401. S. van Velzen, D. R. Pasham, S. Komossa, L. Yan, E. A. Kara, *SSRv* **217**, 63, arXiv: 2107.12268 (astro-ph.HE) (Aug. 2021).
402. A. W. Hotan *et al.*, *PASA* **38**, e009, arXiv: 2102.01870 (astro-ph.IM) (Mar. 2021).
403. E. J. Murphy *et al.*, presented at the Science with a Next Generation Very Large Array, ed. by E. Murphy, vol. 517, p. 3, arXiv: 1810.07524 (astro-ph.IM).
404. G. Hallinan *et al.*, presented at the Bulletin of the American Astronomical Society, vol. 51, 255, p. 255, arXiv: 1907.07648 (astro-ph.IM).
405. C. L. Hale *et al.*, *PASA* **38**, e058, arXiv: 2109.00956 (astro-ph.GA) (Nov. 2021).
406. A. Mainzer *et al.*, *ApJ* **792**, 30, arXiv: 1406.6025 (astro-ph.EP) (Sept. 2014).

407. R. Sunyaev *et al.*, *arXiv e-prints*, arXiv:2104.13267, arXiv: 2104 . 13267 (astro-ph.HE) (Apr. 2021).
408. I. Sfaradi *et al.*, MNRAS **527**, 7672–7680, arXiv: 2308 . 01965 (astro-ph.HE) (Jan. 2024).
409. P. Charalampopoulos *et al.*, A&A **659**, A34, arXiv: 2109 . 00016 (astro-ph.HE) (Mar. 2022).
410. T. Hung *et al.*, ApJ **903**, 31, arXiv: 2003 . 09427 (astro-ph.HE) (Nov. 2020).
411. P. Clark *et al.*, MNRAS **528**, 7076–7102, arXiv: 2307 . 03182 (astro-ph.HE) (Mar. 2024).
412. J. T. Hinkle, B. J. Shappee, T. W. -. Holoiien, MNRAS **528**, 4775–4784, arXiv: 2303 . 05525 (astro-ph.HE) (Mar. 2024).
413. J. J. Somalwar *et al.*, *arXiv*, arXiv:2310.03791, (<https://ui.adsabs.harvard.edu/abs/2023arXiv231003791S/abstract>) (2023).
414. Planck Collaboration *et al.*, A&A **594**, A13, arXiv: 1502 . 01589 (astro-ph.CO) (Sept. 2016).
415. P. Charalampopoulos, G. Leloudas, M. Pursiainen, R. Kotak, *Transient Name Server AstroNote* **115**, 1 (May 2023).
416. D. E. Osterbrock, G. J. Ferland, *agna*, (<https://ui.adsabs.harvard.edu/abs/2006agna.book.....0/abstract>) (2006).
417. G. Leloudas *et al.*, ApJ **887**, 218, arXiv: 1903 . 03120 (astro-ph.HE) (Dec. 2019).
418. K. Heng, PASA **27**, 23–44, arXiv: 0908 . 4080 (astro-ph.GA) (Mar. 2010).
419. C. Bilinski *et al.*, MNRAS **475**, 1104–1120, arXiv: 1712 . 03370 (astro-ph.SR) (Mar. 2018).
420. J. Japelj, S. D. Vergani, R. Salvaterra, M. Renzo, E. Zapartas, S. E. de Mink, L. Kaper, S. Zibetti, A&A **617**, A105, arXiv: 1806 . 10613 (astro-ph.HE) (Sept. 2018).
421. F. Taddia *et al.*, A&A **621**, A71, arXiv: 1811 . 09544 (astro-ph.HE) (Jan. 2019).
422. Y. Wang, G. J. Ferland, M. L. Lykins, R. L. Porter, P. A. M. van Hoof, R. J. R. Williams, MNRAS **440**, 3100–3112, arXiv: 1403 . 3076 (astro-ph.IM) (June 2014).
423. M. G. Allen, B. A. Groves, M. A. Dopita, R. S. Sutherland, L. J. Kewley, ApJS **178**, 20–55, arXiv: 0805 . 0204 (astro-ph) (Sept. 2008).
424. A. Franchini, G. Lodato, S. Facchini, MNRAS **455**, 1946–1956, arXiv: 1510 . 04879 (astro-ph.HE) (Jan. 2016).

425. S. van Velzen, G. R. Farrar, *ApJ* **792**, 53, arXiv: 1407.6425 (astro-ph.GA) (Sept. 2014).
426. N. C. Stone, E. Vasiliev, M. Kesden, E. M. Rossi, H. B. Perets, P. Amaro-Seoane, *SSRv* **216**, 35, arXiv: 2003.08953 (astro-ph.HE) (Mar. 2020).
427. J. Guillochon, E. Ramirez-Ruiz, *ApJ* **767**, 25, arXiv: 1206.2350 (astro-ph.HE) (Apr. 2013).
428. E. R. Coughlin, C. J. Nixon, *ApJL* **883**, L17, arXiv: 1907.03034 (astro-ph.GA) (Sept. 2019).
429. E. Bortolas, T. Ryu, L. Broggi, A. Sesana, *MNRAS* **524**, 3026–3038, arXiv: 2303.03408 (astro-ph.HE) (Sept. 2023).
430. A. V. Payne *et al.*, *ApJ* **910**, 125, arXiv: 2009.03321 (astro-ph.HE) (Apr. 2021).
431. Z. Liu *et al.*, *A&A* **669**, A75, arXiv: 2208.12452 (astro-ph.HE) (Jan. 2023).
432. T. Wevers *et al.*, *MNRAS* **488**, 4816–4830, arXiv: 1903.12203 (astro-ph.HE) (Oct. 2019).
433. J. Hampel, S. Komossa, J. Greiner, T. H. Reiprich, M. Freyberg, T. Erben, *Research in Astronomy and Astrophysics* **22**, 055004, arXiv: 2202.11187 (astro-ph.HE) (May 2022).
434. A. Malyali *et al.*, *MNRAS* **520**, 3549–3559, arXiv: 2301.05501 (astro-ph.HE) (Apr. 2023).
435. Z. Lin *et al.*, *ApJL* **971**, L26, arXiv: 2405.10895 (astro-ph.HE) (Aug. 2024).
436. J. T. Hinkle *et al.*, *arXiv e-prints*, arXiv:2412.15326, arXiv: 2412.15326 (astro-ph.HE) (Dec. 2024).
437. P. A. Evans *et al.*, *Nature Astronomy* **7**, 1368–1375, arXiv: 2309.02500 (astro-ph.HE) (Nov. 2023).
438. M. Guolo *et al.*, *Nature Astronomy* **8**, 347–358, arXiv: 2309.03011 (astro-ph.HE) (Mar. 2024).
439. D.-W. Bao *et al.*, *ApJ* **977**, 279, arXiv: 2311.16726 (astro-ph.HE) (Dec. 2024).
440. J. Sun *et al.*, *arXiv e-prints*, arXiv:2501.01824, arXiv: 2501.01824 (astro-ph.HE) (Jan. 2025).
441. T. Alexander, *ARA&A* **55**, 17–57, arXiv: 1701.04762 (astro-ph.GA) (Aug. 2017).
442. W. Lu, E. Quataert, *MNRAS* **524**, 6247–6266, arXiv: 2210.08023 (astro-ph.HE) (Oct. 2023).

443. J. Nordin *et al.*, *A&A* **631**, A147, arXiv: 1904.05922 (astro-ph.IM) (Nov. 2019).
444. T. W. -. Holoiien *et al.*, *MNRAS* **445**, 3263–3277, arXiv: 1405.1417 (astro-ph.GA) (Dec. 2014).
445. P. Charalampopoulos, M. Pursiainen, G. Leloudas, I. Arcavi, M. Newsome, S. Schulze, J. Burke, M. Nicholl, *A&A* **673**, A95, arXiv: 2209.12913 (astro-ph.HE) (May 2023).
446. M. Nicholl *et al.*, *MNRAS* **499**, 482–504, arXiv: 2006.02454 (astro-ph.HE) (Nov. 2020).
447. N. Blagorodnova *et al.*, *ApJ* **844**, 46, arXiv: 1703.00965 (astro-ph.HE) (July 2017).
448. N. Blagorodnova *et al.*, *ApJ* **873**, 92, arXiv: 1809.07446 (astro-ph.HE) (Mar. 2019).
449. P. Short *et al.*, *MNRAS* **498**, 4119–4133, arXiv: 2003.05470 (astro-ph.GA) (Nov. 2020).
450. A. V. Payne *et al.*, *ApJ* **951**, 134, arXiv: 2206.11278 (astro-ph.HE) (July 2023).
451. J. S. Brown *et al.*, *MNRAS* **473**, 1130–1144, arXiv: 1704.02321 (astro-ph.HE) (Jan. 2018).
452. S. B. Cenko *et al.*, *ApJL* **818**, L32, arXiv: 1601.03331 (astro-ph.HE) (Feb. 2016).
453. T. Hung *et al.*, *ApJ* **879**, 119, arXiv: 1903.05637 (astro-ph.HE) (July 2019).
454. T. Hung *et al.*, *ApJ* **917**, 9, arXiv: 2011.01593 (astro-ph.HE) (Aug. 2021).
455. C. Gabriel, M. Denby, D. J. Fyfe, J. Hoar, A. Ibarra, E. Ojero, J. Osborne, R. D. Saxton, U. Lammers, G. Vacanti, presented at the Astronomical Data Analysis Software and Systems (ADASS) XIII, ed. by F. Ochsenbein, M. G. Allen, D. Egret, vol. 314, p. 759.
456. K. A. Arnaud, presented at the Astronomical Data Analysis Software and Systems V, ed. by G. H. Jacoby, J. Barnes, vol. 101, p. 17.
457. J. F. Steiner, R. Narayan, J. E. McClintock, K. Ebisawa, *PASP* **121**, 1279, arXiv: 0810.1758 (astro-ph) (Nov. 2009).
458. L. L. Thomsen, T. Kwan, L. Dai, S. Wu, E. Ramirez-Ruiz, *arXiv e-prints*, arXiv:2206.02804, arXiv: 2206.02804 (astro-ph.HE) (June 2022).
459. R. J. Assef *et al.*, *ApJ* **772**, 26, arXiv: 1209.6055 (astro-ph.CO) (July 2013).

460. F. K. Liu, S. Li, X. Chen, *ApJL* **706**, L133–L137, arXiv: 0910.4152 (astro-ph.HE) (Nov. 2009).
461. A. Ricarte, P. Natarajan, L. Dai, P. Coppi, *MNRAS* **458**, 1712–1727, arXiv: 1510.04693 (astro-ph.HE) (May 2016).
462. S. Gomez *et al.*, *MNRAS* **497**, 1925–1934, arXiv: 2003.05469 (astro-ph.HE) (Sept. 2020).
463. C. R. Angus *et al.*, *Nature Astronomy* **6**, 1452–1463, arXiv: 2209.00018 (astro-ph.HE) (Dec. 2022).
464. A. V. Payne *et al.*, *ApJ* **926**, 142, arXiv: 2104.06414 (astro-ph.HE) (Feb. 2022).
465. Z. Liu *et al.*, *A&A* **683**, L13, arXiv: 2401.14091 (astro-ph.HE) (Mar. 2024).
466. L. Sun *et al.*, *A&A* **692**, A262, arXiv: 2410.09720 (astro-ph.HE) (Dec. 2024).
467. C. Ricci *et al.*, *ApJL* **898**, L1, arXiv: 2007.07275 (astro-ph.HE) (July 2020).
468. M. Cufari, E. R. Coughlin, C. J. Nixon, *ApJL* **929**, L20, arXiv: 2203.08162 (astro-ph.HE) (Apr. 2022).
469. G. Lodato, A. R. King, J. E. Pringle, *MNRAS* **392**, 332–340, arXiv: 0810.1288 (astro-ph) (Jan. 2009).
470. C.-H. Chan, T. Piran, J. H. Krolik, D. Saban, *ApJ* **881**, 113, arXiv: 1904.12261 (astro-ph.HE) (Aug. 2019).
471. W. Lu, P. Kumar, *ApJ* **865**, 128, arXiv: 1802.02151 (astro-ph.HE) (Oct. 2018).
472. A. Mummery, *arXiv e-prints*, arXiv:2104.06212, arXiv: 2104.06212 (astro-ph.HE) (Apr. 2021).
473. A. Mummery, T. Wevers, R. Saxton, D. Pasham, *MNRAS* **519**, 5828–5847, arXiv: 2301.07419 (astro-ph.HE) (Mar. 2023).
474. L. Dai, J. C. McKinney, N. Roth, E. Ramirez-Ruiz, M. C. Miller, *ApJL* **859**, L20, arXiv: 1803.03265 (astro-ph.HE) (June 2018).
475. B. Curd, R. Narayan, *MNRAS* **483**, 565–592, arXiv: 1811.06971 (astro-ph.HE) (Feb. 2019).
476. A. Munoz-Arancibia, L. Hernandez-Garcia, F. E. Bauer, A. M. Mourão, P. Lira, M. Catelan, F. Forster, *Transient Name Server AstroNote* **138**, 1 (May 2023).
477. B. P. Abbott *et al.*, *The Astrophysical Journal Letters* **882**, L24, ISSN: 2041-8205, (<https://ui.adsabs.harvard.edu/abs/2019ApJ...882L..24A/abstract>) (Sept. 2019).

478. P. Natarajan, *MNRAS* **501**, 1413–1425, arXiv: 2009.09156 (astro-ph.GA) (Feb. 2021).
479. W. B. Hoogendam *et al.*, *Monthly Notices of the Royal Astronomical Society* **530**, 4501–4518, (<http://arxiv.org/abs/2401.05490>) (<http://dx.doi.org/10.1093/mnras/stae1121>) (Jan. 2024).
480. T. W.-S. Holoién *et al.*, *The Astrophysical Journal* **898**, 161, ISSN: 0004-637X, (<https://ui.adsabs.harvard.edu/abs/2020ApJ...898.161H/abstract>) (Aug. 2020).
481. T. W.-S. Holoién *et al.*, *The Astrophysical Journal* **883**, 111, ISSN: 0004-637X, (<https://ui.adsabs.harvard.edu/abs/2019ApJ...883.111H/abstract>) (Oct. 2019).
482. J. T. Hinkle *et al.*, *Monthly Notices of the Royal Astronomical Society* **519**, 2035–2045, ISSN: 13652966, (<https://ui.adsabs.harvard.edu/abs/2023MNRAS.519.2035H/abstract>) (Feb. 2023).
483. Y. Yao *et al.*, *ApJ* **976**, 34, ISSN: 0004-637X, (<https://ui.adsabs.harvard.edu/abs/2024ApJ...976...34Y/abstract>) (Nov. 2024).
484. Y. Yao *et al.*, *arXiv*, arXiv:2502.17661, (<https://ui.adsabs.harvard.edu/abs/2025arXiv250217661Y/abstract>) (Feb. 2025).
485. B. D. Metzger, *ApJ* **932**, 84, arXiv: 2203.04331 (astro-ph.HE) (June 2022).
486. S. J. Prentice *et al.*, *ApJL* **865**, L3, arXiv: 1807.05965 (astro-ph.HE) (Sept. 2018).
487. D. L. Coppejans *et al.*, *ApJL* **895**, L23, arXiv: 2003.10503 (astro-ph.HE) (May 2020).
488. C. P. Gutiérrez *et al.*, *arXiv e-prints*, arXiv:2408.04698, arXiv: 2408.04698 (astro-ph.HE) (Aug. 2024).
489. D. A. Perley *et al.*, *MNRAS* **484**, 1031–1049, arXiv: 1808.00969 (astro-ph.HE) (Mar. 2019).
490. A. Y. Q. Ho *et al.*, *ApJ* **949**, 120, arXiv: 2105.08811 (astro-ph.HE) (June 2023).
491. A. Y. Q. Ho *et al.*, *ApJ* **895**, 49, arXiv: 2003.01222 (astro-ph.HE) (May 2020).
492. A. A. Chrimes *et al.*, *MNRAS* **527**, L47–L53, arXiv: 2307.01771 (astro-ph.HE) (Jan. 2024).
493. J. S. Bright *et al.*, *ApJ* **926**, 112, arXiv: 2110.05514 (astro-ph.HE) (Feb. 2022).

494. A. Y. Q. Ho, B. Margalit, M. Bremer, D. A. Perley, Y. Yao, D. Dobie, D. L. Kaplan, A. O'Brien, G. Petitpas, A. Zic, *ApJ* **932**, 116, arXiv: 2110.05490 (astro-ph.HE) (June 2022).
495. A. A. Chrimes, D. L. Coppejans, P. G. Jonker, A. J. Levan, P. J. Groot, A. Mummery, E. R. Stanway, *A&A* **691**, A329, arXiv: 2406.13821 (astro-ph.HE) (Nov. 2024).
496. A. Inkenhaag, P. G. Jonker, A. J. Levan, A. A. Chrimes, A. Mummery, D. A. Perley, N. R. Tanvir, *MNRAS* **525**, 4042–4056, arXiv: 2308.07381 (astro-ph.HE) (Nov. 2023).
497. G. Migliori *et al.*, *ApJL* **963**, L24 (Mar. 2024).
498. L. Li, S.-Q. Zhong, D. Xiao, Z.-G. Dai, S.-F. Huang, Z.-F. Sheng, *ApJL* **963**, L13, arXiv: 2402.15067 (astro-ph.HE) (Mar. 2024).
499. D. Tsuna, W. Lu, *arXiv e-prints*, arXiv:2501.03316, arXiv: 2501.03316 (astro-ph.HE) (Jan. 2025).
500. D. R. Pasham *et al.*, *Nature Astronomy* **6**, 249–258, ISSN: 23973366, (<https://ui.adsabs.harvard.edu/abs/2022NatAs...6..249P/abstract>) (Feb. 2022).
501. D. J. Schlegel, D. P. Finkbeiner, M. Davis, *ApJ* **500**, 525–553, ISSN: 0004-637X, arXiv: 9710327 (astro-ph), (<https://ui.adsabs.harvard.edu/abs/1998ApJ...500..525S/abstract>) (June 1998).
502. M. Pursiainen *et al.*, *arXiv e-prints*, arXiv:2411.03272, arXiv: 2411.03272 (astro-ph.HE) (Nov. 2024).
503. S. J. v. d. Walt, A. Crellin-Quick, J. S. Bloom, *Journal of Open Source Software* **4**, 1247, ISSN: 2475-9066, (<https://joss.theoj.org/papers/10.21105/joss.01247>) (May 2019).
504. M. W. Coughlin *et al.*, *The Astrophysical Journal Supplement Series* **267**, 31, ISSN: 0067-0049, (<https://iopscience.iop.org/article/10.3847/1538-4365/acdee1>), (<https://iopscience.iop.org/article/10.3847/1538-4365/acdee1/meta>) (July 2023).
505. N. Blagorodnova *et al.*, *Publications of the Astronomical Society of the Pacific* **130**, 035003, ISSN: 00046280, (<https://ui.adsabs.harvard.edu/abs/2018PASP...130c5003B/abstract>) (Mar. 2018).
506. M. Rigault *et al.*, *Astronomy and Astrophysics* **627**, A115, ISSN: 14320746, (<https://ui.adsabs.harvard.edu/abs/2019A&A...627A.115R/abstract>) (July 2019).
507. J. Sollerman, C. Fremling, D. Perley, T. D. Laz, *TNSTR* **2024-2511**, 1, (<https://ui.adsabs.harvard.edu/abs/2024TNSTR2511...1S/abstract>) (2024).

508. K. De *et al.*, *PASP* **132**, 025001, ISSN: 0004-6280, (<https://ui.adsabs.harvard.edu/abs/2020PASP...132b5001D/abstract>) (2020).
509. R. M. Cutri *et al.*, *tmc*, (<https://ui.adsabs.harvard.edu/abs/2003tmc...book.....C/abstract>) (2003).
510. N. Gehrels *et al.*, *ApJ* **611**, 1005–1020, ISSN: 0004-637X, arXiv: 0405233 (astro-ph), (<https://ui.adsabs.harvard.edu/abs/2004ApJ...611.1005G/abstract>) (2004).
511. F. A. Harrison *et al.*, *ApJ* **770**, 103, arXiv: 1301.7307 (astro-ph.IM) (June 2013).
512. R. P. Kraft, D. N. Burrows, J. A. Nousek, *ApJ* **374**, 344 (June 1991).
513. M. Nicholl *et al.*, *The Astrophysical Journal Letters* **954**, L28, ISSN: 2041-8205, (<https://ui.adsabs.harvard.edu/abs/2023ApJ...954L..28N/abstract>) (Sept. 2023).
514. F. D. Albareti *et al.*, *ApJS* **233**, 25, arXiv: 1608.02013 (astro-ph.GA) (Dec. 2017).
515. K. Barbary, *Journal of Open Source Software* **1**, 58, ISSN: 2475-9066, (<https://joss.theoj.org/papers/10.21105/joss.00058>) (Oct. 2016).
516. E. Bertin, S. Arnouts, E. Bertin, S. Arnouts, *A&AS* **117**, 393–404, ISSN: 0365-0138, (<https://ui.adsabs.harvard.edu/abs/1996A&AS...117..393B/abstract>) (1996).
517. C. C. Steidel, W. L. W. Sargent, *ApJS* **80**, 1, ISSN: 0067-0049, (<https://ui.adsabs.harvard.edu/abs/1992ApJS...80....1S/abstract>) (May 1992).
518. H. Zou, J. Gao, X. Xu, X. Zhou, J. Ma, Z. Zhou, T. Zhang, J. Nie, J. Wang, S. Xue, *The Astrophysical Journal Supplement Series* **253**, 56, ISSN: 0067-0049, (<https://ui.adsabs.harvard.edu/abs/2021ApJS...253...56Z/abstract>) (Apr. 2021).
519. Z. L. Wen, J. L. Han, *The Astrophysical Journal Supplement Series* **272**, 39, ISSN: 0067-0049, (<https://ui.adsabs.harvard.edu/abs/2024ApJS...272...39W/abstract>) (June 2024).
520. A. Anand, G. Kauffmann, D. Nelson, *Monthly Notices of the Royal Astronomical Society* **513**, 3210–3227, ISSN: 13652966, (<https://ui.adsabs.harvard.edu/abs/2022MNRAS.513.3210A/abstract>) (July 2022).
521. Y.-H. Huang, H.-W. Chen, S. A. Sheckman, S. D. Johnson, F. S. Zahedy, J. E. Helsby, J.-R. Gauthier, I. B. Thompson, *MNRAS* **502**, 4743–4761, arXiv: 2009.12372 (astro-ph.GA) (Apr. 2021).
522. A. Peres, *Physical Review*, vol. 128, Issue 5, pp. 2471-2475 **128**, 2471, ISSN: 1536-6065, (<https://ui.adsabs.harvard.edu/abs/1962PhRv...128.2471P/abstract>) (Dec. 1962).

523. J. D. Bekenstein, *Astrophysical Journal*, Vol. 183, pp. 657-664 (1973) **183**, 657, ISSN: 0004-637X, ([https://ui.adsabs.harvard.edu/search/q=doi%3A%2210.1086%2F152255%22&sort=date%20desc%2C%20bibcode%20desc&p\\_=0](https://ui.adsabs.harvard.edu/search/q=doi%3A%2210.1086%2F152255%22&sort=date%20desc%2C%20bibcode%20desc&p_=0)) (July 1973).
524. J. Leja, B. D. Johnson, C. Conroy, P. G. v. Dokkum, N. Byler, *The Astrophysical Journal* **837**, 170, ISSN: 0004-637X, (<https://ui.adsabs.harvard.edu/abs/2017ApJ...837..170L/abstract>) (Mar. 2017).
525. C. Conroy, J. E. Gunn, C. Conroy, J. E. Gunn, *ascl*, ascl:1010.043, (<https://ui.adsabs.harvard.edu/abs/2010ascl.soft10043C/abstract>) (2010).
526. J. Skilling, <https://doi.org/10.1214/06-BA127> **1**, 833–859, ISSN: 1936-0975, (<https://projecteuclid.org/journals/bayesian-analysis/volume-1/issue-4/Nested-sampling-for-general-Bayesian-computation/10.1214/06-BA127.full%20https://projecteuclid.org/journals/bayesian-analysis/volume-1/issue-4/Nested-sampling-for-general-Bayesian-computation/10.1214/06-BA127.short>) (Dec. 2006).
527. E. N. Kirby, J. G. Cohen, P. Guhathakurta, L. Cheng, J. S. Bullock, A. Gallazzi, *The Astrophysical Journal* **779**, 102 (2013).
528. D. A. Perley *et al.*, *MNRAS* **508**, 5138–5147, arXiv: 2103.01968 (astro-ph.HE) (Dec. 2021).
529. Y. Yao *et al.*, *ApJ* **934**, 104, arXiv: 2112.00751 (astro-ph.HE) (Aug. 2022).
530. S. Schulze *et al.*, *The Astrophysical Journal Supplement Series* **255**, 29, ISSN: 0067-0049, (<https://iopscience.iop.org/article/10.3847/1538-4365/abff5e%20https://iopscience.iop.org/article/10.3847/1538-4365/abff5e/meta>) (Aug. 2021).
531. J. Leja, J. S. Speagle, Y.-S. Ting, B. D. Johnson, C. Conroy, K. E. Whitaker, E. J. Nelson, P. van Dokkum, M. Franx, *ApJ* **936**, 165, arXiv: 2110.04314 (astro-ph.GA) (Sept. 2022).
532. Y. Chen, M. R. Drout, A. L. Piro, C. D. Kilpatrick, R. J. Foley, C. Rojas-Bravo, K. Taggart, M. R. Siebert, M. R. Magee, *ApJ* **955**, 42, arXiv: 2303.03500 (astro-ph.HE) (Sept. 2023).
533. B. D. Metzger, D. A. Perley, *ApJ* **944**, 74, arXiv: 2210.01819 (astro-ph.HE) (Feb. 2023).
534. D. A. Verner, G. J. Ferland, K. T. Korista, D. G. Yakovlev, *ApJ* **465**, 487, arXiv: astro-ph/9601009 (astro-ph) (July 1996).
535. C. Fransson, P. Lundqvist, R. A. Chevalier, *ApJ* **461**, 993, ISSN: 0004-637X, (<https://ui.adsabs.harvard.edu/abs/1996ApJ...461..993F/abstract>) (Apr. 1996).

536. G. B. Rybicki, A. P. Lightman, *Radiative processes in astrophysics*.
537. E. Takeo, K. Inayoshi, K. Ohsuga, H. R. Takahashi, S. Mineshige (2019).
538. J. C. McKinney, L. Dai, M. J. Avara, MNRAS **454**, L6–L10, arXiv: 1508.02433 (astro-ph.HE) (Nov. 2015).
539. Y.-F. Jiang, L. Dai, *arXiv e-prints*, arXiv:2408.16856, arXiv: 2408.16856 (astro-ph.HE) (Aug. 2024).
540. Y. F. Jiang, J. M. Stone, S. W. Davis, *Astrophysical Journal* **796**, 106, ISSN: 15384357, (<https://ui.adsabs.harvard.edu/abs/2014ApJ...796..106J/abstract>) (Dec. 2014).
541. W. D. Arnett, Arnett, W. D., *ApJ* **253**, 785–797, ISSN: 0004-637X, (<https://ui.adsabs.harvard.edu/abs/1982ApJ...253..785A/abstract>) (Feb. 1982).
542. Nadyozhin, D. K., *ApJS* **92**, 527, ISSN: 0067-0049, (<https://ui.adsabs.harvard.edu/abs/1994ApJS...92..527N/abstract>) (June 1994).
543. J. Guillochon, M. Nicholl, V. A. Villar, B. Mockler, G. Narayan, K. S. Mandel, E. Berger, P. K. G. Williams, *The Astrophysical Journal Supplement Series* **236**, 6, ISSN: 0067-0049, (<https://ui.adsabs.harvard.edu/abs/2018ApJS..236....6G/abstract>) (May 2018).
544. A. King, J. P. Lasota, M. Middleton, *New Astronomy Reviews* **96**, 101672, ISSN: 13876473, (<https://ui.adsabs.harvard.edu/abs/2023NewAR..9601672K/abstract>) (June 2023).
545. D. K. Khatami, D. N. Kasen, *The Astrophysical Journal* **972**, 140, ISSN: 0004-637X, (<https://ui.adsabs.harvard.edu/abs/2024ApJ...972..140K/abstract>) (Sept. 2024).
546. E. Karamehmetoglu *et al.*, *Astronomy & Astrophysics* **602**, A93, ISSN: 0004-6361, ([https://www.aanda.org/articles/aa/full\\_html/2017/06/aa29619-16/aa29619-16.html](https://www.aanda.org/articles/aa/full_html/2017/06/aa29619-16/aa29619-16.html)) (<https://www.aanda.org/articles/aa/abs/2017/06/aa29619-16/aa29619-16.html>) (June 2017).
547. E. Nakar, A. L. Piro, *Astrophysical Journal* **788**, 193, ISSN: 15384357, (<https://ui.adsabs.harvard.edu/abs/2014ApJ...788..193N/abstract>) (June 2014).
548. S. Tuna, B. D. Metzger, Y.-F. Jiang, C. J. White, S. Tuna, B. D. Metzger, Y.-F. Jiang, C. J. White, *arXiv*, arXiv:2501.13157, (<https://ui.adsabs.harvard.edu/abs/2025arXiv250113157T/abstract>) (Jan. 2025).
549. B. T. Draine, A. Li, *The Astrophysical Journal* **657**, 810–837, ISSN: 0004-637X, (<https://ui.adsabs.harvard.edu/abs/2007ApJ...657..810D/abstract>) (Mar. 2007).

550. C. Chen, R.-F. Shen, C. Chen, R.-F. Shen, *arXiv*, arXiv:2411.18985, (<https://ui.adsabs.harvard.edu/abs/2024arXiv241118985C/abstract>) (2024).
551. L. E. Sandoval, T. J. Maccarone, A. Corsi, P. J. Brown, D. Pooley, J. C. Wheeler, *Monthly Notices of the Royal Astronomical Society: Letters* **480**, L146–L150, ISSN: 1745-3925, (<https://dx.doi.org/10.1093/mnrasl/sly145>) (Oct. 2018).
552. J. G. Hills, *Nature* **254**, 295–298 (Mar. 1975).
553. V. V. Lidskii, L. M. Ozernoi, *Pisma v Astronomicheskii Zhurnal* **5**, 28–33 (Feb. 1979).
554. A. Ulmer, *ApJ* **514**, 180–187 (Mar. 1999).
555. D. Matthews *et al.*, *Research Notes of the American Astronomical Society* **7**, 126, arXiv: 2306.01114 (astro-ph.HE) (June 2023).
556. C. S. Reynolds, Reynolds, C. S., *ASPC* **161**, 178, ISSN: 1050-3390, arXiv: 9810018 (astro-ph), (<https://ui.adsabs.harvard.edu/abs/1999ASPC..161..178R/abstract>) (1999).
557. Y. Chen, M. R. Drout, A. L. Piro, C. D. Kilpatrick, R. J. Foley, C. Rojas-Bravo, M. R. Magee, *ApJ* **955**, 43, arXiv: 2303.03501 (astro-ph.HE) (Sept. 2023).
558. N. C. Sun, J. R. Maund, P. A. Crowther, L. D. Liu, *Monthly Notices of the Royal Astronomical Society: Letters* **512**, L66–L70, ISSN: 17453933, (<https://ui.adsabs.harvard.edu/abs/2022MNRAS.512L..66S/abstract>) (May 2022).
559. N. Earl *et al.*, *ApJ* **983**, 28, arXiv: 2412.12991 (astro-ph.HE) (Apr. 2025).
560. Y. Yao *et al.*, *The Astrophysical Journal* **937**, 8, ISSN: 0004-637X, (<https://iopscience.iop.org/article/10.3847/1538-4357/ac898a%20https://iopscience.iop.org/article/10.3847/1538-4357/ac898a/meta>) (Sept. 2022).
561. A. Y. Q. Ho *et al.*, *arXiv*, arXiv:2502.07885, (<https://ui.adsabs.harvard.edu/abs/2025arXiv250207885H/abstract>) (Feb. 2025).
562. D. A. Perley *et al.*, *ApJ* **904**, 35, arXiv: 2009.01242 (astro-ph.HE) (Nov. 2020).
563. C. Fremling *et al.*, *The Astrophysical Journal* **895**, 32, ISSN: 0004-637X, (<https://ui.adsabs.harvard.edu/abs/2020ApJ...895...32F/abstract>) (May 2020).
564. O. D. Elbert, J. S. Bullock, M. Kaplinghat, *Monthly Notices of the Royal Astronomical Society* **473**, 1186–1194, ISSN: 0035-8711, (<https://dx.doi.org/10.1093/mnras/stx1959>) (Jan. 2018).

565. A. Sicilia, A. Lapi, L. Boco, M. Spera, U. N. D. Carlo, M. Mapelli, F. Shankar, D. M. Alexander, A. Bressan, L. Danese, (<https://doi.org/10.3847/1538-4357/ac34fb>) (2022).
566. A. E. Reines, M. Volonteri, *ApJ* **813**, 82, arXiv: 1508.06274 (astro-ph.GA) (Nov. 2015).
567. S. Repetto, M. B. Davies, S. Sigurdsson, *Monthly Notices of the Royal Astronomical Society* **425**, 2799–2809, ISSN: 13652966, (<https://ui.adsabs.harvard.edu/abs/2012MNRAS.425.2799R/abstract>) (Oct. 2012).
568. A. Ricarte, M. Tremmel, P. Natarajan, T. Quinn, *ApJL* **916**, L18, arXiv: 2107.02132 (astro-ph.GA) (Aug. 2021).
569. J. A. González, M. Hannam, U. Sperhake, B. Brügmann, S. Husa, *Physical Review Letters* **98**, 231101, ISSN: 00319007, (<https://ui.adsabs.harvard.edu/abs/2007PhRvL..98w1101G/abstract>) (June 2007).
570. V. Rodríguez-Gomez *et al.*, *Monthly Notices of the Royal Astronomical Society* **449**, 49–64, ISSN: 0035-8711, (<https://dx.doi.org/10.1093/mnras/stv264>) (May 2015).
571. K. Maguire, M. Eracleous, P. G. Jonker, M. MacLeod, S. Rosswog, *SSRv* **216**, 39, arXiv: 2004.00146 (astro-ph.HE) (Mar. 2020).
572. L. Dai, J. C. McKinney, M. C. Miller, *ApJL* **812**, L39, arXiv: 1507.04333 (astro-ph.HE) (Oct. 2015).
573. K. Kremer, W. Lu, A. L. Piro, S. Chatterjee, F. A. Rasio, C. S. Ye, *ApJ* **911**, 104, arXiv: 2012.02796 (astro-ph.HE) (Apr. 2021).
574. S. C. Wu, J. Fuller, *ApJL* **940**, L27, arXiv: 2210.10187 (astro-ph.HE) (Nov. 2022).
575. N. Scoville *et al.*, *The Astrophysical Journal Supplement Series* **172**, 1–8, ISSN: 0067-0049, (<https://ui.adsabs.harvard.edu/abs/2007ApJS..172....1S/abstract>) (Sept. 2007).
576. N. A. Grogin *et al.*, *Astrophysical Journal, Supplement Series* **197**, 35, ISSN: 00670049, (<https://ui.adsabs.harvard.edu/abs/2011ApJS..197..35G/abstract>) (Dec. 2011).
577. A. M. Koekemoer *et al.*, *Astrophysical Journal, Supplement Series* **197**, 36, ISSN: 00670049, (<https://ui.adsabs.harvard.edu/abs/2011ApJS..197...36K/abstract>) (Dec. 2011).
578. H. Nayyeri *et al.*, *The Astrophysical Journal Supplement Series* **228**, 7, ISSN: 0067-0049, (<https://iopscience.iop.org/article/10.3847/1538-4365/228/1/7%20https://iopscience.iop.org/article/10.3847/1538-4365/228/1/7/meta>) (Jan. 2017).

579. S. Y. Sazonov, J. P. Ostriker, R. A. Sunyaev, *Monthly Notices of the Royal Astronomical Society* **347**, 144–156, ISSN: 00358711, (<https://ui.adsabs.harvard.edu/abs/2004MNRAS.347..144S/abstract>) (Jan. 2004).
580. J. T. Hinkle *et al.*, *arXiv*, arXiv:2405.08855, (<https://ui.adsabs.harvard.edu/abs/2024arXiv240508855H/abstract>) (May 2024).
581. M. S. Tashiro *et al.*, <https://doi.org/10.1117/12.2565812> **11444**, 293–303, ISSN: 1996756X, (<https://www.spiedigitallibrary.org/conference-proceedings-of-spie/11444/1144422/Status-of-x-ray-imaging-and-spectroscopy-mission-XRISM/10.1117/12.2565812.full%20https://www.spiedigitallibrary.org/conference-proceedings-of-spie/11444/1144422/Status-of-x-ray-imaging-and-spectroscopy-mission-XRISM/10.1117/12.2565812.short>) (Dec. 2020).
582. X. Collaboration *et al.*, *The Astrophysical Journal Letters* **973**, L25, ISSN: 2041-8205, (<https://iopscience.iop.org/article/10.3847/2041-8213/ad7397%20https://iopscience.iop.org/article/10.3847/2041-8213/ad7397/meta>) (Sept. 2024).
583. A. Lupi, A. Trinca, M. Volonteri, M. Dotti, C. Mazzucchelli, *Astronomy & Astrophysics* **689**, A128, ISSN: 0004-6361, ([https://www.aanda.org/articles/aa/full\\_html/2024/09/aa51249-24/aa51249-24.html%20https://www.aanda.org/articles/aa/abs/2024/09/aa51249-24/aa51249-24.html](https://www.aanda.org/articles/aa/full_html/2024/09/aa51249-24/aa51249-24.html%20https://www.aanda.org/articles/aa/abs/2024/09/aa51249-24/aa51249-24.html)) (Sept. 2024).
584. Ž. Ivezić *et al.*, (<http://arxiv.org/abs/0805.2366%20http://dx.doi.org/10.3847/1538-4357/ab042c>) (May 2008).
585. S. R. Kulkarni *et al.*, *arXiv*, arXiv:2111.15608, (<https://ui.adsabs.harvard.edu/abs/2021arXiv211115608K/abstract>) (Nov. 2021).
586. D. J. Reardon *et al.*, *ApJL* **951**, L6, arXiv: 2306.16215 (astro-ph.HE) (July 2023).
587. H. Xu *et al.*, *Research in Astronomy and Astrophysics* **23**, 075024, arXiv: 2306.16216 (astro-ph.HE) (July 2023).
588. EPTA Collaboration *et al.*, *A&A* **678**, A50, arXiv: 2306.16214 (astro-ph.HE) (Oct. 2023).
589. P. Amaro-Seoane *et al.*, *arXiv*, arXiv:1702.00786, (<https://ui.adsabs.harvard.edu/abs/2017arXiv170200786A/abstract>) (Feb. 2017).
590. Đ. V. Savić *et al.*, *The Astrophysical Journal* **953**, 138, ISSN: 0004-637X, (<https://ui.adsabs.harvard.edu/abs/2023ApJ...953..138S/abstract>) (Aug. 2023).

591. I. Linial, B. D. Metzger, *The Astrophysical Journal* **957**, 34, ISSN: 0004-637X, (<https://iopscience.iop.org/article/10.3847/1538-4357/acf65b%20https://iopscience.iop.org/article/10.3847/1538-4357/acf65b/meta>) (Oct. 2023).
592. M. Nicholl *et al.*, *Nature* 2024 634:8035 **634**, 804–808, ISSN: 1476-4687, (<https://www.nature.com/articles/s41586-024-08023-6>) (Oct. 2024).
593. J. Chakraborty *et al.*, *ApJL* **983**, L39, ISSN: 0004-637X, (<https://ui.adsabs.harvard.edu/abs/2025ApJ...983L..39C/abstract>) (Apr. 2025).
594. E. Quintin *et al.*, *Astronomy & Astrophysics* **675**, A152, ISSN: 0004-6361, ([https://www.aanda.org/articles/aa/full\\_html/2023/07/aa46440-23/aa46440-23.html%20https://www.aanda.org/articles/aa/abs/2023/07/aa46440-23/aa46440-23.html](https://www.aanda.org/articles/aa/full_html/2023/07/aa46440-23/aa46440-23.html%20https://www.aanda.org/articles/aa/abs/2023/07/aa46440-23/aa46440-23.html)) (July 2023).